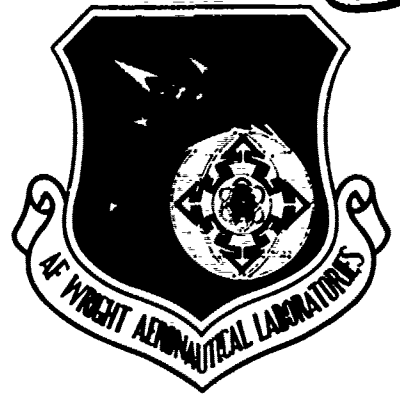


12

AFWAL-TR-84-3089
Volume I



AD-A178 313

**AEROSPACE STRUCTURES TECHNOLOGY
DAMPING DESIGN GUIDE
VOLUME I — TECHNOLOGY REVIEW**

J. SOOVERE
LOCKHEED CALIFORNIA COMPANY
P.O. BOX 551
BURBANK, CALIFORNIA 91520

M.L. DRAKE
UNIVERSITY OF DAYTON RESEARCH INSTITUTE
300 COLLEGE PARK AVENUE
DAYTON, OHIO 45469

DECEMBER 1985

Final Report for Period September 1981 — July 1984

Approved for Public Release; Distribution is Unlimited

DTC FILE COPY



FLIGHT DYNAMICS LABORATORY
AIR FORCE WRIGHT AERONAUTICAL LABORATORIES
AIR FORCE SYSTEMS COMMAND
WRIGHT-PATTERSON AIR FORCE BASE, OHIO 45433

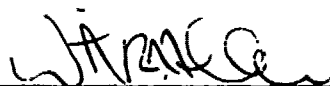
87 3 30 015

NOTICE .

When Government drawings, specifications, or other data are used for any purpose other than in connection with a definitely related Government procurement operation, the United States Government thereby incurs no responsibility nor any obligation whatsoever; and the fact that the government may have formulated, furnished, or in any way supplied the said drawings, specifications, or other data, is not to be regarded by implication or otherwise as in any manner licensing the holder or any other person or corporation, or conveying any rights or permission to manufacture, use, or sell any patented invention that may in any way be related thereto.

This report has been reviewed by the Office of Public Affairs (ASD/PA) and is releasable to the National Technical Information Service (NTIS). At NTIS, it will be available to the general public, including foreign nations.

This technical report has been reviewed and is approved for publication.



Vincent R. Miller
Project Engineer



John T. Ach, Actg Chief
Structural Vibrations Branch
Structures & Dynamics Division

FOR THE COMMANDER



ROBERT M. BADER
Acting Chief
Structures & Dynamics Division

"If your address has changed, if you wish to be removed from our mailing list, or if the addressee is no longer employed by your organization please notify AFWAL/FIBGD, W-PAFB, OH 45433 to help us maintain a current mailing list".

Copies of this report should not be returned unless return is required by security considerations, contractual obligations, or notice on a specific document.

AFWAL-TR-84-3089
Volume I



AEROSPACE STRUCTURES TECHNOLOGY DAMPING DESIGN GUIDE VOLUME I — TECHNOLOGY REVIEW

J. SOOVERE
LOCKHEED CALIFORNIA COMPANY
P.O. BOX 551
BURBANK, CALIFORNIA 91520

M.L. DRAKE
UNIVERSITY OF DAYTON RESEARCH INSTITUTE
300 COLLEGE PARK AVENUE
DAYTON, OHIO 45469

DECEMBER 1985

Final Report for Period September 1981 — July 1984

Approved for Public Release; Distribution is Unlimited

Accession For	
NTIS GRA&I	<input checked="" type="checkbox"/>
DTIC TAB	<input checked="" type="checkbox"/>
Unannounced	<input type="checkbox"/>
Justification	
By _____	
Distribution/	
Availability Codes	
Dist	Avail and/or Special
A-1	



FLIGHT DYNAMICS LABORATORY
AIR FORCE WRIGHT AERONAUTICAL LABORATORIES
AIR FORCE SYSTEMS COMMAND
WRIGHT-PATTERSON AIR FORCE BASE, OHIO 45433

NOTICE

When Government drawings, specifications, or other data are used for any purpose other than in connection with a definitely related Government procurement operation, the United States Government thereby incurs no responsibility nor any obligation whatsoever; and the fact that the government may have formulated, furnished, or in any way supplied the said drawings, specifications, or other data, is not to be regarded by implication or otherwise as in any manner licensing the holder or any other person or corporation, or conveying any rights or permission to manufacture, use, or sell any patented invention that may in any way be related thereto.

This report has been reviewed by the Office of Public Affairs (ASD/PA) and is releasable to the National Technical Information Service (NTIS). At NTIS, it will be available to the general public, including foreign nations.

This technical report has been reviewed and is approved for publication.



Vincent R. Miller
Project Engineer



John T. Ach, Actg Chief
Structural Vibrations Branch
Structures & Dynamics Division

FOR THE COMMANDER



ROBERT M. BADER
Acting Chief
Structures & Dynamics Division

"If your address has changed, if you wish to be removed from our mailing list, or if the addressee is no longer employed by your organization please notify AFWAL/FIBGD, W-PAFB, OH 45433 to help us maintain a current mailing list".

Copies of this report should not be returned unless return is required by security considerations, contractual obligations, or notice on a specific document.

AD-A178 213

REPORT DOCUMENTATION PAGE

1a. REPORT SECURITY CLASSIFICATION UNCLASSIFIED			1b. RESTRICTIVE MARKINGS			
2a. SECURITY CLASSIFICATION AUTHORITY			3. DISTRIBUTION/AVAILABILITY OF REPORT Approved for Public Release: Distribution is unlimited			
2b. DECLASSIFICATION/DOWNGRADING SCHEDULE						
4. PERFORMING ORGANIZATION REPORT NUMBER(S)			5. MONITORING ORGANIZATION REPORT NUMBER(S) AFWAL-TR-84-3089, Vol. I			
6a. NAME OF PERFORMING ORGANIZATION Lockheed-California Company		6b. OFFICE SYMBOL (If applicable)	7a. NAME OF MONITORING ORGANIZATION Air Force Wright Aeronautical Laboratories Flight Dynamics Laboratory (AFWAL/FIBGD)			
6c. ADDRESS (City, State and ZIP Code) P. O. Box 551 Burbank, California 91520			7b. ADDRESS (City, State and ZIP Code) Wright-Patterson AFB, Ohio 45433			
8a. NAME OF FUNDING/SPONSORING ORGANIZATION Flight Dynamics Laboratory		8b. OFFICE SYMBOL (If applicable) AFWAL/FIBGD	9. PROCUREMENT INSTRUMENT IDENTIFICATION NUMBER F33615-81-C-3213			
8c. ADDRESS (City, State and ZIP Code) Wright-Patterson AFB, Ohio 45433			10. SOURCE OF FUNDING NOS.			
			PROGRAM ELEMENT NO. 62201F	PROJECT NO. 2401	TASK NO. 01	WORK UNIT NO. 50
11. TITLE (Include Security Classification) (see reverse)						
12. PERSONAL AUTHOR(S) Soovere, J., Drake, M.L.						
13a. TYPE OF REPORT Final		13b. TIME COVERED FROM Sept. '81 to Jul. '84		14. DATE OF REPORT (Yr., Mo., Day) December 1985		15. PAGE COUNT 513
16. SUPPLEMENTARY NOTATION						
17. COSATI CODES			18. SUBJECT TERMS (Continue on reverse if necessary and identify by block number)			
FIELD	GROUP	SUB. GR.	Fundamental of damping, viscoelastic damping theory, free layers, constrained (see reverse) →			
01	03					
22	02					
19. ABSTRACT (Continue on reverse if necessary and identify by block number) This volume contains a summary of the current technology used in the application of viscoelastic damping to primarily aerospace structures. The topics covered include the fundamentals of damping, the level of the damping present in metals, composites and aerospace structures made from these materials, and methods for measuring this damping; the fundamentals of viscoelastic damping materials, the test methods used to obtain the damping material data and the method of presenting these data; the basic viscoelastic damping theory for the free and constrained layer damping designs and for tuned dampers, and the finite element analysis used in the design of more complex viscoelastic damping applications. A brief review of the classical methods for predicting the vibration response of aircraft type structures is also included together with a discussion of the effect of damping on the noise transmission loss of these types of aircraft structures. <i>Keywords</i>						
20. DISTRIBUTION/AVAILABILITY OF ABSTRACT UNCLASSIFIED/UNLIMITED <input checked="" type="checkbox"/> SAME AS RPT. <input type="checkbox"/> DTIC USERS <input type="checkbox"/>			21. ABSTRACT SECURITY CLASSIFICATION UNCLASSIFIED			
22a. NAME OF RESPONSIBLE INDIVIDUAL Vince Miller			22b. TELEPHONE NUMBER (Include Area Code) 513-255-5066		22c. OFFICE SYMBOL AFWAL/FIBGD	

Block 11: Title:

Aerospace Structures Technology Damping Design Guide Volume I - Technology Review

Block 18: Subject Terms:

ed. ~~layers, tuned dampers,~~ finite element analysis, fundamentals of damping materials, test methods, structural vibration theories, measurement of resonant frequency, measurement of damping, damping in metals, damping in composites, damping in structures, effect on noise transmission.

FOREWORD

This report was prepared jointly by the Lockheed-California Company, Burbank, California and the University of Dayton Research Institute, Dayton, Ohio for the Structural Integrity Branch, Flight Dynamics Laboratory, Air Force Wright Aeronautical Laboratory, Wright-Patterson Air Force Base, Ohio under contract F33615-81-C-3213, "Aerospace Structures Technology Damping Design Guide." Mr. V. R. Miller of the Structural Integrity Branch was the Project Engineer. Dr. J. Soovere of the Lockheed-California Company was the overall Program Manager and Mr. M. L. Drake was the Program Manager for the University of Dayton. The authors wish to acknowledge the contribution to this report provided by Mr. M. Bouchard, Dr. M. Soni, Mr. M. F. Kluesener, Mr. R. Nash, Mr. R. Dominic, Mr. P. Graf, and Mr. D. M. Hopkins from the University of Dayton, and by Mr. M. A. Gamon from Lockheed-California Company.

This report consists of three volumes. Volume I provides a summary of the current technology in the application of viscoelastic damping, Volume II is the design guide for viscoelastic damping applications, and Volume III contains the damping material data for use with Volume II.

The damping material data in Volume III are presented in a simplified format, suitable for use by designers. All of the damping material data are believed to be accurate, but no guarantee of accuracy or completeness is made. No responsibility is assumed for changes in these data due to batch-to-batch variation in the commercially manufactured damping materials. The damping material data should be verified independently under the proposed operating conditions, for each damping material, prior to its use.

TABLE OF CONTENTS

<u>Section</u>	<u>Page</u>
FOREWORD	iii
LIST OF FIGURES	ix
LIST OF TABLES	xxi
1 INTRODUCTION	1-1
2 FUNDAMENTALS OF DAMPING AND DAMPING MATERIALS	2-1
2.1 NATURE OF DAMPING	2-1
2.1.1 Physical Mechanisms of Material Damping	2-1
2.1.2 Measure of Damping	2-3
2.2 CHARACTERIZATION OF LINEAR DAMPING BEHAVIOR: COMPLEX MODULI	2-7
2.2.1 Effects of Temperature and Frequency and Strain	2-12
2.2.2 The Time-Temperature Superposition Principle	2-14
2.2.3 A Reduced-Temperature Nomogram	2-16
2.3 DAMPING MATERIAL CHARACTERIZATION TECHNIQUES	2-18
2.3.1 Resonant Beam Test	2-18
2.3.2 Dynamic Mechanical Analyzer	2-28
2.3.3 Resonant Test	2-37
2.3.4 The Rheovibron	2-43
2.3.5 The Progressive Wave Technique	2-46
2.3.6 Impedance Testing	2-48
2.3.7 3M Piezoelectric Oscillatory Rheometer	2-49
3 FUNDAMENTALS OF DAMPING TREATMENT	3-1
3.1 FREE LAYER DAMPING TREATMENTS	3-c
3.1.1 Euler-Bernoulli Beam Equations for Free Layer Damping	3-13
3.1.2 Partial Coverage of Beams	3-28
3.1.3 Vibration of Unstiffened Plates with a Free Layer Damping Treatment	3-31
3.1.4 Summary	3-34
3.2 CONSTRAINED-LAYER DAMPING TREATMENTS	3-34
3.2.1 Single Constrained Layer	3-34

TABLE OF CONTENTS (Continued)

<u>Section</u>	<u>Page</u>	
3.2.2	Single Constrained-Layer Damping Treatment Analysis	3-48
3.2.3	Flexural Rigidity of Single Constraining-Layer Configurations	3-52
3.2.4	Single Damping Material Multiple Layer Design	3-58
3.2.5	Analysis for Multiple Constrained-Layer Treatment	3-62
3.2.6	Complex Mathematical Approach to the Three-Layer Sandwich	3-71
3.3	TUNED VISCOELASTIC DAMPERS	3-72
3.3.1	Tuned Dampers (TD)	3-73
3.3.2	Energy Dissipation in a Simple Damper	3-76
3.3.3	Two Degree-of-Freedom	3-82
3.3.4	Tuned Viscoelastic Damper Attached to a Structure	3-87
3.3.5	Multi-Span Structures	3-94
4	CLASSICAL STRUCTURAL VIBRATION RESPONSE THEORIES	4-1
4.1	INTRODUCTION	4-1
4.2	CLASSIFICATION OF VIBRATION ANALYSIS METHODS	4-2
4.2.1	Differential Equation Methods	4-3
4.2.2	Integral Equation Methods	4-4
4.2.3	Energy Methods	4-4
4.3	SIMPLIFIED ANALYSIS METHODS	4-10
4.3.1	Forced Vibration Theory	4-10
4.3.2	Simplification of the Forced Vibration Theory	4-13
5	FINITE ELEMENT PROCEDURE IN DAMPING DESIGN	5-1
5.1	THE FINITE ELEMENT METHOD (FEM)	5-2
5.1.1	Formulation of Finite Element Equations	5-2
5.1.2	Evaluation of the Damping of the Structure	5-5
5.1.3	Solution Methods	5-9
5.1.4	Computer Programs	5-28
5.2	INTEGRATION OF FINITE ELEMENT MODELING INTO THE DESIGN PROCESS	5-31
5.2.1	Analytical Procedure in Damping Design	5-31

TABLE OF CONTENTS (Continued)

<u>Section</u>		<u>Page</u>
5.2.2	Example Damping Analysis	5-33
5.3	A NOTE ON FINITE ELEMENT DISCRETIZATION OF LAYERED DAMPING DESIGNS	5-39
5.3.1	Results Using High Aspect Ratios	5-39
5.3.2	Modeling Techniques to Reduce the DOF	5-44
5.4	SUMMARY AND CONCLUSIONS	5-49
6	MEASUREMENT OF RESONANT FREQUENCIES AND DAMPING	6-1
6.1	INTRODUCTION	6-1
6.2	BASIC METHODS	6-1
6.2.1	Time Domain Analysis	6-2
6.2.2	Frequency Domain Analysis	6-10
6.3	DEVELOPMENT OF THE BASIC METHODS	6-22
6.3.1	Structural Response to Random Excitation	6-25
6.3.2	Fourier and Laplace Analysis of Transient Response	6-41
6.3.3	Nonlinear Response and Electrodynamical Shakers	6-47
6.4	CORRECTION OF SMOOTHING ERRORS IN DAMPING OBTAINED FROM SPECTRAL ANALYSIS	6-51
6.4.1	Introduction	6-51
6.4.2	Basic Smoothing Theory	6-53
6.4.3	Methods for Correcting Smoothing Affected Damping	6-58
6.4.4	Effect of Smoothing on Curve Fitting	6-62
6.4.5	Evaluation of the Smoothing Theory	6-70
7	DAMPING IN STRUCTURAL MATERIALS AND STRUCTURES	7-1
7.1	INTRODUCTION	7-1
7.2	BASIC DAMPING MECHANISMS IN STRUCTURES	7-1
7.2.1	Acoustic Radiation	7-2
7.2.2	Friction Damping	7-10
7.2.3	Gas Pumping at the Fastener Lines	7-18
7.2.4	Material Damping	7-19

TABLE OF CONTENTS (Continued)

<u>Section</u>		<u>Page</u>
7.3	DAMPING LEVELS IN AEROSPACE STRUCTURES	7-87
7.3.1	Damping in Stiffened Aluminum and Composite Honeycomb Panels	7-89
7.3.2	Damping in Riveted and Bonded Multibay Metal Panels and Box Structures	7-97
7.3.3	Damping in Bonded and Integrally Stiffened Multi-bay Composite Panels and Fastener Attached Box Structure	7-107
7.3.4	Damping in Stiffened Panels under Inplane Axial, Tension, Compression and Shear Load	7-108
7.3.5	Damping in Stiffened Cylinders	7-109
7.3.6	Effect of Fluid Loading on Stiffened Panels	7-116
7.3.7	Measured Damping in Jet Engine Components	7-116
7.3.8	Printed Circuit Board Damping	7-116
8	EFFECT OF DAMPING ON INTERIOR NOISE IN AIRCRAFT	8-1
8.1	INTRODUCTION	8-1
8.2	INTERIOR NOISE IN AIRCRAFT	8-1
8.2.1	Sources of Interior Noise	8-1
8.2.2	Basic Noise Transmission Loss Theory	8-2
8.2.3	Behavior of Stiffened Aircraft Panels	8-12
8.2.4	Behavior of Shells	8-15
8.3	EFFECT OF ACOUSTIC TRIM AND DAMPING TREATMENT ON FUSELAGE DAMPING	8-25
8.3.1	Effect of Damping Treatment on Interior Noise	8-25
8.3.2	Effect of Acoustic Trim on the Fuselage Damping	8-26
8.3.3	Flight Test Procedures for Developing Viscoelastic Damping Treatments	8-30
8.4	SUMMARY OF CURRENT INTERIOR NOISE PREDICTION METHODOLOGY	8-36

LIST OF FIGURES

<u>Figure</u>		<u>Page</u>
1.1	Life extension obtained with additive damping on existing hardware	1-1
1.2	Application of damping technology	1-2
1.3	Purpose for use of damping technology	1-3
1.4	Classification of individuals active in the application of damping technology	1-4
2.1	Typical experimentally determined material hysteresis loop	2-9
2.2	Hypothetical hysteresis loop	2-9
2.3	Young's modulus and loss factor versus temperature at a constant frequency	2-13
2.4	Young's modulus and loss factor versus frequency at a constant temperature	2-13
2.5	Illustration of reduced variable time-temperature superposition	2-15
2.6	Illustration of the reduced-temperature nomogram	2-16
2.7	Block diagram of the beam test fixture	2-19
2.8	Resonant beam test specimens	2-19
2.9	One half of a sandwich beam specimen with recommended specimen dimensions	2-25
2.10	Typical graphs of η_n , f_n , and f_{on} versus temperature	2-27
2.11	4th and 6th order variation in material loss factor	2-29
2.12	4th and 6th order variation in material modulus	2-30
2.13	Comparison of 4th and 6th order modulus in mode five	2-31
2.14	Comparison of 4th and 6th order loss factor in mode five	2-32
2.15	Data comparison of 4th and 6th order in reduced temperature nomogram	2-33
2.16	Test geometry for DuPont 981 dynamic mechanical analyzer (DMA)	2-34
2.17	98C DMA electronics block diagram	2-35
2.18	Specimen dimensions and suggested $\frac{L}{t}$ values for the test regions	2-36

LIST OF FIGURES (Continued)

<u>Figure</u>		<u>Page</u>
2.19	Sample deformation in DuPont 981 DMA apparatus	2-37
2.20	Resonance test system	2-39
2.21	Resonance test specimen	2-39
2.22	A simplified diagram of the equipment and concepts for Rheovibron	2-44
2.23	Progressive wave apparatus	2-47
2.24	Wave equation governing the motion of material sample	2-49
2.25	Shear generator diagram	2-51
2.26	Hardware system configuration including shear generator	2-53
3.1	Free layer damping treatments	3-6
3.2	Optimum temperature range for free layer treatment	3-7
3.3	Typical variation of material properties for a polymer blend of materials	3-8
3.4	Fixed thickness ratio (h_D/h_2) = 2 for single materials and a polymer blend	3-9
3.5	Multiple layer broadening effect	3-10
3.6	Typical variation of material properties for Corning 9871 (Enamel) at 200 Hz	3-11
3.7	Enamel elastomer loss modulus comparison	3-12
3.8	Element of a deformed beam	3-14
3.9	Beam coated with viscoelastic material	3-21
3.10	Infinitesimal element of deformed coating	3-21
3.11	Material loss factor ratio as a function of the modulus ratio and the thickness ratio	3-26
3.12	Beam partially covered with viscoelastic material	3-28
3.13	Viscoelastic layer on a plate	3-32
3.14	Single constrained layer illustrating shear deformations of the damping layer	3-35
3.15	Optimum temperature range for constrained layer treatments	3-36
3.16	Wave length dependency on shear deformation	3-39

LIST OF FIGURES (Continued)

<u>Figure</u>		<u>Page</u>
3.17	Maximum energy dissipation when shear stresses approach the fatigue strength of the viscoelastic material	3-40
3.18	Symmetric sandwich panel	3-41
3.19	Spacer used with damping layer	3-42
3.20	Viscoelastic corrugated configuration	3-43
3.21	Multilayer anchored treatment	3-44
3.22	Multilayer spaced treatment	3-44
3.23	Deformations in multiple layers of damping tape	3-45
3.24	Beam damping with multiple layers of tape	3-46
3.25	Damping in multiple material constrained layer system	3-47
3.26	Single constrained layer damping treatment	3-48
3.27	Tension in a beam on an elastic foundation	3-50
3.28	Single constraining layer element	3-53
3.29	Elements of a three-layer system	3-59
3.30	Elements of N constrained layer system on a structure	3-63
3.31	Bent element of multilayer beam	3-65
3.32	Response of a single degree of freedom system with a dynamic absorber	3-74
3.33	Effects of a tuned damper on different types of structures	3-75
3.34	Idealized tuned damper	3-77
3.35	Effect of loss factor on energy dissipation	3-82
3.36	E_D and η_D versus temperature for typical elastomer	3-83
3.37	Effect of damper tuning	3-83
3.38	Two degree-of-freedom system	3-84
3.39	Response of a single degree of freedom system with a dynamic absorber	3-87
3.40	Variation of $ w_1/w_0 $ versus β for different α 's	3-88
3.41	Tuned damper mounted on structure	3-89
3.42	Reduction in force from the addition of damping	3-90
3.43	Number of tuned dampers on a beam	3-90

LIST OF FIGURES (Continued)

<u>Figure</u>		<u>Page</u>
3.44	Nondimensional response versus frequency parameter	3-94
3.45	Effects of a tuned damper on different types of structures	3-95
3.46	Effect of elastomeric tuned dampers on the response of a curved skin-stringer structure	3-96
5.1	Common element configuration in FEM modeling	5-3
5.2	Synopsis of dynamic response analysis methods	5-11
5.3	Determination of viscoelastic modulus for modal response analysis	5-12
5.4	Finite element analysis in damping design procedure	5-32
5.5	Engine exhaust duct	5-35
5.6	Finite element model	5-36
5.7	Mode shapes of engine exhaust duct (perspective view)	5-37
5.8	Mode shapes of engine exhaust duct (end-on view)	5-37
5.9	Effect of damping treatment on the amplitude and frequency response of the second mode of engine exhaust duct	5-38
5.10	Detailed model with damping layer and constraining layer	5-38
5.11	Cantilever plate finite element model	5-40
5.12	Cross-section of Plate 1 damping system	5-40
5.13	Analytical and experimental results for Plate 1, second bending mode	5-42
5.14	Cross-section of Plate 2 damping system	5-42
5.15	Experimental and analytical results for Plate 2, 2nd bending mode	5-43
5.16	Experimental and analytical results for Plate 2, 1st torsional mode	5-44
5.17	Plate 1 modeling scheme using membrane elements	5-46
5.18	FEA results comparing all solid model to membrane model	5-46
5.19	Equivalent solid beam test specimen	5-47
5.20	Plate 2 modeling scheme using the equivalent solid approach	5-48

LIST OF FIGURES (Continued)

<u>Figure</u>		<u>Page</u>
5.21	Analytical results comparing the all solid model to the equivalent solid model for the second bending mode	j-48
5.22	Analytical results comparing the all solid model to the equivalent solid model for Plate 2 first torsion mode	5-49
6.1	Free vibration response of damped single degree-of-freedom system	6-4
6.2	Effect of bandpass filter on the impulse response function	6-9
6.3	Typical aircraft stick pulse excited free decay with beating	6-10
6.4	Typical magnification factors for single degree-of-freedom system with viscous damping, including the half power points	6-13
6.5	Modulus of a stiffened Kevlar honeycomb panel vibration response to discrete frequency acoustic excitation	6-15
6.6	Modulus of a typical aircraft vibration response corresponding to the free decay in Figure 6.3	6-15
6.7	Vibration response of a stiffened Kevlar honeycomb panel to discrete frequency acoustic excitation	6-20
6.8	Frequency domain representation of the stick pulse excited decay in Figure 6.3	6-23
6.9	Curve fit to the vibration response of a stiffened Kevlar honeycomb panel due to rapid sine sweep acoustic excitation	6-24
6.10	Real part of a transfer function with poles at $s = -1 \pm i5$	6-37
6.11	Randomdec signature analysis procedures	6-39
6.12	Typical rapid sine weep waveform and spectrum	6-42
6.13	Typical measured mode shapes of an integrally stiffened graphite/epoxy panel	6-45
6.14	Force spectra produced with various hammer tip materials	6-46
6.15	Hammer force spectra from tapping at panel center and over stiffener flange	6-46
6.16	Coherence functions between force and both panel center displacement and acceleration - tapping over stiffener flange	6-48

LIST OF FIGURES (Continued)

<u>Figure</u>		<u>Page</u>
6.17	Measured viscous damping ratio for integrally stiffened graphite/epoxy panels	6-49
6.18	Typical linear and nonlinear strain power spectral densities for an integrally stiffened graphite/epoxy panel subjected to random acoustic loading	6-50
6.19	Rectangular, Hanning and Bartlett smoothing or weighting functions and the corresponding spectral windows	6-52
6.20	Smoothing error in the normalized power and cross spectral peaks at resonance	6-58
6.21	Effect of Hanning smoothing on the cross spectrum of a single degree-of-freedom system	6-59
6.22	Effect of Hanning smoothing on normalized power spectral density	6-60
6.22	Damping correction curves for unsmoothed cross spectral density	6-63
6.23	Damping correction curves for Hanning smoothing affected cross spectral density	6-64
6.24	Damping correction curves for Bartlett smoothing affected cross spectral density	6-65
6.25	Damping correction curves for unsmoothed power spectral density	6-65
6.26	Damping correction curves for Hanning smoothing affected power spectral density	6-66
6.27	Damping correction curves for Bartlett smoothing affected power spectral density	6-67
6.28	Typical effect of smoothing on curvature, change in arc length and measured damping ratio for normalized cross spectrum of a single degree-of-freedom system	6-68
6.29	Response of composite aileron panel to hammer tap excitation	6-71
6.30	Measured aircraft wing response to stick pulse	6-72
6.31	Unsmoothed Fourier spectra of aircraft wing free decay	6-72
6.32	Bartlett smoothed Fourier spectra of aircraft wing free decay	6-73
6.33	Restored Fourier spectra of aircraft wing response to stick pulse	6-73

LIST OF FIGURES (Continued)

<u>Figure</u>		<u>Page</u>
7.1	Composite honeycomb panel damping measured in a large baffle test facility	7-3
7.2	Comparison of theoretically predicted and measured viscous damping ratios for fundamental mode of stiffened composite honeycomb panels	7-4
7.3	Comparison of theoretically predicted and measured viscous damping ratios for fundamental mode of stiffened aluminum honeycomb panels	7-5
7.4	Comparison of theoretically predicted and measured viscous damping ratios of blade stiffened mini-sandwich graphite/epoxy panel	7-6
7.5	Variation of the fundamental mode viscous damping ratio of stiffened aluminum panels with axial inplane load	7-8
7.6	Comparison of graphite/epoxy free-free beam damping measured in air and in vacuum	7-9
7.7	Low-amplitude acoustic radiation damping in the fundamental mode of thin cantilever beams as a function of length-thickness ratio	7-11
7.8	Variation of equivalent friction coefficient during sinusoidal motion with normal load, frequency and maximum relative velocity	7-12
7.9	Variation of the Galileo spacecraft high gain antenna frequencies with amplitude	7-13
7.10	Comparison of typical damping levels measured on the ground and in orbit	7-14
7.11	Typical damping levels measured during Galileo spacecraft modal tests	7-15
7.12	Damping schedule for Titan launch vehicle	7-15
7.13	Equivalent viscous damping ratios (damping factors) measured during space shuttle ascent vehicle Stage 1 vibration tests	7-16
7.14	Comparison of predicted and measured material damping in aluminum	7-23
7.15	Variation of the viscous damping ratio with stress amplitude for materials listed in Table 7.2	7-28

LIST OF FIGURES (Continued)

<u>Figure</u>		<u>Page</u>
7.16	Variation of the viscous damping ratio with stress amplitude for materials listed in Table 7.3	7-30
7.17	Viscous damping ratio for various alloys at a stress level equal to one tenth of the yield stress as a function of the elastic modulus.	7-33
7.18	Variation of viscous damping ratio with fiber volume in early beam tests	7-34
7.19	Comparison of viscous damping ratios, as a function of fiber volume, measured in early beam flexure tests	7-35
7.20	Theoretical correction factor for the Young's modulus obtained from measured flexural beam resonant frequencies as a function of mode number	7-36
7.21	Comparison of predicted and measured Young's modulus and viscous damping ratio as a function of the outer ply fiber orientation	7-37
7.22	Effect of fiber aspect ratio on the loss and storage moduli of discontinuous aligned composites	7-39
7.23	Variation of damping with uniaxial fiber orientation relative to beam axis for Scotchply 1002 measured by double cantilever beam tests in air	7-44
7.24	Variation of storage modulus and damping with frequency for chopped E-glass/polyester composites	7-45
7.25	Measured Young's modulus and damping for graphite/epoxy composite at ambient temperature	7-55
7.26	Comparison between the damping behavior of epoxy and that of graphite/epoxy composite, as a function of temperature	7-56
7.27	Young's modulus and damping of discontinuous aligned and random fiber graphite/epoxy composites	7-58
7.28	Graphite/epoxy composite Young's modulus and viscous damping ratio as a function of frequency for difference fiber lengths	7-60
7.29	Measured damping and Young's modulus for boron/epoxy composite	7-62
7.30	Measured damping in free-free Kevlar honeycomb panels and beams	7-64

LIST OF FIGURES (Continued)

<u>Figure</u>		<u>Page</u>
7.31	Kevlar/epoxy Young's modulus and viscous damping ratio as a function of frequency and fiber length	7-65
7.32	Variation of damping with frequency of graphite reinforced aluminum and magnesium matrix composites	7-70
7.33	Variation of damping with frequency of aluminum oxide fiber reinforced lithium-aluminum and magnesium matrix composites	7-71
7.34	Variation of damping with frequency of silicon carbide reinforced aluminum matrix composites	7-72
7.35	Damping of metal matrix specimens versus frequency superimposed on the σ - ϵ curve for AZ916 magnesium	7-73
7.36	Typical method for measuring material damping in air with a free-free resonant beam	7-75
7.37	A method for measuring material damping under near vacuum conditions with a free-free resonant beam	7-77
7.38	Schematic of coil and magnet drive used with large test specimens	7-77
7.39	Test sequence of the tunable excitation launch mechanism, showing the launcher, specimen and signal wire carrier	7-78
7.40	Typical double cantilever test specimens used in measuring material damping	7-80
7.41	Experimental arrangement for resonant dwell tests	7-81
7.42	Forced vibration test setup used for frequency sweep tests	7-81
7.43	Driving arrangement for shear tests	7-82
7.44	Combined loading apparatus	7-84
7.45	Combined loading apparatus	7-85
7.46	Principle of blade test rig	7-85
7.47	Computer aided data acquisition system	7-86
7.48	Measured viscous damping ratios for flat skin-stringer panels	7-88
7.49	Damping ratio versus frequency for typical structure	7-90
7.50	Measured stiffened aluminum and composite honeycomb panel damping	7-91

LIST OF FIGURES (Continued)

<u>Figure</u>		<u>Page</u>
7.51	Measured fundamental and higher mode damping in selected composite honeycomb panels	7-93
7.52	Actual measured variation of fundamental mode damping with frequency for stiffened honeycomb panels	7-94
7.53	Correlation achieved in predicting the higher order panel damping on the basis of the fundamental mode damping	7-96
7.54	Variation of the measured damping in the fundamental mode of riveted and bonded multi-bay skin-stringer aluminum panels with frequency	7-98
7.55	Measured damping in aluminum multi-bay panels and box specimens	7-99
7.56	Measured damping in aluminum and titanium multi-bay panels	7-100
7.57	Curved skin and stringer panels	7-101
7.58	Built-up structures with integrally machined skins	7-101
7.59	Damping in hat stiffened, corrugated and built-up integrally stiffened panels	7-102
7.60	Comparison of measured and predicted damping in the fundamental mode of riveted and bonded multi-bay skin-stringer aluminum panels	7-105
7.61	Comparison of measured and predicted damping of riveted multi-bay aluminum panels with predictions for higher mode damping.	7-106
7.62	Fundamental mode shape of integrally blade stiffened graphite/epoxy minisandwich panel	7-108
7.63	Measured damping in multibay integrally J-stiffened graphite/epoxy panels and graphite/epoxy box structure assembled with fasteners.	7-109
7.64	Fundamental mode of integrally J-stiffened graphite/epoxy panel	7-110
7.65	Variation of the J-stiffened minisandwich panel resonant frequencies with jack load	7-112
7.66	Variation of damping with jack load for J-stiffened minisandwich panel	7-113

LIST OF FIGURES (Continued)

<u>Figure</u>		<u>Page</u>
7.67	Variation of J-stiffened monolithic panel damping with jack load	7-114
7.68	Damping measured on bare stiffened shells and a trimmed stiffened shell as a function of frequency	7-115
7.69	Damping measured on a welded stiffened steel structure in air and immersed in water	7-117
8.1	Plane acoustic wave incident on a panel	8-3
8.2	Schematic of acoustic transmission loss curve for a finite panel	8-5
8.3	Panel transmission loss both with and without acoustic treatment	8-8
8.4	Transmission loss characteristics of graphite/epoxy mini-sandwich panel with a 1mm thick syntactic core	8-9
8.5	Typical radiation ratio for a baffled panel as a function of frequency normalized to the critical frequency	8-10
8.6	Field incidence transmission loss of a stiffened flat panel	8-11
8.7	Mode shapes of a stiffened panel array	8-13
8.8	Acoustic plane wave excitation of infinite cylinder	8-16
8.9	Transmission loss for stringer-stiffened infinite length shell	8-16
8.10	Natural frequencies of a finite, frame-stiffened cylinder	8-18
8.11	Stiffened cylinder mounted in acoustic test facility	8-18
8.12	Typical strain response of a panel in a stiffened shell due to broad band random acoustic loading at grazing incidence	8-19
8.13	Typical measured stiffened shell overall mode shapes in the circumferential direction	8-20
8.14	Typical in-flight fuselage acceleration response and radiated noise	8-21
8.15	Radiation ratio of a cylindrical shell	8-23
8.16	Variation of frequency index β with frequency	8-24
8.17	Power spectral density of interior noise (Mach 0.85)	8-25

LIST OF FIGURES (Continued)

<u>Figure</u>		<u>Page</u>
8.18	Small diameter stiffened cylinder	8-27
8.19	Summary of loss factors measured on bare shells and a trimmed shell	8-28
8.20	Bare Metroliner Fuselage Shell	8-29
8.21	Vibration data measured during flight on the 747 upper deck panels both with and without acoustic trim	8-31
8.22	Honeycomb panel damping increased by acoustic impedance effect in acoustic progressive wave tunnel	8-32
8.23	Effect of damping tape on bare panel vibration in comparison to that from acoustic trim	8-33
8.24	Effect of damping tape on 747 upper deck sound levels	8-34
8.25	Noise reduction achieved with I-beam damping	8-35

LIST OF TABLES

<u>Table</u>		<u>Page</u>
2.1	List of Symbols for Section 2.1	2-8
2.2	List of Symbols for Section 2.2	2-11
2.3	List of Symbols for Subsection 2.3.1	2-21
2.4	Abbreviations and List of Symbols for Subsection 2.3.2	2-38
2.5	List of Symbols for Subsection 2.3.3	2-41
2.6	List of Symbols for Subsection 2.3.4	2-45
2.7	Auxiliary Equipment Requirements	2-52
3.1	List of Symbols Up to and Including Section 3.1	3-2
3.2	Roots of Cantilever Beam	3-19
3.3	List of Symbols for Section 3.2	3-37
3.4	List of Symbols for Section 3.3	3-78
5.1	Linear Dynamic Response Analysis Capabilities	5-29
5.2	List of Symbols for Section 5.	5-51
6.1	Calculation of the Viscous Damping Ratio Using the K-P Method	6-21
6.2	Error in Measuring PSD for 90% Confidence Limits as a Function of the Statistical Degrees-of-Freedom	6-27
6.3	Blackman and Tuckey Analysis Parameters for Determining Power Spectral Density (PSD)	6-28
6.4	FFT Analysis Parameters for Determining Power Spectral Density (PSD)	6-32
5.5	Comparison of Viscous Damping Ratio Determined by Various Methods	6-75
7.1	Typical Viscous Damping Ratios for Structural Materials at Small Amplitudes and Room Temperature in the Audio Frequency Range	7-25
7.2	Identification and Damping Mechanisms for Materials in Figure 7.15	7-26
7.3	Identification for Materials in Figure 7.16 Having Magnetomechanical Damping Mechanism	7-29
7.4	Classification of High Damping Metals	7-31
7.5	Summary of Alloys Tested with Type of Damping Mechanism	7-32

LIST OF TABLES (Continued)

<u>Table</u>		<u>Page</u>
7.6	Summary of Measured Fiberglass Composite Material Damping	7-40
7.7	Summary of Measured Graphite-Epoxy and Polyester Composite Material Damping	7-47
7.8	Effect of Resin Damping on the Damping of Chopped Aligned Graphite Fiber Composite	7-57
7.9	Damping in Discontinuous Aligned and Random Fiber Graphite/Epoxy Composites	7-57
7.10	Summary of Measured Boron/Epoxy Composite Material Damping	7-61
7.11	Summary of Measured Kevlar/Epoxy Material Damping	7-63
7.12	Summary of Measured Metal Matrix Composite Material Damping	7-57
7.13	Values of Friction and Material Damping Assumed in Honeycomb Panel Analysis	7-95
7.14	Measured Damping in Bonded Graphite/Epoxy Panels	7-110
7.15	Measured Damping in Integrally Hat Stiffened Graphite/Epoxy Flat and Curved Panels	7-111
7.16	Measured Damping Values for Engine Components	7-118
7.17	Typical Range of Measured Printed Circuit Board Damping Values	7-119
8.1	Effect of Curvature and Pressure	8-22

SECTION 1

INTRODUCTION

Aerospace structures and equipment mounted in these structures are required to operate under a wide range of dynamic loads. When structural resonances are excited, the dynamic loads can produce excessive vibration levels in the structures and equipment. High interior noise levels can be produced by excessive vibration of the surrounding structure. The resonant vibration levels can be significantly reduced by increasing the damping in the dominant modes through the application of viscoelastic damping technology.

The above vibration problems are often encountered following some initial in-service exposure. The high cost of subsequent structural changes has made the application of viscoelastic damping technology both attractive and cost-effective in solving these problems. In many instances the reduction in resonant vibration response has been quite dramatic (Figure 1.1), exceeding that possible with stiffening for the same weight increment. Viscoelastic damping

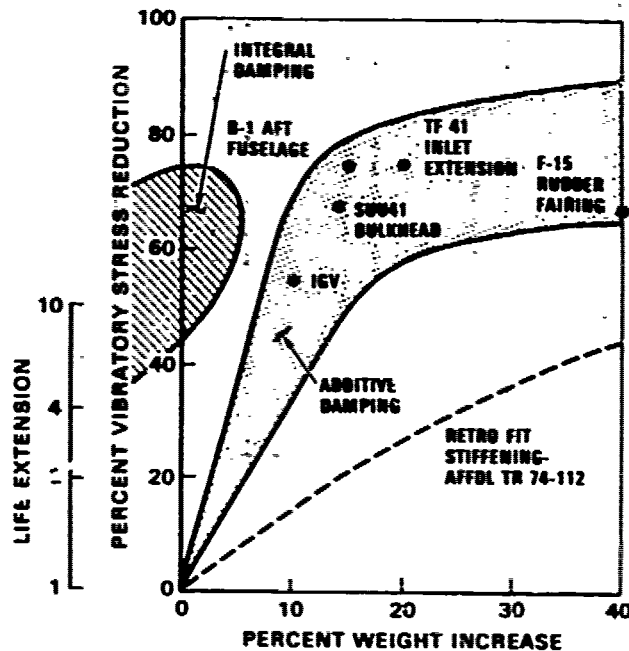


Figure 1.1. - Life extension obtained with additive damping on existing hardware.

has been applied successfully in many fields of engineering as indicated by the results (Figure 1.2) of a survey conducted in the United States of America as part of this program. It has also been used in Civil Engineering to reduce the noise transmission in buildings. The main use of viscoelastic damping has been for the purposes of vibration control, noise control, and preventing high cycle fatigue failures and sonic fatigue in that order (Figure 1.3). Controlling vibration can improve the accuracy of optical systems and guidance systems as well as the reliability of electronic equipment. The use of viscoelastic (passive) damping is also expected to increase in space applications, in conjunction with active damping, since the inherent damping is very low in aerospace metals and high-modulus, graphite/epoxy composites. These latter materials are being used in increasing quantities in space structures.

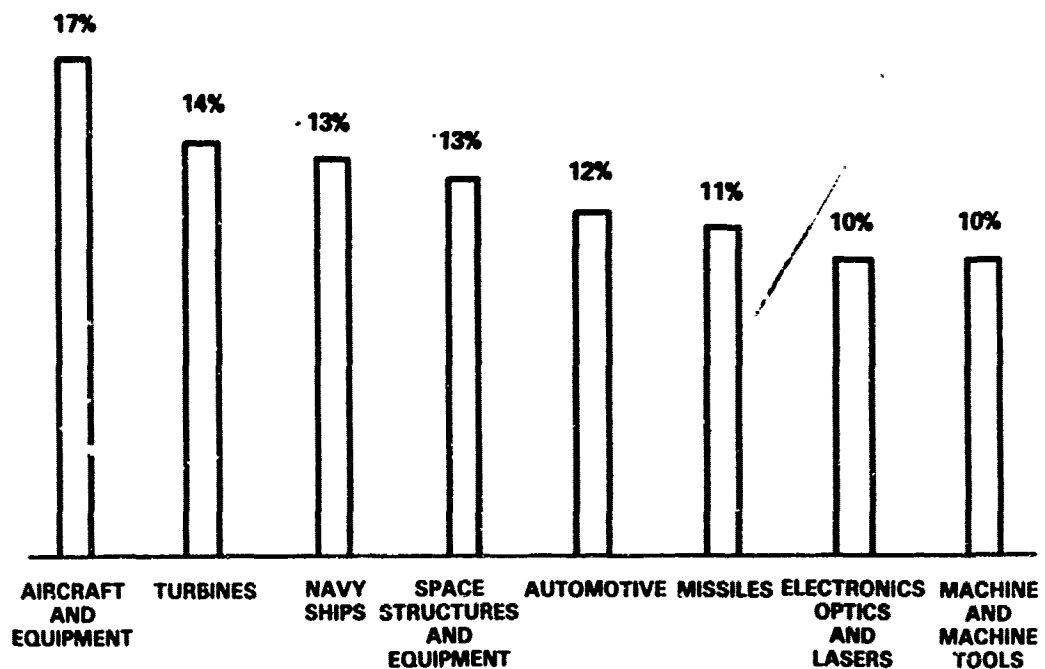


Figure 1.2. - Application of damping technology.

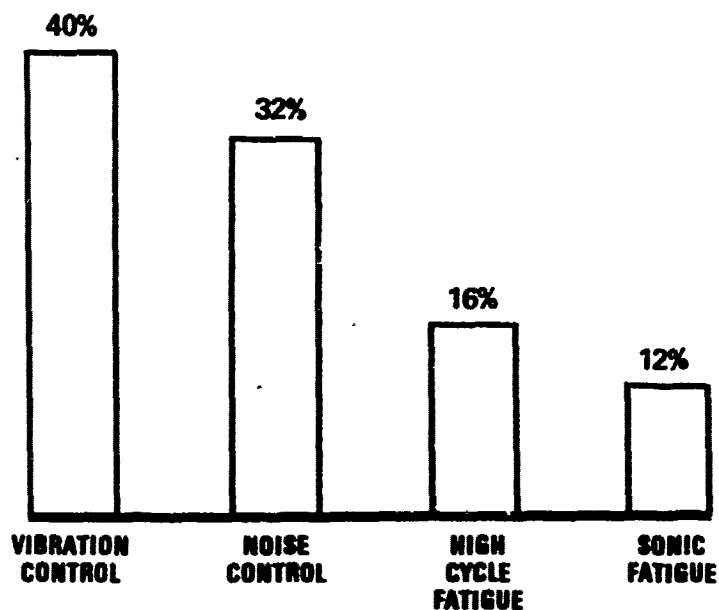


Figure 1.3. - Purpose for use of damping technology.

Vibration testing and data analysis capability has increased dramatically in recent years. The resonant frequencies and damping in structures can now be determined much quicker and with a greater accuracy. The dynamic loads and vibration environments encountered by aerospace structures and equipment are reasonably well known. Damping materials for use in a temperature range from -65°F (-54°C) to 1500°F (816°C) have been developed. The theory for simultaneously curve fitting the measured modulus and loss factor, for improved accuracy and consistency, has been developed for these materials. The basic Ross-Kerwin-Ungar analysis methods for application of viscoelastic damping to beams and plates and the subsequent work by many authors, have been complemented by the development of finite element methods which enable the damping technology to be applied to more complex structural designs. Many successful applications of the viscoelastic damping technology have been reported in the literature. Consequently, it should be possible to anticipate resonant vibration problems and apply the damping technology at the design stage. This approach would not only reduce the cost relative to a subsequent design change, but could also result in a lighter design (integral damping in Figure 1.1).

The viscoelastic damping technology has reached a sufficient state of maturity to take its place as a practical design tool for overcoming resonant

vibration problems. The Damping Design Guide has been developed to speed this process by bringing together much of the information available in literature on the application of viscoelastic damping technology. For a wide appeal, the Damping Design Guide should be suitable for use by designers. This objective represents a very difficult task, as was revealed by the results of the survey (Figure 1.4). Most of the personnel, currently involved in the application of damping technology, are research and development (R&D) engineers. These R&D engineers and their immediate management represent 93 percent of the personnel active in the field (Figure 1.4). Consequently, the R&D engineers are also currently involved in the design and production effort. The bar chart in Figure 1.4 was not normalized, on purpose, to illustrate this point.

To make this technology available to a wider range of engineers and designers, the analysis methods used in this design guide have been simplified, wherever possible, through the use of approximate methods that exhibit acceptable engineering accuracies. Knowledge of structural dynamics would, however, be an advantage. The damping design guide is organized into three volumes.

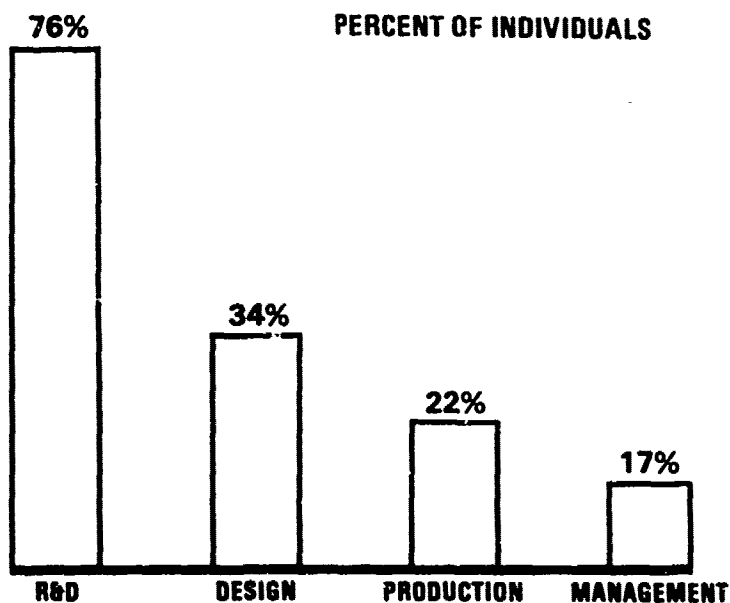


Figure 1.4. - Classification of individuals active in the application of damping technology.

- Volume I is intended to be more of a reference volume providing a broad background of information on viscoelastic damping technology and the related fields. This volume contains reference sources and provides the basis for the data and equations used in Volume II of the Design Guide.
- Volumes II and III represent the user-oriented Design Guide, intended for use by designers and engineers.
 - Volume II contains a brief introduction to vibration, damping, and damping materials. It also contains design equations, design procedures, worked examples and other data useful to the design of damping treatments. The worked examples are intended to illustrate the use of the design procedures and equations.
 - Volume III contains the damping material data that are to be used with the design equations in Volume II. It also contains a list of vendors where these damping materials can be obtained.

SECTION 2

FUNDAMENTALS OF DAMPING AND DAMPING MATERIALS

2.1 NATURE OF DAMPING

When an elastic body is deformed cyclically, a very large part of the stored mechanical energy is recoverable. The remaining part of this mechanical energy is dissipated irreversibly. This irreversible dissipation of mechanical energy is known as damping.

Damping is produced by a variety of energy loss mechanisms. In the basic materials, including the viscoelastic damping materials, the damping is primarily derived from the conversion of mechanical energy into heat through internal friction. This type of damping is known as hysteresis or material damping. Damping is also derived from friction due to relative motion between fluids or solid surfaces and from energy transport to adjacent structural components or fluids (including acoustic radiation). Because of the variety of damping mechanisms, it is difficult to both predict and eliminate the damping. These mechanisms, however, provide insight into various means of increasing the damping [2.1].

2.1.1 Physical Mechanisms of Material Damping [2.2]

The energy dissipating mechanisms contributing to the material damping are themselves very complex and depend on a great number of factors [2.3]. In particular, energy dissipation depends on:

- Internal factors such as type of material, chemical composition, internal crystalline or noncrystalline structure.
- External factors such as temperature, preload, initial strain.
- Factors connected with motion, amplitude and frequency of deformation, state of stress.
- Specimen factors such as geometry, scale, state of surfaces, bonding.

Originally, the damping in materials was thought to be a homogeneous process. It is now understood that the dissipation of mechanical energy within a material involves the transference of the internal structure from one state of thermal equilibrium to another state of equilibrium, corresponding to the newly imposed conditions. This transfer process is accomplished through a reorganization of the internal structure at the macro and micro structural levels. The mechanisms of internal reconstruction include magnetic effects (magnetoelastic, magnetomechanical hysteresis, eddy currents, and magnetostrictive effects) and thermal effects (thermoelastic, thermal conductivity, thermal diffusion, and thermal flow effects). The latter group includes effects connected with diffusion, dislocations, concentrated defects of crystal lattices, photoelectronic effects, stress relaxation at grain boundaries, blocks in polycrystalline materials, phase processes in solid solutions, etc.

During deformation, the above mechanisms contribute to the overall material damping. Each process is, however, associated with a certain frequency and temperature range at which it provides the most effective contribution. This frequency and temperature range can vary with external conditions, the stress state and the stress amplitude. The processes, responsible for the internal structure reorganization, can be both irreversible and reversible. These processes include:

- Relaxation damping which is dependent on frequency and temperature but independent of the deformation amplitude. Actually the process is reversible at small amplitudes, depending on the time, and is called "anelasticity of materials". At larger amplitudes the process becomes irreversible and is known as "viscoelasticity".
- Resonant damping which is dependent on the resonant frequency of the particular mechanism.
- Hysteretic damping ("structural") which is independent of the velocity of deformation, but dependent on the amplitude.
- Nonlinear viscous damping which is dependent on the amplitude and the velocity of deformation and other factors (mainly temperature).

2.1.2 Measure of Damping

In spite of the extreme complexity of the energy dissipating mechanisms, a number of parameters have been proposed that provide an adequate measure of the total energy dissipated within the materials as well as in the structure using the materials. It is common practice to separate the material damping from the total damping of the built-up structure. There has been a concerted effort over many years to separate and quantify all of the damping mechanisms, such as acoustic radiation, and dissipation in mechanical joints, that contribute to the overall damping in the structure. The material damping and the dissipation of energy in joints freed from the effects of gravity are important in space applications.

The energy dissipated per unit time, in a unit volume of a macroscopically homogeneous material [2.3], provides a useful measure of the material damping, and is defined by

$$D = \int \sigma \dot{\epsilon} dv \quad (2.1)$$

where σ is the instantaneous stress and $\dot{\epsilon}$ is the corresponding strain. The quantity D , known as the specific damping energy, is a measure of the capability of a given homogeneous material to dissipate energy when cyclically strained.

Generally, nondimensional parameters, describing the energy dissipating capacity of material, are more useful. One such parameter is the specific damping capacity ψ , which represents the fraction of the system's vibrational energy that is dissipated in one cycle of vibration. It is given by

$$\psi = D_s / U_s$$

where

$$D_s = \frac{2\pi}{\omega} \int_{vol} \sigma \dot{\epsilon} dv \quad (2.2)$$

is the energy dissipated in the total volume, v , of the specimen during one cycle, and

$$U_s = \frac{1}{2} \int_{\text{vol}} \sigma_o \epsilon_o dv \quad (2.3)$$

is the maximum strain energy stored in the specimen during the same cycle. In the above equation σ_o and ϵ_o are the maximum (zero to peak) stress and strain amplitudes, respectively.

Another measure of damping, which is related to the ratio of energy dissipated to energy stored per cycle, is represented by the system damping coefficient or loss factor, which is defined by

$$\eta_s = D_s / 2\pi U_s \quad (2.4)$$

where D_s and U_s are given by Equations 2.2 and 2.3.

There are several measures of damping related to the rate of decay of free vibration. The logarithmic decrement is defined as:

$$\delta = \ln \left(\frac{X_n}{X_{n+1}} \right) \quad (2.5)$$

where X_n and X_{n+1} are two successive amplitudes (strain, acceleration, or displacement) of the decaying free vibration.

Two other decay rate related damping parameters are Δ_t and T_{60} . The parameter Δ_t , which represents the rate of reduction of the vibration in dB/sec is given by

$$\Delta_t = \frac{1}{t_2 - t_1} 20 \log_{10} \frac{\epsilon(t_1)}{\epsilon(t_2)} \quad (2.6)$$

where t_1 and t_2 are points in time an integer number of periods apart. T_{60} denotes the reverberation time (in seconds) (in analogy to the related room-acoustic measure) that it takes for the vibration amplitude of a system, vibrating freely at frequency f_n (Hz), to decrease by 60 dB or to 1/1000 of its initial value.

Another measure of damping is related to the spatial decay of the vibration along the specimen. For such specimens, use has been made of a logarithmic attenuation coefficient [2.3,2.4]:

$$\delta_y = \ln \frac{\epsilon(x_1)}{\epsilon(x_2)} \quad (2.7)$$

a spatial attenuation coefficient [2.3, 2.4]:

$$\theta_y = \frac{1}{x_1 - x_2} \ln \frac{\epsilon(x_1)}{\epsilon(x_2)} \quad (2.8)$$

and a decibel attenuation coefficient rate in space [2.3, 2.4]:

$$\Delta_\lambda = \frac{1}{x_1 - x_2} 20 \log_{10} \frac{\epsilon(x_1)}{\epsilon(x_2)} \quad (2.9)$$

where x_1 , x_2 are the space coordinates of two points in the specimen, integral wave lengths apart, and $\epsilon(x_1)$ and $\epsilon(x_2)$ are the corresponding strains.

Most materials are not ideally elastic. Under cyclic tension-compression loading, a characteristic hysteresis loop is obtained in the resulting stress-strain (or force-displacement) relationship. The area enclosed by the hysteresis loop can be used as a measure of dissipated energy since the area is proportional to the specific damping energy, D , even for nonlinear materials [2.4].

Some of the most commonly used measures of damping are based on the viscoelastic damping model. The damping force in this model is proportional to the velocity. The ratio of the damping force to the velocity is called the viscous damping coefficient, c . The simplest model of a viscoelastically damped system is provided by the single mass-spring-dashpot system, in which the dashpot provides the damping proportional to velocity. If this system, with a modest viscoelastic damping force, is disturbed from the equilibrium position and then released, the mass will oscillate about the equilibrium position with decreasing amplitude. However if c is made large enough, no oscillations will occur. Instead, the mass will creep toward its equilibrium position without crossing it. The viscous damping coefficient at which the motion of the mass first becomes nonoscillatory is called the critical (viscous) damping coefficient, $c_c = 2(KM)^{1/2}$, where M denotes mass and K the spring stiffness. The viscous damping ratio, c/c_c , also called the fraction of critical damping or percent of critical damping, is widely used to indicate damping magnitudes.

Two other measures of damping are derived from the steady state behavior of an ideal linear mass-spring-dashpot system that is driven by a sinusoidal force of constant amplitude. The amplification at resonance, often called the "Q" of the system, is defined as the ratio of the amplitude of the displacement at resonance to the static displacement (the amplitude of the displacement at zero frequency). The proportional bandwidth, $\Delta f/f_n$, takes account of the damping-related broadening of the peak in a plot of response amplitude versus frequency. In this expression, Δf denotes the difference between the two half power point frequencies, one above, and one below the resonance frequency, f_n , at which the square of the response amplitude is one-half of the maximum value at the resonance frequency.

All of the damping measures are related. To illustrate this point, let us consider the relative energy dissipation coefficient for a process of free vibration. The energy, U_s , is here proportional to c^2 and so we have:

$$\eta = - \int_t^{t+T} \frac{D_s}{2\pi U_s} dt = - \frac{1}{\pi} \int_t^{t+T} \frac{\epsilon_o(t) d(\epsilon_o(t))}{\epsilon_o^2(t)} \quad (2.10)$$

$$= \frac{1}{\pi} \ln \frac{\epsilon_o(t)}{\epsilon_o(t+T)} = \frac{1}{\pi} \ln \left(\frac{\epsilon_n}{\epsilon_{(n+1)}} \right) = \frac{\delta}{\pi}$$

where δ is the logarithmic decrement. The interrelationship between all of the damping measures are [2.1,2.2,2.3]

$$\eta = \frac{\psi}{2\pi} = \frac{2.20}{f_n \cdot 60} = \frac{\Delta_t}{27.3 f_n} = \frac{\Delta f}{f_n} = \frac{\delta}{\pi} = \frac{D_s}{2\pi U_s} = \frac{2c}{c_c} = 2\zeta = \frac{1}{Q} \quad (2.11)$$

The symbols used in this section are also defined in Table 2.1.

2.2 CHARACTERIZATION OF LINEAR DAMPING BEHAVIOR: COMPLEX MODULI

For many rubberlike or linear viscoelastic materials, the hysteresis loop of the stress-strain relationship under cyclic deformation is not thin, and may be thick, and is in the shape of an ellipse [2.5]. The shape of the ellipse does not change greatly with changing amplitude, at least within a certain range of conditions, and the area enclosed by the loop is nearly proportional to the square of the strain amplitude, other things being equal. In this case, although the shape of the stress-strain curve is not a straight line, the damping is nevertheless linear and a very convenient and simple representation of the stress-strain relationship in algebraic form is possible, namely the complex modulus [2.3,2.4]. Figure 2.1 shows a typical measured hysteresis loop [2.6] for which these features are evident. Consider the hypothetical elliptical hysteresis loop shown in Figure 2.2. The approximate equation of this ellipse is:

$$\sigma = \sigma_o \left[\epsilon/\epsilon_o \pm \eta (1 - (\epsilon/\epsilon_o)^2)^{1/2} \right] \quad (2.12)$$

TABLE 2.1. LIST OF SYMBOLS FOR SECTION 2.1

SYMBOL	DEFINITION
c	Viscous damping coefficient
c _c	Critical (viscous) damping coefficient
c/c _c	Viscous damping ratio or fraction of critical damping
D	Specific damping energy
D _s	Energy dissipated in the total volume of the specimen
f _n	Resonance frequency
Δf	Difference between the two frequencies above and below the resonance frequency
K	Spring stiffness
M	Mass
Q	Amplification at resonance
T ₆₀	Time within which the vibration level of a system vibrating freely at frequency f _n decreases by 60 dB (reverberation time)
t ₁ , t ₂	Time points an integer number of periods apart
U _s	Energy of vibration (strain energy)
V	Total volume of the specimen
X _n , X _{n+1}	Two successive amplitudes of the free decay
x ₁ , x ₂	Space coordinates of two points in specimen integral wave lengths apart
Δt	Rate of reduction of vibration
Δλ	Decibel attenuation coefficient rate in space
δ	Logarithmic decrement
δ _y	Logarithmic attenuation coefficient
e	Strain
ė	Strain rate
e ₀	Amplitude of strain
e(x ₁), e(x ₂)	Strains corresponding to x ₁ and x ₂
η	Loss factor
η _s	System damping coefficient or loss factor
θ _y	Spatial attenuation coefficient
σ	Instantaneous stress
σ ₀	Amplitude of stress
Ψ	Specific damping capacity

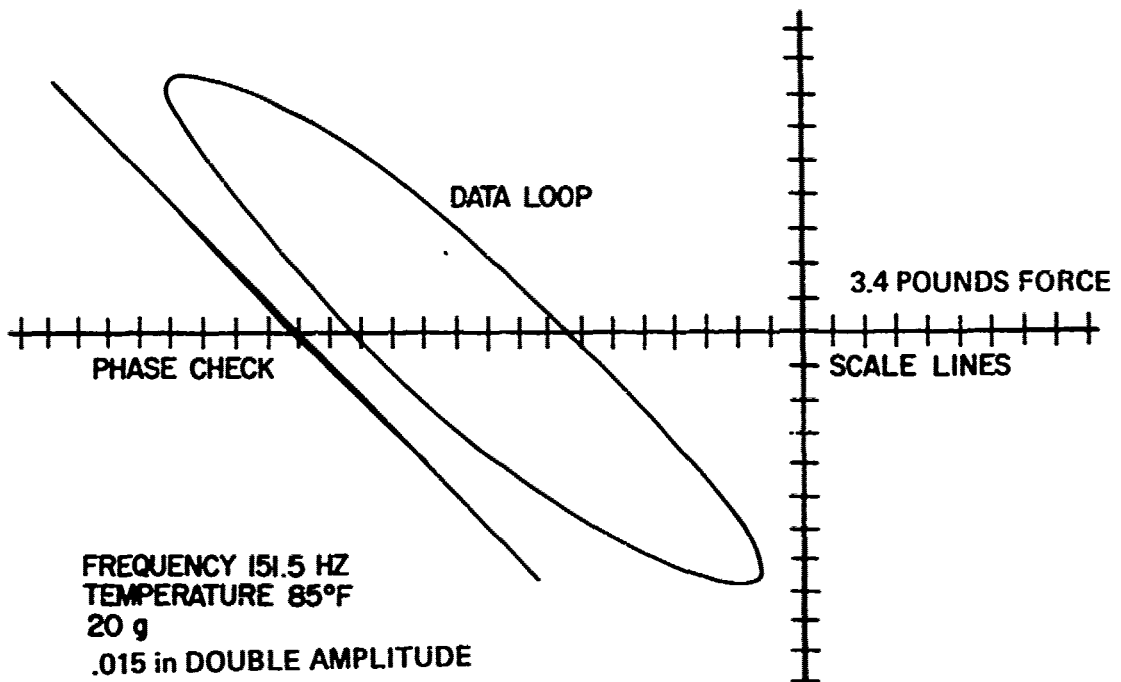


Figure 2.1. - Typical experimentally determined material hysteresis loop.

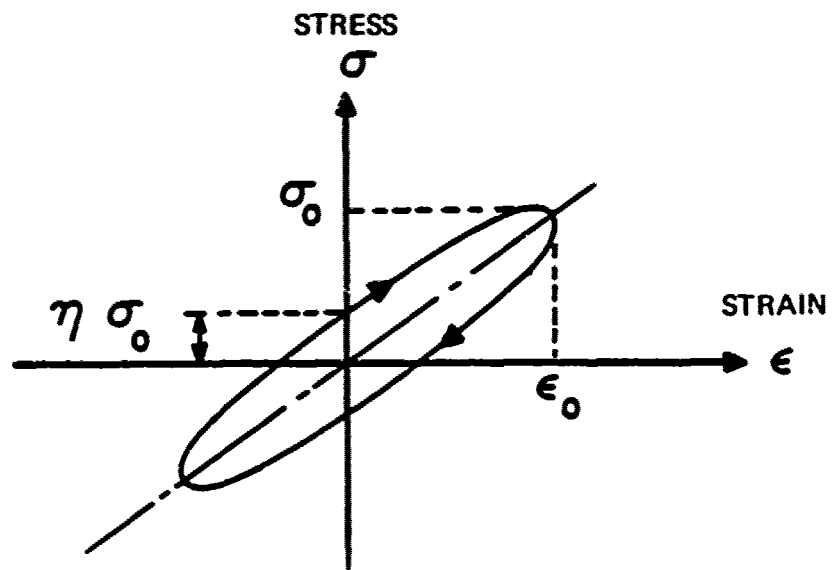


Figure 2.2. - Hypothetical hysteresis Loop.

where σ , σ_0 , ϵ_0 , and η are defined in Figure 2.2 and in Table 2.2, the list of symbols for this section. The nondimensional ratio, η , is simply the ratio of the minor axis of the ellipse to the major axis, but later will be seen to be the loss factor of the material. In this equation, the + sign relates to the loading part of the cycle and the - sign to the unloading part. The positive square root is implied in Equation (2.12). Now, if we let $\epsilon = \epsilon_0 \sin \omega t$, where ω is the frequency, then Equation (2.12) becomes:

$$\begin{aligned}\sigma &= \sigma_0 [\sin \omega t \pm \eta |\cos \omega t|] \\ &= \sigma_0 [\sin \omega t + \eta \cos \omega t]\end{aligned}\tag{2.13}$$

since $\cos \omega t$ is positive from $\omega t = -90^\circ$ to $+90^\circ$ (i.e., the loading part of the cycle corresponding to the + sign), and $\cos \omega t$ is negative from $\omega t = +90^\circ$ to $+270^\circ$ (i.e., the unloading part of the cycle corresponding to the - sign). Since $\cos \omega t$ is the first derivative of $\sin \omega t$ with respect to the time, t , equation 2.13 can be written in the form:

$$\sigma = (\sigma_0/\epsilon_0) [\epsilon + (\eta/|\omega|) (d\epsilon/dt)]\tag{2.14}$$

Clearly, σ_0/ϵ_0 has the dimensions of a modulus and depends on the slope of the major axis of the ellipse. It reduces to the real Young's modulus for purely extensional deformation of the specimen with $\eta = 0$, so we can write:

$$\sigma = E [\epsilon + (\eta/|\omega|) \dot{\epsilon}]\tag{2.15}$$

Finally, we introduce the notation that $\epsilon = \epsilon_0 e^{i\omega t}$, in which only the real part (or only the imaginary part) can represent the actual deformation as a function of time. With this complex notation, equation 2.14 becomes:

$$\sigma = E(1 + i\eta)\epsilon\tag{2.16}$$

since $\epsilon = i\omega e^{i\omega t}$. This equation is the well-known complex modulus representation of linear damping material behavior under harmonic excitation. Note the

TABLE 2.2. LIST OF SYMBOLS FOR SECTION 2.2

SYMBOL	DEFINITION
E	Young's modulus
f	Frequency
f_0	Frequency at temperature T_0
f_{aT}	Reduced frequency
G	Real part of the shear modulus
G_0	Real part of the shear modulus at temperature T_0
T, T_1, T_2	Temperature
T_0	Reference temperature
ΔT	Temperature increment between T_0 and T_1, T_2 , etc.
a_T	Temperature shift factor
ϵ	Strain
$\dot{\epsilon}$	Strain rate
ϵ_0	Amplitude of strain
η	Loss factor
η'	Shear loss factor
ρ	Beam density
ρ_0	Beam density at temperature T_0
σ	Instantaneous stress
σ_0	Amplitude of stress
ω	Circular frequency

restrictions; namely, that it must be harmonic motion and the complex notation must be interpreted in terms of real numbers eventually. It can be shown that this η , known as the loss factor, is the same as the η defined earlier. In practice, E and η are functions of frequency and temperature, and for any given material there exists a threshold strain level beyond which the apparent values of E and η also become dependent on the strain. The material behaviour is then nonlinear.

Similar considerations apply to deformation in shear, so that the relationship between the shear stress and the shear strain, γ , is:

$$\tau = G(1 + i\eta')\gamma \quad (2.17)$$

where G is the real part of the shear modulus and $\eta' \approx \eta$.

2.2.1 Effects of Temperature and Frequency and Strain

One of the ways in which the large number of available linear damping materials differ from each other is in the variation of E (or G) and η with frequency, temperature and strain amplitude, and prestress or prestrain. Temperature is by far the most important factor, since E can vary by as much as four orders of magnitude over a narrow temperature range. The variation of Young's modulus E and loss factor η with temperature at fixed frequency and strain amplitude are typically of the form shown in Figure 2.3. Three distinct regimes are observed; namely, the glassy region, the transition region, and the rubbery region. In the glassy region, E is high and η is low. In the transition region, E varies rapidly with temperature and η is high. In the rubbery region, E is low and varies quite slowly with temperature and η is low but not as low as in the glassy region. At the very highest temperatures, irreversible thermal decomposition of the material takes place.

Figure 2.4 shows the variation of Young's modulus E and η with frequency at a fixed temperature and strain amplitude for a typical damping material. Note that the modulus curve is the mirror image of that in Figure 2.3. The same three distinct regions in the modulus curve exist with the same description applying. It should be noted that the property variation shown in Figure 2.4 occurs across many decades of frequency while the variation shown in Figure 2.3 can occur across as small a temperature range as 20 degrees.

At high strain levels, the measured values of E and η begin to depend on the value of peak strain amplitude, and nonlinear behavior begins to occur. In this case, the complex modulus representation is useful only in a more qualitative sense since it represents an average value over a complete cycle and over the volume of the specimen. Nonlinear behavior of materials will be discussed later.

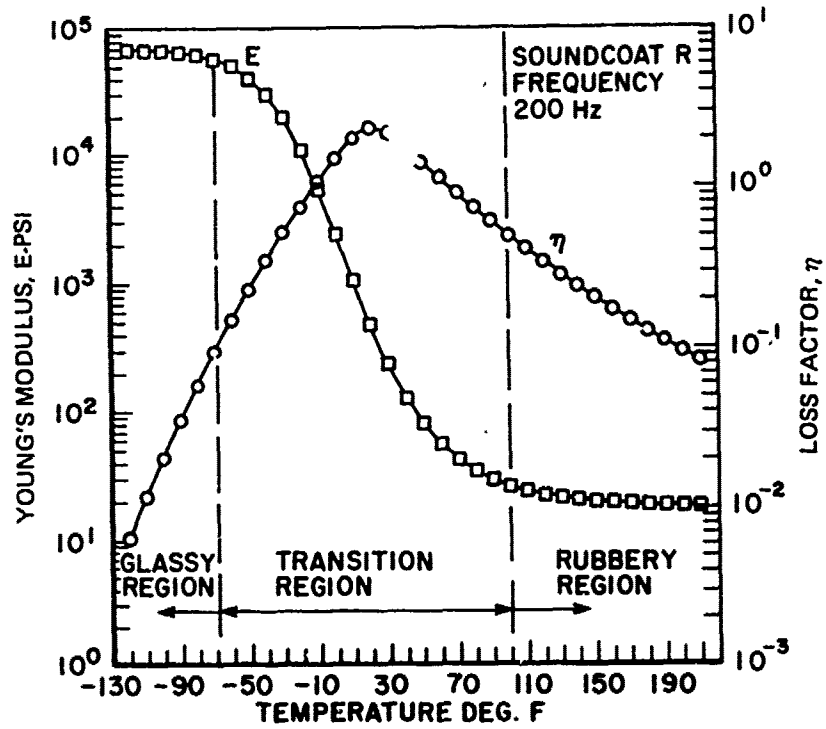


Figure 2.3. - Young's modulus and loss factor versus temperature at a constant frequency.

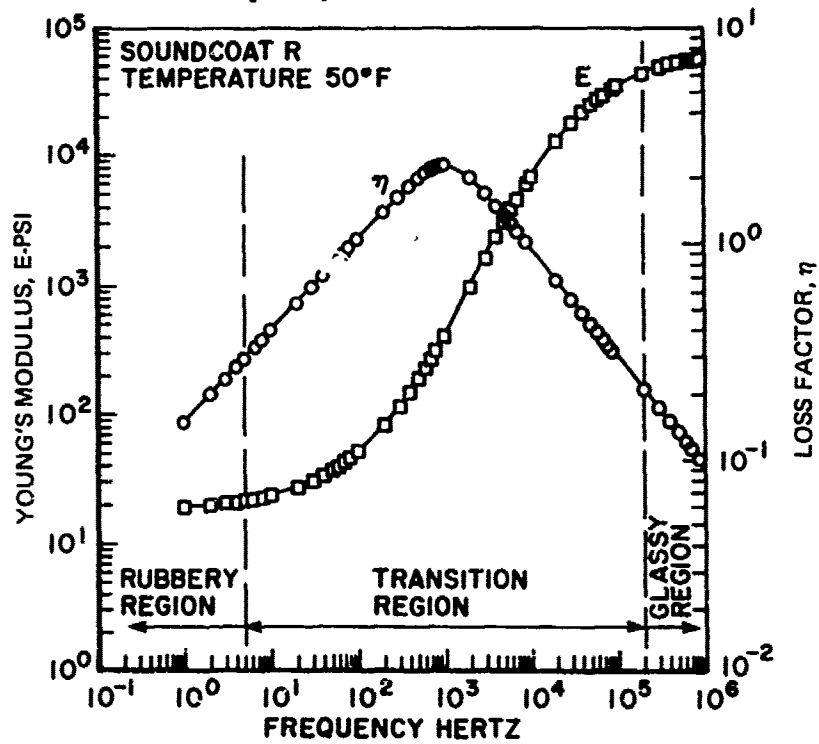


Figure 2.4. - Young's modulus and loss factor versus frequency at a constant temperature.

2.2.2 The Time-Temperature Superposition Principle

The similarity between time- and temperature-dependent viscoelastic properties can be seen in Figures 2.3 and 2.4. This similarity was first noted by Leaderman [2.6] who observed that creep recovery data obtained at different temperatures could be superposed by horizontal translation along the logarithmic time axis. This empirical time-temperature superposition principle was formalized by Tobolsky and Andrews [2.7] and Ferry [2.8]. Its practical significance is that experimental data taken over a limited range of time or frequency at a number of different temperatures can be superposed to give a single composite curve for a particular viscoelastic function, over an extended interval of time.

The basis of the time-temperature superposition principle is that the effect of a change in temperature on viscoelastic properties is to multiply or divide the time scale by a shift factor which is constant for a given temperature. Although when the principle was first applied there was no fundamental theory to support its validity, it was subsequently found to be a logical consequence of the flexible chain molecular theory of polymer viscoelasticity [2.9].

Ferry [2.8,2.10] combined all temperature effects into a single shift factor, α_T , which relates relaxation times at a temperature T to those at an arbitrary reference temperature T_0 . The effect of temperature on the modulus function such as G or E is expressed as the ratio

$$\frac{G}{G_0} = \frac{\rho T}{\rho_0 T_0} \quad (2.18)$$

Since α_T is the same for all relaxation times, an increase in temperature from T_0 to T shifts a logarithmic G curve upward and to the right as shown in Figure 2.5 while the shape of the curve is unchanged. In considering the horizontal shift direction for G , it should be noted that α_T is negative because as T increases intermolecular friction decreases. Therefore, $\alpha_T = f_0/f$ or $f = f_0/\alpha_T$, giving the shift to higher frequencies at higher temperatures. Similarly,

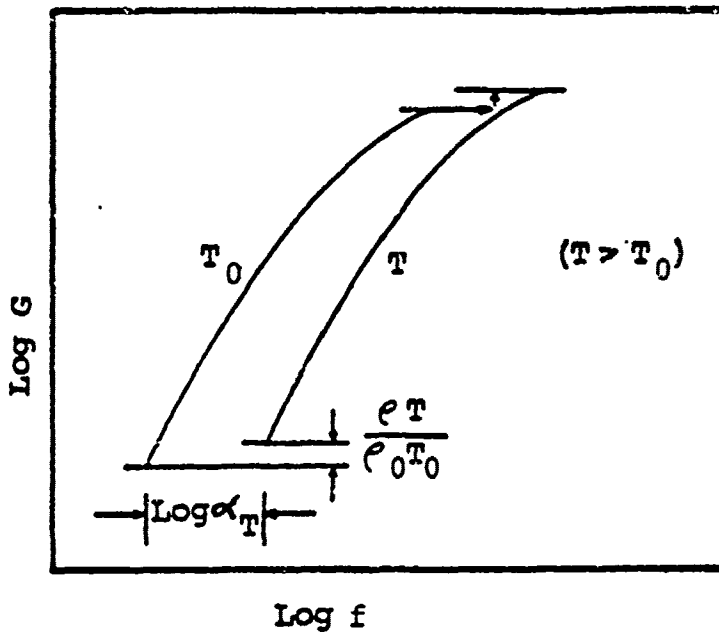


Figure 2.5. - Illustration of reduced variables time-temperature superposition.

an experimental G curve determined at temperature T can be shifted to temperature T_0 by plotting $\log G \frac{\rho_0 T_0}{\rho T}$ versus $\log \alpha_T$. The choice of T_0 is completely arbitrary. Shift factors, α_T , are determined empirically for each temperature.

Thus, by using the superposition principle, it is possible to separate the complex time and temperature dependence of a viscoelastic function in terms of a function of time (or frequency) and one of temperature, $\alpha_T(T)$. It is clear that α_T is a dimensionless quantity, since it is used to reduce viscoelastic data taken at various temperatures to the reference temperature T_0 ; the reduction procedure is often referred to as the reduced variable method or simply the temperature-frequency equivalence method.

In using this approach for the Young's Modulus, E , $(T_0 \rho_0 / T \rho)E$ and η are plotted against the reduced frequency, $f \alpha_T$. Often the density ratio ρ_0 / ρ and the temperature ratio T_0 / T may be regarded as unity over the range of usefulness

of the material. The preparation of "master curves" of E and η versus $f\alpha_T$ is a very useful technique for extrapolation of data to frequency, or temperature ranges where test data are not available. To prepare these curves, one must first use the available data to estimate α_T . This is often best accomplished empirically by arbitrarily selecting an initial T_0 and then judging the value of α_T needed to shift the curve of $\log E$ versus $\log f$ at temperature T_1 to best match the curve at T_0 , while at the same time matching curves of $\log \eta$ versus $\log f$. The process is illustrated in Figure 2.6 where the hypothetical curves of $\log E$ and $\log \eta$ versus $\log f$ at various temperatures have been shifted as indicated, and the appropriate α_T versus T curve drawn. If T_0 is improperly chosen, the matching will not be satisfactory and a new value should be tried.

2.2.3 A Reduced-Temperature Nomogram [2.11]

The graphs of E and η versus reduced frequency, $f\alpha_T$, represents a fundamental relationship between the various parameters for many damping materials. Its use, to directly read off the modulus and loss factor at any given

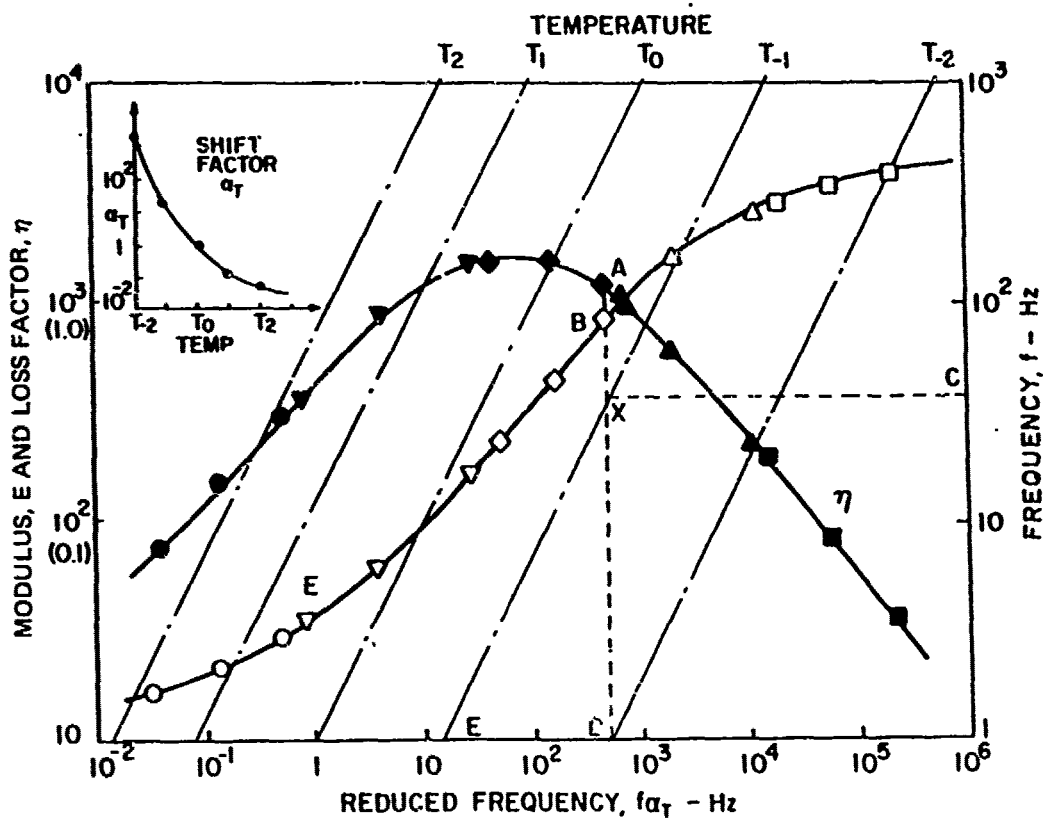


Figure 2.6. - Illustration of the reduced-temperature nomogram.

temperature and frequency, is tedious and inconvenient since it is necessary to read off α_T , calculate $f \alpha_T$, and only then read off E and η . If the scales of this graph are relabelled, a very simple nomogram can readily be created. Simply use the right-hand scale for frequency, as indicated in Figure 2.6, and continue to use the lower horizontal scale for α_T . For the line $f = 1$, which is the lower axis of the graph, then $f \alpha_T = \alpha_T$ and hence the points corresponding to each temperature $T_0, T_1, T_2 \dots$ can be marked out since α_T is assumed known for each T_i ($i=1, 2\dots$). Similarly, for the horizontal line one decade higher, for which $f = 10$, then $f \alpha_T = 10\alpha_T$ and again, since α_T is known for each T , the points can be marked. If the process is repeated for $f = 1000$ or whatever, the set of points corresponding to each T_i can be filled in to form the set of diagonal lines shown in Figure 2.6. Once the nomogram is made in this way, for the required f and T , move along the horizontal f line and along the diagonal T line to the point of intersection (X). The point X corresponds to the appropriate value of $f \alpha_T$, at X, construct a vertical line intersecting the E and η curves and read off the appropriate value.

Another use for the nomogram is to reduce data in the first instance without directly having to estimate α_T for each temperature. For, if one selects the proper position to correspond to T_0 and selects the proper temperature interval, ΔT , between T_0 and T_1, T_2, \dots , the grid of lines can be used to position the test points, in effect by calculating $f \alpha_T$ according to the assumed T_0 and ΔT . Only one combination of T_0 location and ΔT will give a satisfactory reduction of the data, just as in the reduced frequency approach. If the chosen combination is not satisfactory, one must change the position of T_0 and/or ΔT .

In summary, the reduced temperature nomogram displays, on one plot, the materials modulus and loss factor data. From the limited number of data points taken at specific temperature and frequencies, interpolations can be made on the reduced temperature nomogram to obtain the material properties for any combination of temperature and frequency. The use of the nomogram in the design procedure is discussed in volumes II and III.

2.3 DAMPING MATERIAL CHARACTERIZATION TECHNIQUES

The essential first step in using damping technology to control vibration problems is the accurate determination of damping material properties. It is important for the designer to have a general knowledge of the various characterization techniques so that an evaluation of the data obtained from the material suppliers can be made and suggestions on how to conduct quality assurance testing can be offered.

The following paragraphs will discuss several techniques for determining the dynamic properties of materials. The techniques discussed are:

- Resonant Beam
- Dynamic Mechanical Analyzer
- Resonance Tests
- Rheovibron
- Progressive Wave
- Impedance
- Shear Rheometer

2.3.1 Resonant Beam Test

The resonant beam test technique is the test procedure which forms the basis of ASTM standard E756-80. Either "digital" or "analog" systems can be used to generate and handle data from resonant beam tests. Typical analog vibrating beam test equipment is shown in Figure 2.7. The four types of specimen beams (uniform, "Oberst," "modified Oberst" and sandwich), are shown in Figure 2.8.

The appropriate beam specimen for testing a particular material is determined from the following criteria:

- a. The uniform beam is used for stiff materials, such as epoxies and plastics, which are self-supporting at test temperatures, that is, have Young's moduli E_D greater than 10^6 psi ($6.98 \times 10^9 \text{N/m}^2$).

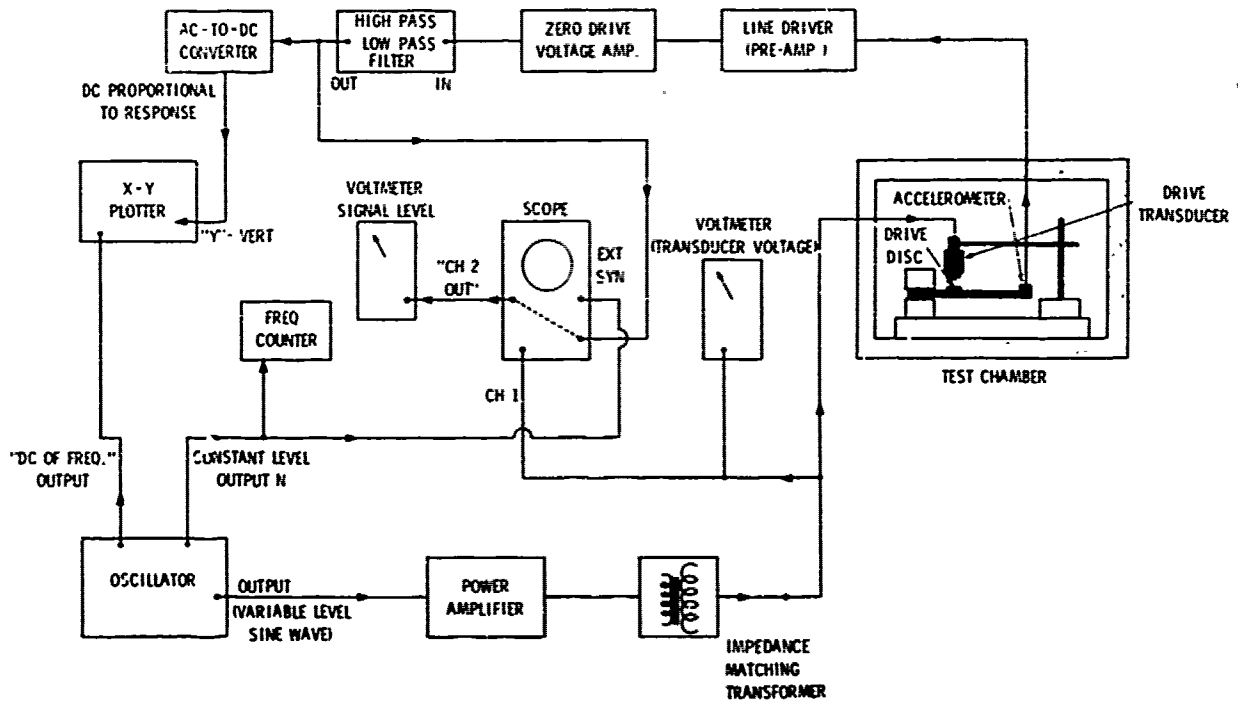


Figure 2.7. - Block diagram of the beam test fixture.

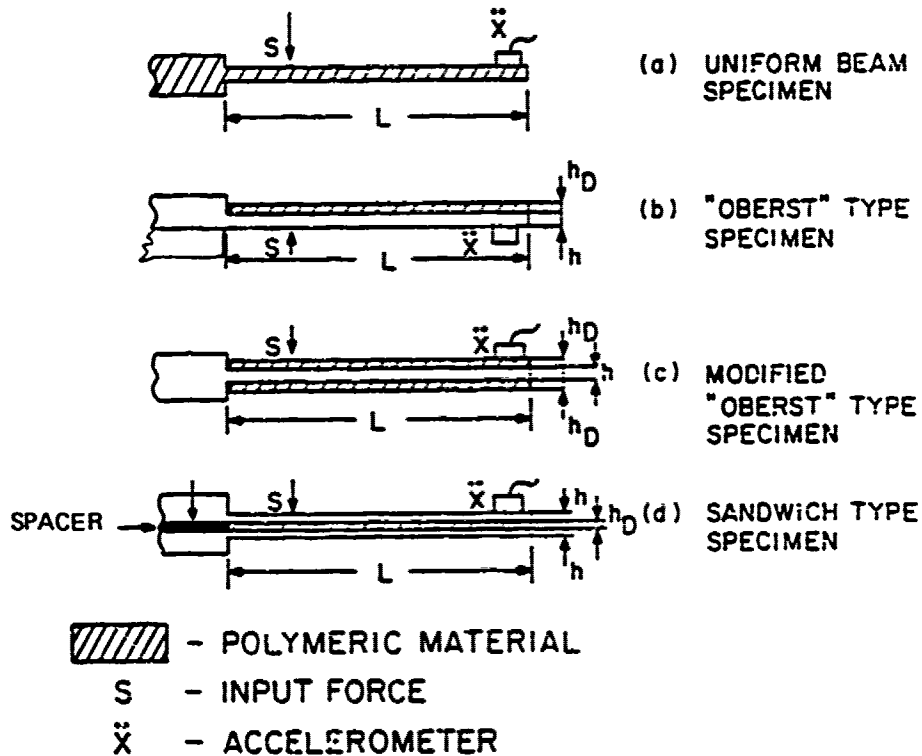


Figure 2.8. - Resonant beam test specimens.

- b. The "Oberst" (nonsymmetric) or "modified Oberst" (symmetric) beams are used for materials in which E_D is between 10^4 psi (6.89×10^7 N/m²) and 10^6 psi (6.89×10^9 N/m²). As E_D falls toward the lower limit, h_D/h for these beams can increase.
- c. The symmetric sandwich beam is used for materials in which E_D is between 10 psi (6.89×10^4 N/m²) and 10^5 psi (6.89×10^8 N/m²). Since the sandwich beam relies on shear of the damping material between two support beams, it yields better results for this range of values of E_D .

The following equations are used in the ASTM standard to calculate the value of E_D or G_D for various damping materials, according to the specimen beam used in the test. The symbols used in the following equations are listed in Table 2.3.

- a. For an "Oberst" beam (with damping material coated on only one side of the beam), the complex Young's modulus is derived from formulae developed originally by Oberst [2.12]. These are:

$$Z^2 = \left[1 + \frac{\rho_D h_D}{\rho h} \right] \left[\frac{f_n}{f_{on}} \right]^2 = \frac{1 + 2en(2 + 3n + 2n^2) + e^2 n^4}{1 + ne} \quad (2.19)$$

$$\frac{\eta_n}{\eta_D} = \frac{en}{1 + en} \left[\frac{3 + 6n + 4n^2 + 2en^3 + e^2 n^4}{1 + 2en(2 + 3n + 2n^2) + e^2 n^4} \right] \quad (2.20)$$

where $e = E_D/E$ and $n = h_D/h$. In these formulae, Z^2 is calculated from the measured resonance frequency, f_n , of the n th mode of the damped beam and the measured frequency, f_{on} , of the undamped beam. The ratio e is then deduced from equation 2.19 and η_D is calculated from equation 2.20, using the value of e , and the measured value of modal damping, η_n . In fact, after some algebraic manipulation, the following equation for e in terms of Z^2 and n can be derived:

$$e = \left[-(4+6n+4n^2-Z^2)n + \left((4+6n+4n^2-Z^2)^2 n^2 + 4n^4 (Z^2-1) \right)^{1/2} \right] / 2n^4 \quad (2.21)$$

TABLE 2.3. LIST OF SYMBOLS FOR SUBSECTION 2.3.1.

SYMBOL	DEFINITION
A,B	Nondimensional parameters (equations 2.29 and 2.30)
b	Breadth of beam
e	Modulus ratio E_D/E
E	Young's modulus of beam material
E _D	Real part of complex Young's modulus of damping material
f	Frequency (Hertz)
(EI) _e	Equivalent complex flexural rigidity (equation 2.25)
f _{0n}	n th natural frequency of bare beam
f _n	n th resonant frequency of damped beam
f _L	Lower half-power bandwidth frequency
f _R	Higher half-power bandwidth frequency
Δf	Total half-power bandwidth (f _R - f _L)
G _D	Real part of complex shear modulus of damping material
g*	Shear parameter (equation 2.26)
h	Thickness of beam
h _D	Thickness of polymeric material
h _R	Thickness of root
L	Length of beam
l	Length of beam root
n	Thickness ratio (h _D /h); mode number
T	Temperature
T ₀	Reference temperature
Z	Nondimensional parameter (equation 2.19)
ω _T	Temperature shift factor
η _D	Extensional loss factor of damping material
η _D '	Shear loss factor
η _n	Loss factor of beam specimen in n th mode
ξ _n	n th eigen value for beam
ρ _n	Density of beam; also density in general
ρ _D	Density of damping material
ω _{0n}	n th circular frequency of bare beam

These equations give accurate results provided that $Z^2 - 1 > 0.1$. If $Z^2 > 1.0$, the error in e resulting from an error in Z^2 becomes prohibitively high.

- b. For a "modified Oberst" beam (with damping material coated symmetrically on both sides of the beam) the complex Young's modulus is derived from the formulae

$$E_D = E(Z^2 - 1) / [en^3 + i2n^2 + 6n] \quad (2.22)$$

$$\eta_D = \eta_n Z^2 / (Z^2 - 1) \quad (2.23)$$

where

$$Z^2 = (1 + 2\rho_D n/\rho) (f_n/f_{on})^2 \quad (2.24)$$

Again, the equations give reasonably accurate results whenever $Z^2 - 1 > 0.1$.

- c. For the symmetrical sandwich beam, calculation of values of the shear modulus, C_D , and the loss factor, η_D , for the damping material is based on a set of equations developed by Ross, Kerwin, and Ungar [2.13]. In current notation the now classical equation is;

$$(EI)_e^* = \frac{Eh^3}{6} + Eh(h + h_D)^2 \frac{E^*}{1 + 2g^*} \quad (2.25)$$

where $(EI)_e^*$ is the equivalent complex flexural rigidity of the three layer sandwich $[\approx (EI)_3 (1 + i\eta_n)]$ and g^* is the shear parameter given by:

$$g^* = \frac{G_D^* L^2}{Eh_D \xi_n^2} \quad (2.26)$$

Equations (2.25) and (2.26) may be solved to give simple algebraic equations for G_D and n_D^i , namely:

$$G_D = \frac{[(A - B) - 2(A - B)^2 - 2(A\eta_n)^2] [Eh_D \xi_n^2 / L^2]}{(1 - 2A + 2B)^2 + 4(A\eta_n)^2} \quad (2.27)$$

$$n_D^i = A\eta_n / [A - B - 2(A - B)^2 - 2(A\eta_n)^2] \quad (2.28)$$

where

$$A = (f_n / f_{on})^2 (2 + \rho_D h_D / \rho h) (B/2) \quad (2.29)$$

and

$$B = 1/6(1 + h_D/h)^2 \quad (2.30)$$

for most polymeric materials in the rubbery and transition regions, $E_D \sim 3G_D$ and $n_D \sim n_D^i$.

Most tests cover only the first seven modes of the cantilever beam. The eigenvalues of the system are given by:

$$\begin{aligned} \xi_1^2 &= 3.515 \\ \xi_2^2 &= 22.0345 \\ \xi_3^2 &= 61.6970 \\ \xi_4^2 &= 120.902 \\ \xi_5^2 &= 199.866 \\ \xi_6^2 &= 298.560 \end{aligned} \quad (2.31)$$

$$\frac{\omega_n^2}{\xi_n^2} = 416.990$$

The eigenvalues define the relationship between the resonant frequencies of the uncoated individual beams and the modulus E by the classical relationship

$$\rho h \omega_{on}^2 L^4 / (Eh^3 / 12) = \xi_n^4 \quad (2.32)$$

2.3.1.1 A Review of Specimen Beam Criteria

To obtain satisfactory test results, specimen beams must be prepared carefully. Paying careful attention to specimen dimensions helps avoid machining difficulties and helps to insure accurate test results. Figure 2.9 shows a typical bare beam, with appropriate dimensions indicated.

Recommended materials for specimen beams depend on the test temperatures. For low temperature tests (below 300°F (149°C)), aluminum or steel beams can be used. It is important to note that if a stiffer beam is used, clamping conditions become more critical.

For high temperature tests (up to 2,000°F (1,093°C)), steel or superalloy beams must be used.

The thickness of the damping material, h_D , should not be less than 0.004-inch (0.127 mm). Preferably, the damping material should be thicker; otherwise, it is difficult to control the dimensions of the composite specimen beam.

2.3.1.2 Error Sources

For resonant beam testing, as for any measurement technique, errors can arise from several sources. Errors in the measured complex moduli of the polymeric material may be the result of:

- Errors in specimen preparation, such as poor adhesion, voids (air bubbles), joint damping in clamping fixture, or nonuniform thicknesses.

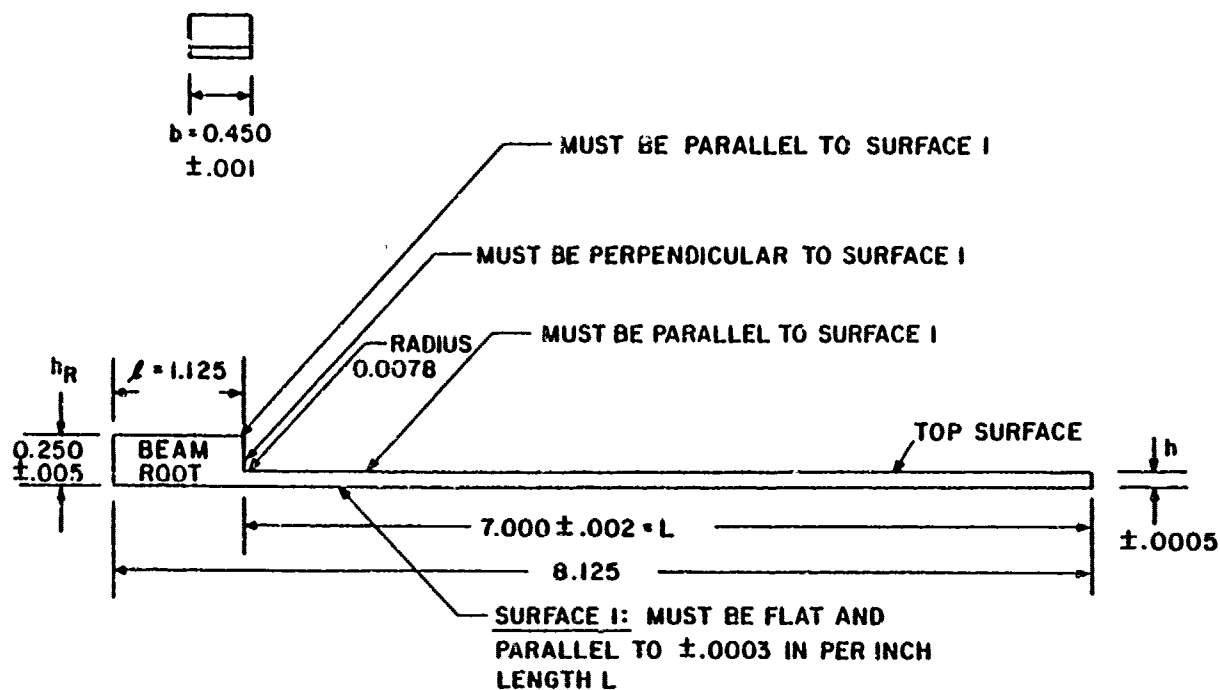


Figure 2.9. - One half of a sandwich beam specimen with recommended specimen dimensions.

- Errors in temperature control. The thermocouple may not indicate the specimen temperature accurately because of thermal lag (insufficient time for reaching thermal equilibrium or because of nonuniform temperature distribution within the specimen).
- Errors in measuring resonant frequencies, as a result of too high frequency sweep rate, mechanical relaxation of the specimen, or low level signals (hence the need to always monitor "input" and "output").
- Errors in measuring modal damping. Problems could include closely spaced modes, extraneous damping sources (such as damping in the clamp), or incorrect interpretation of nonlinear response as apparent increased damping.
- Error magnification, because of unstable regions in the equations. For example, in "Oberst" equations 2.19 and 2.20, and "modified Oberst" equations 2.22 and 2.23, the term $(Z^2 - 1)^{-1}$ acts to magnify errors in η_n or E . As $Z^2 \rightarrow 1$, the loss factor becomes infinite.

While conducting resonant beam tests, it is important to constantly be aware of these and other possible sources of erroneous data, and to apply every possible precaution while obtaining, interpreting, and utilizing the data.

2.3.1.3 Test Data Set

For any beam specimen, each test "point" consists of a set of simultaneously measured values of temperature, mode number, resonant frequency, and modal damping. The complete set of data points for each test includes these measured values for the undamped beams and for the damped specimen beams. The raw test data for each damping material evaluated include the values of temperature, damped resonant frequency, f_n , the half-power frequencies, f_L and f_R , bandwidth, Δf , and the modal loss factor, η .

It is important to evaluate the validity of raw test data being generated by a particular resonant beam test. One way to evaluate the raw test data is to examine the plot of η_n , f_n , and f_{on} versus temperature. This plot may be generated manually as shown in Figure 2.10 or automatically as part of the test system [2.14,2.15]. In either case, subjective evaluation of the test data at this point is an important step in the testing process.

The valid raw data can now be used in conjunction with the appropriate set of equations to produce a set of material properties for the specific temperatures and frequencies measured during the beam tests.

2.3.1.4 Advantages and Disadvantages

Advantages of this test set-up method include: (a) the system is reasonably simple to use; (b) errors can be assessed and kept within limits; (c) a single specimen can be used to cover a wide band of frequencies and temperatures; (d) the damping materials is bonded to the beam which simulates the actual use of the damping material.

Disadvantages of this test set-up are: (a) the test can be conducted only at low strain levels; (b) the test is time consuming and costly.

2.3.1.5 Six Order Theory Data Analysis

An improvement in the material property data obtained from resonant beam tests can be realized if the test data are reduced using 6th order beam theory instead of the ASTM standard 4th order beam theory.

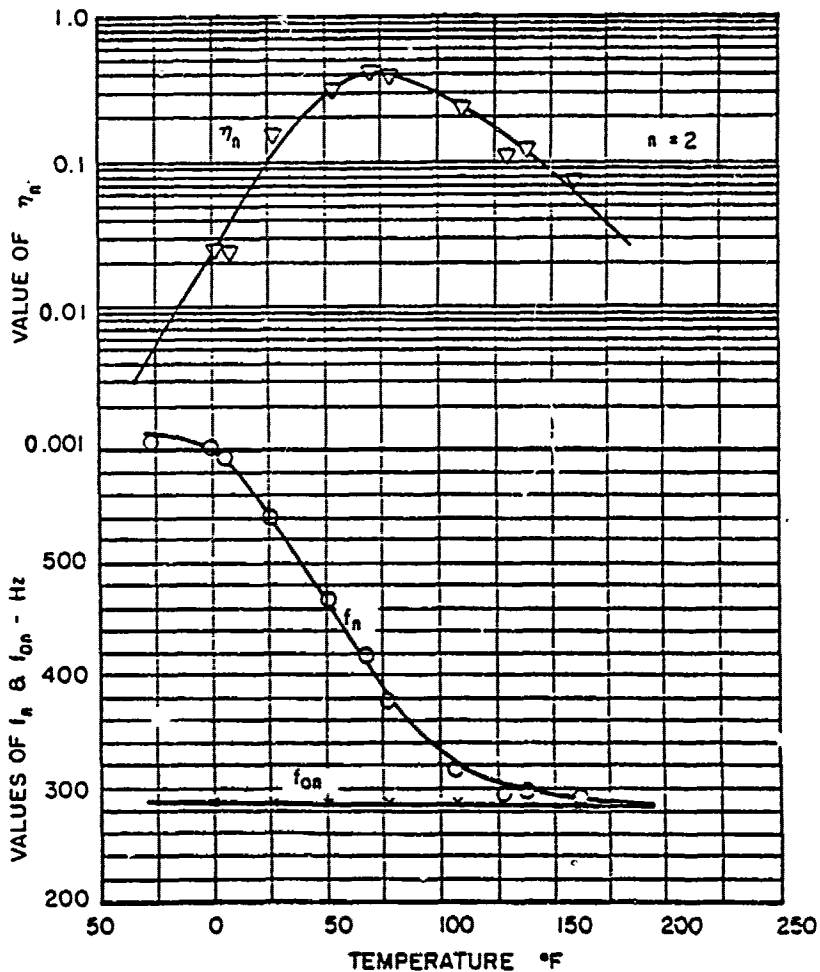


Figure 2.10. - Typical graphs of η_n , f_n , and f_{on} versus temperature.

The advantage of the 6th order theory is the ability to match the cantilever beam boundary conditions exactly, therefore reducing the error when analyzing the test data. The development of this analysis is detailed in References [2.16] and [2.17].

The basic assumptions for the analysis are:

- The beam deflection is small and uniform across a section
- The axial displacements are continuous
- The base and constraining layers bend according to the Euler hypothesis

- The damping layer deforms only in shear: ($E_D \ll E$)
- Longitudinal and rotary inertia effects are insignificant

The variation in the material properties, obtained by the 4th and 6th order analysis, is shown in Figures 2.11 through 2.14. Figure 2.11 shows the variation in material loss factor and Figure 2.13 shows the variation in material modulus for the data taken from the second mode of a cantilever beam. The trends seen here are typical results. Figures 2.13 and 2.14 illustrate the same type of data variation except that the data are for mode six of a cantilever beam. As would be expected, the error reduces as the mode number increases because the importance of the boundary conditions is reduced.

In general, the loss factor values predicted by the 4th order theory are lower than those predicted by the 6th order theory, primarily near the maximum loss factor. The 4th order theory also predicts higher modulus values in the rubbery region and lower modulus values in the glassy region. A comparison of the 4th and 6th order data in a reduced temperature nomogram format is illustrated in Figure 2.15. As can be seen, the major differences occur in the glassy and rubbery regions. The major disadvantage of the 6th order data reduction is the increased computer cost that is directly related to the increased complexity of the analysis.

The sixth order theory was used to reduce the damping material data for the design guide in instances where the materials were tested in a sandwich configuration. A description of the 6th order data reduction used in the design guide is given in Volume III.

2.3.2 Dynamic Mechanical Analyzer

The dynamic mechanical analyzer is a valuable tool in a polymer laboratory. Among the various tests that can be run on the machine is the test to determine damping properties. The following paragraphs explain how to obtain damping properties using the Dupont 981 Dynamic Mechanical Analyzer, DMA.

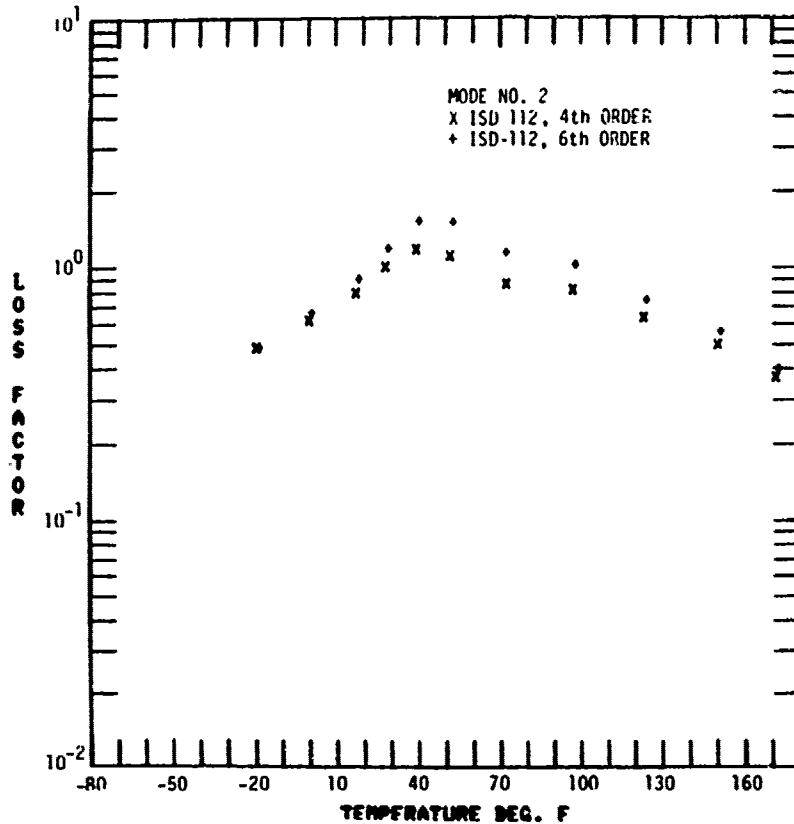


Figure 2.11. - 4th and 6th order variation in material loss factor.

2.3.2.1 The Test Set-up

A schematic diagram of the DMA system is shown in Figure 2.16. The mechanical portion of the systems consists of two parallel balanced sample support arms which are free to oscillate around flexure pivots. The arms are connected by the sample. The instrumentation used in the DMA test is shown in Figure 2.17. This test set-up can be used for constant temperature or range temperature tests.

A servo control system controls the power input into the electro-magnetic drive to maintain a constant amplitude level vibration on the driven arm. The displacement is measured by a Linear Variable Differential Transducer, LVDT.

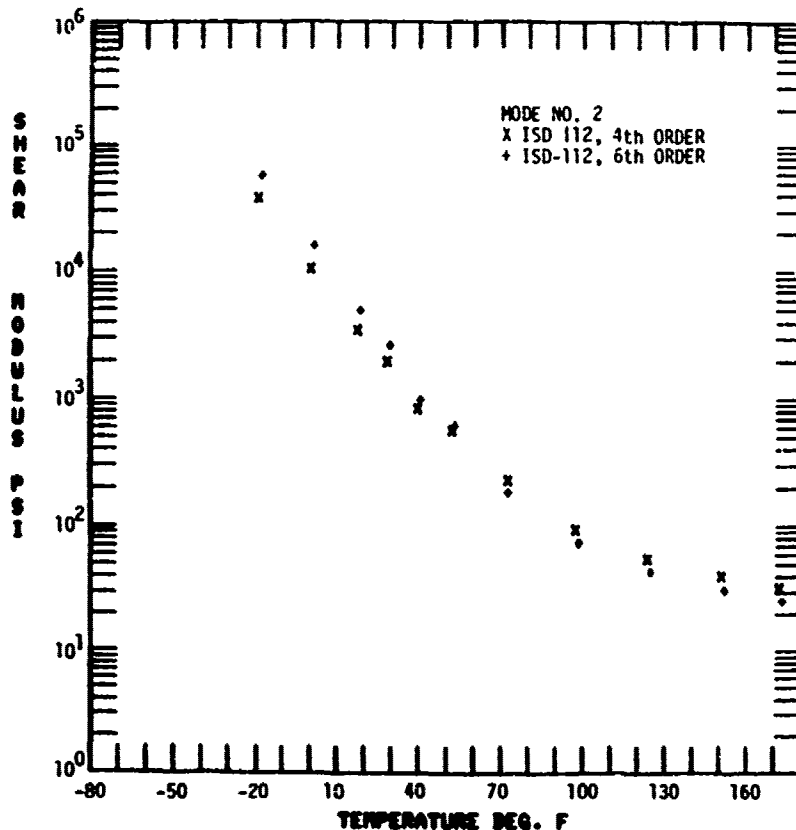


Figure 2.12. - 4th and 6th order variation in material modulus.

The test set-up incorporates an X-Y plotter, used to plot both the power into the driver and the frequency of the system versus temperature. These measurements are used to calculate the complex Young's modulus, $E(1 + i\eta_D)$, for the material.

2.3.2.2 Specimen Selection Criteria

The specimen for a DMA test is generally rectangular. The nominal specimen dimensions are shown in Figure 2.18. Experience has shown that two specimens are required to obtain the most accurate data across the entire test temperature range. The lower temperature range data are best collected with a specimen which has an aspect ratio of approximately 10 to 12. The high temperature data, just below maximum damping temperature and above (see Figure 2.18), are most accurately obtained from a specimen with an aspect ratio of 4 to 6. Aspect ratio is defined as length/thickness, $\frac{L}{T}$.

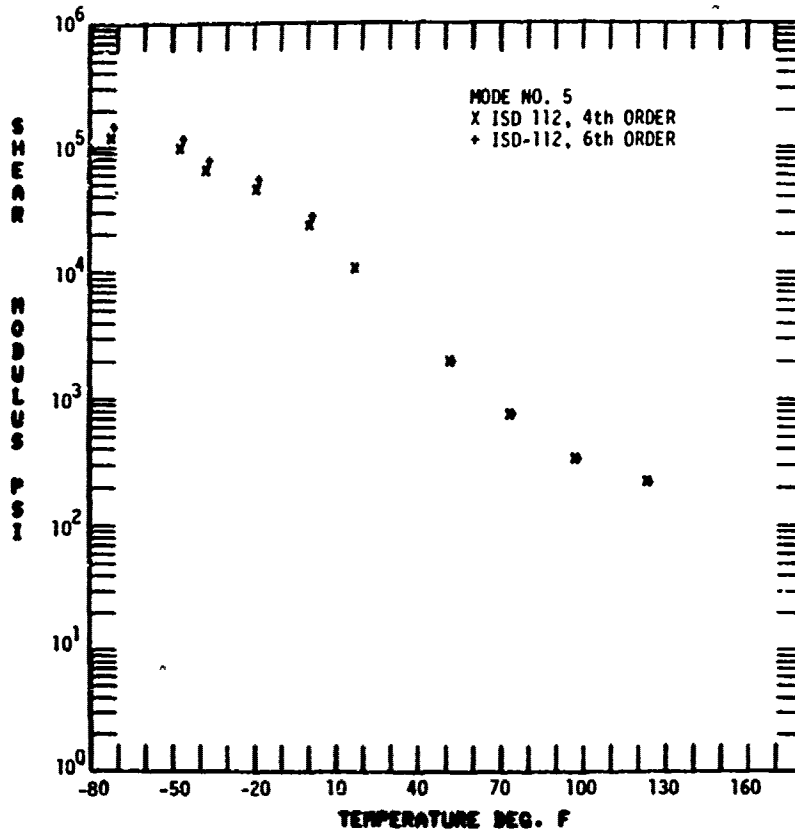


Figure 2.13. - Comparison of 4th and 6th order modulus in mode five.

2.3.2.3 Data Reduction Equations

The sample and the pivot arms, as shown in Figure 2.16, form a compound resonance system. Because of the low natural resonant frequency of the arm-pivot system, the resonant frequency is dependent almost entirely on the configuration and modulus of the sample. In oscillation, the sample is deformed via the geometry shown in Figure 2.19. In the equilibrium position before the oscillation, the sample, the centerlines of the two arms, and an imaginary line connecting the centers of the two flexure pivots form a rectangle represented by the broken lines. The deformation of the specimen is obtained from standard frame analysis except that the clamps for holding the specimen extend a distance D beyond the center line of each pivot arm toward the opposite arm.

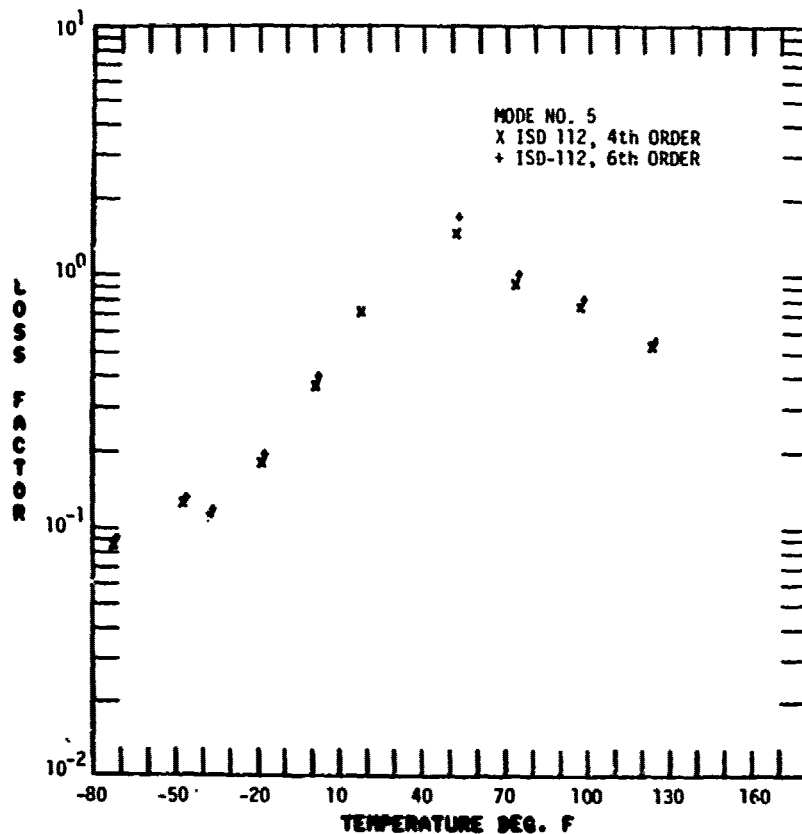


Figure 2-14. - Comparison of 4th and 6th order loss factor in mode five.

If the compound resonance system is deflected away from the equilibrium position to a new position (represented by the solid lines in Figure 2.19), the two ends of the sample remain parallel to each other and perpendicular to the arms. The center of gravity of the sample and the arms, however, translate to new positions. During each cycle the sample is subjected to an alternating flexural deformation. The solution for the dynamic equation of motion for the system [2.18] gives the relationship between Young's modulus and frequency:

$$E = \frac{(4\pi^2 f^2 J - K)}{2[\frac{L}{2} + D]^2} \left[\frac{L}{t} \right]^3, \quad (2.33)$$

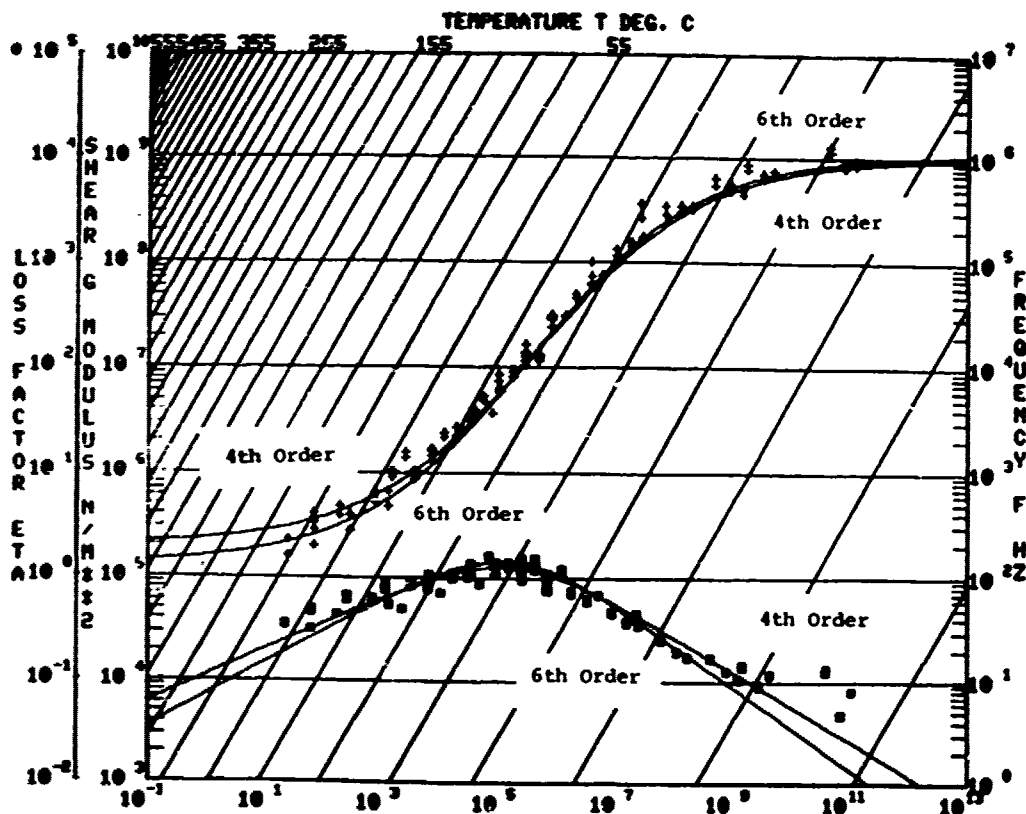


Figure 2.15. - Data comparison of 4th and 6th order in reduced temperature nomogram.

where E = Young's modulus (Pa), f = DMA frequency (Hz), J = Moment of inertia of arm ($\text{kg}\cdot\text{m}^2$), K = Spring constant of pivot ($\text{N}\cdot\text{m}/\text{rad}$), D = Clamping distance (m), W = Sample width (m), t = Sample thickness (m), and L = Sample length (m).

Sample loss factor is calculated from:

$$\eta = \frac{CV}{f^2} \quad (2.34)$$

where V = DMA Damping Signal (mV), f = DMA Resonant Frequency (Hz), and C = System Constant ($\sim 0.25 \text{ Hz}^2/\text{mV}$). See also the list of symbols in Table 2.4.

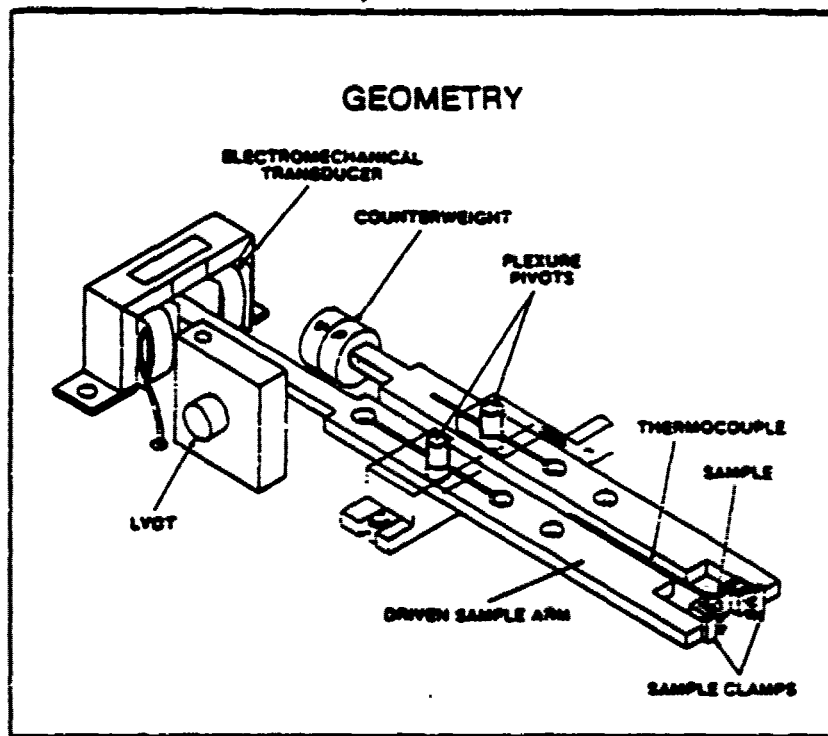


Figure 2.16. - Test geometry for DuPont 981 dynamic mechanical analyzer (DMA).

2.3.2.4 Error Sources

The principle error in DMA damping data is a thermal lag problem. Great care must be exercised not to sweep temperature at a rate of more than 3-6°F (2°C) per minute. Other errors to watch for are:

- Improper aspect ratio
- Improper clamping pressure or alignment
- Improper temperature read out due to poor thermocouple location

2.3.2.5 Advantages and Disadvantages

The advantages of this test procedure are:

- Small samples are required; this is particularly helpful for newly synthesized materials where only a few grams are available.

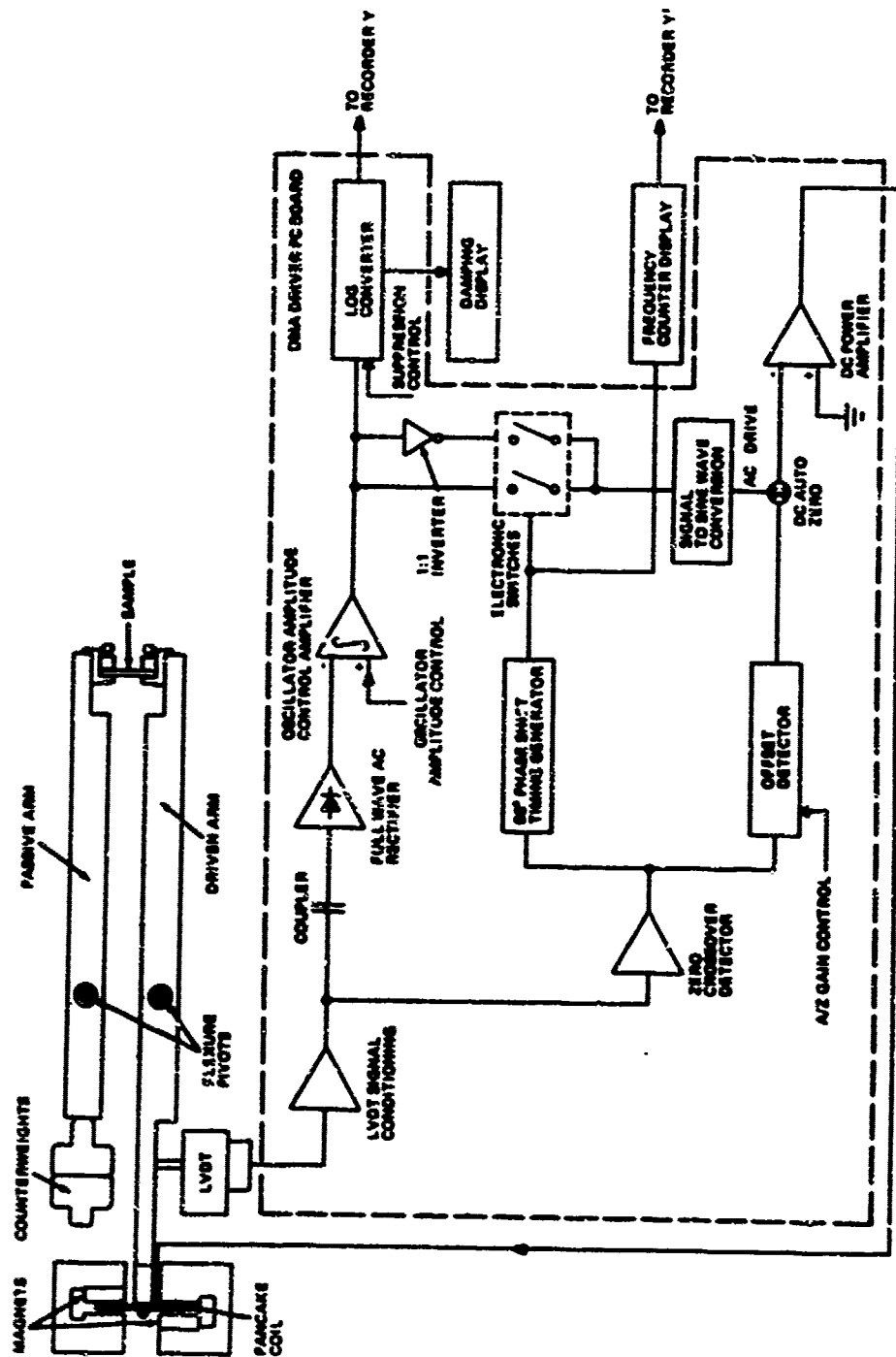


Figure 2.17. - 980 DMA electronics block diagram.

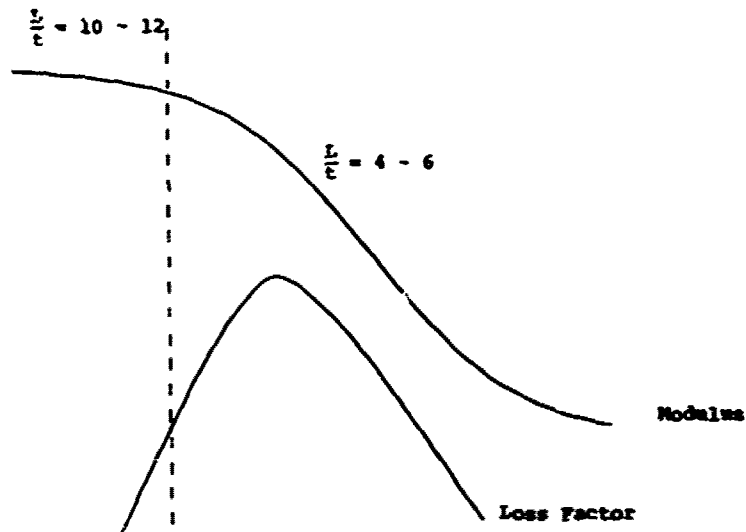
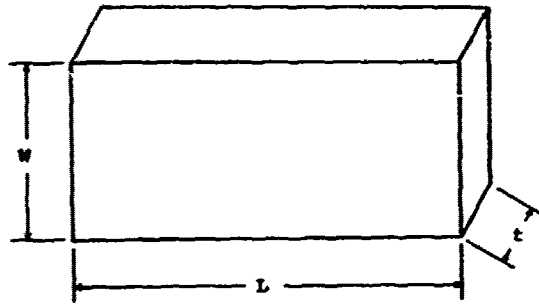


Figure 2.18. - Specimen dimensions and suggested $\frac{L}{t}$ values for the test regions.

- The samples do not need to be bonded to a metal beam.
- The temperature range scanned runs from -184°F (-120°C) to $+932^{\circ}\text{F}$ ($+500^{\circ}\text{C}$).
- Data are obtained quickly; the entire temperature range can be scanned in a few hours.
- The amplitude of oscillation can be varied so that linearity of viscoelastic response can be verified.
- Data are recorded continuously so that the modulus and loss factor are plotted as continuous analog functions of temperature.

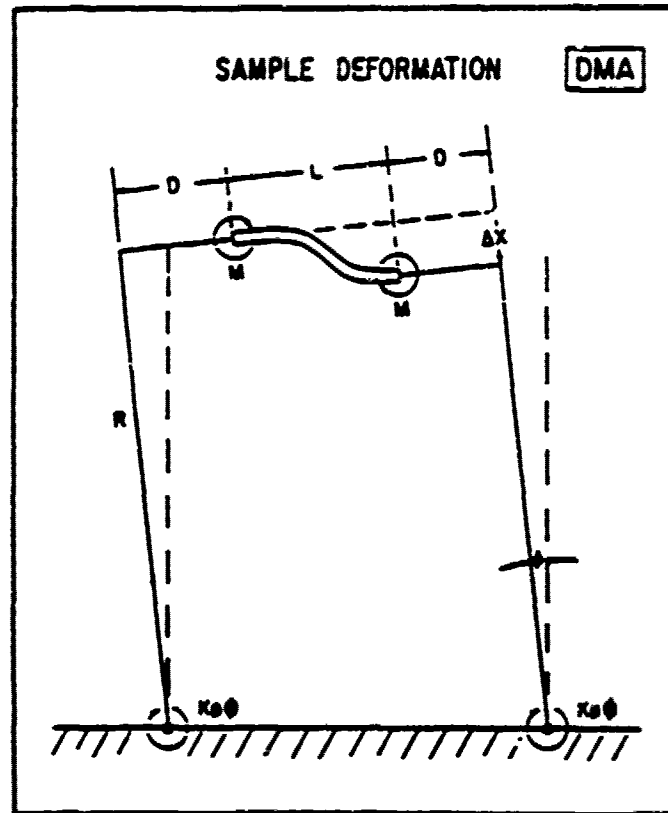


Figure 2.19. - Sample deformation in DuPont 981 DMA apparatus.

The disadvantages of the DMA are:

- Only a single resonant mode is measured.
- The frequency range of measurement is quite limited.
- The temperature accuracy of the data has been known to cause a problem.
- The DMA test does not accurately reflect the structural behavior of a polymer, since the polymer is not bonded directly to a metal substrate as it would be in application.

2.3.3 Resonant Test

The following paragraphs describe the resonant test for measuring the damping properties of materials. This set-up is perhaps the most simple procedure to implement.

TABLE 2.4. ABBREVIATIONS AND LIST OF SYMBOLS FOR SUBSECTION 2.3.2

SYMBOL	DEFINITION
DMA	Dynamic Mechanical Analyzer
LVDT	Linear Variable Differential Transformer
C	System constant ($\sim 0.25 \text{ Hz}^2/\text{mV}$)
D	Clamp-distance
E	Young's modulus
f	DMA resonant frequency
J	Moment of inertia of arm
K	Spring constant of pivot
L	Sample length
R	Arm length
t	Sample thickness
V	DMA damping signal
W	Sample width
Δx	Difference in sample end displacements
η_D	Damping material loss factor
ϕ	Arm rotation

2.3.3.1 The Test Set-Up

The instrumentation and test set-up for the resonant test are shown in Figure 2.20. The types of specimens used are illustrated in Figure 2.21.

A continuous sine sweep oscillator is used to power an electromagnetic shaker which excites the test specimens. An accelerometer monitors the response of the shaker head and another accelerometer monitors the response of the test specimen. The system incorporates a frequency counter, an oscilloscope, and a dB meter to make the required measurements. The measurements made are: 1) shaker acceleration, 2) test specimen acceleration, 3) resonant frequency, and 4) temperature. From these values complex Young's modulus $E(1 + i\eta_D)$ or shear modulus $G(1 + i\eta_D)$ can be calculated.

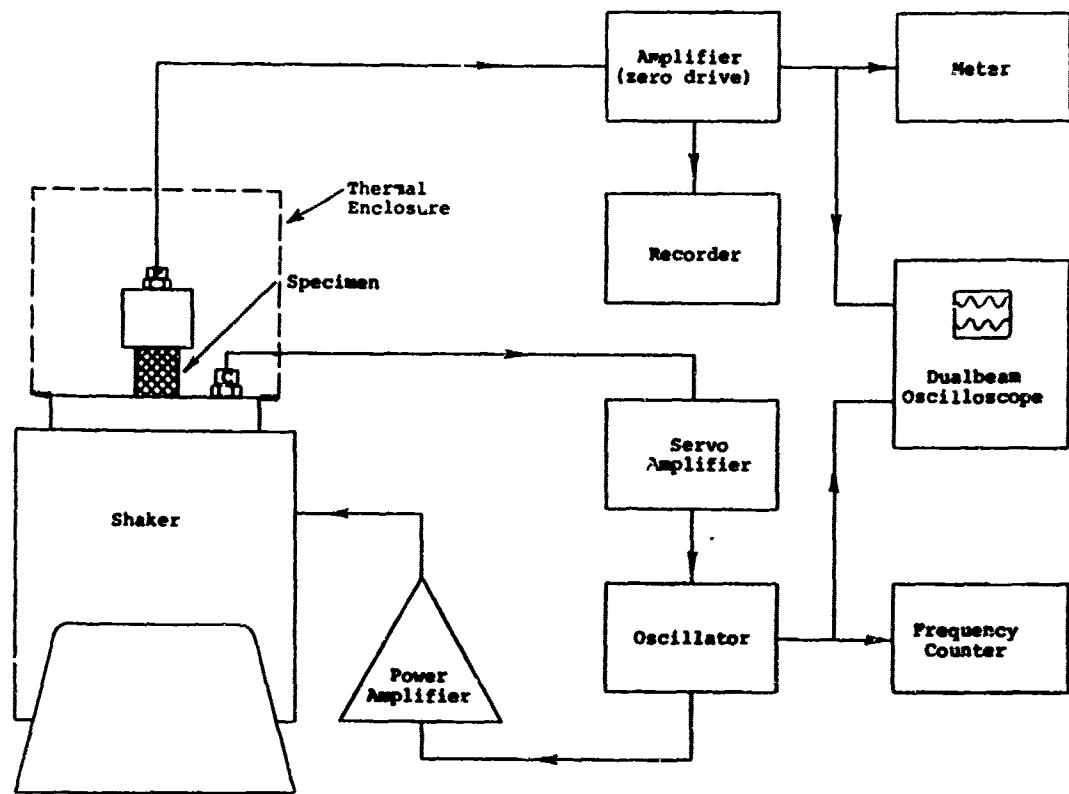


Figure 2.20. - Resonance test system.

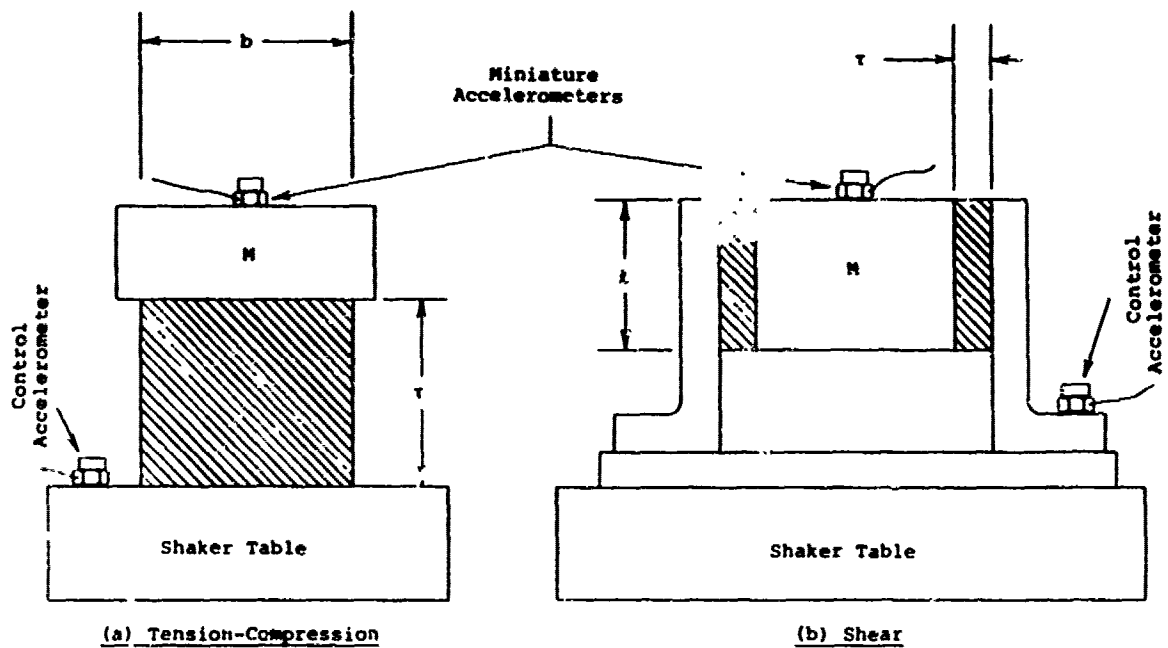


Figure 2.21. - Resonance test specimen.

2.3.3.2 Specimen Selection Criteria

The criteria on specimen selection are quite simple. The specimens should be designed to have a height to diameter ratio greater than two to avoid error resulting from nonuniform strain distribution in the specimen. Specimen design must also consider the possibility of a standing wave developing in the specimens. The data reduction equations are invalid for a test where standing waves occur.

2.3.3.3 Data Reduction Equations

The data reduction equations are:

$$\eta_D' \text{ and } \eta_D = (A^2 - 1)^{-\frac{1}{2}} \quad (2.35)$$

for the loss factor in both tests,

$$E_D = 4\pi^2 f_n^2 \tau (M + m_o/3) / S (1 + \beta S^2 / S_1^2) \quad (2.36)$$

for the tension - compression resonance test

$$G_D = 4\pi^2 f_n^2 \tau (M + m_o/3) (1 + \tau^2 / 36R^2) / S \quad (2.37)$$

and for the shear resonance test, respectively. The symbols are defined in Table 2.5. These equations are developed in Reference [2.19]. A modified version of the shear resonance test method is described in Reference [2.20].

2.3.3.4 Test Procedure

The test procedure is to place the test specimen on the shaker with a mass, M, attached to the polymer. A frequency sweep is conducted to locate the resonant frequency. Once the resonant frequency is established, the required measurements of shaker acceleration, specimen acceleration, temperature and frequency are made. Varying the input level allows measurement to be made at various strain levels. Varying M allows measurements to be

TABLE 2.5. LIST OF SYMBOLS FOR SUBSECTION 2.3.3

SYMBOL	DEFINITION
A	Ratio of resonant mass acceleration to shaker acceleration
E	Young's modulus of damping material (real)
f	Excitation frequency
f_n	Resonant frequency of mass
G	Shear modulus of damping material (real)
ℓ	Length of damping material (shear test)
M	Mass
m_D	Mass of viscoelastic material in resonance test
R	Radius of gyration of shear specimen about horizontal axis ($=R/\sqrt{12}$ for a rectangular section)
S	Load of carrying area of damping material (extension test) or total area of damping material in contact with resonant mass (shear test)
S_1	Wetted surface area (non-load bearing) of damping material (extensional test)
β	Shape factor
τ	Height of specimen (spring length) in extensional test or thickness of specimen in shear test
η_D	Damping material loss factor (extension)
η'_D	Damping material loss factor (shear)
ϕ	Phase angle between resonant mass and shaker table accelerations

made at various frequencies, and placing the system in an environmental chamber allows temperature variation.

Results of error analysis in Reference [2.21], supported by test results, indicate that damping measurements can be made with the resonant shear test method at frequencies on either side of the resonant frequency, but not below 0.7 times the resonant frequency for a material loss factor of 0.5. The below resonance error is greater for a lower material loss factor. It is, however, necessary to measure phase angle ϕ between the mass and the shaker table. The loss factor is obtained from

$$\eta'_D = \frac{\sin \phi}{A - \cos \phi} \quad (2.38)$$

and the resonant frequency f_n , for use in equation 2.37 from

$$f_n = f \left(\frac{A^2 - A \cos \phi}{A^2 - 2A \cos \phi + 1} \right)^{1/2} \quad (2.39)$$

where f is the excitation frequency. Test time is saved with this procedure, since exact tuning onto resonance is not required. It is especially useful when investigating the effect of strain level on the shear modulus and loss factor since the resonant frequency tends to change with increasing excitation level.

2.3.3.5 Error Sources

Errors in the resonant test system can result from:

- Poor specimen geometry
- Improper temperature measurement
- Poor signal-to-noise ratio of the accelerometers.

Care should be taken in measuring temperature of the specimen. If the system is allowed to dwell at resonance for a short period of time, there will be a temperature rise in the polymer material due to the energy it is dissipating. If not detected, this will result in a thermal shift of the data. This effect can be minimized by off resonance testing, making use of phase data.

2.3.3.6 Advantages and Disadvantages

The principle advantages of this test procedure are:

- A simple test to set-up and run
- Simple data reduction equations
- Capability to assess the effect of strain amplitudes

- Does not need to be tuned exactly to resonance if phase difference is measured

The disadvantages are:

- Mass must be changed to change frequency
- Frequency limited by the frequency limits of the shaker

2.3.4 The Rheovibron

The purpose of the Rheovibron is to measure the temperature dependence of the complex modulus of high polymers in both amorphous and crystalline states at a constant frequency. A simplified diagram of the equipment and concept are shown in Figure 2.22.

The basic principle behind the operation of the Rheovibron is the fact that a sinusoidal tensile strain applied on one end of a test sample in a viscoelastic state will generate a sinusoidal stress at the other end. There will be a phase difference between the two signals of δ . The Rheovibron is built to read $\text{Tan } \delta (= \eta_D)$ directly. The storage modulus can then be calculated from the values of the stress, strain, and δ .

The system equations are very straightforward.

$$\eta_D = \text{Tan } \delta = a_1 - a_2 \quad (2.40)$$

$$E' = E^* \text{ Cos } \delta \quad (2.41)$$

$$E^* = 2.0 \left(\frac{1}{(A)(D)} \times 10^9 \right) \text{ (L/S)} \quad (2.42)$$

The symbols are defined in Table 2.6.

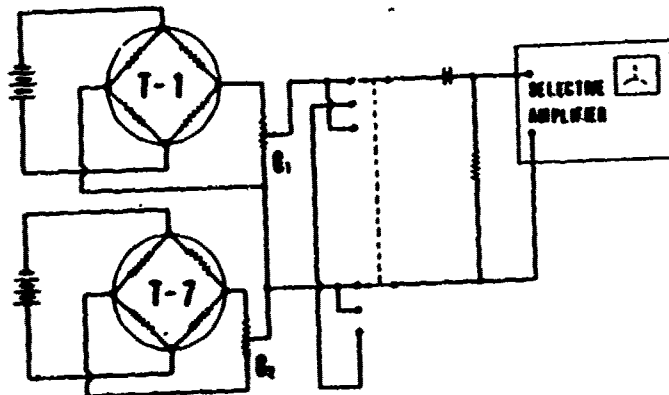
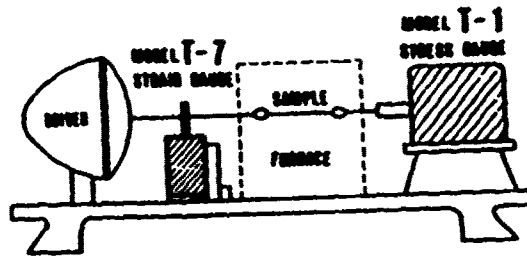


Figure 2.22. - A simplified diagram of the equipment and concept for Rheovibron.

TABLE 2.6. LIST OF SYMBOLS FOR SUBSECTION 2.3.4

SYMBOL	DEFINITION
A	Value defined from amplitude factor in measuring $\tan \delta$
D	Value of dynamic force dial in measuring $\tan \delta$
E'	Storage modulus
E*	Dynamic elastic modulus
L	Sample length
S	Sample section area
a_1	Stress transducer vector
a_2	Strain transducer vector

The test procedure consists of attaching both ends of the sample such as fiber or plastics film to two strain gages of unbonded type (Figure 2.22, one of which is a transducer of displacement (MODEL T.7) and the other of which is a transducer of generated force (MODEL T.1). After the absolute values of the electrical vectors transduced from force and displacement are adjusted to unity (full scale of meter), vector subtraction is made by changing the connection of the output circuit of two strain gages (Figure 2.22). By this operation the value of $\tan \delta$ can be read directly from the meter.

The dynamic modulus can be easily calculated from the readings of the dividers G_1 and G_2 in Figure 2.22.

The advantages of the system are:

- The data are obtained at a constant frequency
- The material loss factor can be read directly

The disadvantages are:

- The data are operator dependent
- The test is time consuming
- The test apparatus is temperature limited

Additional information for the Rheovibron is in Reference [2.22].

2.3.5 The Progressive Wave Technique

The progressive wave technique has been used widely to determine the dynamic properties of rubber components. The block diagram of the test equipment is shown in Figure 2.23. An electromagnetic shaker is used to drive a rubber test specimen at the bottom end while the top end is suspended under constant tension. A phonograph cartridge is used to measure the mechanical response of the vibrating strip. The shaker, test specimen, and cartridge are placed in an environmental chamber. A frequency synthesizer powers the shaker and controls the frequency of the test. The network analyzer measures the phase angle and amplitude differences between the reference output signal and the measured response.

The basic system equations are:

$$\eta_D = 2 \gamma / (1 - \gamma^2) \quad (2.43)$$

$$E' = \rho C^2 (1 - \gamma^2) / (1 + \gamma^2)^2 \quad (2.44)$$

$$\gamma = 6.59 A/P \quad (2.45)$$

where

C = 360 FL/P

A = amplitude

P = phase angle

C = sound speed

F = frequency

L = length

ρ = density

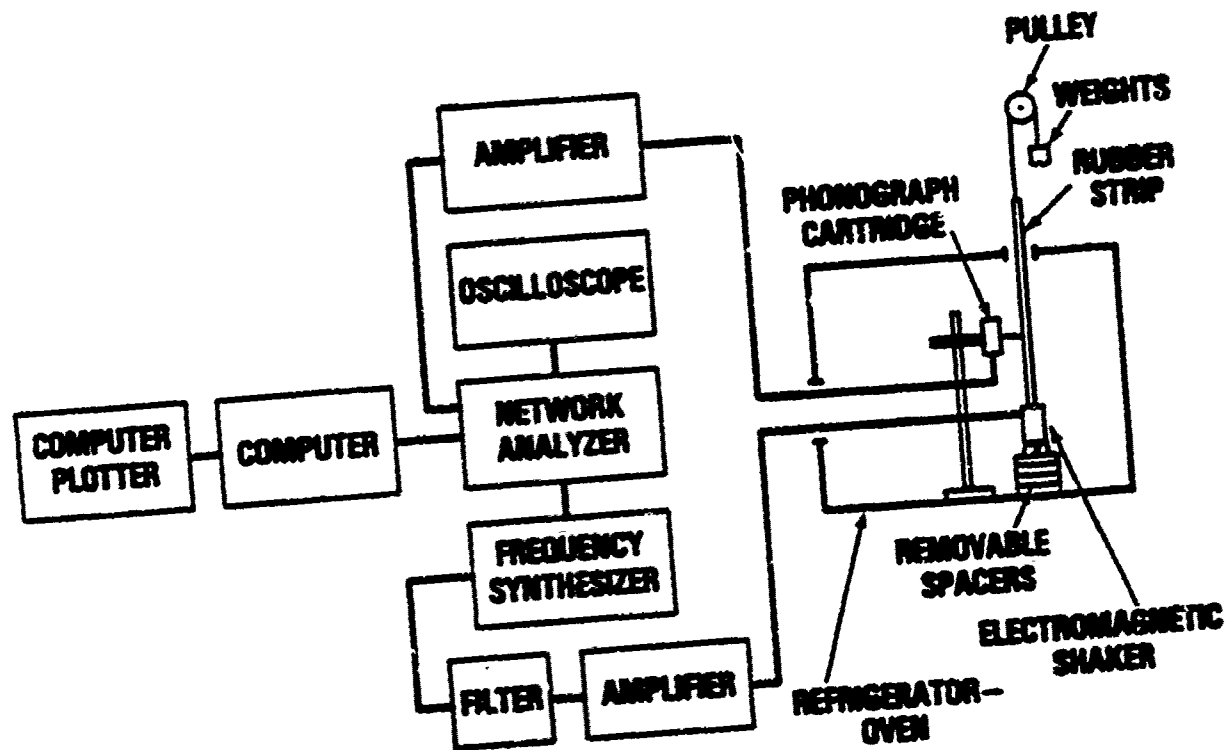


Figure 2.23. - Progressive wave apparatus.

The advantages of the system are:

- Data analysis is simple and can be automated
- Tests can be completed rapidly

The disadvantages are:

- Loss factor data not repeatable
- Difficult to measure materials with either low damping and high modulus or high damping and low modulus

Additional information on the progressive wave technique is given in Reference [2.23].

2.3.6 Impedance Testing

There have been many variations of the mechanical impedance technique suggested and used to measure viscoelastic damping material properties [2.24, 2.25, 2.26]. The general purpose of the impedance techniques is to measure the complex modulus properties of viscoelastic materials as a function of temperature and frequency while operating the system in a nonresonant condition.

One experimental set-up for impedance measurements is shown in Figure 2.24. The system consists of an electromagnetic shaker used as the driver, an impedance head to measure the force and acceleration at the driven end of the material sample, the material sample and a large mass. The dynamic signals from the impedance head should be measured with a digital Fast Fourier Analyzer.

The wave equation governing the motion of the material sample shown in Figure 2.24 can readily be solved, subject to the boundary conditions of a known, or measured, input displacement, U , at the point $X = 0$ and acceleration, \ddot{U} , equal to F/M at $X = L$ (the sample length), where F is the force. The ratio of displacement to force at the transducer end, i.e., the compliance, can be shown to be

$$\frac{U}{F}_{x=0} = \frac{h}{E_D^* A \alpha} \left(\frac{B \cos \alpha - \alpha \sin \alpha}{\alpha \cos \alpha + B \sin \alpha} \right) \quad (2.46)$$

where U is the displacement, F the force, $E_D^* = E_D (1 + i\eta_D)$ is the complex modulus, A and h are the cross-sectional area and length, respectively, of the material sample, E_D is the real part of the complex modulus, and

$$\alpha = (PW^2 E_D^*)^{1/2} h; \quad B = Ph A/M \quad (2.47)$$

where;

W is the frequency, P material density, M mass of attached weight.

Data obtained using this method compare well with data obtained from other procedures. The technique is useful for materials with loss factors

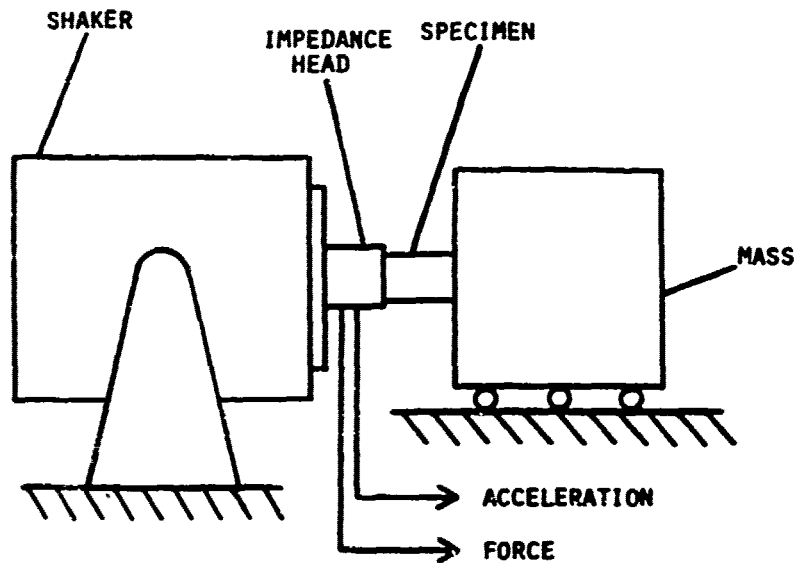


Figure 2.24. - Wave equation governing the motion of material sample.

varying from about 0.1 to 1.5 and Young's Moduli varying from about 200 to 200,000 psi (1.38×10^6 to 1.38×10^9 N/m²).

Accurate data are obtainable if care is taken in selecting specimen geometry, temperature measurements are exact and the strain level is in the linear region. Since the material is in a bulk form, energy dissipation can cause a temperature rise in the material.

The principle advantages of this procedure are the simple test set-up and the capability to assess various strain amplitudes.

2.3.7 3M Piezoelectric Oscillatory Rheometer

The 3M Piezoelectric Oscillatory Rheometer provides measurements of the shear properties of a wide variety of solid materials, such as filled and unfilled rubbers, psa's and molten plastics, under controlled conditions of temperature and frequency.

The Piezoelectric Oscillatory rheometer permits analysis of these materials under conditions of shear over a rigidity range of 10^5 to 10^8 N/m².

2.3.7.1 Test Set-up

The heart of the rheometer system is a shear generator shown in Figure 2.25. The sample under test is mounted between a driver plate which applies a shear force to the sample and parallel monitor plate. A monitor transducer converts the force that is transmitted through the test sample into a proportional voltage which is used in calculating the shear modulus of the sample.

Auxiliary equipment that is required to supply the driving power and temperature controls for the shear generator and to amplify and to measure the output from the monitor transducer is listed in Table 2.7. The entire test set-up is illustrated in Figure 2.26.

Specifications for the Piezoelectric Shear are:

- Test temperature range: -112°F (-80°C) to 266°F ($+130^{\circ}\text{C}$)
- Test frequency range of plus or minus one degree phase angle drift is as follows:

$$G' < 10^6 \text{ N/m}^2 \quad 30 \text{ to } 2000 \text{ Hertz}$$

$$G' > 10^6 \text{ N/m}^2 \quad 5 \text{ to } 2000 \text{ Hertz}$$

- Amplitude of Oscillation - approximately 600 angstroms at approximately 8.7 volts RMS stack driving voltage
- Test specimen size:
 - 0.197 in (5 mm) < length < 0.394 in (10 mm)
 - 0.075 in (2 mm) < width < 0.157 in (4 mm)
 - 0.010 in (0.26 mm) < thickness < 0.059 in (1.5 mm)
- Viscoelastic Range:
 - 7.25 psi ($5 \times 10^4 \text{ N/m}^2$) < G'' < $2.9 \times 10^4 \text{ psi}$ ($2 \times 10^8 \text{ N/m}^2$),
 - $0.04 < \tan \delta < 12.0$
- Precision:

Estimated to be plus or minus 5 percent for both G'' and $\tan \delta$

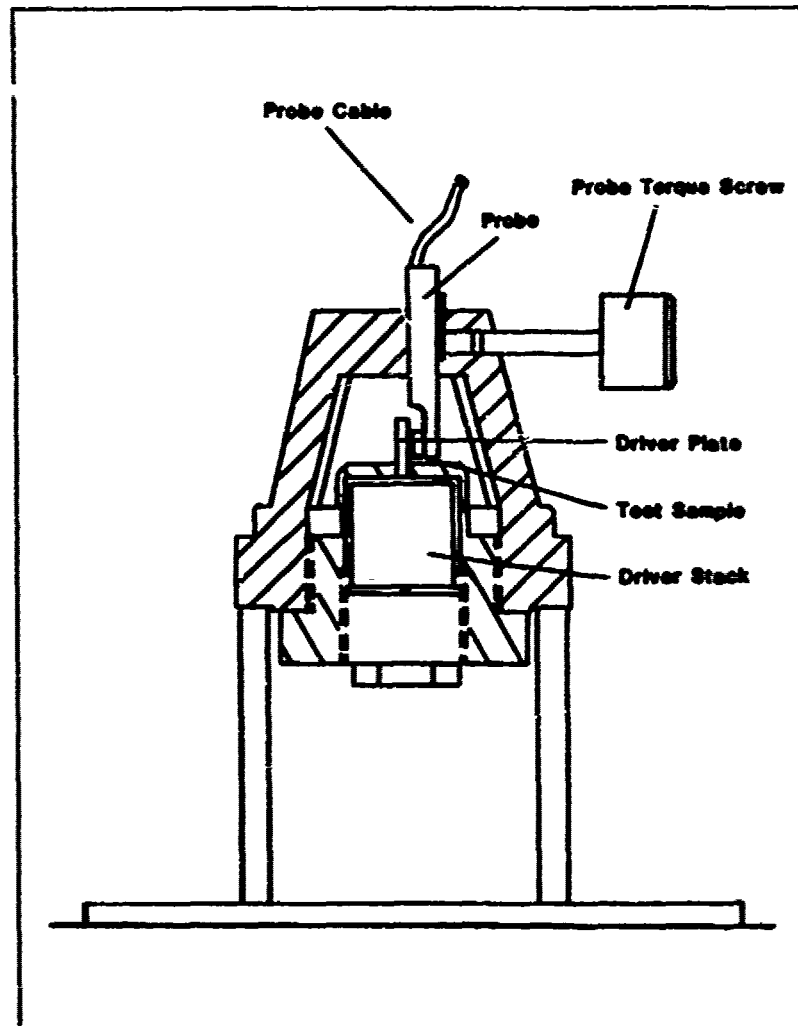


Figure 2.25. - Shear generator diagram.

- Minimum voltage output from high-impedance amplifier for adequate signal to noise ratio is approximately 20 millivolts
- Degree of parallelism of sample gap is as follows:

For sample thickness > 0.010 in (0.25 mm) gap parallelism is not critical (i.e. ± 0.0012 in (0.03 mm))

For sample thickness > 0.005 in (0.13 mm) gap parallelism is critical

In the above specifications, G' is the shear of storage modulus, G'' is the shear loss modulus and $\text{Tan } \delta$ is the loss factor.

TABLE 2.7. AUXILIARY EQUIPMENT REQUIREMENTS

Description	Type	Selection Characteristics
Oscillator - Power Amplifier	HP 3320B Frequency Synthesizer Krohn-hite 7500 Power Amplifier	
High Impedance Amplifier	Special model manufactured and designed by 3M specifically for use with the MELABS Rheometer	a. Frequency range 1 to 1000 Hz. b. Input impedance of 10^{10} ohms (or greater). c. Phase shift of less than 1 degree.
Phase Meter + Network Analyzer	Dranetz - Model 30E South Plainfield, New Jersey 07000 Dranetz - Model 305 PA-308SA Fluke Digital Voltmeter #6600A	a. Accurate to $\pm 0.05\%$ - 50 - 50 kHz, to $\pm 25\%$ - 50 kHz to 500 kHz b. Input level - 10 MV-300 VRMS decreasing to 50 V above 100 kHz (maximum 700 kHz) c. Input level - 10 MVRMS - 40 VRMS d. Frequency range - 2 Hz - 700 kHz.
Temperature Controller	Tenny Jr. Fluke 210DA Digital Thermometer	
Oscilloscope	Tektronix Type 561A	
Microprocessor	Intel Microprocessor Teletype Model 43 Terminal	

NOTE: The oscilloscope is not an integral part of the Rheometer system but is used for trouble-shooting purposes.

2.3.7.1 Sample Preparation and Test Procedure

Rubbers and plastics samples are tested in this instrument. The sample preparation is:

1. Loosen clamping screw for monitor plate
2. Place sample between probe and driver plates
3. Carefully tighten screw

The final sample thickness should be between 0.010 inch (0.254 mm) to 0.040 inch (1.016 mm)

The measurement procedure is:

1. Measure sample thickness to nearest 0.001 inches (0.025 mm) with a micrometer.
2. Place a suitable set of shims in instrument so that sample will be squeezed about 10 percent when clamped in place.

For example, if the sample thickness is 0.030 in. (0.762 mm) use a set of shims that will result in a final thickness of 0.027 in. (0.686 mm).

3. Cut a 0.394 in. (10 mm) by 0.276 in. (7 mm) (maximum) piece of rubber.
4. Place rubber piece between probe and driver plates.
5. Tighten clamping screw.
6. Close chamber door.
7. Allow temperature to come to equilibrium.
8. Take readings with digital voltmeter at desired frequencies.
9. Take readings with phasemeter at desired temperatures.
10. Repeat Steps 7 through 9 for all desired temperatures.

For oscilloscope measurements use amplitude, V , and phase angle, θ .

The shear moduli are obtained by the following equations:

$$G' = v^k 10^b S \cos \theta \quad (2.48)$$

$$G'' = v^k 10^b S \sin \theta \quad (2.49)$$

$$\tan \theta = G''/G' \quad (2.50)$$

where:

G' = shear storage modulus

G'' = shear loss modulus

$\text{Tan}\delta$ = loss factor

V = output voltage measured on DVM (volts)

k = slope of least squares log-log calibration

θ = phase angle measured on phasemeter

S = sample shape factor

The sample shape factor is given by

$$S = t_s^2 b/bt_o$$

where:

t_s = shim thickness (cm)

t_o = sample thickness (cm)

l = sample length (cm)

b = sample width (cm)

REFERENCES

- 2.1 Ungar, Eric C., "Fundamental Concepts of Structural Damping for Noise and Vibration Control," 10th International Congress on Acoustics-Satellite Symposium on Engineering for Noise Control, July 1980, pp. A1 to A8.
- 2.2 Jones, D.I.G. and Henderson, J.P., "Fundamentals of Damping Materials," University of Dayton Vibration Damping Short Course, Section 2.
- 2.3 Lazan, B.J., Damping of Materials and Members in Structural Mechanics, Pergamon Press, New York, 1968.
- 2.4 Crandall, S.H., "The Pole of Damping in Vibration Theory," J. Sound & Vibration, 11(1), pp. 3-18, 1970.
- 2.5 Henderson, J.P., "An Investigation of a Viscoelastic Damper.," M.S. Thesis, The Ohio State University, 1965.
- 2.6 Leaderman, H., "Elastic and Creep Properties of Filamentous Materials, Textile Foundation," Washington, D.C., 1943.
- 2.7 Tobolsky, A.V. and Andrews, R.D., J. Chem. Phys., 13, 3 (1945).
- 2.8 Ferry, J.D., J. Amer. Chem. Soc., 72, 3746 (1950).
- 2.9 Ferry, J.D., Viscoelastic Properties of Polymers, 2nd ed., Wiley, New York, 1970, Ch. 10.
- 2.10 Ferry, J.D., loc. cit., Ch. 11.
- 2.11 Jones, D.I.G., "A Reduced Temperature Nomogram for Characterization of Damping Material Behavior," Shock and Vibration Bulletin 48, Part 2, pp. 13-22, 1978 (D.O.D.).
- 2.12 Oberst, H., "Über die Dämpfung Biegeschwingungen Dünner Bleche Durch fest Haftende Beläge," Acoustics (Akustische Beiträge) 4, pp. 181-194, 1952.
- 2.13 Ross, D., Ungar, E.E. and Kerwin, E.M., Jr., "Damping of Plate Flexural Vibrations by Means of Viscoelastic Laminæ," Structural Damping, ed. J.E. Ruzicka, Proc. ASME Colloq., 1959.
- 2.14 King, C.S., Jr., "Computerized Processing and Graphic Representation of Viscoelastic Material Property Data," University of Dayton, May 1978, UDR-TR-78-49.
- 2.15 Jones D.I.G., "A Reduced-Temperature Nomogram for Characterization of Damped Material Behavior," Shock and Vibration Bulletin 48, 1978.

REFERENCES (Continued)

- 2.16 Rao, D.K., "Frequency and Loss Factors of Sandwich Beams Under Various Boundary Conditions," *Journal of Mechanical Engineering Science*, Vol. 20 No. 5, 1978.
- 2.17 Mead, D.J., "Comparison of Some Equations for the Flexural Vibration of Damped Sandwich Beams," *Journal of Sound and Vibration*, (1982), 83(3), pp. 363-377.
- 2.18 Dupont Instruments "Thermal Analysis Review: Dynamic Mechanical Analysis" product bulletin, 1978.
- 2.19 Jones, D.I.G., "Techniques for Measuring Damping Properties of Viscoelastic Layers," *Journal of Sound and Vibration*, (1972) 24(2), pp. 201-210.
- 2.20 Coote, C.T., "Measurement of Damping Properties of Silicone-Based Elastomers Over Wide Temperature Ranges," *Journal of Sound and Vibration*, (1972) 21(2), pp. 133-147.
- 2.21 Soovere, J., "High Modulus Graphite Fiber Constrained Layer Damping Treatment for Heavy Aerospace Structures," *Conference of Aerospace Polymeric Viscoelastic Damping Technology for the 1980's*, L.C. Rogers Ed., AFFDL-TM-78-78-F88, 1978.
- 2.22 Rheovibron Instruction Manual Model DDV-II, August 1969.
- 2.23 Madegosky, W.M., and Lee, G.F., "Automated Dynamic Young's Modulus and Loss Factor Measurements," *J. Acoust. Soc. Am.* 66 (2), August 1979.
- 2.24 Parsons, J., Yates, W. and Schiess, F., "The Measurement of Dynamic Properties of Materials Using a Transfer Impedance Technique," *Naval Ships Res. L. Ctr. Res. Develop. Rep.* 2981 (1969).
- 2.25 Edwards, J.L. and Hicks, D.R., "Mechanical Impedance Technique for Measurement of Dynamic Properties of Materials," *Proc. 1971 AFSC Sci. Eng. Symp.*, Dayton, Ohio, Vol. II (1971).
- 2.26 Miller, H.E., Jurgens, J.L. and Plunkett, R., "Measurement of Complex Shear Modulus of Thin Viscoelastic Layers," *U.S. Navy: Bureau of Ships*, Code 345, TR-65-4.

SECTION 3

FUNDAMENTALS OF DAMPING TREATMENT

The effects of temperature, frequency, and strain on the basic material properties of viscoelastic material have already been discussed. The usual design problem centers around the question of how to use a material with these properties to introduce significant amounts of damping into a structure having an undesirable resonant response characteristic. "Significant amount" of damping is the key phrase here, since it is the intention to increase the material damping in the structure to a level where it is much higher than the damping from all other sources, such as the damping from joints and acoustic radiation. To accomplish this, the damping material must be used in a configuration that will assure that sufficient energy is dissipated, D_s , compared with the elastic energy stored in the structure or, as already shown, the loss factor, η_s , of the structure or the system (equation 3.1) needs to be increased.

$$\eta_s = \frac{D_s}{2\pi U_s} \quad (3.1)$$

The elastic strain energy in a simple specimen (or structure) can be expressed as the area under the stress-strain curve integrated over the volume of the specimen.

$$U_s = \frac{1}{2} \int_{vol} \sigma \epsilon \, dv$$

or

$$U_s = \frac{1}{2} E \int_{vol} \epsilon^2 \, dv \quad (3.2)$$

E , σ and ϵ are the Young's modulus, the dynamic stress and the dynamic strain of the specimen (or structure), respectively. The integration is taken over volume, v , of the specimen. The symbols used in all equations up to the end of Section 3.1 are listed in Table 3.1.

TABLE 3.1. LIST OF SYMBOLS UP TO AND INCLUDING SECTION 3.1

\bar{A}	thickness ratio parameter (equation 3.67)
A', B'	terms defined by equations 3.98 and 3.99 respectively
a	length of plate
b	width of beam or plate
C_1, C_2, C_3, C_4	mode shape constants in equation 3.29
D	flexural stiffness $Eh^3/12(1 - \nu)$
D_c	flexural stiffness of coated plate
D_D, D_2	flexural stiffness of damping material and plate about the coated plate neutral axis
D_d	energy dissipated in damping material
D_s	energy dissipated in structure or system
E	Young's modulus of beam or plate material
E''	imaginary part of complex modulus
E'	real part of complex modulus
$E_c I_c$	Equation 3.78 ($= E_2 I_2 + E_D I_D$)
E_D	damping material Young's modulus
E_r	modulus ratio E_D/E_2 for beam
E_1, E_2, E_3	Young's modulus of beam material
e	modulus ratio E_D/E for plate
Fa_T	reduced frequency
f_{cmn}	natural frequency of coated plate
f_{cn}	natural frequency of coated beam
f_{mn}	natural frequency of bare plate
f_n, f_{2n}	natural frequency of bare beam
g	acceleration due to gravity
h	thickness of beam or plate
h_D	damping material thickness
h_{D1}, h_{D2}	two-layer damping material thickness
h_r	thickness ratio h_D/h_2

TABLE 3.1. LIST OF SYMBOLS UP TO AND INCLUDING SECTION 3.1 (Continued)

h_2	thickness of beam segment
I, I_1, I_3	second moment of area of beam about the bare beam neutral axis
I_D	second moment of area of damping material about the coated beam neutral axis
I_2	second moment of area of beam about the coated beam neutral axis
i	square root of minus one; as a subscript, beam segment i
J, \bar{n}	constants (characteristics of material)
k	wave number (equation 3.26)
k_n	wave number at resonance
L	length of beam
M_x	moment in beam
m, n	mode numbers
$P(x)$	transverse loading on beam
$P(x), P(x,t)$	pressure acting on beam
$P(x, y)$	pressure acting on plate
Q	ratio of resonant displacement to static displacement (amplification factor)
q	roots of the characteristic equation
R	radius of curvature
T, s	thickness related constants (figure 3.10)
T	temperature
T_0	reference temperature
U_s	elastic strain energy in structure or system
V	shear force in beam
v, vol	volume
$w, w(x)$	displacement of beam parallel to z axis
$w, w(x, y)$	displacement of plate parallel to z axis
$w_n(x)$	mode shape
w_n	modal intensity

TABLE 3.1. LIST OF SYMBOLS UP TO AND INCLUDING SECTION 3.1 (Continued)

w_1, w_2, w_3	beam segment displacements parallel to z axis
x, y, z	coordinate axes
α, β	lengths associated with partial coverage (Figure 3.12)
$\bar{\gamma}$	thickness ratio parameter (equation 3.74)
Δx	length of fiber along neutral axis in beam element
$\Delta x'$	length of fiber at a distance from neutral axis in deformed beam element
$\Delta \phi$	angle subtended by deformed beam element
ϵ	localized dynamic strain
ϵ_x	dynamic strain in beam or plate parallel to x axis
η	loss factor (ratio of imaginary part to real part of modulus E''/E')
η_D	damping material loss factor
$\eta_D E_D$	loss modulus of damping material
η_s	loss factor of the structure or system
λ_n	eigenvalue for the n^{th} mode
μ_D	mass per unit length of damping material
μ_s	mass per unit length of coated beam
μ, μ_1	mass per unit length of bare beam
ν	Poisson's ratio
ρ	density of beam or plate material
ρ_D	density of damping material
σ	dynamic stress
σ_x, σ_y	stress parallel to x and y axes
$\phi_n(x_i/L_i)$	mode shape function (equation (equation 3.85))
ω	circular frequency
ω_n, ω_{2n}	natural circular frequency of the bare beam
ω_{cn}	natural circular frequency of the coated beam

The energy dissipated in a specimen has been shown by Lazan [3.1] to be

$$D_s = \int_{vol} J \sigma^{\bar{n}} dv \quad (3.3)$$

where J and \bar{n} are constants characterizing the material. On considering the case of a "linear" viscoelastic material, where $\bar{n} = 2$, the energy dissipated in the viscoelastic material is

$$D_s = \pi \int_{vol} \eta_D E_D \epsilon^2 dv \quad (3.4)$$

where the integral is performed over the volume of the viscoelastic material.

The important point about Equation (3.4) is that the energy dissipated depends on two kinds of terms. The " $\eta_D E_D$ " term (loss modulus) in the integral is a damping material property term, and the " ϵ^2 " term is a measure of the localized dynamic strain, which is a function of the geometry of the damping treatment and the deformations associated with particular modes of vibration of the structure.

Thus the optimization of a damping treatment involves not only the proper choice of a damping material, but an understanding of the effects of the geometry of the damping treatment and the modal characteristics of the structure being damped.

In this section three basic categories of damping treatments, namely, free or unconstrained layers, constrained layers, and tuned damping devices are considered. Each of these damping concepts is discussed in detail starting with an emphasis on the qualitative concepts of damping of simple structures and the relationships between the material properties and the geometric arrangement of each type of damping treatment and ending with detailed beam and plate analysis. Finite element analysis procedures are contained in Section 5.

3.1 FREE LAYER DAMPING TREATMENTS

The free or unconstrained layer treatment is the simplest way of introducing damping into a sheet-metal type of structure. The treatment consists of a simple layer of an appropriate damping material bonded to those surfaces of the structure which are vibrating primarily in a bending type of mode, as shown in Figure 3.1. As these surfaces bend, the treatments on the surfaces are deformed cyclically in tension-compression and so dissipate energy. The simplest way to visualize this configuration is to think of polymeric coating on a sheet metal panel to reduce impact noise.

In analyzing these types of treatments it is usually appropriate to assume that normals to the undeformed neutral plane of the structure remain straight and normal to the deformed neutral plane. Or, in other words, we can ignore

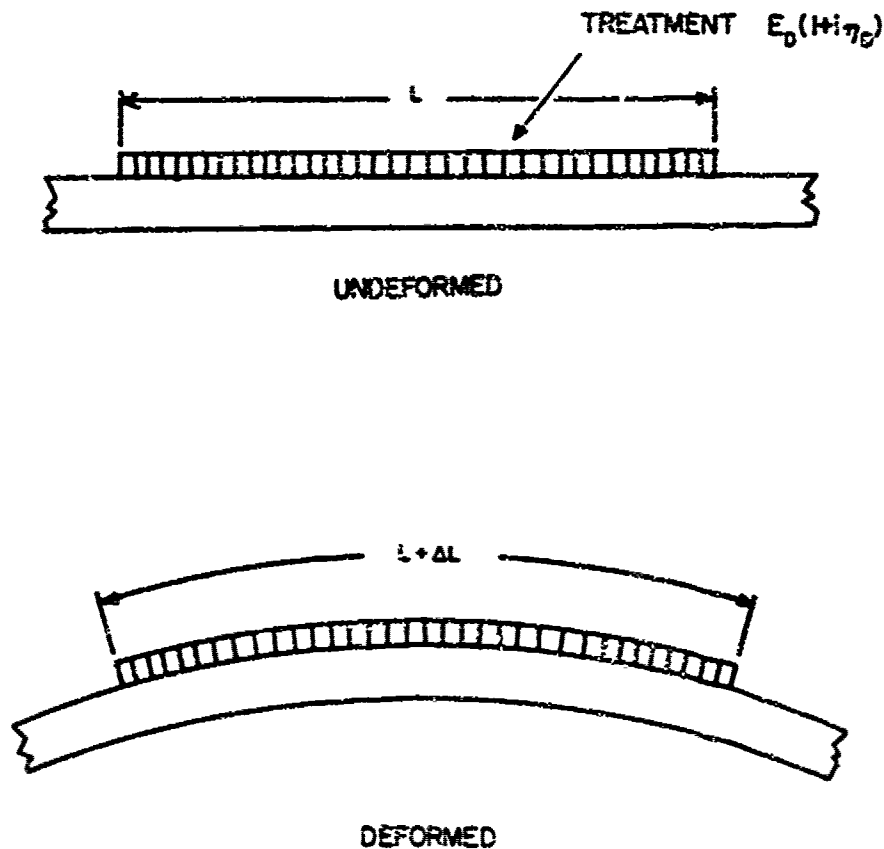


Figure 3.1. - Free layer damping treatments.

shear deformations and use simple beam or plate bending theory for layered structures [3.2]. This means that the localized strain will depend strictly upon the distance from the neutral bending plane and on the localized curvature of the structure caused by dynamic bending. Therefore, since the magnitudes of strain are generally limited by practical thickness restrictions, a designer must maximize D_s , as expressed in Equation 3.4, by selecting a damping material with maximum loss modulus ηE . Obviously good free layer damping materials are both stiff and exhibit high damping loss factors.

The typical variation of Young's modulus E and loss factor η with temperature, for a fixed frequency and strain level, is illustrated in Figure 3.2. The area between the dotted lines indicates the temperature range in which a material would be most useful as a free-layer damping treatment. For most viscoelastic polymers this temperature range is fairly narrow, on the order

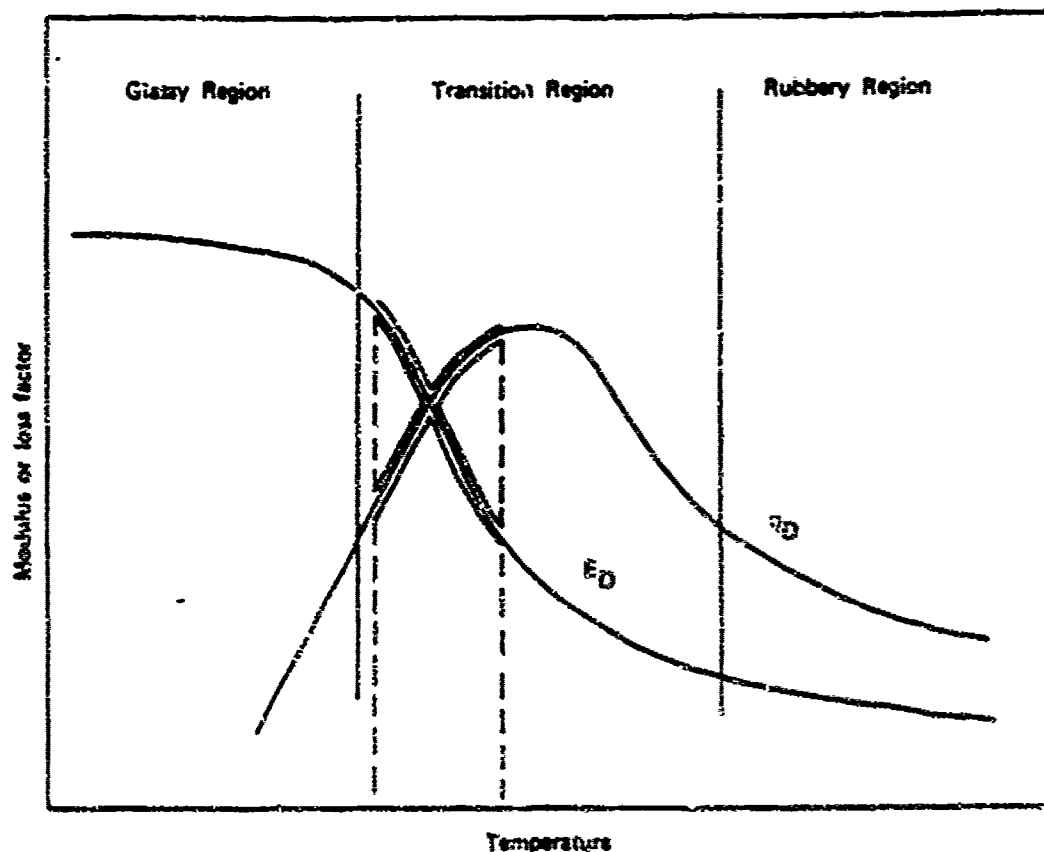


Figure 3.2. - Optimum temperature range for free layer treatment.

of about 50F° (28C°) or less. An obvious question is how can high damping be obtained from a single free layer over a fairly wide temperature range? This question has been partially resolved through the development of polymer blends that exhibit more than one glass transition temperature [3.3]. Figure 3.3 shows the variation of the real part of Young's modulus and loss factor for a polymer blend of three materials, compared with similar data on two commercially available damping materials with single transition temperatures. It can be seen that the polymer blend literally has three peaks in the loss factor-temperature curve. The composite loss factor, for a fixed thickness ratio for each of the three materials, is shown in Figure 3.4. If the design criterion is maximum system loss factor, then material A would be the designer's choice. If the minimum required system loss factor was 0.1,

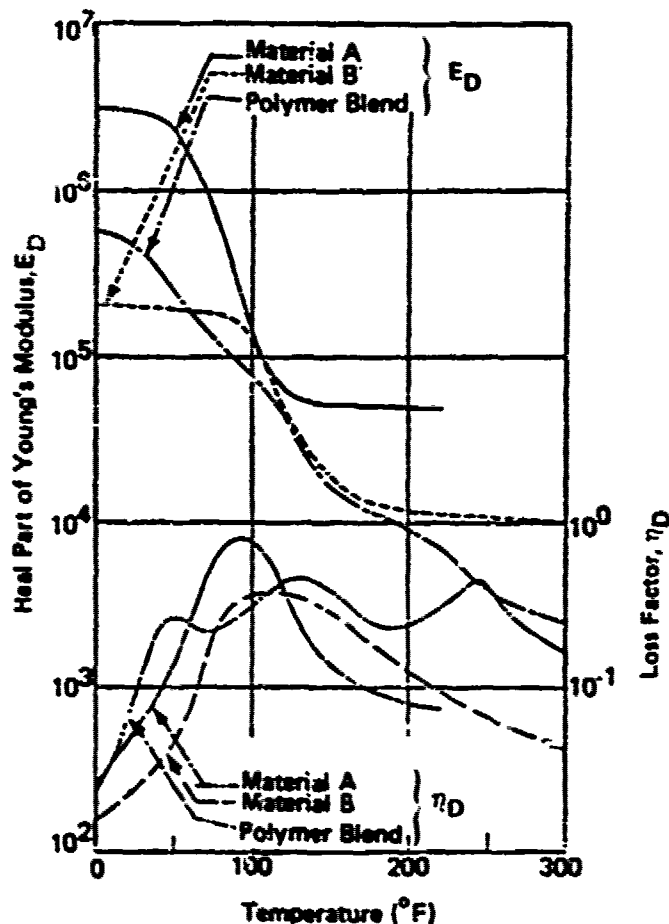


Figure 3.3. - Typical variation of material properties for a polymer blend of materials.

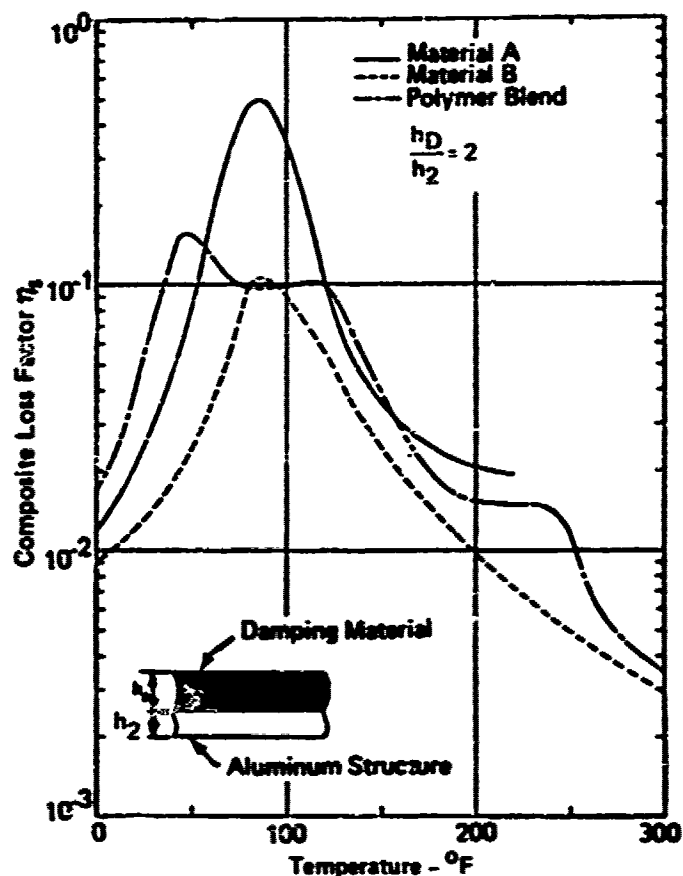


Figure 3.4. - Fixed thickness ratio (h_D/h_2) = 2 for single materials and a polymer blend.

material A would have an effective temperature range from 50°F (10°C) to 125°F (52°C), material B's effective temperature range from 80°F (27°C) to 95°F (35°C) while the polymer blend's range would be from 30°F (-1°C) to 125°F (52°C). If $\eta_s > .1$ and maximum temperature range were the design points, the poly-blend would be the proper choice.

Another way of broadening the temperature range, over which the maximum damping can be achieved by the unconstrained-layer damping treatment, is by applying multiple materials with peaks in the loss modulus occurring at different temperatures. For instance, if the temperature range for which the treatment has to operate is from 50°F (10°C) to 150°F (66°C), it may be necessary to select one material that has its optimum value around 70°F (27°C) and

another material that has its optimum value at approximately 120°F (49°C). Then it will be possible to place one material on each side of the structure and their performance can be combined to give wide temperature coverage. It is also possible to use a multiple layer system as shown in Figure 3.5. Provided that layer 1 (nearest to the structure) has the higher temperature of peak damping, the wide range damping performance shown will result.

Another method of optimizing a free layer damping treatment for a particular structure is to carefully select the locations of the damping treatment. Little, if any, benefit is gained from damping material located near nodes or locations of minimum bending moments. For instance, it has been shown [3.4] that for a fixed weight of damping material, applied to a simply supported beam vibrating in its fundamental mode, maximum damping occurs when the damping material is distributed over the center 40 percent of the beam.

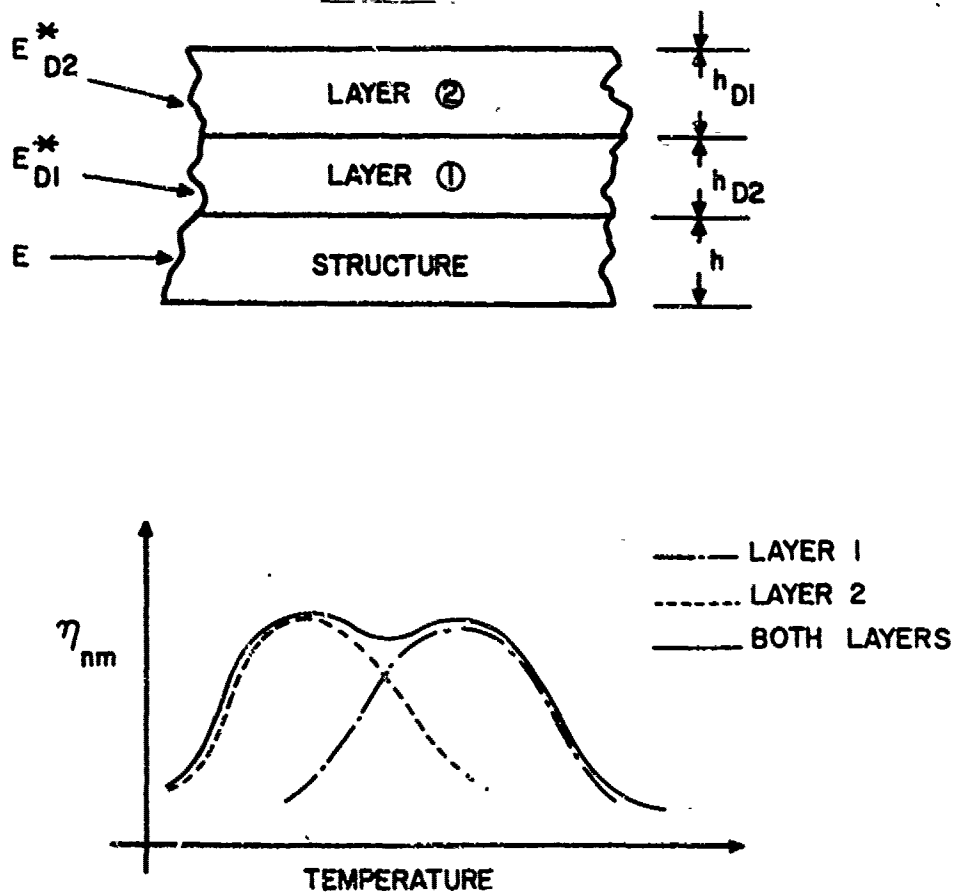


Figure 3.5. - Multiple layer broadening effect.

Although free layer damping treatments are often thought of in terms of elastomeric or rubberlike polymers, the concept is not limited to this class of materials. It has been shown that many porcelain enamel coatings have extremely high loss moduli at elevated temperatures [3.5 - 3.12]. As shown in Figure 3.6 a typical porcelain enamel exhibits material characteristics as a function of temperature similar to damping polymers. In fact, as illustrated in Figure 3.7, the peak loss modulus of some porcelain enamels is typically much higher and the temperature bandwidth wider than for even an efficient polymeric free-layer damping material. The implications of this point are quite significant when one considers the damping of high-temperature structures such as components of jet engines.

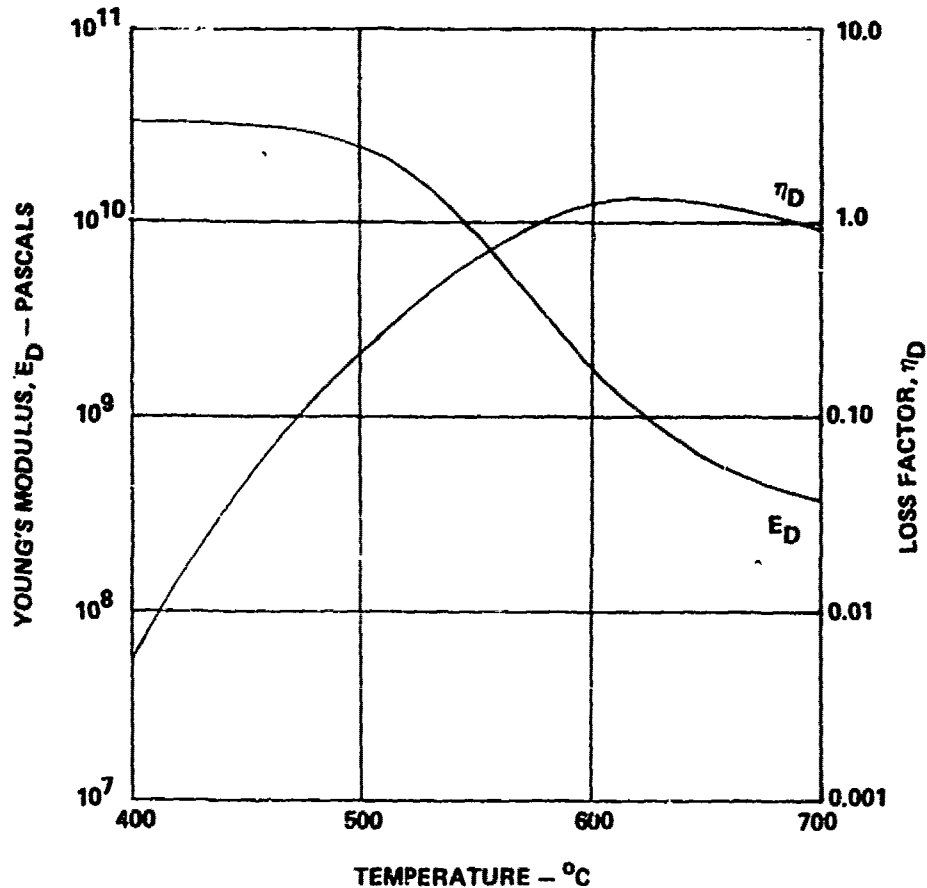


Figure 3.6. - Typical variation of material properties for Corning 8871 (Enamel) at 200 Hz.

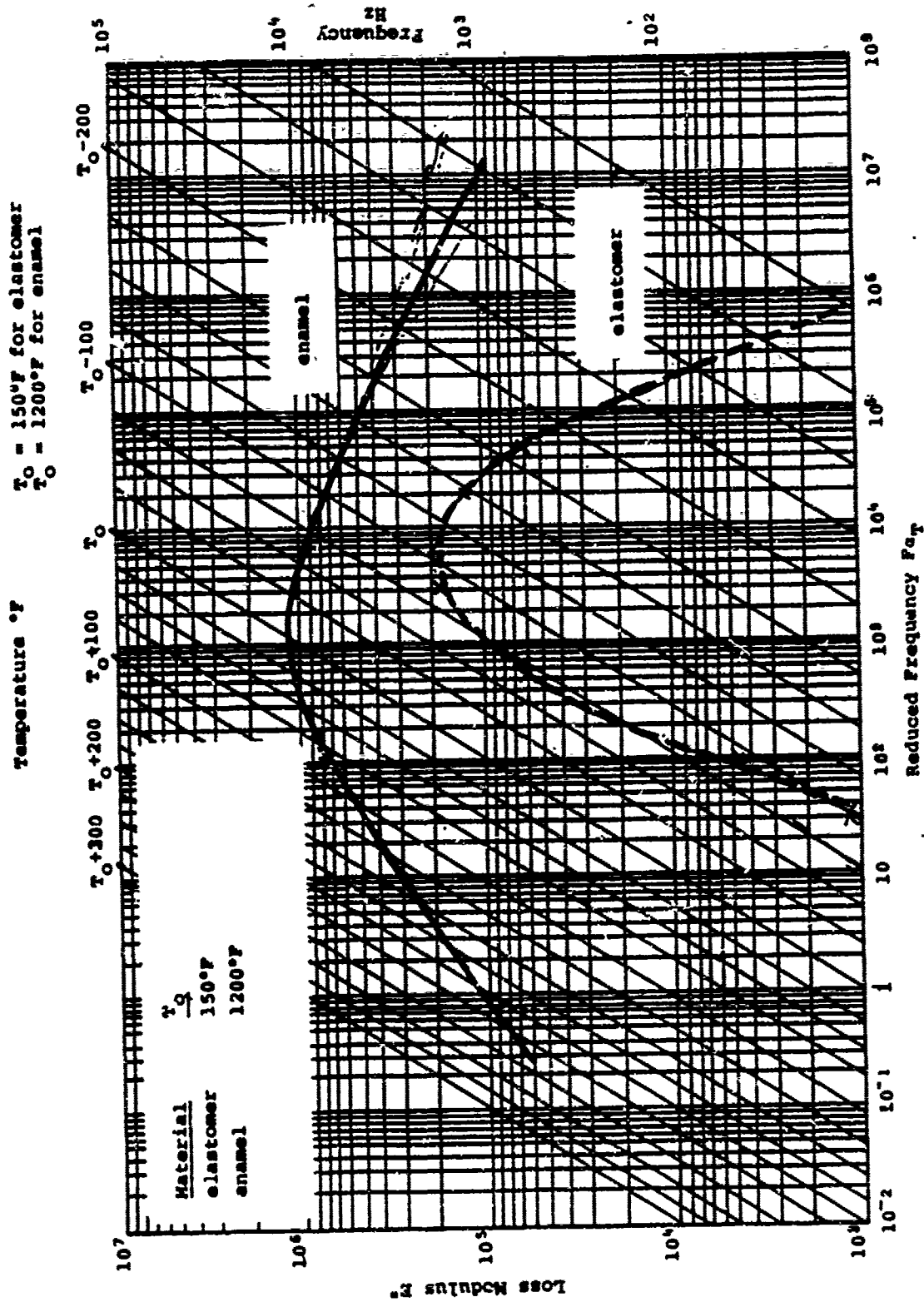


Figure 3.7. - Enamel elastomer loss modulus comparison.

Techniques and analytical methods to predict the effect of free-layer damping treatments on the vibrational response of beams, plates, and stiffened structures follows.

3.1.1 Euler-Bernoulli Beam Equations for Free Layer Damping

To date, a majority of the damping analyses have been based on 4th order beam theory. In the following paragraphs, a review of the basis of this theory is presented.

3.1.1.1 Beam Vibration

The first system to be analyzed will be a simple beam. Structures such as automobile frames and columns in buildings can be analyzed as beam structures. In the pure bending analysis of a long-slender beam, plane sections are assumed to remain plane, shear deformation and rotary inertia are neglected and the deformations are small. Many engineering structures meet these assumptions. These assumptions also lead to equations which are fairly easy to solve and, at the same time, give very good insight into the dynamic behavior of the structure.

Consider an element of a deformed beam as shown in Figure 3.8 where Δx is the length of the neutral axis. At a distance z above the neutral axis, the length of the element is $\Delta x'$. Therefore

$$\Delta\phi = \frac{\Delta x}{R} = \frac{\Delta x'}{R-z} \quad (3.5)$$

$$\Delta x' = \frac{R-z}{R} \Delta x$$

On rearranging equation 3.5

$$\frac{\Delta x' - \Delta x}{\Delta x} = -\frac{z}{R} \quad (3.6)$$

By definition, the strain is given by

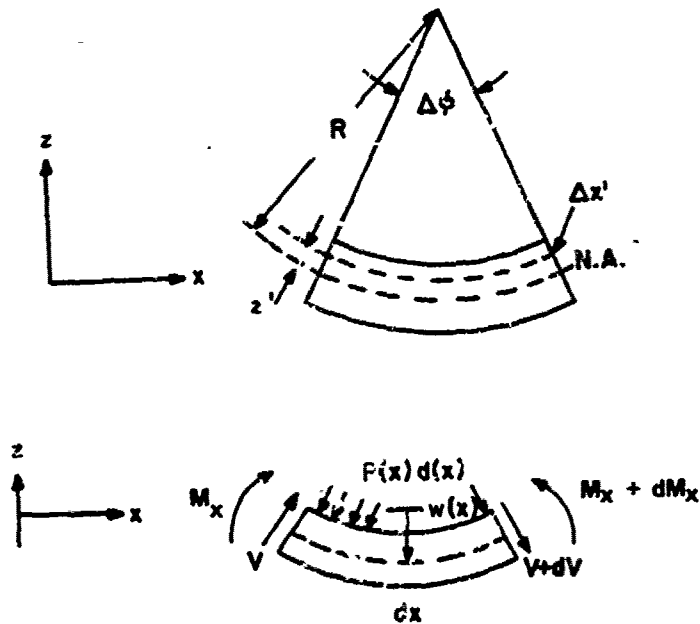


Figure 3.8. - Element of a deformed beam.

$$\epsilon_x = \frac{\Delta x' - \Delta x}{\Delta x} \quad (3.7)$$

Therefore, from equations 3.6 and 3.7,

$$\epsilon_x = -\frac{z}{R} \quad (3.8)$$

Using Hooke's law,

$$\epsilon_x = \frac{\sigma_x}{E} \quad (3.9)$$

And on substituting for ϵ_x , the normal stress becomes

$$\sigma_x = -E \frac{z}{R} \quad (3.10)$$

Consider, now, the forces acting on an element of the beam. It can be shown from analytical geometry that

$$\frac{1}{R} = \frac{d^2 w / dx^2}{[1 + (\frac{dw}{dx})^2]^{3/2}} \quad (3.11)$$

where w is the displacement of the beam from the neutral axis. Since small deformations are assumed,

$$\left(\frac{dw}{dx}\right)^2 \ll 1 \quad (3.12)$$

and equation 3.11 can be approximated by

$$\frac{1}{R} = \frac{d^2 w}{dx^2} \quad (3.13)$$

The moment acting on the section, of cross sectional area A , is

$$\begin{aligned} M_x &= - \iint \sigma_x z dA \\ &= - \iint \frac{Ez}{R} dA = \frac{E}{R} \iint z^2 dA = \frac{EI}{R} \end{aligned} \quad (3.14)$$

Substituting for $\frac{1}{R}$

$$M_x = EI \frac{d^2 w}{dx^2} \quad (3.15)$$

Summing forces in the vertical direction and moments about the right hand side,

$$dV + P(x)dx = 0 \quad (3.16)$$

$$dM_x - V d(x) + 1/2 P(x) (dx)^2 = 0 \quad (3.17)$$

where $P(x)$, the sum of the inertia forces and the external loads, is given by

$$P(x) = -\frac{\mu}{g} \frac{d^2 w}{dt^2} + p(x,t) \quad (3.18)$$

In the above equation, $p(x,t)$ is the pressure acting on the elemental beam, g is the acceleration due to gravity, and μ is the mass per unit length given by

$$\mu = \rho b h \quad (3.19)$$

where ρ is the density, b is the width and h is the thickness of the beam. Equation 3.16 becomes

$$\frac{dV}{dx} = -P(x) \quad (3.20)$$

On differentiating with respect to x , and ignoring second order terms, equation 3.17 yields the relationship

$$\frac{dV}{dx} = \frac{d^2 M}{dx^2} \quad (3.21)$$

On using this relationship together with those in equation 3.15, 3.18 and 3.20, the following equation of motion is obtained

$$EI \frac{d^4 w}{dx^4} + \frac{\mu}{g} \frac{d^2 w}{dt^2} = p(x,t) \quad (3.22)$$

It is common practice to first obtain a solution to the free vibration problem with

$$p(x,t) = 0 \quad (3.23)$$

The displacement w is a function of the variables x and t . On assuming a separation of variables of the form

$$w = w(x)e^{i\omega t} \quad (3.24)$$

The equation of motion becomes

$$\frac{d^4 w}{dx^4} - k^4 w = 0 \quad (3.25)$$

where

$$k^4 = \frac{\mu \omega^2}{EIg} \quad (3.26)$$

The solution to equation 3.25 is of the form

$$w = w_0 e^{qt} \quad (3.27)$$

which leads to the following equation for the roots

$$q^4 - k^4 = 0$$

or

$$q = \pm k, \pm ik$$

(3.28)

The general solution may be written as

$$w = C_1 \sin kx + C_2 \cos kx + C_3 \cosh kx + C_4 \sinh kx \quad (3.29)$$

Four boundary conditions are required to evaluate the four constants in the above equation. These are obtained from the following

$$\text{Clamped: } w = \frac{dw}{dx} = 0 \quad (3.30)$$

$$\text{Simply Supported: } w = \frac{d^2 w}{dx^2} = 0 \quad (3.31)$$

$$\text{Free: } \frac{d^2 w}{dx^2} = \frac{d^3 w}{dx^3} = 0 \quad (3.32)$$

For a simply supported beam, the boundary conditions lead to the following equation for the eigenvalues

$$\sin kL = 0 \quad (3.33)$$

from which

$$kL = \pi, 2\pi, 3\pi, \dots \quad (3.34)$$

or, for the m th mode;

$$k_m = \frac{m\pi}{L} \quad m = 1, 2, 3, \dots \quad (3.35)$$

From equation 3.26 the natural circular frequency ω_n is given by

$$\omega_n = k_m^2 \sqrt{\frac{EIg}{\mu}} \quad (3.36)$$

$$= \left(\frac{m\pi}{L}\right)^2 \sqrt{\frac{EIg}{\mu}}$$

and the natural frequency f_n by

$$f_n = \frac{\omega_n}{2\pi} = \frac{\pi}{2} \left(\frac{m}{L}\right)^2 \sqrt{\frac{EIg}{\mu}} \quad (3.37)$$

The simply supported beam mode shape, for the m th mode, is

$$w_m(x) = w_m \sin \frac{m\pi x}{L} \quad (3.38)$$

For a cantilever beam the boundary conditions lead to the eigenvalue equation

$$\cos kL \cdot \cosh kL = -1 \quad (3.39)$$

The general expression for the natural frequency of a beam, including the cantilever beam, is

$$f_n = \frac{\lambda_m^2}{2\pi L^2} \sqrt{\frac{EI}{\mu}} \quad (3.40)$$

where

$$\lambda_m = k_m L \quad (3.41)$$

The roots of equation 3.39 are listed in Table 3.2 for the first eight modes, of the cantilever beam. The corresponding cantilever beam mode shape is

TABLE 3.2. ROOTS OF CANTILEVER BEAM

$k_n L$	kL	$(kL)^2$
$k_1 L$	1.8751041	3.5160153
$k_2 L$	4.6940911	22.034492
$k_3 L$	7.8547574	61.697214
$k_4 L$	10.995541	120.90192
$k_5 L$	14.137168	199.85953
$k_6 L$	17.279760	298.55553
$k_7 L$	20.520352	416.99079
$k_8 L$	23.561945	555.16525

$$w_{\text{B}}(x) = w_{\text{B}} \left[\cos kx - \cosh kx + \frac{\sin kL - \sinh kL}{\cos kL - \cosh kL} (\sin kx - \sinh kx) \right] \quad (3.42)$$

On assuming harmonic motion, and harmonic excitation of the form

$$p(x,t) = p(x)e^{i\omega t}$$

equation 3.22 becomes

$$EI \frac{d^4 w}{dx^4} + \frac{\mu}{8} \omega^2 w = p(x) \quad (3.43)$$

which is the Euler-Bernoulli equation of motion for a vibrating beam.

3.1.1.2 Beam Vibration with One-Sided Coating

If the beam is made of a material whose modulus is complex, then

$$E = E'(1+i\eta) \quad (3.44)$$

where η is the ratio of the imaginary to the real part of the modulus, given by

$$\eta = \frac{E''}{E'} \quad (3.45)$$

The parameter η is the material damping or the loss factor. On substituting the complex modulus into the Euler-Bernoulli equation (equation 3.43), it becomes

$$EI(1+i\eta) \frac{d^4 w}{dx^4} - \frac{\mu}{8} \omega^2 w = p(x) \quad (3.46)$$

Now consider a beam that is coated on one side with a layer of viscoelastic material as illustrated in Figure 3.9. An infinitesimal element

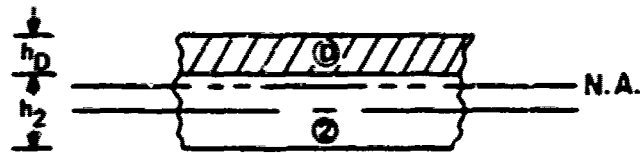


Figure 3.9. - Beam coated with viscoelastic material.

in the deformed coating is illustrated in Figure 3.10. A fiber in coating,

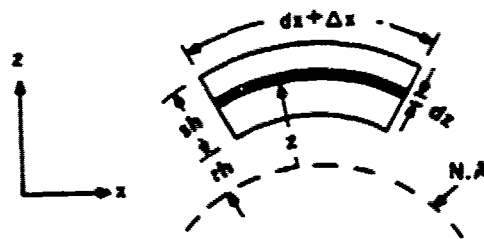


Figure 3.10. - Infinitesimal element of deformed coating.

at a distance, z , from the neutral axis, has a thickness, dz , and an undeformed length, dx . During deformation, this fiber elongates by a distance, Δx . Therefore, the strain is

$$\epsilon_x = \frac{\Delta x}{dx} = -z \frac{d^2 w}{dx^2} \quad (3-47)$$

Following equations 3.1, 3.2 and 3.45, the energy dissipated per cycle in the length of the fiber is

$$\delta D_d = \pi b E_D'' (\epsilon_x)^2 dx dz \quad (3-48)$$

where

$$E_D'' = \gamma_D E_D \quad (3-49)$$

The total energy dissipated in the viscoelastic coating over one cycle is

$$D_d = \pi b E_D'' \int_{rh}^{(r+s)h} z^2 dz \int_0^L \left(\frac{d^2 w}{dx^2} \right)^2 dx \quad (3.50)$$

Alternatively,

$$D_d = \pi E_D'' I_D \int_0^L \left(\frac{d^2 w}{dx^2} \right)^2 dx \quad (3.51)$$

where I_D is the second moment of area about the coated beam neutral axis given by

$$I_D = b \int_{rh}^{(r+s)h} z^2 dz \quad (3.52)$$

The maximum strain energy stored in a beam is

$$U_s = \frac{1}{2} \int_{\text{length}} \left(\frac{d^2 w}{dx^2} \right)^2 E I dx \quad (3.53)$$

Therefore, the maximum strain energy stored in the coated beam is

$$U_s = \frac{1}{2} \int_0^L E_2 I_2 \left(\frac{d^2 w}{dx^2} \right)^2 dx + \frac{1}{2} \int_0^L E_D I_D \left(\frac{d^2 w}{dx^2} \right)^2 dx \quad (3.54)$$

Since only the viscoelastic coating is assumed to provide the damping in the beam, then

$$D_s = D_d \quad (3.55)$$

in equation 3.1 and the system loss factor η_s given by equation 3.1 becomes

$$\eta_s = \frac{E_D'' I_D \int_0^L \left(\frac{d^2 w}{dx^2} \right)^2 dx}{E_2 I_2 \int_0^L \left(\frac{d^2 w}{dx^2} \right)^2 dx + E_D I_D \int_0^L \left(\frac{d^2 w}{dx^2} \right)^2 dx} \quad (3.56)$$

for a uniform thickness beam with a uniform thickness coating. This equation reduces to

$$\eta_s = \frac{\eta_D E_D I_D}{E_2 I_2 + E_D I_D} \quad (3.57)$$

Making the same assumptions as for the Euler-Bernoulli beam (plane sections remain plane, neglecting rotating inertia and assuming small deformations), and using the derivation for the single material, it can be shown that

$$(E_2 I_2 + E_D I_D) \frac{d^4 w}{dx^4} - \frac{1}{8} (\mu_2 + \mu_D) \omega^2 w = p(x) \quad (3.58)$$

where μ_2 and μ_D are the beam and the viscoelastic coating mass per unit lengths, respectively. On assuming that only E_D is complex, equation 3.58 becomes

$$(E_2 I_2 + E_D I_D) \left(1 + i \eta_D \frac{E_D I_D}{E_2 I_2 + E_D I_D} \right) \frac{d^4 w}{dx^4} - \frac{1}{8} (\mu_2 + \mu_D) \omega^2 w = p(x) \quad (3.59)$$

This equation is the same as equation 3.25 if

$$EI = E_2 I_2 + E_D I_D = E_c I_c \quad (3.60)$$

and $\eta = \eta_s$ given by equation 3.57. The ratio of the damped beam loss factor to the loss factor of the viscoelastic damping material is

$$\frac{\eta_s}{\eta_D} = \frac{E_D I_D}{E_2 I_2 + E_D I_D} \quad (3.61)$$

The resonant circular frequencies ω_{cm} and ω_{2m} for the m th mode of the coated and uncoated beam respectively, are related by

$$\mu_c \omega_{cm}^2 L^4 / E_c I_c g = \mu_2 \omega_{2m}^2 L^4 / E_2 I_2 g = \lambda_m^4 \quad (3.62)$$

where λ_m is the eigenvalue for the m th mode and is a constant. The value of λ_m is determined by the mode and boundary conditions of the beam. From equations 3.60 and 3.62, the ratio of the damped beam to the undamped beam natural circular frequencies for the n th mode is given by

$$\left(\frac{\omega_{cm}}{\omega_{2m}} \right)^2 = \frac{\mu_2 E_c I_c}{\mu_c E_2 I_2} = \frac{\mu_2 (E_2 I_2 + E_D I_D)}{\mu_c E_2 I_2} \quad (3.63)$$

$$\frac{f_{cm}}{f_{2m}} = \frac{\mu_1}{\mu_2} \left[1 + \frac{E_D I_D}{E_2 I_2} \right]$$

where f_{sm} and f_{1m} are respective natural frequencies in Hz. In the above equations

$$I_2 = \frac{h_2^3}{24} \left[\frac{\left[1 - \left(\frac{h_D}{h_2}\right)^2 \frac{E_D}{E_2}\right]^3 + \left[1 + \left(2\frac{h_D}{h_2} + \frac{h_D^2}{h_2^2}\right) \frac{E_D}{E_2}\right]^3}{\left(1 + \frac{h_D}{h_2} \frac{E_D}{E_2}\right)^3} \right] \quad (3.64)$$

and

$$I_D = \frac{h_2^3}{24} \left[\frac{\left[\left(2\frac{h_D}{h_2} + 1\right) + \left(\frac{h_D}{h_2}\right)^2 \frac{E_D}{E_2} \right]^3 - \left[1 - \left(\frac{h_D}{h_2}\right)^2 \frac{E_D}{E_2} \right]^3}{\left(1 + \frac{h_D}{h_2} \frac{E_D}{E_2}\right)} \right] \quad (3.65)$$

After some algebraic manipulation, equation 3.61 becomes

$$\frac{\eta_s}{\eta_D} = \frac{\left\{ \left(\frac{E_2}{E_2}\right) \left(\frac{h_2}{h_D}\right) \left[2\bar{A} + 2\left(\frac{E_D}{E_2}\right) \left(\frac{h_D}{h_2}\right)^3 + \left(\frac{E_D}{E_2}\right)^2 \left(\frac{h_D}{h_2}\right)^4 - 1\right] \right\}}{\left\{ 1 + \left(\frac{E_D}{E_2}\right) \left(\frac{h_D}{h_2}\right) \right\} \left\{ 1 + 2\bar{A}\left(\frac{E_D}{E_2}\right) \left(\frac{h_D}{h_2}\right) + \left(\frac{E_D}{E_2}\right)^2 \left(\frac{h_D}{h_2}\right)^4 \right\}} \quad (3.66)$$

where

$$\bar{A} = 2 + 3 \left(\frac{h_D}{h_2}\right) + 2 \left(\frac{h_D}{h_2}\right)^2 \quad (3.67)$$

On using the simplified notation,

$$E_r = \frac{E_D}{E_2} \text{ and } h_r = \frac{h_D}{h_2} \quad (3.68)$$

then

$$Q = \frac{(1 + E_r h_r) (1 + 2\bar{A} E_r h_r + E_r^2 h_r^2)}{\eta_D E_r h_r [2\bar{A} + 2E_r h_r^3 + E_r^2 h_r^4 - 1]} \quad (3.69)$$

where Q is the ratio of the displacement at resonance to the static displacement (the amplification factor).

The modal damping that can be introduced into the beam is a function of the thickness ratio, h_r , modulus ratio, E_r , and material loss factor, η_2 .

Consider the plot of $\frac{\eta_s}{\eta_D}$ for various thickness ratios h_r and damping material modulus ratios E_r on an aluminum beam, shown in Figure 3.11.

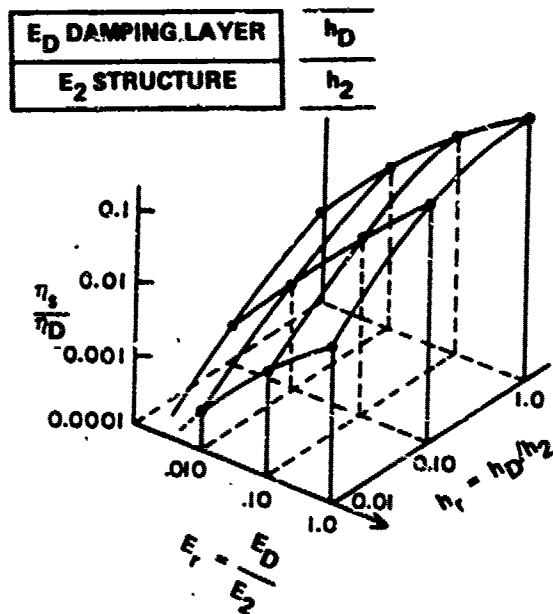


Figure 3.11. - Material loss factor ratio as a function of the modulus ratio and the thickness ratio.

The stiffer and thicker the damping material, the higher the modal damping. The modal damping cannot exceed the loss factor of the damping material. That is, as

$$\frac{E_r h_r}{r} \rightarrow \infty$$

then

(3.70)

$$\eta_s \rightarrow \eta_D$$

Therefore, in order to damp a beam-like structure, it is necessary to decide what modal damping is required and then determine from a plot, similar to the previous one, the thickness of the damping material necessary to achieve the desired damping. This approach does not provide any control over the weight penalty required to achieve the desired damping. The other approach is to determine the acceptable weight penalty, and the modal damping that can be obtained from a material of a given loss factor and Young's modulus.

3.1.1.3 Beam Vibration with Both Sides Coated

For a beam coated on both sides, the equations predicting the modal damping, η_s , and resonant frequencies become much less cumbersome because of symmetry. In this instance

$$I_2 = \frac{1}{12} b h_2^3 \quad (3.71)$$

$$I_D = 2b[\bar{\gamma} h_D^3 / 12 + \bar{\gamma} h_D (h_2 + h_D)^2 / 4] \quad (3.72)$$

and

$$\frac{\eta_s}{\eta_D} = \frac{\bar{\gamma} E_D}{\bar{\gamma} E_D + E_2} = \frac{\bar{\gamma} E_r}{\bar{\gamma} E_r + 1} \quad (3.73)$$

where

$$\gamma = 8 (h_D/h_2)^3 + 12 (h_D/h_2)^2 + 6 (h_D/h_2) \quad (3.74)$$

or

$$Q = \frac{(1 + \frac{E_1}{\gamma E_D})}{\eta_D} = \frac{1 + \frac{1}{\gamma E_r}}{\eta_D} \quad (3.75)$$

Again it can be seen that the stiffer and thicker the damping material, the higher the damping that can be introduced into the composite beam. This result reemphasizes the basic conclusion that in designing free-layer damping treatments the designer needs to consider damping materials with high Young's modulus and high loss factor.

3.1.2 Partial Coverage of Beams [3.4]

Consider the beam illustrated in Figure 3.12. The beam is divided into three sections of which the center section is coated with a damping material.

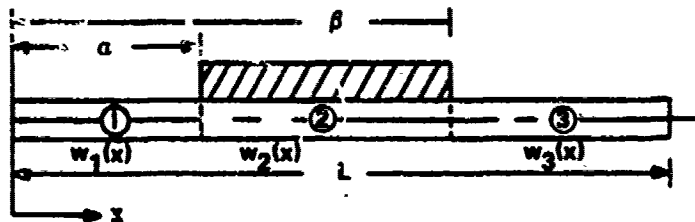


Figure 3.12. - Beam partially covered with viscoelastic material.

By definition,

$$2\eta_s = \frac{\text{The energy dissipated per cycle by the damping treatment}}{\text{The maximum strain energy stored in the beam and coating during the cycle}}$$

Following equation 3.51, the total energy dissipated in the viscoelastic coating is

$$D_d = \pi E_D'' I_D \int_{\alpha}^{\beta} \left(\frac{d^2 w}{dx^2} \right)^2 dx \quad (3.76)$$

The maximum strain energy stored in the beam under consideration (equation 3.53) is the sum of the strain energies stored in the individual portion of the beam, which is

$$U_s = \frac{1}{2} \int_0^{\alpha} \left(\frac{d^2 w_1}{dx^2} \right)^2 E_1 I_1 dx + \frac{1}{2} \int_{\alpha}^{\beta} \left(\frac{d^2 w_2}{dx^2} \right)^2 E_c I_c dx + \frac{1}{2} \int_{\beta}^L \left(\frac{d^2 w_3}{dx^2} \right)^2 E_3 I_3 dx \quad (3.77)$$

where

$$E_c I_c = (E_D I_D + E_2 I_2) \quad (3.78)$$

and I_D and I_2 are the moments of inertia for the damping material and the beam, respectively, about the combined beam neutral axis, the same as in equation 3.60, but with suffix 1 now replaced by suffix 2.

For sake of simplicity and illustrative purposes, it is assumed that

$$E_2 I_2 \sim E_1 I_1 = E_3 I_3 \quad (3.79)$$

Then

$$\eta_s = \frac{E_D'' I_D \int_{\alpha}^{\beta} \left(\frac{d^2 w_2}{dx^2} \right)^2 dx}{E_1 I_1 \left[\int_0^{\alpha} \left(\frac{d^2 w_1}{dx^2} \right)^2 dx + \int_{\alpha}^{\beta} \left(\frac{d^2 w_2}{dx^2} \right)^2 dx + \int_{\beta}^L \left(\frac{d^2 w_3}{dx^2} \right)^2 dx \right] + E_D I_D \int_{\alpha}^{\beta} \left(\frac{d^2 w_2}{dx^2} \right)^2 dx} \quad (3.80)$$

Again, for illustrative purposes, it is assumed that the damping treatment does not change the normal modes of vibration of the beam. Then,

$$\int_0^{\alpha} \left(\frac{d^2 w}{dx^2}\right)^2 dx + \int_{\alpha}^{\beta} \left(\frac{d^2 w}{dx^2}\right)^2 dx + \int_{\beta}^L \left(\frac{d^2 w}{dx^2}\right)^2 dx = \int_0^L \left(\frac{d^2 w}{dx^2}\right)^2 dx \quad (3.81)$$

and

$$\eta_s = \frac{\eta_D E_D I_D}{E_1 I_1 \frac{\int_0^L \left(\frac{d^2 w}{dx^2}\right)^2 dx}{\int_{\alpha}^{\beta} \left(\frac{d^2 w}{dx^2}\right)^2 dx} + E_D I_D} \quad (3.82)$$

which shows that as the coverage approaches complete coverage,

$$\eta_s \rightarrow \frac{\eta_D E_D I_D}{E_1 I_1 + E_D I_D} \quad (3.83)$$

the same as equation 3.57 for a beam with complete coverage. The integral, for each section of the beam denoted by i ,

$$\int_{\substack{\text{length} \\ \text{section } i}} \left(\frac{d^2 w_i}{dx^2}\right)^2 dx \quad (3.84)$$

can be determined in a number of ways. If the normal modes are known, that is

$$w(x) = \sum w_m \phi_m \left(\frac{x_i}{L_i}\right) \quad (3.85)$$

then $d^2 w/dx^2$ and the integrals can be readily determined. The function $\phi_m(x_i/L_i)$ is dependent on the boundary conditions and loading. If

$$EI \frac{d^4 w(x)}{dx^4} - \frac{\mu}{g} \omega^2 w(x) = p(x). \quad (3.86)$$

then a solution to the above equation can be obtained of the form given by equation 3.29. Whichever solution method is used, either the direct or the normal mode method, expressions for $w(x)$ are obtained. The resonant frequency can be determined along with the moment distribution $d^2 w/dx^2$.

3.1.3 Vibration of Unstiffened Plates with a Free Layer Damping Treatment [3.13]

The equation of motion of a simple plate is

$$D\nabla^4 w - \frac{\rho}{g} h\omega^2 w = p(x, y) \quad (3.87)$$

where

$$\nabla^4 w = \frac{\partial^4 w}{\partial x^4} + 2 \frac{\partial^4 w}{\partial x^2 \partial y^2} + \frac{\partial^4 w}{\partial y^4} \quad (3.88)$$

$$D = \frac{E h^3}{12(1-\nu^2)} \quad (3.89)$$

and

h = thickness of the plate

ρ = density of the plate

ν = Poisson's ratio of the plate material.

Consider now the completely covered plate illustrated in Figure 3.13.

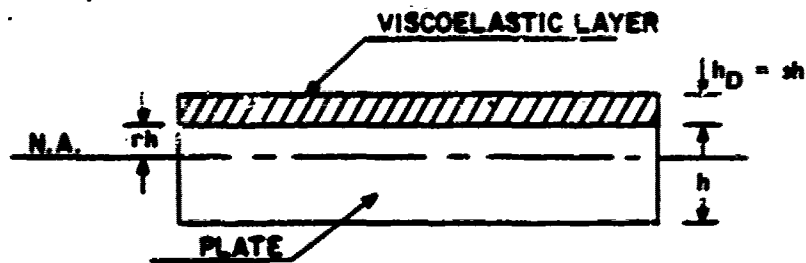


Figure 3.13. - Viscoelastic layer on a plate.

In much the same way as for a coated beam, the Euler-Bernoulli equation for the composite plate can be written in the form:

$$D_c \nabla^4 w - \frac{1}{g} (\rho h + \rho_D h_D) \omega^2 w = p(x,y) \quad (3.90)$$

where ρ_D and h_D are the density and thickness of the damping layer, respectively, and

$$D_c = D_2 + D_D \quad (3.91)$$

where D_2 and D_D are the flexural rigidities of the metal plate and the damping layer, respectively, about the coated plate neutral axis. In deriving equation 3.90, it is also assumed that the plate is undergoing harmonic excitation of the form

$$w(x,y,t) = w(x,y) e^{i\omega t} \quad (3.92)$$

Using the fact that

$$\int \sigma_x dz = \int \sigma_y dz = 0, \quad (3.93)$$

that is the net force in the x and y directions must be zero in the absence of body forces, it can be shown

$$r = (1-s^2 e) / 2(1-se) \quad (3.94)$$

where

$$s = \frac{h_D}{h} \text{ and } e = \frac{E_D}{E} \quad (3.95)$$

The flexural rigidities are then

$$D_2 = \int_{-(1-r)b}^{rh} [E/(1-\nu^2)] z^2 dz = E h^3 A' / [24(1-\nu^2)] \quad (3.96)$$

$$D_D = \int_{rh}^{(r+s)h} [E_D(1+i \eta_D)/(1-\nu^2)] z^2 dz = E_D h^3 B' (1+i \eta_D) / [24(1-\nu^2)] \quad (3.97)$$

where it is assumed $z_D = z_1$ and

$$A' = \left\{ (1-s^2e)^3 + (1+[2s+s^2]e)^3 \right\} (1+se)^{-3} \quad (3.98)$$

$$B' = \left\{ (2s+1+s^2e)^3 - (1-s^2e)^3 \right\} (1+se)^{-3} \quad (3.99)$$

Also, on noting that

$$D_c = D_c' (1 + i\eta_s) \quad (3.100)$$

for the damped plate, it can be shown that

$$\eta_s = \eta_D (1+A'/B'e)^{-1} \quad (3.101)$$

$$\left(1 + \frac{\rho_D h_D}{\rho h} \right) \left(\frac{f_{cmn}}{f_{mn}} \right)^2 = 1 + (A' - 2 + B'e) / 2 \quad (3.102)$$

Here f_{mn} is the resonant frequency of the undamped plate for the mn^{th} mode and f_{cmn} is the resonant frequency of the coated (damped) plate for the mn^{th} mode.

The natural frequency, f_{mn} , is determined by solving the equation of motion for the free vibrations of the undamped plate, given by

$$D\nabla^4 w - \frac{\rho}{g} h \omega^2 w = 0 \quad (3.103)$$

and is dependent on the boundary conditions.

3.1.4 Summary

The analyses and equations were derived in a general manner without referring to any specific examples. For solutions of specific examples (such as stiffened plates) there are a number of references listed where solutions of various examples of layered damping treatments are discussed and illustrated [3.14, 3.15, 3.16].

3.2 CONSTRAINED-LAYER DAMPING TREATMENTS

Constrained-layer damping treatments are among the most efficient ways of introducing damping into a structure. There are many variations of constrained-layer treatments including damping tapes, sandwich plates, multiple-layer treatments; and a multitude of special configurations including the use of corrugations, spacers, selected cuts, and schemes for alternately anchored constraining layers.

3.2.1 Single Constrained Layer

To understand the concepts involved in constrained-layer treatments, let us consider one of the simplest and most familiar forms of these treatments, the single constrained layer consisting of a thin layer of damping material combined with a constraining layer of metallic foil. Such a treatment is shown schematically in Figure 3.14 with the typical dimensions grossly out of scale for illustrative purposes. The damping mechanism, in this configuration, is the cyclic shear deformation of the damping layer, as illustrated in Figure 3.14.

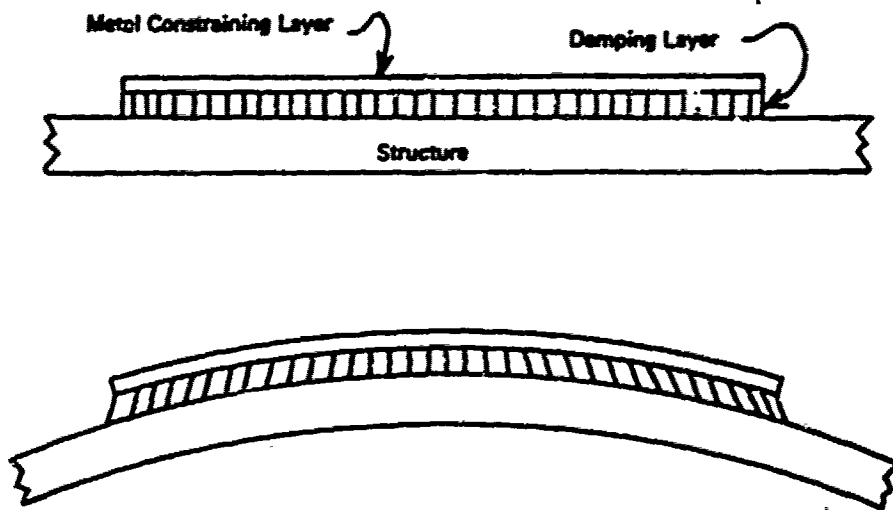


Figure 3.14. - Single constrained layer illustrating shear deformations of the damping layer.

In analyzing constrained-layer treatments it is usually appropriate to neglect bending deformations (elongation and compression, which in contrast are the most important in free-layer treatments), and to assume that all deformation in the damping material is shear. With this in mind, consider the shear deformation version of Equation 3.4.

$$D_s = \tau \int_{\text{vol}} \eta G \gamma^2 dv \quad (3.83)$$

where G is the shear modulus, γ is the shear strain and η is the loss factor. Unlike the case of free layer damping, the level of cyclic strains in the damping material of a constrained-layer treatment is greatly affected by the geometry of the treatment and the relative stiffness of the damping material, constraining layer, and base structure. Often, a decrease in the shear loss modulus, ηG , of the damping material, will increase both the strain, γ , and the energy dissipated, D_s , since D_s is proportional to the square of the strain and only to the first power of the shear loss modulus. It must be kept in mind, that for any given geometric configuration, there is shear modulus which will optimize D_s and if the modulus is increased or decreased from this

optimum point, D_g will decrease. The area shown in Figure 3.15 illustrates the temperature range in which most shear damping materials are efficient.

The symbols used in equation 3.104 and all other equations in Section 3.2 are listed in Table 3.3.

The design of an optimized constrained-layer damping treatment is much more involved than the simple chore of picking a material with the highest possible loss modulus for a free layer treatment. For instance, it has been shown [3.17] that a constrained-layer treatment has an inherent frequency, or more precisely, a wave length dependency not present in the free-layer treatments. Figure 3.16 illustrates how this wave length dependency can affect the shear deformation in damping treatments with different lengths of constraining layers. In long treatments with long bending wave lengths, the center portion of the damping layer does not experience high shear deformation, due to the stretching of the constraining layer. On the other hand, in very short

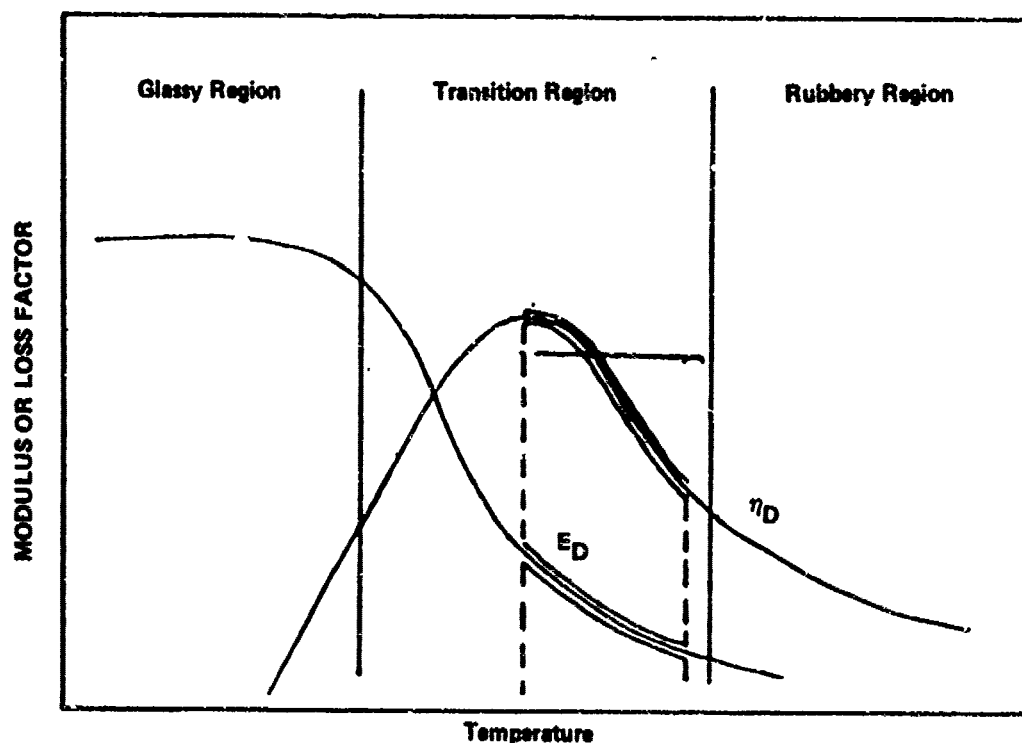


Figure 3.15. - Optimum temperature range for constrained layer treatments.

TABLE 3.3. - LIST OF SYMBOLS FOR SECTION 3.2

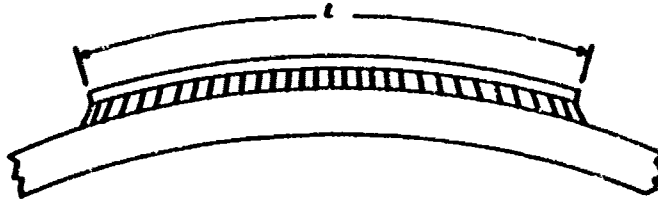
SYMBOL	DEFINITION
A	Cross-sectional area
A_3	Beam area
a	Plate length
b	Plate width
D_s	Energy dissipated in structure or system
E	Young's modulus
F_i	Net extensional force on the i^{th} layer
F_3	Tension in the beam
G	Shear modulus
\bar{G}	Dimensionless shear parameter (equation 3.142)
G_2^*	Damping material complex shear modulus
G_2	Shear modulus of the elastic foundation
g_0	Exponent in expression for longitudinal displacement (equation 3.111)
H_{i0}	Distance from the center of the i^{th} layer to the reference neutral plane of the laminate
H	Thickness of material
I	Moment of inertia
K_i	Extensional stiffeners of layer i
k	Wave number

TABLE 3.3. - LIST OF SYMBOLS FOR SECTION 3.2 (Continued)

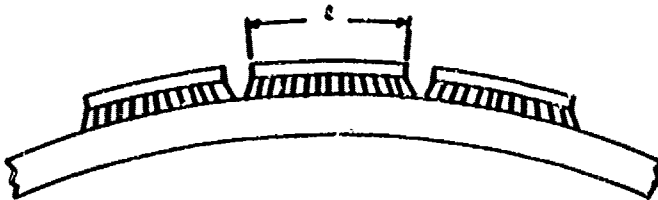
SYMBOL	DEFINITION
L	Beam length
l	Optimum length of constraining layer
M_{i1}	Moment exerted by the forces on the i^{th} layer about its own neutral plane
S_i	Cross-sectional area of layer i
η	Loss factor
η_D	Damping material loss factor
γ	Shear strain
μ	Mass density per unit area of composite plate
ν	Poisson's ratio of composite plate
ϕ	Beam slope (flexural angle)
ψ	Shear strain
τ	Shear stress in the elastic foundation
τ_i	Extensional stress
ξ	Beam longitudinal displacement
ζ	Density

EFFECT OF LENGTH OF CONSTRAINING LAYER
(on a beam with uniform bending moment)

- In a very long treatment center portion of damping layer does not experience high shear deformation due to stretching of the constraining layer.



- In a very short treatment the constraining layer provides little constraint and maximum shear deformation is small.



- An optimum length can be calculated for a constant temperature and uniform bending moment.

Figure 3.16. - Wave length dependency on shear deformation.

treatments, the maximum shear deformation at the ends of the segments can be quite small. These factors, therefore, suggest that, for a given viscoelastic material, constraining layer, frequency range, and temperature there is an optimum length of constraining layer. The length has been calculated by Plunkett and Lee [3.18] to be

$$l = 3.28 H_2 H_3 \frac{E_3}{|G_2^*|} \quad (3.105)$$

where H_2 and H_3 are the thicknesses of the damping material and the constraining layer respectively, E_3 is the Young's modulus of the constraining layer and $|G_2^*|$ is the absolute value of the damping material complex shear modulus. This analysis is valid for cases in which the half wave length (or approximately the distance between node lines in the structure) is much greater than the optimum

length λ . Actually, this analysis illustrates the importance of considering wave length effects in the design of constrained-layer damping treatments, since if the thicknesses and stiffnesses of the damping treatments were chosen so as to have λ nearly equal to the half wave length in the structure, then no cuts would be necessary in the constraining layer for optimum damping.

As shown in Figure 3.17 maximum energy dissipation is achieved with shear stresses approaching the fatigue strength of the viscoelastic material. For instance, it has been demonstrated [3.19] that some viscoelastic materials can

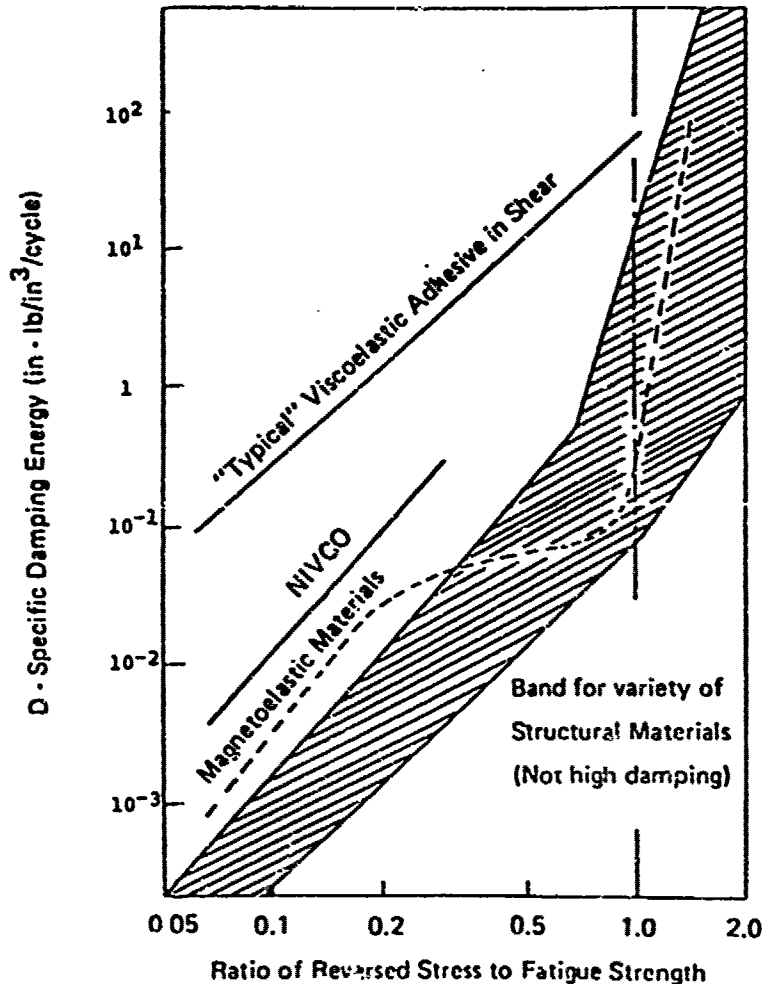


Figure 3.17. - Maximum energy dissipation when shear stresses approach the fatigue strength of the viscoelastic material.

withstand millions of reversed cycles of strain as large as unity without evidence of fatigue failure. It is apparent therefore, that if a full damping potential is to be realized from one of these adhesives, then ideally it should be strained to much higher levels than the structural materials with which it is used. Most practical applications of constrained-layer damping treatments are limited in effectiveness because of the small strains obtainable in the viscoelastic layer. This is particularly true on thin metal panels where the plane of the damping layer is displaced only slightly from the neutral bending axis.

One of the factors limiting the strain achieved in the viscoelastic layer is the stretch in the constraining layer. It is important to note, however, that the temperature at which maximum damping is achieved, will decrease with increasing constraining-layer stiffness if the viscoelastic layer remains the same. There is also a practical limit to the stiffness of the constraining layer, for when the constraining layer becomes stiffer than the original panel, the shear deformations in the viscoelastic material are limited by stretch in the original structure. Therefore, the symmetric sandwich panel, shown in Figure 3.18 is one of the most efficient single constrained layer configurations for damping of sheet metal panels. Unfortunately, sandwich panels usually have to be designed into the original structure because they are difficult if not impossible to add to a structure after it is fabricated.

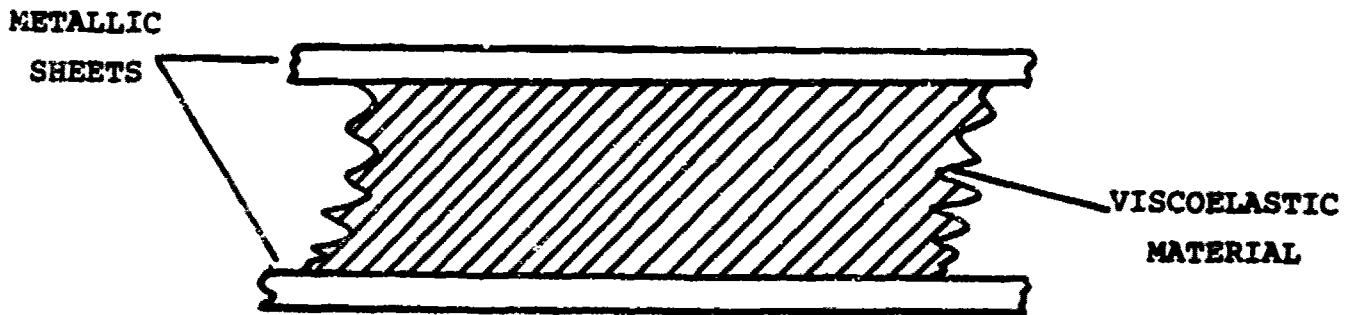
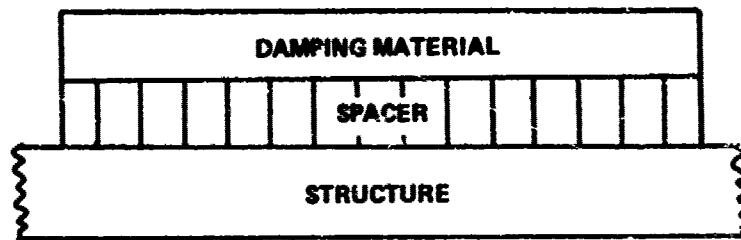


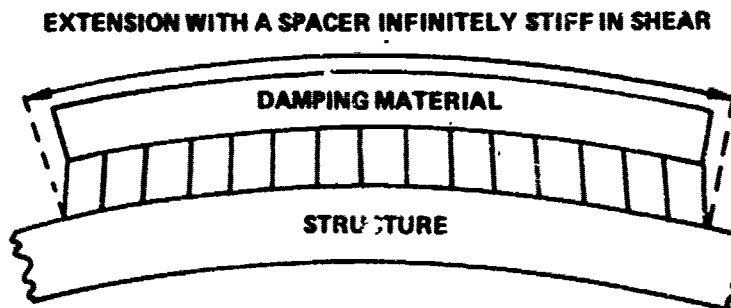
Figure 3.18. - Symmetric sandwich panel.

3.2.1.1 Special Configurations

Several unique configurations have been investigated as a means of increasing the shear deformations in constrained-layer damping treatments. A spacer, which increases the distance between the neutral axis and the damping layer, as shown in Figure 3.19a, can greatly increase the effectiveness of layer treatments provided that the spacer is sufficiently stiff in shear [3.20]. The problem is that lightweight, low-cost materials usually considered for spacers have a relatively low shear modulus. Shear deformations, therefore, occur in the spacer, as shown in Figure 3.19b, which detract from the theoretical advantage gained with the spacer assumed rigid in shear [3.21].



(a) UNSTRAINED CASE



(b) STRAINED CASE

Figure 3.19. - Spacer used with damping layer.

To circumvent this problem, Torvik and Lazan [3.22] investigated a corrugated configuration as shown in Figure 3.20. Damping material was applied between bands attached to the beam or panel, over a filler material. The bands were thin, but constructed of material with a high Young's modulus so that they could withstand compressive as well as tensile loads. The filler material did not need to be stiff in either bending or shear to ensure negligible deformations normal to the beam. Analysis and experiments demonstrated increased panel damping by a factor of 20 over the untreated panel, compared with a 1 percent improvement resulting from the same viscoelastic matter applied to the panel. This treatment has not been used due to the difficulty in fabrication, but the investigation did serve as a basis for further developments.

Later, Lazan [3.22, 3.23, 3.24] developed a multiple-layer, alternately anchored treatment which was easier to fabricate but still showed increased effectiveness over conventional multilayer treatments. Figure 3.21 shows a schematic of this concept which used rigid connections between alternate constraining layers and the structure to increase the shear deformation in the outer damping layer. Another configuration for increasing strain in the damping layers was proposed by Plunkett and Lee [3.18]. Figure 3.22 is a schematic showing how the constraining layers were cut to optimal lengths to increase

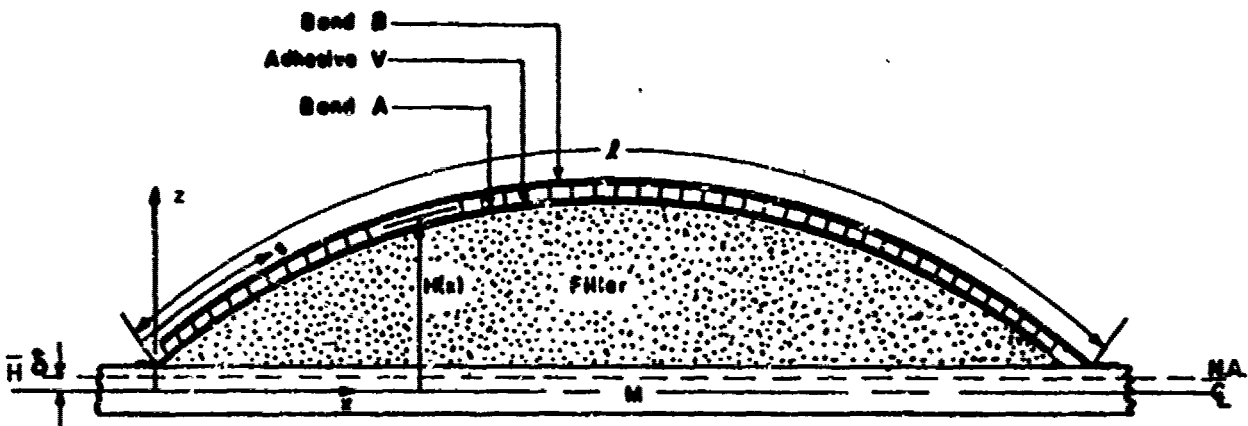


Figure 3.20. - Viscoelastic corrugated configuration.

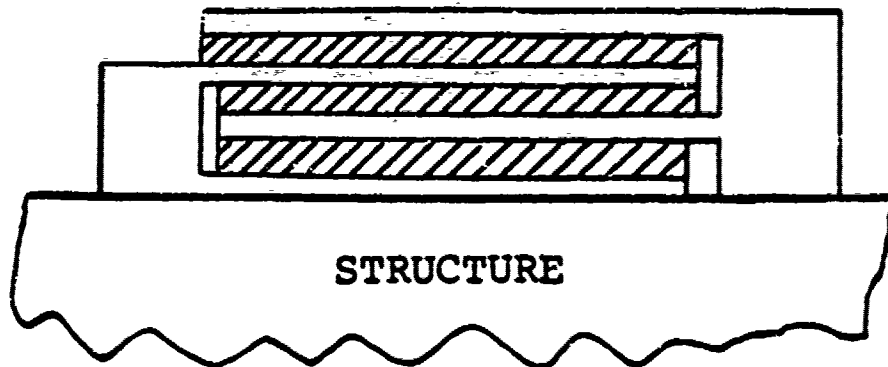


Figure 3.21. - Multilayer anchored treatment.

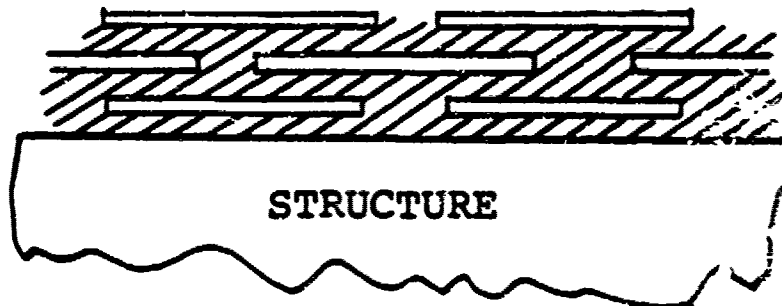


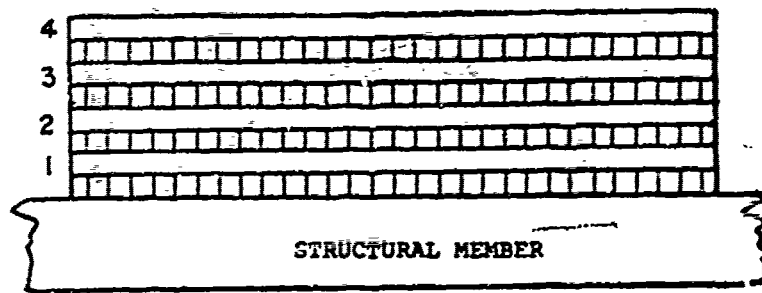
Figure 3.22. - Multilayer spaced treatment.

the strain in the damping layers. These optimal lengths were calculated for stiffness properties of the constraining layer and the shear modulus of the damping material.

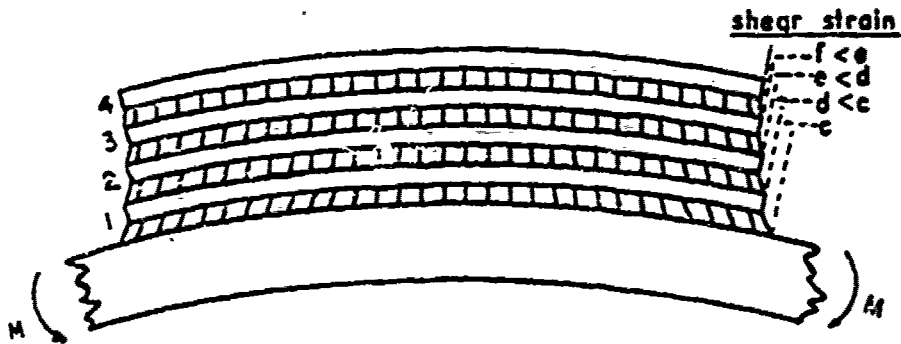
3.2.1.2 Multiple Constrained Layers

Multiple layers of damping systems are frequently used to increase damping of structures. The deformation that occurs in multiple layer treatments is illustrated in Figure 3.23, which shows a decreasing shear strain in each subsequent layer from the structure surface outward. In fact, if the same material is used in each layer, most of the damping in a multiple

constrained-layer treatment occurs as a result of shear of the viscoelastic layer closest to the structure. The additional layers contribute primarily to



(A) UNSTRAINED CASE



(B) STRAINED CASE

Figure 3.23. - Deformations in multiple layers of damping tape.

the apparent stiffness of the first constraining layer. Typical measured damping of a beam with 1 to 7 layers of damping tape is shown as a function of temperature in Figure 3.24. As would be expected, there is a diminishing gain from each successive additional layer and a shift of the damping peak to lower temperatures. One of the main advantages of using multiple layers is that this type of treatment often conforms better to an existing structure than a single damping layer with a very stiff thick constraining layer.

As in the case of free-layer treatments, damping materials with different transition temperatures can be combined in a multiple constrained-layer treatment to achieve an effective temperature range broader than possible with a single material. This is illustrated in Figure 3.25 [3.25], which shows the results of damping tests of three beams with different multiple constrained layer treatments. The beam with three constrained layers of Adhesive I show a

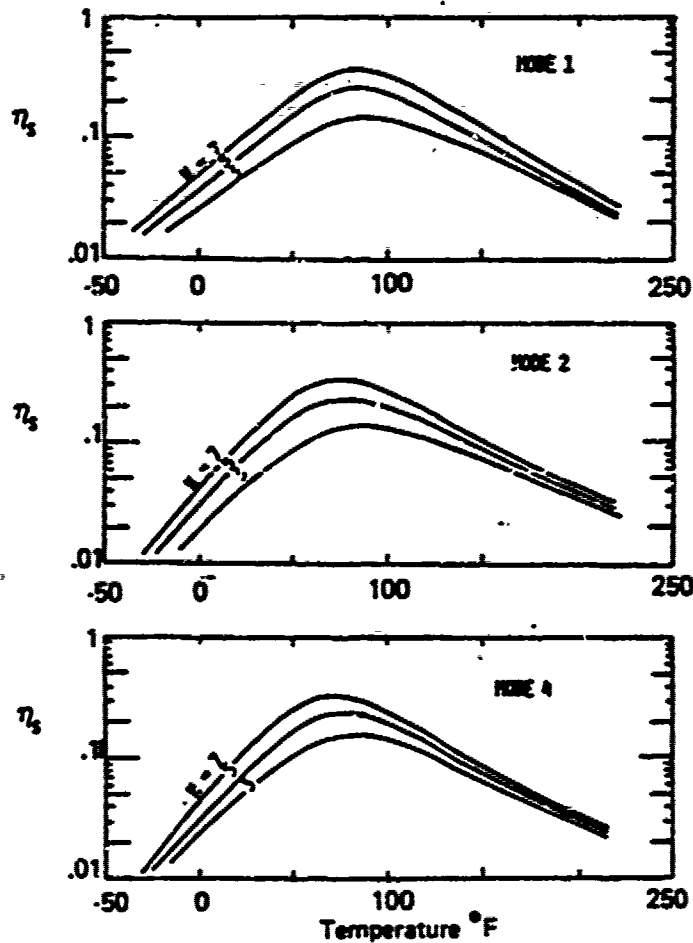


Figure 3.24. - Beam damping with multiple layers of tape.

damping peak at a temperature slightly below 100°F for each of the first three modes of a clamped-clamped beam.

Analytical predictions of the damping (the curves) can be compared with experimental data (the points). A damping treatment with the same geometry but using a different viscoelastic material (Adhesive II), on a similar beam, produced a damping peak at 0°F. When the two damping treatments were combined into a six layer treatment with the higher temperature treatment closest to the beam, a broad temperature damping curve was obtained which approximates the superposition of the damping of the two different treatments. It is important to note that the high-temperature treatment must be closest to the

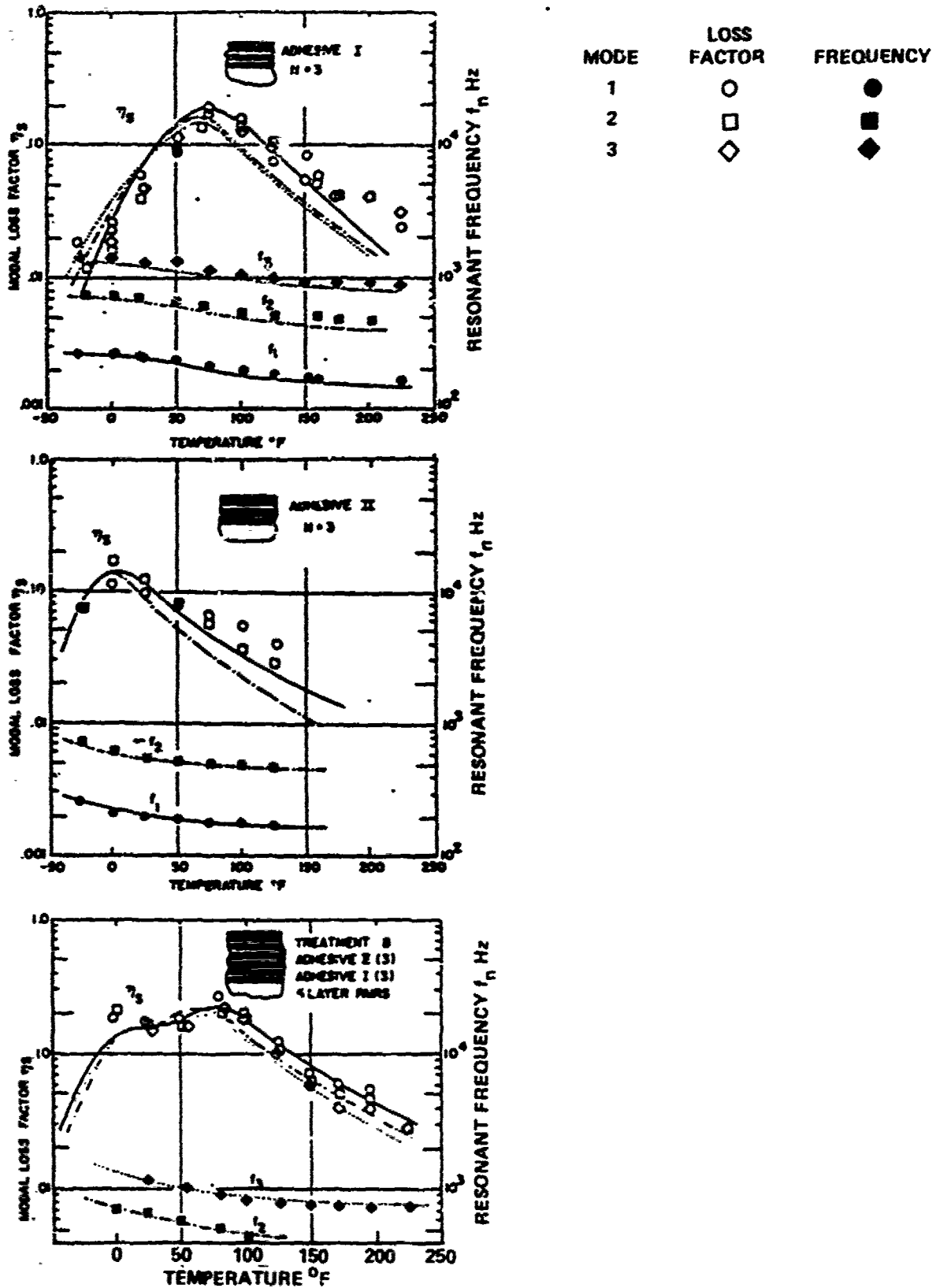


Figure 3.25. - Damping in multiple material constrained layer systems.

beam to obtain this broad temperature performance. Otherwise, at high temperatures the lower temperature material is so soft that the higher temperature material is never deformed efficiently.

3.2.1.3 Optimization of Constrained Layer Treatments

Design of an optimum constrained layer damping treatment involves examining the tradeoffs of varying damping materials, thicknesses, and constraining layers, allowing for the effects of temperature, frequency, and wave lengths. In the examples that have just been discussed, all but one or two of the design parameters have been fixed and the effect of changing these variables has been shown. While this gives insight to the behavior of constrained layer damping treatments, it does not in itself constitute an effective design procedure. Analytical approaches have been formulated to assist in the design of this multiparameter optimization problem, and are presented in another section.

3.2.2 Single Constrained-Layer Damping Treatment Analysis

The term "single constrained-layer damping treatment" signifies a single layer of viscoelastic material (VEM) between two elastic layers (Figure 3.26).

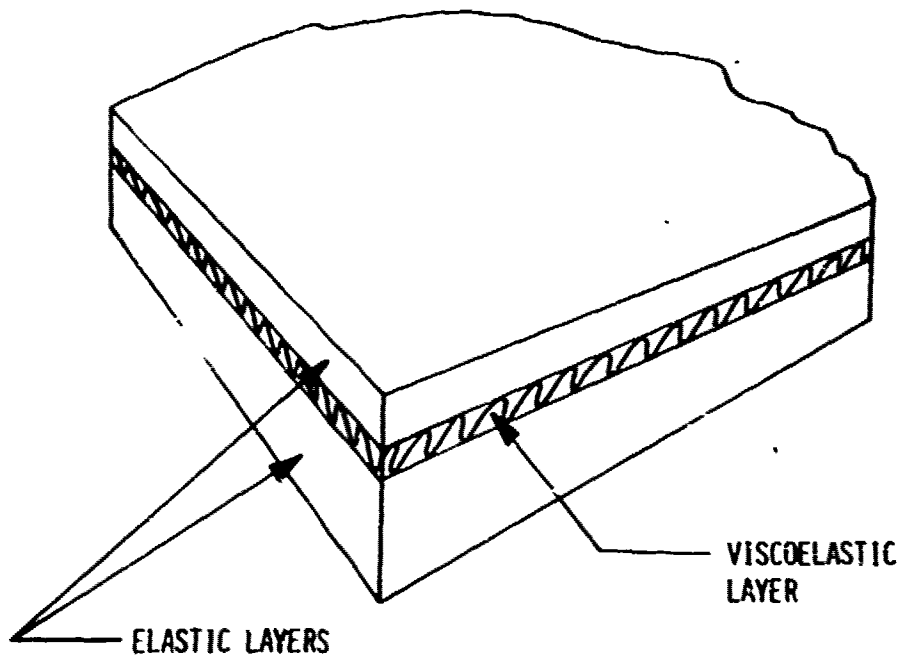


Figure 3.26. - Single constrained layer damping treatment.

When a foil is used as one of the elastic layers and added to an existing structure with self-adhesive VEM, it is commonly referred to as "damping tape." Damping tape dates to the early 1950s and it was claimed that the vibrational energy of the treated panel was reduced "substantially to zero so as to minimize the noise below auditory levels ...". [3.26]

Damping tape is used extensively in commercial airlines to control noise due to turbulent boundary layer at cruise conditions.

When the elastic layers are approximately equal in thickness, the system is typically referred to as a "sandwich" or a "damped laminate." This form is finding increasing use, especially in the consumer goods industry, particularly in Europe. In the United States, valve covers and oil pans of diesel engines have been made of this type of construction.

3.2.2.1 Stretching of a Beam on an Elastic Foundation

It is instructive, when studying constrained layer damping, to consider the stretching of a semi-infinite beam on an elastic foundation of finite thickness (Figure 3.27). Under a tension applied to the end, the beam is stretched and the elastic foundation is sheared. The equilibrium of the beam segment of length dx gives

$$\frac{\partial F_3}{\partial x} = -G_2 \psi = -G_2 \frac{\xi}{H_2} \quad (3.106)$$

and the stress relationship for a unit width beam is

$$\frac{F_3}{A_3} = \frac{F_3}{H_3} = E_3 \frac{\partial \xi}{\partial x} \quad (3.107)$$

where

A_3 is the area of the beam,

E_3 is Young's modulus of the beam,

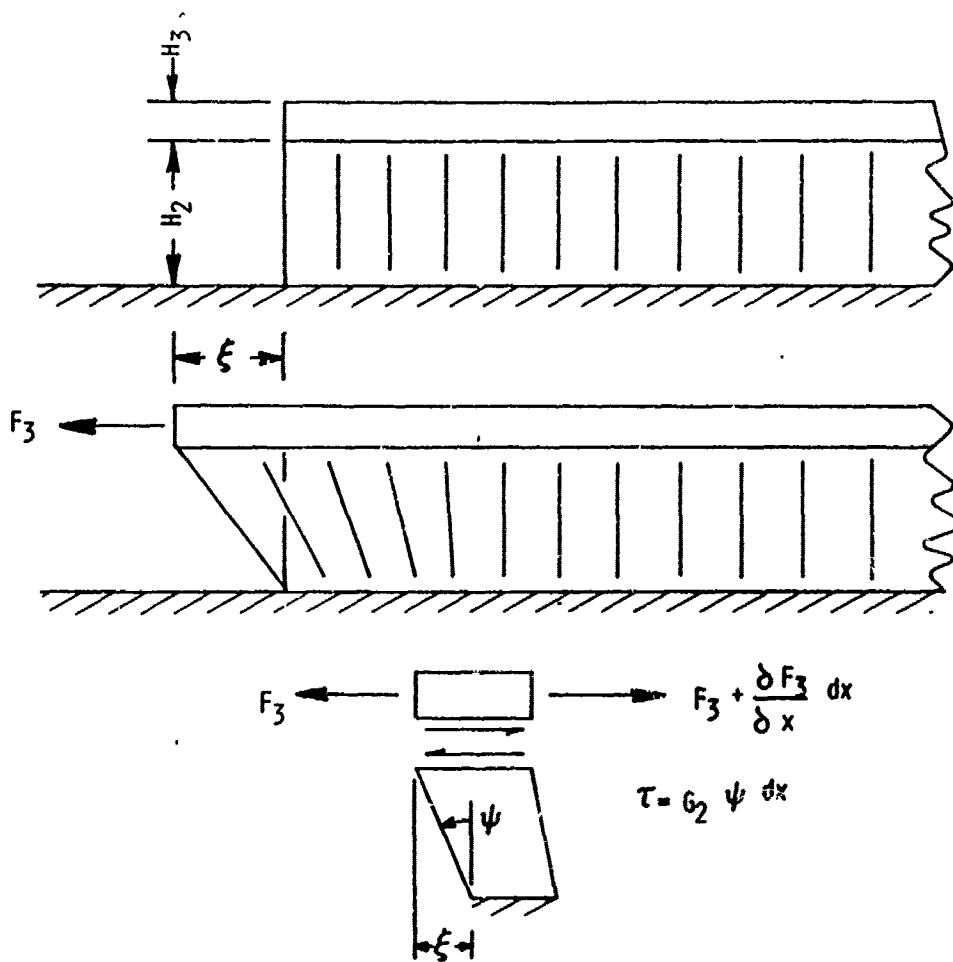


Figure 3.27. - Tension in a beam on an elastic foundation.

H_3 is the thickness of the beam,

F_3 is tension in the beam,

τ is the shear stress in the VEM, (Elastic foundation)

G_2 is the shear modulus of the VEM,

H is the thickness of the VEM,

ψ is the shearing strain of the VEM, and

ξ is the longitudinal displacement of the beam.

Differentiating Equation 3.86 gives

$$\frac{\partial F_3}{\partial x} = E_3 H_3 \frac{\partial^2 \xi}{\partial x^2} \quad (3.108)$$

and substituting into Equation 3.106 and collecting terms yields the differential equation for

$$\frac{\partial^2 \xi}{\partial x^2} - \frac{G_2}{E_3 H_3 H_2} \xi = 0. \quad (3.109)$$

The solution for Equation 3.109 is of the form

$$\xi = c_1 e^{-g_0 x} + c_2 e^{g_0 x} \quad (3.110)$$

where

$$g_0 = \sqrt{\frac{G_2}{E_3 H_3 H_2}}. \quad (3.111)$$

The coefficient c_2 must be zero if ξ is finite for large x . For the other boundary condition we obtain,

$$\xi(0) = -\xi_0 = c_1, \quad (3.112)$$

the solution for the displacement becomes

$$\xi = -\xi_0 e^{-g_0 x} \quad (3.113)$$

and the tension is

$$F_3 = E_3 H_3 g_0 \xi_0 e^{-g_0 x} \quad (3.114)$$

Thus the tension and displacement at the end of the beam obey the relationship

$$F_3 = E_3 H_3 g_0 \xi_0 \quad (3.115)$$

Equations 3.113 and 3.114 show that the displacement and tension decay exponentially. The parameter g_0 governs the rate and consists of two parts, G_2/H_2 and $E_3 H_3$. The effects of changes in these parts on the displacements are consistent with intuition; i.e., a softer foundation or a stiffer beam increases the distance required for the displacements to die out.

3.2.3 Flexural Rigidity of Single Constraining-Layer Configurations

Class [3.27] analyzed such an arrangement; both outer layers were considered to be very thin, and shear effect in the core was included. This analysis basically follows Ross, Kerwin, and Ungar. [3.28]

On considering the forces acting on the deformed beam element in Figure 3.8, it can be shown that the inertia force is related to the bending moment M_x , in the free vibration of the beam, by the following equation

$$\frac{\rho A}{g} \frac{\partial^2 w}{\partial t^2} = \frac{\rho A}{g} \ddot{w} = - \frac{\partial^2 M_x}{\partial x^2} \quad (3.116)$$

In order to solve this equation for a layered beam, it is first necessary to express $\partial^2 M_x / \partial x^2$ in terms of the geometry of the layered beam. Consider the unit width element of the layered beam in Figure 3.28, the total bending moment may be expressed by

$$M_x = EI \frac{\partial \phi}{\partial x} = \sum M_{ii} + \sum F_i H_{io} \quad (3.117)$$

where

M_{ii} is the moment exerted by the forces on the i^{th} layer about its own neutral plane,

F_i is the net extensional force on the i^{th} layer, and

H_{io} is the distance from the center of the i^{th} layer to the reference neutral plane of the laminate.

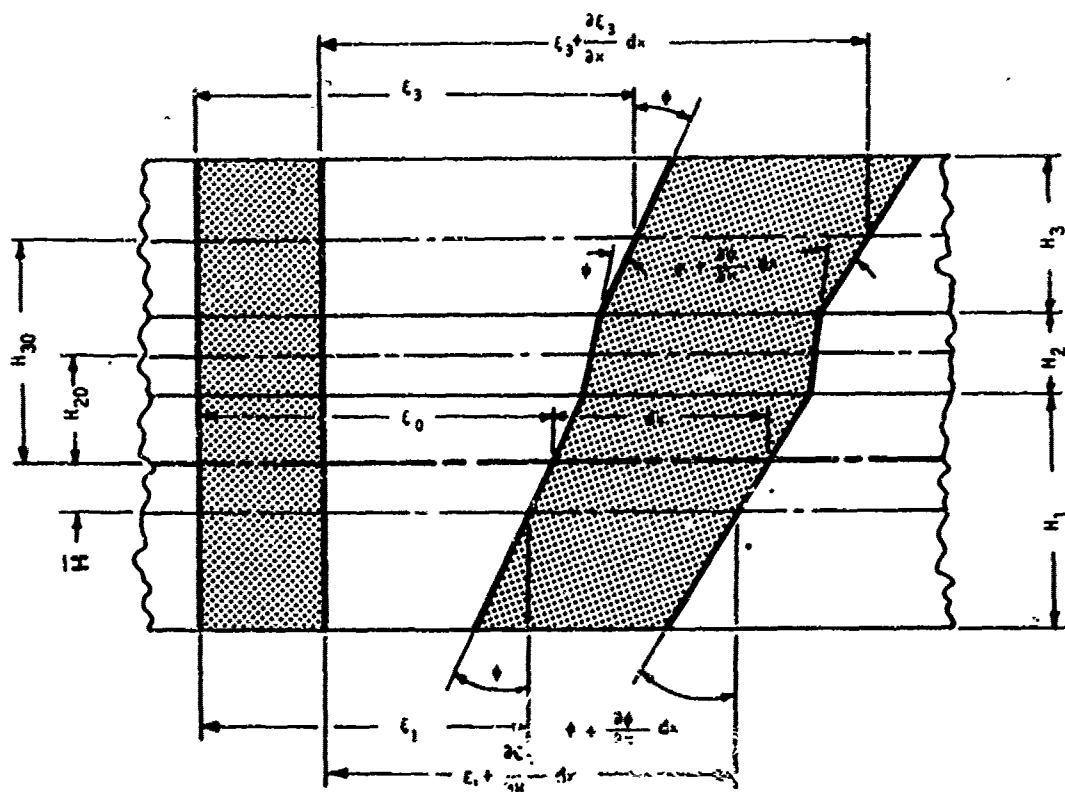


Figure 3.28. - Single constraining layer element.

The individual moments may be given in terms of curvatures as

$$M_{11} = E_1 I_1 \frac{\partial \psi}{\partial x} \quad (3.118)$$

$$M_{22} = E_2 I_2 \left(\frac{\partial \phi}{\partial x} - \frac{\partial \psi}{\partial x} \right) \quad (3.119)$$

$$M_{33} = E_3 I_3 \frac{\partial \psi}{\partial x} \quad (3.120)$$

The extensional strains at the mid planes are

$$\epsilon_1 = \frac{(\xi_1 + \frac{\partial \xi_1}{\partial x} dx) - \xi_1}{dx} = \frac{\xi_0 - \bar{H}(\phi + \frac{\partial \phi}{\partial x} dx) - (\xi_0 - \bar{H}\phi)}{dx} = \bar{H} \frac{\partial \phi}{\partial x} \quad (3.121)$$

$$\begin{aligned} \epsilon_2 = & \left\{ \left[\epsilon_o + H_{20} \left(\psi + \frac{\partial \psi}{\partial x} dx \right) - \frac{H_2}{2} \left(\psi + \frac{\partial \psi}{\partial x} dx \right) \right] \right. \\ & \left. - \left[\epsilon_o + H_{20} \psi - \frac{H_2}{2} \psi \right] \right\} \frac{1}{dx} = H_{20} \frac{\partial \psi}{\partial x} - \frac{H_2}{2} \frac{\partial \psi}{\partial x} \end{aligned} \quad (3.122)$$

$$\begin{aligned} \epsilon_3 = & \left\{ \left[\epsilon_o + H_{30} \left(\psi + \frac{\partial \psi}{\partial x} dx \right) - H_2 \left(\psi + \frac{\partial \psi}{\partial x} dx \right) \right] \right. \\ & \left. - \left[\epsilon_o + H_{30} \psi - H_2 \psi \right] \right\} \frac{1}{dx} = H_{30} \frac{\partial \psi}{\partial x} - H_2 \frac{\partial \psi}{\partial x} \end{aligned} \quad (3.123)$$

where

$$\begin{aligned} H_{10} &= -\bar{H} \\ H_{20} &= H_{21} - \bar{H} \\ H_{30} &= H_{31} - \bar{H} \\ H_{21} &= \frac{H_1 + H_2}{2} \\ H_{31} &= \frac{H_1 + 2H_2 + H_3}{2} \end{aligned} \quad (3.124)$$

The net extensional force on each layer is the product of the extensional strain at the midplane and the extensional stiffness, which, in turn, is the Young's modulus times the area.

$$F_1 = E_1 H_1 H_{10} \frac{\partial \psi}{\partial x} \quad (3.125)$$

$$F_2 = E_2 H_2 \left(H_{20} \frac{\partial \psi}{\partial x} - \frac{H_2}{2} \frac{\partial \psi}{\partial x} \right) \quad (3.126)$$

$$F_3 = E_3 H_3 \left(H_{30} \frac{\partial \psi}{\partial x} - H_2 \frac{\partial \psi}{\partial x} \right) \quad (3.127)$$

The net extensional force on the unit width element is zero for pure bending

$$\begin{aligned} \Sigma F = 0 = E_1 H_1 H_{10} \frac{\partial \phi}{\partial x} \\ + E_2 H_2 (H_{20} \frac{\partial \phi}{\partial x} - \frac{H_2}{2} \frac{\partial \psi}{\partial x}) \\ + E_3 H_3 (H_{30} \frac{\partial \phi}{\partial x} - H_2 \frac{\partial \psi}{\partial x}) \end{aligned} \quad (3.128)$$

from which

$$\begin{aligned} - E_1 H_1 \bar{H} \phi' + E_2 H_2 \left[(H_{21} - \bar{H}) \phi' - \frac{H_2}{2} \psi' \right] \\ + E_3 H_3 \left[(H_{31} - \bar{H}) \phi' - H_2 \psi' \right] = 0 \end{aligned} \quad (3.129)$$

which becomes

$$\begin{aligned} - (E_1 H_1 + E_2 H_2 + E_3 H_3) \bar{H} \phi' \\ + (E_2 H_2 H_{21} + E_3 H_3 H_{31}) \phi' \\ - \left(\frac{E_2 H_2}{2} + E_3 H_3 \right) H_2 \psi' = 0 \end{aligned} \quad (3.130)$$

where each prime above a symbol represents partial differentiation with respect to x. On solving for \bar{H} , the following equation is obtained

$$\bar{H} = \frac{E_2 H_2 H_{21} + E_3 H_3 H_{31} - \left(\frac{E_2 H_2}{2} + E_3 H_3 \right) H_2 \frac{\psi'}{\phi'}}{E_1 H_1 + E_2 H_2 + E_3 H_3} \quad (3.131)$$

Equation 3.117 may be solved for the flexural rigidity and becomes, after substitution of equations 3.118 to 3.120 and 3.124 to 3.127,

$$\begin{aligned}
EI = \frac{M}{\phi'} &= E_1 \frac{H_1^3}{12} - E_1 H_1 \bar{H}(-\bar{H}) \\
&+ \frac{E_2 H_2^3}{12} \left(1 - \frac{\phi'}{\phi'}\right) + E_2 H_2 \left[(H_{21} - \bar{H}) - \frac{H_2}{2} \frac{\phi'}{\phi'} \right] (H_{21} - \bar{H}) \\
&+ \frac{E_3 H_3^3}{12} + E_3 H_3 \left[(H_{31} - \bar{H}) - H_2 \frac{\phi'}{\phi'} \right] (H_{31} - \bar{H})
\end{aligned} \tag{3.132}$$

which simplifies to

$$\begin{aligned}
EI &= \frac{E_1 H_1^3}{12} + \frac{E_2 H_2^3}{12} + \frac{E_3 H_3^3}{12} \\
&+ E_1 H_1 \bar{H}^2 + E_2 H_2 (H_{21} - \bar{H})^2 + E_3 H_3 (H_{31} - \bar{H})^2
\end{aligned} \tag{3.133}$$

The beam is assumed to be undergoing simple harmonic motion and have a simply supported mode shape given by

$$\omega(x) = \sin kx \tag{3.134}$$

where k is the wave number given by equation 3.26. The slope is

$$\phi = \omega' = k \cos kx \tag{3.135}$$

and the second derivative of the slope is

$$\phi'' = -k^3 \cos kx = -k^2 \phi. \tag{3.135}$$

On assuming that all laminates undergo the same lateral displacement, the shear strain γ of the viscoelastic layer is proportional to the flexural angle ϕ .

Therefore,

$$\psi = \kappa \phi \quad (3.137)$$

and

$$\psi' = \kappa \phi' ; \psi'' = \kappa \phi'' \quad (3.138)$$

Taking the partial derivative of F_3 in equation 3.127 and setting it equal to equation 3.106 gives

$$\frac{\partial F_3}{\partial x} = E_3 H_3 \left[(H_{31} - \bar{H}) \phi'' + H_2 \psi'' \right] = -G_2 \psi \quad (3.139)$$

which with equation 3.136 leads to

$$\frac{(H_{31} - \bar{H})}{H_2} \phi'' + \psi'' = \frac{-G_2 \psi}{E_3 H_3 H_2} = \frac{G_2 \psi''}{E_3 H_3 H_2 k^2} \quad (3.140)$$

or

$$H_2 \frac{\psi''}{\phi''} = \frac{H_{31} - \bar{H}}{1 + \frac{G_2}{E_3 H_3 H_2 k^2}} = \frac{H_{31} - \bar{H}}{1 + \bar{G}} \quad (3.141)$$

where the dimensionless parameter

$$\bar{G} = \frac{G_2}{E_3 H_3 H_2 k^2} \quad (3.142)$$

is known as the shear parameter. From equation 3.138

$$H_2 \frac{\psi'}{\phi'} = \frac{H_2 \psi''}{\phi''} \quad (3.143)$$

Substituting equation 3.141 into 3.131 gives

$$\bar{H} = \frac{E_2 H_2 H_{21} + E_3 H_3 H_{31} - \left(\frac{E_2 H_2}{2} + E_3 H_3 \right) \frac{H_{31} - \bar{H}}{1 + \bar{G}}}{E_1 H_1 + E_2 H_2 + E_3 H_3} \quad (3.144)$$

which, when solved for \bar{H} , leads to

$$\bar{H} = \frac{E_2 H_2 (H_{21} - \frac{H_{31}}{2}) + \bar{G} (E_2 H_2 H_{21} + E_3 H_3 H_{31})}{\frac{E_1 H_1 + E_2 H_2 + \bar{G} (E_1 H_1 + E_2 H_2 + E_3 H_3)}{2}} \quad (3.145)$$

Substituting equation 3.141 into 3.133 gives the expression for the flexural rigidity

$$EI = \frac{E_1 H_1^3}{12} + \frac{E_2 H_2^3}{12} + \frac{E_3 H_3^3}{12} + E_1 H_1 \bar{H}^2 + E_2 H_2 (H_{21} - \bar{H})^2 + E_3 H_3 (H_{31} - \bar{H})^2 - \left[\frac{E_2 H_2^2}{12} + \frac{E_2 H_2}{2} (H_{21} - \bar{H}) + E_3 H_3 (H_{31} - \bar{H}) \right] \frac{H_{31} - \bar{H}}{1 + \bar{G}} \quad (3.146)$$

Equation 3.146 is used in calculating the modal damping. Any or all of the quantities EI , E_1 , E_2 , E_3 , and \bar{G} may be treated as complex. A complex E_1 would represent the baseline damping of an untreated structural member. A complex E_2 and \bar{G} with $H_3 = 0$ and $E_3 = 0$ would approximate a free-layer (extensional damping) treatment. ($H_3 = E_3 = 0$ is not valid because it results in $\bar{G} = 0$). A complex E_3 would represent a viscoelastic constraining layer. Thus, the equation is seen to be very useful. It should be noted that there is no shear deformation allowed in layers 1 or 3.

3.2.4 Single Damping Material Multiple Layer Design

The analysis used for this investigation is based on the equations that were just developed [3.5]. The analytical approach is modified to handle multiple-layer configurations using the same damping material in each layer. Experiments were performed to verify the analytical results.

The flexural rigidity, EI , of the three-layer system shown in Figure 3.29 is given by

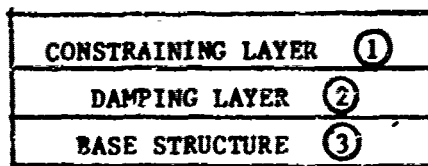


Figure 3.29. - Elements of a three-layer system.

$$EI = \frac{E_1 H_1^3}{12} + \frac{E_2 H_2^3}{12} + E_3 \frac{H_3^3}{12} + E_1 H_1 \bar{H}^2 + E_2 H_2 (H_{21} - \bar{H})^2 + E_3 H_3 (H_{31} - \bar{H})^2$$

$$- \left[\frac{E_2 H_2^2}{12} + \frac{E_2 H_2}{2} (H_{21} - \bar{H}) + E_3 H_3 (H_{31} - \bar{H}) \right] \frac{H_{31} - \bar{H}}{1 + \bar{G}} \quad (3.147)$$

where

$$\bar{H} = \frac{E_2 H_2 (H_{21} - \frac{H_{31}}{2}) + \bar{G} (E_2 H_2 H_{21} + E_3 H_3 H_{31})}{E_1 H_1 + \frac{E_2 H_2}{2} + \bar{G} (E_1 H_1 + E_2 H_2 + E_3 H_3)} \quad (3.148)$$

$$H_{31} = \frac{H_1 + H_3}{2} + H_2 \quad (3.149)$$

$$H_{21} = \frac{H_1 + H_2}{2} \quad (3.150)$$

$$\bar{G} = \frac{G_2}{E_3 H_3 H_2 k^2} \quad (3.151)$$

E is the Young's modulus of elasticity,

G is the shear modulus,

I is the moment of inertia

H is the thickness, and

k is the wave number.

G is the shear parameter

m is the mode number

For the m th mode of vibration of a simply supported beam, the wave number, k_m , and the natural frequency, ω_n , are:

$$k_m = \frac{m\pi}{L} \quad (3.152)$$

$$\omega_n = k_m^2 \sqrt{\frac{EIg}{\rho A}} \quad (3.153)$$

where

L is the length of the beam,

ρ is the density, and

A is the cross-sectional area.

Similarly, the wave number k_{mn} and the natural circular frequency ω_n for the m, n th mode of a simply supported plate are:

$$k_{mn}^2 = \left(\frac{m\pi}{a}\right)^2 + \left(\frac{n\pi}{b}\right)^2 \quad \text{and} \quad (3.154)$$

$$\omega_n = k_{mn}^2 \sqrt{\frac{EH^3g}{12(1-\nu^2)\mu}} \quad (3.155)$$

where

a is the length of the plate,

b is the width of the plate,

μ is the mass density per unit area of the composite plate, and

ν is the Poisson's ratio of the composite plate.

Introducing complex modulus terms and making certain simplifying assumptions:

- a. The damping of the base structure is negligible.
- b. The extensional stiffness of the damping layer is small,

$$(E_2 \ll E_3 \text{ and } E_2 \ll E_1)$$

Equation 3.47 becomes

$$EH^3 = E_1 H_1^3 + E_3 H_3^3 + \frac{12}{c^2 + d^2} [\alpha - B - \beta]_{RE} \quad (3.156)$$

$$EH^3 \eta_B = E_3 H_3^3 \eta_3 + \frac{12}{c^2 + d^2} [\alpha - B - \beta]_{Im} \quad (3.157)$$

where

$$\alpha = \bar{G} E_1 H_1 E_3 H_3 H_{31}^2 \left\{ c(1 - \eta_2 \eta_3) + d(\eta_2 + \eta_3) + 1 [c(\eta_2 + \eta_3)] \right\} \quad (3.158)$$

$$B = E_1 H_1 E_2 H_2 H_{31} [c + d\eta_2 + 1(c\eta_2 - d)] \quad (3.159)$$

$$\begin{aligned} \beta = & 2\bar{G} E_2 H_2 E_3 H_3 H_{21} H_{31} [c(1 - 2\eta_2 \eta_3 - \eta_2^2) + d(2\eta_2 - \eta_3 - \eta_2^2 \eta_3)] \\ & + 1 [c(2\eta_2 + \eta_3 - \eta_2^2 \eta_3) - d(1 - 2\eta_2 \eta_3 - \eta_2^2)] \end{aligned} \quad (3.160)$$

$$c = E_1 H_1 (1 + G) + \bar{G} E_3 H_3 (1 - \eta_2 \eta_3) \quad (3.161)$$

$$d = \bar{G} E_1 H_2 \eta_2 + \bar{G} E_3 H_3 (\eta_2 + \eta_3). \quad (3.162)$$

The above equations can be used to predict the performance of simply supported beams or rectangular plates with constrained layer damping treatments. For a three-layer sandwich, which is equivalent to a single constrained-layer system as already discussed, the equations can be used directly, and for multiple constrained treatments they can be used in a step-by-step procedure.

For the single constrained layer, equations 3.156 through 3.162 can be used without modifications to predict the performance of the treatment. To use these equations, it is necessary to know the complex modulus properties of the damping material (modulus and loss factor), which are dependent on both temperature and frequency. It is necessary to go through the following steps.

1. First it is assumed that either the natural frequency, ω , or the semiwave length of vibration is known. Regardless of which is known, the other quantity can be calculated from equations 3.152 and 3.153 for beams, or 3.154 and 3.155 for plates.
2. The undamped natural frequency can be determined (if not known) from equation 3.153 for a beam or 3.155 for a plate.
3. The material properties should be determined for the frequency of Step 2 and for the desired temperature range to which the structure and damping material are subjected.
4. Using the material properties of Step 3, the term EH^3 of equation 3.155 is calculated.
5. Use this value of EH^3 in equation 3.153 for beams or 3.155 for plates to calculate the frequency of the 3 layer sandwich. With the new frequency recalculate the material properties and the EH^3 term (Steps 3 and 4). Repeat this process until the frequency converges (within 10 percent).
6. The loss factor is calculated from equations 3.156 and 3.157.
7. The above procedure is repeated for each desired temperature.

3.2.5 Analysis for Multiple Constrained-Layer Treatment

As a result of many tests on the performance of multiple constrained layers constructed with the same damping material in each layer, it has been observed that most of the shear deformation occurs in the shear damping layer closest to the structure. [3.29] All the outer layer pairs act as a thick constraining layer which restrains the first shear damping layer. Therefore, if the stiffness of all subsequent layers can be determined, then the damping of multiple constrained layers can be predicted. This can be done by using

the three-layer equation and working from the outside of the treatment (away from the structure) to the first layer. The steps for carrying out this procedure are described below (also refer to Figure 3.30).

1. Repeat Steps 1 through 3 for a single layer application.
4. Consider the n th constraining layer, n th damping layer, and the $N - 1$ constraining layer. Calculate the term EH^3 from equation 3.157, and hence E and H .
5. Take E and H from Step 4 and use them as the new properties of a constraining layer acting on the $N - 1$ damping layer and $N - 2$ constraining layer.
6. Repeat Steps 4 and 5 until the first shear damping layer is reached. At that point, the first damping layer will have one equivalent constraining layer with a given E and H .
7. Repeat Steps 4 through 7 of Section 2 for the single constraining layer.

3.2.5.1 Multiple-Layer, Multiple-Material Constrained-Layer Damping Analysis [3-30]

The method of using a multiple-layered constrained-layer damping design to obtain a broad temperature range of damping was discussed early and has been successfully applied to various problems. [3.21,3.25,3.29]

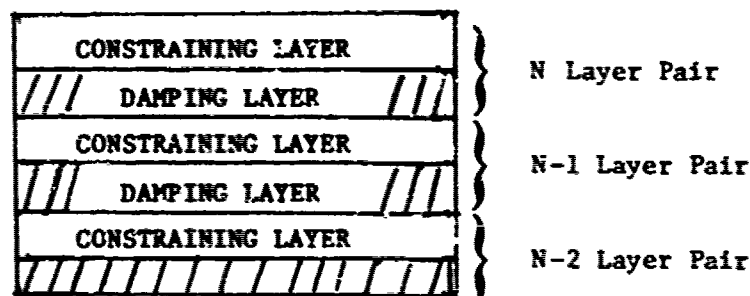


Figure 3.30. - Elements of N constrained layer system on a structure.

Numerous methods exist to analytically model certain types of multiple layer treatments [3.31-3.34]. This section presents an analysis technique for a general multilayer prediction approach based on a generalization of the theory of a single constrained layer system developed by Koss, Kerwin, and Ungar [3.35]. The method used in this analysis is to derive the equation of motion for the bending of an N layered beam that is simply supported. Limiting the analysis to this simple boundary condition permits a tremendous simplification of the equations so that minimal computational skill is required for their evaluation. The complex natural frequencies of the damped beam are calculated, and from there, the damping effectiveness is determined.

The approach is similar to that used in Section 3.2.3. The task is to express $\partial^2 M_x / \partial x^2$ in equation 3.116 in terms of the geometry of an N layered beam. The total bending moment M may be expressed in terms of the moments of each layer about the composite neutral axis

$$M_x = \sum_{i=1}^N M_{ii} + \sum_{i=1}^N F_i H_{io} , \quad (3.163)$$

Where M_{ii} is the bending moment of the ith layer about its own centroid; F_i is the extensional force in the ith layer; and H_{io} is the distance between the centroid of the ith layer and that of the composite beam. This is illustrated in Figure 3.31. The bending moment of the ith layer may be expressed as

$$M_{ii} = \frac{\partial^2}{\partial x^2} E_i I_i , \quad (3.164)$$

where E_i and I_i are the Young's Modulus and moment of inertia.

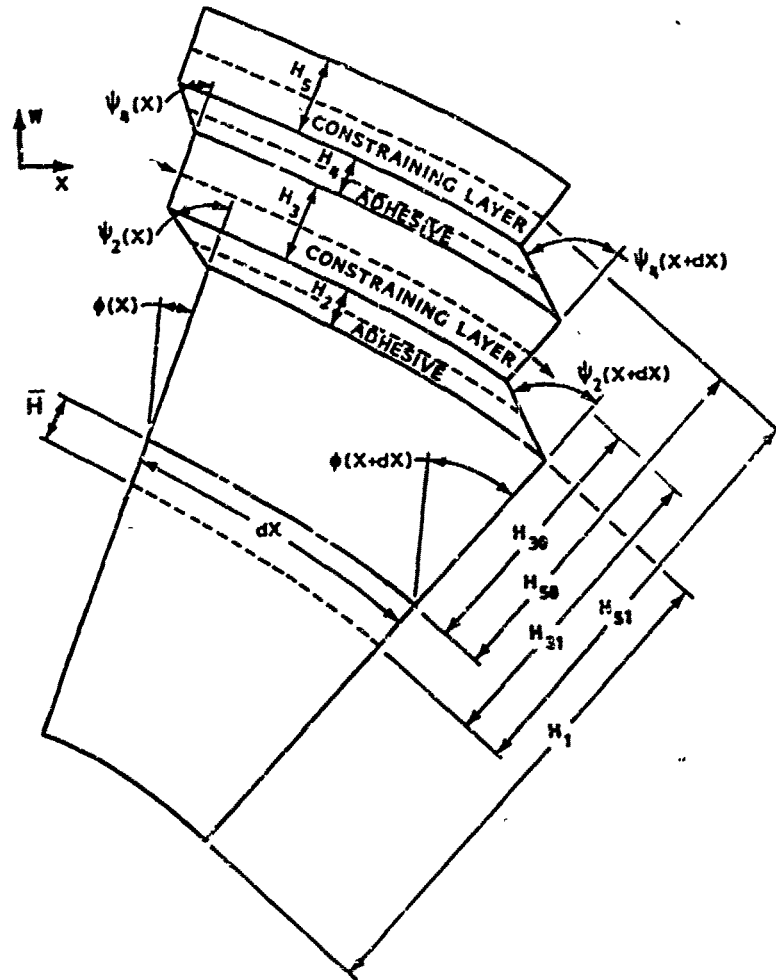


Figure 3.31. - Bent element of multilayer beam.

To calculate M_x it is necessary to determine F_i and H_{j0} for each layer. From Figure 3.31 it may be seen that for $i = 3, 5, 7, N$ the (areawise) average extensional strain is

$$\gamma_i = H_{i0} \frac{\phi(x) - \phi(x+dx)}{dx} - \sum_{j=2,2}^{i-1} H_j \frac{(\psi_j(x) - \psi_j(x+dx))}{dx} \quad (3.165)$$

$$\gamma_i = H_{i0} \frac{\partial \phi}{\partial x} - \sum_{j=2,2}^{i-1} H_j \frac{\partial \psi_j}{\partial x} \quad i = 3, 5, 7, \dots, N \quad (3.166)$$

and

$$\gamma_i = \bar{h} \frac{\partial \phi}{\partial x} \quad (3.167)$$

Here it is assumed that the viscoelastic layers maintain a constant thickness during bending so that all layers bend with the same curvature. The notation $\sum_{j=2,2}^{i-1}$ means that i takes on even values only.

The extensional stress, τ_i , the product of the strain and Young's Modulus E_i ,

$$\tau_i = E_i \gamma_i \quad (3.168)$$

The extensional force is

$$F_i = S_i \tau_i = S_i E_i \gamma_i = K_i \gamma_i \quad i = 1, 3, 5, \dots, N \quad (3.169)$$

where S_i is the cross sectional area of layer i and K_i is the extensional stiffness. Since the Young's modulus of the metal layers is much higher than that of the viscoelastic layers it is assumed that F_i is zero when i is even.

To evaluate equation 3.169 it is necessary to determine the viscoelastic shear strain ψ_i in equation 3.166. For small deflections of a simply supported beam, the shear strain in each layer is proportional to the slope of the beam. This can be seen from the geometry as shown in Figure 3.31.

$$\psi_i = A_i w' \quad (3.170)$$

The coefficient A_i , will be determined later. Differentiating equation 3.170 gives

$$\psi_i' = A_i w'' \quad (3.171)$$

Substituting the derivative of the adhesive shear strain, as obtained from equation 3.171 into the extensional strain γ_i , in equation 3.166 permits the calculation of the extensional force F_i in each elastic layer from equation 3.169.

$$F_i = K_i \left[H_{i0} w'' - \sum_{j=2,2}^{i-1} H_j A_j w'' \right] \quad i=3,5,7,\dots,n \quad (3.172)$$

Also,

$$F_i = K_i \bar{H} w'$$

Substituting this equation into the bending moment equation (equation 3.163) and then into equation 3.116 gives the equation of motion of the multiple layered beam,

$$w'''' \left(\sum_{i=1,2}^N D_{ii} + \sum_{i=1,2}^N K_i H_{i0}^2 - \sum_{i=3,2}^N K_i H_{i0} \sum_{j=2,2}^{i-1} H_j A_j \right) + \frac{1}{g} \rho A \ddot{w} = 0 \quad (3.173)$$

When the beam is driven by an applied loading $F(x,t)$ the equation of motion may be written as

$$D^* w'''' + \frac{1}{g} \rho A \ddot{w} = F(x,t) \quad (3.174)$$

where

$$D^* = \sum_{i=1,2}^N \left(D_{ii} + K_i H_{i0}^2 \right) - \sum_{i=3,2}^N K_i H_{i0} \sum_{j=2,2}^{i-1} H_j A_j \quad (3.175)$$

D^* is the composite complex bending stiffness of the N layered beam.

It will be shown later that A_j , (Note $A_i = A_j$), and hence H_{i0} take on complex values when the viscoelastic layers are capable of dissipating energy. This causes the bending stiffness B to also be complex. The complex natural frequency for the m th mode of the beam is

$$\omega_n^{*2} = \frac{P_m^4 g D^*}{\rho A} = \frac{P_m^4 g D (1 - i \eta_s)}{\rho A} = \omega_n^2 (1 - i \eta_s) \quad (3.176)$$

where * denotes a complex number and η_s is the composite loss factor of the damped beam.

In order to calculate the bending stiffness in equation 3.178 it is necessary to find H_{10} and A_j . From Figure 3.31

$$H_{10} = H_{11} - \bar{H} \quad (3.177)$$

where \bar{H} is the distance between the neutral axis of the composite and that of the primary beam. If there are N layers in the composite beam there will be $\frac{N-1}{2}$ adhesive layers and there will be $\frac{N-1}{2}$ values needed for A_j ($j=2,4,6,\dots, n-1$).

Including D , there are then $\frac{N-1}{2}$ unknowns in equation 3.179. To calculate the bending stiffness in equation 3.175, $\frac{N+1}{2}$ more equations must be generated in D and A_j . One equation may be obtained by summing the forces in the X direction,

$$\sum_{1,2}^N F_i = 0. \quad (3.178)$$

It is assumed here that the inertia forces are much less than the extensional restoring forces in the metal layers. From equations 3.172 and 3.176 this becomes

$$\sum_{1,2}^N F_i = \sum_{1,2}^N K_i \left[H_{10} - \sum_{j=2,2}^{i-1} H_j A_j \right] w'' = 0 \quad (3.179)$$

$$\bar{H} = \frac{\sum_{1,2}^N K_i \left(H_{11} - \sum_{j=2,2}^{i-1} H_j A_j \right)}{\sum_{1,2}^N K_i} \quad (3.180)$$

To evaluate A_j it is necessary to know the relationship between the shear strains of the adhesive layers. This may be obtained from the stress-strain relation for the shear of each adhesive layer

$$\phi_i = \frac{1}{G_i b_i} \sum_{j=1,2}^{i-1} \frac{\partial F_j}{\partial x} = \frac{-1}{G_i b_i} \sum_{j=i+1,2}^N \frac{\partial F_j}{\partial x} \quad (3.181)$$

Where G_i is the shear modulus of the adhesive and b_i is the width. Substituting equations 3.170 and 3.172 gives

$$A_i w' = \frac{-1}{G_i b_i} \sum_{j=i+1,2}^N K_j H_j w'' - \sum_{j=i+1,2}^N K_j \sum_{m=2,2}^{i-1} H_m A_m w'' \quad (3.182)$$

For simply supported beams,

$$w'' = -\frac{P}{n} w' \quad (3.183)$$

and equation 3.182 becomes

$$A_i w' = \frac{P}{G_i b_i} \sum_{j=i+1,2}^N K_j H_j - \sum_{j=i+1,2}^N K_j \sum_{m=2,2}^{i-1} H_m A_m \quad (3.184)$$

$i=2,4,6,\dots,n-1$

Substituting equations 3.177 and 3.180 and rearranging gives

$$\sum_{j=2,2}^{n-1} C_{ij} A_j = d_i \quad i=2,4,6,\dots,N-1 \quad (3.185)$$

where

$$C_{ii} = \frac{G_i b_i}{P_m^2} + \left(H_i \sum_{m=i+1,2}^N K_m \right) \left(1 - \frac{\sum_{m=i+1,2}^N K_m}{\sum_{m=1,2}^N K_m} \right) \quad \text{For } i = j \quad (3.186)$$

$$C_{ij} = \begin{pmatrix} N \\ H_j \\ \Sigma \\ m=j+1,2 \\ K_m \end{pmatrix} \left(1 - \frac{\begin{matrix} N \\ \Sigma \\ m=i+1,2 \\ K_m \end{matrix}}{\begin{matrix} N \\ \Sigma \\ m=1,2 \\ K_m \end{matrix}} \right) \quad \text{For } j < i \quad (3.187)$$

$$C_{ij} = \begin{pmatrix} N \\ H_j \\ \Sigma \\ m=j+1,2 \\ K_m \end{pmatrix} \left(1 - \frac{\begin{matrix} N \\ \Sigma \\ m=i+1,2 \\ K_m \end{matrix}}{\begin{matrix} N \\ \Sigma \\ m=1,2 \\ K_m \end{matrix}} \right) \quad \text{For } j > i$$

$$d_1 = \Sigma_{m=i+1,2}^N K_m H_{mi} - \left(\Sigma_{m=i+1,2}^N K_m \right) \frac{\begin{pmatrix} N \\ \Sigma \\ m=3,2 \\ K_m H_{mi} \end{pmatrix}}{\begin{matrix} N \\ \Sigma \\ m=1,2 \\ K_m \end{matrix}} \quad (3.188)$$

Equation 3.185 is a linear system of $\frac{N-1}{2}$ equations with $\frac{N-1}{2}$ unknowns which may be solved for the A_j . D may then be evaluated from equation 3.180. The composite bending stiffness and the complex natural frequencies may now be determined from equations 3.175 and 3.176.

The damping ability of each viscoelastic layer is included by allowing the shear modulus to be complex

$$G_j^* = G_j (1+i\eta_j) \quad , \quad (3.189)$$

where η_j is the viscoelastic loss factor. This will cause the system of equations (equation 3.185) to be complex and the resulting solutions, A_i , will be complex.

The above analysis may be used to predict the effectiveness of a general multiple constrained-layer damper.

3.2.6 Complex Mathematical Approach to the Three-Layer Sandwich

A review of the literature on the analysis of constrained-layer damping system rapidly revealed that the major contributions were developed before computers were so prevalent. Another interesting observation is that most of the modifications in the beam theory approach regardless of the time they were developed have continued along the same lines. A totally non-novel idea is interjected here for all the new comers to the area who are about to develop computer codes for constrained-layer analysis.

The three-layer-sandwich equation is repeated here for convenience. Therefore

$$EI = \frac{E_1 H_1^3}{12} + \frac{E_2 H_2^3}{12} + \frac{E_3 H_3^3}{12} + E_1 H_1 \bar{H}^2 + E_2 H_2 (H_{21} - \bar{H})^2 + E_3 H_3 (H_{31} - \bar{H})^2 - \left[\frac{E_2 H_2^2}{12} + \frac{E_2 H_2}{2} (H_{21} - \bar{H}) + E_3 H_3 (H_{31} - \bar{H}) \right] \frac{H_{31} - \bar{H}}{1 + \bar{G}} \quad (3.190)$$

where

$$D = \frac{E_2 H_2 (H_{21} - \frac{H_{31}}{2} + \bar{G}(E_2 H_2 H_{21} + E_3 H_3 H_{31}))}{E_1 H_1 + \frac{E_2 H_2}{2} + \bar{G}(E_1 H_1 + E_2 H_2 + E_3 H_3)} \quad (3.191)$$

$$H_{31} = \frac{H_1 + H_3}{2} + H_2 \quad (3.192)$$

$$H_{21} = \frac{H_1 + H_2}{2} \quad (3.193)$$

$$\bar{G} = \frac{G_2}{E_3 H_3 H_2 k^2} \quad (3.194)$$

E is the Young's modulus of elasticity,

G is the shear modulus,

I is the moment of inertia,

H is the thickness,

k is the wave number,

\bar{G} is the shear parameter, and

n is the mode number.

Note that this equation is based on the assumptions that:

- 1) No shear can occur in layer 1 or 2
- 2) The beam is simply supported

If E, E₁, E₂, E₃, and G₂ are allowed to be complex and the complex algebra routines are used that are available on most mini-computers, a simple equation is obtained which is very powerful. This approach applies to any of the analyses whether it is free- or constrained-layer or is single or multilayer. The approach eliminates the need to separate the real part from the imaginary part analytically making the computer code much easier to develop.

3.3 TUNED VISCOELASTIC DAMPERS

The various layered damping treatments operate effectively only in structures with plate-like bending modes of vibration, for which high surface strains occur. For structures which have low surface strains involving non-plate-like behavior, as in the case of very highly curved elements, or space-frame type structures, the auxiliary mass damper (AMD) concept may be of greater utility. Although the vibration mode shapes might dictate the use of

AMD, other considerations in the total design procedure for a platelike vibration problem might also lead to an AMD design as optimum.

The two types of AMD's are:

- 1) Dynamic Absorbers - added mass-spring dampers with no damping.
- 2) Tuned viscoelastic dampers or damped absorber ALIAS - "Tuned Damper" - added mass-spring damping with a complex spring stiffness.

The dynamic absorber, consisting essentially of a mass suspended on a spring, has been used to eliminate sharp resonance peaks at specific frequencies (revolutions per second) in rotating machinery and other devices being excited by a single frequency. The function of a dynamic absorber is to convert a single-resonant frequency into two-system resonant frequencies, one lower than the initial frequency and one higher.

A dynamic absorber is effective if the two new system frequencies are outside the frequency range of the excitation input. The typical structural response, with a dynamic absorber attached is shown in Figure 3.32. It can be seen that the vibration response at the old resonant frequency is eliminated.

The emphasis here will be placed on the tuned damper. Additional design information on dynamic absorbers can be obtained from Reference [3.36].

3.3.1 Tuned Dampers (TD)

For structures excited by broadband noise, or machinery operating over a wide frequency range, dynamic absorbers are not practical as they will introduce other resonances which may be excited and, therefore, as damaging as the original resonance. That is, eliminating a problem at one frequency may introduce problems at other frequencies.

The use of tuned viscoelastic dampers can compensate for the problem of introducing resonances at other frequencies. Essential prerequisites for a tuned damper to be of value are that the damper be located at a point of high

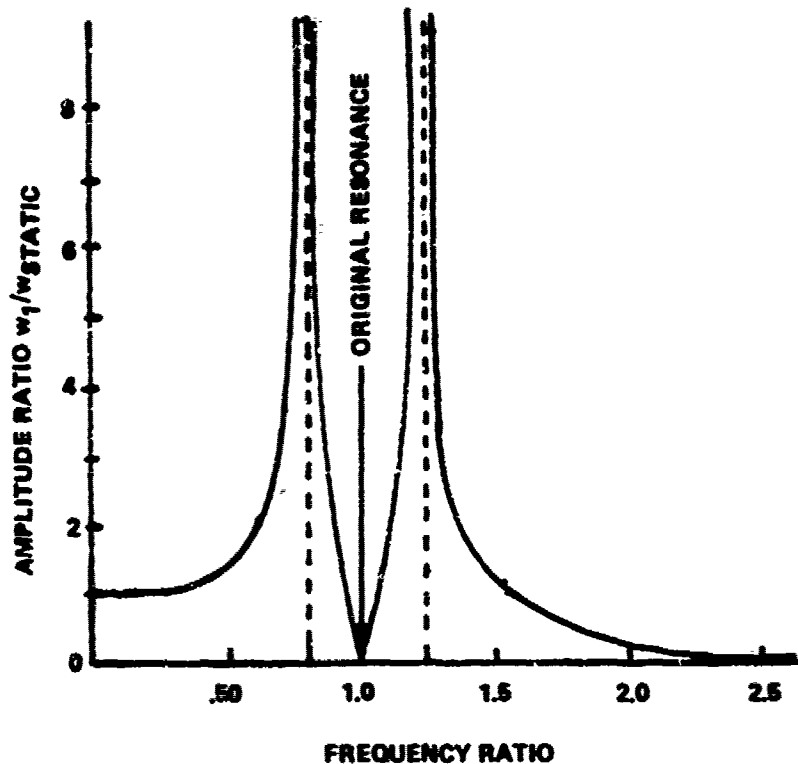


Figure 3.32. - Response of a single degree-of-freedom system with a dynamic absorber.

amplitude response, such as an antinode, and that the frequency spectrum of the response have a single resonance, a number of widely separated resonances, or in some cases, a number of resonances in a frequency band of an octave or less. The effects of a TD for each of these cases is shown in Figure 3.33.

Figure 3.34 shows an idealized sketch of a tuned damper, consisting of a mass attached to a spring exhibiting viscoelastic damping behavior. Energy dissipation in the damper occurs through the cyclic deformation of the viscoelastic material. This type of damper differs from the dynamic absorber, which functions as an energy transfer device at a tuned resonant frequency [3.37]. In the viscoelastic damper, mechanical energy is converted into heat. The TD is effective over a frequency range rather than a single frequency. TD's have been studied for many years. Classical analyses consider the effect of attaching a mass to a vibrating body through an elastic

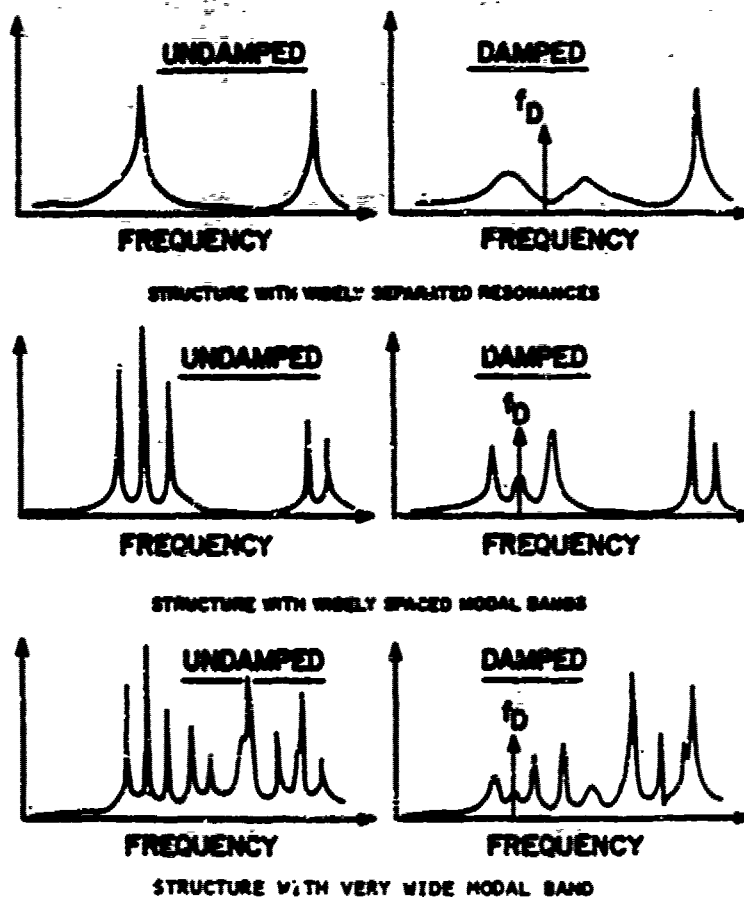


Figure 3.33. - Effects of a tuned damper on different types of structures.

spring and viscous dashpot [3.36,3.38]. More recent investigations have refined these analyses by introducing complex modulus notation to represent damping in a dynamic absorber that uses a spring made from rubberlike, or elastomeric, material which both stores and dissipates energy [3.39,3.40].

If the structure is relatively simple to the extent that it either has only a single resonance or a number of very widely separated resonances, a tuned damper can be designed very readily simply by assuring that the damper frequency $\omega_D = \sqrt{K/M}$ is close to the frequency of the mode to be damped. The effect of the damper on the response of the structure is to split the original mode into two. The lower frequency branch corresponds to the damper mass M and the structure surface moving essentially in phase with each other, while

the higher frequency peak corresponds to the mass and surface moving essentially out of phase.

3.3.2 Energy Dissipation in a Simple Damper

The essential features of tuned viscoelastic damper behavior can be understood by considering the energy, D_s , dissipated per cycle for given cyclic displacement of amplitude, w_0 , at the point of attachment to the structure.

Consider the spring mass system (Figure 3.34) excited at the base of the spring by a displacement $w_0(t) = w_0 e^{i\omega t}$ (or $w_0(t) = w_0 \cos \omega t$).

The equation of motion of the system can be written as

$$M \frac{d^2 w}{dt^2} + K^* (w_r) e^{i\omega t} = 0 \quad (3.195)$$

The list of symbols used in this and other equations in Section 3.3 are listed in Table 3.4. Since

$$w(t) = (w_0 + w_r) e^{i\omega t}$$

then

$$-M\omega^2 (w_0 + w_r) + k^* (w_r) = 0 \quad (3.196)$$

and,

$$-M\omega^2 w_r + K^* w_r = M\omega^2 w_0$$

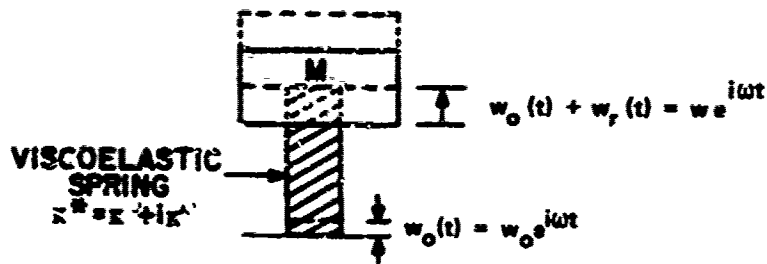


Figure 3.34. - Idealized tuned damper.

or,

$$(K^* - M\omega^2) v_r = M\omega^2 w_0 \quad (3.197)$$

Thus,

$$\frac{v_r}{w_0} = \frac{M\omega^2}{K^* - M\omega^2} \quad \text{remembering } K^* = K' + iK'',$$

$$\frac{v_r}{w_0} = \frac{M\omega^2}{K' + iK'' - M\omega^2} = \frac{M\omega^2 (K' - M\omega^2 - iK'')}{(K' - M\omega^2)^2 + K''^2} \quad (3.198a)$$

$$\frac{v_r}{w_0} = \frac{M\omega^2}{\sqrt{(K' - M\omega^2)^2 + K''^2}} \quad (3.198b)$$

then

$$v_r = \frac{M\omega^2 w_0}{\sqrt{(K' - M\omega^2)^2 + K''^2}} \quad (3.199a)$$

TABLE 3.4. - LIST OF SYMBOLS FOR SECTION 3.3

SYMBOL	DEFINITION
D_s	Energy dissipated per cycle in tuned damper
F	Force in tuned damper
K'	Real part of complex stiffness K^*
K''	Imaginary part of complex stiffness K^*
K^*, K_2^*	Complex stiffness of tuned damper
H	Mass of tuned damper
M_1	Intermediate mass in two degree-of-freedom system
M_2	Tuned damper mass in two degree-of-freedom system
$p(x)$	Harmonic beam loading function
U	Strain energy
$w(\epsilon)$	Displacement of tuned damper
$w_0(t)$	Displacement at base of tuned damper
$w(x)$	Beam displacement as function of position x
w_1, w_2	Displacement of M_1 and M_2
α	Ratio of resonant frequency tuning mass to resonant frequency of system
β	Ratio
η	Loss factor
η_s	Structural loss factor
Λ	Ratio of damper mass to mass of system to be damped
μ	Mass per unit length of beam
ω	Radian frequency of harmonic motion at base of tuned damper
ω_D	Natural frequency of tuned damper

From this, resonance occurs when

$$K' = M\omega^2 \quad (3.199b)$$

or

$$\omega^2 = \frac{K'}{M} \quad (3.200)$$

which is the undamped frequency.

The force tending to deform the spring or the force opposing the motion of the base of the spring is

$$F = K^* w_r \quad (3.201)$$

Also, the work done in a cycle of motion is

$$\text{work/cycle} = \int \frac{2\pi}{\omega} F \cdot \frac{dw_r}{dt} dt \quad (3.202)$$

where f and $\frac{dw_r}{dt}$ are vectors.

Integrating, it can be shown that the energy dissipated per cycle is

$$D_s = \pi w_r^2 K'' \quad (3.203)$$

On substituting for w_r from equation 3.219a,

$$D_s = \frac{\pi K'' M^2 \omega_o^4 w_o^2}{(K' - M\omega^2)^2 + K''^2} \quad (3.204)$$

Since $K'' = \eta K'$

$$D_s = \frac{\pi \eta K' \eta^2 \omega^4 \omega_0^2}{(K' - M\omega^2)^2 + (\eta K')^2} \quad (3.205a)$$

With $\omega_D^2 = \frac{K'}{M}$ and $\beta = \frac{\omega}{\omega_D}$, and divide numerator and denominator of equation 3.205a by $\frac{1}{(K')^2}$ results in

$$D_s = \frac{\eta \omega_0^2 K' \beta^4 \pi}{\eta^2 + (1 - \beta^2)^2} \quad (3.205b)$$

By definition, the structural loss factor is

$$\eta_s = \frac{D_s}{2\pi U} \quad (3.205c)$$

It is readily apparent that the effectiveness of a TD is controlled by

- 1) $\omega_0 \rightarrow$ the displacement of the structure where the TD is attached.
- 2) η and K' \rightarrow the material properties of the viscoelastic spring.
- 3) $\beta = \frac{\omega}{\omega_D} \rightarrow$ the frequency ratio or tuning of the TD.

The fact that $\eta_s \propto \omega_0$ explains why the tuned damper needs to be placed at or near an antinode of the mode of vibration which is to be controlled. Obviously, if $\omega_0 = 0$ or the TD is placed on a node, there will be no effect on the structural response.

The material property effects are not as straight forward for a tuned damper design as they are for the layered damping designs. Review of equation 3.205b shows that η and K' are in the numerator and η^2 is in the denominator. Also, ω_D , the damped natural frequency, is dependent on K' . To evaluate the effect of η , assume $\omega_D = \omega$. Then $D_s \propto \frac{1}{\eta}$, which means that the higher the loss factor the smaller D_s and η , resulting in a less effective TD at the design frequency. This point is illustrated in Figure 3.35. Note in Figure 3.38 that there is an advantage in the TD design gained as η is increased which is the increased effective frequency range of the TD. The level of material damping chosen for a TD is a design parameter which will affect the frequency range over which the TD will be effective and will affect the total amount of energy dissipated.

The other material property of interest in a TD design is the modulus. As can be seen from equation 3.200, the modulus is a controlling parameter for the TD resonant frequency. Since precise tuning is important for proper utilization of a TD, the modulus is required to be relatively constant. This tuning effect has a profound influence on the choice of elastomer used in the damper. If an elastomeric tuned damper were to be operated within the transition temperature range, where the loss factor is high and the modulus changes rapidly with temperature, then the internal heating of the damper due to energy dissipation would cause the resonant frequency to change and the damper to detune itself. Therefore, elastomeric materials in tuned dampers should be used in the rubbery temperature region, as shown in Figure 3.36, where small changes in temperature do not have a large effect on the stiffness of the viscoelastic materials.

The final parameter which the designer has control over in equation 3.205b is β the tuning ratio ($\frac{\omega}{\omega_D}$). The effect of the tuning is shown in Figure 3.37. If the ω_D is significantly different than ω one of two peaks will be reduced more than the other as shown in Figure 3.37. Optimum system control is obtained with $\beta=1$.

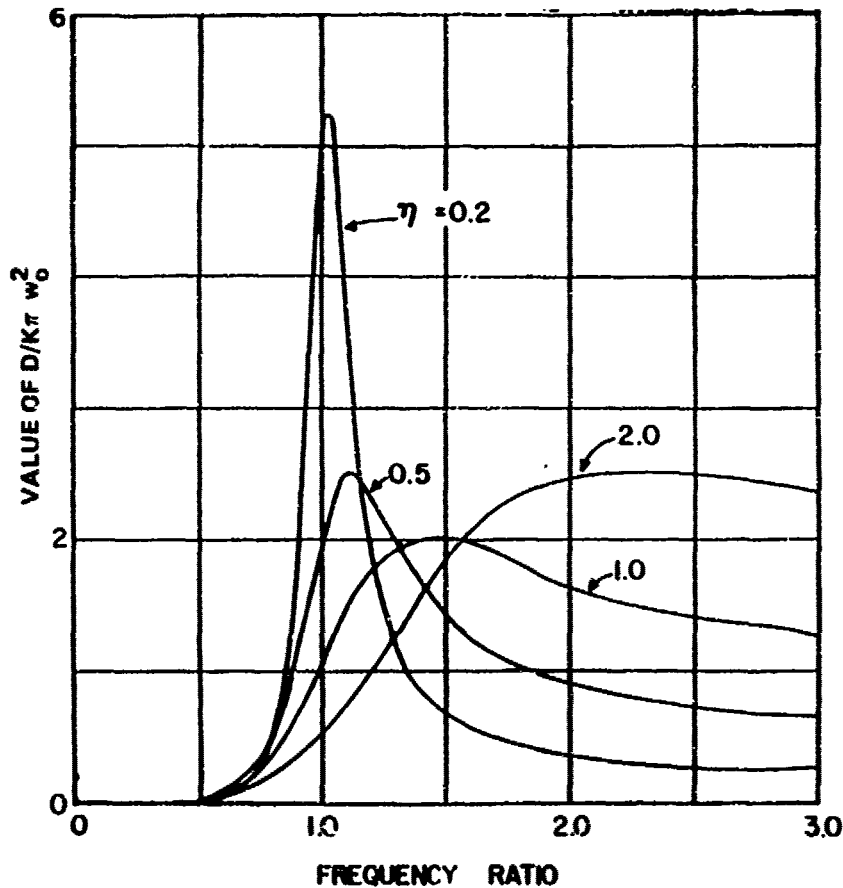


Figure 3.35. - Effect of loss factor on energy dissipation.

The effects of TD placement, damping material properties, and tuning have been discussed here to emphasize basic principle. Design procedures for structures which give additional insight into TD design and function follow.

3.3.3 Two Degree-of-Freedom

Let us now investigate the system illustrated in Figure 3.38.

An example of such a system may be an electronics package mounted to the fuselage on some structural member of an airframe or engine, where the support is moving and causing undesirable vibration of the package. We will show that the spring-mass system of M_2 and K_2^* can be designed in such a way as to control the amplitude of M_1 .

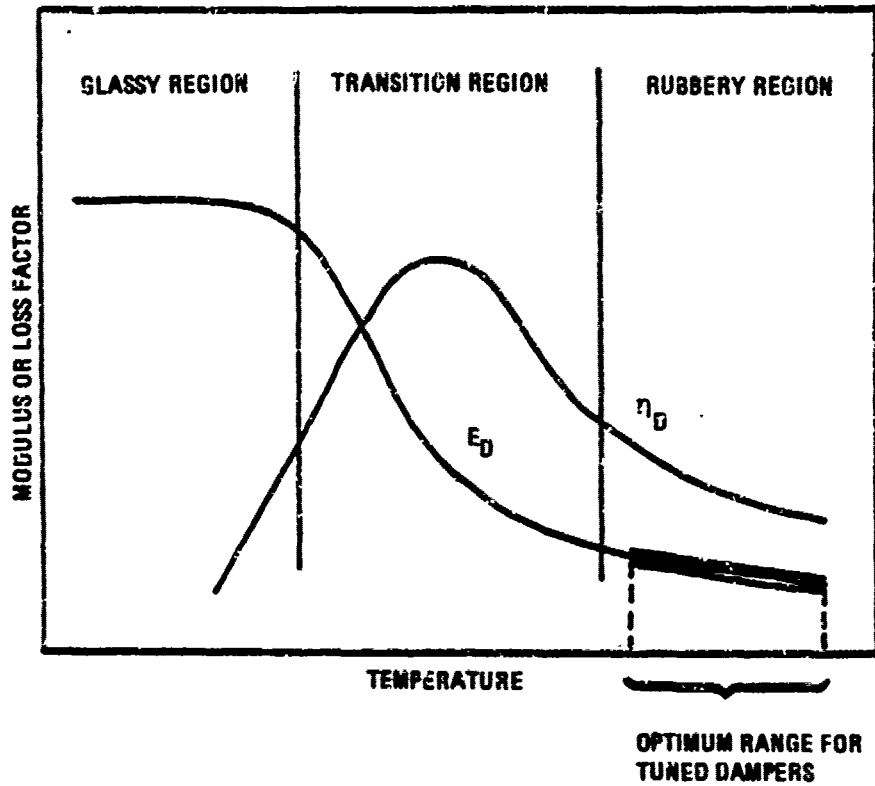


Figure 3.36. - E_D and η_D versus temperature for typical elastomer.

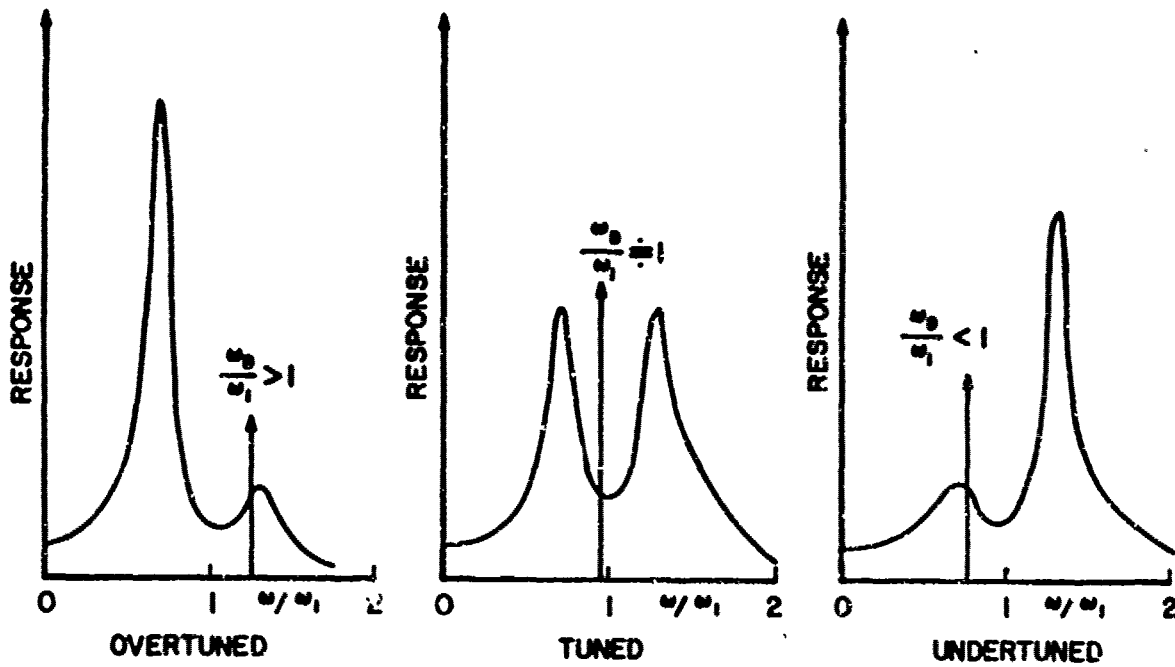


Figure 3-37. - Effect of damper tuning.

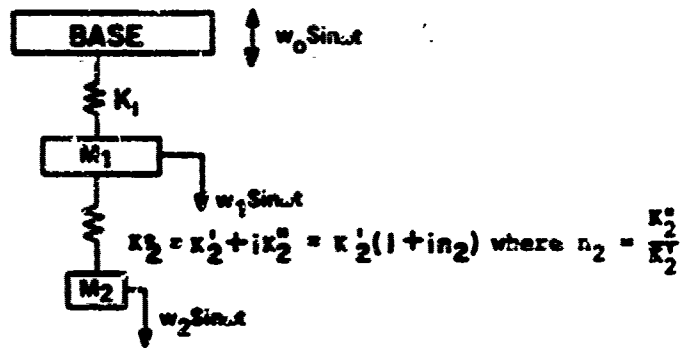


Figure 3.38. - Two degree-of-freedom system.

The equations of motion of this system are as follows.

$$M_1 \ddot{w}_1 + K_1 w_1 - K_2^* (w_2 - w_1) = 0 \quad (3.206)$$

$$M_2 \ddot{w}_2 + K_2^* (w_2 - w_1) = 0. \quad (3.207)$$

We assume w_1 and w_2 are undergoing harmonic displacements, so

$$w_1 = w_1 \sin \omega t \quad (3.208)$$

$$w_2 = w_2 \sin \omega t.$$

The equations of motion are then

$$-M_1 \omega^2 w_1 + K_1 w_1 - K_2^* (w_2 - w_1) = 0 \quad (3.209)$$

$$-M_2 \omega^2 w_2 + K_2^* (w_2 - w_1) = 0 \quad (3.210)$$

$$K_1 w_1 + (M_1 \omega^2 + K_2^*) w_1 = K_2^* w_2, \text{ and} \quad (3.211)$$

$$K_2^* w_1 = (K_2^* - M_2 \omega^2) w_2. \quad (3.212)$$

After collecting terms and solving the simultaneous linear equations, we can show [3.36]

$$\frac{w_1}{w_0} = \left\{ \frac{(\alpha^2 - \beta^2)^2 + (2\sigma\alpha\beta)^2}{[(\alpha^2 - \beta^2)(1 - \beta^2) - \alpha^2 \beta^2 \lambda]^2 + (2\sigma\alpha\beta)^2 (1 - \beta^2 - \beta^2 \lambda)^2} \right\}^{1/2} \quad (3.213)$$

where

$$\alpha = \frac{\omega_2}{\omega_1}, \quad \beta = \sqrt{\frac{M_1 \omega^2}{K_1}} = \frac{\omega}{\omega_1}$$

$$\lambda = \frac{M_2}{M_1}, \quad \sigma_1 = \sqrt{\frac{K_1}{M_1}}$$

$$\omega_2 = \sqrt{\frac{K_2^*}{M_2}}, \quad \sigma = \sqrt{\frac{K_2^*}{2 K_2^* M_2}} = \frac{\eta_2 \omega_2}{2\omega}$$

$$\eta_2 = 2 \frac{\omega \sigma}{\omega_2}$$

where ω is the forcing frequency and ω_1 and ω_2 are the undamped natural frequencies of systems 1 and 2 by themselves.

Using the definition $\sigma = \frac{\eta_2 \omega_2}{2\omega}$, equation 3.213 becomes

$$\frac{w_1}{w_0} = \left\{ \frac{(\alpha^2 - \beta^2)^2 + (\eta_2 \alpha^2 \beta^2)^2}{[(\alpha^2 - \beta^2)(1 - \beta^2) - \alpha^2 \beta^2 \lambda]^2 + (\eta_2 \alpha^2 \beta^2)^2 (1 - \beta^2 - \beta^2 \lambda)^2} \right\}^{1/2} \quad (3.214)$$

The damping term in the above equation is independent of frequency if η_2 is constant with frequency, which is generally a good assumption for certain viscoelastic damping materials. That is

$$\eta_2 \alpha^2 = \text{Constant.}$$

Parameters are ratios of resonant frequency of tuning mass to resonant frequency of system, α , forcing frequency to resonant frequency of system, β , mass of damper to mass of system to be damped, λ , and loss factor, η .

For many applications, the mass ratio, λ , and loss factor (η) are already determined; the mass ratio, because of size, weight and space considerations; the loss factor, because it is unique to the viscoelastic material chosen for the spring. Consider an example in which the purpose is to control the resonant vibrations of a spring mass system of an electronics package.

Adding a properly designed tuned absorber (a spring mass system with no damping) will eliminate the response at the resonance of the package, but introduces two other resonances with very high response levels as illustrated in Figure 3.39. The response amplitude levels of these resonances may also be undesirable, especially if the excitation is broadband. In the illustration as to how the amplitude of these two peaks can be controlled by using a viscoelastic spring material, it is assumed that the mass ratio, λ , and the loss factor of the spring material, η have already been chosen. For the purpose of the illustration, assume that

$$\lambda = 0.3$$

and that

$$\eta = 0.2$$

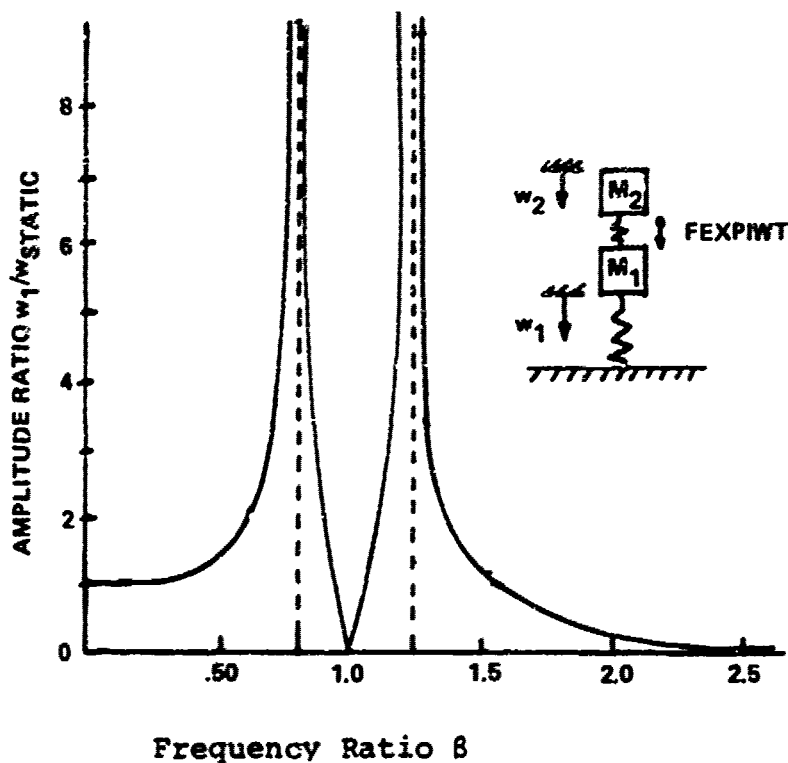


Figure 3.39. - Response of a single degree of freedom system with a dynamic absorber.

both reasonable values. The amplitudes of the two peaks can be controlled by controlling the ratio of the resonant frequency of the tuning mass to the resonant frequency of the package, α . This control is illustrated in Figure 3.39. Usually, optimum tuning for a fixed mass ratio, μ , and loss factor, η , is defined as the frequency ratio, α , at which the two peaks are equal in amplitude.

3.3.4 Tuned Viscoelastic Damper Attached to a Structure

Consider a mass M attached through a viscoelastic spring to a point on a structure as illustrated in Figure 3.40. Let $w e^{i\omega t}$ be the response of the mass M relative to a point fixed in space due to a structural vibration $w_0 e^{i\omega t}$ at the point of attachment, where ω is the frequency of excitation. The force of the spring is

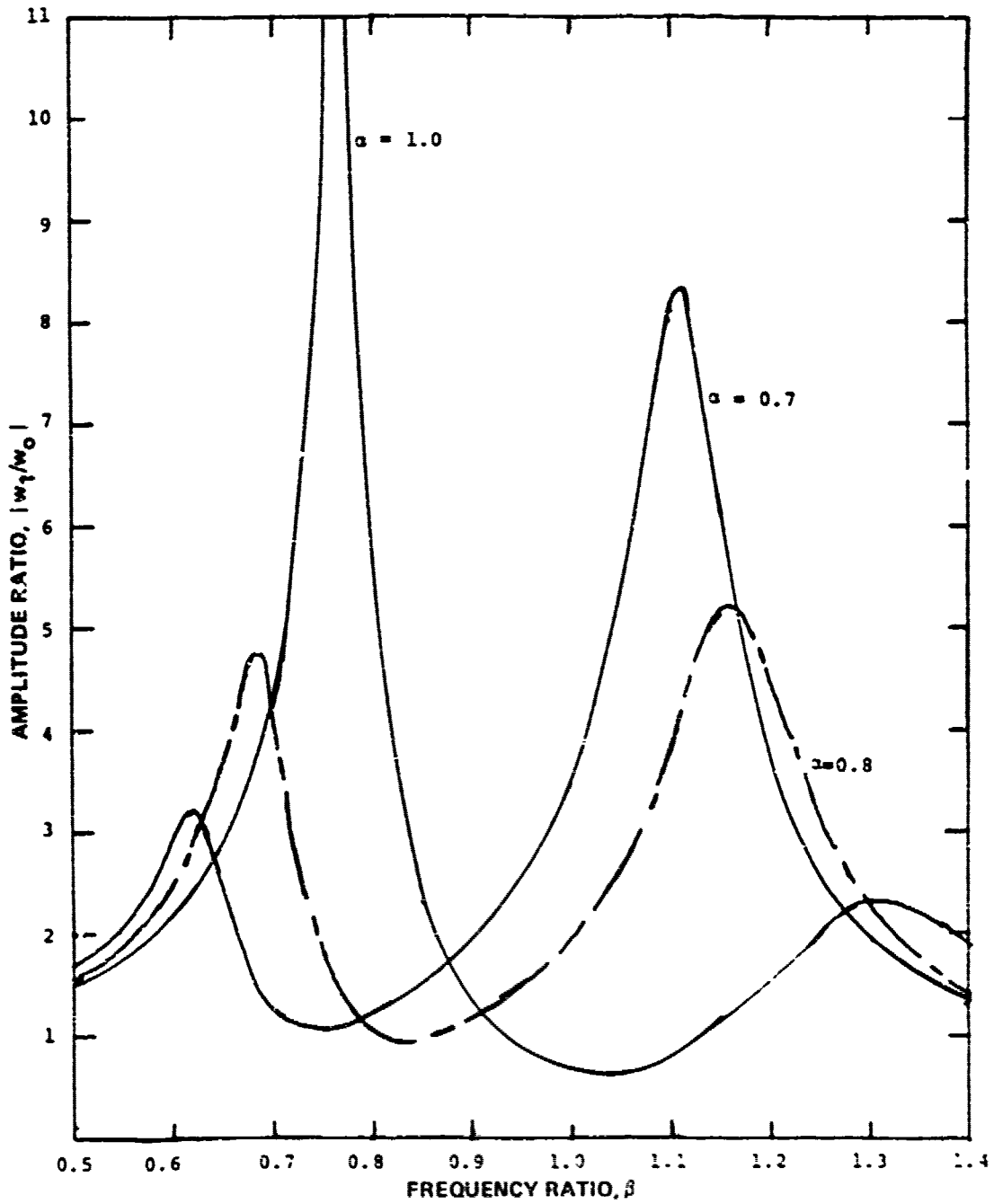


Figure 3.40. - Variation of $|w_1/w_0|$ versus β for different α 's.

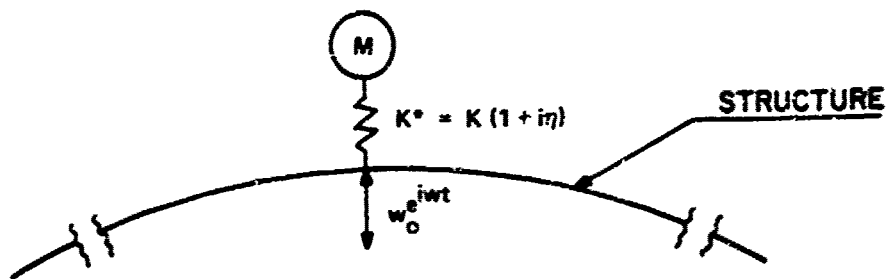


Figure 3.41. - Tuned damper mounted on structure.

$$F = K^*(w - w_0) e^{i\omega t} \quad (3.215)$$

and the equation of motion of the spring mass system is

$$M \left(\frac{d^2 w}{dt^2} \right) + K' (1 + i\eta) (w - w_0) e^{i\omega t} = 0 \quad (3.216)$$

Then

$$w = \frac{K' (1 + i\eta) w_0}{K' (1 + i\eta) - M\omega^2} \quad (3.217)$$

and the force in the spring (also the force transmitted back to the structure) is

$$F = \frac{M\omega^2 K' (1 + i\eta) w_0 e^{i\omega t}}{K' (1 + i\eta) - M\omega^2} \quad (3.218)$$

Again, as in the previous section, define

$$\omega_D^2 = \frac{K'}{M} \quad (3.219)$$

Therefore

$$\frac{F}{K' w_0} = \frac{1 + i\eta \frac{\omega}{\omega_D}}{1 - \frac{\omega}{\omega_D}^2 + i\eta} \quad (3.220)$$

or

$$\frac{F}{K'w_0} = \frac{\left(\frac{\omega}{\omega_D}\right)^2 \sqrt{1+\eta^2}}{\left[1-\left(\frac{\omega}{\omega_D}\right)^2\right]^2 + \eta^2} \quad (3.221)$$

If $F/K'w_0$ is plotted against ω/ω_D then plots similar to those illustrated in Figure 3-41 are obtained.

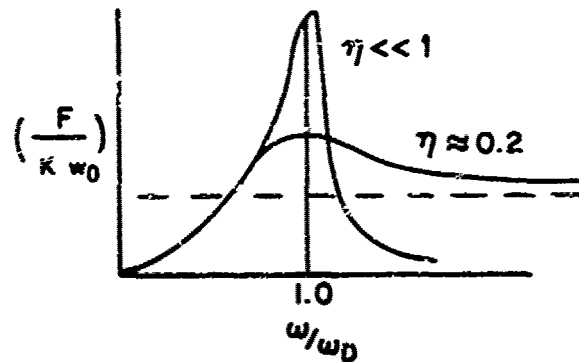


Figure 3.42. - Reduction in force from the addition of damping.

This figure shows that adding damping lowers the force transmitted back to the structure at the resonant point ($\omega/\omega_D = 1$) but gives a still significant force transmission over a wider frequency range.

Consider now a single span beam of length L with a tuned viscoelastic damper attached to a number of points $x = x_j$ ($j = 1 \dots j$) as in Figure 3.42.

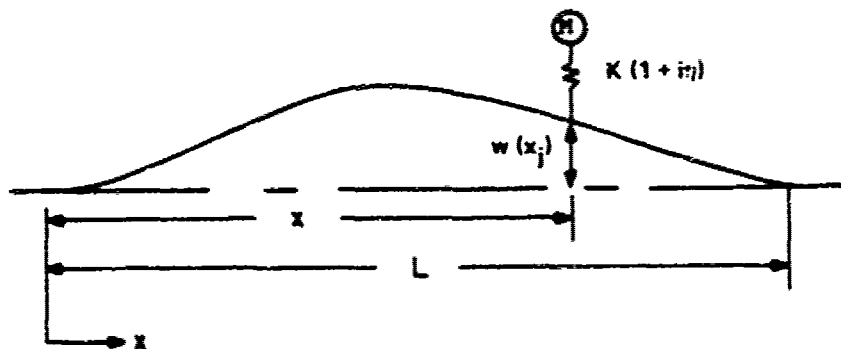


Figure 3.43. - Number of tuned dampers on a beam.

Making use of equation 3.218, the force transmitted back to the structure by the damper at point $x = x_j$ is

$$F_j = \frac{-M\omega^2 w(x_j) \delta(x-x_j)}{1 - M\omega^2 / [K'(1 + i\eta)]} \quad (3.222)$$

where

$\delta(x-x_j)$ is the Dirac delta function and

$\delta(x-x_j) = 0$ when $x \neq x_j$

$\delta(x-x_j) = 1$ when $x = x_j$.

The Euler-Bernoulli equation for the beam with harmonic loading $p(x)$ is then

$$EI \frac{d^4 w}{dx^4} - \frac{U}{R} \omega^2 w - \frac{M\omega^2}{1 - \frac{M\omega^2}{K(1+i\eta)}} \sum_{j=1}^I w(x_j) \delta(x-x_j) = p(x) \quad (3.223)$$

If $w(x)$ and $p(x)$ are expanded as a series of normal modes $\phi_m(\frac{x}{L})$ as the undamped beam, that is,

$$w(x) = \sum_{m=1}^{\infty} w_m \phi_m(\frac{x}{L}) \quad (3.224)$$

$$p(x) = \sum_{m=1}^{\infty} p_m \phi_m(\frac{x}{L}) \quad (3.225)$$

where w_m and p_m are the corresponding modal intensities in the m th mode.

Looking at vibrations in the vicinity of the first mode only, equation (3.224) becomes

$$\frac{EI g \lambda_1^4 w_1}{P_1 L} = \left\{ 1 - \left(\frac{\lambda}{\lambda_1}\right)^4 - \frac{[\psi_{\text{eff}} \left(\frac{\lambda}{\lambda_1}\right)^4]}{\left[1 - \frac{\psi_{\text{eff}} \left(\frac{\lambda}{\lambda_1}\right)^4}{\Gamma_{\text{eff}}(1+i\eta)}\right]} \right\}^{-1} \quad (3.226)$$

Where

$$\psi_{\text{eff}} = \psi \sum_{j=1}^J \phi_1^2(\Delta_j) / \int_0^1 \phi_1^2(\Delta) d\Delta$$

$$\Gamma_{\text{eff}} = \Gamma \sum_{j=1}^J \phi_1^2(\Delta_j) / \int_0^1 \phi_1^2(\Delta) d\Delta$$

and

$$x \Delta_j = \frac{x_j}{L} \quad \Delta = \frac{x}{L}$$

$$\lambda = (\mu \omega^2 L^4 / EI g)^{1/4}$$

$$\lambda_m = (\mu \omega_n^2 L^4 / EI g)^{1/4}$$

μ = mass/unit length of the beam

$$\psi = \frac{m}{\mu L} \quad \Gamma = \frac{KL^3}{EI g^4}$$

$\phi_1(\Delta)$ is the first normal mode of the beam.

Equation 3-226 can be written in the form

$$\frac{EI g \lambda_1^4 w_1}{P_1 L} = \frac{1}{z_r + iz_i} \quad (3.227)$$

Where

$$z_r = 1 - \left(\frac{\lambda}{\lambda_1}\right)^4 - \frac{\psi_{\text{eff}} \left(\frac{\lambda}{\lambda_1}\right)^4 [\Gamma_{\text{eff}} - \psi_{\text{eff}} \left(\frac{\lambda}{\lambda_1}\right)^4 + n^2 \Gamma_{\text{eff}}] \Gamma_{\text{eff}}}{[\Gamma_{\text{eff}} - \psi_{\text{eff}} \left(\frac{\lambda}{\lambda_1}\right)^4]^2 + n^2 \Gamma_{\text{eff}}^2} \quad (3.228)$$

$$z_i = \frac{n \Gamma_{\text{eff}} \psi_{\text{eff}}^2 \left(\frac{\delta}{\lambda_1}\right) \delta}{[\Gamma_{\text{eff}} - \psi_{\text{eff}} \left(\frac{\lambda}{\lambda_1}\right)^4]^2 + \Gamma_{\text{eff}}^2 n^2} \quad (3.229)$$

Then,

$$\frac{\lambda_1^4 w_1 g F'}{P_1 L} = \frac{1}{\sqrt{z_r^2 + z_i^2}} \quad (3.230)$$

A typical plot of the nondimensional response versus $\left(\frac{\lambda}{\lambda_1}\right)^2$, which is the ratio of the forcing frequency to the undamped natural frequency of the beam, is as shown in Figure 3.47.

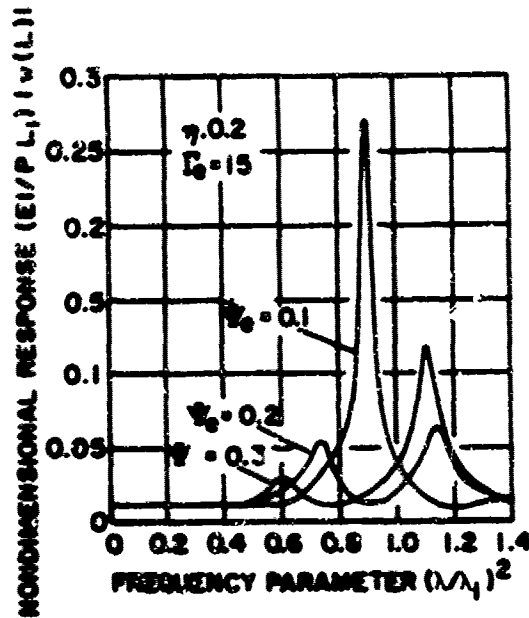


Figure 3.44. - Nondimensional response versus frequency parameter.

Optimum damping is defined as the value ψ_{eff} which makes the amplitude of the two peaks of the response the same. It can be shown that

$$\omega_D/\omega_1 = (\Gamma_{eff}/\psi_{eff})^{1/2}$$

for optimal tuning. This implies that if we determine the optimal value of ψ_{eff} for a given Γ_{eff} and loss factor, γ , we can calculate the resonant frequency, ω_D , of the damper and thus the dimension of the spring.

A paper by D.I.C. Jones, "Response and Damping of a Simple Beam with Tuned Dampers," (Reference [3.41]) discusses these details.

3.3.5 Multi-Span Structures

It has been previously demonstrated that tuned viscoelastic dampers can be effective in damping the response of simple spring mass types of structures or single modes in simple vibrating beam structures. Another attractive feature of tuned viscoelastic dampers is that when applied to structures with closely spaced modes, a single damper can reduce the response in several modes as illustrated in Figure 3.45.

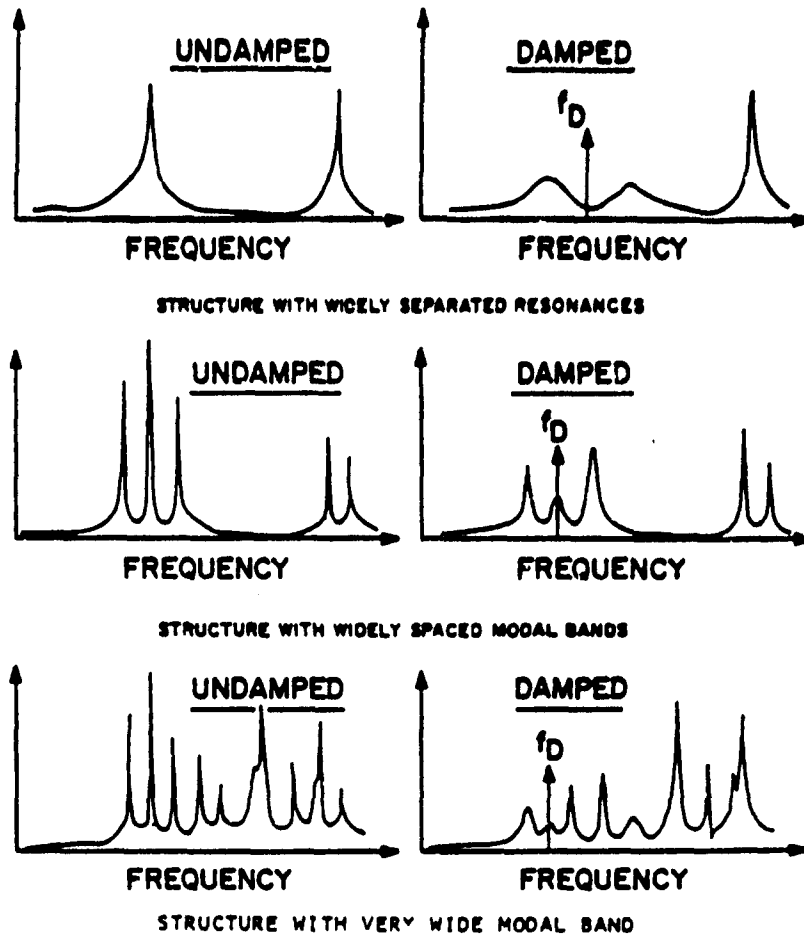


Figure 3.45. - Effects of a tuned damper on different types of structures.

To better describe this behavior, consider two different types of structures, with tuned dampers attached. The first structure is a clamped-clamped beam with a tuned damper attached at mid-span. If the damper is optimized for the fundamental mode, there will be little effect on the other modes, as shown in Figure 3.45 for the case of widely-separated frequencies. The damper will not have any effect on the second mode since it is at a node line and it will also have negligible damping effect on the third mode. This latter can be understood from examination of the equation where loss factor, η_s , for the beam with the damper attached is defined as $\eta_s = D_s / (2\pi U_s)$, where D_s is the total energy dissipated per cycle and U_s is the total strain energy in both the damper and the beam. In the case of the clamped-clamped beam,

the strain energy in the third mode is much greater (about 30 times) than the strain energy in the fundamental mode with the same displacement at the center of the beam. Therefore, even if the energy dissipated per cycle remains the same for both modes, the effect of damping in the third mode will be much lower.

The second type of structure to be considered is a row of curved skin-stringer panels typical of aircraft construction, with a lightweight tuned damper in the center of each panel. This structure is of the type characterized in Figure 3.46 as having closely spaced resonances. Yet, the modes in a given octave band have very similar strain energies, U_p , associated with them. So it is possible for a single tuned-damper to be effective over an octave band of frequencies in such a structure, as shown in Figure 3.46.

Analysis to predict the effect of tuned viscoelastic dampers on the response of multispan structures is given in References [3.42] and [3.43].

Analysis on the effects of TDs on other structures is given in References [3.44 to 3.52].

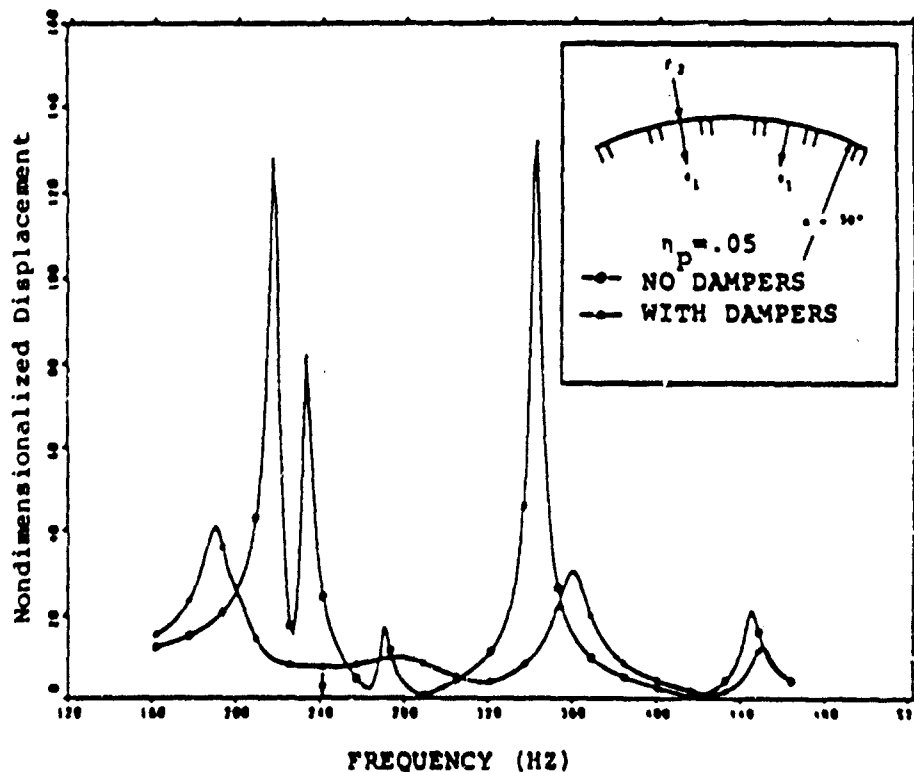


Figure 3.46.- Effect of elastomeric tuned dampers on the response of a curved skin-stringer structure.

REFERENCES

- 3.1 Lazan, B.J., "Damping of Materials and Members in Structural Mechanics." Pergamon Press, New York, 1968.
- 3.2 Oberst H., and K. Frankenfeld, "Uber die Dämpfung dünner Bleche durch festhaltende Beläge," Acoustics, 1952, Vol. 2, pp. 181-194.
- 3.3 Owens, F.S., "Elastomers for Damping Over Wide Temperature Ranges," Shock and Vibration Bulletin 36, Part 4, pp 25-35, 1967.
- 3.4 Mead, D.H., and T.G. Pearce, "The Optimum Use of Unconstrained Layer Damping Treatments," Air Force Materials Laboratory Technical Report ML-TDR-64-51, 1964.
- 3.5 Wirt, L.S., "Development of High Temperature Vibration Coatings," Air Research Technical Report, U.S. Army Contract Da-44-009-AMC-838(T), Air Research Manufacturing Company, Phoenix, Arizona, February 1966.
- 3.6 Nashif, A.D., "Materials for Vibration Control in Engineering," Shock and Vibration Bulletin No. 43, Part 4, June 1973 (D.O.D.)
- 3.7 Sridharan, R.I., "Damping in Porcelain Enamel Coatings," AFML-TR-74-191, Air Force Materials Laboratory, Wright-Patterson AFB, Ohio 1976 (also published as a Ph.D. dissertation, University of Minnesota, 1975).
- 3.8 Jones, D.I.G., and C.M. Cannon, "Control of Gas Turbine Stator Blade Vibrations by Means of Enamel Coatings," J. Aircraft, Vol. 12, No. 4, April 1975, pp 226-230.
- 3.9 Graves, G.A., Jr., C.M. Carson, and B. Kumar, "A Study to Determine the Effects of Glass Compositioned Variations on Vibration Damping Properties," AFWAL-TR-80-4061, May 1980.
- 3.10 Hopkins, D.M., and M.L. Drake, "Porcelain Enamel Material Testing Procedures to Determine the Damping Properties and the Results of Selected Materials," AFWAL-TR-80-4116, September 1980.
- 3.11 Brentnall, W.D., A.R. Stetson, A.G. Metcalf, A.D. Nashif, "Enamels for Engine Structure Damping," AFWAL-TR-83-
- 3.12 Kumar, B., and M.L. Drake, "Constrained Layer Damping with Vitreous Enamel," Journal of Sound and Vibration, Vol. 93, No. 3, 8 April 1984.
- 3.13 Jones, David I.G., "Effect of Free Layer Damping on Response of Stiffened Plate Structures," Shock and Vibration Bulletin, 41, Part 2, December 1970.

- 3.14 Nashif, A.D., "New Method for Determining Damping Properties of Viscoelastic Materials," Shock and Vibration Bulletin 36, Part 4, pp 37-47, January 1967.
- 3.15 Nashif, A.D. and T. Nicholas, "An Analytical and Experimental Investigation of a Two-Layer Damping Treatment," Shock and Vibration Bulletin 39, Part 4, April 1969.
- 3.16 Mead, D.J. and Wilby, J.F. "The Damping of Beam Vibration by Rotational Damping at the Supports," AFML-TR-67-233, Air Force Materials Laboratory, Wright-Patterson Air Force Base, Ohio, August 1967.
- 3.17 Kerwin, E.M., Jr. "Damping of Flexural Waves of a Constrained Viscoelastic Layer," Jour. Acoust. Soc. Am., Vol. 31, July 1959.
- 3.18 Plunkett, R. and C.I. Lee, "Length Optimization for Constrained Viscoelastic Layer Damping," JASA Vol. 48, No. 1, Part 2, pp 150-161, July 1970.
- 3.19 Whittier, J.S., "Rheological Properties of Adhesive; Considered for Interface Damping," WADD TF 60-280, June 1960.
- 3.20 Ross, D., E.E. Ungar, and E.M. Kerwin, Jr., "Damping of Plate Flexural Vibrations by Means of Viscoelastic Laminae," Section III of Structural Damping, ASME, 1959, pp 49-88.
- 3.21 Henderson, J.P., "New Techniques and Materials for Damping," ASME paper 64-MD-22, 1964; design abstract in Machine Design, July 30, 1964, pp 119-124.
- 3.22 Torvik, B.J. and B.J. Lazan, "A Corrugated Addition for Increased Damping in Flexure," AFML-TR-64-73, Air Force Materials Laboratory, Wright-Patterson Air Force Base, Ohio, 1964.
- 3.23 Lazan, B.J., A.F. Metherell, and G. Sokol, "Multiple Band Surface Treatments for High Damping," Air Force Materials Laboratory Report AFML-TR-65-269, Wright-Patterson Air Force Base, Ohio, 1965.
- 3.24 Lazar, B.J., U.S. Patent No. 3,327,812, "Damping Means," June 1967.
- 3.25 Jones, D.I.G., "Design of Constrained Layer Treatments for Broad Temperature Damping," Shock and Vibration Bulletin No. 44, Part 5, pp 1-12, August 1974.
- 3.26 Patent 2,819,032 filed October 20, 1953.
- 3.27 Plass, H.J., "Damping of Vibrations in Elastic Rods and Sandwich Structures by Incorporation of Additional Viscoelastic Materials," Proc. 3rd Midwest Conference Solid Mechanics, p. 48, 1957.

- 3.28 Ross, D., E.E. Ungar, and E.M. Kerwin, "Damping of Plate Flexural Vibrations by Means of Viscoelastic Laminae," *Poc. Colloq. Struct. Damping ASME*, pp 49-87, 1959.
- 3.29 *Vibration Damping Short Course Notebook*, University of Dayton Research Institute, Dayton, Ohio, 1983.
- 3.30 Miles, R.N., "The Prediction of the Damping Effectiveness of Multiple Constrained Layer Damping Treatments," presented at the Meeting of the Acoustical Society of America at the Massachusetts Institute of Technology, June 1979.
- 3.31 Ungar, E.E., and D. Ross, "Damping of Flexural Vibrations by Alternate Visco-Elastic and Elastic Layers," Fourth Midwestern Conference on Fluid and Solid Mechanics, University of Texas, 1959.
- 3.32 Jones, D.I.G., "Damping of Stiffened Plates by Multiple Layer Treatments," *Journal of Sound and Vibration*, Vol. 35, 1974, pp 417, 427.
- 3.33 Nakra, B.C., "Vibration Analysis of an Unsymmetrical Five Layer," *Journal of the Acoustic Society of India*, Vol. IV, No. 1, January/April, 1976 pp 45, 54.
- 3.34 Jones, D.I.G., "Design of Constrained Layer Treatments for Broad Temperature Damping," *The Shock and Vibration Bulletin*, No. 44, August, 1974, Part 5.
- 3.35 Ross, D., E.E. Ungar, and E.M. Kerwin, "Damping of Plate Flexural Vibrations by Means of Viscoelastic Laminae," Sec. 3 of *Structural Damping*, ASME 1959.
- 3.36 Reed, F.E., "Dynamic Vibration Absorbers and Auxiliary Mass Dampers," *Shock and Vibration Handbook*, Chapter 6, edited by C.M. Harris and C.E. Crede, McGraw-Hill Book Company, New York, New York, 1961.
- 3.37 Ormondroyd, J. and J.P. Den Hartog, "The Theory of the Dynamic Vibration Absorber," *Trans, ASME, APM-50-7*, 1928.
- 3.38 Den Hartog- J.P., *Mechanical Vibrations*, Fourth Edition, McGraw-Hill Book Company, New York, New York, 1956.
- 3.39 Snowden, J.C., "Steady State Behavior of the Dynamic Absorber," *The Journal of the Acoustical Society of America*, Vol. 36, No. 6, June 1964.
- 3.40 Soroka, W.W., "Hysteretically Damped Vibration Absorber and Equivalent Electrical Circuit," *Experimental Mechanics*, pp 53-58, February 1965.
- 3.41 Jones, D.I.G., A.D. Nashif, and R.L. Adkins, "Effect of Tuned Dampers on Vibrations of Simple Structures," *AIAA Journal*, Vol. 5, No. 2, 1967.

- 3.42 Bruns, G.A., "Effect of Tuned Viscoelastic Dampers on Response of Multi-Span Structures," Shock and Vibration Bulletin, 36, Part 4, January 1967.
- 3.43 Henderson, J.P., "Vibration Analysis of Curved Skin-Stringer Structures Having Tuned Elastomeric Dampers," AFML-TF-72-240, Air Force Materials Laboratory, Wright-Patterson Air Force Base, Ohio, October 1972.
- 3.44 Jones, D.I.G., "Performance of Tuned Damper Treatments," Acoustical Fatigue in Aerospace Structures, pp 673-681, Syracuse University Press, Syracuse, New York, 1965.
- 3.45 Henderson, J.P., "Energy Dissipation in a Vibration Damper Utilizing a Viscoelastic Suspension," AFML-TR-67-403, Air Force Materials Laboratory, Wright-Patterson Air Force Base, Ohio, November, 1965.
- 3.46 Cannon, C.M., and D.I.G. Jones, "Damping Measurements on Soft Viscoelastic Materials Using a Tuned Damper Technique," Shock and Vibration Bulletin, 38, November 1968.
- 3.47 Jones, D.I.G., "Response and Damping of a Simple Beam with Tuned Dampers," The Journal of the Acoustical Society of America, Vol. 42, No. 1, pp 157-185, 1971.
- 3.48 Jones, D.I.G., and W.J. Trap, "Influence of Additive Damping on Resonance Fatigue of Structures," Journal of Sound and Vibration, Vol. 17, 92, pp 157-195, 1971.
- 3.49 Nasrif, A.D., "Development of Practical Tuned Dampers to Operate Over a Wide Temperature Range," Shock and Vibration Bulletin, 38, November 1968.
- 3.50 Bruns, G.H. and A.D. Nashif, "Experimental Verification of Theory of Damping of a Simple Structure by Distributed Tuned Dampers," AFML-TR-67-44C, Air Force Materials Laboratory, Wright-Patterson Air Force Base, Ohio, June 1967.
- 3.51 Jones, D.I.G., "Analytical and Experimental Investigation of the Effect of Tuned Viscoelastic Dampers on Response of Simple Beams with Various Boundary Conditions," AFML-TR-67-214, Air Force Materials Laboratory, Wright-Patterson Air Force Base, Ohio, June 1967.
- 3.52 Snowden, J.C., "Steady State Behavior of the Dynamic Absorber Addendum," The Journal of the Acoustical Society of America, Vol. 36, No. 6, June 1964.

SECTION 4

CLASSICAL STRUCTURAL VIBRATION RESPONSE THEORIES

4.1 INTRODUCTION

The natural frequencies and mode shapes of structures are required to predict the vibration amplitudes and stresses that will be encountered by these structures when exposed to the in-service vibration environments. The formulation and solution of the equations of motion, for the purposes of obtaining the above information, can range from a simple calculation to those requiring solution by computer. These formulations are based on the stiffness and mass properties of the structure. Resonant frequencies, which include a contribution from the modal damping, are encountered in actual structures, but not the natural frequencies obtained from the above analyses. Because of the relatively low damping observed in most structures, the natural frequencies represent a very close approximation to these structural resonant frequencies. The mode shapes are also assumed to be unaffected by the presence of damping.

The accuracy achieved in predicting the resonant frequencies of structures by these methods is dependent on factors such as the accuracy of the modelling. One of the major problem areas has been the reproduction in the analysis of the actual edge conditions. Another problem area is the engineering tolerances within most practical aerospace structures. These tolerances combine to produce a scatter band of frequencies about a mean frequency for each mode. Consequently, an accuracy of plus or minus ten percent in predicting the resonant frequencies, based on engineering drawing dimensions, is considered acceptable. A higher accuracy can sometimes be achieved for structures with very regular shapes. Normally the reverse is true, especially for more complex structures.

Accurate knowledge of resonant frequencies may be required when attempting to detune structures that are excited by constant frequency type harmonic excitation, which may include higher harmonics of the basic excitation

frequency. Most environments tend to be broadband random in nature which tend, together with transient excitation, to excite many modes. The overall stress, which generally determines if or when the structure will fail, is obtained by taking the square root of the sum of the mean square stresses in the individual modes. Often, the overall stress is due to the dominant response in the fundamental mode. Variations in the resonant frequency of the individual modes will not produce as great an effect on the overall stresses in structures experiencing single mode or the multimode response, as that produced by variations in the modal damping. The modal damping can vary by as much as a factor of two or more in practice. Variations in the level of the vibration environments also tend to have a significant impact on the overall stresses. Consequently, approximate methods for predicting the resonant frequencies of structures, often based on assumed mode shapes, provide sufficient accuracy for preliminary design purposes and, often, for final design purposes. The vibration response can sometimes be reduced to that of a single or two degree-of-freedom lumped mass-spring-damper systems. The development of the governing equations of motion for lumped parameter systems can be found in any standard textbook on mechanical vibration [4.1, 4.2]. More advanced methods can be found in References [4.3] and [4.4].

The purpose in Section 4.2 is to briefly describe some of the basic methods used in the vibration analysis of light weight aerospace structures. Except for a change in emphasis, the discussion is taken almost ad verbatim from the text of a similar discussion in Reference [4.5]. Emphasis is placed in Section 4.3 on simplified analysis methods that are compatible with those available for designing damping treatments in Section 3. Consequently, methods that can only be solved by computer will be excluded unless nondimensional curves or tabulation parameters are available.

4.2 CLASSIFICATION OF VIBRATION ANALYSIS METHODS

Methods of vibration analysis may be classified under three general categories according to the mathematical form of the governing equations [4.3, 4.6]. These three general categories are differential equation methods,

integral equation methods, and energy methods. The distinction between the three categories is logical on a mathematical basis and, hence, to some extent on the degree of effort required to obtain quantitative results. The most salient distinction between the three categories is the manner in which the boundary conditions are handled. In addition, the degree of structural complexity that may be easily included in the model (discontinuities, etc.) is somewhat dependent upon the method. Of the three techniques, energy methods have found the most widespread and common use as an analysis tool. These energy methods provide a means of extending the structural analysis to include the addition of viscoelastic damping treatments to the basic structure, based on assumptions that the mode shapes are not affected by the added treatment. A brief discussion of differential equation methods and integral equation methods is presented with a more detailed consideration given to the energy methods.

4.2.1 Differential Equation Methods

The vibration analysis of a structure requires the solution of the governing partial differential equations describing the motion of the system. For the natural vibrations, the prescribed boundary conditions must be satisfied explicitly to obtain unique solutions. The frequency or characteristics equation results directly from the mathematical conditions imposed by enforcing the boundary conditions on the general solution. Using this method, it is not possible to obtain frequency or mode shape estimates that do not satisfy the boundary conditions. The types of structures for which solutions to the governing equations of motion are possible are strings, bending and twisting of beams, membranes, circular plates and rectangular plates with simply supported edges [4.4]. The bending and torsional vibration of beams have many engineering applications. A good source of solutions to the beam vibration problem, with both classical and nonclassical boundary conditions, is contained in Reference [4.7]. Similarly, the simply supported rectangular plate equation has been used as the basis for approximating the response of plates with fixed edge conditions [4.8] and those with rotationally flexible edge conditions [4.9, 4.10, 4.11, 4.12]. Solutions to the plate vibration problem are also discussed in Reference [4.13].

4.2.2 Integral Equation Methods

Integral equation methods involve the solution of governing integral equations. An integral equation is an equation in which the function to be determined (i.e., the solution) appears under an integral sign. The kernel of these integral equations (4.14) include influence functions (Green's Functions) that will, by usual methods of derivation, satisfy the boundary conditions of the problem. That is, auxiliary conditions are, in a sense, already written into the equation so that the boundary conditions are implicitly satisfied through the use of appropriate influence functions. This method is used extensively in solving acoustics problems but rarely in solving structural dynamics problems.

4.2.3 Energy Methods

Energy methods are based upon the use of one or more of the energy principles of mechanics: conservation of energy, virtual work, Hamilton's principle, Lagrange's equations, etc. Energy methods are the most practical approach for the vibration analysis of complex structures such as plates with edge conditions [4.13] other than simply supported and both unstiffened and stiffened shells [4.15 through 4.19]. A basic discussion of the energy methods is presented in Reference [4.20] with applications of these methods in References [4.3], [4.5] and [4.6] to name a few. Basically, energy methods make use of one or more displacement functions selected somewhat arbitrarily to approximate the natural mode functions. If the natural modes determined by the analysis are to satisfy the prescribed boundary conditions, it is necessary that the approximate or assumed displacement functions satisfy the boundary conditions. The accuracy of the solution, however, depends upon whether or not the boundary conditions are satisfied.

4.2.3.1 Rayleigh Method

Rayleigh's method is based upon a principle stated by Lord Rayleigh in his famous work Theory of Sound in 1877 [4.21]. Rayleigh's principle, stated in modern terminology, is as follows [4.4]: In a natural mode of vibration of a conservative system the frequency of the vibration is a minimum. That is, at any instant the energy of a conservative system in free vibration is partly

kinetic and partly potential with the total energy being constant and the time rate of change of the total energy being zero. Denoting the kinetic energy by $T(t)$ and the potential energy by $U(t)$ at an instant of time, t , the principle of conservation of energy is stated as

$$T(t) + U(t) = \text{constant} \quad (4.1)$$

and the time rate of change of the total energy is

$$\frac{d}{dt} (T(t) + U(t)) = 0 \quad (4.2)$$

Both the kinetic and potential energy are proportional to the square of the amplitude of the mode, and the displacements vary harmonically in time with frequency ω . Hence, for a linear system, the amplitude of the mode is arbitrary when using Rayleigh's method to determine the frequency. From the above result, it is evident that the maximum value of the kinetic energy and that the maximum value of the potential energy must be equal. Hence, an alternate form of Equation 4.2 is

$$T_{\max} = U_{\max} \quad (4.3)$$

Since the motion is harmonic, $T_{\max} = \frac{1}{2} \omega^2 M A^2$ and $U_{\max} = \frac{1}{2} K A^2$ where M is called the modal mass (or generalized mass) and K is called the modal stiffness (or generalized stiffness). Hence, Rayleigh's method yields the result for the normal mode response frequency

$$\omega^2 = K/M \quad (\text{rad/sec})^2 \quad (4.4)$$

The application of Rayleigh's method requires that the frequency be a minimum. That is, the first variation of the frequency must minimize Equation 4.4 such that

$$\delta(\omega^2) = \delta(K/M) = 0 \quad (4.5)$$

Hurty (4.4) has shown that the requirement stated in Equation 4.5 implies that the assumed mode function used to obtain K and M must satisfy the governing differential equation and the natural boundary conditions of the problem. If the assumed mode does not satisfy these conditions completely, then the frequency estimate is not a minimum but slightly higher than the exact result.

Rayleigh's method is extremely useful since reasonably accurate frequency estimates can be obtained explicitly for many structural configurations. Other more refined methods using more than a single assumed mode require extensive computation to obtain quantitative results. Additionally, Rayleigh's method is a very versatile and direct method in that one only needs to make a reasonable guess at the mode and to use this result to obtain the expressions for the kinetic and potential energy of the structure. Leissa (4.13) has shown that in some cases Rayleigh's method provides frequency estimates as accurate as the more refined Rayleigh-Ritz procedure for the vibration analysis of rectangular thin plates.

4.2.3.2 Rayleigh-Ritz Method

This method is an extension of the Rayleigh method and is based upon the premise that a number of assumed functions can be linearly superimposed to provide a closer approximation of the exact natural modes than can be had using a single function as in Rayleigh's method. This method was proposed by Ritz (4.22) and allows not only a better approximation of the fundamental mode frequency and mode shape but also allows the calculation of higher mode frequencies and mode shapes. Using several approximate functions leads to the more accurate results at the expense of increased effort in computation.

The Rayleigh-Ritz procedure assumes that N functions, $\phi_i(x)$, that satisfy at least the geometric boundary conditions are used to approximate the assumed displacement function, $w(x)$, as a series

$$w(x) = \sum_{i=1}^N \phi_i(x) W_i \quad (4.6)$$

The coefficients W_i are determined so that the "best" approximation to the natural modes is obtained by requiring the frequency to be stationary at the natural frequencies, W_i , as required by the Rayleigh Principle (Equation 4.5). By substituting the assumed deflection $w(x)$ given by Equation 4.6 into Equation 4.5 and differentiating the result with respect to each of the coefficients, W_i , a set of N homogenous equations are obtained in the form

$$\frac{\partial \omega^2}{\partial W_i} = 0 \quad i = 1, \dots, N \quad (4.7)$$

These equations contain the undetermined frequency parameter, ω^2 , so that the resulting problem is an n dimensional eigenvalue problem. The solution of this eigenvalue problem requires a computer for $N > 3$ so that the technique is not readily applied to problems that do not justify extensive calculation.

The Rayleigh-Ritz method can be improved [4.23] by the use of the bending moment $M(x)$ at any section of, for example, a beam, rather than the differential of the deflected shape, in deriving the maximum strain energy. The bending moment is obtained by integrating the deflected shape. The deflected mode shape is used to obtain the distributed acceleration force over the beam. The distributed force is integrated to obtain the shear force $Q(x)$ at any cross section. The constant of integration is obtained from the shear force at the boundary ($x = 0$). The moment at any section is obtained by integration of the shear force where the constant of integration is obtained by the bending moment at the boundary ($x = 0$). These two integration constants are known as boundary conditions. If these boundary conditions are not known, then the integration process can be repeated twice more to yield another two boundary conditions. However, this step is usually not required. The advantage of this approach is that good accuracy can be achieved in the predicted natural frequencies with a fewer number of assumed terms in the displacement function.

An alternate approach to the Rayleigh-Ritz Method is the use of Lagrange's equations to obtain the equations of motion based upon an assumed series

expansion of a deflection shape. The results obtained are identical. The utility of using this approach is that the system of governing equations can be developed and estimates made as to the effect of increasing the number of terms in an attempt to improve accuracy. If the effect is small, then it is possible to rationalize an assumed single mode approximation to obtain simple design equations.

4.2.3.3 Numerical Methods

The techniques described previously in Section 4.2 are classified as analytical methods since they are basically focused at obtaining explicit closed-form quantitative results for simple structural configurations. The analysis techniques discussed here are applicable to the analysis of complex structure such as found in aircraft design. For such complex structure, numerical methods must invariably be employed in order to accurately model the structural configuration.

Numerical methods can be subdivided into two categories: numerical solutions to differential equations and matrix methods based upon discrete-element idealization. Numerical solutions to differential equations are somewhat restricted so that these techniques can be practically applied only to simple structural configurations.

Matrix methods develop the complete structural theory using matrix algebra through all stages of the analysis. The structure is first idealized into an assembly of discrete structural elements with an assumed form of displacement or stress distribution. The complete solution is obtained by combining these individual approximate displacement or stress distributions in a manner which satisfies, respectively, the force-equilibrium and displacement-compatibility conditions at the junctions of these elements. The formulation of the analysis in matrix algebra is convenient in that one does not have to write out the lengthy equations and the result is in a form ideally suited for solution on a digital computer.

Examples of matrix methods that are used in all space structures include the finite element method and the transfer matrix method. The finite element method is discussed separately in Section 5. The transfer matrix method is an iterative matrix technique that can be used for structural configurations that are idealized as one dimensional structures. Aircraft structure between two heavy supports, such as fuselage frames, consists of a row of panels that are transversely supported by flexible stringers. The properties of the structure are considered constant in the direction lateral to the frames, with boundary conditions along these frames, assumed to be either simply supported or clamped. The stiffener spacing and the elastic characteristics in the lengthwise direction, parallel to the frames, are taken as variables. The application of the transfer matrix method to stiffened aircraft panel structures was made possible by the discovery [4.24] that the correlation between the vibration response of two adjacent equal size panels that are separated by a heavy stiffener such as a frame, is very small. The correlation between two such panels, when divided by a light stiffener such as a stringer, is very significant.

Prentis and Leckie [4.25] present a basic description of the derivation of the transfer matrix for simple structural configurations and the application of the method to simple lumped parameter mechanical systems. The general analysis techniques to apply the transfer matrix method to structural systems is presented in the textbook by Pestel and Leckie [4.26]. The first application of the transfer matrix method to aircraft skin-stringer panel arrays is described in Reference [4.27]. This work has been continued by other authors [4.28, 4.29, 4.30, 4.31, 4.32] involving the application to flat panel arrays with uneven stiffener spacing [4.29] and curved panel arrays [4.31, 4.32]. The problem of forced response of the panel array to random excitation is discussed in Reference [4.33]. All of the above methods require solution by computer. A simplified method for predicting the natural frequencies of a panel array with even stringer spacing, that does not require solution by computer, is given in Reference [4.34].

4.3 SIMPLIFIED ANALYSIS METHODS

4.3.1 Forced Vibration Theory

The majority of vibration environments encountered by aerospace structures are random in nature, although some discrete frequency environments, such as propeller noise, do exist. Most of these random environments produce pressure fluctuations on the surface of the stiffened panel type structures that are usually convected along the structure. The basic theory for predicting the response of a panel in such structure has been developed by Powell [4.35] using the normal modes approach. This work is based on the linear differential equation of motion for flat plates with small deflections

$$M \ddot{w} + C \dot{w} + K w = p(x, y, t) \quad (4.8)$$

where each dot represents differentiation once with respect to time and where

M = Mass per unit area

C = Damping coefficient

K = Stiffness

$p(x, y, t)$ = Surface pressure fluctuations

w = The displacement

The displacement, w, is a function of both location and time. Therefore the displacement can be expressed [4.36] by

$$w = \sum_{r=1}^N w_r(x, y) q_r(t) \quad (4.9)$$

where $w_r(x, y)$ is the rth mode shape, $q_r(t)$ is the corresponding generalized coordinate and the summation is taken over N modes. Considering only the rth mode for simplicity, equation 4.8 can be written in the form

$$M_r \ddot{q}_r + C_r \dot{q}_r + K_r q_r = L_r(t) \quad (4.10)$$

where

$$M_r = \int_A M w_r^2(x, y) dA \quad (4.11)$$

$$C_r = \int_A C w_r^2(x, y) dA \quad (4.12)$$

$$K_r = \omega_r^2 M_r \quad (4.13)$$

$$L_r(t) = \int_A w_r(x, y) p(x, y; t) dA \quad (4.14)$$

The terms M_r , C_r , K_r and $L_r(t)$ are known as the generalized mass, the generalized damping coefficient, the generalized stiffness and the generalized force, respectively. A is the panel surface area and ω_r is the natural circular frequency of the r th mode.

For random excitation, the Fourier transform of equation 4.14 is first taken to obtain the Fourier spectrum, $\hat{z}_r(i\omega)$, of the generalized force given by

$$\hat{z}_r(i\omega) = \int_A w_r(x, y) p(x, y; i\omega) dA \quad (4.15)$$

where $p(x, y; i\omega)$ is the Fourier spectrum of the fluctuating pressure. The single-sided power spectral density of the generalized force, $G_L(\omega)$, is derived from the equation

$$G_L(\omega) = \lim_{T \rightarrow \infty} \frac{\hat{z}_r^*(i\omega) \hat{z}_r(i\omega)}{2T} \quad (4.16)$$

where the asterisk denotes a complex conjugate and T is the duration of the data sample. Therefore,

$$C_L(\omega) = \int_A \int_A w_r(x, y) w_r(x', y') G_p(x, y; x', y'; \omega) dA dA \quad (4.17)$$

where x, y and x', y' two points on the panel and G(x, y; x', y'; ω) is the simple-sided cross spectral density of the pressure between these points. The power spectral density, $G_w(x, y, \omega)$ of the displacement is obtained by applying the same analytical approach to equation 4.9 but, in this instance, including summation over all N modes. Therefore

$$G_w(x, y, \omega) = \sum_{\substack{r \\ (r=s)}} \frac{\{w_r(x, y)\}^2}{|Z_r(\omega)|^2} \int_A \int_A w_r(x, y) w_r(x', y') G_p(x, y; x', y'; \omega) dx dy dx' dy'$$

$$+ \sum_{\substack{r \ s \\ (r \neq s)}} \frac{w_r(x, y) w_s(x, y)}{|Z_r^*(\omega)| |Z_s(\omega)|} \int_A \int_A w_r(x, y) w_s(x', y') G_p(x, y; x', y'; \omega) dx dy dx' dy' \quad (4.18)$$

where

$$Z_r(\omega) = M_r(\omega_r^2 - \omega^2 + 2i\zeta_r\omega\omega) \quad (4.19)$$

and r and s represent two different modes, ζ_r is the viscous damping ratio for the rth mode and the asterisk denotes a complex conjugate. For the sth mode

the subscript r is replaced by s. The first term in equation 4.19 represents the contribution from each of the modes and the second term represents the contribution from the cross coupling between the modes.

On assuming that the power spectral density of the fluctuating pressures is essentially constant with frequency, equation 4.18 can be reduced to

$$G_w(x, y; \omega) = \frac{A^2 G_p}{4} \left[\sum_r \frac{w_r^2(x, y)}{|Z_r(\omega)|^2} j_{rr}^2 + \sum_{\substack{r \neq s}} \sum_s \frac{w_r(x, y) w_s(x, y)}{|Z_r^*(\omega)| |Z_s(\omega)|} j_{rs}^2 \right] \quad (4.20)$$

where

j_{rr} is the joint acceptance

j_{rs} is the cross acceptance

G_p is the excitation power spectral density

4.3.2 Simplification of the Forced Vibration Theory

Calculation of the power spectral density of the response of a simple plate with equation 4.20 is time consuming even when using a computer. It has been shown [4.35] that for panels with lightly damped modes, that are well separated in frequency, the contribution from the cross terms is negligible. This result has been confirmed in Reference [4.37] even for modes that are reasonably close together. Hence the analysis can be restricted to include only the direct contribution from each of the modes. The calculation still remains complex since the excitation can be from turbulent boundary layer [4.37], separated flow and acoustic excitation [4.36, 4.38], all of which have different spatial characteristics. The panel edge conditions usually fall somewhere between the simply supported or fixed edge conditions. These two bounding edge conditions are usually assumed in most analyses although the analysis with fixed edges is much more complex [4.38].

Considerable simplification can still be achieved by restricting the analysis to simply supported panels that are subjected to acoustic progressive wave excitation parallel to the x axis of the panel. This approach appears rather drastic but it is considerably simpler to "adjust" the structural analysis through the use of the equivalent simply supported mode shape than it is to perform the calculation for a complex mode shape. The use of equivalent simply supported modes shapes in the analysis of structures with fixed edges is not new, having previously been used in the vibration analysis of shells [4.16], panels [4.8, 4.9, 4.10] and of turbulent boundary layer excitation of panels [4.36]. Also, it has been possible to replace the turbulent boundary layer excitation with an equivalent plane wave acoustic excitation as discussed in Section 2, Volume II of the design guide.

The above approach has been adopted for the analysis of structural response to the random fluctuating pressure environment in Section 3, Volume II of the design guide. A random acoustic plane wave, $p(x, t)$, that is travelling parallel to the x axis of a simply supported panel, and incident on the panel surface at an angle ϕ , can be represented by [4.36].

$$p(x, t) = \sum_{k=1}^{\infty} d_k \cos \left\{ \omega_k \left(t - \frac{x \cos \phi}{c} \right) + \beta_k \right\} \quad (4.21)$$

This pressure wave is composed of a continuous spectrum of travelling waves, denoted by the subscript k, at all wavelengths. In the above equation c is the speed of sound in air and d_k and β_k are constants. On assuming well separated modes and a constant spectrum level, G_p , for the acoustic pressure, the power spectral density of the response, $G_w(x, y, \omega)$, at a circular frequency, ω , and a location, x, y, on the surface of the panel, is given by

$$G_w(x, y, \omega) = a^2 b^2 G_p \sum_{r=1}^N \frac{w_r^2(x, y) j_{rr}^2}{|Z_r(\omega)|^2} \quad (4.22)$$

where a and b are the panel length and width, respectively, and j_{rr} is the joint acceptance for the r th mode, given by the expression

$$j_{rr}^2 = \frac{8}{\pi^4 m^2 n^2} \frac{\left\{ 1 - \cos(m\pi) \cos\left(\frac{\omega_r a \cos \phi}{c}\right) \right\}}{\left\{ 1 - \left(\frac{\omega_r a \cos \phi}{\pi mc}\right)^2 \right\}^2} \quad \begin{matrix} n \text{ odd} \\ n \text{ even} \end{matrix} \quad (4.23)$$

$$= 0 \quad n \text{ even}$$

For a progressive acoustic wave used in acoustic fatigue test facilities, $\phi = 0$. If a fully correlated pressure field is assumed, then equation 4.23 becomes

$$j_{rr}^2 = \frac{16}{\pi^4 m^2 n^2} \quad \begin{matrix} m \text{ and } n \text{ odd} \\ n \text{ even} \end{matrix} \quad (4.24)$$

$$= 0 \quad n \text{ even}$$

The overall or mean square displacement, $\bar{w}^2(x, y)$, at location, x, y , on the panel, is obtained by integrating equation 4.21 over the entire frequency range. Therefore,

$$\bar{w}^2(x, y) = \frac{G_p}{2\pi^4 H^2} \sum_{r=1}^N \frac{w_r^2(x, y) j_{rr}^2}{\zeta_r f_r^3} \quad (4.25)$$

The above analysis, based on the equivalent simply supported mode shapes, has been applied recently to stiffened fastener attached metal and composite honeycomb panels [4.40]. Good correlation was obtained between the measured and predicted root mean square strains. This agreement was only possible because a realistic model of the local edge deformation at the fastener line was used.

REFERENCES

- 4.1 Thomson, W. T., "Vibration Theory and Applications," Prentice-Hall, Inc., Englewood Cliffs, N.J., 1965.
- 4.2 Bishop, R.E.D., and Johnson, D.C., "The Mechanics of Vibration," Cambridge University Press, 1960.
- 4.3 Hurty, W.C., and Rubinstein, M.F., "Dynamics of Structures," Prentice-Hall, Inc., Englewood Cliffs, N.J., 1964.
- 4.4 Nowacki, W., "Dynamics of Elastic Systems," John Wiley and Sons, Inc., New York, 1963.
- 4.5 Rudder, F.F. and Plumblee, H.E., "Sonic Fatigue Design Guide for Military Aircraft," AFFDL-TR-74-112, May 1975.
- 4.6 Bisplinghoff, R.L., Ashley, H., and Halfman, R.L., "Aeroelasticity," Addison-Wesley Publishing Company, Inc., 1955.
- 4.7 Goman, D.J., "Free Vibration Analysis of Beams and Shafts," John Wiley and Son, 1975.
- 4.8 Szechenyi, E., "Approximate Methods for Determination of the Natural Frequencies at Stiffened and Curved Plates," Current Developments in Sonic Fatigue, Conference at I.S.V.R., University of Southampton, England, on 6-9 July 1970.
- 4.9 Bolotin, V.V., "Dynamic Edge Effect in Vibration of Plates," Inzhenernyi Sbornik, No. 31, 1960, p. 3.
- 4.10 Ungar, E.E. and Lee, K.S., "Considerations in the Design of Supports for Panels in Fatigue Tests," AFFDL-TR-67-86, September 1967.
- 4.11 Elishakoff, I., "Bolotin's Dynamic Edge Effect," Shock and Vibration Digest, Vol. 8, No. 1, January 1976, p. 95.
- 4.12 Carmichael, T.E., "The Vibration of a Rectangular Plate with Edges Elastically Restrained Against Rotation," Quarterly Journal of Mechanics and Mathematics, Vol. 12, Pt. 1, 1959. pp. 29-42.
- 4.13 Leissa, A.W., "Vibration of Plates," NASA SP-160, National Aeronautics and Space Administration, Washington, D.C., 1969.
- 4.14 Hildebrand, F.B., "Methods of Applied Mathematics," Prentice-Hall, Inc., Englewood Cliffs, N.J., 1960.

- 4.15 Arnold, R.N. and Warburton, G.B., "Flexural Vibrations of the Walls of Thin Cylindrical Shells Having Freely Supported Ends," Proceedings of the Royal Society, Vol. 197, 1949, p. 238.
- 4.16 Arnold, R.N. and Warburton, G.B., "The Flexural Vibration of Thin Cylinders," Proceedings of the Institute of Mechanical Engineering A, Vol. 1967, 1953, p. 62.
- 4.17 Sewall, J.L. and Naumann, E.C., "An Experimental and Analytical Vibration Study of Thin Cylindrical Shells With and Without Longitudinal Stiffeners," NASA TN D-4705. September 1968.
- 4.18 Egle, D.M. and Soder, K.E., "A Theoretical Analysis of the Free Vibration of Discretely Stiffened Cylindrical Shells With Arbitrary End Conditions," NASA CR-1316, June 1969.
- 4.19 Leissa, A.W., "Vibration of Shells," NASA SP-288, 1973.
- 4.20 Langhaar, H.L., "Energy Methods in Applied Mechanics," John Wiley and Sons, Inc., 1962.
- 4.21 Lord Rayleigh, "The Theory of Sound," (1st Ed.), 1877, (2nd Ed.), 1894, Republished by Dover Publications, Inc., New York, 1945.
- 4.22 Ritz, W., "Gesammelte Werke," Paris, 1911.
- 4.23 Bhat, R.B., "Obtaining Natural Frequencies of Elastic Systems by Using an Improved Strain Energy Formulation in the Rayleigh-Ritz Method," Journal of Sound and Vibration, Vol. 93, No. 2, 1984, p. 3i4.
- 4.24 Clarkson, B.L. and Ford, R.D., "The Response of Typical Aircraft Structure to Jet Noise," Journal of the Royal Aeronautical Society, Vol. 66, January 1962, p. 31.
- 4.25 Prentis, J.M. and Leckie, F.A., "Mechanical Vibrations: An Introduction to Matrix Methods," Longmans, Green & Co. Ltd., London, 1963.
- 4.26 Pestel, E., and Leckie, F., "Matrix Methods in Elastomechanics," McGraw-Hill Publishing Company, New York, 1963.
- 4.27 Lin, Y.K., "Free Vibration of Continuous Skin-Stringer Panels," Journal of Applied Mechanics, December 1960, p. 669.
- 4.28 Lin, Y.K., Brown, I.D. and Deutschle, P.C., "Free Vibration of a Finite Row of Continuous Skin-Stringer Panels," Journal of Sound and Vibration, Vol. 1, 1964, p. 14.
- 4.29 Mercer, C.A. and Seavey, "Prediction of Natural Frequencies and Normal Modes of Skin-Stringer Panel Rows," Journal of Sound and Vibration, Vol. 6, No. 1, 1967, p. 149.

- 4.30 Lin, Y. K., and Donaldson, B. K.; "A Brief Survey of Transfer Matrix Techniques with Special Reference to the Analysis of Aircraft Panels," *Journal of Sound and Vibration*, Vol. 10, No. 1, pp. 103-143, 1969.
- 4.31 McDaniel, T. J.; "Dynamics of Stiffened Cylindrical Shells with Spatially Varying Curvature," AFML-TR-72-134, Air Force Materials Laboratory, Wright-Patterson Air Force Base, Ohio, 1972.
- 4.32 Henderson, J. P.; "Vibration Analysis of Curved Skin-Stringer Structures Housing Tuned Elastomeric Dampers," AFML-TR-72-240, Air Force Materials Laboratory, Wright-Patterson Air Force Base, Ohio, 1972.
- 4.33 Lin, Y. K., "Stresses in Continuous Skin-Stiffener Panels Under Random Loading," *Journal of the Aerospace Sciences*, January 1962, p. 67.
- 4.34 Thompson, A. G. R., "Acoustic Fatigue Design Data: Part I," AGARD-AG-162-Part I, May 1972.
- 4.35 Powell, A., "On the Fatigue Failure of Structures Due to Vibration Excited by Random Pressure Fields," *The Journal of the Acoustical Society of America*, Volume 30, No. 12, December 1958, p. 1130.
- 4.36 Richards, E. J. and Mead, D. J., "Noise and Acoustic Fatigue in Aeronautics," J. Wiley & Sons, 1968.
- 4.37 Wilby, J. F., "The Response of Simple Panels to Turbulent Boundary Layer Excitation," AFFDL-TR-67-70, 1967.
- 4.38 Bozich, D. J., "Spatial Correlation in Acoustic-Structural Coupling," *The Journal of the Acoustical Society of America*, Vol. 36, No. 1, January 1964.
- 4.39 Szechenyi, E., "The Response of and the Acoustic Radiation from Panels Excited by Turbulent Boundary Layers", AFFDL-TR-70-94, June 1970.
- 4.40 Soovere, J. "Dynamic Response of Acoustically Excited Stiffened Composite Honeycomb Panels", Ph.D. Thesis, Institute of Sound and Vibration Research, Southampton University, England, March 1984.

SECTION 5

FINITE ELEMENT PROCEDURE IN DAMPING DESIGN

An accurate and efficient analysis is of great importance in the design of reliable structures which include damping materials. At the conceptual design stage, the use of experimental technique to verify candidate design is not an option unless either full scale or scaled models are built. This fabrication, and the subsequent testing, can involve considerable expenditures in both funds and time, especially if multiple tests on several trial designs need to be performed in order to optimize the design for minimum cost and weight. It is apparent that appropriate analysis tools can be used to great advantage in this design process. Many trial designs can be investigated analytically, with experimentation confined to verification of the final design.

In recent years the finite element methods have found increasing application in the analysis of complex structures. The ability to model very general structural configurations, supports, loading conditions and the availability of high-speed computers are primarily the reasons for its success.

The objective of this chapter is to provide for the designer an overview of the finite element method (FEM) and its application in the design of visco-elastically damped structures. The presentation is divided into three basic parts. In the first part the basic theory and the available computer software for the finite element analysis are described. The displacement-based FEM, modeling of damping, and methods of solving finite element equations in order to assess the effectiveness of damping design are considered. In the second part the integration of the FEM into the damping design process is presented. An example problem illustrating the essential features of the design process is also given. Some general comments for discretizing layered damping designs are given in the final section.

5.1 THE FINITE ELEMENT METHOD (FEM)

The finite element method is an approximate technique of describing the mechanics of a continuous structure. From a mathematical viewpoint the method is an extension of the classical Rayleigh-Ritz method discussed in the preceding chapter. A detailed account of the FEM may be found in textbooks [5.1 - 5.3]. In the following the basic equations of the method are given for later discussion.

5.1.1 Formulation of Finite Element Equations

In the FEM the continuous body is discretized using a number of fictitious subdomains called finite elements. Figure 5.1 depicts some commonly used basic elements. Then within each element, e , in the displacement-based-FEM, the displacements, \underline{U}^e , at any point, x_i ($i=1,2,3$), are expressed in terms of the nodal displacements, \underline{U}^e , as

$$\underline{U}^e(x_i) = \underline{N}^{eT}(x_i)\underline{U}^e \quad (5.1)*$$

where \underline{N}^e is called the matrix of shape functions; the strain, $\underline{\epsilon}^e$, is given as

$$\underline{\epsilon}^e = \underline{B}^e \underline{U}^e \quad (5.2)$$

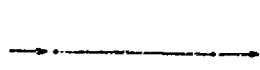
where \underline{B}^e is the element strain displacement matrix. The stress, $\underline{\sigma}^e$, is related to strain as

$$\underline{\sigma}^e = \underline{D}^e \underline{\epsilon}^e \quad (5.3)$$

where \underline{D}^e is the elasticity matrix. A list of symbols used in these and all subsequent equations in Section 5 is included at the end of Section 5.4.

The finite element equations of motion are derived from the consideration of the principle of virtual work [5.1] which can be written as

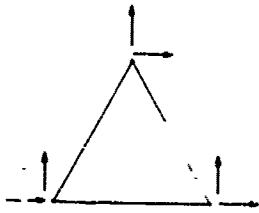
*A single underbar denotes a vector, while a double underbar denotes a matrix. The superscript T denotes the transpose, and superpose dots denote derivatives with respect to time, t .



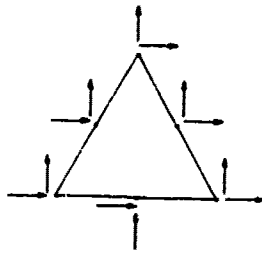
BAR



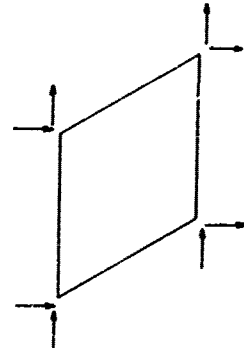
BEAM



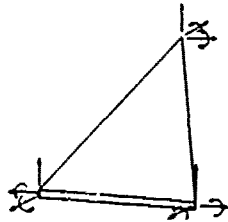
TRIANGULAR MEMBRANE
LINEAR DISPLACEMENT



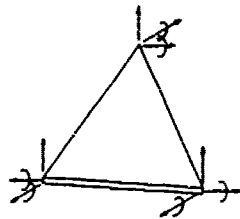
TRIANGULAR MEMBRANE
QUADRATIC DISPLACEMENTS



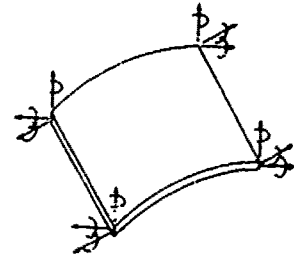
QUADRILATERAL
MEMBRANE



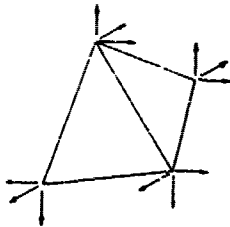
TRIANGULAR PLATE
CUBIC BENDING DISPLACEMENT



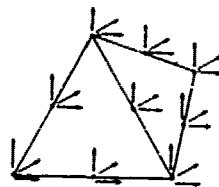
TRIANGULAR PLATE
BENDING & MEMBRANE DISP.



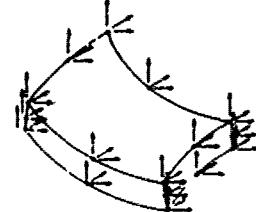
RECTANGULAR CYLINDRICAL
SHELL



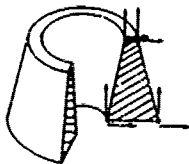
TETRAHEDRON
LINEAR DISPLACEMENTS



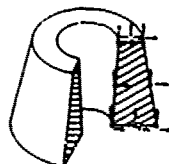
TETRAHEDRON
QUADRATIC DISPLACEMENTS



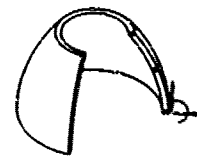
THREE DIMENSIONAL
ISOPARAMETRIC SOLID



AXISYMMETRICAL SOLID
LINEAR



AXISYMMETRICAL SOLID
QUADRATIC DISPLACEMENT



AXISYMMETRIC
THIN SHELL

Figure 5.1. - Common element configuration in FEM modeling.

$$\int_V (\sigma_{ij} \delta_{ij} + \rho u_i \delta u_j \delta_{ij}) dv = \int_{S_\sigma} \bar{t}_i \delta u_j \delta_{ij} dA \quad (5.4)$$

where δ is the variational operator, δ_{ij} is the kronecker delta. S_σ is the portion of the surface of body V where external traction, \underline{t} , is specified, ρ is the mass density of the structural material. Substituting Equations 5.1 to 5.3 into Equation 5.4 and carrying out the integrations, the discretized virtual work for the finite element assemblage becomes

$$\sum_{e=1}^n [\delta \underline{u}^e \underline{K}^e \underline{u}^e + \delta \underline{u}^e \underline{M}^e \underline{\dot{u}}^e] = \sum_{e=1}^n \delta \underline{u}^e \underline{F}^e \quad (5.5)$$

where n is the total number of finite elements in the assembly and

$$\underline{K}^e = \int_V \underline{B}^e \underline{D}^e \underline{B}^e dv \quad (5.6a)$$

is the stiffness matrix,

$$\underline{M}^e = \int_V \rho^e \underline{N}^e \underline{N}^e dv \quad (5.6b)$$

is the consistent mass matrix, and

$$\underline{F}^e = \int_{S_\sigma} \underline{N}^e \underline{t} dA \quad (5.6c)$$

is the vector of concentrated nodal forces. When the element continuity is taken into account, equation 5.5 can be written in the form

$$\delta \underline{U}^T \underline{K} \underline{U} + \delta \underline{U}^T \underline{M} \underline{\dot{U}} = \underline{U}^T \underline{F} \quad (5.7)$$

where \underline{U} is the vector of all independent node displacements and \underline{K} and \underline{M} are assembled stiffness and mass matrices respectively and \underline{F} is the assembled load vector. Finally in view of the fact that the discrete virtual displacements, $\delta \underline{U}$, are arbitrary and independent, the final form of the finite element equations of motion, that govern the time-dependent response of a general finite element model of a three dimensional structure, are obtained from equation 5.7

as follows:

$$\underline{M} \ddot{\underline{U}} + \underline{K} \underline{U} = \underline{F} \quad (5.8)$$

In the presence of energy dissipating mechanisms within the structure, the finite element equations can be derived in an analogous manner leading to

$$\underline{M} \ddot{\underline{U}} + \underline{C} \dot{\underline{U}} + (\underline{K} + j\underline{H}) \underline{U} = \underline{F} \quad (5.9)$$

where \underline{C} and \underline{H} are respectively the viscous and hysteretic damping matrices, and $j = (-1)^{1/2}$. Construction of these matrices from known damping data is discussed in the following.

5.1.2 Evaluation of the Damping of the Structure

Two forms of damping representations are commonly used in the finite element analysis damping design; viscous and hysteretic. Various other forms of damping representation have also been proposed in recent years and are given in references 5.4 through 5.7. The methods used to arrive at a damping model of a structure are as follows. If the mechanism and the distribution of damping are known precisely, then by following the procedure for calculating stiffness and inertia, consistent damping matrices can be calculated for the element. Finite element assembly then leads to the structural damping matrix. The damping properties seldom are known in such a detail however. Instead, damping values associated with vibration modes are generally known from experimental tests and the damping matrices are calculated indirectly using mass and stiffness characteristics of the structure. For more general cases, where the damping mechanism varies widely throughout the structure and is not a simple function of vibration amplitude, frequency, level of excitation, etc. damping values are known only in an average sense, such as via a correlation of total energy dissipated per cycle and maximum stored energy in a given element. For this class of problems the system damping is determined using an energy ratio method described in the next section. In the following paragraph the calculation of viscous and hysteretic damping matrices is described.

5.1.2.1 Viscous Damping

In the viscous form, where the damping in the structure is assumed to be dependent on the coordinate velocities, the damping force vector is expressed as

$$\underline{F} = \underline{C} \dot{\underline{U}} \quad (5.10)$$

where \underline{C} is the viscous damping matrix of the structure. Various techniques are available to derive the \underline{C} matrix corresponding to given set of modal damping ratios. In the commonly used form, known as Rayleigh damping, the \underline{C} matrix is given by a linear combination of damping matrices proportional to the mass and stiffness matrices (equations 5.7 to 5.9) by

$$\underline{C} = A_0 \underline{M} + A_1 \underline{K} \quad (5.11)$$

The constants A_0 and A_1 are determined from the relation

$$\zeta_n = \frac{A_0}{2\omega_n} + \frac{A_1 \omega_n}{2} \quad (5.12)$$

where ω_n is the modal frequency and ζ_n is the corresponding modal damping ratio which is assumed known. If the damping properties of the structure are uniform throughout, the same value of the constants A_0 and A_1 will apply everywhere in the structure and the complete damping matrix ("proportional damping") can be formed by combination of the complete mass and stiffness matrices as indicated in equation 5.11. If damping varies between different parts of the structure (e.g., from element to element), different A_0 and A_1 must be determined for each element using appropriate damping ratios and equation 5.12. The frequencies to be used in these equations are the undamped frequencies of the element. When A_0 and A_1 have been defined for each element of the structure, the damping matrix for the element is constructed using an equation equivalent to equation 5.11 such as

$$\underline{C}^e = A_0^e \underline{M}^e + A_1^e \underline{K}^e \quad (5.13)$$

where the element mass and stiffness matrices are used. The damping matrix for the complete structure is then obtained by assembling the element matrices. The structure damping matrix so obtained is not proportional to any combination of structure mass and/or stiffness matrix [5.8].

In the Rayleigh Damping described above, damping can be controlled only in any two modes. In all other modes damping ratios are as given by equation 5.12. A more general form of equation 5.11 that permits the specification of damping ratios in more than two modes is [5.9]

$$\underline{C} = \underline{M} \sum_{s=0}^{p-1} A_s [\underline{M}^{-1} \underline{K}]^s \quad s = 0, 1, \dots, p-1 \quad (5.14)$$

where p is the number of modes in which damping is specified and the constants A_s are obtained from the p simultaneous equations

$$\zeta_r = \frac{1}{2} \left(\frac{A_0}{\omega_r} + A_1 \omega_r + A_2 \omega_r^3 + \dots + A_{p-1} \omega_r^{2p-3} \right) \quad r=1, 2, \dots, p \quad (5.15)$$

In using the above procedure, numerical difficulties may arise when the number of modes used is large due to the rapid increase in the numerical values of the frequency terms. A more direct and efficient procedure to establish \underline{C} is [5.7]

$$\underline{C} = \sum_{r=1}^p \underline{C}_r \quad (5.16)$$

where \underline{C}_r is the contribution to the structure damping matrix due to a specified damping ratio in the r th mode, given as

$$\underline{C}_r = 2\zeta_r \omega_r \underline{\theta}_r \underline{\theta}_r^T \quad (5.17)$$

$\underline{\theta}_r$ being the r th mass normalized mode shape of the undamped structure. Both representations, equations 5.14 and 5.16, permit nonuniform distribution of damping throughout the structure. In References [5.10] and [5.11] methods of constructing viscous damping matrices from measured modal data are given. The matrices so derived generally lead to coupled modal damping matrices and are a

more accurate representation of the material behavior than the ones based on stiffness and mass properties.

5.1.2.2 Hysteretic Damping

If the structural material possesses stress-strain hysteresis and is undergoing harmonic motion, the damping force is proportional to displacement but in phase with the velocity. In this case the finite element damping matrix is obtained in a manner similar to the stiffness matrix. Using the stress-strain law [5.13,5.14,5.15]

$$\underline{\sigma} = [\underline{D} + j\underline{G}] \underline{\epsilon} \quad (5.18a)$$

where \underline{D} and \underline{G} are respectively the material property matrices characterizing energy storage and dissipative behavior of the material, and $j = (-1)^{1/2}$, and $\underline{\sigma} = (\sigma_{11}, \sigma_{22}, \sigma_{33}, \sigma_{23}, \sigma_{31}, \sigma_{12})^T$, and $\underline{\epsilon} = (\epsilon_{11}, \epsilon_{22}, \epsilon_{33}, \epsilon_{23}, \epsilon_{31}, \epsilon_{12})^T$. The element damping matrix associated with equation 5.18a is

$$\underline{H}^e = \int_{V^e} \underline{B}^{eT} \underline{G} \underline{B}^e dv \quad (5.18b)$$

This damping matrix is usually combined with the element stiffness matrix to form a complex stiffness matrix. The complex stiffness matrix for the structure is obtained in the usual assembly procedure.

In practice, the elements of the damping matrix G are obtained from those of the elasticity matrix D through experimentally measured proportionality constants known as the loss factors, η_s and η_d , associated with the dissipation behavior in shear and dilatational modes of vibration respectively. Thus

$$\mu^i = \eta_s \mu^r \quad (5.19a)$$

$$\lambda^i = \eta_d \lambda^r + 2(\eta_d - \eta_s) \mu^r \quad (5.19b)$$

where λ^r , μ^r are the Lamé parameters of the isotropic elastic material in the elasticity matrix \underline{D} .

$$\underline{D} = \begin{bmatrix} (\lambda^r+2\mu^r) & \lambda^r & \lambda^r & 0 & 0 & 0 \\ \lambda^r & (\lambda^r+2\mu^r) & \lambda^r & 0 & 0 & 0 \\ \lambda^r & \lambda^r & (\lambda^r+2\mu^r) & 0 & 0 & 0 \\ 0 & 0 & 0 & \mu^r & 0 & 0 \\ 0 & 0 & 0 & 0 & \mu^r & 0 \\ 0 & 0 & 0 & 0 & 0 & \mu^r \end{bmatrix} \quad (5.20a)$$

and μ^i , λ^i are the material parameters of the damping matrix \underline{G} ;

$$\underline{G} = \begin{bmatrix} (\lambda^i+2\mu^i) & \lambda^i & \lambda^i & 0 & 0 & 0 \\ \lambda^i & (\lambda^i+2\mu^i) & \lambda^i & 0 & 0 & 0 \\ \lambda^i & \lambda^i & (\lambda^i+2\mu^i) & 0 & 0 & 0 \\ 0 & 0 & 0 & \mu^i & 0 & 0 \\ 0 & 0 & 0 & 0 & \mu^i & 0 \\ 0 & 0 & 0 & 0 & 0 & \mu^i \end{bmatrix} \quad (5.20b)$$

In the event the two loss factors are equal i.e., $\eta_s = \eta_d = \eta$

$$\underline{G} = \eta \underline{D} \quad (5.21)$$

and the element complex stiffness is obtained directly by scaling the elastic stiffness matrix by the factor η .

5.1.3 Solution Methods

Once a structure is modeled using the finite element method a number of possibilities exist for computing the dynamic behavior. The following discussions are restricted to the methods for calculating natural vibration frequency, mode shapes and damping ratios, response-time histories under arbitrary time-dependent excitation, and response to harmonic excitation. The method chosen

in the damping design analysis will depend upon the required results (which may vary at different stages of the design process) as well as the amount of time and expense deemed allowable.

The methods of dynamic response analysis can be classified as

- transient response by direct integration
- frequency response by direct solution, and
- dynamic response by modal analysis methods.

A synopsis of the solution procedures is given in Figure 5.2. The direct methods of solution employ the finite element equations (9) in the physical coordinates, whereas the modal methods employ vibration modes of the structure as the basis. The direct methods are more general but require more computational resources than their modal counterparts. The modal methods may employ undamped normal modes or damped complex modes as the basis for its formulation depending upon the magnitude and distribution of damping. The modal methods are of advantage in linear problems if the load frequency content corresponds to lower frequency spectrum. These methods are discussed in the following paragraphs.

5.1.3.1 Transient Response by Direct Integration

In this solution method the finite element equation

$$\underline{M} \ddot{\underline{U}} + \underline{C} \dot{\underline{U}} + \underline{K} \underline{U} = \underline{F}(t) \quad (5.22)$$

represents linear algebraic equations in physical displacements, \underline{U} , and second-order differential equations in time, are solved step-by-step in time to obtain the response behavior under arbitrary time-dependent loads, $\underline{F}(t)$. Two methods of time integration along with their numerical stability and accuracy are discussed in [5.16]. The time integration method is the most general of the response analysis methods shown in Figure 5.3 and permits the specification

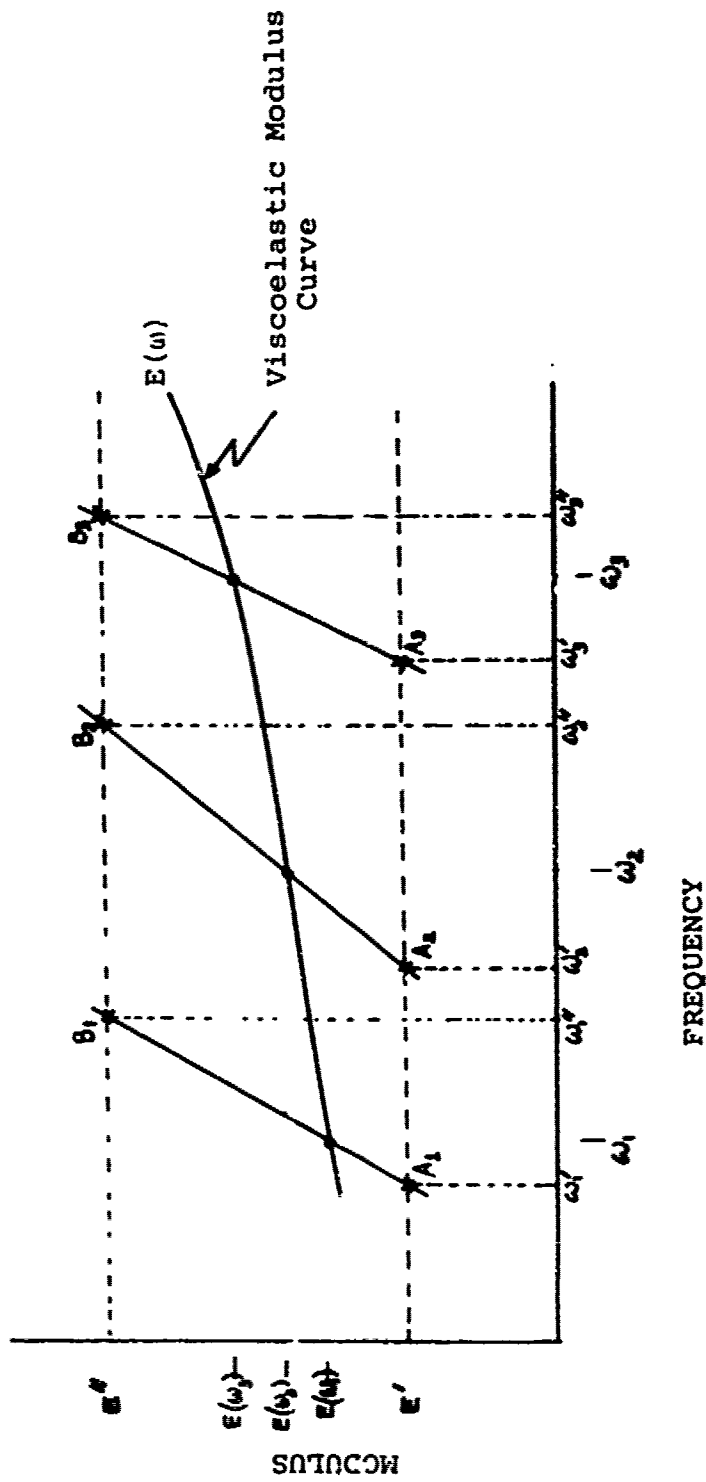


Figure 5.3. - Determination of viscoelastic modulus for modal response analysis.

of certain nonlinearities in structural stiffness and/or damping properties [5.4,5.5,5.16]. The method is relatively expensive because it deals with a large number of coupled equations; one equation corresponding to each active physical degree of freedom in the model.

The results produced by the method are displacement, velocity, acceleration, and stress versus time. These results are of little direct use to a designer. Commonly, the analysis is made with different types, amount, and distribution of damping and its effect on response amplitude is taken as a measure of effectiveness of the damping design.

Since the hysteretic damping is not defined for other than harmonic motion, to treat this class of problems including any frequency dependent damping terms, the solution is obtained using transform techniques. The equations of motion are first transformed to frequency domain and then the frequency dependent damping is incorporated into the transformed equations of motion. After a solution is obtained in the frequency domain, an inverse Fourier transform is used to return to time domain. With the development of Fast Fourier Transform algorithm this procedure can be efficiently treated numerically. In recent papers [5.17,5.19] the application of this procedure is demonstrated. No general purpose computer programs provide this capability, however.

5.1.3.2 Frequency Response by Direct Solution

Consider the case when the applied forces in equation (22) are harmonic in time; that is

$$F = \underline{F} e^{j\omega t} \quad (5.23)$$

where \underline{F} is the peak amplitude of harmonic force, ω is the forcing frequency, t is the time and $j = (-1)^{1/2}$. In the absence of any nonlinearities, the response to harmonic loading is also harmonic of the form

$$\underline{U} = \underline{\hat{U}} e^{j\omega t} \quad (5.24)$$

where $\underline{\hat{U}}$ is a vector of nodal displacements that characterize the spatial form of the response. The elements of $\underline{\hat{U}}$ are in general complex owing to possible phase difference (due to damping) between the response quantities and the forcing function. Substituting equations 5.23 and 5.24 into equation 5.23, and eliminating $e^{j\omega t}$ from side term, leads to

$$[-\omega^2 \underline{M} + j\omega \underline{C} + j\underline{H} + \underline{K}] \underline{\hat{U}} = \underline{\hat{F}} \quad (5.25)$$

where the matrices \underline{K} , \underline{C} , and \underline{H} can be general frequency dependent. For a given excitation frequency, ω_i , Equation 5.25 is solved directly to yield the displacement amplitude and phase angle at every point in the finite element model. This technique is repeated at any desired frequency to generate complete frequency response information.

The amplitude/phase-versus-frequency response generated by the above method can be used to obtain system damping estimates using half-power bandwidth or phase plot methods (discussed elsewhere in this design guide). Alternately, the system damping may be computed from the knowledge of stored and dissipated energies in the system. The system damping ratio, ζ_i , is calculated as [5.18 - 5.23]

$$2\zeta_i = \frac{\underline{\hat{U}}^* (\omega_i \underline{C} + \underline{H}) \underline{\hat{U}}}{\underline{\hat{U}}^* \underline{K} \underline{\hat{U}}} \quad (5.26)$$

where $\underline{\hat{U}}$ is the displacement vector and $\underline{\hat{U}}^*$ its transposed complex conjugate corresponding to the excitation frequency, ω_i . Equation 5.26 can be written in terms of the parameters of each element of the structures as

$$2\zeta_i = \frac{\sum_{e=1}^n (2\omega_i \frac{\zeta^e}{i\omega^e} + \eta_1^e) (SE)_{\max}^e}{\sum_{e=1}^n (SE)_{\max}^e} \quad (5.27)$$

where the element viscous damping, \underline{C}^e , is assumed proportional to its stiffness matrix, \underline{K}^e , (equation (11) with $A_0 = 0$) and

$$\underline{C}^e = 2 \frac{\zeta^e}{\omega^e} \underline{K}^e \quad (5.28)$$

ζ^e and ω^e being the viscous modal damping ratio and natural frequency, respectively. The hysteretic damping is assumed proportional to stiffness matrix,

$$\underline{H}^e = \eta_1^e \underline{K}^e \quad (5.29)$$

η_1^e , being the loss factors of the element material at the excitation frequency, ω_1 . The element stored energy is calculated as

$$(SE)_{\max}^e = \frac{1}{2} \underline{\dot{U}}^{*e} \underline{K}^e \underline{\dot{U}}^e \quad (5.30)$$

where $\underline{\dot{U}}^e$ is the vector of element nodal displacement. Equation 5.27 thus permits the calculation of damping ratio of the finite element assemblage, knowing the element stored energy and its damping constants.

The use of above methods is recommended to correlate the results with experimental tests. It should be noted however that the damping value given by equation 5.28 is not modal damping unless the forced vibration shape used in the calculation is also an eigenvector. With increasing damping coupling between modes and/or close spacing of the modes the forced mode is contaminated and the results diverge from a true modal value.

5.1.3.3 Dynamic Response by Normal Modal Method

The modal method presents an alternate and economical means of dynamic response analysis. First the method yields directly the system dynamic characteristics such as the frequency of natural vibrations, mode shapes, stored energy distribution, and modal damping. Second, through the use of a truncated set of modal properties, the size of the response analysis problem is reduced significantly.

In the following discussion, the classical normal mode method and its utility in determining system damping and response is described.

A. Normal Mode Analysis

The normal mode methods are based on the eigensolution of the free vibration problem

$$\underline{K} \underline{\phi}_s = \omega_s^2 \underline{M} \underline{\phi}_s \quad (5.31)$$

where damping is ignored, however the elastic and inertia contributions of the damping treatments are taken into account. The eigensolution of equation 5.31 leads to undamped frequencies, ω_s , and corresponding mode shapes, $\underline{\phi}_s$, with the properties

$$\underline{\phi}_r^T \underline{M} \underline{\phi}_r = 1 \quad (5.32)$$

$$\underline{\phi}_r^T \underline{K} \underline{\phi}_r = \omega_r^2$$

and

$$\underline{U} = \underline{\phi} \underline{\xi} \quad (5.33)$$

where \underline{U} is the physical displacement and $\underline{\xi}$ the vector of modal coordinates. Substitution of equation 5.33 into the equations of motion with viscous damping included leads to

$$\ddot{\underline{\xi}} + \underline{C}_{\xi} \dot{\underline{\xi}} + \underline{\Gamma} \omega_r^2 \underline{\xi} = \underline{Q}(\tau) \quad (5.34)$$

where $\underline{\Gamma} \omega_r^2 \underline{\Gamma}$ is nxn diagonal matrix with element in rth row and column being ω_r^2 , \underline{C}_{ξ} is the nxn generalized damping matrix defined as

$$\underline{C}_{\xi} = \underline{\phi}^T \underline{C} \underline{\phi} \quad (5.35)$$

The generalized damping matrix, \underline{C}_ζ , is in general fully populated, and the coefficients, $C_{\zeta rs}$, are related to the modal damping ratio, ζ_r , as

$$\zeta_{rr} = \frac{C_{\zeta rr}}{2\omega_r} \quad (5.36)$$

and to modal damping coupling ratio, ζ_{rs} , as

$$\zeta_{rs} = \frac{C_{\zeta rs}}{2\sqrt{\omega_r \omega_s}} \quad (5.37)$$

The formulation of the dynamic response analysis problem in the normal mode method thus requires (a) the eigensolution of equation 5.31; (b) the transformation of the load vector to modal coordinates; and (c) the computation of the matrix \underline{C}_ζ .

B. Modal Strain Energy Method (MSE)

Methods of constructing matrix \underline{C} are discussed in Section 5.2.2. In the event the damping in the structure is distributed such that the damping coupling given by equation 5.37 vanishes (proportional damping) or is at least negligible (see Reference 5.25 for a criteria for neglecting modal damping coupling), the structure modal damping can be calculated by modal strain energy method [5.26,5.27], without having to construct and assemble the finite element damping matrices. The method is analogous to that given in Section 5.1.3.2, the difference being in the use of undamped normal modes instead of the damped deflection shapes. Thus the system damping ratio, ζ_r , is given as [5.20]

$$\zeta_r = \frac{\sum_{e=1}^n \left(\omega_r \frac{x}{\omega^e} + \frac{1}{2} \eta_r^e \right) (SE)_{\max}^e}{\sum_{e=1}^n (SE)_{\max}^e} \quad (5.38)$$

where ζ^e is the element damping ratio evaluated at its resonance frequency, ω^e , η_r^e is the material loss factor at frequency ω_r , and $(SE)_{\max}^e$ is the peak stored energy in the element. In the absence of viscous damping the loss factor in rth mode is

$$\eta_r = \frac{\sum_{e=1}^n \eta_r^e (SE)_{\max}^e}{\sum_{e=1}^n (SE)_{\max}^e} \quad (5.39)$$

where η_r is as defined in the modal equation of motion

$$\ddot{\xi}_r + \eta_r \omega_r \dot{\xi}_r + \omega_r^2 \xi_r = Q_r(t) \quad (5.40)$$

It must be noted that the energy method does not yield off-diagonal damping terms. Furthermore, with an increasing amount of damping, the damped resonance frequency departs further from the undamped one which introduces errors through incorrect material property values. This situation is further aggravated in the presence of nonuniform distribution of damping in the structure.

In reference [5.27] an empirical correction procedure is given for improving the accuracy of the MSE prediction for frequency dependent material properties. Since the modal frequency depends upon the value of material modulus which is not known a priori, the problem of determining correct material properties in the modal calculation is resolved as follows. A sequence of normal mode runs is made for a range of assumed material property values. Then by correlating the material property versus frequency curve with the mode frequency versus material property curves, the required consistent material property values are obtained for each mode (Figure 5.3). Normal mode analysis must again be performed for each mode to get the correct energy distribution to use in equation 5.38.

C. Transient Response Analysis

The equation 5.34 may be integrated step-by-step in time to solve for the response due to arbitrary $\underline{F}(t)$ as is done in the direct solution method. In reference [5.28], the methods of time integration and the accuracy and stability aspects of the numerical computations are discussed. The number of governing equations 5.34 can be made much smaller than in the direct method by retaining only the significant modes in the modal superposition equation 5.33. The criteria being that under a given loading only the first few modes are significantly excited and the contribution of the higher modes is negligible. Two situations arise depending upon whether the damping is proportional or non-proportional. For proportional damping the equations uncouple, giving

$$\ddot{\xi}_r + 2\zeta_r \omega_r \dot{\xi}_r + \omega_r^2 \xi_r = Q_r(t) \quad (5.41)$$

the number of equations being the number of modes retained in the modal expansion equation 5.33. The solution of equation 5.41 yields the values of the modal participation factors, ξ_r . The physical displacements of discrete points in the finite element model are recovered using equation 5.33. The analysis leads to a response-time history.

D. Frequency Response Analysis

Response to harmonic inputs is governed by the modal equation (5.34) with the right hand side defined as

$$\underline{Q} = \underline{\phi}^T \underline{F}_0 e^{i\omega t} \quad (5.42)$$

\underline{F}_0 being the real force vector, and ω the excitation frequency. The discussion concerning coupling of the modal equations in this case is similar to that for the transient case.

In [5.29] an extension of the modal response method is given to treat problems involving frequency dependent material properties. The

method is similar to that used in [5.27]. The eigen problem of undamped structure is solved for two values E' and E'' of storage modulus, E , of the damping material. These two values bracket the variation of the actual modulus values in frequency range of interest. Corresponding to the two modulus values, two sets of natural frequencies $\omega_1', \omega_2', \dots$ and $\omega_1'', \omega_2'', \dots$, are obtained.

The natural frequencies vary linearly with the modulus as shown in Figure 5.3. More precise variations can be obtained if modal analyses are made for intermediate values of the material modulus. The intersections of the lines A_1B_1, A_2B_2 etc., with the curve of the material characteristic leads to the values of the storage modulus that should be used in calculating modal properties. Then eigenproblems are solved for each mode to be used in the modal superposition, each modal solution using the storage modulus values appropriate to that natural frequency. Having thus obtained the modal properties (mode shapes, generalized mass, stiffness and damping) for each frequency, the equation of motion is obtained in a manner similar to that for equation 5.41, which can be solved for desired forcing frequency. The analysis leads to amplitude versus frequency response behavior.

5.1.3.4 Dynamic Response by Complex Mode Methods

In the presence of widely varying magnitudes of damping in the structure, the undamped normal modes become coupled and cannot be used to specify a single damping ratio or loss factor corresponding to any one mode by which to measure or quote the modal damping. This difficulty is overcome through the use of damped complex modes. For structures with viscous damping the method is given by Foss [5.30], and for structures with hysteretic damping by Mead [5.33].

In the Foss method, amplitudes of damped free vibration eigenmodes are chosen as the generalized coordinates, and the amplitudes of damped forced

vibration modes are used in the Mead method. The two methods are described in the following paragraphs.

A. Damped Eigenmode Method

The complex mode shapes and eigenvalues of the damped structure are determined from the homogeneous solution of the equation:

$$\underline{A} \dot{\underline{Y}} + \underline{B} \underline{Y} = \underline{Q} \quad (5.43)$$

where

$$\underline{A} = \begin{bmatrix} \underline{0} & \underline{M} \\ \underline{M} & \underline{C} \end{bmatrix}, \quad \underline{B} = \begin{bmatrix} -\underline{M} & \underline{0} \\ \underline{0} & \underline{K} \end{bmatrix}, \quad \underline{Y} = \begin{bmatrix} \underline{U} \\ \underline{U} \end{bmatrix}, \quad \underline{Q} = \begin{bmatrix} \underline{Q} \\ \underline{F}(t) \end{bmatrix} \quad (5.44)$$

The eigensolution of the form $\underline{Y} = \underline{\psi} e^{\lambda t}$ leads to a set of $2n$ (n being the order of the \underline{K} or \underline{M} matrices) numbers of eigenvalues, λ_r , and corresponding $2n$ number of eigenvectors, both complex, with the property that the eigenvectors diagonalize the matrix equation 5.43 i.e.

$$\begin{aligned} \underline{\psi}_r^t \underline{A} \underline{\psi}_s &= 0 \\ &\text{if } r \neq s \\ \underline{\psi}_r^t \underline{B} \underline{\psi}_s &= 0 \end{aligned} \quad (5.45)$$

The eigenvalue is denoted by

$$\lambda_r = \sigma_r + j\omega_r$$

The imaginary part defines the damped natural frequency while σ defines an associated decay rate related to the amount of modal damping. In terms of an undamped frequency, ω_0 , and a critical damping ratio, ζ , σ and ω are of the form

$$\sigma = -\zeta\omega_0 \quad (5.46)$$

$$\omega = \omega_0 \sqrt{1-\zeta^2} \quad (5.47)$$

This method, like the normal mode method, does not permit frequency or amplitude dependent material properties. However, no restrictions regarding the magnitude or the distribution of the damping are needed for the method to be applicable. The major drawback of the methods based on the complex modes is that it is computationally expensive, the number of equations being twice that in the normal mode case.

Equations of motion in the complex mode coordinate, \underline{Z} , are obtained, using the transformation.

$$\underline{Y} = \underline{\psi} \underline{Z} \quad (5.48)$$

Where $\underline{\psi}$ is the complex mode matrix. Using equation 5.48 in 5.43 and premultiplying by $[\lambda] \underline{\psi}^T$ leads to the uncoupled matrix equation

$$[\lambda] \dot{\underline{Z}} - [\lambda^2] \underline{Z} = [\lambda] \underline{\psi}^T \underline{Q} \quad (5.49)$$

where $[\lambda]$ is $2n \times 2n$ diagonal mode value matrix, and use is made of the orthogonality properties expressed by equations 5.45. Again the use of a modal method is advantageous only if a severely truncated mode set is used in equation 5.48.

In a manner similar to that described in the normal mode method, the transient and frequency response can be calculated using the complex modal equation 5.49. For further details see references [5.31,5.32].

B. Damped Forced Vibration Mode Method

This method is applicable to harmonic vibration only since it is based on hysteretic damping.

In reference [5.33] Mead shows that a unique specification of the damping of the modes can only be made by considering the forced vibration modes excited by a harmonic external loading which is

proportional to the local inertia loading but which is in phase with the local velocity. This method is a special case of the more general characteristic phase lag method [5.34]. The general case however does not have the computational simplicity of Mead's method. The Mead method is as follows.

Consider the equation of motion

$$\underline{\underline{M}} \ddot{\underline{U}} + (\underline{\underline{K}} + i\underline{\underline{H}}) \underline{U} = \underline{\phi} e^{i\omega t} \quad (5.50)$$

where $\underline{\phi}$ is a column of forces equal to $i\eta$ times the inertia force corresponding to the harmonic vibration

$$\underline{U} = \underline{\psi} e^{i\omega t} \quad (5.51)$$

$$\underline{\phi} = i\eta\omega^2 \underline{\underline{M}} \underline{\psi} \quad (5.52)$$

Putting both equations 5.51 and 5.52 into 5.50, we find

$$[\underline{\underline{K}} - \omega^2(1 + i\eta)\underline{\underline{M}} + i\underline{\underline{H}}] \underline{\psi} = \underline{0} \quad (5.53)$$

From which the complex eigenvalues, $\omega_r^2(1 + i\eta_r)$, and corresponding complex modal columns, $\underline{\psi}_r$, can be determined. The modal columns satisfy the orthogonality condition

$$\frac{\underline{\psi}_r^T}{\underline{\underline{M}}} \underline{\underline{M}} \underline{\psi}_s = 0 \quad r \neq s \quad (5.54)$$

$$\underline{\psi}_r^T (\underline{\underline{K}} + i\underline{\underline{H}}) \underline{\psi}_s = 0$$

and

$$\frac{\underline{\psi}_r^T}{\underline{\underline{M}}} \underline{\underline{M}} \underline{\psi}_r = m_r, \quad \frac{\underline{\psi}_r^T}{\underline{\underline{K}}} \underline{\underline{K}} \underline{\psi}_r = k_r, \quad \frac{\underline{\psi}_r^T}{\underline{\underline{H}}} \underline{\underline{H}} \underline{\psi}_r = h_r \quad (5.55)$$

are the complex modal coefficients.

Next introduce the new column of damped forced normal mode coordinates, v , so that

$$\underline{U} = \underline{\psi} v \quad (5.56)$$

and the modal equation of motion becomes

$$[m_r (\omega_r^2 (1 + i\eta) - \omega^2)] v = \underline{\psi}^T \underline{f} e^{i\omega t} \quad (5.57)$$

which can be solved to give

$$v_r = \frac{\underline{\psi}_r^T \underline{f} e^{i\omega t}}{m_r (\omega_r^2 (1 + i\eta_r) - \omega^2)} \quad (5.58)$$

The above equation has the form of a single degree of freedom frequency response function, resonating at frequency ω_r with the loss factor, η_r . The system vibrates in the complex mode, $\underline{\psi}_r$.

It is interesting to note that when the damping is distributed in proportion to the stiffness of the system, the damped forced normal modes are identical to the undamped normal modes from equation 5.53, and undamped normal modes can be excited at their natural frequencies by forces which are equal to the $i\eta$ times the inertia forces, where η is the system loss factor.

5.1.3.5 Substructuring Methods

The substructural analysis methods are the best and sometimes the only approach for dynamic analysis of large or complex structures. The methods are based on subdividing the large structure into smaller parts which are analyzed separately. The system dynamics is then obtained by solving the system equations obtained by analytically coupling the dynamic characteristics of each substructure. Through certain reduction techniques applied at the substructure level, the size of the coupled problem is reduced considerably, as compared to the size of the original direct system problem.

Two classes of methods for dynamic reductions are used with the finite element method. The first class, known as dynamic condensation [5.35] is widely used when finite element models of all the components are available. The method involves elimination of degrees-of-freedom that are assumed to have negligible effect on mode shapes and thus vibration response of the structure. Dynamic results are sensitive to the choice of the degrees-of-freedom to be eliminated.

In the second class of dynamic reduction methods termed component mode synthesis [5.36], the component dynamics are specified in terms of a truncated set of its generalized coordinates. Many techniques in the category of modal synthesis have been devised. These techniques are ideally suited for systems involving components that are characterized in experimental modal tests.

A brief discussion of these methods follows; details may be found in references [5.3, 5.36-5.39, 5.45].

A. Dynamic Condensation:

Consider an isolated substructure consisting of simple finite elements. The undamped free vibration equation of the structure is

$$\begin{bmatrix} \underline{K}^{mm} & \underline{K}^{ms} \\ \underline{K}^{sm} & \underline{K}^{ss} \end{bmatrix} \begin{Bmatrix} \underline{U}^m \\ \underline{U}^s \end{Bmatrix} - \omega_1^2 \begin{bmatrix} \underline{M}^{mm} & \underline{M}^{ms} \\ \underline{M}^{sm} & \underline{M}^{ss} \end{bmatrix} \begin{Bmatrix} \underline{U}^m \\ \underline{U}^s \end{Bmatrix} = \underline{0} \quad (5.59)$$

where the matrix equations are partitioned in terms of the degrees-of-freedom (DOF) 'm' to be retained and DOF 's' to be reduced out. The m DOF includes substructure connection interface as well as any interior DOFs. The basis of reduction is that the inertia forces on the 's' degrees of freedom are negligible compared to static forces. This leads to the following relation between the m and s DOFs.

$$\underline{U}^s = \underline{T} \underline{U}^m \quad (5.60)$$

where

$$\underline{T} = -\underline{K}^{ss}{}^{-1} \underline{K}^{sm}$$

the reduced stiffness, mass, and damping matrices are given as

$$\begin{aligned} \underline{K}_G &= \underline{K}^{mm} + \underline{K}^{ms} \underline{T} \\ \underline{M}_G &= \underline{M}^{mm} + \underline{T}^T \underline{M}^{ss} \underline{T} + \underline{T}^T \underline{M}^{sm} + \underline{M}^{ms} \underline{T} \\ \underline{C}_G &= \underline{C}^{mm} + \underline{T}^T \underline{C}^{ss} \underline{T} + \underline{T}^T \underline{C}^{sm} + \underline{C}^{ms} \underline{T} \end{aligned} \quad (5.61)$$

and the load vector as

$$\underline{F} = \underline{T} \underline{P}$$

Each substructure has its mass, stiffness, damping, and load similarly partitioned and reduced. Assembly of the reduced substructure matrices leads to the system equations of motion. Geometric compatibility between substructures is automatically assured by the use of the 'm' DOF as generalized coordinates. The accuracy of these methods is very sensitive to the choice of the 'm' degrees-of-freedom.

B. Component Mode Synthesis

A number of variants of this method exist differing mainly in the manner the substructure matrices are reduced and subsequently coupled to form system equations. A representative method is briefly described here.

Consider the equations of motion of an uncoupled substructure

$$\underline{M} \ddot{\underline{U}} + \underline{C} \dot{\underline{U}} + (\underline{K} + i\underline{H}) \underline{U} = \underline{F} \quad (5.62)$$

The substructure physical DOF, \underline{u} , are represented in terms of substructure generalized coordinates, \underline{p} , so that the number of substructure DOF can be reduced, thus

$$\underline{u} = \underline{\phi} \underline{p} \quad (5.63)$$

The $\underline{\phi}$ matrix contains substructure vibration modes, static deflection functions, etc. Changing the basis from physical coordinate to generalized coordinates the substructure equation of motion becomes

$$\left(\underline{\phi}^T \underline{M} \underline{\phi} \right) \ddot{\underline{p}} + \left(\underline{\phi}^T \underline{C} \underline{\phi} \right) \dot{\underline{p}} + \underline{\phi}^T (\underline{K} + i\underline{H}) \underline{\phi} \underline{p} = \underline{\phi}^T \underline{F} \quad (5.64)$$

Equations of the above form may be written for each substructure and formally assembled to give

$$\underline{m} \ddot{\underline{q}} + \underline{c} \dot{\underline{q}} + (\underline{k} + i\underline{h}) \underline{q} = \underline{f} \quad (5.65)$$

where the matrices \underline{m} , \underline{c} , etc are the assembled system matrices in uncoupled system coordinates, \underline{q} . Constraint relations of the type

$$\underline{A} \underline{q} = 0 \quad (5.66)$$

exist between the components of \underline{q} due to geometric compatibility at the substructure interfaces. Equation 5.65, together with the constraint equation 5.66, defines the problem of the assembled structure. Specific modal synthesis methods are defined by the choice of displacement functions used in the $\underline{\phi}$ matrices in equation (5.63) and the procedure used to treat the constraint equation (5.66).

It should be noted that the substructure dynamic matrices \underline{m} , \underline{c} , \underline{h} , and \underline{k} in equation (5.65) do not need to be derived from a finite element model, and may be obtained experimentally. Modal synthesis procedures are also available that admit dynamic characterization of substructures in terms of frequency response functions obtained conveniently in modal testing, references [5.40, 5.41].

5.1.4 Computer Programs

A large number of computer programs are available for dynamic response analysis of damped structures. Since early 1970 several bibliographies, data sheets, and tables have been compiled about finite element software. Most recent surveys of computer programs for linear and nonlinear dynamic analysis are in references [5.42-5.45].

A summary of available computer programs relevant to damping design analysis is given in Table 5.1. The table is essentially the same as that given in reference [5.43], except for some updates. Modeling features vary from one code to the other and therefore it is often difficult to identify the proper code that meets a specific need. Some basic factors which affect the selection of a code are as follows:

- **Structural Elements** - The program should provide a complete element library including rod and beam elements, membrane, plate and shell elements of various shapes, three-dimensional elements and axisymmetric solid and shell elements.
- **Mass and Damping Models** - The program should provide a choice between lumped and consistent mass models. Likewise it should permit modeling of structures with variable amount and distribution of damping. It is desirable to have both the viscous as well as hysteretic damping models.
- **Analysis Capabilities** - These include the solution methods for eigen-reduction, time integration and response analysis, energy distribution in free and forced vibration modes, damped frequencies, and mode shapes.
- **Substructure Synthesis Capabilities** - To analyze structures with a large number of degrees-of-freedom or with substructures that are represented by their modal properties. Methods such as substructure analysis and component mode synthesis are a desirable feature.

In addition, several other vital features of the program such as allowable material properties, data generation, graphics, user interface, etc., need to be considered in selecting a code. For a detailed discussion of the code selection criteria see References [5.43, 5.46, 5.47].

The majority of the computer programs use normal mode based modal superposition methods for analysis. Viscous damping is most commonly used. The use of modal superposition using complex eigen solution is very limited. For hysteretically damped structures, the complex stiffness model is used and the analysis is restricted to harmonic response calculation. The method of damped forced vibration modes, although applicable to hysteresis damping is not implemented in any program.

Some special purpose computer programs for the analysis of damped structures are described in reference [5.42]. The programs ASTRE, DAMP, KSHELL, and SAMYS, surveyed in [5.42], all have the complex frequency and mode shape calculation capability.

A partial list of software dissemination and users group sources is given in the following list. A more complete list may be found in Reference [5.48].

- ASIAC - Aerospace Structures Information and Analysis Center, AFFDL/FBR Wright Patterson Air Force Base, Dayton, Ohio 45433.
- CEPA - Society for Computer Application in Engineering, Planning and Architecture, Inc., 358 Hungerford Drive, Rockville, MA 20850.
- COSMIC - Computer Software Management and Information Center, 112 Barrow Hall, University of Georgia, Athens, GA 30602.
- CES - Users Group, Inc., P.O. Box 8243, Cranston, RI 02920.
- ICP - International Computer Programs, Inc., 9000 Keystone Crossing, Indianapolis, IN 46240.
- NISEE - National Information of Service for Earthquake Engineering, 519 Davis Hall, University of California, Berkley, CA 94720.
- NTIS - National Technical Information System, U.S. Department of Commerce, 5285 Port Royal Road, Springfield, VA 22161.

5.2 INTEGRATION OF FINITE ELEMENT MODELING INTO THE DESIGN PROCESS

The finite element technique provides the designer with an accurate and economical means of predicting the dynamic behavior of either damped or undamped structures. As such, finite element analysis can play an important role at several stages in the design of damping treatments. This section describes a procedure for integrating finite element analysis into the damping design process and gives an example to illustrate the procedure. In references [5.49 - 5.51] a variety of damping design analysis problems are illustrated.

5.2.1 Analytical Procedure in Damping Design

The procedure may be divided into the following steps:

1. Perform an assessment of vibration problems present in a preliminary undamped design.
2. Evaluate different damping concepts for specific application.
3. Evaluate alternate damping treatment design.
4. Qualify final design configurations.

Each of these applications is discussed in greater detail in the following paragraphs. A schematic of the damping process with the finite element method is shown in Figure 5.4.

In the preliminary design phase, finite element modeling of a structure is a valuable tool in determining the existence of potential vibration problems. Conclusions can be drawn on the basis of either a natural frequency solution (to identify critical excitation frequencies and troublesome modes) or a frequency response analysis. Furthermore, examination of the vibration mode shapes will often help to determine those locations in which the application of damping treatments will prove most effective.

During the actual design of a damping treatment, a rational choice of the type and location of the treatment can be made much more easily by the

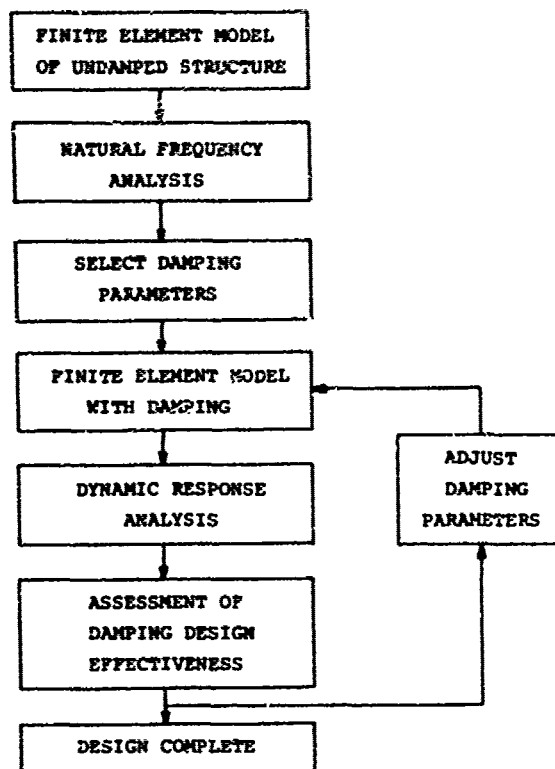


Figure 5.4. - Finite element analysis in damping design procedure.

use of trial simulations, again performed using finite element methodology. If a model has been developed during the preliminary design stage, simple modifications of such a model will often suffice for identifying the most desirable type of damping treatment to be used. Experience is frequently a sufficient guide to the selection of a damping concept for a particular application. However, in more complex situations, finite element analysis can often provide this same familiarity with the problem, at only modest expenditures of time and money.

Once a damping treatment has been selected (either on the basis of experiments or analytical studies), finite element techniques are readily employed to determine the exact design configuration based upon costs, weight, or performance criteria. A single finite element model can generally serve as a means of evaluating a great number of minor design changes, such as

variation in amount and distribution of damping, constraining layer thicknesses, material properties, etc.

Finally, the finite element method can be used for the final qualification of a damping treatment design. The performance of the final design can be assessed accurately and efficiently for a variety of operating environments (temperatures, loading, excitation, frequency). Besides the displacement response, stress information can also be generated in the finite element solution to identify potential fracture or fatigue problems which would not otherwise be anticipated prior to production.

Obviously, the finite element method represents a potentially powerful tool in several stages of the design process. Finite element simulations can, in most instances, be performed more quickly and economically than prototype testing, and can provide the opportunity for modeling the structural response under operating conditions which may not be easily obtained in laboratory testing.

The recent interest in finite element technology as an aid to the designer has been sparked at least, in part, by the development of computer graphics methods which can assist in both the preparation and interpretation of finite element data. The computer graphic processors can aid in:

- Generation of finite element data
- Model verification
- Assimilation of analysis results

An example illustrating the above design analysis procedure is summarized in the following paragraphs.

5.2.2 Example Damping Analysis

This example illustrates how the finite element method can be used efficiently within the general process of designing a damping treatment to reduce the amplitude of forced vibrations. First, a hypothetical structure

is defined which is presumed to have natural frequencies of vibration in the vicinity of the steady-state input frequency. A finite element model of the structure is constructed, and the natural frequencies are determined using a finite element computer program. Structural damping is then assumed in various parts of the structure. The results of the finite element program are used to determine the most effective areas to apply layered damping treatment. Finally, constrained damping is applied strategically, and the finite element program is used to determine the effectiveness of the damping treatment.

- a. Problem Definition - The particular problem selected for illustration of the application of finite element analysis in damping treatment design is similar to the engine exhaust duct shown in Figure 5.5.
- b. Finite Element Model - Figure 5.6 shows the finite element model used in this demonstration study. A cylindrical shroud with three flat vanes was modeled with variable 8-27 node solid finite elements. The boundary conditions and dimensions are shown in Figure 5.6. Although the full structure is shown, only a symmetric half of the structure on one side of a plane of symmetry through the bottom vane was actually modeled for computation.
- c. Natural Frequency Analysis - The finite element program of reference [5.52] was used to compute the natural frequencies and mode shapes of the model of Figure 5.6. Perspective plots of the first three vibration modes are shown in Figure 5.7 and end-on views of the same modes are shown in Figure 5.8. The modes were obtained by solving the eigenvalue problem defined by equation [5.31].
- d. Preliminary Damping Analysis - In practice, damping treatment is applied to one or more exposed surfaces of a structure. A complete finite element model containing multiple added layers would be quite complex and relatively expensive to analyze. Therefore, a preliminary damping analysis can be performed in which the elements of the original finite element model are assumed to be internally damped. In this case, four different cases are considered:
 1. No damping
 2. The vane elements have 5 percent damping
 3. The shroud elements have 5 percent damping
 4. Both the vane elements and the shroud elements have 5 percent damping.

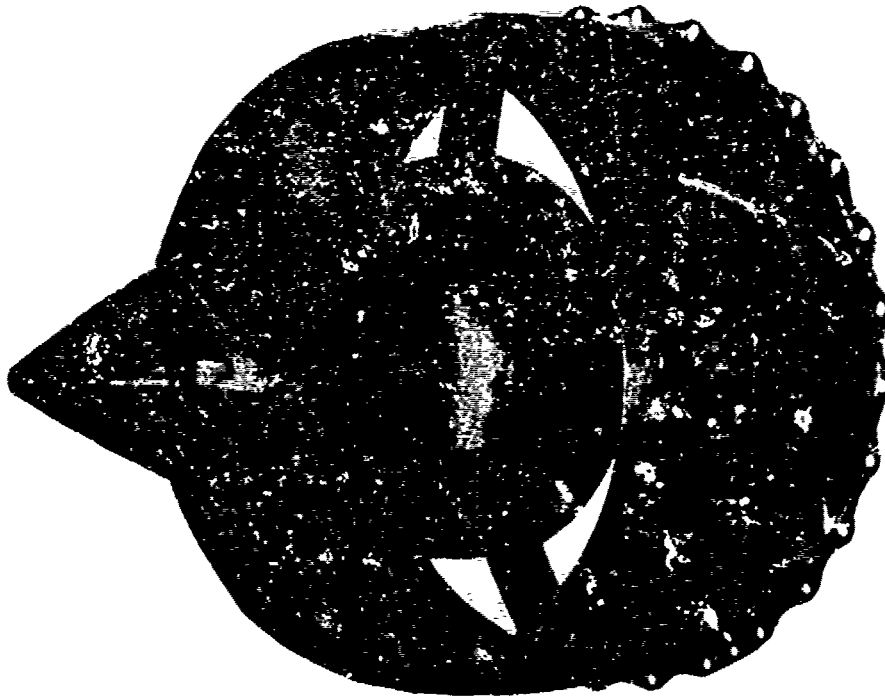


Figure 5.5. - Engine exhaust duct.

The results of the four cases for mode 2 are shown in Figure 5.9. In this case the amplitude and phase angle for the displacement of No. 1 (Figures 5.8 and 5.9) are plotted versus input frequency. The curves are generated by solving Equation 5.40 for several values of the input frequency for each of the four cases shown. Equation 5.25 was used to compile the system loss factors. Figure 5.9 indicates that considerable reduction in amplitude can be obtained if damping is present.

- e. Final Damping Design Analysis - The preliminary damping analysis of the preceding section provides the designer valuable information which can be used along with other data to select a damping treatment. After the damping treatment has been designed, another finite element analysis can be performed. This time the damping treatment is modeled separately to obtain an accurate representation of the effectiveness of the damping design. Figure 5.10 shows a detailed finite element model of the structure under consideration having a hypothetical damping treatment. In this case, for illustration, the shroud has a constrained damping layer applied to the outside diameter, while the vanes have an unconstrained damping layer applied to both sides. The detailed model can be used to proof-check the final design or used at each stage of an iterative design process.

Shroud
10" ID
.05" Thick
3" Wide
Steel

Vanes
2.5" Long
.1" Thick
1" Wide
Steel

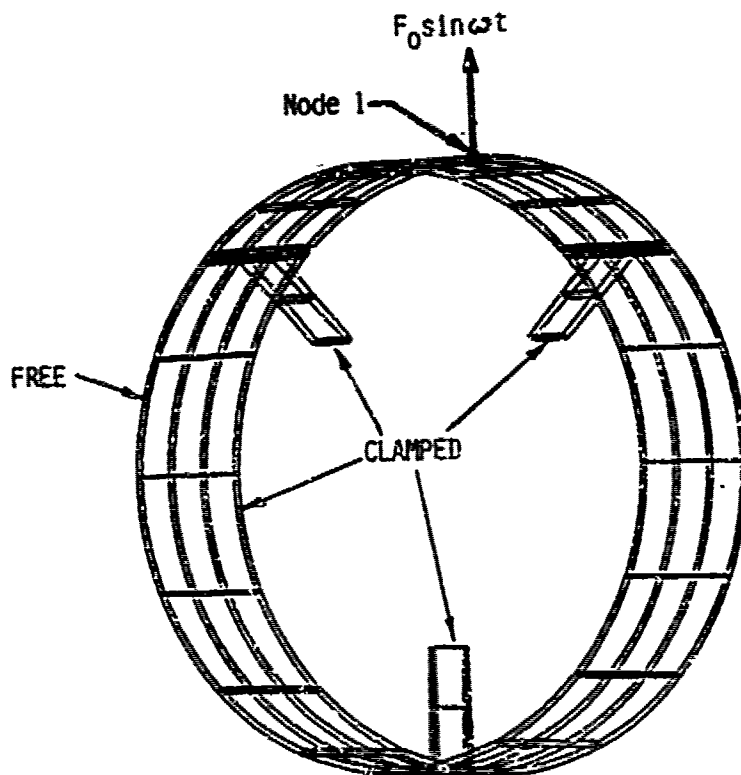


Figure 5.6. - Finite element model.

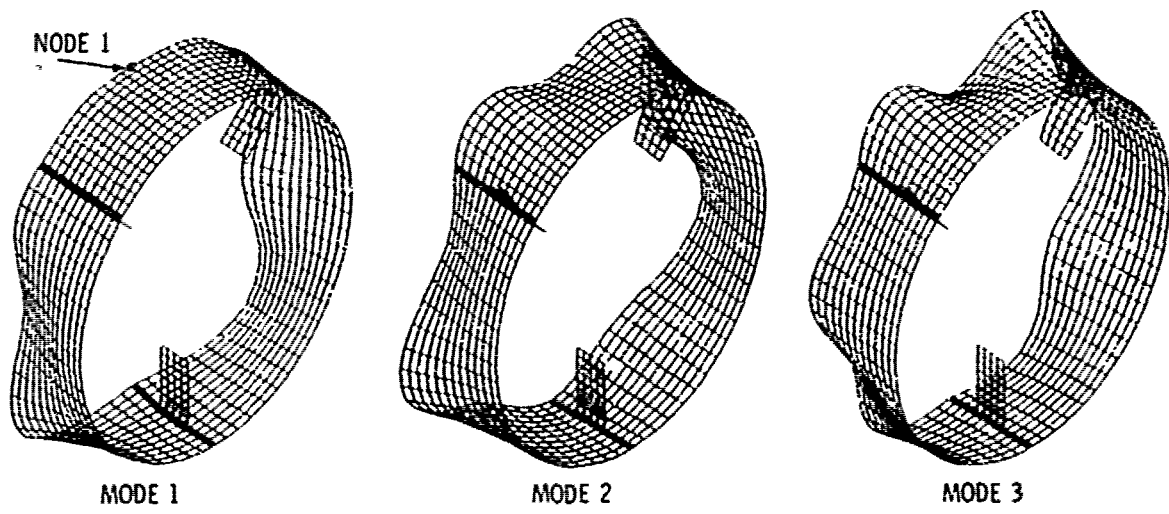


Figure 5.7. - Mode shapes of engine exhaust duct (perspective view).

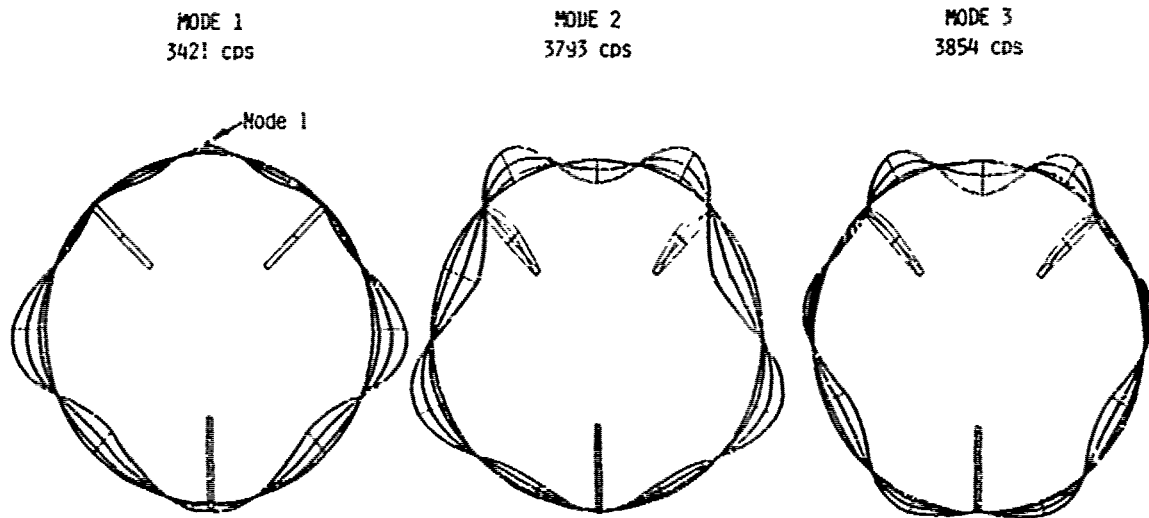


Figure 5.8. - Mode shapes of engine exhaust duct (end-on view).

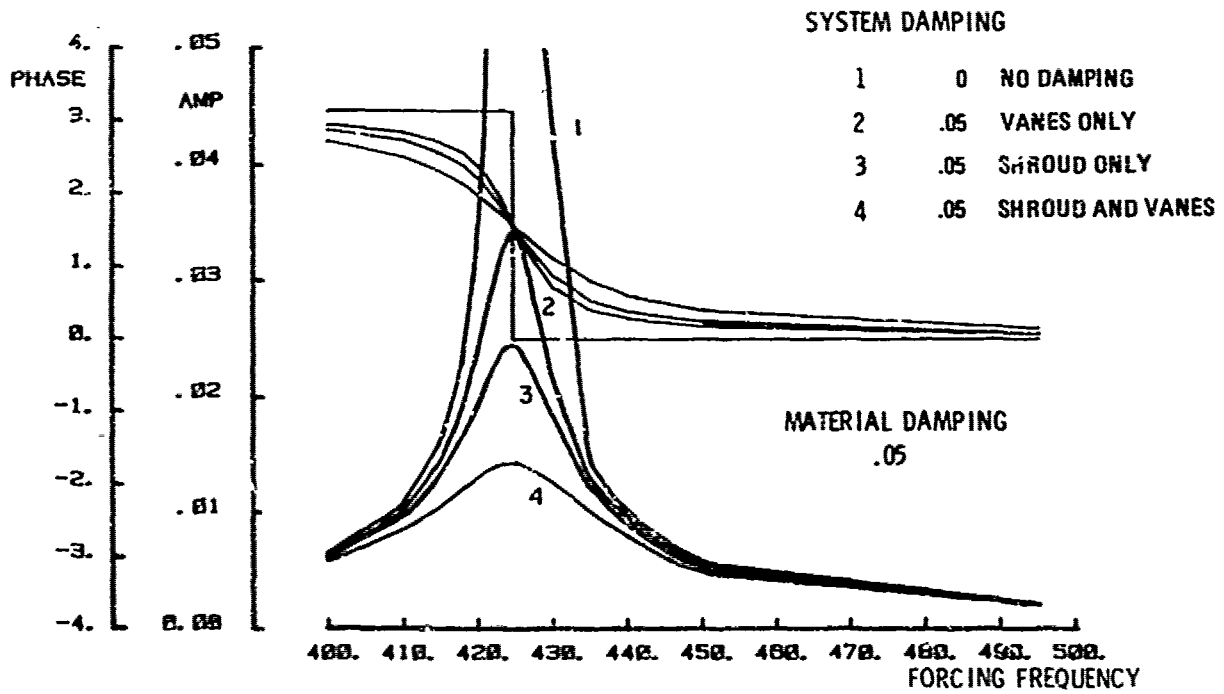


Figure 5.9. - Effect of damping treatment on the amplitude and frequency response of the second mode of engine exhaust duct.

DETAILED MODEL WITH DAMPING
LAYER AND CONSTRAINING LAYER

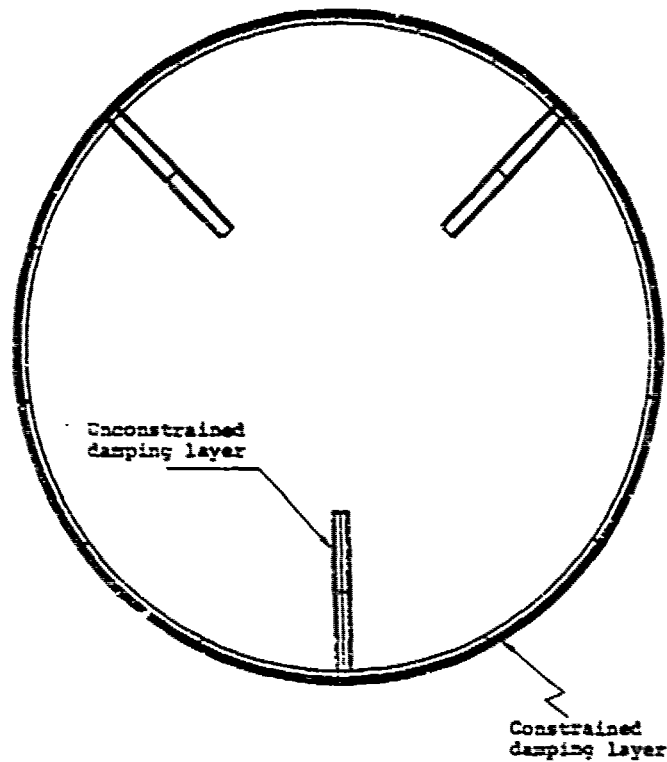


Figure 5.10. - Detailed model with damping layer and constraining layer.

5.3 A NOTE ON FINITE ELEMENT DISCRETIZATION OF LAYERED DAMPING DESIGNS

Finite element analysis because of its versatility in modeling general structures is ideally suited for modeling passive damping configurations on integrally damped structures. However, the modeling of layered damping designs on complex structures poses two problems. First of all, the thin damping layers result in high aspect ratios (length ÷ thickness) of the 3D solid elements representing the damping system. Secondly, if a multilayered damping system is being modeled, there are a large number of degrees-of-freedom. This section discusses ways to reduce the number of elements representing the damping system and the accuracy of the damping prediction using high aspect ratios. The recommendations made in the following paragraphs are based on a very limited number of practical applications [5.53].

5.3.1 Results Using High Aspect Ratios

The construction of an FE model for dynamic analysis is usually governed by giving consideration to the number and type of modes that are to be determined from the model. The length and width of the elements in the base structure are thus determined by accepted modeling practice. If a constrained layer damping system is then modeled on the structure and if the damping and/or constraining layers are thin relative to the base structure, the damping and/or constraining layers may have high aspect ratios (length ÷ thickness).

Experimental tests and corresponding FEA evaluation [5.53] of a cantilever plate with a double constrained layer system showed that aspect ratios up to 1000:1 yield very good analytical results. The undamped FE model of the plate is shown in Figure 5.11. Figure 5.12 shows the cross section of one of the damping configurations tested and analyzed. This configuration, referred to as Plate 1, consisted of the 0.25-inch (6.35 mm) thick plate with 0.002-inch (0.051 mm) thick 3M ISD-110 damping material, 0.007-inch (0.178 mm) thick stainless steel middle constraining layer, 0.003-inch (0.076 mm) thick Soundcoat MN damping material, and 0.007-inch (0.178 mm) thick stainless steel outer constraining layer. All layers in the FE model were modeled with 3D solid thick shell elements. Since the elements were 2 inches (50.8 mm) long and some elements were as thin as 0.002 in (0.051 mm), the aspect ratio on some elements were 1000 to 1.

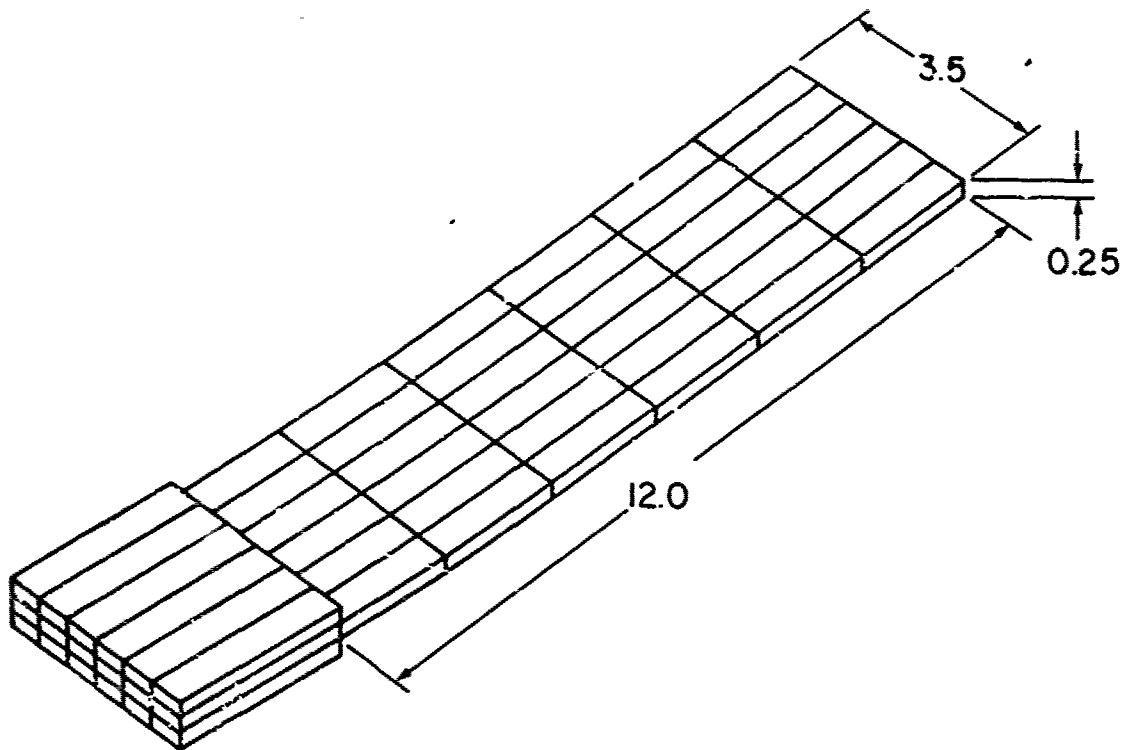


Figure 5.11. - Cantilever plate finite element model.

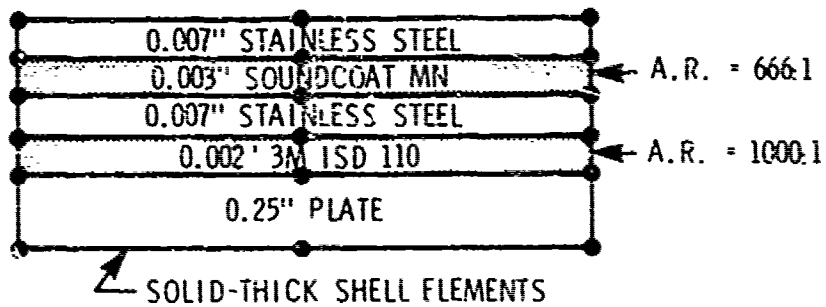


Figure 5.12. - Cross-section of Plate 1 damping system.

The results of the FEA and test of Plate 1 are shown in Figure 5.13, for the second bending mode. It can be seen that there is very good agreement between the test results and the FE forced vibration results. The results from the FE normal mode are considerably higher than the test results. It is felt in this case that the strain energy method using the forced response more closely matches the test. In both the test and the forced response analysis the plate was subjected to a small tip load. Another cause of the discrepancy could be that the tip load does not excite a pure mode. Indeed damping couples mode together. Perhaps if the test had been conducted with the clamped end of the cantilever mounted on a shaker, the mode shape of the cantilever plate may have been more nearly a pure mode rather than exciting the cantilever at the tip. Then perhaps the normal mode method would more closely match the shaker test.

A second damping configuration evaluated, referred to as Plate 2, is shown in cross section in Figure 5.14. This damping system had two layers of the same damping material, each 0.002 in. (0.051 mm) thick 3M ISD-112, separated by a 0.003-in. (0.076 mm) thick middle constraining layer. The outer constraining layer was 0.007-in. (0.178 mm) thick stainless steel. All layers were modeled with 3D solid-thick shell elements. The aspect ratios of the damping layers were 1000 to 1.

The results of the FEA and test of Plate 2 are shown in Figure 5.15 for the second bending mode. Again there is very good agreement between the test results and the FE forced vibration results. As for the Plate 2, the normal mode results are higher than the test results; the same explanation given for Plate 1, holds here as well.

Results for the first torsion mode are shown in Figure 5.16. The forced vibration results agree well with the test results, as do the normal mode results. In this instance, driving at the tip of the cantilever for the forced response (and test results) yields approximately the same results as the normal mode.

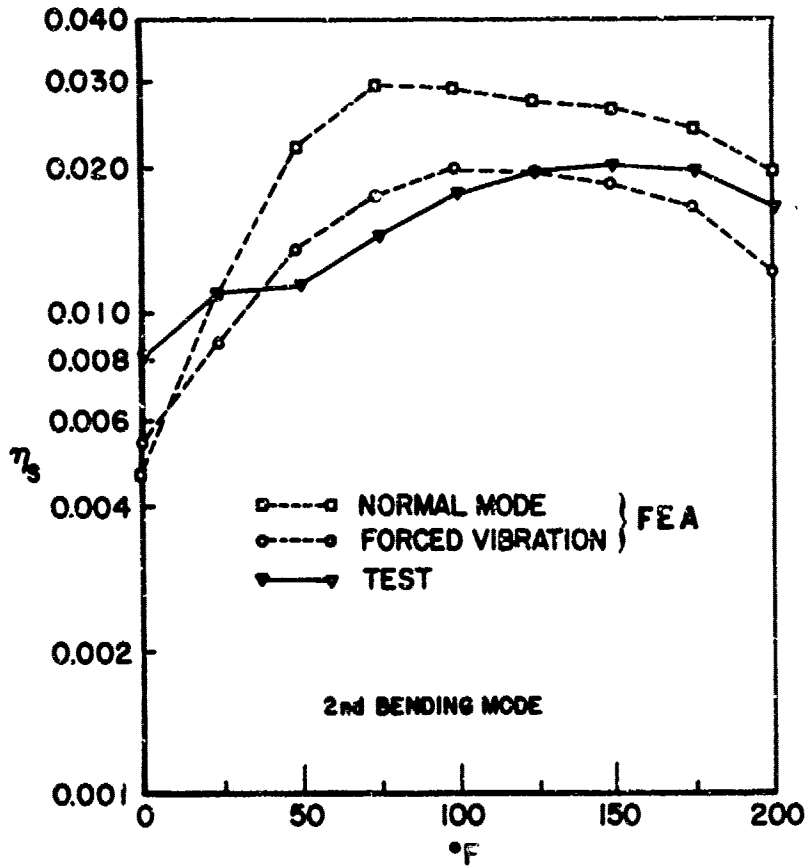


Figure 5.13. - Analytical and experimental results for Plate 1, second bending mode.

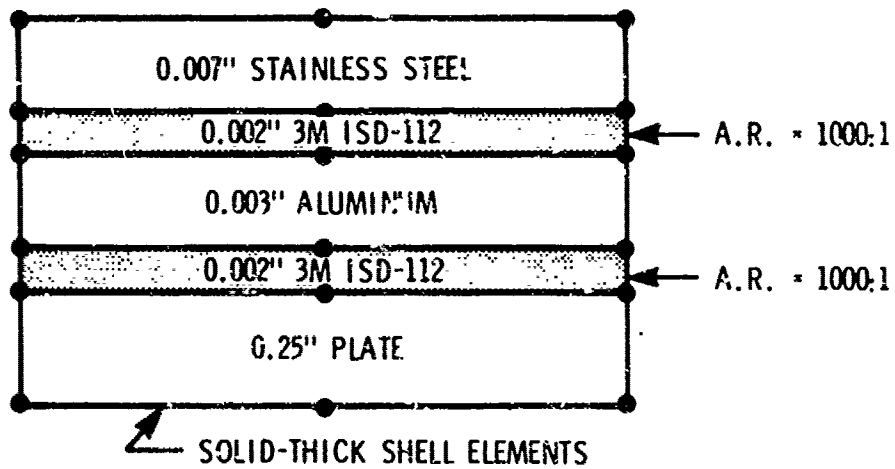


Figure 5.14. - Cross-section of Plate 2 damping system.

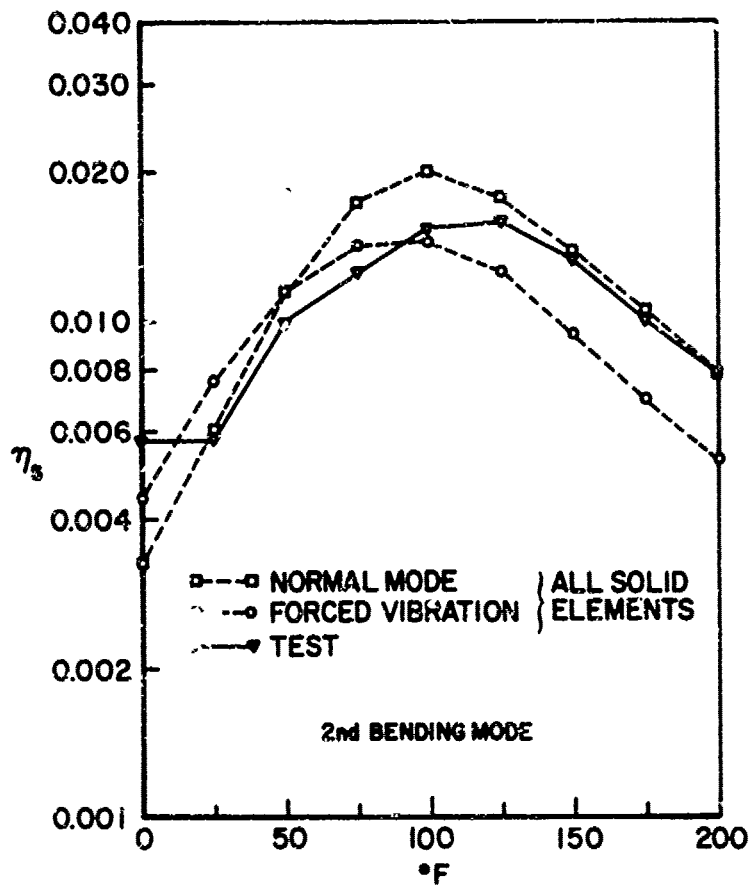


Figure 5.15. - Experimental and analytical results for Plate 2, 2nd bending mode.

It is observed, in the Plate 1 and Plate 2 results presented so far, that although the magnitude of the peak damping and the shape of the loss factor curve predicted by the FE forced vibration is nearly identical to the test results, the forced vibration curve is shifted to 25°F (-4°C) to the left of the test data. This temperature shift could be the result of two causes. The finite element model of the cantilever plate could be stiffer than the actual specimen; this is in fact the case, with the second bending mode frequency approximately 8 percent high. The other cause could be that the actual damping material is stiffer than the properties being input into the FE model. It is likely that the cause is a combination of these two factors.

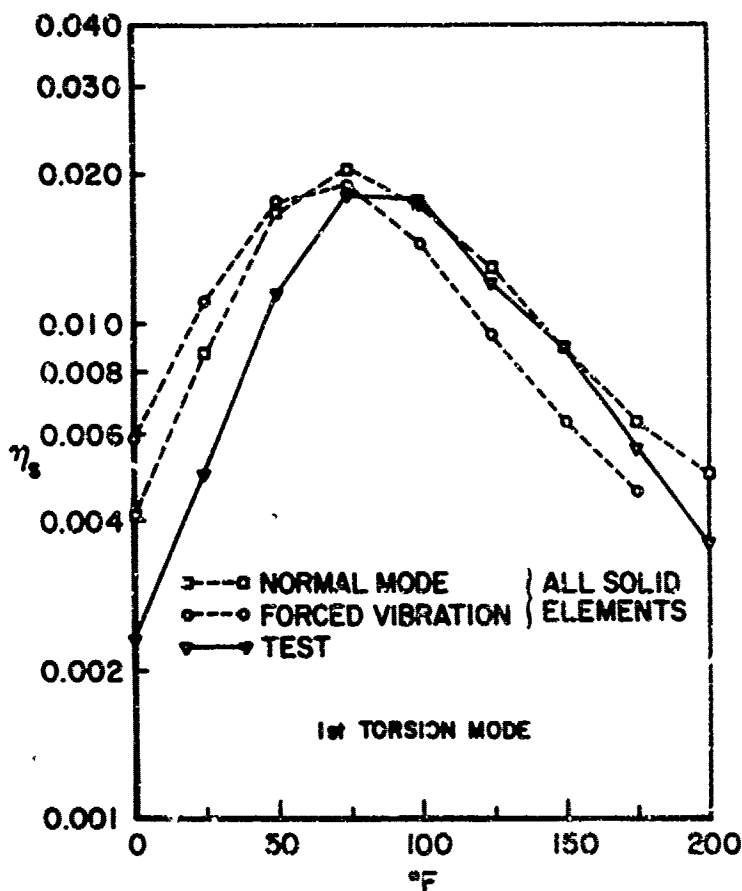


Figure 5.16. - Experimental and analytical results for Plate 2, 1st torsional mode.

The results presented so far have been for aspect ratios up to 1000 to 1. To see if the prediction of loss factors could be improved, the FE model was changed. Twelve elements were used along the length of the cantilever instead of six and the aspect ratio was correspondingly cut by a factor of two. The change in the results due to the lower aspect ratio were insignificant. Therefore, the use of aspect ratios up to 1000 to 1 was acceptable. The use of aspect ratios greater than 1000 to 1 needs further investigation.

5.3.2 Modeling Techniques to Reduce the DCF

Even a simple structure with a multiconstrained layer damping system can have a large number of DOFs. As an example, the cantilever plate discussed previously has 1300 DOFs.

Therefore, two means of reducing the number of DOFs were investigated. The first method involves the use of membrane elements to model the constraining layers. The second approach is to replace several layers in the damping system by an "equivalent" element.

- a. Use of Membrane Elements for Constraining Layers - The purpose of the constraining layer in a constrained-layer damping system is, as its name implies, to constrain the damping material. During bending, the constraining layer places the damping material in a state of shear stress and thus dissipates energy. The constraining layer, being stiff and usually very thin, undergoes very little shear deformation and is subjected to in-plane loading. Thus it has the characteristics of a membrane and can be represented by a membrane element. The damping layer on the other hand undergoes considerable shear deformation and therefore must be modeled with shear deformable elements such as a 3D solid thick shell (solid) element.

The use of membrane elements for constraining layers as applied to the Plate 1 damping configuration is shown in Figure 5.17. The nodes of the membrane elements are coincident with the nodes on the upper surface of the damping layers. Therefore, the membrane elements do not add any DOFs to the three solid elements used for the damping layers and plate. Thus the damping system shown in Figure 5.12, which was modeled by five solid elements through the thickness, is modeled by three solid elements and two membrane elements, resulting in a 33 percent reduction in DOF.

Figure 5.18 shows the FE forced vibration results using the membrane and solid elements model. Also shown are the FE forced vibration results using all solid elements, previously shown in Figure 5.13. It is seen that the two methods compare very favorably. Notice that the damping predicted by the use of the membrane elements is nearly uniformly lower than the results using all solid elements. This is probably due to the outer damping material and outer constraining layer not being as far away from the neutral bending axis because the membrane elements have no physical thickness.

A small error is introduced for structures with constraining layers that are thin relative to the base structure, such as Plate 1. Thick constraining layers would produce a greater error. The reader is also cautioned about using the membrane elements on curved surfaces as the membrane bending coupling is neglected, and the effect of its absence cannot be generalized.

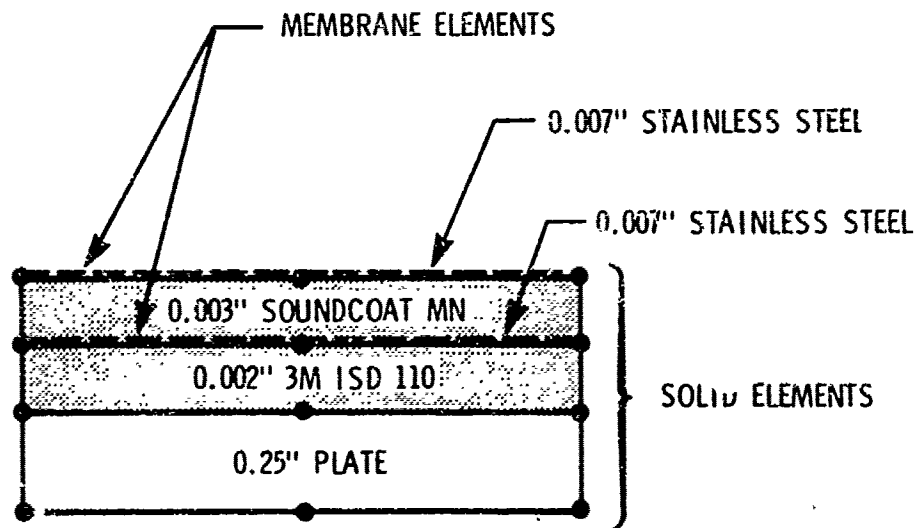


Figure 5.17. - Plate 1 modeling scheme using membrane elements.

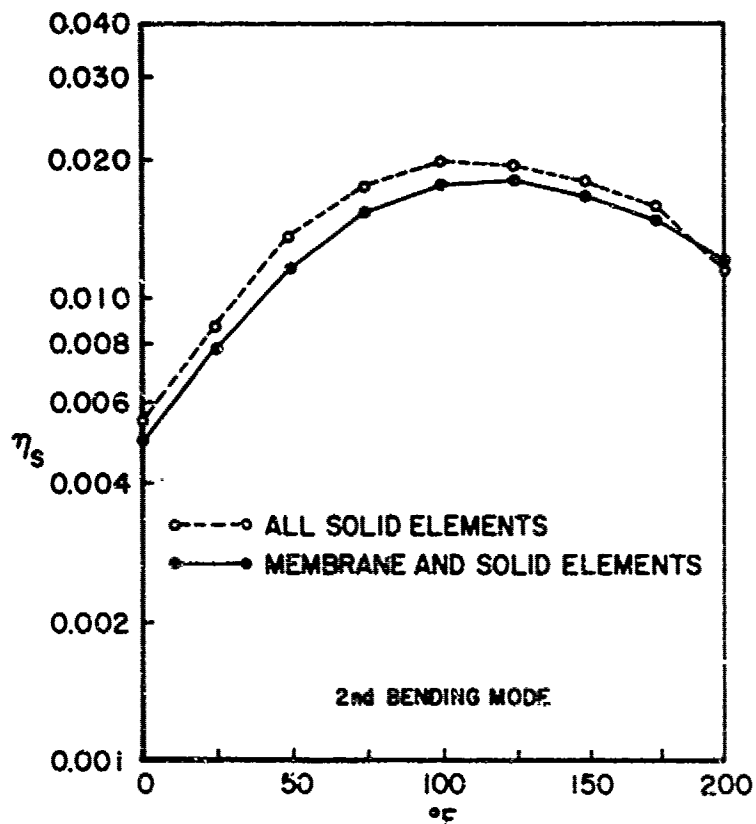


Figure 5.18. - FEA results comparing all solid model to membrane model.

- b. Use of Equivalent Solid Element - The other means of reducing the number of DOF become apparent from studying the Plate 2 configuration (see Figure 5.14). Since the two damping layers are the same thickness and of the same material and are separated by a thin middle constraining layer, it seemed that the overall behavior of the three-layer system would be governed by the soft damping materials. Furthermore, it seemed that the three layers could be represented by a single "equivalent" layer. It only remained to determine the dynamic properties of the three layers. The properties were determined from a symmetric sandwich beam test. Usually to determine the properties of a constrained layer damping material the material is placed between symmetric sandwich beams and tested over broad temperature and frequency ranges, as discussed in Volume I, Section 2. In the present case, the three layer system was placed between symmetric sandwich beams, as shown in Figure 5.19, and tested as if it were a typical damping material. The properties could also have been determined analytically thus avoiding the test procedures.

The application of this modeling technique to the Plate 2 configuration is shown in Figure 5.20. Figure 5.21 shows the second bending mode FE forced vibration results using all solid elements

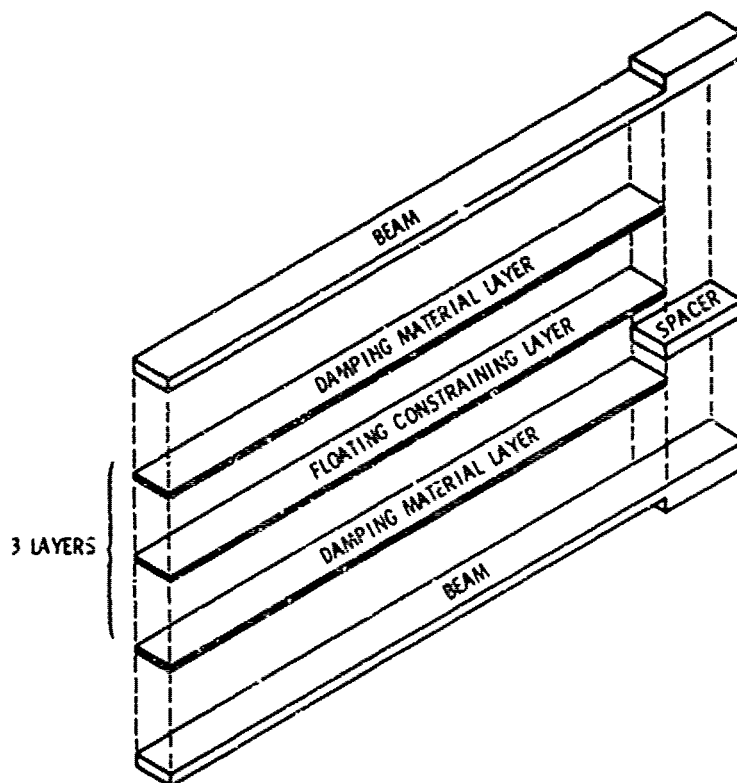


Figure 5.19. - Equivalent solid beam test specimen.

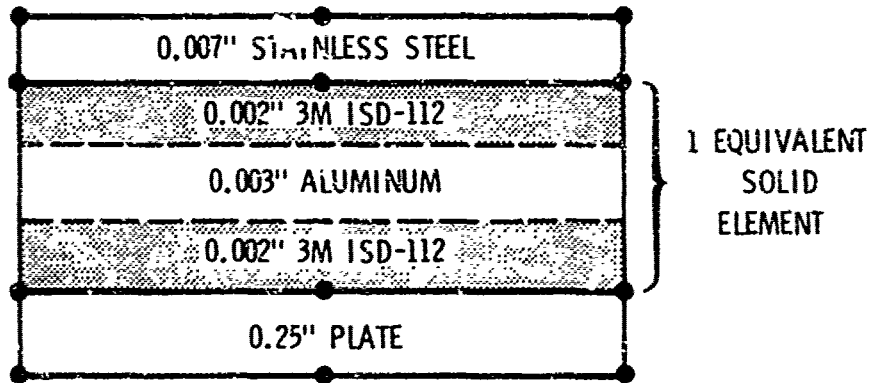


Figure 5.20. - Plate 2 modeling scheme using the equivalent solid approach.

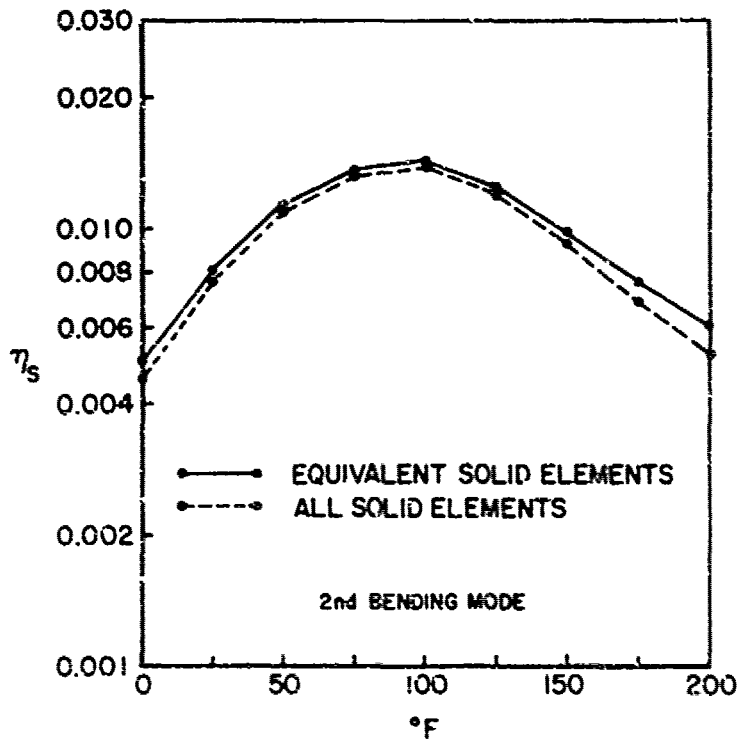


Figure 5.21. - Analytical results comparing the all solid model to the equivalent solid model for the second bending mode.

(previously shown in Figure 5.15) and the equivalent solid element. The results are nearly identical. The same is true for the first torsion mode shown in Figure 5.22.

To summarize, the modeling techniques for reducing the DOF were found to be accurate. The use of membrane elements for constraining layers predicts a slightly lower value of damping than the standard approach and reduced computer costs 44 percent in the present analyses. An equivalent solid element replacing the two damping materials and middle constraining layer gave nearly identical results as the standard modeling approach. This technique reduced computer costs 60 percent.

5.4 SUMMARY AND CONCLUSIONS

An overview of the finite element modeling procedure in the design of damped structures is presented. First a brief derivation of the discretized equations of motion is given primarily to define the notations and fix the ideas for subsequent discussion. Methods of modeling damping within the

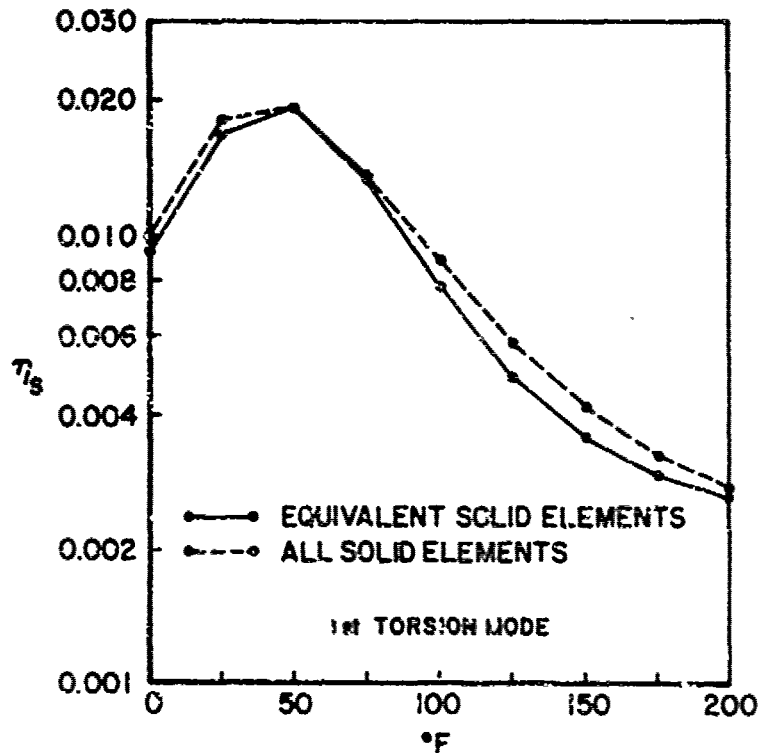


Figure 5.22. - Analytical results comparing the all solid model to the equivalent solid model for Plate 2 first torsion mode.

framework of finite element analysis are discussed next. Procedures are given for constructing damping matrices using known damping data and stiffness and mass characteristics of the structure. Frequency dependent, proportional and nonproportional, viscous and hysteretic damping models are discussed. Other models which may be a better representation of material damping behavior, but are not well developed for practical applications are relegated to the cited literature. Response analysis methods, relevant to the effectiveness of assessing damped designs, are described. It is noted that the direct response analysis methods permit greater generality in regard to modeling complex material behavior and loading conditions but at an increased computational cost. The modal strain energy method is seen as a computationally convenient, though less accurate, alternate for a cost-effective analysis at the preliminary design stage. The limitations of this as well as other methods are noted. For structures with heavy and nonuniformly distributed damping, the coupling of classical normal modes can not be ignored; complex mode methods are given to treat such problems. Analysis methods are described for structures which require solution by partitioning the system owing to computer and/or organizational constraints. Major commercially available finite element computer programs, their response analysis capabilities and information concerning their availability are described. It is observed that for the most part, response analysis methods based on direct solution and normal mode superposition are implemented in the existing codes. Few programs have complex mode capability for viscously damped systems. None of the general-purpose programs have the capability to treat transient or complex modal response problems of hysteretically damped systems. Substructure methods are implemented in some general-purpose finite element computer programs. For the most part, this capability is developed independent of the finite element programs. A procedure is described next for integrating the finite element analysis into damping design. An example is given illustrating the important points of this procedure. Finally, two case studies are presented that discuss practical ways to reduce the size of the discretized problem of damped structures.

TABLE 5.2. LIST OF SYMBOLS FOR SECTION 5

SYMBOL	DEFINITION
B^e	Element strain displacement matrix
C	Viscous damping matrix
D^e	Elasticity matrix
F	Assembled load vector
F^e	Vector of concentrated nodal forces
F_0	Peak amplitude of harmonic force
G	Damping matrix
H	Hysteretic damping matrix
H^e	Element damping matrix
H	Substructure dynamic matrix
J	$(-1)^{\frac{1}{2}}$
K	Assembled stiffness matrix
K^e	Stiffness matrix
K_G	Reduced stiffness matrix
K	Substructure dynamic matrix
M	Assembled mass matrix
M^e	Consistent mass matrix
M_G	Mass matrix
n	Degrees-of-freedom to be retained in isolated substructure matrix equations
n	Substructure dynamic matrices
m_r	Generalized mass

TABLE 5.2. LIST OF SYMBOLS FOR SECTION 5 (Continued)

SYMBOL	DEFINITION
\underline{N}^e	Matrix of shape functions
n	Total number of finite elements in the assembly or the order of \underline{K} or \underline{M} matrices
\underline{P}	Substructure generalized coordinates
p	Number of modes in which damping is specified
$\underline{Q}(t)$	Uncoupled system coordinates
S_σ	Portion of surface of V where \underline{t} is specified
$(SE)_{\max}^e$	Peak stored energy in the element
s	Degrees-of-freedom to be reduced out of isolated substructure matrix equations
\underline{T}	Matrix defined in equation 5.60
t	Time
\underline{t}	External traction
\underline{U}	Vector of all independent node displacements
\underline{U}^e	Nodal displacements
\underline{u}_i^e	Vector of element nodal displacement
\underline{v}_i	Vector of nodal displacements that characterize the spatial form of the response
\underline{u}_i^*	Transposed complex conjugate of \underline{U} corresponding to excitation frequency, ω_i
V	Body
\underline{Y}	Eigensolution matrix
Y	Modal intensity matrix

TABLE 5.2. LIST OF SYMBOLS FOR SECTION 5 (Continued)

SYMBOL	DEFINITION
\underline{Z}	Complex mode coordinate
δ	Variational operator
$\delta \underline{U}$	Discrete virtual displacements
δ_{ij}	Kronecker delta
$\underline{\epsilon}^e$	Strain
η_d	Loss factor associated with dissipation behavior in dilatational modes of vibration
η_1^e	Loss factor of the element material at excitation frequency, ω_1
η_s	Loss factor associated with dissipation behavior in shear modes of vibration
$\{ \lambda \}$	2n x 2n diagonal mode value matrix
λ^r, μ^r	Lame's parameters of the isotropic elastic material in the elasticity matrix D
μ^i, λ^i	Material parameters of the damping matrix, G
v	Damped forced normal mode coordinates
ω	Forcing frequency
ω^e	Natural frequency
ω_n	Modal frequency
$\{ \omega_r^2 \}$	NXN diagonal matrix with element in r th row and column being ω_r^2
ω_s	Undamped frequencies
$\underline{\Phi}$	Column of forces equal to $i\eta$ times the inertial force corresponding to harmonic vibration $\underline{U} = \underline{Y}e^{i\omega t}$

TABLE 5.2. LIST OF SYMBOLS FOR SECTION 5 (Continued)

SYMBOL	DEFINITION
$\underline{\phi}_s$	Mode shapes corresponding to ω_s
$\underline{\Psi}$	Complex mode matrix
ρ	Mass density of the structural material
$\underline{\sigma}^e$	Stress
$\frac{\theta}{r}$	r^{th} mass normalized mode shape of undamped structure
$\underline{\xi}$	Vector of modal coordinates
ζ^e	Viscous modal damping ratio
ζ_i	System damping ratio
ζ_n	Modal damping ratio
ζ_{rs}	Modal damping coupling ratio

REFERENCES

- 5.1 Zienkiewicz, O.C., "The Finite Element Method," 3rd edition, McGraw-Hill Book Company, New York, NY, 1977.
- 5.2 Bathe, K.J., "Finite Element Procedures in Engineering Analysis," Prentice-Hall, Inc., Englewood Cliffs, New Jersey, 1982.
- 5.3 Przemieniecki, J.S., "Theory of Matrix Structural Analysis," McGraw-Hill Book Company, New York, NY, 1968.
- 5.4 Key, Samuel W., et al, "Hondo II, A Finite Element Computer Program for the Large Deformation Dynamic Response of Axisymmetric Solids," Sandia Laboratories, Report SAND-78-0422, October 1978.
- 5.5 Rousos, L.A., Kyer, M.W., Thornton, F.A., "Finite Element Modes with Nonviscous Damping," AIAA Journal, Vol. 20, No. 6, June 1982, pp. 831-836.
- 5.6 Bagley, R.L., Torvik, P.J., "Fractional Calculus - a Different Approach to the Finite Element Analysis of Viscoelastically Damped Structures," AIAA Journal, Vol. 21, No. 5, May 1983, pp. 741-748.
- 5.7 Wilson, E.L., Penzien, J., "Evaluation of Orthogonal Damping Matrices," Intl. J. for Numerical Methods in Engineering, Vol. 4, 1972, pp. 5-10.
- 5.8 Clough, R.W., Mojtahedi, S., "Earthquake Response Analysis Considering Nonproportional Damping," Earthquake Engineering and Structural Dynamics, Vol. 4, 1976, pp. 489-496.
- 5.9 Caughey, T.K., "Classical Normal Modes in Damped Linear Dynamic Systems," Journal of Applied Mechanics, ASME Transactions, Ser. E, Vol 27, July 1960, pp. 269-271.
- 5.10 Hasselman, T.K., "Method for Constructing a Full Modal Damping Matrix from Experimental Measurements," AIAA Journal, Vol. 10, No. 4, April 1972, pp. 526-527.
- 5.11 Breitbach, E., "A Semiautomatic Modal Survey Test Technique for Complex Aircraft and Spacecraft Structures," ESRO-SP-99, March 1974, pp. 519-528.
- 5.12 Jezequel, L., "A Method of Damping Synthesis from Substructure Tests," Transactions of the ASME, Journal of Mechanical Design, paper no. 79-DET-11.
- 5.13 Williams, M.L., "Structural Analysis of Viscoelastic Materials," AIAA Journal, Vol. 2, No. 5, May 1964, pp. 788-808.

REFERENCES (Continued)

- 5.14 Nelson, F.C., Grief, R., "On the Incorporation of Damping in Large, General-Purpose Computer Programs," Nuclear Engineering and Design, 37, 1976, pp. 65-72.
- 5.15 Kalinowski, A.J., "Modeling Structural Damping for Solids having Distinct Shear and Dilatational Loss Factors," Seventh NASTRAN User's Colloquim, NASA-CP-2062, 1978.
- 5.16 Belytschko, T., "A Survey of Numerical Methods and Computer Programs for Dynamic Structural Analysis," Nuclear Engineering and Design, 37, 1976, pp. 23-24.
- 5.17 Van Overmeire, "A Fast-Fourier Method for the Dynamic Analysis of Linear Structures with Frequency Dependent Properties," Zeitschrift Angewandte Mathematic Und Mechanik, 63, 1983, pp. 84-86.
- 5.18 Jones, D.I.G., "Transient Response of Damped Space Systems," Paper no. 83-0090, 24th Structures, Structural Dynamics and Materials Conference, Lake Tahoe, Nevada, May 2-4, 1983, pp 304-313.
- 5.19 Lunden, R., Dahlberg, T., "Frequency-Dependent Damping in Structural Vibration Analysis by Use of Complex Series Expansion of Transfer Functions and Numerical Fourier Transformation," Journal of Sound and Vibration, 80 (2), 1982, pp. 161-178.
- 5.20 Roesset, J.M., Whitman, R.V., Dobry, R., "Modal Analysis for Structures with Foundation Interaction," Journal of Structural Division, Proceedings of the American Society of Civil Engineers, Vol. 99, No. ST3, March 1973, pp 399-415.
- 5.21 Brockman, R.A., "Finite Element Analysis of Forced Vibrations in Viscoelastic Layered Panel Structures," University of Dayton, Report UDR-TR-78-31, March 1978.
- 5.22 Soni, M.L. "Finite Element Analysis of Vibrations of Initially Stressed Viscoelastic Structures," University of Dayton, Report UDR-TR-79-113, November 1979.
- 5.23 Soni, M.L., "Finite Element Analysis of Viscoelastically Damped Sandwich Structures," The Shock and Vibration Bulletin 51, Part 1, May 1981, pp. 97-108.
- 5.24 Soni, M.L., Bogner, F.K., "Finite Element Vibration Analysis of Damped Structures," AIAA Journal, Vol. 20, No. 5, May 1982, pp. 700-707.
- 5.25 Hasselman, T.K., "Mode Coupling in Lightly Damped Structures," AIAA Journal, Vol. 14, No. 11, November 1976, pp. 1627-1628.

REFERENCES (Continued)

- 5.26 Ungar, E.E., Kerwin, E.M., Jr., "Loss Factors of Viscoelastic Systems in Terms of Energy Concepts," *Journal of the Acoustical Society of America*, Vol. 34, July 1962, pp. 954-957.
- 5.27 Rogers, L., Johnson, C.D., Keinholz, D.A., "The Modal Strain Energy Finite Element Analysis Method and its Application to Damped Laminated Beams," 51st Shock and Vibration Symposium, San Diego, CA, October 21-23, 1980.
- 5.28 Belytschko, T., Mindle, W.L., "The Treatment of Damping in Transient Computations," *Proceedings, Winter Annual Meeting of the ASME*, Chicago, IL, November 16-21, 1980, pp. 123-132.
- 5.29 Lalanne, M., Paulard, M., Trompette, P., "Response of Thick Structures Damped by Viscoelastic Material with Application to Layered Beams and Plate," *Shock and Vibration Bulletin* circa 1975.
- 5.30 Foss, K.A., "Coordinates Which Uncouple the Equations of Motion of Damped Linear Dynamic Systems," *Journal of Applied Mechanics*, Vol. 25, September, 1958, pp. 361-366.
- 5.31 Hurty, M.F., Rubenstein, M.F., *Dynamics of Structures*, Prentice-Hall, Inc., Englewood Cliffs, NJ, 1964.
- 5.32 Itoh, T., "Damped Vibration Mode Superposition Method for Dynamic Response Analysis," *Earthquake Engineering and Structural Dynamics*, Vol. 2, 47-57 (1973).
- 5.33 Mead, D.J., "Existence of Normal Modes of Linear Systems with Arbitrary Damping," *Proc. Symposium on Structural Dynamics*, Loughborough University of Tech., Vol. 1, pp. 5.1-16, 1970.
- 5.34 Fraeijs de Veubeke, B.M., "A Variational Approach to Pure Mode Excitation Based on Characteristic Phase Lag Theory," *AGARD Report 39*, 1958.
- 5.35 Guyan, R.J., "Reduction of Stiffness and Mass Matrices," *AIAA Journal*, Vol. 3, pp. 380, 1965.
- 5.36 Hurty, W.C., "Dynamic Analysis of Structural Systems Using Component Modes," *AIAA Journal*, Vol. 3, No. 4, 1965, pp. 678-685.
- 5.37 Meirovitch, L., "Computational Methods in Structural Dynamics," Sijthoff and Noordhoff, Alphen aan des Rijn, Netherlands, 1980.
- 5.38 Craig, R.R. Jr., "Structural Dynamics: An Introduction to Computer Methods," John Wiley & Sons, New York, 1981.

REFERENCES (Continued)

- 5.39 The NASTRAN THEORETICAL MANUAL Level 17.5. NASA SP 221 (03) December, 1978.
- 5.40 Soni, M.L., "DFLEX: A Computer Program for Modal and Damping Synthesis of Flexible Spacecraft Appendages," University of Dayton, Report UDR-TR-82-128, October 1982.
- 5.41 Klosterman, A.L., "On the Experimental Determination and Use of Modal Representations of Dynamic Characteristics," Ph.D. thesis, University of Cincinnati, 1971.
- 5.42 Nelson, F.C., Greif, R., "Damping", in Shock and Vibration Computer Programs: Reviews and Summaries," The Shock and Vibration Information Center, Naval Research Lab., Washington, D.C., DVM-10, 1975.
- 5.43 Imbert, J.F., "A Survey of Current Capability for Dynamic Analysis of Complex Structures," Proceedings of Conference on Finite Element Method in the Commercial Environment. Bournemouth, U.K., 1978, paper 20, pp. 421-464.
- 5.44 Noor, A.K., "Survey of Computer Programs for Solution of Nonlinear Structural and Solid Mechanics Problems," Computers and Structures, Vol. 13, No. 1-3, June 1981, pp. 425-465.
- 5.45 Schmidt, R.J., Dodds, R.H. Jr., "Theoretical and Software Considerations for Nonlinear Dynamic Analysis," The University of Kansas Center for Research Report SM-8, February 1983.
- 5.46 Tajg, I.C., "Selection Criteria for Structural Analysis Programs," Space AGARD Report No. 670, NATO-AGARD, pp. 11-20, Neuilly Sur Seine, France, January 1979.
- 5.47 Sollogobo, P., Wahl, L., Dreyer, F., "Main Computer Systems Programs, Presentation, Criteria for Selection," CNEOX/CTICM, 1978 (available from CNEOX, B.P. 337, F-29273, Brest, or: CTICM, 20 Rue Jean Jaures F-93807, Puleaux).
- 5.48 Pilkey, B.F., "Computerized Sources of Abstracts of the Engineering Literature," Structural Mechanics Software Series, Vol. 3, pp. 29-39, The University Press of Virginia, Charlottesville, VA, 1980.
- 5.49 Kluesener, M.F., Drake, M.L., "Damped Structures Design Using Finite Element Analysis," The Shock and Vibration Bulletin 51, part 5, May 1982, pp. 1-12.

REFERENCES (Continued)

- 5.50 Holman, R.E., Liu, C.P., Bauer, J.L., "Damping of Precision Pointing Systems and the Use of Finite Element Computational Program for Performance Prediction," Hughes Aircraft Company, Air Force Weapons Laboratory Contract No. F29604-80-C-0015.
- 5.51 Kienholz, D.A., Johnson, C.D., Parekh, J.C., "Design Methods for Visco-elastically Damped Plates," Paper no. 83-0904, 24th Structures, Structural Dynamics and Materials Conference, Lake Tahoe, Nevada, May 2-4, 1983, pp. 334-343.
- 5.52 Brockman, R.A., "MAGNA Computer Program User's Manual," University of Dayton, Report UDR-TR-80-107, November 1980.
- 5.53 Kluesener, M.F., "Practical Methods of Applying Finite Element Analysis to the Design of Complex Damped Structures," AIAA Paper no. 84-0971-CP.

SECTION 6

MEASUREMENT OF RESONANT FREQUENCIES AND DAMPING

6.1 INTRODUCTION

The purpose in this section is to briefly review the methods used in determining the resonant frequencies and the damping of structural modes. This field is still undergoing considerable change, spurred on by the need for modal parameter identification in the presence of nonlinear response, the resolution of modes with identical frequencies in the presence of noise and the avoidance of truncation or smoothing errors. A review of parameter identification methods, and developments in these methods, is contained in Reference [6.1] with emphasis on ground vibration testing of aircraft. The intention here is to concentrate on the well established methods rather than on the newest developments in the field, with emphasis placed on accurate measurement of modal damping. System identification [6.2], which involves changing the analytical model of the structure on the basis of measured modal parameters, is beyond the scope of this review.

The basic methods are discussed in Section 6.2 and the subsequent development of these methods based on the Fourier and the Laplace transforms, are discussed in Section 6.3. The errors in the measured damping resulting from the use of the above periodic transforms in analyzing nonperiodic data and the means of overcoming these errors are discussed in Section 6.4.

6.2 BASIC METHODS

The basic methods for measuring the modal frequencies and damping include the free vibration decay method in the time domain [6.3, 6.4, 6.5], and the half power point [6.3, 6.4, 6.5] and the Kennedy-Pancu (K-P) [6.6] methods in the frequency domain. These methods work best with well separated modes in which each mode can be treated as a single degree-of-freedom system. Most vibration response measurements, from a variety of structures, can be analyzed on the basis of a single mode response. The basic K-P method can also be used to analyze multimodal response provided the modes do not have close or

identical resonant frequencies. Even this problem can often be overcome by selecting a different measurement location where the response in one or the other of the modes dominates. All of these methods are degraded by the presence of spurious noise in the response data. Damping is especially sensitive to the presence of such noise, accounting in part for the large scatter observed in the measured damping data.

The basic theory for the above methods is summarized in some detail in the following sections, assuming a single mode response. All methods of measuring damping are based on either the free vibration decay or the complex frequency domain representation of the resonant vibration response.

6.2.1 Time Domain Analysis

The structural damping or loss factor, η , can be used in steady state vibration analysis but has some limitations [6.7] when used in free vibration or transient analyses. This problem is not encountered with the viscous damping ratio, ζ . Since most structures, including those damped with viscoelastic materials, have a viscous damping ratio of less than 0.2, the viscous damping ratios extracted by all of the methods can be expressed in terms of the loss factor by means of the following relationship

$$\eta \approx 2\zeta \quad (6.1)$$

6.2...1 Free Vibration Theory

The equation of motion for the free vibration of a single degree-of-freedom system with viscous damping can be written as

$$M\ddot{w}(t) + C\dot{w}(t) + Kw(t) = 0 \quad (6.2a)$$

where M is the mass, C is the viscous damping coefficient, K is the stiffness, and $\ddot{w}(t)$, $\dot{w}(t)$ and $w(t)$ are the acceleration, velocity and displacement of the mass, respectively. On dividing by the mass, the above equation becomes

$$\ddot{w} + 2\zeta \omega_n \dot{w} + \omega_n^2 w = 0 \quad (6.2b)$$

where ω_n is the natural circular frequency given by

$$\omega_n = \sqrt{\frac{K}{M}} \quad (6.3)$$

and ζ is the previously mentioned viscous damping ratio defined by

$$\zeta = \frac{C}{C_c} \quad (6.4)$$

where C_c , the critical viscous damping coefficient, is

$$C_c = 2 \sqrt{KM} = 2M \omega_n \quad (6.5)$$

The general solution to equation 6.2b can be written as

$$w(t) = e^{-\zeta \omega_n t} \left\{ A \sin \left(\sqrt{1-\zeta^2} \omega_n t \right) + B \cos \left(\sqrt{1-\zeta^2} \omega_n t \right) \right\} \quad (6.6)$$

where A and B are constants defined by the initial conditions. The velocity corresponding to the above displacement is

$$\begin{aligned} \dot{w}(t) = & e^{-\zeta \omega_n t} \omega_n \sqrt{1-\zeta^2} \left\{ A \cos \left(\sqrt{1-\zeta^2} \omega_n t \right) - B \sin \left(\sqrt{1-\zeta^2} \omega_n t \right) \right\} \\ & - \zeta \omega_n e^{-\zeta \omega_n t} \left\{ A \sin \left(\sqrt{1-\zeta^2} \omega_n t \right) + B \cos \left(\sqrt{1-\zeta^2} \omega_n t \right) \right\} \end{aligned} \quad (6.7)$$

If the system is given an initial displacement w_0 , at a time $t = 0$ ($B = w_0$) and then released with a zero initial velocity, that is $\dot{w}(0) = 0$ ($A = w_0 \zeta / \sqrt{1-\zeta^2}$), the resulting displacement becomes

$$w(t) = w_0 e^{-\zeta \omega_n t} \left\{ \cos \left(\sqrt{1-\zeta^2} \omega_n t \right) + \frac{\zeta}{\sqrt{1-\zeta^2}} \sin \left(\sqrt{1-\zeta^2} \omega_n t \right) \right\}$$

$$= \frac{w_0 e^{-\zeta \omega_n t}}{\sqrt{1-\zeta^2}} \text{Cos} (\omega_d t - \phi) \quad (6.8)$$

where ϕ is the phase angle given by

$$\text{Tan } \phi = \frac{\zeta}{\sqrt{1-\zeta^2}} \quad (6.9)$$

and ω_d is

$$\omega_d = \omega_n \sqrt{1-\zeta^2} \quad (6.10)$$

An exponentially decaying oscillation is obtained (Figure 6.1(a)) when $\zeta < 1$, which is the case for most structures. Critical damping is obtained when $\zeta = 1$ and the vibration decays to zero without oscillating (Figure 6.1(b)).

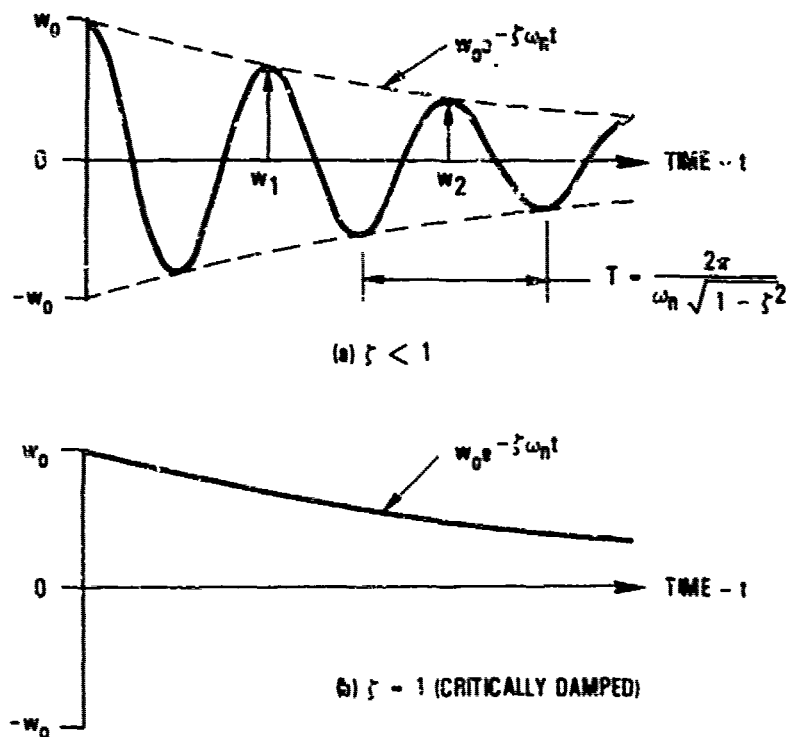


Figure 6.1. Free vibration response of damped single degree-of-freedom system

The critical damping coefficient corresponding to this unit viscous damping ratio is given in equation 6.5.

Equation 6.8 contains the natural circular frequency and the viscous damping ratio in an extractable form. Thus, for a single degree-of-freedom system, it is only necessary to displace the mass and then to release it suddenly in order to reproduce the exponentially decaying oscillation represented by equation 6.8. The quick stop method is another means of achieving the same result. The mass in this method is excited by a harmonic force that is first tuned onto the resonant frequency of the single degree-of-freedom system and then suddenly removed. The resulting exponentially decaying oscillation can also be represented, over most of the decay, by equation 6.8.

6.2.1.2 Impulsive Loading

The velocity of the mass of a single degree-of-freedom system, that is subjected to an impulse I , is changed suddenly by I/M without undergoing any significant displacement. On substituting these initial conditions into equations 6.6 and 6.7, it follows that the resulting displacement of the mass is given by

$$w(t) = I h(t) \quad (6.11)$$

where

$$h(t) = \frac{1}{M \omega_d} e^{-\zeta \omega_n t} \sin \omega_d t \quad (6.12)$$

is the impulse response function of the single degree-of-freedom system. This impulse response function represents an exponentially decaying oscillation similar to that in equation 6.8. For an impulse $I(t)$, of arbitrary shape and duration, t , the displacement in equation 6.11 becomes

$$w(t) = \int_0^t I(t-\tau) h(\tau) d\tau \quad (6.13)$$

where τ is another time variable.

If an impulse, of duration, t , is applied at the base of the spring, producing a base displacement of $w_B(t)$, the relative displacement, $w_R(t)$, of the mass becomes

$$w_R(t) = \frac{1}{\omega_d} \int_0^t \ddot{w}_B(\tau) e^{-\zeta\omega_n(t-\tau)} \sin(\omega_d(t-\tau)) d\tau \quad (6.14)$$

where

$$w_R(t) = w(t) - w_B(t) \quad (6.15)$$

and $\ddot{w}_B(t)$ is the acceleration of the base. Equations 6.13 and 6.14 both represent exponentially decaying oscillations, subsequent to the initial disturbance.

6.2.1.3 Logarithmic Decrement Method

The method used in extracting the natural frequency and the viscous damping ratio from the exponentially decaying oscillation of a single degree-of-freedom system is known as the logarithmic decrement method. This method, basically, involves measuring the zero to peak amplitudes w_1 and w_2 of two adjacent decay peaks, as illustrated in Figure 6.1a. The log decrement δ is given by

$$\delta = \ln \left\{ \frac{w_1}{w_2} \right\} = \ln \left\{ \frac{e^{-\zeta\omega_n t_1} \cos(\omega_d t_1 - \phi)}{e^{-\zeta\omega_n (t_1+T)} \cos(\omega_d (t_1+T) - \phi)} \right\} \quad (6.16)$$

where \ln indicates a natural logarithm, t_1 corresponds to the time at peak w_1 and T is the period of the decaying oscillation given by

$$T = \frac{2\pi}{\omega_n \sqrt{1-\zeta^2}} \quad (6.17)$$

The value of the cosine term is the same at time t_1 and time $t_1 + T$, i.e., one period later. Therefore, using the relationship in equation 6.17, equation 6.16 reduces to

$$\begin{aligned} \delta &= \ln \left\{ \frac{e^{-\zeta\omega_n t_1}}{e^{-\zeta\omega_n (t_1+T)}} \right\} = \ln \left\{ \frac{1}{e^{-\zeta\omega_n T}} \right\} \\ &= \zeta\omega_n T = \frac{2\pi\zeta}{\sqrt{1-\zeta^2}} \quad (6.18) \end{aligned}$$

Since ζ , for most structures, is less than 0.2, $\sqrt{1-\zeta^2} \approx 1$. With this approximation, the following relationship is obtained.

$$\zeta \approx \frac{\delta}{2\pi} \quad (6.19)$$

In practice, it is more accurate to measure the amplitude after an elapse of a number of cycles, for example N . If the amplitude after N cycles is w_{N+1} , then

$$\delta = \frac{1}{N} \ln \left\{ \frac{w_1}{w_{N+1}} \right\} \quad (6.20)$$

and the viscous damping ratio is given by

$$\zeta = \frac{1}{2\pi N} \ln \left\{ \frac{w_1}{w_{N+1}} \right\} \quad (6.21)$$

the natural circular frequency ω_n is extracted from equation 6.17 and the viscous damping ratio from equation 6.21.

6.2.1.4 Multimodal Response, Circuit Noise and Filtering Effects

A sharp impulse contains energy over a wide frequency range and will, therefore, excite many resonant modes simultaneously. Even displacing and suddenly releasing the structure will excite more than one mode. Noise will also be present in the measurement circuits, producing a random ripple superimposed on the multimodal decay time history. Filtering is used to isolate the mode of interest and to reduce, to some extent, the level of the noise ripple. The filter must, however, be wide enough so as not to affect the free vibration decay in the selected mode [6.8, 6.9].

The effect of such a filter on the free decay can be illustrated by considering the effect of an ideal rectangular bandpass filter on the impulse response function (equation 6.12) of a single degree-of-freedom system. After passing through such a filter, the resulting impulse response function, $\hat{h}(t_1)$, can be represented by the equation

$$\hat{h}(t_1) = \frac{1}{\pi} \int_{-\infty}^{\infty} h(t) \left\{ \frac{\sin 2\pi f_2(t-t_1) - \sin 2\pi f_1(t-t_1)}{t-t_1} \right\} dt \quad (6.22)$$

where f_2 and f_1 are the bandpass filter upper and lower frequency limits, respectively. The effect of the bandpass filter on the impulse response function is illustrated [6.9] in Figure 6.2, for the following parameters:

$$\begin{aligned} f_n &= 20 \text{ Hz} & f_2 &= 36 \text{ Hz} \\ \zeta &= 0.02 & f_1 &= 25 \text{ Hz} \end{aligned}$$

Leakage, represented by the waveform below $t=0$, has been introduced by the filter. The impulse response function is similarly affected above $t=0$. This leakage effect extends as much into the positive time region as it does into the negative time region. The viscous damping ratio, extracted by the logarithmic decrement method from the positive decay time history in Figure 6.2, beyond the fifth positive peak, could be lower than the actual damping ratio by as much as thirty percent. Widening the filter increases both the noise level and the possibility of multimodal response. A free decay with two modes, such as illustrated in Figure 6.3, cannot be analyzed accurately by the basic logarithmic decrement method.

The quick stop method has an advantage over the impulse excitation method since all of the excitation energy is concentrated at a discrete frequency that is tuned onto the resonant frequency of the mode of interest. Thus one mode at-a-time is excited. Circuit noise can be minimized by the use of bandpass filters subject to the previously discussed limitations. Even with this

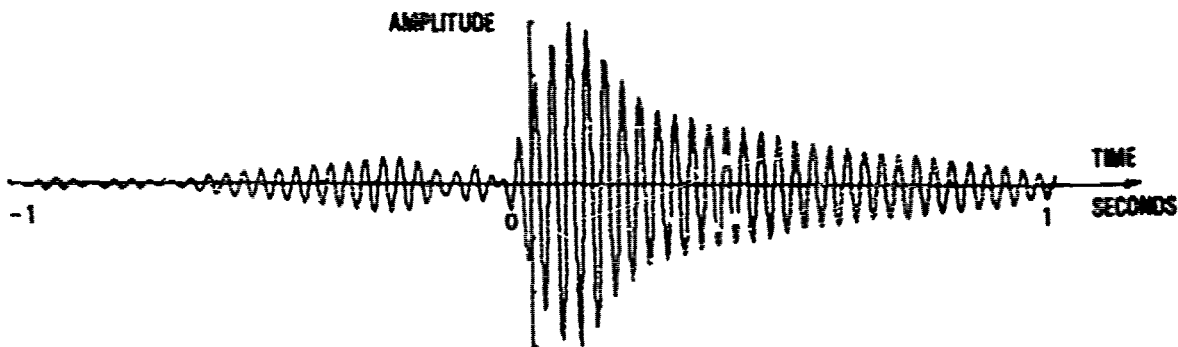


Figure 6.2. Effect of bandpass filter on the impulse response function

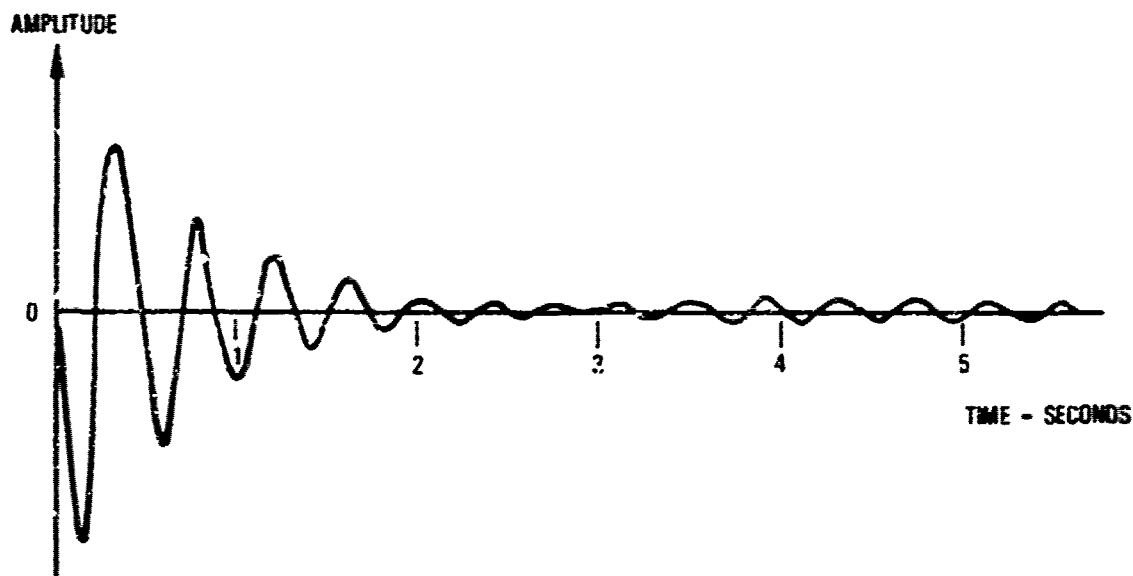


Figure 6.3. Typical aircraft stick pulse excited free decay with beating

form of excitation, the free decay can be contaminated by a contribution from an adjacent close mode.

The effect of circuit noise on the decay time history can also be minimized by the use of a least squares type curve fit [6.10, 6.11] of test data to both single and multimodal free vibration theory. Thus, both of the above problem areas can be overcome. The implementation of these least squares curve fit theories was made possible by the development of analog to digital (A to D) converters over two decades ago, thereby placing the burden of the analysis on the computer.

6.2.2 Frequency Domain Analysis

6.2.2.1 Forced Vibration With Viscous Damping

If the mass of a spring-mass-damper system is excited by a harmonic force $F \cos \omega t$, the equation of motion can be expressed by

$$M\ddot{w}(t) + C\dot{w}(t) + Kw(t) = F \cos \omega t \quad (6.23)$$

where F is the amplitude of the force and ω is the excitation circular frequency. Equation 6.23 can also be expressed in complex form by

$$w(t) = H(i\omega) F e^{i\omega t} \quad (6.24)$$

where

$$H(i\omega) = \frac{1}{M \left(\omega_n^2 - \omega^2 + 2i \zeta \omega \omega_n \right)} \quad (6.25)$$

is known as the frequency response function of the single degree-of-freedom system and i represents the square root of minus one. The resulting displacement to the harmonic force, obtained by taking the real part of equation 6.24, can be expressed by

$$w(t) = w_0 \cos(\omega t - \phi) \quad (6.26)$$

after the start-up transients have decayed, where ϕ is the phase angle. After substituting equation 6.26 into equation 6.23 the resulting zero-to-peak amplitude, w_0 , of the displacement becomes

$$w_0 = \frac{F}{M \left\{ \left(\omega_n^2 - \omega^2 \right)^2 + 4\zeta^2 \omega_n^2 \omega^2 \right\}^{1/2}} \quad (6.27)$$

The phase angle can be obtained from the relationship

$$\tan \phi = \frac{2\zeta \omega_n \omega}{\omega_n^2 - \omega^2} = \frac{2\zeta \left(\frac{\omega}{\omega_n} \right)}{1 - \left(\frac{\omega}{\omega_n} \right)^2} = \frac{2\zeta \left(\frac{f}{f_n} \right)}{1 - \left(\frac{f}{f_n} \right)^2} \quad (6.28)$$

where f and f_n are the frequency and the natural frequency, respectively. The maximum amplification of the vibration is obtained when equation 6.27 is a maximum. This occurs when

$$f_r = f_n \sqrt{1 - 2\zeta^2} \quad (6.29)$$

which is also known as the resonant frequency. For small damping $f_r \approx f_n$.

Since $M \omega_n^2 = K$ is the static stiffness, equation 6.27 can also be expressed by

$$\frac{w_o K}{F} = \frac{1}{\sqrt{\left\{1 - \left(\frac{f}{f_n}\right)^2\right\}^2 + 4\zeta^2 \left(\frac{f}{f_n}\right)^2}} \quad (6.30)$$

which represents the nondimensional amplitude of the vibration or the magnification factor. It has the value of unity at zero excitation frequency ($f=0$). At the resonant frequency, the nondimensional vibration amplitude becomes

$$\frac{w_o K}{F} = \frac{1}{2\zeta \sqrt{1 - \zeta^2}} \approx \frac{1}{2\zeta} = Q \quad (6.31)$$

In the above equation, Q is called the amplification factor or the quality factor. This factor represents the ratio of the dynamic displacement at resonance to the static displacement. Typical magnification factors are illustrated in Figure 6.4 for a viscous damping ratio of 0.125 and for critical damping.

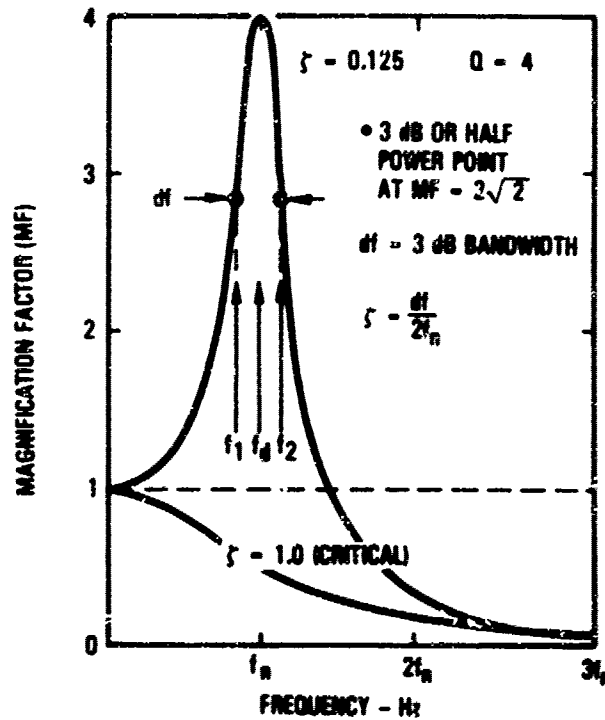


Figure 6.4. Typical magnification factors for single degree-of-freedom system with viscous damping, including the half power points

6.2.2.2 Half Power Point Method

The viscous damping ratio can be calculated from the response curve given by equation 6.27, using the half power point method. The amplitude of the displacement at resonance is given by

$$w_o = \frac{F}{M \omega_n^2} \frac{1}{2\zeta \sqrt{1 - \zeta^2}} = \frac{F}{M \omega_n^2} \frac{1}{2\zeta} \quad (6.32)$$

The amplitude of the displacement at the half power, or three dB (decibel) points is $\sqrt{2}/2$ times the amplitude at resonance. Therefore, when $w_o = \sqrt{2}F / (M \omega_n^2 4\zeta)$ is substituted back into equation 6.27, two frequencies are obtained.

$$f_1 = f_n (1 - \zeta) \quad \text{and} \quad f_2 = f_n (1 + \zeta) \quad (6.33)$$

In equation 6.33, f_1 is the frequency of the lower half power point and f_2 is that of the higher half power point. The frequency bandwidth df at the half power points is

$$df = f_2 - f_1 = 2\zeta f_n \quad (6.34)$$

and the viscous damping ratio is simply

$$\zeta = \frac{f_2 - f_1}{2f_n} \quad (6.35)$$

This procedure for measuring the damping is illustrated in Figure 6.4, with the magnification factor (MF) given by equation 6.30. The method is based on the fact that the area under the curve within the half power point bandwidth is equal to half of the total area under the curve.

The problems with this method are illustrated in Figures 6.5 and 6.6 which depict a single mode response of a Kevlar honeycomb panel to harmonic acoustic excitation and a two-mode aircraft wing response, respectively. The latter figure corresponds to the vibration decay shown in figure 6.3. The "modal response" in Figure 6.5 represents the true single degree-of-freedom response whereas the "total response" is usually obtained experimentally, reflecting the contribution from the other modes. Errors could be obtained in the measured resonant frequency and the damping when the total response curve is used. For reasonably close modes such as those illustrated in Figure 6.6, the half power points cannot be resolved.

6.2.2.3 Forced Vibration With Hysteretic Damping

The equation of motion with hysteretic damping, corresponding to equation 6.23 with viscous damping, is

$$M\ddot{w}(t) + \frac{H}{\omega} \dot{w}(t) + Kw(t) = F \cos \omega t \quad (6.36)$$

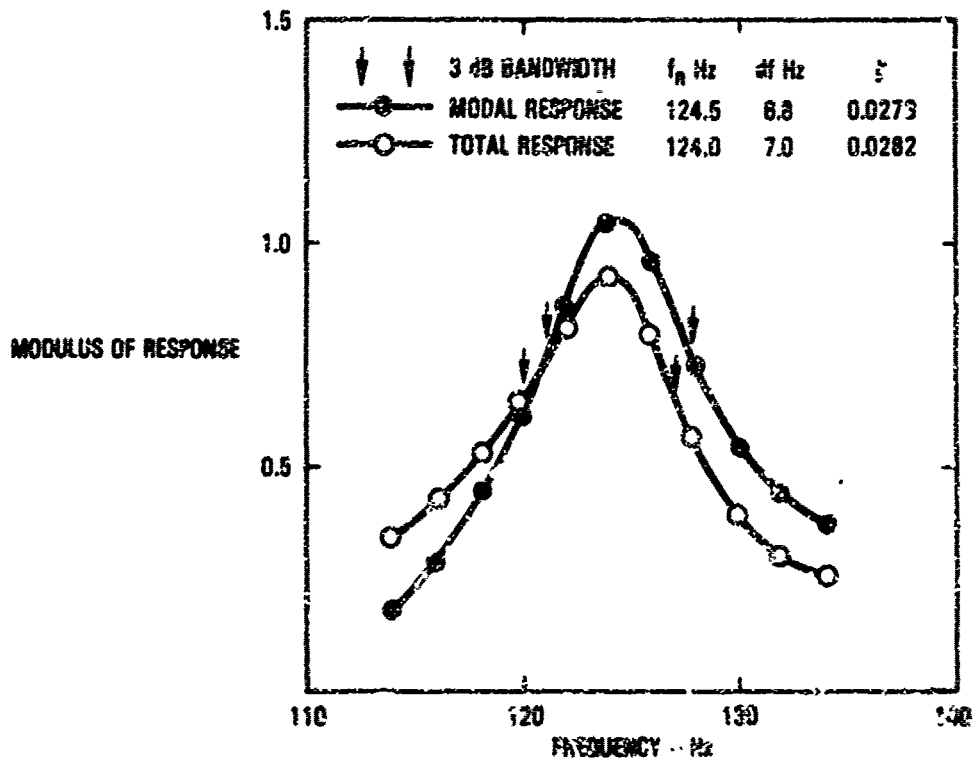


Figure 6.5. Modulus of a stiffened Kevlar honeycomb panel vibration response to discrete frequency acoustic excitation

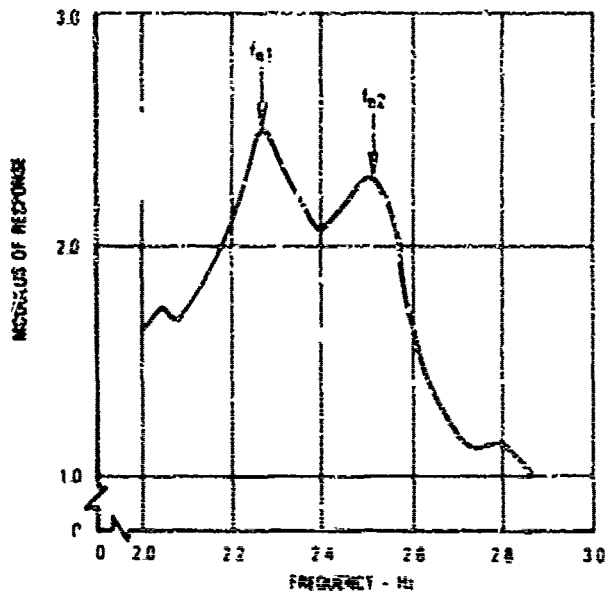


Figure 6.6. Modulus of a typical aircraft vibration response corresponding to the free decay in Figure 6.3

where $\bar{\eta}/\omega$ is the hysteretic damping coefficient. The displacement can again be expressed by equation 6.26, but with the zero-to-peak amplitude given by

$$w_0 = \frac{F}{M \left\{ \left(\omega_n^2 - \omega^2 \right)^2 + \frac{4}{\bar{\eta}^2} \omega^4 \right\}^{1/2}} \quad (6.37)$$

and the phase angle by

$$\tan \phi = \frac{\eta \omega_n^2}{\omega_n^2 - \omega^2} = \frac{\eta}{1 - \left(\frac{f}{f_n} \right)^2} \quad (6.38)$$

where η is the loss factor or structural damping defined by

$$\eta = \frac{\bar{H}}{K} \quad (6.39)$$

The phase angle remains finite at zero frequency with hysteretic damping but is zero with viscous damping (equation 6.27). Equation 6.36 can also be expressed in complex form by equation 6.24, but $H(i\omega)$ is now given by

$$H(i\omega) = \frac{1}{M \left(\omega_n^2 - \omega^2 + i\eta \omega_n^2 \right)} \quad (6.40)$$

The half power point method can also be used with hysteretic damping. In this instance, the loss factor is

$$\eta = \frac{f_2 - f_1}{f_n} = \frac{df}{f_n} \quad (6.41)$$

Also,

$$Q = \frac{1}{\eta} \quad (6.42)$$

6.2.2.4 The Kennedy-Rancu Method

The derivation of this method is based on the assumption of hysteretic damping. On using the complex form of the equation of motion, determined by combining equations 6.24 and 6.40, the complex displacement can be expressed by

$$w(t) = \frac{F e^{i(\omega t - \psi)}}{M \left\{ \left(\omega_n^2 - \omega^2 \right)^2 + \eta^2 \omega_n^4 \right\}^{1/2}} = \left\{ R(\omega) + iI(\omega) \right\} e^{i\omega t} \quad (6.43)$$

where

$$R(\omega) = \frac{F \left(\omega_n^2 - \omega^2 \right)}{M \left\{ \left(\omega_n^2 - \omega^2 \right)^2 + \eta^2 \omega_n^4 \right\}} \quad (6.44)$$

and

$$I(\omega) = - \frac{F \eta \omega_n^2}{M \left\{ \left(\omega_n^2 - \omega^2 \right)^2 + \eta^2 \omega_n^4 \right\}} \quad (6.45)$$

represent the real and imaginary parts of the displacement. Now

$$R(\omega)^2 + I(\omega)^2 = \frac{F^2}{M^2 \left\{ \left(\omega_n^2 - \omega^2 \right)^2 + \eta^2 \omega_n^4 \right\}} = - \frac{I(\omega) F}{M \eta \omega_n^2} \quad (6.46)$$

or

$$R(\omega)^2 + \left\{ I(\omega) + \frac{F}{2M\eta \omega_n^2} \right\}^2 = \frac{F^2}{4M^2 \eta^2 \omega_n^4} \quad (6.47)$$

Equation 6.47 represents an equation of a circle, centered at $(0, -F/2M\eta \omega_n^2)$ on the complex plane with a diameter equal to $F/(M\eta \omega_n^2)$. This diameter is the modal diameter which is equal to the zero-to-peak amplitude at resonance.

The resonant frequency is located where the above circle intersects the complex axis, away from the origin. Another more practical method for establishing the resonant frequency, that also works well with multimodal response, is to determine where the rate of change of arc length, s , along the circumference with respect to the frequency (or frequency squared), is a maximum. This condition is represented by the following equation

$$\frac{ds}{d(\omega^2)} = \frac{1}{M \left\{ \left(\omega_n^2 - \omega^2 \right)^2 + \eta^2 \omega_n^4 \right\}} \quad (6.48)$$

which has a maximum at the resonant frequency, where $\omega = \omega_n$.

The damping can be obtained from the half power points, which for a single degree-of-freedom system, coincide with the maximum and minimum values, respectively, of $R(\omega)$, the real part of the complex displacement given by equation 6.44. In practice the full circle is not always obtained. Consequently, it is more practical to measure the angle ϕ subtended at the modal origin A by the arc of the circle between the resonant frequency, f_n , and another frequency, f , on either side of the resonant frequency. The loss factor is defined by

$$\eta = \frac{2(f_n - f)}{f_n} \cot \phi \quad f < f_n \quad (6.49a)$$

or

$$\zeta = \frac{2(f - f_n)}{f_n} \cot \theta \quad f > f_n \quad (6.49b)$$

At the half power points $\theta = 45^\circ$.

The above theory is also valid for viscous damping. Because of the relationship in equation 6.29, the maximum response is obtained just before the circle crosses the imaginary axis. The viscous damping ratio is extracted from the circular vector loop by means of the following relationships:

$$\zeta = \frac{f_n - f}{f_n} \cot \theta \quad f < f_n \quad (6.50a)$$

and

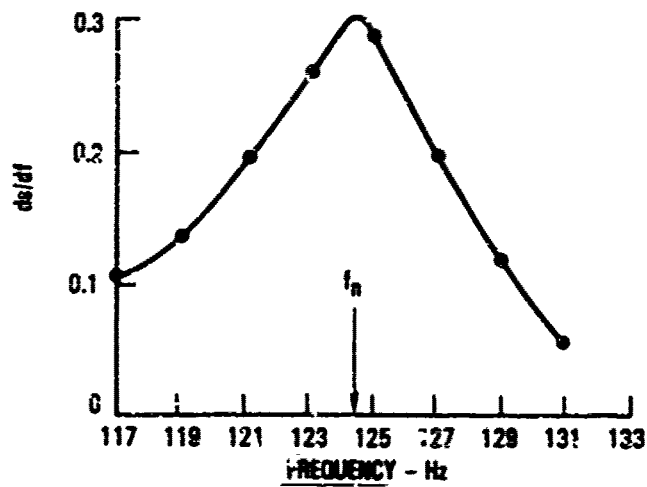
$$\zeta = \frac{f - f_n}{f_n} \cot \theta \quad f > f_n \quad (6.50b)$$

and the resonant frequency by the location on the circle where ds/df is a maximum, the same as before.

6.2.2.5 Application of the Kennedy-Pancu Method

A resolved components indicator is usually used with the K-P method to measure the inphase and out-of-phase vibration response, at discrete frequency increments, relative to the constant level harmonic force. The resulting modal circles, obtained from these data when plotted on the complex plane, are called vector loops.

Typical results obtained with the K-P method are illustrated in Figure 6.7. They represent the measured vibration response, in the fundamental



(a) RATE OF CHANGE OF ARC LENGTH WITH FREQUENCY

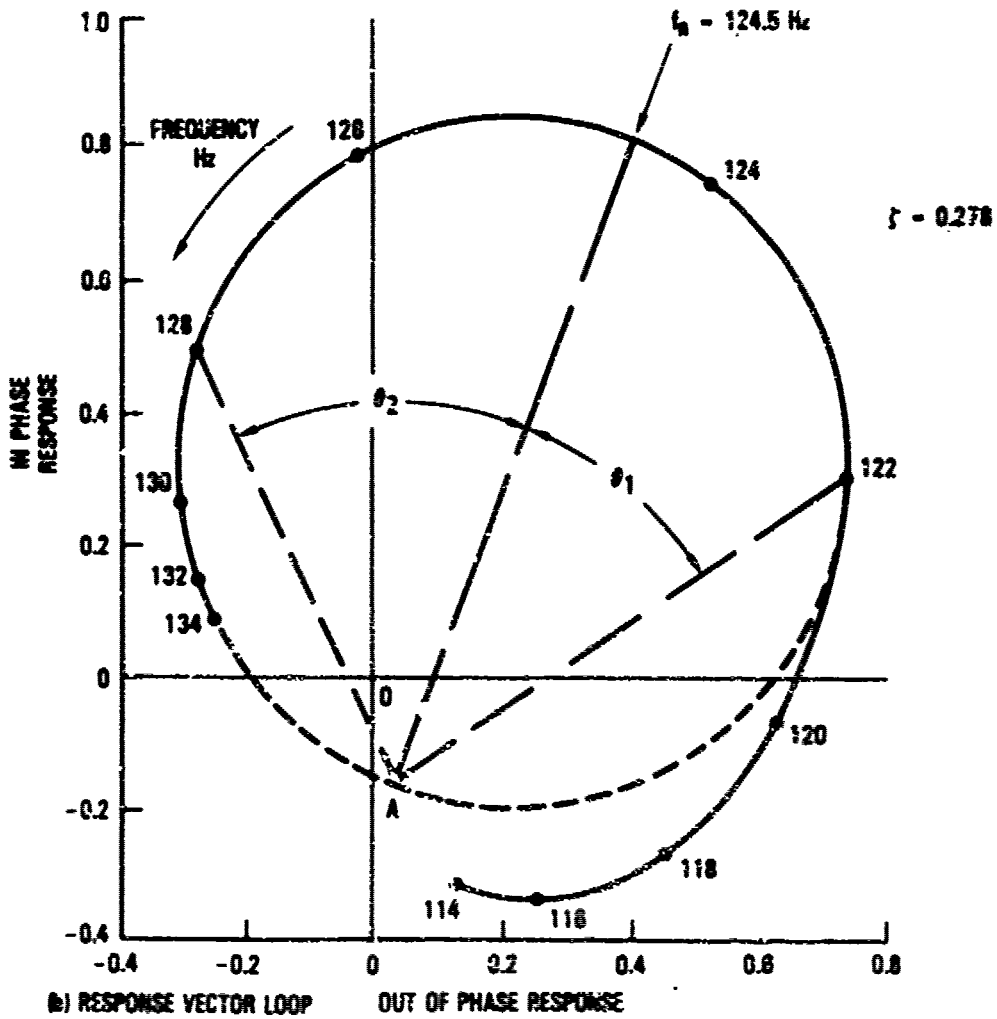


Figure 6.7. Vibration response of a stiffened Kevlar honeycomb panel to discrete frequency acoustic excitation

mode of a stiffened Kevlar honeycomb panel, due to discrete frequency acoustic excitation. The modulus of this vibration response is illustrated in Figure 6.5. The resonant frequency of 124.5 Hz was established in Figure 6.7a, by measuring ds/df along the vector loop in Figure 6.7b. The viscous damping ratio was computed (Table 6.1) by taking the average of two damping ratios calculated with angles θ_1 and θ_2 on either side of the resonance, as illustrated in Figure 6.7b. The difference in the measured damping values indicates that the resonant frequency may not have been physically located at its correct position on the vector loop, the main reason for selecting an angle on both sides of the resonant frequency.

The origin of the modal response is located at point A in Figure 6.7b. The distance OA represents the contribution from the other modes. The total response is measured relative to the origin O. The two curves in Figure 6.5 were obtained by taking the modulus of the response, first relative to the origin at O (the total response), and then relative to A (the modal response). The mode shapes are obtained by measuring the modal diameter at different locations on the structure, taking account of the phase. Except close to nodal lines, all the modal vectors at resonance are either in phase or 180 degrees out-of-phase.

TABLE 6.1. CALCULATION OF THE VISCOUS DAMPING RATIO USING THE K-P METHOD

f_n	f	$ f - f_n $	θ°	$\text{Cot } \theta$	ζ
124.5	122	2.5	35.15	1.42	0.0285
124.5	128	3.5	46.08	0.963	<u>0.0271</u>
					$\zeta_{\text{AVE}} = 0.0278$

The K-P method can also be used to extract the resonant frequencies and damping values for multimodal response such as illustrated in Figure 6.8. These multimodal vector loops were obtained by taking the Fourier Transform of the stick pulse excited decay in Figure 6.3. The difference between the modal and total response is illustrated more clearly in this figure. The damping for both modes can still be extracted from these vector loops by means of equations 6.45 or 6.46, but not from the modulus of these vector loops, illustrated in Figure 6.6. Modes that have closer resonant frequencies than those shown in Figure 6.8 may not be resolved by the basic K-P method.

The accuracy of the K-P method is degraded by the presence of both noise in the measurement circuit and distortion in the excitation waveform. The resolved components indicator has some noise rejection capability on account of the averaging time used in the instrument. In most instances, filtering is also required, subject to the limitations discussed in Section 6.2.1.4. A high as possible signal-to-noise ratio should be used if accurate damping measurements are to be obtained.

The main disadvantages of the basic K-P method are that it is very time consuming to apply and very tedious to analyze by hand if many modes are present, especially when measuring mode shapes since many measurement locations are involved. The results are also subject to human error, especially if the vector loops are distorted by spurious noise. These problem areas stimulated the development of curve fitting algorithms [6.12, 6.13, 6.14] which can extract the modal parameters interactively while minimizing the effects of measurement circuit noise and the presence of random noise (or distortion) in the excitation signal [6.15]. This latter effect produces the greatest scatter in the test data at the resonance peak, as illustrated in Figure 6.9c.

6.3 DEVELOPMENT OF THE BASIC METHODS

The need for reducing test time has resulted in the development of alternate shorter duration methods for exciting structures. These include the broad band random excitation [6.16], the rapid sine sweep excitation [6.17] and the impedance head hammer tap excitations [6.14]. The random excitation has

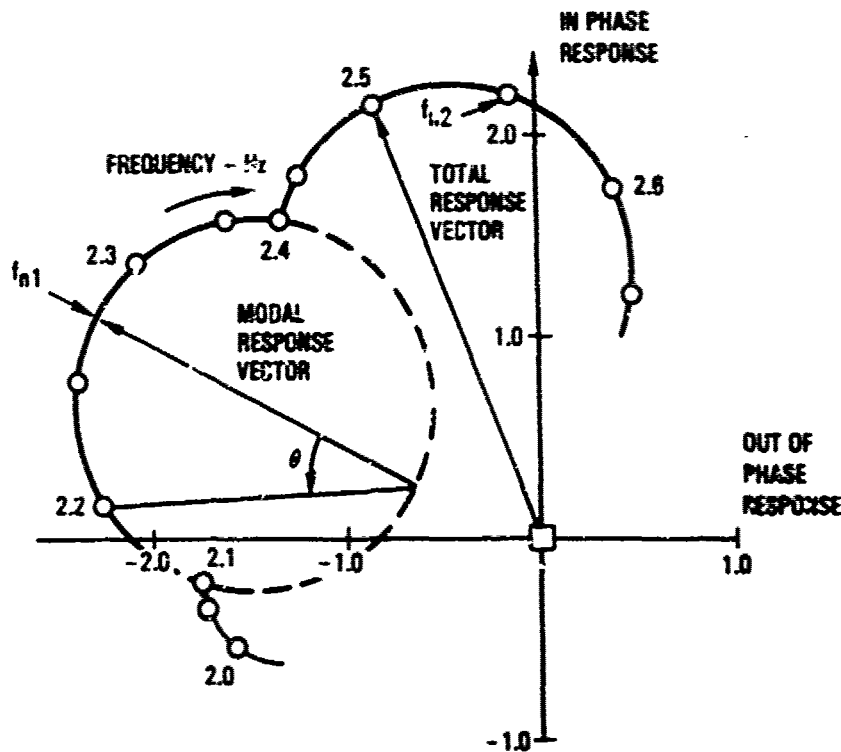
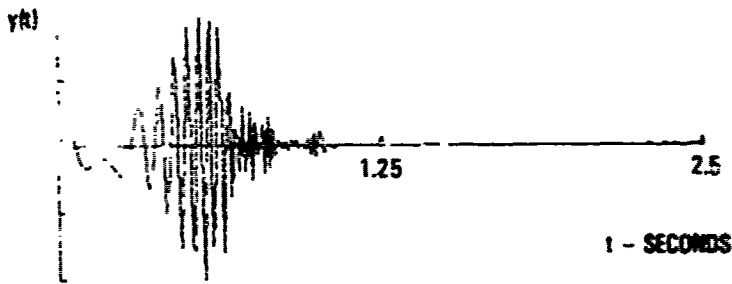
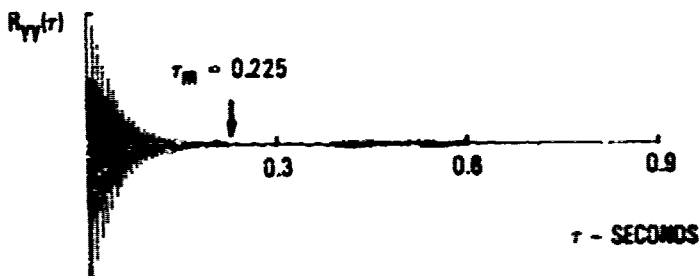


Figure 6.8. Frequency domain representation of the stick pulse excited decay in Figure 6.3

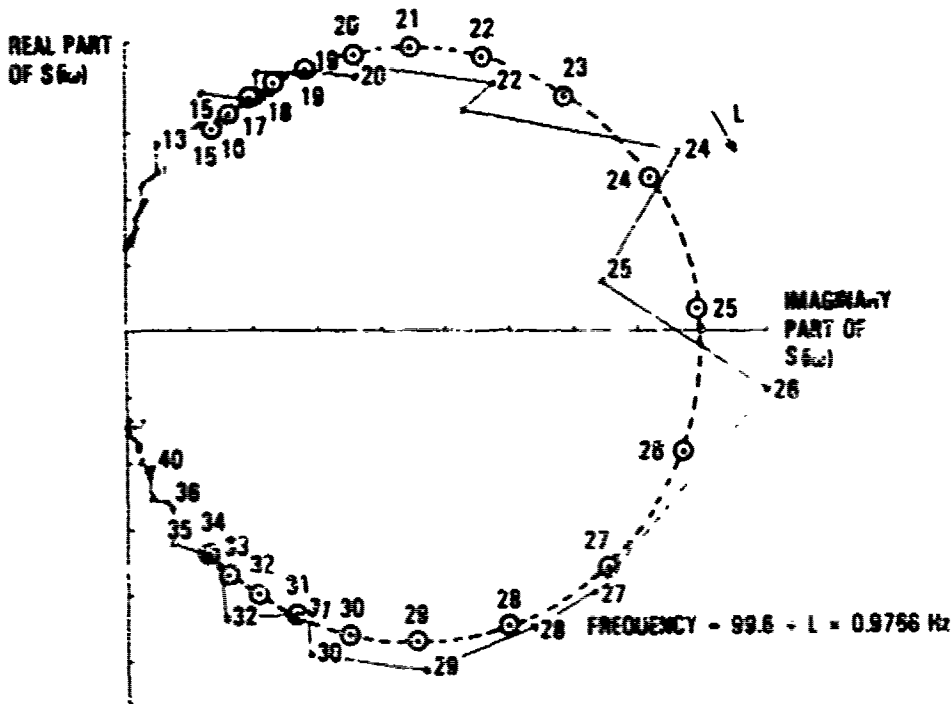
been around for a long time but was time consuming to apply since the cross correlation function had to be determined experimentally, before the cross spectral density could be obtained by means of the Fourier Transform [6.18]. With the advent of the Fast Fourier Transform (FFT) [6.19, 6.20], the auto and cross spectral densities could be calculated directly and in a much shorter time than before. The FFT and the recent advances in computer technology, have revolutionized modal testing by placing the burden of data reduction on the computer while simultaneously permitting an increase in the amount of data being processed. Methods of extracting the modal frequencies and the damping have also increased in number due to the increase in the computational capability. Some of these methods are reviewed briefly in the following section.



(a) RESPONSE TO RAPID SINE SWEEP



(b) AUTO CORRELATION FUNCTION OF THE RESPONSE



(c) FREQUENCY RESPONSE FUNCTION

Figure 6.9. Curve fit to the vibration response of a stiffened Kevlar honeycomb panel due to rapid sine sweep acoustic excitation

6.3.1 Structural Response to Random Excitation

6.3.1.1 Fourier Transform Based Analysis

The autocorrelation function $R_{yy}(\tau)$ of the response $y(t)$ of a single degree-of-freedom system excited by broad band random force $x(t)$ is given by [6.16, 6.18, 6.21]

$$R_{yy}(\tau) = \lim_{T \rightarrow \infty} \frac{1}{2T} \int_{-T}^T y(t) y(t+\tau) dt$$

$$= \frac{\pi S_{xx} e^{-\zeta \omega_n \tau}}{2M^2 \omega_n^3 \zeta} \left(\cos \omega_d \tau + \frac{\zeta}{\sqrt{1-\zeta^2}} \sin \omega_d \tau \right) \quad (6.51)$$

where S_{xx} is the constant power spectral density of the excitation. The displacement $y(t)$, which is the same as the displacement $w(t)$ in the previous section, is used here for convenience. The power spectral density $S_{yy}(\omega)$ of the displacement is given by the Fourier Transform of the correlation function. Therefore

$$S_{yy}(\omega) = \frac{1}{2\pi} \int_{-\infty}^{\infty} R_{yy}(\tau) e^{-i\omega\tau} d\tau$$

$$= \frac{S_{xx}}{M^2 \left\{ \left(\omega_n^2 - \omega^2 \right)^2 + 4\zeta^2 \omega_n^2 \omega^2 \right\}} = |H(i\omega)|^2 S_{xx} \quad (6.52)$$

where $|H(i\omega)|$ is the modulus of equation 6.25. The cross correlation function between the random force $x(t)$ and the corresponding response $y(t)$ of a single degree-of-freedom system is given by [6.16, 6.21]

$$\begin{aligned}
R_{xy}(\tau) &= \lim_{T \rightarrow \infty} \frac{1}{T} \int_0^T x(t) y(t+\tau) dt \\
&= \frac{2\pi S_{xx}}{M\omega_d} e^{-\omega_n \zeta \tau} \sin \omega_d \tau \quad \text{for } \tau > 0 \\
&= 0 \quad \text{elsewhere} \quad (6.53)
\end{aligned}$$

and the cross spectral density $S_{xy}(\omega)$ by

$$\begin{aligned}
S_{xy}(\omega) &= \frac{1}{2\pi} \int_{-\infty}^{\infty} R_{xy}(\tau) e^{-i\omega\tau} d\tau \\
&= H(i\omega) S_{xx} \quad (6.54)
\end{aligned}$$

The above spectra are double-sided spectra in which half of the energy is contained in the negative frequencies. Single-sided, positive-frequency cross and power spectral densities, denoted by $G_{xy}(\omega)$ and $G_{yy}(\omega)$, respectively, are used in practice. These single-sided spectra are related to the corresponding double-sided spectra by

$$G_{xy}(\omega) = 2 S_{xy}(\omega) \quad (6.55)$$

$$G_{yy}(\omega) = 2 S_{yy}(\omega) \quad (6.56)$$

Also, the above spectra can be expressed in terms of the frequency, f , as opposed to the circular frequency, ω , by

$$G_{xy}(f) = 2\pi G_{xy}(\omega) \quad (6.57)$$

$$G_{yy}(f) = 2\pi G_{yy}(\omega)$$

On examining the above equations, it is seen that equations 6.51 and 6.53 are very similar to equations 6.8 and 6.12, respectively, except for multiplication by different constant terms. Thus, the free decay analysis procedures can be used to extract modal parameters from these equations. Similarly, equation 6.52 corresponds to the square of equation 6.27, enabling the damping to be extracted by the half power point method, while equation 6.54 corresponds to equation 6.24, enabling damping to be extracted by the K-P analysis.

The measurement of the cross and power spectral densities usually requires a long record length in order to achieve the required statistical accuracy. The percentage error in measuring the power spectral density with a confidence level of 90 percent is given [6.16] in Table 6.2 as a function of the statistical degrees-of-freedom, k . The relationships used in the Blackman and Tuckey (B-T) analysis for establishing the power spectral density analysis parameters, including the definition of the statistical degrees-of-freedom, are summarized in Table 6.3. The error in the power spectral density is a function of the analysis bandwidth, Δf , and the record length, T ($=N\Delta t$).

TABLE 6.2. ERROR IN MEASURING PSD FOR 90% CONFIDENCE LIMITS AS A FUNCTION OF THE STATISTICAL DEGREES-OF-FREEDOM

Statistical Degrees-of-Freedom, k	\pm Percent Error in PSD
10	65
20	48
30	40
40	35
50	32
100	23
200	16
400	11
1000	7

TABLE 6.3. BLACKMAN AND TUCKEY ANALYSIS PARAMETERS FOR DETERMINING POWER SPECTRAL DENSITY (PSD)

N = total number of samples in record

\hat{T} = record length (seconds)

Δt = time spacing of samples (seconds)

Δf = frequency resolution in PSD (Hz)

f_m = highest frequency in PSD or half of the Nyquist frequency (Hz)

τ_m = maximum correlation time delay (seconds)

m = maximum number of time delays

k = number of statistical degrees-of-freedom

$$\text{Sampling rate} = 2f_m$$

$$\text{Record length} = N\Delta t$$

$$f_m = \frac{1}{2\Delta t} \quad \text{or} \quad \Delta t = \frac{1}{2f_m}$$

$$\Delta f = \frac{f_m}{m} = \frac{1}{2m\Delta t} = \frac{1}{2\tau_m}$$

$$m = \frac{\tau_m}{\Delta t} = \frac{f_m}{\Delta f} = \frac{1}{2\Delta f\Delta t} \approx 0.1 N$$

$$k = \frac{2N}{M} = \frac{2(N\Delta t)}{m} = 2 \frac{\text{Record length}}{\text{Max time delay}}$$

The smaller the analysis bandwidth the greater the error, or the greater the record length for the same error [6.22]. This relationship is usually expressed in the form

$$\Delta f \hat{T} \approx \frac{1}{\epsilon^2} \quad (6.59)$$

where the record length and analysis bandwidth are measured in seconds and Hertz, respectively, and ϵ is the plus or minus fractional error in the power spectral density, which corresponds closely with the error in Table 6.2. On using the relationships in Table 6.3, and equation 6.59, it follows that

$$\Delta f \hat{T} = \Delta f N \Delta t = \frac{N \Delta t}{2\tau_m} = \frac{k}{4} \approx \frac{1}{\epsilon^2} \quad (6.60)$$

A value for $\Delta f \hat{T}$ of around 100 is typically used in power spectral density analysis. This value represents 400 statistical degrees-of-freedom corresponding to an error of ten to eleven percent at the ninety percent confidence level. Even at this level of accuracy, a visible error, in the form of a random ripple superimposed on the true power spectral density, is obtained which may degrade the accuracy of any damping measurement. The above analysis parameters are essentially the same for cross spectral analysis, except that two channels of data, one for the force and the other for the response, need to be recorded simultaneously.

It is necessary, when extracting damping data, to use an analysis bandwidth that is sufficiently small to resolve the 3 dB points in the power spectral density analysis or to provide the necessary number of frequency points for establishing the vector loops in the cross spectral analysis. The criteria for measuring the damping with sufficient accuracy is given by [6.17].

$$f_n \tau_m \zeta \geq 1 \quad (6.61)$$

where f_n , ζ , and τ_m are the natural frequency, the viscous damping ratio and the maximum correlation time delay, respectively. This relationship corresponds to the requirement [6.23] in spectral analysis that the analysis bandwidth, Δf , has to be equal to or less than a quarter of the 3 dB bandwidth, df . Therefore

$$\Delta f \leq \frac{df}{4} \quad (6.62)$$

Equation 6.61 also translates into a requirement for the dynamic range to be equal to or greater than 55 dB when determining the auto and cross correlation functions.

6.3.1.2 The Fast Fourier Transform Analysis

The cross spectral density can also be obtained, by means of the FFT, based on the following equation [6.20, 6.22, 6.24]

$$S_{xy}(\omega) = \lim_{T \rightarrow \infty} \frac{1}{K} \sum_{j=1}^K \frac{2\pi}{T} x_j^*(i\omega, T) y_j(i\omega, T) \quad (6.63)$$

where $x_j^*(i\omega, T)$ and $y_j(i\omega, T)$ represent the j th Fourier spectra of the force $x_j(t)$ and the response $y_j(t)$, respectively, measured over the same time segment j , each duration T ; the asterisk denotes a complex conjugate; and the summation is taken over K spectra in order to obtain convergence [6.24]. The Fourier spectra $x_j(i\omega, T)$ and $y_j(i\omega, T)$ are calculated first by means of the FFT using the relationships

$$x_j(i\omega, T) = \frac{1}{2\pi} \int_0^T x_j(t) e^{-i\omega t} dt \quad (6.64)$$

$$y_j(i\omega, T) = \frac{1}{2\pi} \int_0^T y_j(t) e^{-i\omega t} dt \quad (6.65)$$

for each successive segment of data, the complex conjugate is then taken of the force spectrum and the resulting spectra substituted back into equation 6.63.

The cross correlation function is obtained by taking the inverse Fourier transform of equation 6.63, that is

$$R_{xy}(\tau) = \int_{-\infty}^{\infty} S_{xy}(\omega) e^{i\omega\tau} d\omega \quad (6.66)$$

However some prior manipulation of the data is required [6.19] before the cross correlation function can be obtained from equation 6.66 by means of the FFT analysis. Filtering errors such as discussed in Section 6.2.1.4 may also be possible when taking the inverse FFT.

The power spectral density and the auto correlation function are obtained in the same way as the cross spectral density and the cross correlation function, except that the force $x_j(t)$ and the subscript x in equations 6.63 and 6.66 are now replaced by the response $y_j(t)$ and the subscript y , respectively.

The relationships used in establishing the analysis parameters for the FFT based spectral analysis are summarized in Table 6.4. Since the statistical degrees-of-freedom, k , are approximately equal to four times the number of ensemble averages, K , in the FFT analysis, 100 ensemble averages are required to achieve the same statistical accuracy as given by equation 6.59 for an error of 10 to 11 percent, for the same total record length ($\hat{T} = KL\Delta t$). The number of frequency points in the single sided FFT spectra is equal to $L/2$, not counting the zero frequency point. For accurate measurement of the damping, the requirement in equation 6.62 must also be met by

TABLE 6.4. FFT ANALYSIS PARAMETERS FOR DETERMINING
POWER SPECTRAL DENSITY (PSD)

N = total number of samples in total record

T = duration of data block (seconds)

L = number of samples in data block (256, 512, 1024, 2048, 2^n)

Δt = time spacing of samples (seconds)

Δf = frequency resolution in PSD (Hz)

f_m = highest frequency in PSD (Hz)

K = number of ensemble averages

τ_m = maximum correlation time delay

k = number of statistical degrees-of-freedom

$$\text{Sampling rate} = 2f_m$$

$$\text{Record length} = N\Delta t = K L\Delta t$$

$$K = N/L$$

$$\tau_m = \frac{L \Delta t}{2} \text{ (one half of a data block)}$$

$$\Delta f = \frac{2f_m}{L} = \frac{1}{2\tau_m}$$

$$k = 2 \left(\frac{2|N|}{L} - 1 \right) = 2 (2K-1)$$

the FFT spectral analysis. The basis relationship between the B-T and the FFT analyses is

$$\Delta f = \frac{1}{2\tau_m} \quad (6.67)$$

where Δf is the FFT analysis bandwidth in Hertz and τ_m is the correlation function maximum time delay in seconds, in the B-T analysis.

6.3.1.3 The Band Selectable Fourier Analysis

The band selectable Fourier analysis (BSFA) [6.25], also known as the zcom algorithm, provides a means of increasing the frequency resolution of both the cross and the power spectral densities, and therefore, of meeting the resolution requirements of equation 6.62. This method concentrates the $L/2$ frequency points over a limited frequency band, resulting in a much higher frequency resolution, $\Delta'f$. The number of ensemble averages, K , must be increased to K' where

$$K' = K \Delta f / \Delta'f \quad (6.68)$$

to maintain the same statistical accuracy. Thus the increased resolution is obtained at the expense of increased analysis time.

6.3.1.4 Single-Sided Fourier Transform of the Autocorrelation Function

If the single-sided Fourier transform is taken of the autocorrelation function of the response, $R_{yy}(\tau)$, with limits of integration from zero to infinity, phase information is retained in the response spectrum [6.46]. The resulting response spectrum $S(i\omega)$ is given by

$$S(i\omega) = \frac{S_{xx}}{4M_a^2 n^2 \zeta} \left(\frac{i\omega}{\omega_n} H(i\omega) + 2\zeta H(i\omega) \right) \quad (6.69)$$

The characteristic response function $S(i\omega)/S_{xx}$ has properties similar to the frequency response function $H(i\omega)$ around the resonant frequency. This method

was originally developed for use with rapid sine sweep testing since the autocorrelation function of the impulse response function is the same as the autocorrelation function of a single degree-of-freedom system in equation 6.51 [6.26]. Therefore, this method is also applicable to the autocorrelation function obtained with random excitation. It is a powerful method for extracting modal parameters by means of the K-P analysis (Figure 6.9), without the need for measuring the excitation. The excitation spectrum level has to be reasonably constant in the vicinity of the modal response peaks to obtain accurate damping data. The method can, for example, be used to measure the structural response to turbulent boundary layer [6.27] without having to measure the turbulent boundary layer power spectral density.

6.3.1.5 Exponential Weighting of the Correlation Functions

Weighting of the autocorrelation and cross correlation functions, with a known exponential weighting function [6.28], before taking the Fourier transform, provides a means of improving the quality of the measured damping data by, essentially, increasing the dynamic range. If, for example, the cross correlation function in equation 6.53 is multiplied by an exponential function $e^{-\omega_n \zeta_1 \tau}$, it becomes

$$R_{xy}(\tau) = \frac{2\pi S_{xx}}{M \omega_d} e^{-\omega_n (\zeta + \zeta_1) \tau} \sin \omega_d \tau \quad (6.70)$$

The damping has, in effect, been increased from ζ to $\zeta + \zeta_1$. The added damping ζ_1 can be subtracted from the total damping $\zeta + \zeta_1$ to obtain the actual damping ζ , after the total damping is extracted from the cross spectral density by the K-P analysis. The limitation of this method is that the actual damping must be significantly greater than the error in the measured total damping. Also, the vector loops of close modes tend to coalesce if the total damping is made too large.

6.3.6 The Laplace Transform

The Laplace transform has some distinct advantages over the Fourier transform in determining dynamic response of structures. For example, the Laplace transform of the cross correlation function between the response at two points on a structure, due to a force applied at another location, produces the frequency response function of the structure multiplied by the mode shape function [6.29]. Phase information is retained between the two points on the structure which enable mode shapes to be identified, in addition to obtaining the resonant frequencies and damping ratios from the frequency response function. The Laplace transform of the differential equations of motion for a multi-degree of freedom system has formed the basis for the development of a digital modal analysis test system [6.14, 6.30, 6.31] for structures.

The basic characteristics of the Laplace transform used in studying structural response [6.30] can be illustrated by considering the equation of motion for a single degree-of-freedom system given by

$$M\ddot{y}(t) + C\dot{y}(t) + Ky(t) = x(t) \quad (6.71)$$

where $y(t)$ is the response of the system to a random (or transient) force $x(t)$ and M , C and K are the mass, damping coefficient and stiffness, respectively, of the system. With all initial conditions assumed to be zero, the Laplace transform representation of equation 6.71 is

$$B(s) y(s) = x(s) \quad (6.72)$$

where

$$B(s) = Ms^2 + Cs + K \quad (6.73)$$

and s is the complex Laplace variable, while $y(s)$ and $x(s)$ are the Laplace transforms of $y(t)$ and $x(t)$, respectively. Alternatively,

$$y(s) = H(s) x(s) \quad (6.74)$$

where $H(s)$ is the transfer function given by

$$H(s) = \frac{1/M}{s^2 + \frac{C}{M}s + \frac{K}{M}} \quad (6.75)$$

The transfer function can also be expressed in the following form

$$H(s) = \frac{a}{s-p} + \frac{a^*}{s-p^*} \quad (6.76)$$

where

$$p = -c + i\bar{}$$

$$a = \frac{-i}{2\omega_n (1-\zeta^2)^{1/2}} \quad (6.77)$$

$$\bar{c} = \zeta \omega_n$$

$$\bar{a} = \frac{i}{\omega_n (1-\zeta^2)^{1/2}} = \bar{a}_d$$

and, ω_n and ζ are the natural circular frequency and viscous damping ratio, respectively. The asterisk denotes a complex conjugate. The term, a , represents a complex residue and p is the root or the pole of the transfer function. When the single degree-of-freedom system is subcritically damped, the poles are complex numbers and occur in complex conjugate pairs. A pair of

such poles is illustrated [6.30] in Figure 6.10, occurring at $s = -1 \pm i5$. The Fourier transform is a special case of the Laplace transform as illustrated in Figure 6.10. The inverse Laplace transform of the transfer function (equation 6.76) produces the impulse response function of the single degree-of-freedom system.

The natural frequency and the viscous damping ratio are obtained from

$$f_n = \frac{1}{2\pi} \left\{ \sigma^2 + (\bar{\omega})^2 \right\}^{1/2} \quad (6.78)$$

and

$$\zeta = \frac{\sigma}{\bar{\omega}} \quad (6.79)$$

respectively.

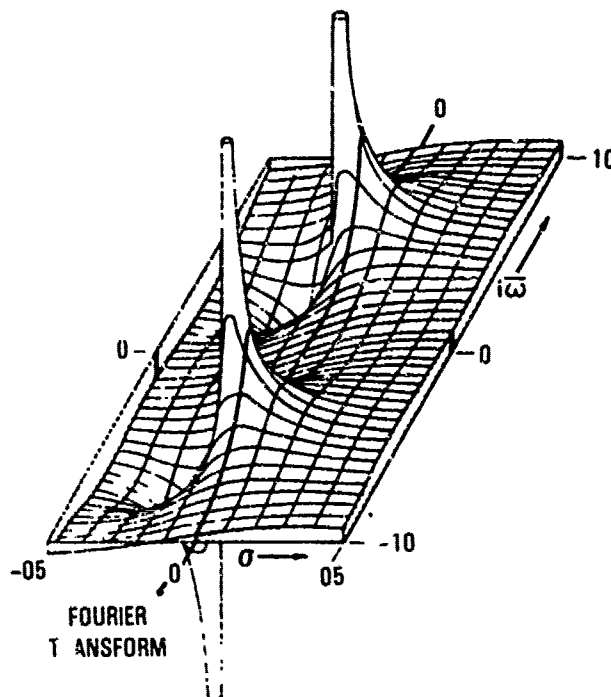


Figure 6.10. Real part of a transfer function with poles at $s = -1 \pm i5$

In the case of multimodal response, equation 6.71 is replaced by a matrix equation. The transfer matrix $[H(s)]$ is obtained [6.30] by inverting the system matrix $[B(s)]$. Therefore, an n-dimensional system,

$$[H(s)] = \begin{bmatrix} h_{11}(s) & \dots & h_{1n}(s) \\ \cdot & & \cdot \\ \cdot & h_{ij}(s) & \cdot \\ \cdot & & \cdot \\ h_{n1}(s) & \dots & h_{nn}(s) \end{bmatrix} \quad (6.80)$$

where $h_{ij}(s)$ is the i,j th complex transfer function of the system. The above transfer matrix contains all of the information necessary to completely specify the dynamic response of the structure [6.30]. Furthermore, the mass, the stiffness and the damping matrices can be recovered once the transfer matrix has been determined. The structural response obtained by this means can be presented in the form of vector loops that have been enhanced by means of a curve fitting algorithm to minimize signal to noise errors. The resolution requirements for accurate damping measurements are the same as those given by equation 6.62.

6.3.1.7 The Random Decrement Method

The random decrement or randomdec method [6.32, 6.33] provides another means of extracting modal data from the time history of the response. It basically involves obtaining a digitized time history of the response, such as illustrated in Figure 6.11, to random excitation. A free vibration decay type randomdec signature is obtained by first shifting or shifting and inverting the time history in the manner illustrated in Figures 11a and b, respectively. This results in a number of ensembles that are then averaged. The frequency and damping data are extracted by the log decrement method or by means of the least squares curve fit method for a one mode, two mode [6.34] or multimodal response, using one measurement location at-a-time. Noise rejection is obtained through ensemble averaging. Generally a large number of

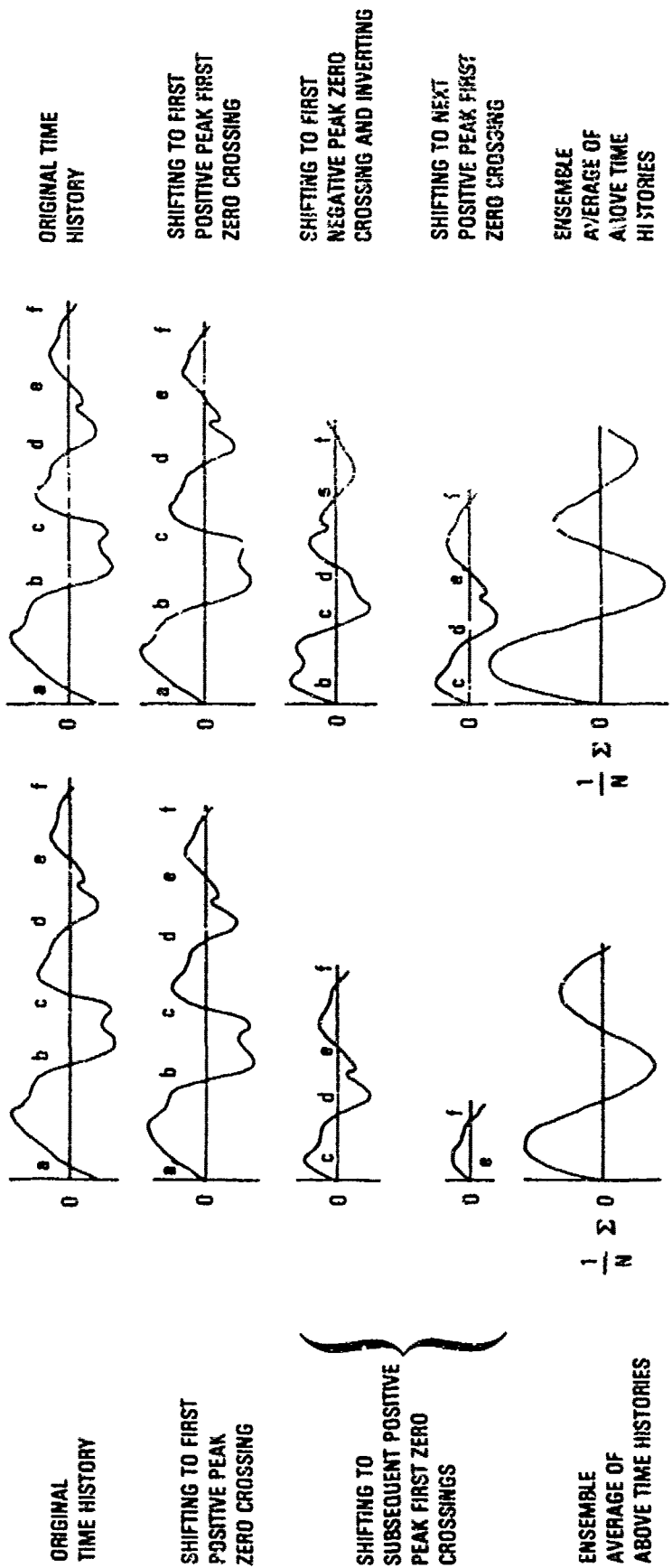


Figure 6.11. Randomdec signature analysis procedures

ensemble averages are required to achieve the necessary accuracy for measuring the damping.

6.3.1.8 Ibrahim Time Domain Method

The randomdec method has been extended [6.35] to permit the analysis of multimodal response based on simultaneous use of multiple measurement locations. The basis of the approach [6.36] can be outlined by considering the equation of motion for a multi-degree-of-freedom system that is excited by random force and given by

$$[M] \{\ddot{y}(t)\} + [C] \{\dot{y}(t)\} + [K] \{y(t)\} = \{x(t)\} \quad (6.81)$$

where $[M]$, $[C]$ and $[K]$ are the mass, damping and stiffness matrices, respectively, and $\{y(t)\}$ and $\{x(t)\}$ are the random response and force vectors, respectively. The time t in the above equation is now replaced by $t_j + \tau$ where the t_j 's are selected according to the triggering method used in starting the randomdec computations. Each ensemble is represented by a value of j , where $j = 1, 2, 3, \dots$, up to a total of N ensembles. After summing and averaging these ensembles, the resulting equation becomes

$$\begin{aligned} [M] \{\ddot{Y}(\tau)\} + [C] \{\dot{Y}(\tau)\} + [K] \{Y(\tau)\} \\ = \frac{1}{N} \sum_{j=1}^N \{x(t_j + \tau)\} \end{aligned} \quad (6.82)$$

The t_j 's were selected in a manner such that the averaged response $\{Y(\tau)\}$ remains finite while the right hand term in equation 6.72 goes to zero, since the random force is assumed to be stationary. Equation 6.82 now becomes

$$[M] \{\ddot{Y}(\tau)\} + [C] \{\dot{Y}(\tau)\} + [K] \{Y(\tau)\} = 0 \quad (6.83)$$

which represents the characteristic equation for multimodal free vibration response. This characteristic equation is then expressed in the form of an eigenvalue problem which includes the inversion of a matrix developed from measured response data. This type of inversion may introduce errors into the analysis since it can be shown that the fractional error in the inverse of a number containing spurious noise, is equal to minus the inverse of the dynamic range. It is therefore suspected that this method may be subjected to the same 55 dB dynamic range requirement for the randomdec signatures as discussed in Section 6.3.1.1.

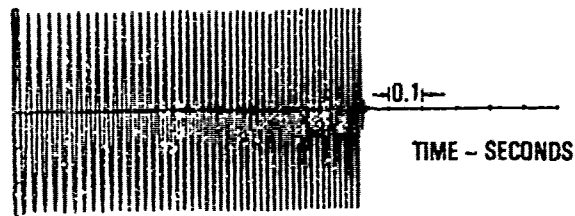
It is stated in Reference [6.36] that the force does not have to be white noise or broad band random. However, it can be shown theoretically that the effect of the forcing function shape is already included in the response $Y(\tau)$. The filter effect in Figure 6.2 was actually obtained by means of a band limited rapid sine sweep excitation. The result is basically the same whether the response of the structure to a broad band excitation is filtered after the application of the excitation or if filtered excitation is applied to the structure. Therefore, it is concluded that for accurate measurement of the damping, the force spectrum should be reasonably constant over the region encompassing the structural resonant peaks.

6.3.2 Fourier and Laplace Analysis of Transient Response

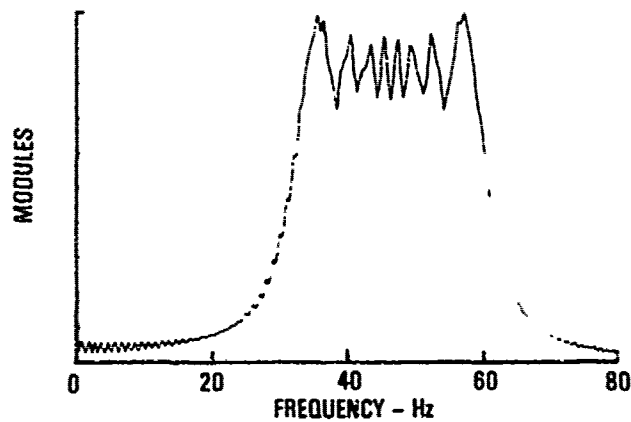
6.3.2.1 Rapid Sine Sweep Excitation Method

The rapid sine or frequency sweep technique was developed [6.17] for rapid measurement of structural response while maintaining control over the excitation force. The constant level sinusoidal force $x(t)$ is varied very rapidly but linearly with frequency (Figure 6.12a) between an initial frequency f_1 and a final frequency f_2 . This form of excitation represents a controlled impulse with approximately an equal energy distribution with frequency between the above frequency limits (Figure 6.12b). The deterministic excitaton is given by the relationship.

$$x(t) = x_0 \sin (at^2 + bt) \quad 0 < t < T \quad (6.84)$$



(a) WAVEFORM



(b) SPECTRUM

Figure 6.12. Typical rapid sine sweep waveform and spectrum

where

$$a = \pi(f_2 - f_1)/T \quad (6.85)$$

$$b = 2\pi f_1$$

The frequency response function (equation 6.25) of a single degree-of-freedom system excited by an impulsive force $x(t)$, such as the rapid sine sweep, is simply

$$H(i\omega) = \frac{y(i\omega)}{x(i\omega)} \quad (6.86)$$

where $x(i\omega)$ and $y(i\omega)$ are the Fourier transform of the force $x(t)$ and the response $y(t)$, respectively, given by

$$x(i\omega) = \frac{1}{2\pi} \int_{-\infty}^{\infty} x(t) e^{-i\omega t} dt \quad (6.87)$$

$$y(i\omega) = \frac{1}{2\pi} \int_{-\infty}^{\infty} y(t) e^{-i\omega t} dt \quad (6.88)$$

The modal frequency and damping can be extracted from equation 6.86 by means of the K-P analysis. The process is also valid for multimodal response.

The vector loops obtained by means of equation 6.86 are usually distorted by the presence of spurious noise. The signal to noise ratio (S/N) can be improved by ensemble averaging of successive test data. If the spurious noise is random gaussian then the improvement that can be achieved in the signal to noise ratio is given by the relationship [6.37]

$$\left(\frac{S}{N}\right)_{\text{Improved}} = \sqrt{K} \left(\frac{S}{N}\right) \quad (6.89)$$

where K is the number of ensemble averages. If the noise is not gaussian the number of averages should be increased by 3.5 times the number given by equation 6.89. The signal to noise ratio can also be improved by first obtaining the autocorrelation function, $R_{yy}(\tau)$, of the response $y(t)$ and then taking the single sided Fourier transform of the autocorrelation function, as discussed in Section 6.3.1.4. This procedure was used in obtaining the fundamental mode response of a Kevlar honeycomb panel to rapid sine sweep acoustic excitation in Figure 6.9. A least squares curve fit analysis was still necessary to extract the modal parameters since some spurious noise effects remained.

There is also a resolution problem with close modes [6.38] with the resolution limits defined approximately by the criterion

$$\frac{\zeta_n f_n}{|\Delta f|} \leq 0.19 + 0.0031 (\text{DR}) \quad 20 < \text{DR} < 60 \quad (6.90)$$

where DR is the dynamic range measured in dB, f_n and ζ_n are the natural frequency and viscous damping ratio of the longest decaying mode, respectively, and Δf is the difference between the resonant frequencies of the two close modes. The term on the right of equation 6.90 becomes 0.37 for the 55 dB dynamic range criterion in equation 6.61, that is also required for accurate damping measurement. A comprehensive summary of the rapid sine sweep testing technique and other potential problem areas is given in Reference [6.38].

6.3.2.2 Impedance Head Hammer Tap Method

The impedance head hammer tap test method was developed [6.30, 6.31] for use in conjunction with the Laplace transform based digital modal analysis system discussed in Section 6.3.1.6. This method of testing provides a simple and rapid means of obtaining measured resonant frequency and damping data from a broad range of structures, since special test fixtures are generally not required. Mode shapes, such as those illustrated in Figure 6.13 for an integrally stiffened graphite/epoxy panel [6.39], require some added effort in defining the tap locations on the structure and storing their coordinates in the computer. Also, a number of hammer taps are, generally, used per tap location in order to improve the signal to noise ratio (see equation 6.89). The zoom algorithm can be used to obtain the required frequency resolution.

The hammer tap represents an "uncontrolled" impulse. Consequently, the hammer contains a force gage to measure the impulse force. The response of the structure is measured either by an accelerometer or a noncontacting displacement transducer [6.39] located on the structure where significant response is obtained from all of the modes of interest. The force and the response are measured simultaneously for each tap. The upper frequency limit

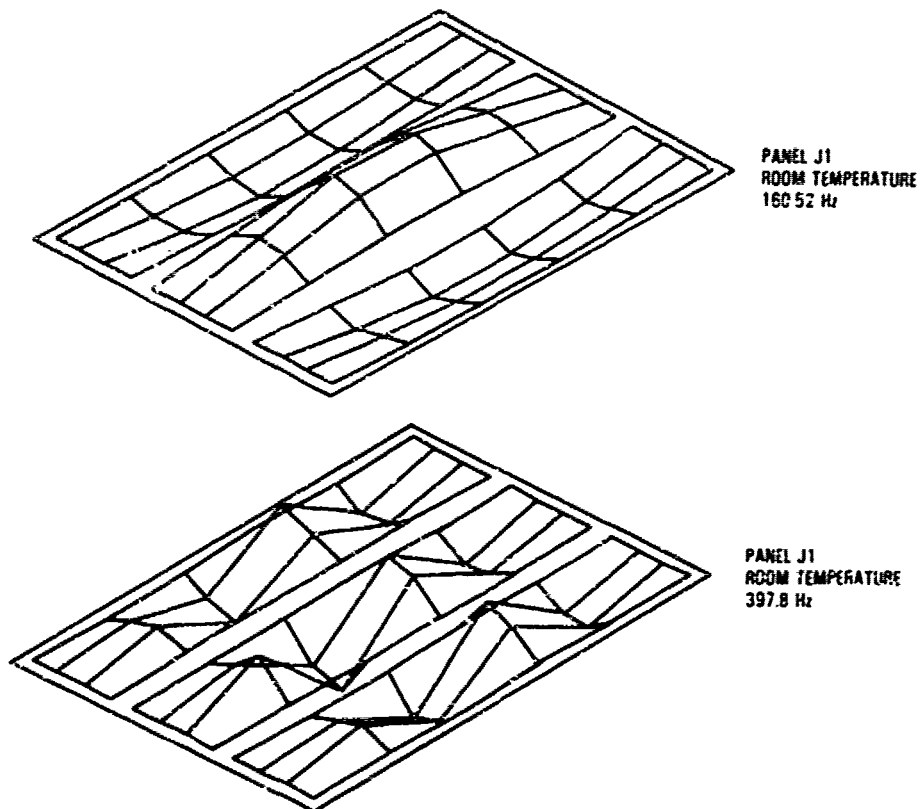


Figure 6.13. Typical measured mode shapes of an integrally stiffened graphite/epoxy panel

of energy imparted to the structure depends on the hardness [6.40] of the hammer tip (Figure 6.14) and the dynamic characteristics of the structure [6.41]. The highest frequency limit is obtained with a hard hammer tip impacting on a very stiff structure. For example, the hammer force spectrum has a much lower energy content when an integrally stiffened graphite/epoxy panel is impacted at the panel center (Figure 6.15) than when it is impacted over the stiffener flange.

An indication as to the accuracy of the measured response data can be obtained by computing the coherence function γ^2 defined by [6.22]

$$\gamma^2 = \frac{|G_{yx}(f)|^2}{G_{xx}(f) G_{yy}(f)} \quad 0 < \gamma \leq 1 \quad (6.91)$$

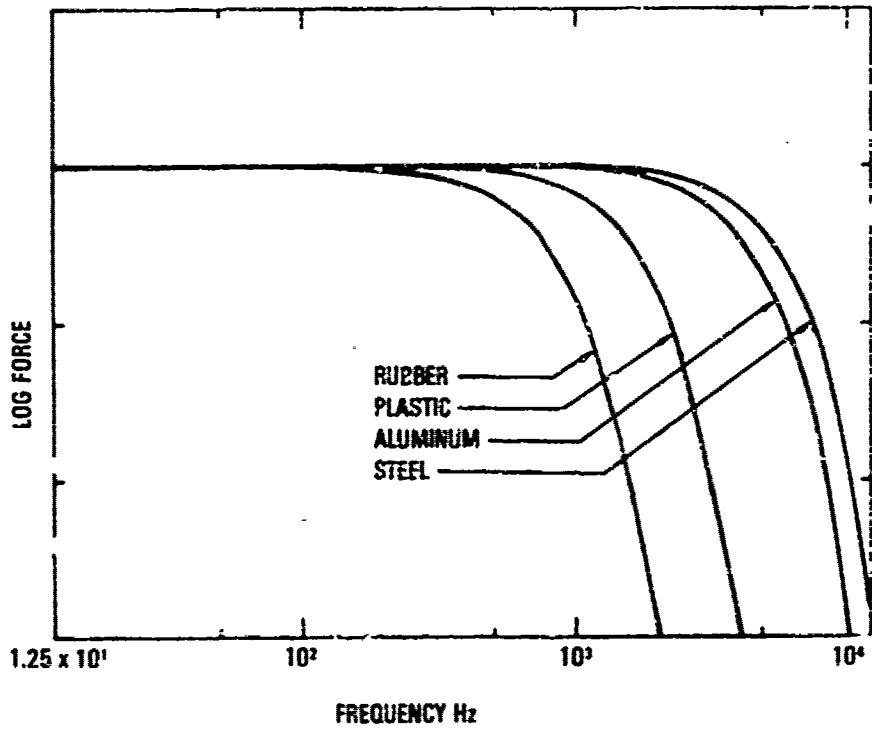


Figure 6.14. Force spectra produced with various hammer tip materials

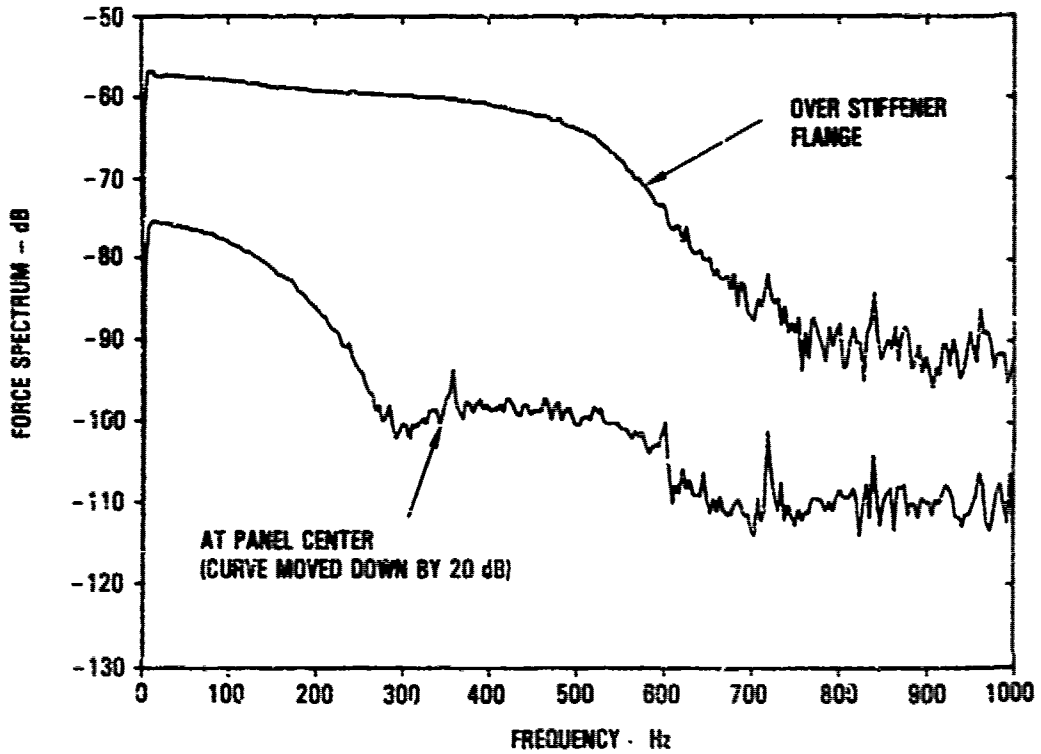
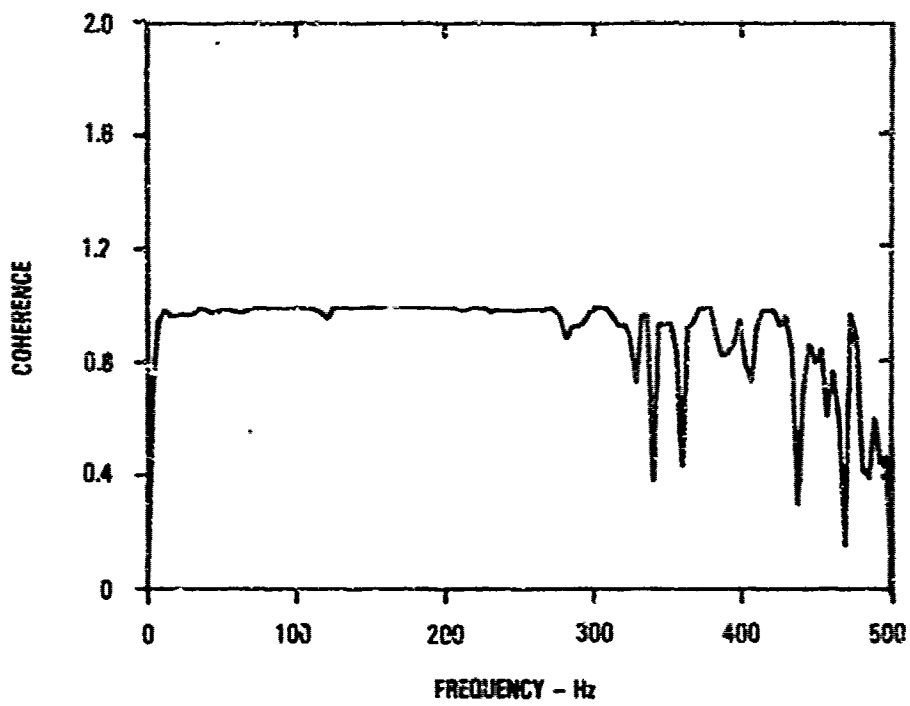


Figure 6.15. Hammer force spectra from tapping at panel center and over stiffener flange

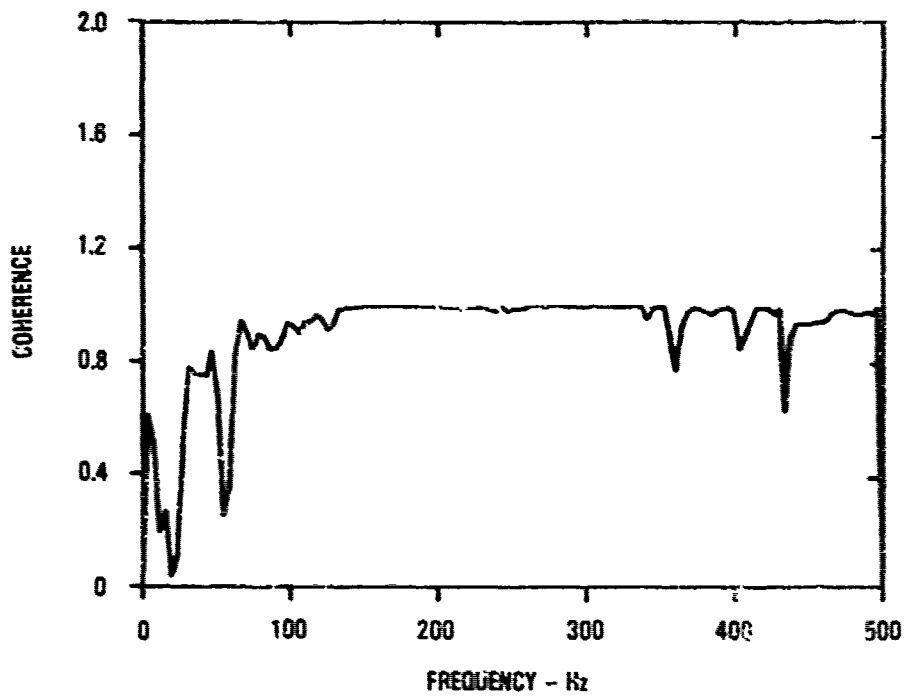
where $G_{xy}(f)$ is the cross spectral density between the force $x(t)$ and the response $y(t)$ and, $G_{xx}(f)$ and $G_{yy}(f)$ are the power spectral densities of the force and the response, respectively. The closer the coherence function is to unity the more accurate the response data. Typical coherence functions obtained with a noncontacting displacement transducer and an accelerometer, with impedance head hammer taps applied over the stiffener flange of an integrally stiffened graphite/epoxy panel, are illustrated in Figure 6.16. The accelerometer provides better data at higher frequencies whereas the displacement transducer is very accurate down to dc. The coherence obtained with the displacement transducer, by tapping at the center of the panel, started to deteriorate at 200 Hz. In spite of this deterioration, it was possible to measure the mode shapes up to a frequency just below 500 Hz (Figure 6.13). The corresponding damping data shown in Figure 6.17, however, exhibited a relatively large scatter at the higher frequencies. Generally, the same dynamic range requirements as discussed in Section 6.3.1.1 are also required for this test method, to obtain accurate damping measurements. The dynamic range cannot be increased by increasing the energy level of the impact since damage could be produced in the structure. It is also difficult to identify the modes when the damping of the structure is increased significantly such as obtained when a panel is approaching buckling [6.42]. The higher order panel modes of complex structures, such as the mode at 397.8 Hz in Figure 6.13, can also reach the data point limit in some of the current analysis systems. Seventy two tap locations were used in deriving the mode shapes in Figure 6.13. This test method is very useful in determining the structural response modes primarily in the lower frequency range. Other forms of excitation that provide a controlled force over a wider frequency range, need to be used for investigating structural response at higher frequencies.

6.3.3 Nonlinear Response and Electrodynamic Shakers

All of the methods discussed in Section 6.3 are based on the assumption of linear structural response. Consequently, significant errors in the resonant frequencies and damping ratios can be obtained when the structural response is highly nonlinear [6.42]. This result is supported by experimental evidence



(a) DISPLACEMENT



(b) ACCELERATION

Figure 6.16. Coherence functions between force and both panel center displacement and acceleration - tapping over stiffener flange

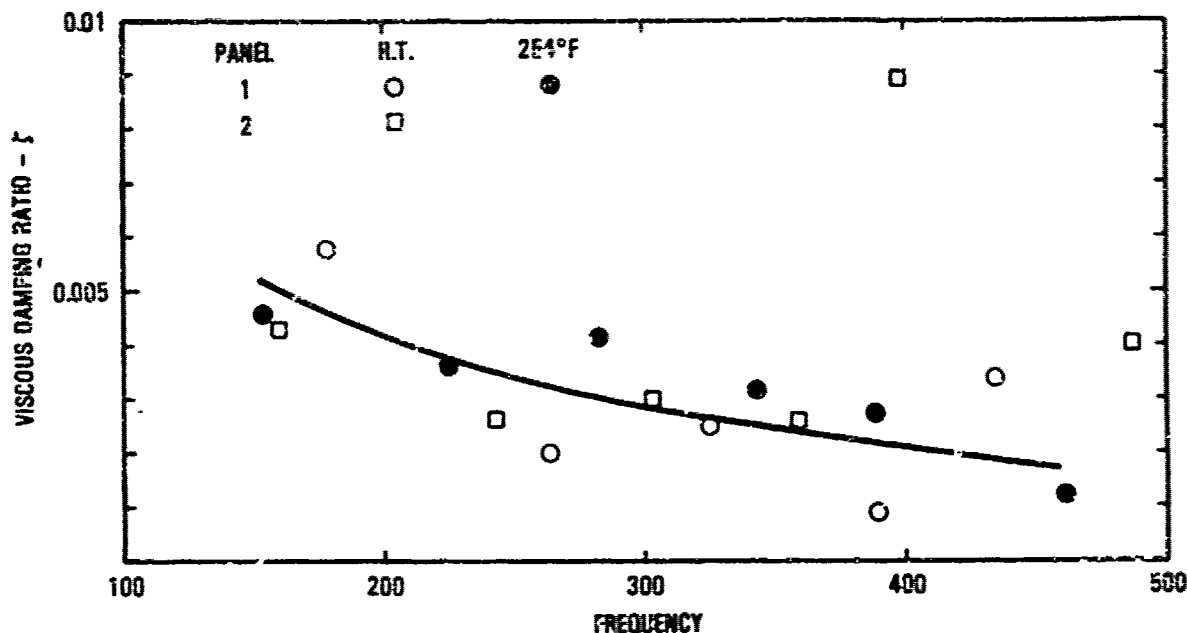


Figure 6.17. Measured viscous damping ratio for integrally stiffened graphite/epoxy panels

in References 6.39 and 6.44. The Fourier and Laplace transforms utilize an averaging process with respect to time. Consequently, nonlinear effects, which are a function of amplitude, are smeared by this averaging process as illustrated [6.39] in Figure 6.18. The integrally stiffened graphite/epoxy panel exhibited a stiffening spring type nonlinear behavior at the higher excitation levels characteristic of large amplitude panel response. The half power point "damping" measurement obtained from the nonlinear vibration spectra are meaningless. No correlation was obtained in the least squares type curve fit of dynamic strain response data to theory when such half power point "damping" values were used [6.44] in the correlation. Other evidence [6.39] suggests that damping values measured in the linear response region at low excitation levels are also applicable at the large panel response amplitudes. Friction damping, which may increase the damping with amplitude, was not present in these panels since the panels were fabricated with cured integral stiffeners.

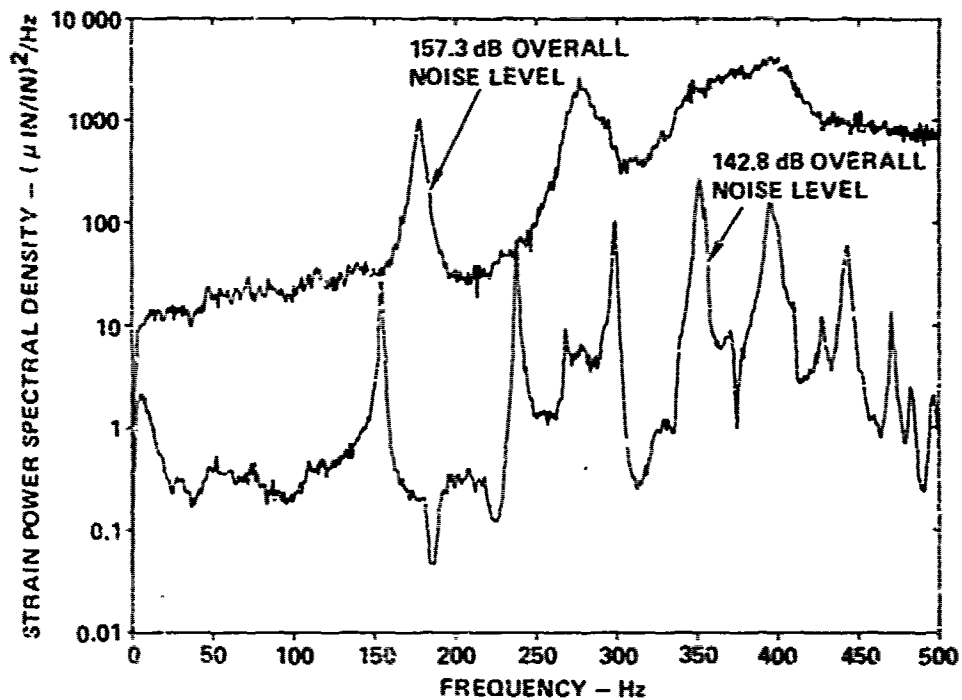


Figure 6.18. Typical linear and nonlinear strain power spectral densities for an integrally stiffened graphite/epoxy panel subjected to random acoustic loading

The sine dwell is considered to be the best method for measuring nonlinear structural response since changes in the resonant frequencies of the modes with force level or vibration amplitude can be readily detected. The damping can be measured from the free decay generated by the quick stop method. The decay rate will vary as a function of amplitude if nonlinear damping is encountered. This method is applied on a mode by mode basis and is, therefore, very time consuming.

If electrodynamic shakers are used to excite the structure, the damping of the structure may be increased by the back EMF within the shaker [6.38]. Quick release couplings should be used when making free decay type damping measurements with electrodynamic shakers. Alternatively, the back EMF can be minimized by making the electrodynamic shaker essentially a constant current device. This change requires the use of nonconducting saddle within the shaker together with a high impedance power amplifier.

The Galileo Spacecraft Development Test Model [6.45] provided an opportunity to evaluate most of the current vibration data analysis methods [6.46] as part of the modal survey effort conducted to verify the analytical dynamic model of the spacecraft. The spacecraft has a three-dimensional vibration response and a high modal density, with approximately thirty modes concentrated in the frequency region between 10 and 45 Hz. The vibration response of the spacecraft is basically nonlinear [6.47]. One electrodynamic shaker was used in the majority of the tests, 3 and 4 shakers were used in the two multi-shaker random tests and up to 8 shakers were used in the sine dwell tests. In general, all of the significant modes were identified by these methods. The variation in each of the modal frequencies, as measured by the various methods, fell within a 10 percent scatter band. The measured damping, however, exhibited a considerably greater scatter. These test methods are discussed in more detail in References [6.46] to [6.50].

6.4 CORRECTION OF SMOOTHING ERRORS IN DAMPING OBTAINED FROM SPECTRAL ANALYSIS

6.4.1 Introduction

The use of the periodic Fourier transform, to analyze nonperiodic random and transient vibration data, introduces leakage into the resulting structural response spectra. This leakage takes the form of spurious side lobes [6.51] which have the appearance of and may be mistaken for actual modes, producing significant errors when multimodal curve fitting algorithms are used to extract the modal parameters. These spurious side lobes can be suppressed by the use of smoothing functions at the expense of increasing the resolution (truncation [6.51] or bias [6.22]) error. The resolution error reduces the level of the spectral response peaks at resonance while increasing the magnitude of the damping extracted from these response peaks. Since the smoothing function and data analysis parameters, such as the analysis bandwidth, are always preselected in any data analysis, their effect on the single degree-of-freedom system can be established theoretically and correction curves developed to compensate for their effect on the extracted modal damping. This

approach has been used for the rectangular, Bartlett and Hanning smoothing (or weighting functions [6.18]) in References [6.51], [6.52] and [6.15], respectively (see Figure 6.19).

Generally, a low resolution error is desirable for measuring modal damping. The unsmoothed data, synonymous with rectangular smoothing, produces the lowest resolution error, but also the highest side lobes. Hanning smoothing has relatively high side lobe suppression capability while producing a slightly larger resolution error. As a consequence, Hanning smoothing is often used as a compromise in modal analysis. The above trend is continued with Bartlett smoothing.

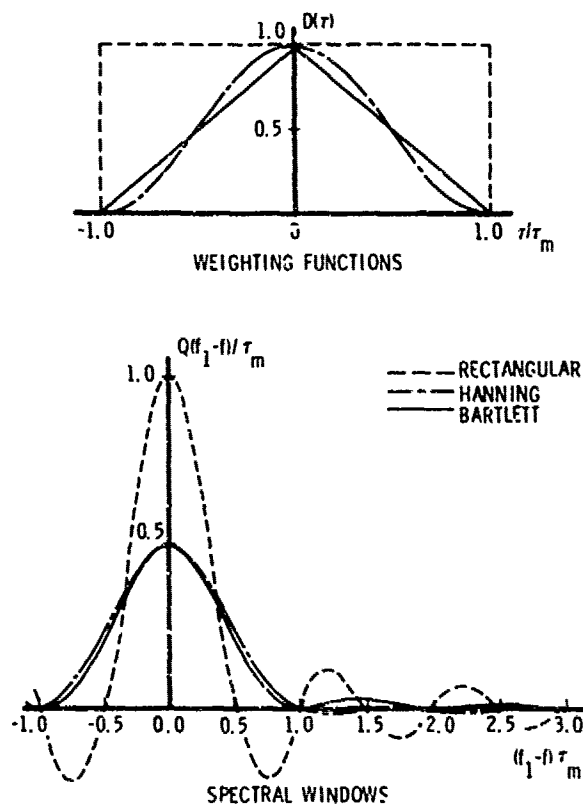


Figure 6.19. Rectangular, Hanning and Bartlett smoothing or weighting functions and the corresponding spectral windows

In general, the effect of the smoothing on the resonant vibration response spectrum is a function of the analysis bandwidth, the resonant frequency and the damping ratio. Therefore, the effect of smoothing cannot be compensated for by a constant factor, such as derived from the spectral analysis of a discrete frequency signal, before the analysis is performed since the modal parameters are usually not known beforehand. In the problem of extracting known discrete frequencies from within random background noise, the suppression of the side lobes is of paramount importance while the resolution bandwidth is much less important. The reverse is true for modal analysis.

In order to obtain accurate damping data, the effects of smoothing on the modal parameters must be understood and means of correcting for their effect established. The limitation imposed on the use of curve fit algorithms by the smoothing must also be established since the data extracted often include parameters other than the resonant frequencies and damping ratios. The purpose in this section is to address these problem areas for the three weighting functions discussed above when used with the Blackman and Tuckey [6.18] spectral analyses. The errors introduced by the FFT spectral analyses are dependent on the way the smoothing is applied within the analysis computer. The basic theory has been developed [6.53] but remains to be verified against test data.

6.4.2 Basic Smoothing Theory

The basic smoothing theory [6.51] is applicable to the spectral analysis of structural response to both random and transient excitation. The basic approach involves calculating the cross correlation function before taking the Fourier transform. The cross correlation function in practice is of finite length, terminated after a maximum time delay τ_m . The expression for the true cross spectral density in equation 6.54 is now replaced by an estimated cross spectral density $P_{xy}(\omega_1)$, at circular frequency ω_1 , that is given by

$$P_{xy}(\omega_1) = \frac{1}{2\tau} \int_{-\infty}^{\infty} D(\tau) R_{xy}(\tau) e^{-i\omega_1 \tau} d\tau \quad (6.92)$$

where $D(\tau)$ is the smoothing or weighting function given by

$$\begin{aligned} D(\tau) &= 1 && \text{for } -\tau_m < \tau < \tau_m \\ &= 0 && \text{elsewhere} \end{aligned} \tag{6.93}$$

for rectangular smoothing,

$$\begin{aligned} D(\tau) &= \frac{1}{2} \left(1 + \cos \frac{\pi \tau}{\tau_m} \right) && \text{for } -\tau_m < \tau < \tau_m \\ &= 0 && \text{elsewhere} \end{aligned} \tag{6.94}$$

for Hanning smoothing, and

$$\begin{aligned} D(\tau) &= \left(1 - \frac{|\tau|}{\tau_m} \right) && \text{for } -\tau_m < \tau < \tau_m \\ &= 0 && \text{elsewhere} \end{aligned} \tag{6.95}$$

for Bartlett smoothing.

The cross correlation function is also given by the inverse Fourier transform of the true cross spectra (equation 6.66). On substituting this expression for the correlation function into equation 6.92, the estimated cross spectral density becomes

$$P_{xy}(\omega_1) = \int_{-\infty}^{\infty} Q(\omega_1 - \omega) S_{xy}(\omega) d\omega \tag{6.96}$$

where the spectral window $Q(\omega_1 - \omega)$ is

$$Q(\omega_1 - \omega) = \frac{1}{2\pi} \int_{-\tau_m}^{\tau_m} D(\tau) e^{-i\tau(\omega_1 - \omega)} d\tau \quad (6.97)$$

The weighting functions in equations 6.93 through 6.95 and the corresponding spectral windows are illustrated in Figure 6.19. The basic theory is equally applicable to the estimated power spectral density $P_{xx}(\omega_1)$ by simply replacing the cross correlation function $R_{xy}(\tau)$ in equation 6.96 with the auto correlation function $R_{yy}(\tau)$. The estimated Fourier spectrum $y(i\omega_1, T)$ of the finite response $y(t)$ of a single degree-of-freedom system to an impulse is given by

$$\begin{aligned} y(i\omega_1, T) &= \frac{1}{2\pi} \int_{-\infty}^{\infty} \int_0^T D(t) e^{-i(\omega_1 - \omega)t} dt y(i\omega) d\omega \\ &= \int_{-\infty}^{\infty} Q(\omega_1 - \omega) y(i\omega) d\omega \end{aligned} \quad (6.98)$$

where the duration of the response is T , $y(i\omega)$ is the true Fourier spectrum, the smoothing function $D(t)$ is the same as $D(\tau)$ in equations 6.93 through 6.95 and the spectral window is

$$Q(\omega_1 - \omega) = \frac{1}{2\pi} \int_0^T D(t) e^{-i(\omega_1 - \omega)t} dt \quad (6.99)$$

The lower limit of the integral in equation (6.97) is also zero when applied to the cross spectral density, since the cross correlation function exists only in positive time (equation 6.53). The same is also true for the single sided Fourier transform of the autocorrelation function. Therefore, all Fourier transform based spectral analyses are prone to smoothing error.

The expression for the estimated cross spectral density for a single degree-of-freedom system that is excited by broad band random noise becomes

$$P_{xy}(\omega_1) = \frac{S_{xx}}{M} \int_{-\infty}^{\infty} \frac{Q(\omega_1 - \omega)}{\left(\omega_n^2 - \omega^2 + 2i\zeta\omega_n\omega\right)} d\omega \quad (6.100)$$

and the estimated power spectral density $P_{yy}(\omega_1)$

$$P_{yy}(\omega_1) = \frac{S_{xx}}{M^2} \int_{-\infty}^{\infty} \frac{Q(\omega_1 - \omega)}{\left(\omega_n^2 - \omega^2\right)^2 + 4\zeta^2\omega_n^2\omega^2} d\omega \quad (6.101)$$

Also, the estimated frequency response function $H(i\omega, T)$ obtained from transient analysis (see equation 6.86) is now

$$H(i\omega, T) = \frac{y(i\omega, T)}{x(i\omega)} = \int_{-\infty}^{\infty} \hat{v}(t) h(t) e^{-i\omega t} dt \quad (6.102)$$

where $h(t)$ is the impulse function of the single degree-of-freedom system.

Equation 6.100 and 6.102 can be solved by contour integration and by direct integration, respectively, and produce identical results for the estimated frequency response function. An approximate solution can be obtained to equation 6.101 from the imaginary part [6.53] of equation 6.100, or the estimated power spectral density can be obtained by direct integration of equation 6.92, with subscript x replaced by y . On dividing the estimated cross and power spectral densities by the corresponding true cross and power spectral densities, respectively, the same resolution error is obtained [6.15] at resonance. The normalized resolution error for the resonance peaks is

$$\frac{P_{xy}(\omega_n)}{S_{xy}(\omega_n)} = \frac{P_{yy}(\omega_n)}{S_{yy}(\omega_n)} = 1 - e^{-\alpha} (1 + 0.5\zeta \sin\beta) \quad (6.103a)$$

for rectangular smoothing [6.51]

$$= -0.25\alpha^2(1 + e^{-\alpha} \cos\beta) \left\{ \frac{1}{(\pi + \beta)^2 + \alpha^2} + \frac{1}{(\pi - \beta)^2 + \alpha^2} + \frac{2}{\beta^2 + \alpha^2} \right\}$$

$$- 0.25\alpha e^{-\alpha} \sin\beta \left\{ \frac{\pi - \beta}{(\pi - \beta)^2 + \alpha^2} - \frac{\pi + \beta}{(\pi + \beta)^2 + \alpha^2} + \frac{2\beta}{\beta^2 + \alpha^2} \right\} \quad (6.103b)$$

$$+ 0.5 \left\{ \frac{2\alpha^2 + \pi^2(1 - e^{-\alpha})}{\alpha^2 + \pi^2} \right\}$$

for Hanning smoothing [6.15] and

$$= 1 - \frac{1 - e^{-\alpha}}{\alpha} \quad (6.103c)$$

for Bartlett smoothing [6.52], where

$$\alpha = \omega_n \tau_m \zeta \quad (6.104)$$

$$\beta = 2\omega_n \tau_m$$

The normalized estimated spectra at resonance are illustrated in Figure 6.20 for the three smoothing functions. It is seen that no error is obtained in the unsmoothed spectra when the criterion in equation 6.61 is satisfied. This condition applies equally to FFT analysis on using equation 6.67 with the relationship in equation 6.61. The error remains finite for the other smoothing functions.

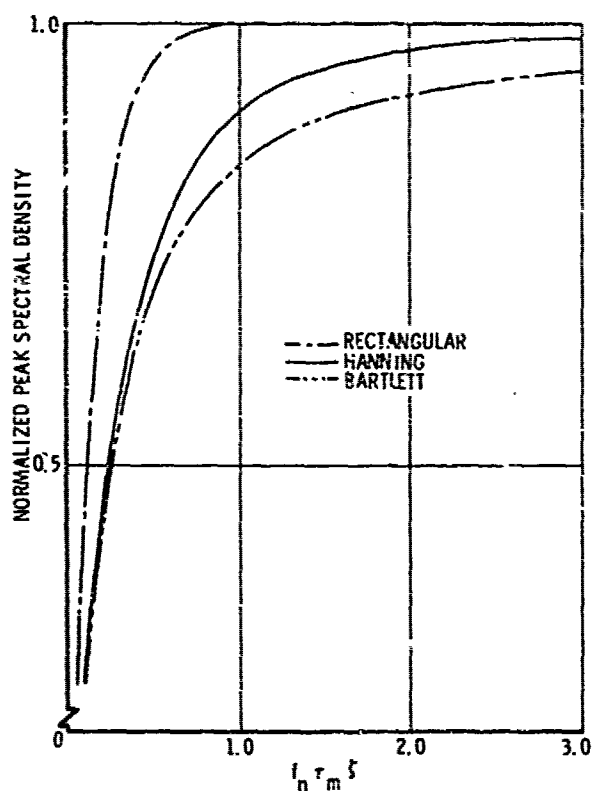


Figure 6.20. Smoothing error in the normalized power and cross spectral peaks at resonance

The effect of Hanning smoothing on the normalized cross and power spectral densities of a single degree of freedom system are illustrated [6.23] in Figures 6.21 and 6.22 respectively.

6.4.3 Methods for Correcting Smoothing Affected Damping

The resonant frequency, of smoothing affected spectra, is extracted by the same method as for the K-P analysis, namely where the rate of change of arc length with frequency (ds/df) is a maximum (see Figure 6.21). However, the extraction of the damping is more involved since special curves have to be developed for this purpose. Originally [6.51] the parameter $\frac{1}{\rho} \frac{ds}{d\omega_n}$, calculated at resonance, formed the basis for such curves where ρ is the radius of curvature of the smoothed vector loop at resonance and $ds/d\omega_n$ is also measured at

REAL PART OF
NORMALIZED
CROSS SPECTRUM

$$\zeta = 0.015$$

$$\frac{df}{f_n} = 0.003$$

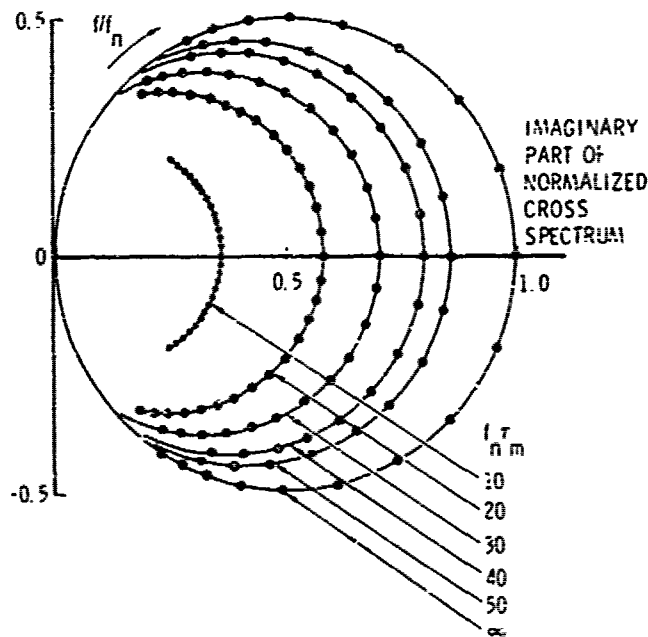


Figure 6.21. Effect of Hanning smoothing on the cross spectrum of a single degree-of-freedom system

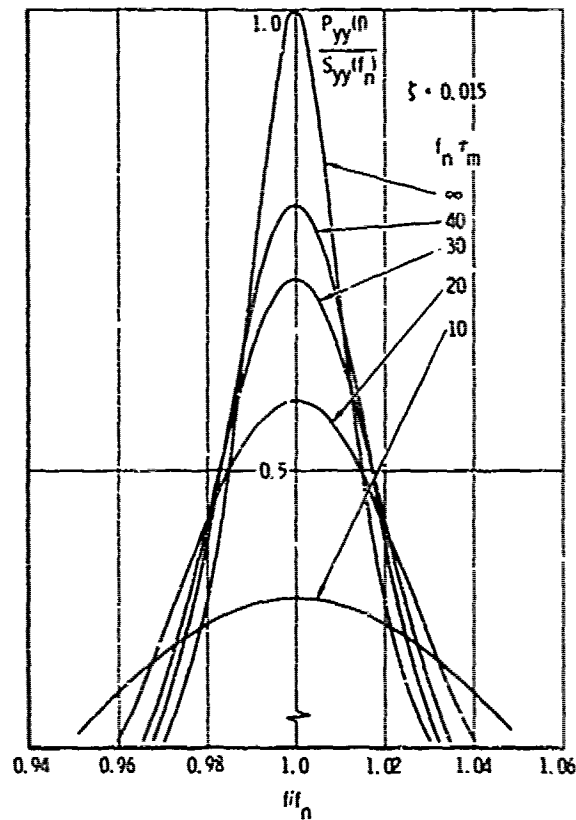


Figure 6.22. Effect of Hanning smoothing on normalized power spectral density

resonance. This parameter produced curves that became asymptotic and consequently impractical to use. Instead, the estimated viscous damping ratio ζ^* given by

$$\zeta^* = \frac{2\rho}{ds} \left(\frac{d\omega}{\omega_n} \right) \quad (6.105)$$

was used to develop the correction curves [6.15, 6.23]. The above expression reduces to the correct damping for unsmoothed spectra given by equation 6.50a since near resonance

$$\cot \theta \approx \frac{1}{\theta} = \frac{2\rho}{ds} \quad (6.106)$$

and

$$\frac{f_n - f}{f_n} = \frac{d\omega}{\omega_n} \quad (6.107)$$

If the cross spectral density in equation 6.69 is expressed by

$$P_{xy}(\omega) = X(\omega) + iY(\omega) \quad (6.108)$$

then, by using the same approach as in Reference [6.51], it is shown in Reference [6.15] that at resonance

$$\zeta^* \approx \frac{2}{\omega_n} \frac{dX(\omega)}{d\omega} \bigg/ \frac{d^2Y(\omega)}{d\omega^2} \quad (6.109)$$

The expressions for ζ^* obtained with rectangular, Hanning and Bartlett smoothing are

$$\zeta^* = \zeta \left[\frac{1 - e^{-\alpha}(1 + \alpha)}{1 - e^{-\alpha}(1 + \alpha + 0.5\alpha^2)} \right] \quad (6.110)$$

$$\zeta^* = -\frac{\zeta}{\gamma} \left[\frac{2 - 8\gamma^2}{(1 + 4\gamma^2)^2} - \frac{1}{2\gamma^2} + e^{-2\pi\gamma} \left[\frac{2 - 8\gamma^2}{(1 + 4\gamma^2)^2} + \frac{1}{2\gamma^2} - \frac{4\pi\gamma}{(1 + 4\gamma^2)} + \frac{\pi}{\gamma} (1 + \delta \sin \beta) \right] \right] \bigg/$$

$$\left[\frac{3\zeta\gamma^3 - 24\gamma}{(1 + 4\gamma^2)^3} + \frac{1}{2\gamma^3} - e^{-2\pi\gamma} \left[\frac{\pi^2}{\gamma} + \frac{1}{2\gamma^3} + \frac{\pi}{\gamma^2} + \frac{32\gamma}{(1 + 4\gamma^2)^3} + \frac{8(\pi - \gamma)}{(1 + 4\gamma^2)^2} \right. \right.$$

$$\left. \left. - \frac{4\pi(\pi\gamma + 1)}{1 + 4\gamma^2} \right] \right] \quad \text{for } \gamma > 20\gamma \quad (6.111)$$

and

$$\zeta^* = \zeta \left\{ \frac{1 - \frac{2}{\alpha} + e^{-\alpha} \left(1 + \frac{2}{\alpha} \right)}{1 - \frac{3}{\alpha} + e^{-\alpha} \left(2 + \frac{\alpha}{2} + \frac{3}{\alpha} \right)} \right\} \quad (6.112)$$

respectively, using the small damping assumptions. In the above equations ζ is the correct viscous damping ratio, α and β are given by equation 6.104 and

$$\gamma = f_n \tau_m \zeta \quad (6.113)$$

The correction curves derived from equations 6.110 through 6.112 are illustrated in Figures 6.22 through 6.24, respectively, as a function of the analysis bandwidth Δf ($= 1/(2\tau_m)$) divided by the resonant frequency. The correct damping can also be extracted from equations 6.21 through 6.23 by means of an iteration procedure [6.23]. Similar correction curves based on the estimated 3 dB damping from the corresponding smoothed power spectral densities are illustrated in Figures 6.25 to 6.27. These curves were obtained by numerical means from the smoothed power spectral densities.

6.4.4 Effect of Smoothing on Curve Fitting

The ability of current curve fitting algorithms to fit many modes simultaneously is advantageous for speeding up the data analysis, but may produce erroneous results when smoothing errors are present in the vector loops. The effect of smoothing on curve fitting of vector loops can be evaluated by considering the variation of the local radius of curvature along the vector loops near resonance with normalized frequency, as illustrated in Figure 6.28a. The radius does vary significantly. Furthermore, equations 6.50a and b, used in extracting the model damping from circular vector loops, are not valid in the presence of smoothing (see equations 6.110 to 6.112). The variation in the rate of change of arc length with normalized frequency, illustrated in Figure 6.28b as a function of the normalized frequency, compensates for the

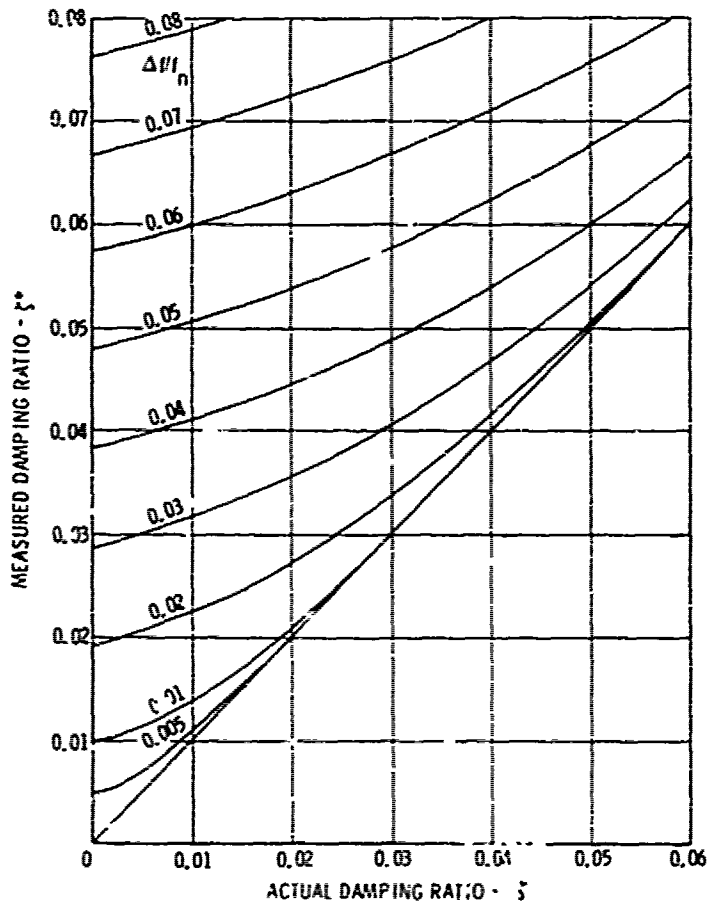


Figure 6.22. Damping correction curves for unsmoothed cross spectral density

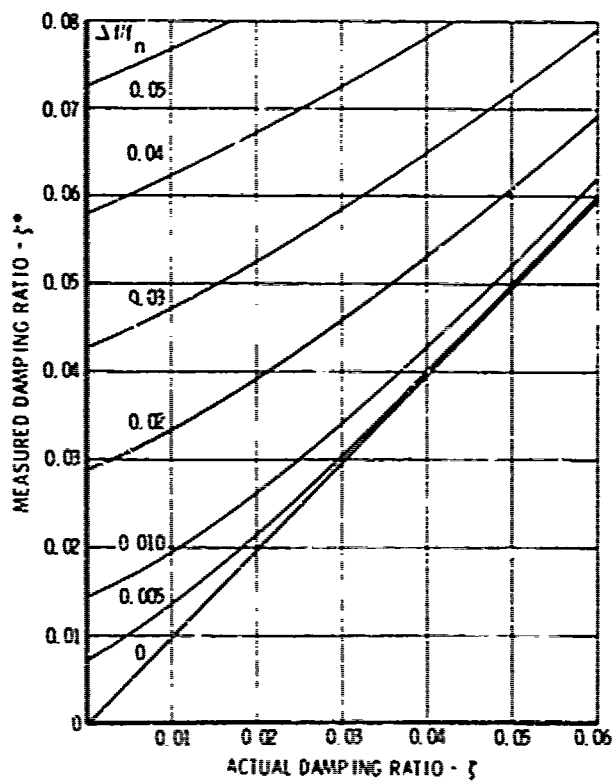


Figure 6.23. Damping correction curves for Hanning smoothing affected cross spectral density

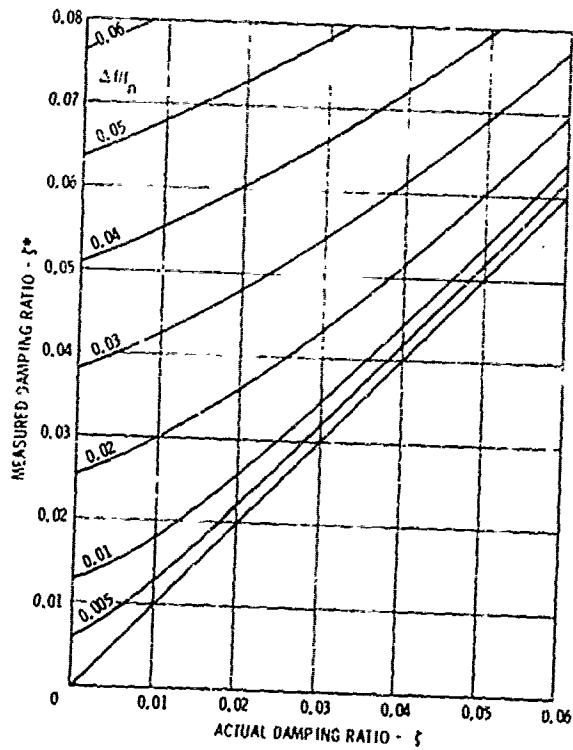


Figure 6.24. Damping correction curves for Bartlett smoothing affected cross spectral density

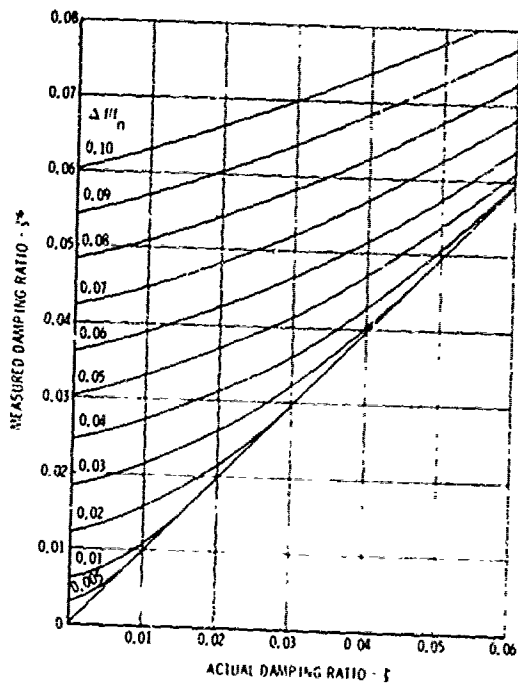


Figure 6.25. Damping correction curves for unsmoothed power spectral density

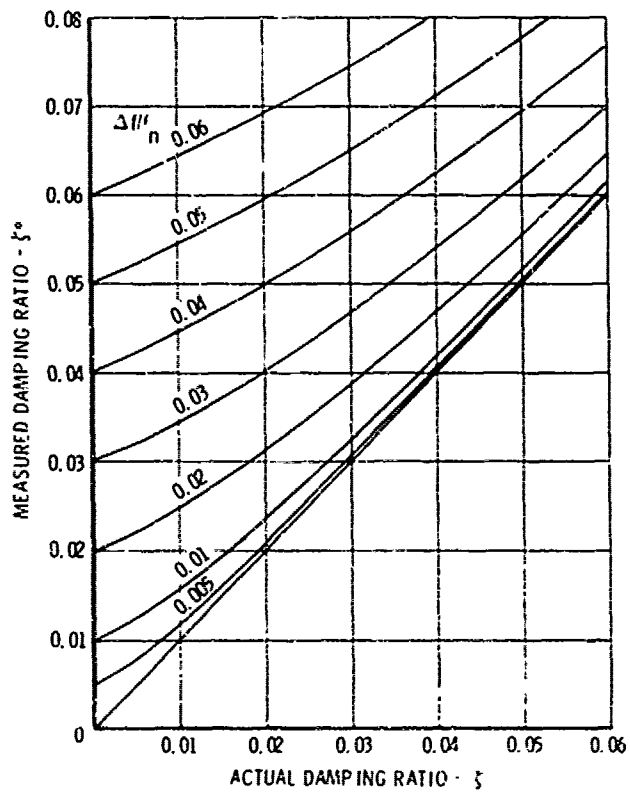


Figure 6.26. Damping correction curves for Hanning smoothing affected power spectral density

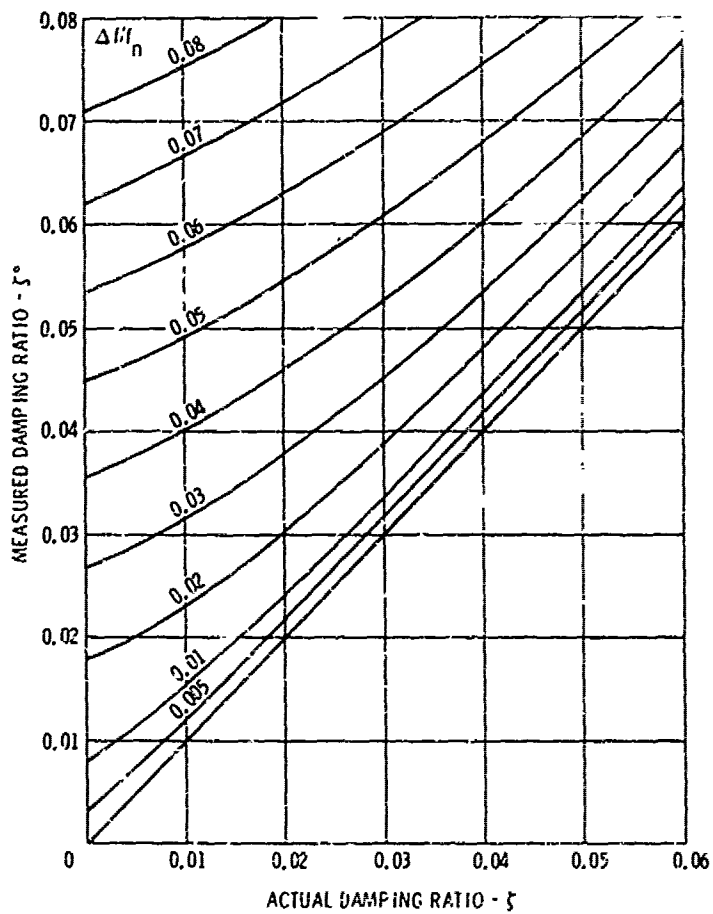


Figure 6.27. Damping correction curves for Bartlett smoothing affected power spectral density

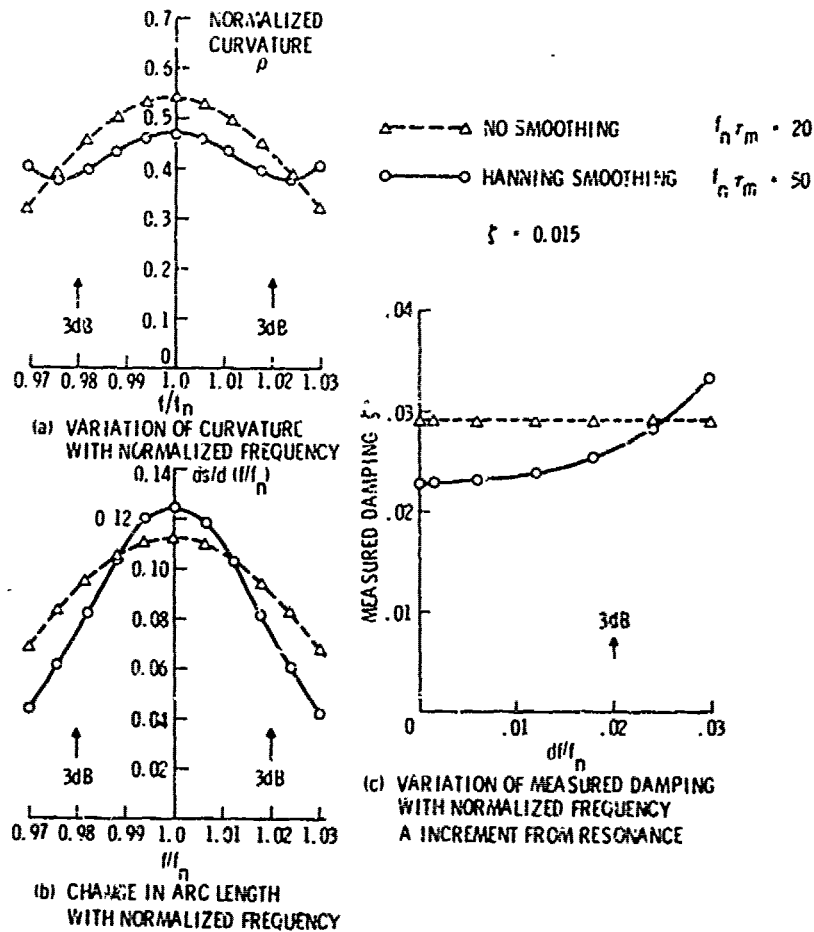


Figure 6.28. Typical effect of smoothing on curvature, change in arc length and measured damping ratio for normalized sinus spectrum of a single degree-of-freedom system

change in curvature when used in equation 6.105. This compensating effect is illustrated in Figure 6.28c where the variation in the measured (estimated) damping ζ^* is shown as a function of the frequency increment df/f_n between two equidistant frequency points on either side of resonance. A good estimate of ζ^* can be obtained with rectangular smoothing using the curve between the two 3 dB points. The estimated damping ratio ζ^* for the other smoothing functions can only be established by the use of the curve around resonance. The correct value for ζ^* is obtained at $df/f_n = 0$ in Figure 6.28c.

The amount of the unsmoothed vector loop that can be included in the curve fit depends on how closely the analysis meets the criteria in equation 6.61 or 6.62. For the vector loop used to derive the curves in Figure 6.28, the parameter $f_n \tau_m \zeta = 0.3$ is obviously too small a value. For the curve fit in Figure 6.9c, the parameter $f_n \tau_m \zeta$ is equal to 0.779, based both on the data in Table 6.1 and the value for τ_m of 0.225 in Figure 6.9b. This value for τ_m corresponded to the point where the autocorrelation function disappeared into the noise. Replacing the correlation function beyond this point with added zeros may improve the signal to noise ratio slightly, but will not change the smoothing effect. The curve fit in Reference [6.15] extracted the following parameters from the noise polluted vector loop in Figure 6.9c:

$$\zeta^* = 0.0313$$

and

$$f_n = 124.5 \text{ Hz}$$

Even with these values, the parameter $f_n \tau_m \zeta^*$ is equal to 0.877, indicating the presence of a smoothing error. Therefore, using the above value for ζ^* and $\Delta f / f_n = 1 / (2 \times 0.225 \times 124.5) = 0.0179$ in Figure 6.22, the corrected viscous damping ratio of $\zeta = 0.028$ is obtained. This damping ratio is in good agreement with that in Table 6.1, measured by the basic K-P method.

In conclusion, it is recommended that only the unsmoothed data should be used in the curve fit and that the criteria in equations 6.61 or 6.62 must be met for accurate damping measurement. A 5 percent error in the vector loop diameter will result if the criterion is relaxed to

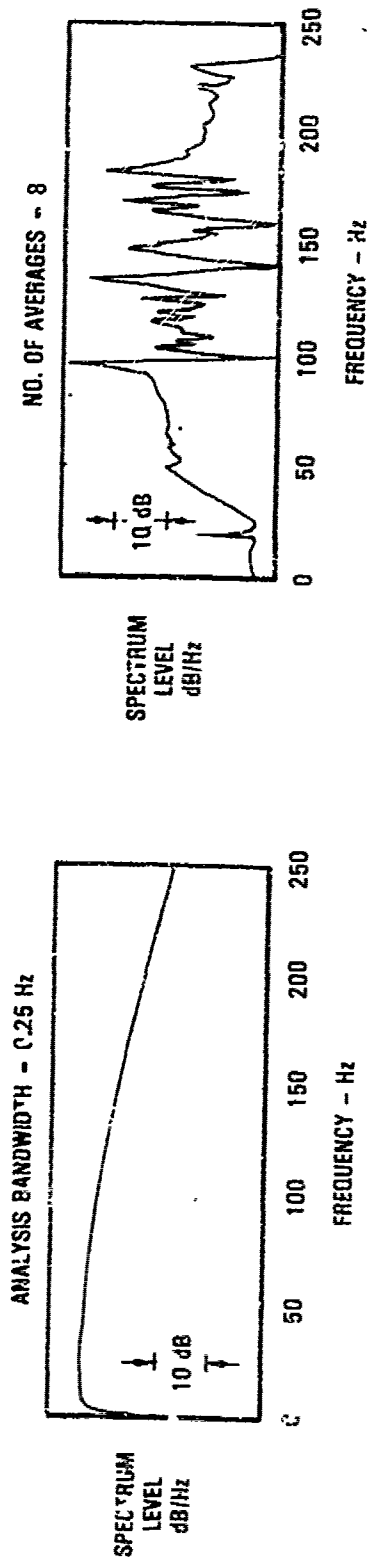
$$f_n \tau_m \zeta \geq 0.05 \quad (6.114)$$

This relaxed criterion is also expected to provide reasonable estimates of the damping provided the damping values are corrected for the smoothing effect. For even lower values of $f_{n,m}$ than in equation 6.114, the curve fit should be applied on a mode-by-mode basis using the curve only between the 3 dB points and again correcting the extracted damping ratio for smoothing error.

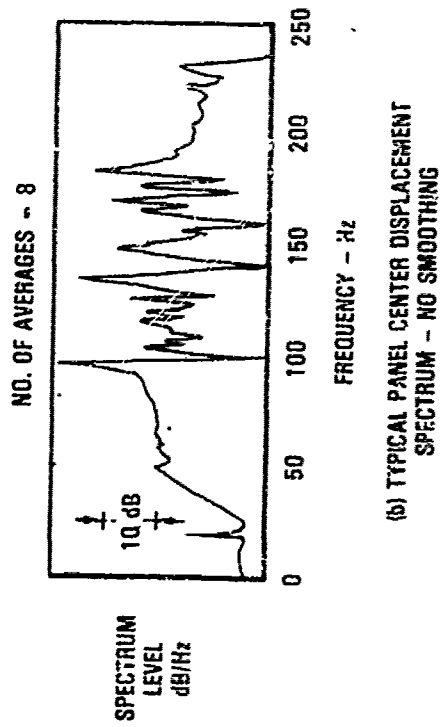
A good procedure for determining whether smoothing errors are present in the response spectrum is to obtain an unsmoothed spectrum such as illustrated in Figure 6.29b. Then obtain a Hanning smoothed spectrum to identify the actual modes (Figure 6.29c). Finally obtain a third unsmoothed spectrum, doubling the resolution. If the spectral peaks are of the same magnitude for the two unsmoothed spectra, then the smoothing error will not be present in the data. If the resonant peaks increase in magnitude when the resolution is increased, then a smoothing error is present in the original unsmoothed spectrum and, possibly, in the higher resolution spectrum. Continuation of this process is limited by the reduction in the frequency range encountered when the resolution is increased.

6.4.5 Evaluation of the Smoothing Theory

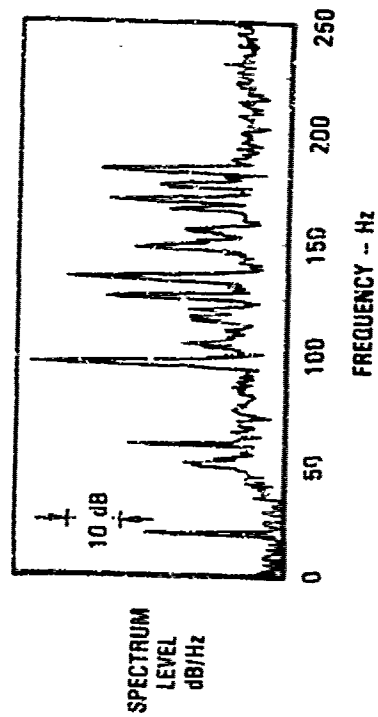
The accuracy of the previously developed methods for correcting smoothing affected damping was evaluated [6.23] by comparing the results obtained from a stick pulse excited free decay by means of the exponential and least squares curve fit methods, with those obtained from the smoothed Fourier spectra of the decay. The single mode aircraft wing decay is illustrated in Figure 6.30. The Fourier spectra obtained with 1 second and 5 seconds of the free decay are illustrated in Figures 6.31 and 6.32 for the unsmoothed and the Bartlett smoothed spectra, respectively. The spurious side lobes are visible for the unsmoothed spectra in Figure 6.31. The oval shape of the vector loops in Figure 6.31 is typical of the smoothing effect. This oval shape also introduces errors when using multimodel curve fitting techniques. The vector loops can be restored to circles by the use of exponential weighting as illustrated in Figure 6.33.



(a) TYPICAL HAMMER SPECTRUM (FORCE)



(b) TYPICAL PANEL CENTER DISPLACEMENT
SPECTRUM - NO SMOOTHING



(c) TYPICAL PANEL CENTER DISPLACEMENT
SPECTRUM - HANNING SMOOTHING

Figure 6.29. Response of composite aileron panel to hammer tap excitation

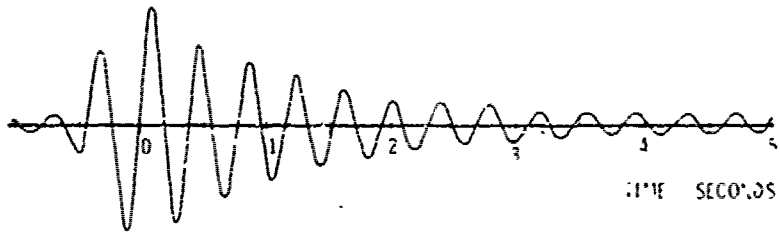


Figure 6.30. Measured aircraft wing response to stick pulse

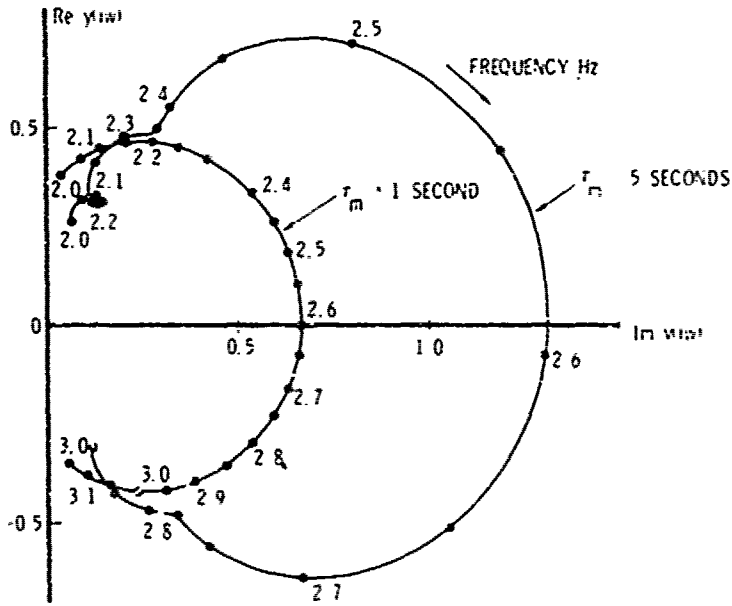


Figure 6.31. Unsmoothed Fourier spectra of aircraft wing free decay

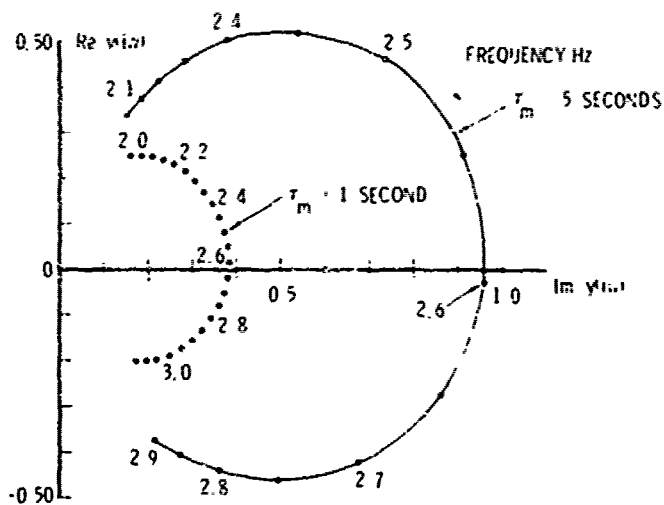


Figure 6.32. Bartlett smoothed Fourier spectra of aircraft wing free decay

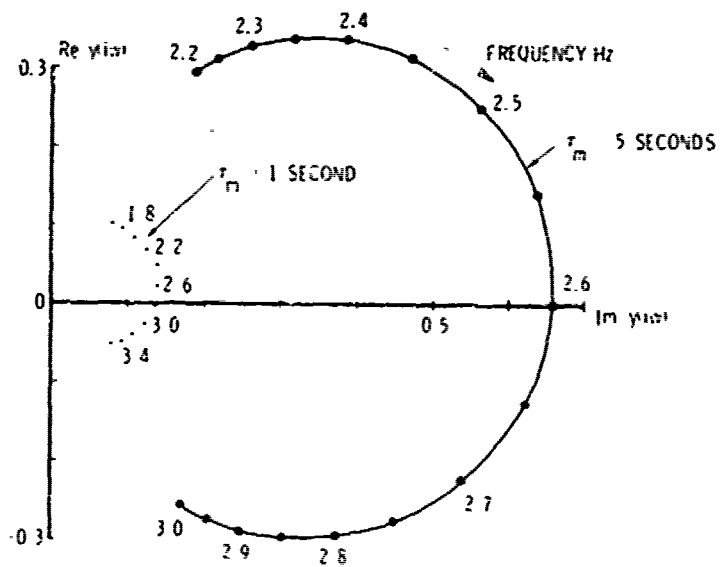


Figure 6.33. Restored Fourier spectra of aircraft wing response to stick pulse

The damping data obtained by the various methods are summarized in Table 6.5. The actual viscous damping ratio of the mode is around 0.038. The raw damping extracted from the smoothing affected spectra exceed the actual damping by significant amounts. The corrected damping, obtained from the unsmoothed (or rectangular smoothed) and Hanning smoothed spectra, are in reasonable agreement with the actual damping. The corrected damping is slightly higher from the Bartlett smoothed spectra. The correction method for the unsmoothed spectra provided the best result for the one second decay time. Also, curve fitting between the 3 dB points on the unsmoothed vector loop appeared to be more accurate than using the data around resonance [6.23] due probably to the presence of some noise in the free decay. This result is supported by the data in Figure 6.28.

The unsmoothed spectra, when used in conjunction with the method for correcting the damping described in the previous section and a single mode partial curve fit, offers the best method for extracting reasonably accurate damping data from smoothing affected spectra. The smoothing error can, generally, be expected to occur in the spectral analysis of structural response modes with low damping.

TABLE 6.5. COMPARISON OF VISCOUS DAMPING RATIO DETERMINED BY VARIOUS METHODS

Viscous Damping Ratio	Decay Time, Seconds	Least Squares Decay	Restored Nyquist Plot	Rectangular Smoothing	Hanning Smoothing	Bartlett Smoothing
Measured Directly from the Smoothed Spectrum	1	-	-	0.186	0.336	0.248
	5	-	-	0.048	0.073	0.068
Determined by the Various Methods	1	0.045	0.092	0.037	-	-
	5	0.038	0.040	0.038	0.037	0.044

REFERENCES

- 6.1. Grimmetad, D. W., "An Improved Ground Vibration Test Method, Vol. I: Research Report," AFWAL-TR-3056 Vol. I, 1981.
- 6.2. "System Identification of Vibrating Structures," American Society of Mechanical Engineers, Editors W.D. Pilkey and R. Cohen, 1972.
- 6.3. Timoshenko, S., "Vibration Problems in Engineering," D. Van Nostrand Company, Inc., 1937.
- 6.4. "Shock and Vibration Handbook," McGraw-Hill Book Company, Inc., Editors C.M. Harris and C.E. Crede, 1961.
- 6.5. Thompson, W.T., "Theory of Vibration With Applications," Prentice-Hall, Inc., 1972.
- 6.6. Kennedy, J.C. and Pancu, C.D.P., "Use of Vectors in Vibration Measurement and Analysis," Journal of the Aeronautical Sciences, Vol. 14, No. 11, November 1947.
- 6.7. Nashif, A.D., Jones, D.I.G., and Henderson, J.P., "Vibration Damping," Wiley, 1985, pp 82-84.
- 6.8. Papoulis, A., "The Fourier Integral and Its Applications", McGraw-Hill, 1963.
- 6.9. Kallianis, F., "Linear System Analysis by Cross Correlation and Its Transform Techniques", I.S.V.R. Technical Report No. 33, November 1970.
- 6.10. Wilcox, P.R. and Crawford, W.L., "A Least Squares Method for Reduction of Free Oscillation Data," NASA TN-D4503, 1968.

- 6.11. Bennet, R.M. and Desmarais, R.N., "Curve Fitting of Aeroelastic Functions," NASA SP-415, 1976, pp 43-58.
- 6.12. Gankroger, D.R., Skingle, C.W. and Heron, K.H., "Numerical Analysis of Vector Response Loci," Journal of Sound and Vibration, Vol. 29, No. 3, 1973.
- 6.13. Klosterman, A., "On the Experimental Determination and Use of Modal Representation of Dynamic Characteristics," Ph.D. Dissertation, University of Cincinnati, 1971.
- 6.14. Richardson, M. and Potter, R., "Identification of the Modal Properties of an Elastic Structure from Measured Transfer Function Data," Instrument Society of America, ISA ASI 74250, 1974, pp 239-246.
- 6.15. Soovere, J., "Truncation Errors in Direct and Cross Power Spectral and Free Decay Structural Response Analyses Due to Finite Data Length," Lockheed Report LR 27069, 1975.
- 6.16. "Random Vibration," Editor S.H. Crandall, Technology Press and John Wiley and Sons, Inc., 1958.
- 6.17. White, R.G., "Use of Transient Excitation in the Dynamic Analysis of Structures," The Aeronautical Journal of the Royal Aeronautical Society, Vol. 73, 1969.
- 6.18. Blackman, R.B. and Tuckey, J.W., "Measurement of Power Spectra," Dover Publications, 1959.
- 6.19. Cooley, J.W. and Tuckey, J.W., "An Algorithm for the Machine Calculation of Complex Fourier Series," Math. Computation, Vol. 19, April 1965.

- 6.20. Enochson, L.D. and Piersol, A.G., "Application of Fast Fourier Transform Procedures to Shock and Vibration Data Analysis," Paper Number 670874, SAE Aeronautic and Space Engineering and Manufacturing Meeting, Los Angeles, California, October 2-6, 1967.
- 6.21. Crandall, S.H. and Mark, W.D., "Random Vibration in Mechanical Systems", Academic Press, 1963.
- 6.22. Bendat, J.S. and Piersol, A.C., "Measurement and Analysis of Random Data," Wiley, 1966.
- 6.23. Soovere, J., "Turbulence Excited Frequency Domain Damping Measurement and Truncation Effects," NASA SP-415, 1976, pp 115-141.
- 6.24. Davenport, W.B. and Root, W.L., "An Introduction to the Theory of Random Signals and Noise," McGraw Hill, 1958.
- 6.25. McKinney, H. W., "Baud - Selectable Fourier Analysis," Hewlett-Packard Journal, April 1975.
- 6.26. Kandianis, F., "Frequency Response of Structures and the Effects of Noise on its Estimates from the Transient Response," Journal of Sound and Vibration, Vol. 15, No. 2, 1971.
- 6.27. Bhat, W.V. and Wilby, J.F., "An Evaluation of Random Analysis Methods for the Determination of Panel Damping," NASA CR-114423, February 1972.
- 6.28. White, R.G., "The Resolution of Close Natural Frequencies in the Impulse Response and Severe Truncation Effects," ISVR Technical Report No. 17, June 1969.

- 6.29. Kallianis, F., "Frequency Response of Structures Excited by Transient or Random Force Using the Cross Correlation and its Laplace Transform," I.S.V.R. Technical Report No. 47, August 1971.
- 6.30. Richardson, M., "Modal Analysis Using Digital Test Systems," Seminar on Understanding Digital Control and Analysis in Vibration Test Systems, Shock and Vibration Information Center Publication, 1975.
- 6.31. Ramsey, K.A., "Effective Measurements for Structural Dynamic Testing," Sound and Vibration, Part I, November 1975, Part II,
- 6.32. Cole, H.A., "On-Line Failure Detection and Damping Measurement of Aerospace Structures Utilizing Randomdec Signatures," NASA CR-2205, March 1973.
- 6.33. Houbolt, J.C., "Subcritical Flutter Testing and System Identification," NASA CR-132480, August 1974.
- 6.34. Abla, M.A., "The Application of Recent Techniques in Flight Flutter Testing," NASA SP-415, 1976, pp 395-411.
- 6.35. Ibrahim, S.R., "A Time Domain Vibration Test Technique," Ph.D. Thesis, The University of Calgary, Calgary, Alberta, Canada, 1973.
- 6.36. Ibrahim, S.R., "Limitations on Random Input Forces in Randomdec Computation for Modal Identification," Shock and Vibration Bulletin, No. 50, Part 3, September 1980.
- 6.37. White, M.F. and White, R.G., "Frequency Response Testing in a Noisy Environment, or with a Limited Power Supply," Journal of Sound and Vibration, Vol. 48, No. 4, 1976.

- 6.38. White, R.G. and Pinnington, R.J., "Practical Application of the Rapid Frequency Sweep Technique for Structural Frequency Response Measurement," The Aeronautical Journal of the Royal Aeronautical Society, May 1982.
- 6.39. Soovere, J., "The Effect of Acoustic/Thermal Environments on Advanced Composite Fuselage Panels," Journal of Aircraft, Vol. 22, No. 4, April 1985.
- 6.40. Halvonsen, W.C. and Brown, W.L., "Impulse Technique for Structural Frequency Response Testing," Sound and Vibration, November 1977.
- 6.41. Gordon, R.W., Wolfe, H.F. and Talmadge, R.D., "Modal Investigation of Lightweight Aircraft Structures Using Digital Techniques," AFFDL-TR-77-124, 1977.
- 6.42. Soovere, J., "Dynamic Response of Flat Integrally Stiffened Graphite/Epoxy Panels Under Combined Acoustic and Shear Loads," Recent Advances in Composites in the United States and Japan, Editors J.R. Vinson and M. Taya, ASTM STP 864, 1985.
- 6.43. White, R.G., "Use of Transient Excitation in the Measurement of the Frequency Response of Systems with Nonlinearities Arising from Large Deflections," I.S.V.R. Technical Report No. 27, February 1970.
- 6.44. Holehouse, J., "Sonic Fatigue Design Techniques for Advanced Composite Aircraft Structures," AFWAL-TR-80-3019, April 1980.
- 6.45. Garba, J.A., Wada, B.K., and Chen, J.C., "Summary of Galileo Spacecraft Nodal Test Activities," AIAA Dynamics Specialists Conference, Paper No. 84-1072, May 1984.

- 6.46. Chen, J., "Evaluation of Modal Testing Methods," AIAA Dynamics Specialists Conference, Paper No. 84-1071, Palm Springs, California, May 1984.
- 6.47. Trubert, M., "Assessment of Galileo Modal Test Results for Mathematical Model Verification," AIAA Dynamics Specialists Conference, Paper No. 84-1066, Palm Springs, California, May 1984.
- 6.48. Chan, J.C. and Hunt, D.L., "Application of Multiple Input Random and Polyreference Analysis Techniques to the Galileo Spacecraft Modal Test," AIAA Dynamics Specialists Conference, Paper No. 84-1069, Palm Springs, California, May 1984.
- 6.49. Stroud, R.C., Pamidi, M.R. and Bausch, H.P., "Some Measurements and Analysis Methods used in the Galileo Spacecraft Modal Survey," AIAA Dynamics Specialists Conference, Paper No. 84-1069-CP, Palm Springs, California, May 1984.
- 6.50. Pappa, R.S. and Juang, J., "Galileo Spacecraft Modal Identification Using an Eigensystem Realization Algorithm," AIAA Dynamics Specialists Conference, Palm Springs, California, May 1984.
- 6.51. Clarkson, B.L. and Mercer, C.A., "Use of Cross Correlation in Studying the Response of Lightly Damped Structures to Random Forces," AIAA Journal Vol. 3, 1965.
- 6.52. Soovere, J. and Clarkson, B.L., "Frequency Response Function from Cross Correlation: Bartlett Weighting Function," AIAA Journal Vol. 5, 1967.
- 6.53. Soovere, J. (Unpublished Research).

SECTION 7

DAMPING IN STRUCTURAL MATERIALS AND STRUCTURES

7.1 INTRODUCTION

The vibration amplitude at resonance is limited only by the damping in the structure. Consequently, prior knowledge of the damping levels within the various aerospace structural materials and in the lightweight aerospace structures made from these materials, would be a great benefit to the design process. Lightweight structures are emphasized since viscoelastic damping can have the greatest beneficial impact on the design of these structures. The purpose here is to review briefly both the damping mechanisms (Section 7.2) and the damping levels (Section 7.3) present in these structures. Because of the increased use of structures in space, the differences between the damping in the earth and space environments need to be discussed.

In this document, damping is presented in terms of the viscous damping ratio ζ . The viscous damping ratio can be converted to loss factor or structural damping, denoted by η , by means of equation 7.1.

$$\eta = 2\zeta \quad (7.1)$$

7.2 BASIC DAMPING MECHANISMS IN STRUCTURES

Most of the damping mechanisms [7.1] are present in stiffened panel type aircraft structures. Consequently, these types of structures represent a good starting point for the review. The damping in these lightweight structures is due to energy loss through acoustic radiation [7.2, 7.3], transmission of the vibration to the surrounding structure [7.4], gas pumping [7.5] and joint friction [7.6, 7.7] at the fastener lines, and internal material damping [7.8]. Obviously, acoustic radiation and gas pumping loss mechanisms do not occur in the space environment. Unmanned spacecraft and satellites

are, generally, constructed with a central structure that supports a number of bolted-on appendages, some of them deployable in space. Consequently, the major source of damping in these structures is due to friction [7.9] generally within the bolted joints, apart from any added active or passive damping. The vibration of the appendages could also produce some acoustic radiation damping during ground vibration tests [7.9] and launch.

7.2.1 Acoustic Radiation

Acoustic radiation from stiffened aircraft panel type structures, has been investigated for more than two decades and has, consequently, been the subject of very many papers. The simplest of the theories, for predicting radiation damping, is given in Reference [7.3] for both simply supported and clamped single panels mounted in an infinite baffle. Based on this work, acoustic radiation damping was, generally, considered to be very small in riveted skin-stiffener type aircraft panels [7.3].

The acoustic radiation damping is proportional to panel area [7.3]. Consequently, if the panels are made large enough, acoustic radiation should become the dominant damping mechanism. This approach was used in a carefully designed experimental study [7.10] in which stiffened graphite/epoxy and Kevlar honeycomb panels were mounted singly in a very large baffle test facility [7.11]. Each panel was installed in a test frame with countersunk fasteners. Jointing compound was used to minimize the effect of gas pumping. The test frame, containing a honeycomb panel, was mounted in the test aperture within the baffle in a manner designed to eliminate the loss of vibration energy to the surrounding structure. The measured viscous damping ratios for these composite honeycomb panels fell into mode-by-mode groups (Figure 7.1). These damping data proved to be repeatable within 10 percent, on reassembly of the test facility from year-to-year. The friction damping at the fastener line was shown to be small, much smaller than originally expected. The material damping was shown to be significant in only the Kevlar honeycomb panels. As a consequence, it was concluded that the dominant contribution to the damping is from the acoustic radiation. The theory

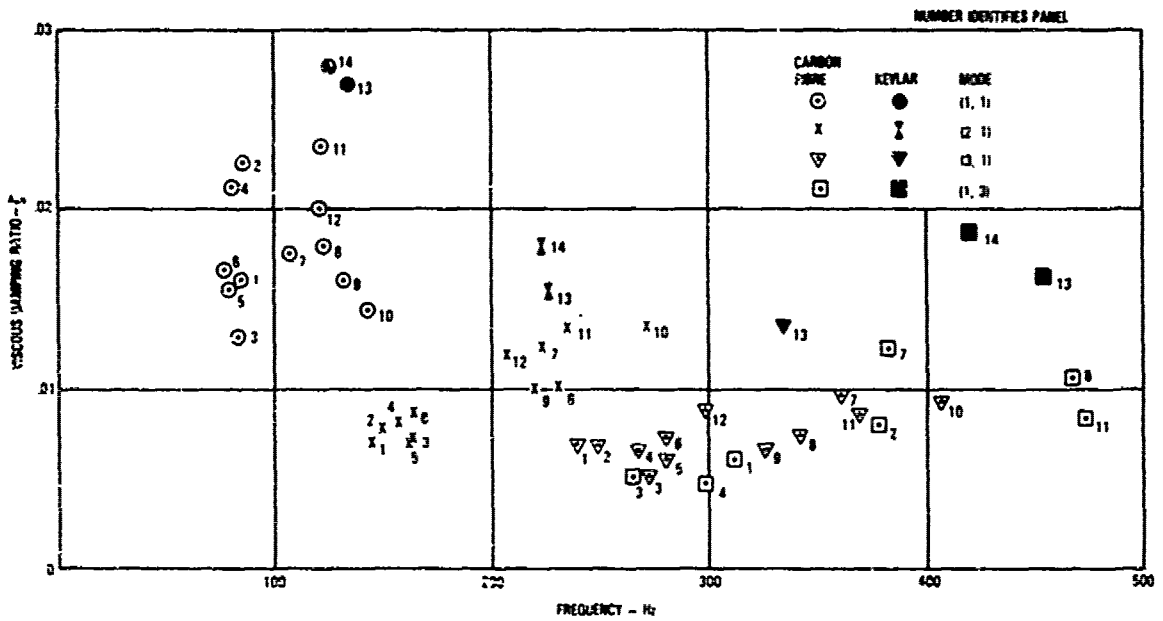


Figure 7.1. Composite honeycomb panel damping measured in a large baffle test facility.

in Reference [7.3] was modified [7.10] for application to larger panels and to include the effects of stiffener flexibility. Since the acoustic radiation damping is highest in the fundamental mode [7.3], the modified acoustic radiation theory was used to predict the damping in this mode. Material damping was added to the predicted damping only for the Kevlar honeycomb panels. A comparison of the measured and predicted damping in the fundamental mode of the composite honeycomb panels is illustrated in Figure 7.2. The theory was also applied to the fundamental mode of the aluminum honeycomb panels [7.12] with clamped edges. The results of this comparison are illustrated in Figure 7.3. In general, the correlation appears to be reasonable for all of these honeycomb panels, when considering the simplicity of the analysis.

Energy losses, due to friction and gas pumping, are nonexistent in integrally stiffened panels. Since the material damping is small in

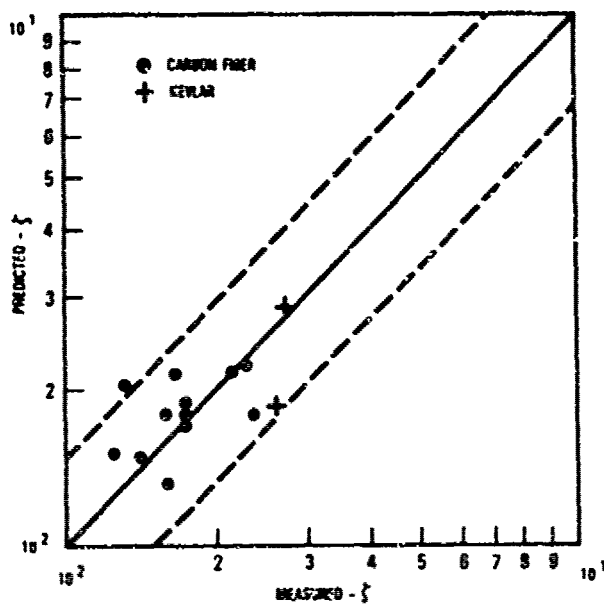


Figure 7.2. Comparison of theoretically predicted and measured viscous damping ratios for fundamental mode of stiffened composite honeycomb panels.

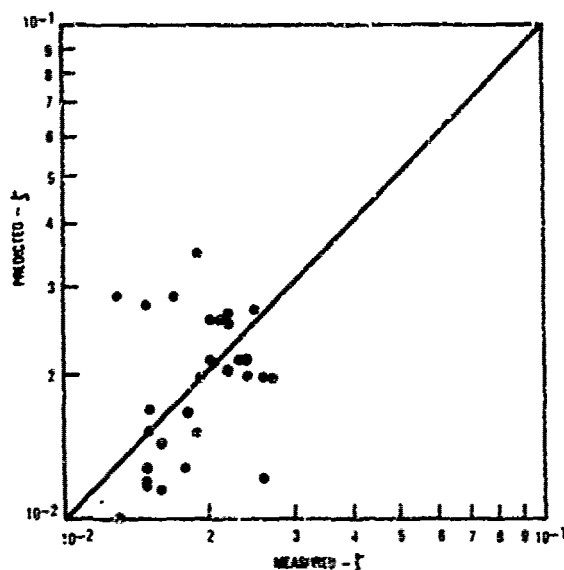


Figure 7.3. Comparison of theoretically predicted and measured viscous damping ratios for fundamental mode of stiffened aluminum honeycomb panels.

graphite/epoxy composites, it is concluded that the damping in integrally stiffened graphite/epoxy panels must be due, primarily, to acoustic radiation. This conclusion was verified [7.13, 7.14] by applying the modified double-sided acoustic radiation theory to an integrally blade-stiffened mini-sandwich panel with a large center bay [7.13], using a sinusoidal approximation to measured mode shapes. Reasonably good correlation (Figure 7.4) was obtained with measured damping data for the fundamental and the higher order panel modes. The cancellation effect [7.3, 7.4], is seen to reduce the damping in the higher order panel modes quite dramatically (Figure 7.4).

The acoustic cancellation effect is also present in panel arrays such as the three-bay integrally J-stiffened graphite/epoxy panels described in Reference [7.13]. The cancellation effect reduced the damping in the fundamental mode of this three-bay panel to a level [7.13] that was an order of

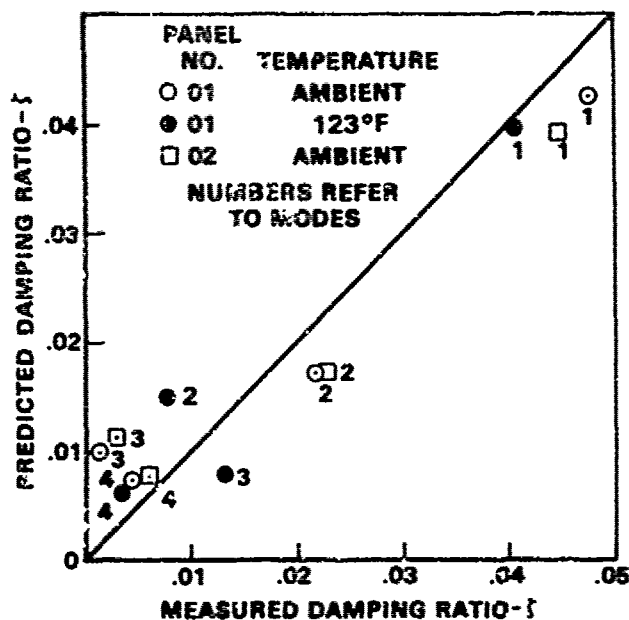


Figure 7.4. Comparison of theoretically predicted and measured viscous damping ratios of blade stiffened mini-sandwich graphite/epoxy panel.

magnitude less than that measured on the mini-sandwich panel with the large center bay. The adjacent bays were vibrating out-of-phase in the fundamental mode. The center bay was just a little larger than the two outer bays. The acoustic radiation damping ratio, predicted by assuming equal bay sizes, was almost two and a half times the measured damping ratio, indicating the importance of using the correct mode shapes. The cancellation effect is also obtained in fastener attached panel arrays in which the out-of-phase vibration of adjacent bays is fully correlated across the stringers. The correlation between the vibration of two panels across a heavy frame is, generally, very low [7.15]. This result allowed the panel array between two frames to be considered separately. When the correlation between two adjacent panels across a stringer is also very low, such as obtained with uneven stringer spacing or with turbulent boundary layer excitation [7.16], the individual panels can be treated as vibrating alone. The sound radiated by such a panel array is equal to the sum of the sound radiated by each panel in the array vibrating alone [7.17].

Acoustic edge conditions also have a significant effect on the damping in stiffened panels. The viscous damping ratio in the fundamental mode of the above composite honeycomb panels dropped down to a value around 0.0035 when removed from the baffle [7.10, 7.11], but remained in the same order of magnitude, as measured in the baffle, for some of the higher frequency modes. The viscous damping ratio in the fundamental mode of a fastener attached stiffened aluminum panel [7.18] was reduced by forty percent to a value around 0.006 (Figure 7.5) when tested later in the unbaffled condition. The viscous damping ratio of 0.0085, measured for the stringer bending mode of a wire suspended unbaffled riveted panel array [7.19] "gave almost the same results" in vacuum. All of the bays vibrate in phase in the stringer bending mode. These results indicate that most, but not all, of the acoustic radiation damping in the lower frequency panel modes is eliminated by the removal of the baffle.

The damping in stiffened aluminum panels remained unaffected by significant axial tension load [7.18], but increased with compression load on approaching panel buckling. A similar increase in damping was obtained in integrally stiffened graphite/epoxy panels on approaching shear buckling [7.20]. It is suspected that this increase in damping may be related to an increase in acoustic radiation.

Acoustic radiation damping, sometimes called air damping, is present to a varying degree in most structures, depending on the structural and acoustic edge conditions. The acoustic radiation damping is lowest in the free-free beams [7.21, 7.22, 7.23, 7.24] and panels [7.11], since the particles of air have to travel laterally from the high pressure regions to the low pressure regions produced by these beams and panels during each vibration cycle. This lateral motion of the air particles is accomplished with a minimum of energy loss. Typical in-air and in-vacuum viscous damping ratios for the first two modes of free-free graphite-epoxy beams [7.22] are illustrated in Figure 7.6. The average contribution from acoustic radiation to the viscous damping ratio of these composite beams is approximately 0.00017. An even lower value was measured in the tests described in Reference [7.23]. The variation of this

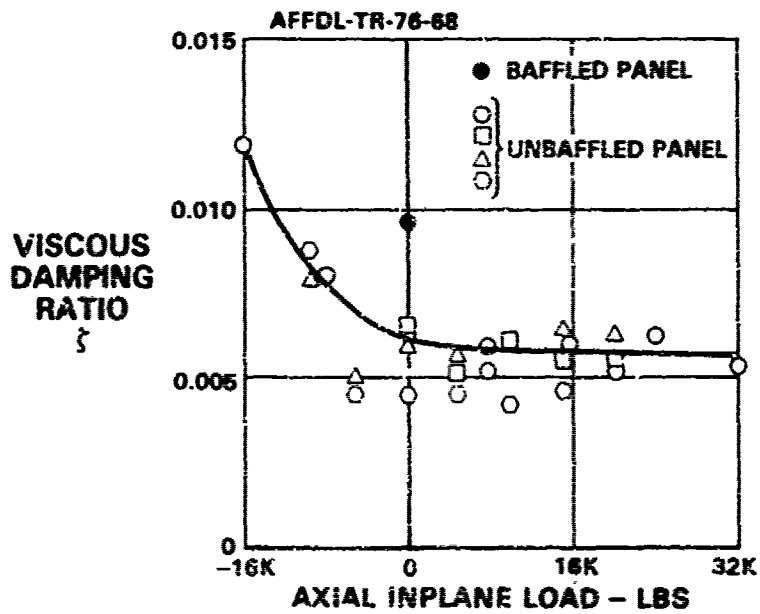


Figure 7.5. Variation of the fundamental mode viscous damping ratio of stiffened aluminum panels with axial inplane load.

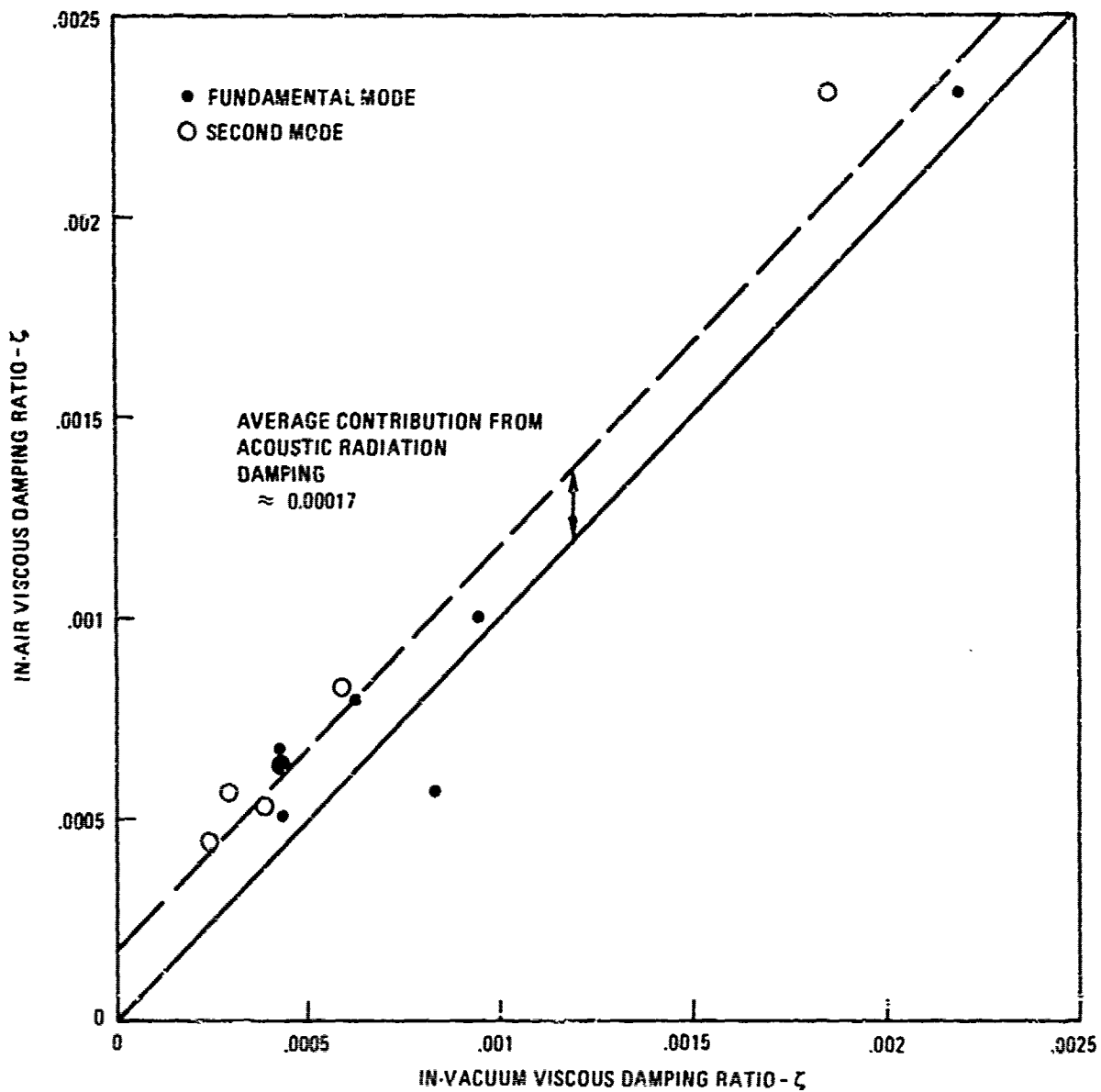


Figure 7.6. Comparison of graphite/epoxy free-free beam damping measured in air and in vacuum.

acoustic radiation damping with amplitude is not expected to be very large. The very low acoustic radiation damping is one reason why the free-free beam vibration tests are used to provide a quick measure of the material damping in aerospace structural materials.

The acoustic radiation or air damping in cantilever beams can be quite significant [7.25, 7.26, 7.27], since the air particles have to flow from one side of the beam to the other. The energy loss is also expected to be amplitude dependent since the path length traveled by the air particles increases with the amplitude. In fact, the acoustic radiation damping increases proportionally with velocity at low vibration amplitudes and with velocity squared at high vibration amplitudes [7.25]. At low amplitudes, it is also a function of the cantilever beam length to thickness ratio [7.25] as illustrated in Figure 7.7. Air damping is also a function of the surface area for cantilever plates [7.26]. Thus, care must be taken when using cantilever beams to measure material damping.

In conclusion, acoustic radiation is the dominant source of damping in stiffened aluminum and composite honeycomb panels as well as integrally stiffened composite panels. The damping in fastener attached skin-stiffener type aircraft panels is due primarily to a combination of acoustic radiation and friction damping at the fastener lines.

7.2.2 Friction Damping

7.2.2.1 General Aerospace Structures

Friction or Coulomb damping is generated by slippage between two contacting surfaces. The damping force is, generally, assumed to be equal to the product of the coefficient of sliding friction and the normal force, but independent of the velocity. In an experiment, described in Reference [7.28], the equivalent coefficient of sliding friction was shown to be independent of both frequency and maximum velocity, but dependent on the normal force, as illustrated in Figure 7.8. The equivalent coefficient of sliding friction was determined from the area of the nearly rectangular measured force - slip

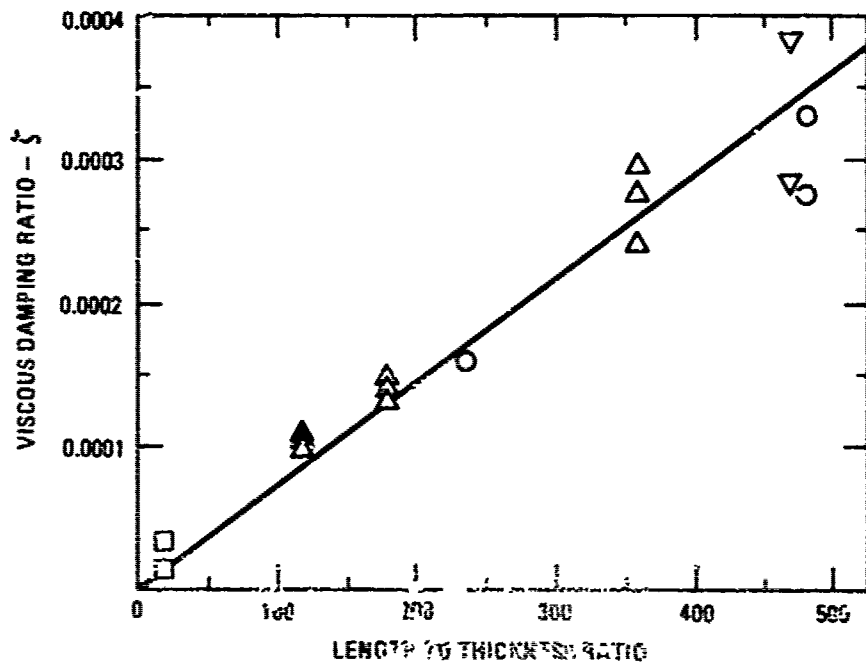


Figure 7.7. Low-amplitude acoustic radiation damping in the fundamental mode of thin cantilever beams as a function of length-thickness ratio.

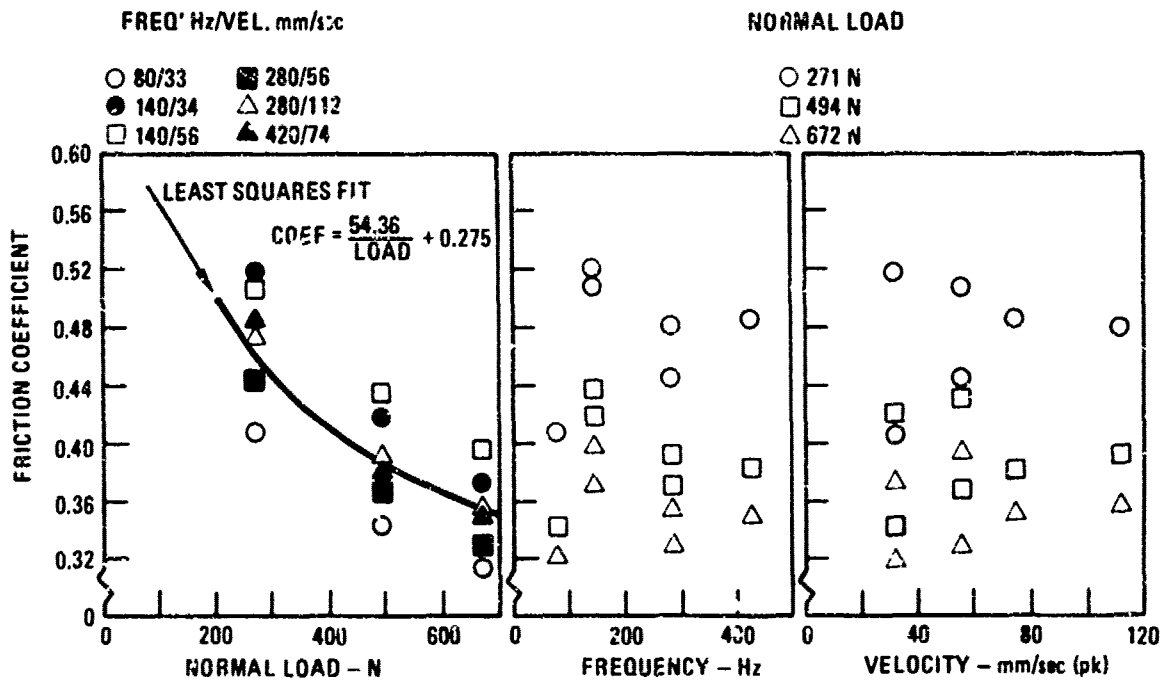


Figure 7.8. Variation of equivalent friction coefficient during sinusoidal motion with normal load, frequency and maximum relative velocity.

loops. The energy loss per cycle, and therefore, the coefficient of friction, can change with time as the contacting surfaces become smooth with wear [7.29]. A review of dry friction damping technology and the basic analytical models used to represent dry friction is also contained in Reference [7.28].

In bolted joints, a threshold force level must be exceeded before slippage can take place. In some multi-jointed structures, for example, complete aeroplanes, more and more joints begin to slip with a progressively increasing excitation level, producing both an increase in the measured damping and a reduction in the resonant frequencies of the modes, as a function of the excitation level. The damping in structures can, in fact, be optimized by controlling the interface slip in joints [7.30, 7.31, 7.32]. In

unmanned spacecraft, the nonlinear behavior of joints can be even more complex [7.33], as illustrated in Figure 7.9 for the high gain antenna on the Galileo spacecraft. The level of the damping in unmanned spacecraft and satellites has been established [7.34, 7.35] during modal testing on the ground (Figures 7.10 and 7.11). Limited damping data measured on a spinning satellite in orbit [7.34] indicate that similar damping levels are also encountered in orbit, as illustrated in Figure 7.10. These results indicate that friction damping is the major source of damping both on the ground and in orbit. Additional sources of information for measured spacecraft modal damping are contained in Reference [7.36].

The damping of vehicles used in launching the above spacecraft is also important for use in launch loads analysis. Such a damping schedule [7.34] is illustrated in Figure 7.12 for the Titan Launch Vehicle. The equivalent viscous damping ratios were also measured [7.37] on the space shuttle ascent vehicle during Stage 1, Stage 2 and Orbiter ground vibration tests. Stage 1 test involved the ascent vehicle consisting of the Orbiter, the external tank and the two solid propellant motors while Stage 2 test involved only the Orbiter and the external tank. The measured damping ratio during launch, ranged between 0.016 to 0.024, with an average value around 0.021. These data were in reasonable agreement with the average value of 0.017 (Figure 7.13)

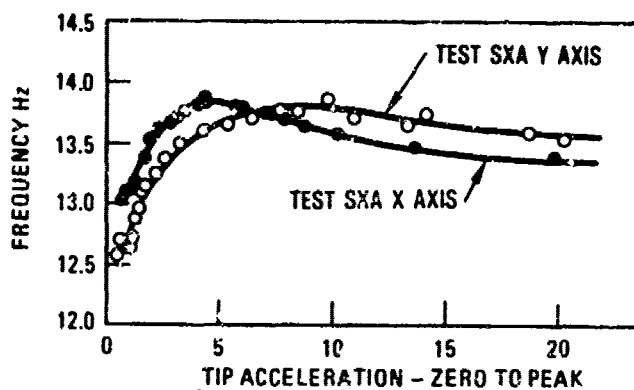


Figure 7.9. Variation of the Galileo spacecraft high gain antenna frequencies with amplitude.

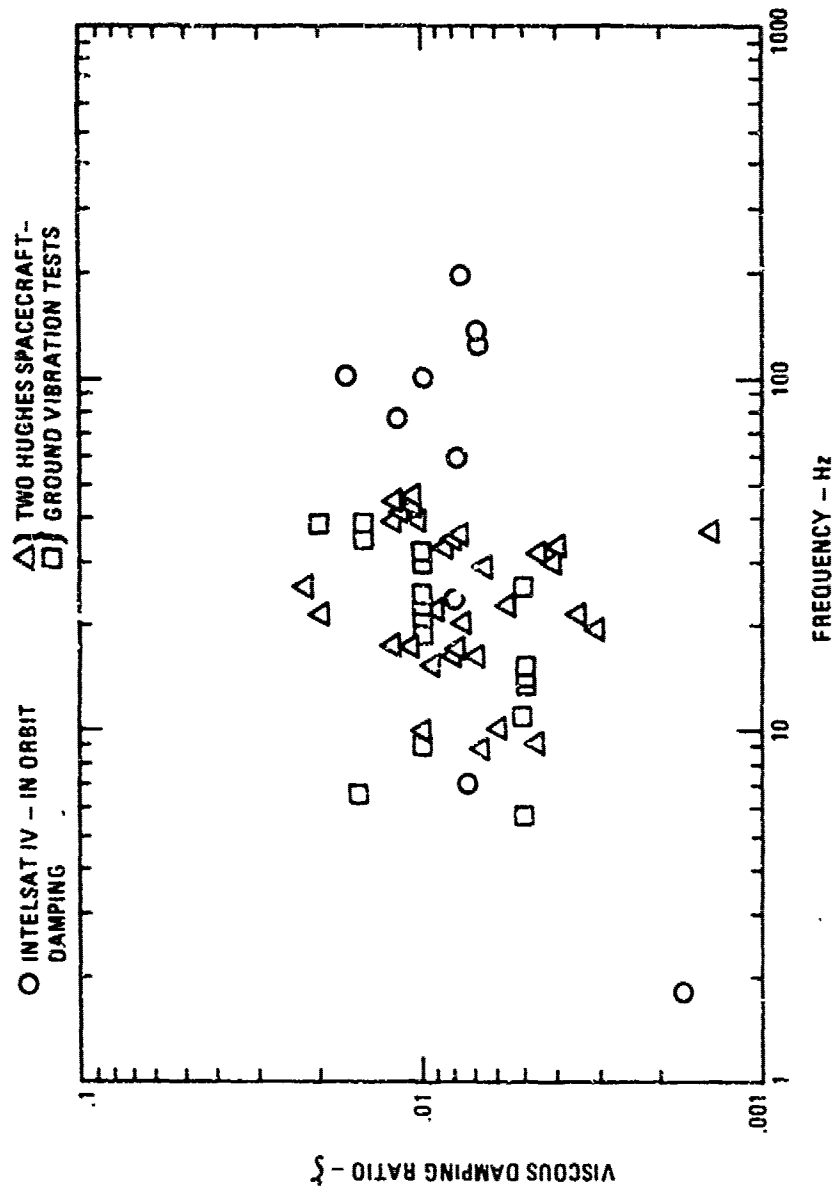


Figure 7.10. Comparison of typical damping levels measured on the ground and in orbit.

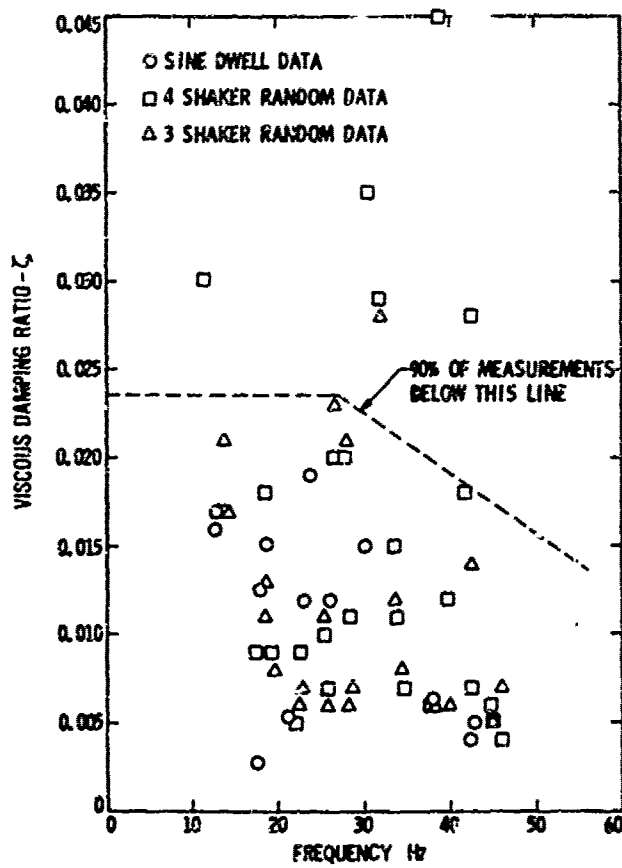


Figure 7.11. Typical damping levels measured during Galileo spacecraft modal tests.

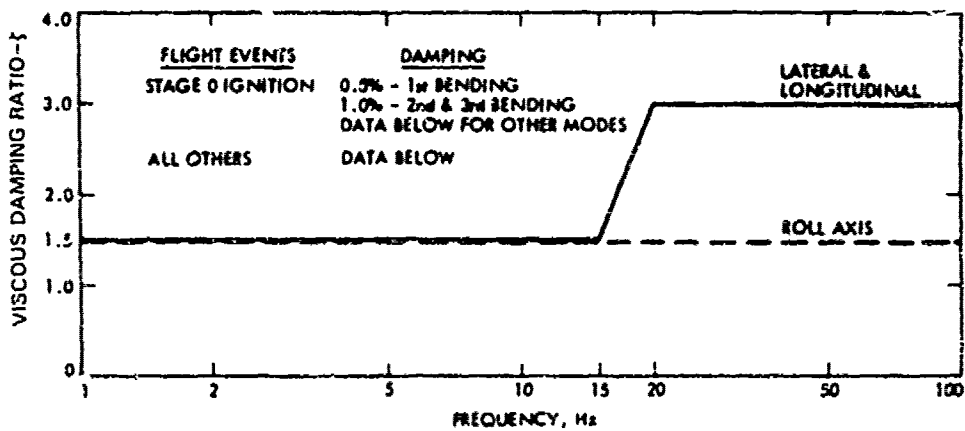


Figure 7.12. Damping schedule for Titan launch vehicle.

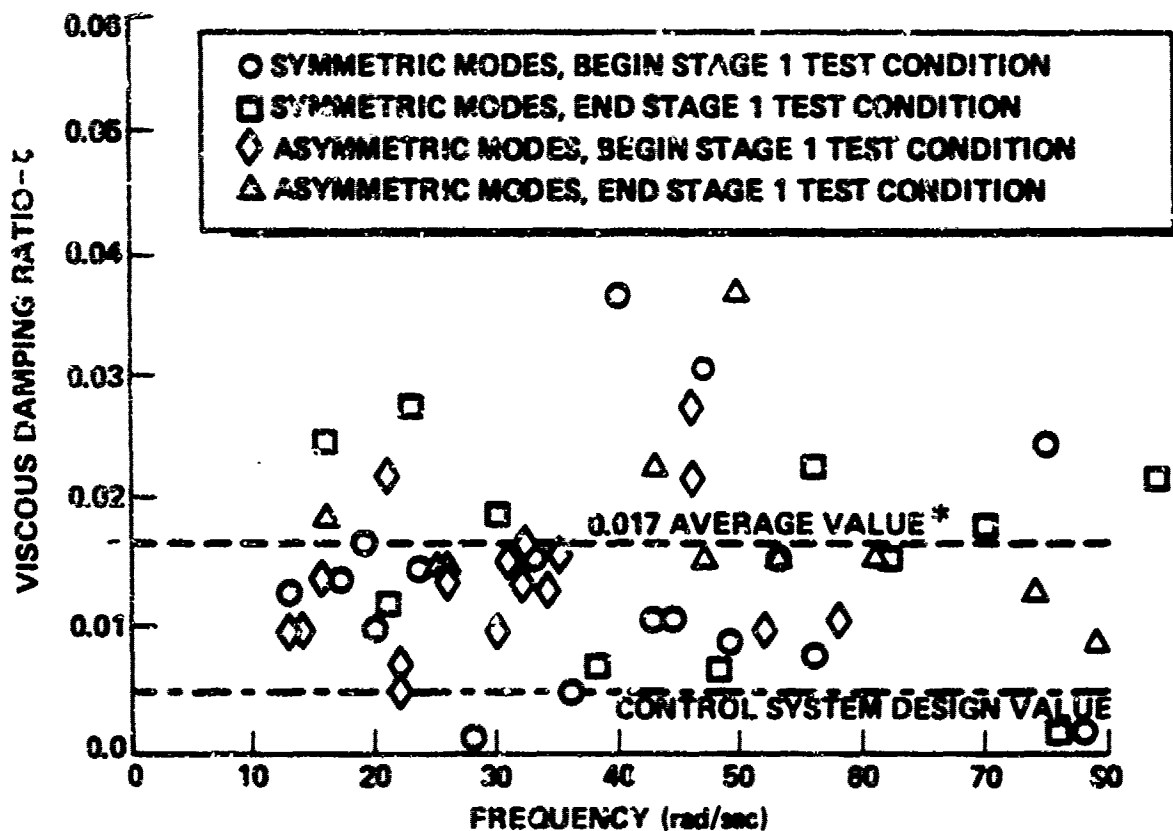


Figure 7.13. Equivalent viscous damping ratios (damping factors) measured during space shuttle ascent vehicle Stage 1 vibration tests.

measured during the Stage 1 test. The average damping ratios, measured during the Stage 2 and Orbiter ground vibration tests, were 0.021 and 0.032, respectively. Generally, the lower levels of the measured damping are used in the design of control systems (Figure 7.13) for these vehicles.

Clip-on joints [7.38, 7.39] may also be used on large space structures such as the space station. Flexibility in these joints will provide friction damping for these structures. Models for representing the friction energy dissipated in these joints are currently being developed [7.40]. However, if high pointing accuracies are required, the supporting structure may have to be fabricated with rigid joints. The resulting damping in the structure will be due entirely to material damping. In this event, the use of active and passive damping will be required to suppress any excessive vibration levels, since the material damping is usually very small in most aerospace structural materials.

Friction damping has been used to suppress resonant vibrations in other fields of engineering such as in shock and vibration isolation by means of multistranded cable vibration isolators [7.40] and in turbine engines [7.41, 7.42], to name a few. Welded (or integral) components such as compressor blades, turbine blades, compressor guide vanes and inlet guide vanes, have a tendency to develop cracks from excessive vibration levels, due to the very low inherent (material) damping in such components. The measured viscous damping ratios, obtained from an integrally machined turbine stage [7.41], were found to fall between 0.00032 to 0.00062, which is comparable to the level of the material damping. Indications are [7.41, 7.42] that friction damping produced by root slip, could increase the blade damping by an equivalent viscous damping ratio of around 0.001. This level of damping is quite small but still significantly greater than the measured damping in the integrally machined turbine stage. The blade damping does increase with the vibration amplitude [7.41, 7.42], but decreases again with increased centrifugal force [7.42].

7.2.2.2 Stiffened Panel Structures

Friction damping, at the fastener lines of stiffened panels, was first investigated many years ago [7.6, 7.7] and continues to be a source of interest in more recent years [7.1, 7.19]. The earlier studies revealed a complicated behavior depending on the load amplitude at the joint. In a more recent study [7.19], the damping of a wire suspended unbaffled panel array, vibrating in the stringer bending mode, was overestimated by a factor of three based on the friction damping measured in simple crossed double cantilever coupon tests, in a vacuum. The measured friction related joint dissipation coefficient, which is proportional to the loss factor, was found to be constant with the joint load amplitude [7.19].

The model assumed a tension-compression type loading on the fastener. A recent dynamic panel edge theory [7.10, 7.43], indicates that the fastener is subjected, basically, to a tension-tension type loading, during the reverse bending cycle of the panel, in both the stringer torsion and bending modes. A net positive-positive bending moment is also acting on the fastener during

the same panel bending cycle in the stringer torsion mode, assuming that a sagging panel bending moment is positive. The above behavior is due to the local deformation produced in the panel during the reverse bending cycle when bending over and away from the stiffener flange takes place. These deformations combine to produce a panel upper-surface fastener-line strain, normal to the panel edge, that is purely compressive during the panel reverse bending cycle. The validity of the above theory has been verified by stress coat patterns in the vicinity of the fastener line [7.44] and by the correlation achieved between the predicted rms strains and those measured on both aluminum honeycomb [7.12, 7.45, 7.46], and composite honeycomb [7.10] panels. The lower surface of the panel makes line contact with the adjacent stiffener flange edges alternately during the stringer torsion mode and simultaneous contact during half of the panel bending cycle in the stringer bending model. Since the crossed double cantilever coupon made line contact along four edges during half of the panel bending cycle, as acknowledged in Reference [7.19], the predicted panel array friction damping based on the coupon data, should be much lower.

The results, in Figure 7.8, show that the sliding friction coefficient is independent of frequency and velocity. The results in Reference [7.19] indicate that the loss factor is independent of the load amplitude at the fastener line, at least for skin-stiffener type panels. It is, therefore, reasonable to conclude that the friction damping at the fastener line of stiffened panels is indeed a constant, dependent only on the number of fasteners along the panel periphery [7.47].

7.2.3 Gas Pumping at the Fastener Lines

The damping in the crossed double cantilever coupon [7.19] was increased by a factor of two when tested in air. This increase was attributed to air or gas pumping in the joint region. Gas pumping [7.1, 7.5] is also encountered in fastener attached stiffened panel type structures vibrating in air. The damping is due to the local displacement of air produced by the relative motion between the stiffener flange and the panel during the vibration cycle.

The mechanism of gas pumping at the fastener lines is, thus, well understood and its contribution to the panel damping generally predictable [7.2, 7.5]. The gas pumping contributes to the panel damping generally at the higher panel frequencies.

7.2.4 Material Damping

The energy dissipated internally within a material is known as material damping. Knowledge of the damping in aerospace structural materials has taken on a greater importance because of the increased activity in space. A considerable amount of information is available on the internal damping in metals. Some of the internal mechanisms responsible for producing the material damping in metals have been identified. More attention is currently being focused on the damping in composite materials. Investigation into the material damping in composites started in the late 1950s. The effort has expanded since that time, to include newer materials such as metal matrix composites. Of interest are the effects of the high stiffness fibers and whiskers on the material damping of the matrix metal. The resin, the type of fiber and the fiber orientation can also affect the material damping of polymer matrix composites. In general, the material damping is very low in both aerospace metals and most uniaxial composites. The low level of the damping also places great demands on the test methods used to measure such data.

This section contains a brief introduction to the basic theoretical representation of the material damping, a brief discussion on the damping mechanisms in metals, and a summary of typical measured material damping levels in both metals and composites. The more recent test methods used in obtaining the damping data are also discussed. In general, the trend has been to use resonant testing under near vacuum conditions, after first demonstrating that the damping due to the fixture is small compared to the measured material damping. Both because of its very low material damping and the theoretical predictability of this damping, aluminum alloy has become the standard material for calibrating such test facilities.

7.2.4.1 Theoretical Basis for Material Damping

No material is perfectly elastic. When the material is cycled under load, a hysteresis loop is obtained when the resulting stress, σ , is plotted against the strain, ϵ . The area enclosed within the hysteresis loop represents the energy dissipated per cycle by the material. This can be expressed, in terms of the instantaneous stress, σ , and strain, ϵ , by

$$D = \int \sigma \, d\epsilon \quad (7.2)$$

where D is the specific damping energy per unit volume. It provides a measure of the capability of a given homogeneous material to dissipate energy under cyclic loading. In the low to intermediate stress range, the specific damping energy is assumed to obey the simple relationship [7.4]

$$D = J \sigma^n \quad (7.3)$$

for many materials, where J is a constant and n takes on a value between 0.5 and 2.5. Both J and n are determined experimentally. The above model for the material damping is linear when $n = 2$. Other linear models for the material damping are discussed in Reference [7.49].

It is more convenient to represent the energy dissipated in a nondimensional form by relating the energy, D_s , dissipated in a volume, v , of the material to the maximum strain energy, U_s , stored in the material. Since, from Section 2.0,

$$D_s = \frac{2\pi}{v} \int_v \sigma \, \dot{\epsilon} \, dv \quad (7.4)$$

and

$$U_s = \frac{1}{2} \int_v \sigma_o \epsilon_o \, dv \quad (7.5)$$

the loss factor η is given by

$$\eta = D_s / 2\pi U_s \quad (7.6)$$

and the viscous damping ratio (equation 7.1) by

$$\zeta = D_s / 4\pi U_s \quad (7.7)$$

In equations 7.4 and 7.5, $\dot{\epsilon}$ is the strain rate, ω is the circular frequency and, σ_0 and ϵ_0 are the maximum (zero to peak) stress and strain amplitudes, respectively. The material damping is often expressed in terms of the specific damping capacity, ψ , given by

$$\psi = D_s / U_s \quad (7.8)$$

7.2.4.2 Material Damping Mechanisms in Metals

There are many linear and nonlinear internal damping mechanisms in metals [7.48, 7.50, 7.51, 7.52]. A linear damping involves a hysteretic stress-strain loop that is basically elliptical in form, with the energy dissipation proportional to the square of the strain. The linear damping is produced by a relaxation mechanism involving thermal processes within the material. The viscous damping ratio, for materials exhibiting these characteristics, is generally dependent on frequency and temperature but not stress amplitude. For example, the major contribution to the material damping of aluminum beams undergoing flexure at room temperature, is due to heat flow from the warmer compression fibers to the cooler tension fibers. The viscous damping ratio due to this linear relaxation mechanism can be calculated from the relationship

$$\zeta = \frac{\pi ET}{2c} \frac{f/f_R}{1 + (f/f_R)^2} \quad (7.9)$$

where

- T = temperature
- α = thermal expansion coefficient
- c = specific heat
- E = Young's modulus
- f_R = relaxation frequency
- f = measurement frequency

The relaxation frequency, derived from the work described in Reference [7.50], is given by

$$f_R = \frac{\pi K}{2 h^2 c} \quad (7.10)$$

where K is the thermal conductivity and h is the beam thickness. A comparison between the predicted and measured [7.26, 7.53] damping is illustrated in Figure 7.14. Additional comparisons between the predicted and measured aluminum material data are given in References [7.24] and [7.28].

Nonlinear damping in metals is the result of the following mechanisms:

- (i) Deformation of inclusions such as graphite flakes in hard metal matrices associated with composition alloys, in which the dissipation of energy takes place within and along the boundaries of the inclusion.
- (ii) Magnetomechanical effect in Ferromagnetic alloys, involving the dissipation of energy during domain wall movements as a result of an externally applied stress or magnetic field.
- (iii) Dislocation movements at high stress amplitudes in metals such as magnesium and its alloys. A linear damping mechanism is obtained at low stress amplitudes.

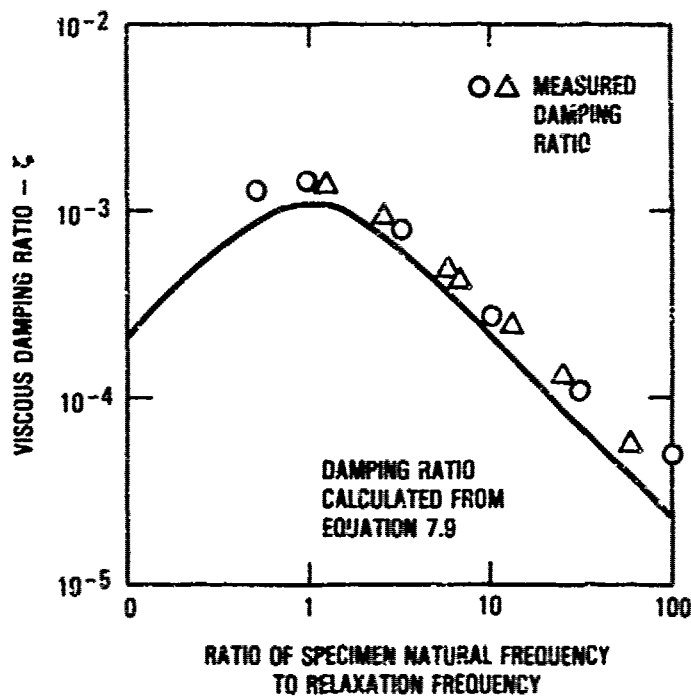


Figure 7.14. Comparison of predicted and measured material damping in aluminum.

- (iv) Two phase boundary movement in metals such as antiferromagnetic and thermoelastic martensitic alloys.

The damping, in most but not all of the metals with nonlinear damping mechanisms, tends to vary with the dynamic stress amplitude. The damping in metals exhibiting the fourth type of nonlinear damping mechanisms described above, tends also to vary with temperature, whereas the damping is constant with temperature for the metals in the other three categories. The damping levels in metals with both linear and nonlinear damping mechanisms are summarized in the following section.

7.2.4.3 Material Damping Levels in Metals and Other Materials

The measured material damping in aluminum and its alloys is very low (Figure 7.14) ranging between a viscous damping ratio of 0.00005 and 0.0012

with the possibility of even lower levels at higher frequencies. Other aerospace metals such as alloy steel have a slightly higher material damping. Typical material damping values for a number of structural materials, are listed in Table 7.1 based on data from Reference [7.51]. The damping mechanisms for a range of materials [7.52] are listed in Tables 7.2 and 7.3 while the corresponding variations in the viscous damping ratios with zero-to-peak stress amplitude are illustrated in Figures 7.15 and 7.16, respectively. The data in these figures have been adapted from Reference [7.52]. A comprehensive summary of the material damping in both metallic and nonmetallic materials is contained in Reference [7.55], in non-reinforced plastics in Reference [7.56] and for highly damped metals in Reference [7.51]. The damping mechanism in these highly damped metals, called 'lidamets,' are summarized in Table 7.4 while the composition of the metals are summarized in Table 7.5. The data in Reference [7.51] include variation of the damping with temperature, dynamic strain amplitude, static strain and frequency. For quick reference purposes, the viscous damping ratios measured at a stress level equal to one tenth of the yield stress, are illustrated in Figure 7.17 together with the data for aluminum and steel for comparison.

7.2.4.4 Material Damping in Composites

The earliest measurements of the material damping in composites were made usually in air using either cantilever [7.57, 7.58] or free-free beam flexure specimens. The free-free beams were supported at the outermost nodal lines either by two polyurethane foam knife edges [7.23] or by two vertical strings [7.11, 7.24, 7.58, 7.59, 7.60]. Free-free [7.59, 7.60] and damped [7.22, 7.23] beam specimens were also tested in torsion to obtain the shear damping. The damping devices used with the cantilever specimens [7.58], the foam knife edges [7.24] and the air (acoustic radiation) damping [7.24, 7.58] all contributed to the damping of the specimens, in addition to the material damping. As previously mentioned, the air damping can be especially significant in single and double cantilever test specimens, a result that encouraged testing under near vacuum conditions [7.58, 7.61, 7.62]. Although the air damping is lowest in the free-free beams (Figure 7.6), this damping can vary from test specimen to test specimen [7.61]. Nevertheless, free-free beam tests in air

TABLE 7.1. TYPICAL VISCOUS DAMPING RATIOS FOR STRUCTURAL MATERIALS
AT SMALL AMPLITUDES AND ROOM TEMPERATURE IN THE AUDIO
FREQUENCY RANGE

Material	Viscous Damping Ratio
Aluminum	0.00005
Brass, bronze	<0.0005
Brick	0.005 - 0.01
Concrete	
Light	0.0075
Porous	0.0075
Dense	0.005 - 0.025
Copper	0.001
Cork	0.065 - 0.085
Glass	0.0003 - 0.001
Gypsum board	0.003 - 0.015
Lead	0.00025 - 0.001
Magnesium	0.00005
Masonry blocks	0.0025 - 0.0035
Oak, fir	0.004 - 0.005
Plaster	0.0025
Plexiglass, Lucite	0.01 - 0.02
Plywood	0.005 - 0.0065
Sand, dry	0.3 - 0.6
Steel, iron	0.00005 - 0.0003
Tin	0.001
Wood fiberboard	0.005 - 0.015
Zinc	0.00015

TABLE 7.2. IDENTIFICATION AND DAMPING MECHANISMS FOR MATERIALS
IN FIGURE 7.15

Sample Number	Material	Damping Mechanism
1	Plexiglass	Viscoelastic
2	Polystyrene	Viscoelastic
	Cast magnesium 99.9% pure	Dislocation
4	Mg - 0.6% Zn	Dislocation
5	Mg - 0.9%	Dislocation
6	Mg - 8.1% Al, 0.5% Zn, 0.2% Mn	Dislocation
7	Austenitic steel Oil quenched from 1000°C, 16 hours, 650°C	Dislocation
8	Pearlitic gray cast iron 3.63% C, 3.39% Si, 0.54% Mn	Graphite flake
9	Pearlitic gray cast iron 3.01% C, 2.49% Si, 0.53% Mn	Graphite flake
10	Pearlitic nodular cast iron	Graphite nodules
11	Mn - 35.9% Cu, 0.24% Fe, Heat 1 hr, 790°C, quench 2 hr, 450°C	Two phase material
12	N - 155 Alloy, Fe 21.7% Cr, 1.9% W, 0.15% C, 19.47 Ni, 1.74% Mn, 19% Co, 0.76% Nb, 2.76% Mo, 0.37% Si quenched, aged	High Temperature Damping (1500°F)
13	Stellite Co - 0.45% C, 1.4% Fe, 0.42% Mn, 24.8% Cr, 0.93% Si, 10.4% Ni, 7.26% W as cast	High Temperature Damping (1500°C)

TABLE 7.2 (continued)

Sample Number	Material	Damping Mechanism
14	Ti - 3.9% Al, 4.3% Mn, 0.1% C annealed	High Temperature Damping (600°F)
15	Sandvik Steel Fe - 1% Cr, 0.2% Si, 1% C, 0.26% Mn, 0.24% Mo, quenched tempered	Not available
16	Free cutting brass Cu - 35% Zn, 3% Pb	Not available
17	Al - 5.5% Cu, 0.5% Pb, 0.5% Bi	Not available
18	Al - 4% Cu, 0.5% Mg, 0.5% Mn	Not available
19	Naval brass Cu - 39% Zn, 1% Sn	Not available

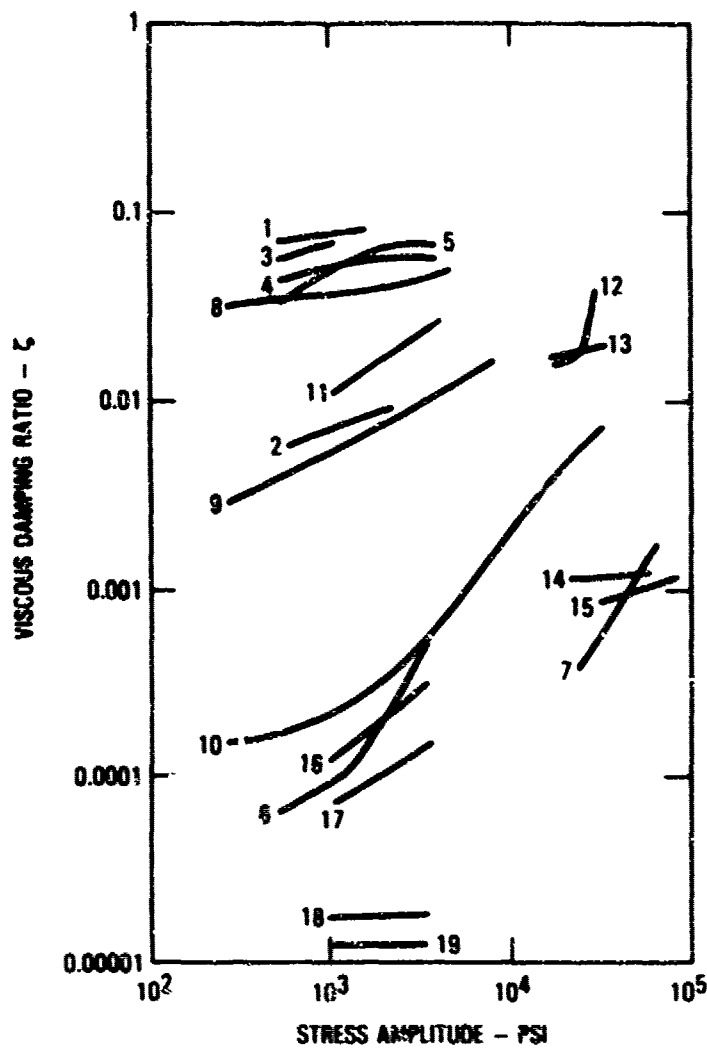


Figure 7.15. Variation of the viscous damping ratio with stress amplitude for materials listed in Table 7.2.

TABLE 7.3. IDENTIFICATION FOR MATERIALS IN FIGURE 7.16 HAVING
MAGNETOMECHANICAL DAMPING MECHANISM

Sample Number	Material
1	Fe - 3.3% Si, anneal 5.5 hr at 1200°C
1S	Sample 1 Saturation Magnetic Field
2	Pure Nickel
2S	Sample 2 Saturation Magnetic Field
3	NiVCO 73.5% Co, 22.5% Ni, 1.8% Ti, 1.1% Zr
4	403 Steel Alloy Fe - 12% Cr, 5% Ni
5	Mild Steel 0.28% C, 0.2% Si, 0.79% Mn, 0.12% Cu, 0.14% Ni, 0.1% Cr, annealed 18 hrs at 625°C
5S	Sample 5 Saturation Magnetic Field
6	Carbon Steel 0.42% C, 0.32% Si, 0.997 Mn, 0.09% Ni, 0.06% Cr, normalized
6S	Sample 6 Saturation Magnetic Field

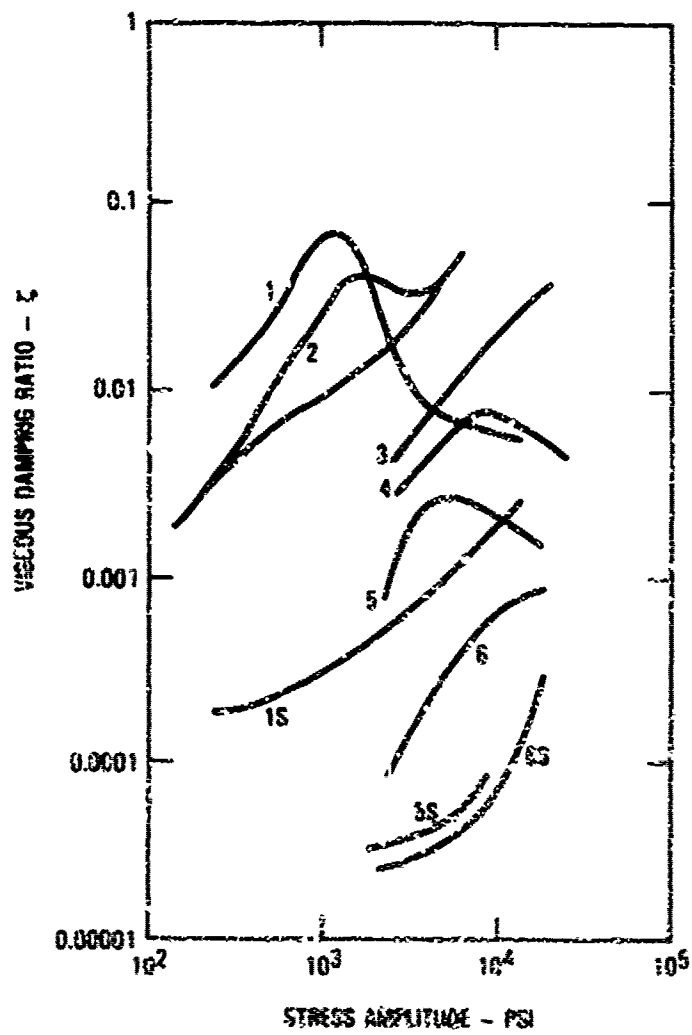


Figure 7.16. Variation of the viscous damping ratio with stress amplitude for materials listed in Table 7.3.

TABLE 7.4. CLASSIFICATION OF HIGH DAMPING METALS

Type	Damping Mechanism	Alloy System	Example
(i) Natural Composite	Viscous or plastic flow across phase boundaries between matrix and the second phase.	Fe-C-Si	Gray cast iron. Rolled nodular iron.
(ii) Ferromagnetic Alloys	Magneto-mechanical static hysteresis due to irreversible movement of ferromagnetic domain walls	Fe and Ni Fe-Cr Fe-Cr-Al Fe or Ni-alloys Co-Ni-Ti	T.D. Nickel 12% Cr-steel Silentalloy Gentalloy Vacrosil NIVCO
(iii) Alloys Based on Dislocation Damping	Static hysteresis due to the movement of dislocation loops, breaking away from pinning points.	Mg Mg-0.6% Zr MG-Mg Ni 2	KIXI-alloy
(iv) Alloys with Movable Twin- or Phase Boundaries	Movement of twin boundaries martensite-martensite boundaries and boundaries between martensite and the matrix-phase	Mn-Cu Mn-Cu-Al Cu-Zn-Al Cu-Al-Ni Ti-Ni Co-Fe	Sonoston Ingramute Proteus Nicalinol

TABLE 7.5. SUMMARY OF ALLOYS TESTED WITH TYPE OF DAMPING MECHANISM

Alloy System and (Type)	Composition	Name
Fe-C-Si (I)	Fe - 3~3, 5% C - 2~2, 5% Si	Cast Iron
Fe-Cr-Mo (II)	Fe - 12% Cr - 3% Mo	Gentalloy
Fe-alloy (II)	Fe - 23% Cr - 3% Al	Vacrosil
Mg (pure) (III)	Mg	Magnesium
Mg-Zn- (III) Rare Earth	Code S499-1	S499-1
Mg-Zn-Cu-Mn (III)	Code S730-6	S730-6
Mn-Cu (IV)	54% Mn - 37% Cu - 4% Al -- 3% Fe - 2% Ni	Sonoston
Ti-Ni (IV)	Ti - 51 at % Ni	Nitinol
Cu-Zn-Al (IV)	Cu - 13~21% Zn - 2~ 8% Al	Proteus
Cu-Zn-Al-Ni (IV)	Cu - 13~21% Zn - 2~ 8% Al - 0~ 2% Ni	Proteus

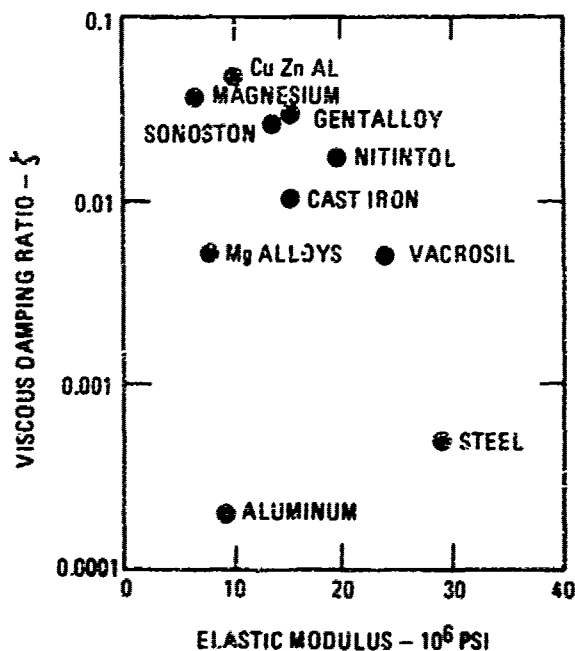


Figure 7.17. Viscous damping ratio for various alloys at a stress level equal to one tenth of the yield stress as a function of the elastic modulus.

provided some of the earliest indications of the low level of damping present in the unidirectional composites. Similar damping measurements have also been performed on free-free graphite/epoxy and Kevlar honeycomb panels that were also supported by two strings [7.11]. These and other test methods are discussed in more detail in Section 7.2.4.5.

Problems were also encountered in fabricating the graphite/epoxy test specimens on account of the resin rich prepreg available at the time. As a consequence, the early composite test specimens tended both to be resin rich and to have a high void content. The importance of fiber volume on the damping [7.23] of composites (Figure 7.18). In addition to the modulus, was recognized early in the damping studies, although the variation of the damping with fiber volume (Figure 7.19) did not always yield the expected results [7.63]. Some problems were encountered in the adhesion between the resin and

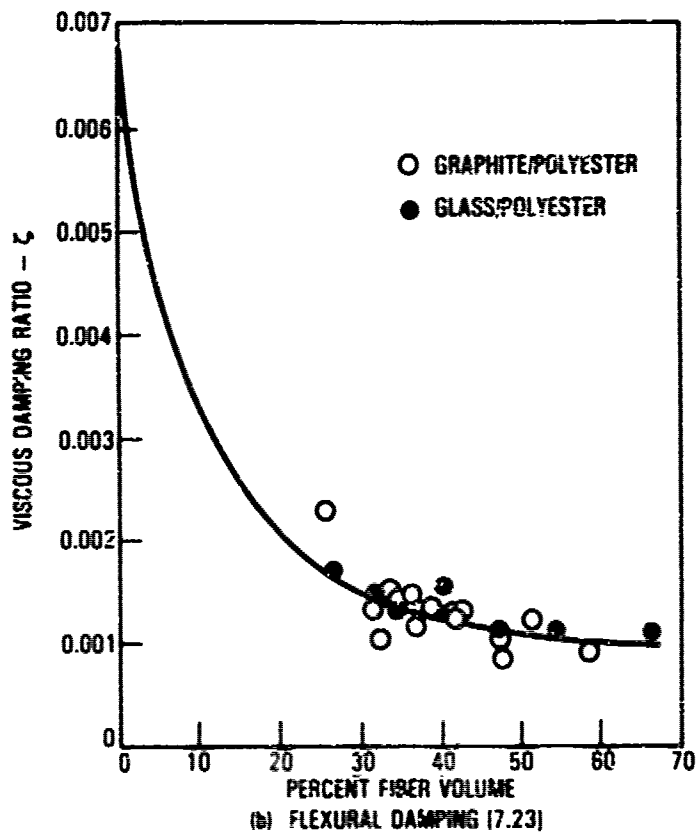
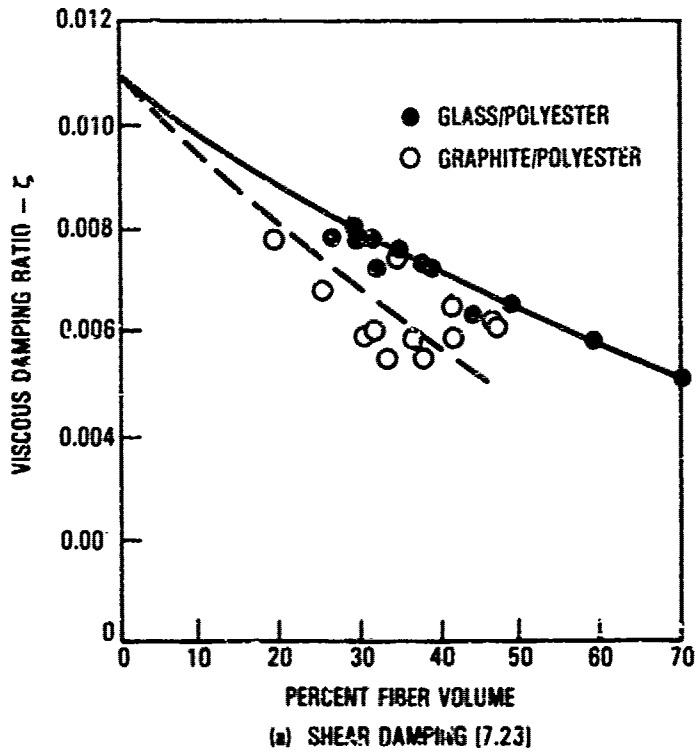


Figure 7.18. Variation of viscous damping ratio with fiber volume in early beam tests.

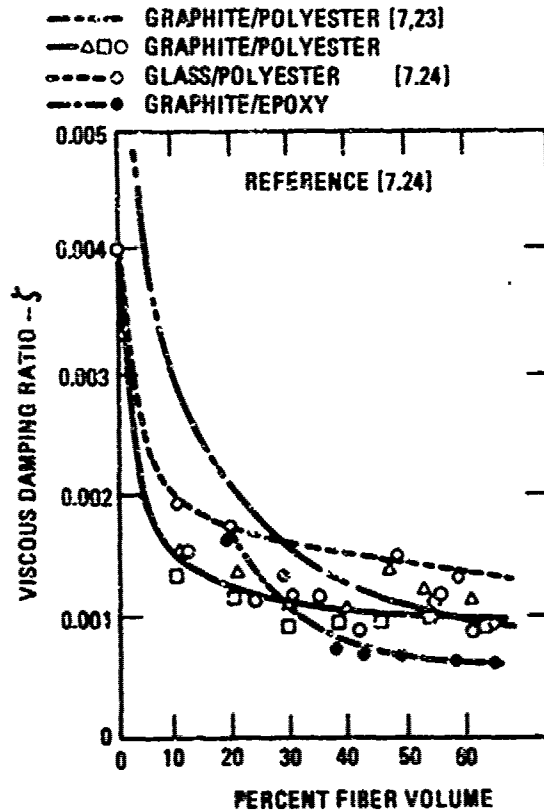


Figure 7.19. Comparison of viscous damping ratios, as a function of fiber volume, measured in early beam flexure tests.

fiber [7.61, 7.63] that were later solved by the use of suitable fiber surface treatments. The lack of adhesion could increase the damping through friction.

On the positive side, it was recognized early that shear effects could be encountered more easily in composites than in metals on account of the high Young's modulus to shear modulus ratio possible in the composites. The test beams are required to have a length to thickness ratio of 100 or more [7.61, 7.64] to minimize the shear effect just in the fundamental mode. This ratio has to be even greater if, for example, the first three modes are to be, essentially, free of shear effects. Alternatively, both the damping [7.61] and the modulus [7.64] need to be corrected for the shear effect, if the above requirement is violated or if even higher modes are included in the development of the damping data. A theoretically derived correction factor for the Young's modulus is illustrated in Figure 7.20 as a function of both the mode number and the ratio of the axial Young's modulus to the shear modulus (E/G).

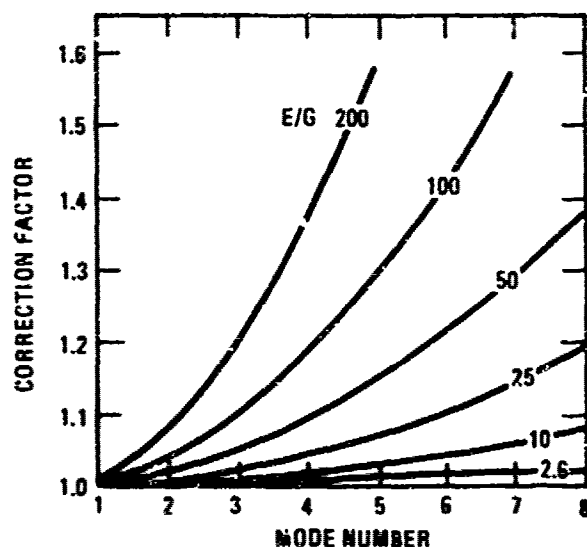


Figure 7.20. Theoretical correction factor for the Young's modulus obtained from measured flexural beam resonant frequencies as a function of mode number.

The earliest research also focused on developing the ability to predict both the axial, shear and flexural damping of unidirectional composites based on the material damping of the resin [7.61, 7.65, 7.66]. The fibers were assumed to provide no damping in this analysis. Thus the material damping of composites is dependent on the damping of the resin, used in the fabrication, the lowest damping being obtained in composite beams with axial fibers. The early theories predicted the form but not the level of the material damping in the composites. Modifications [7.67, 7.68] to these theories produced methods that predict the material damping of cross ply composite beams [7.67] and beams with even more complex fiber orientations [7.68] with good accuracy. The typical agreement achieved between theory and test data [7.68], is illustrated in Figure 7.21.

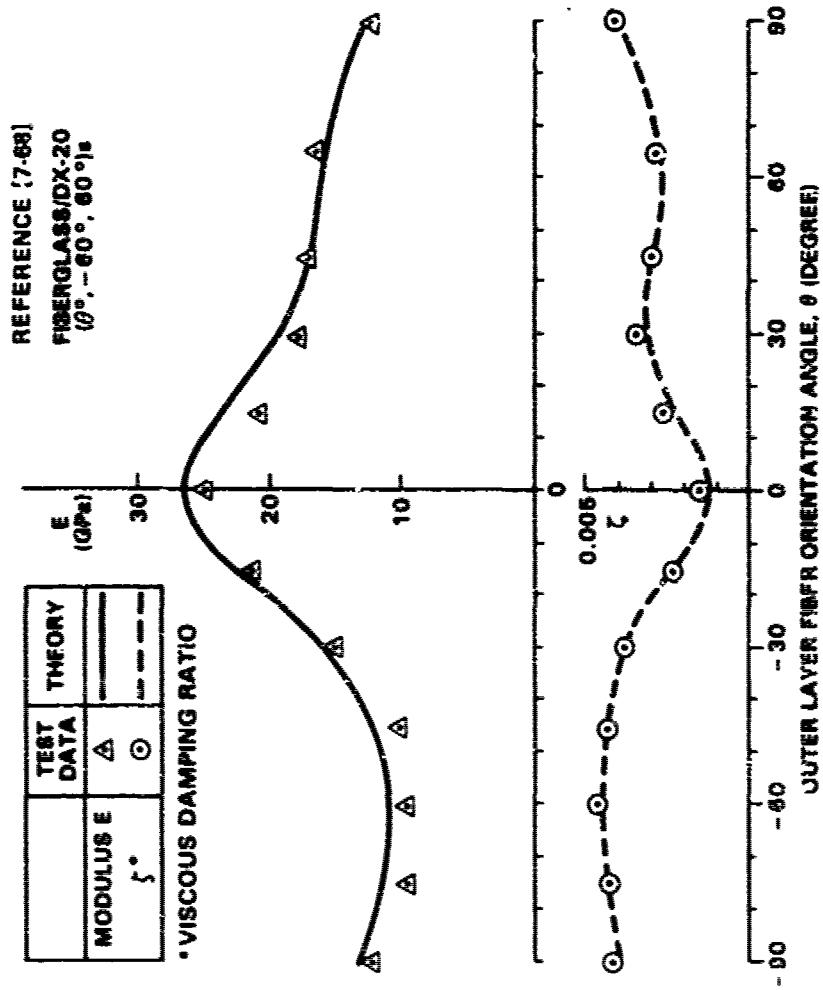
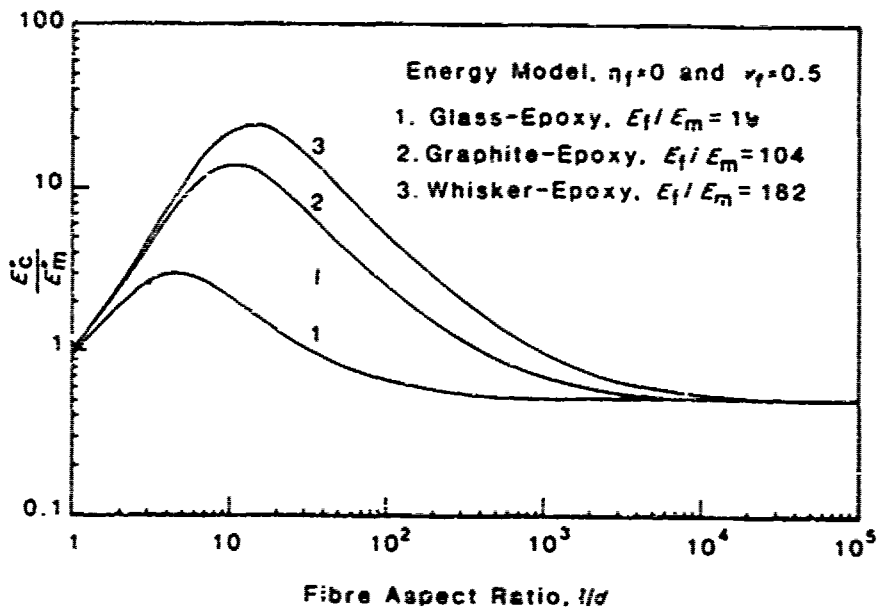


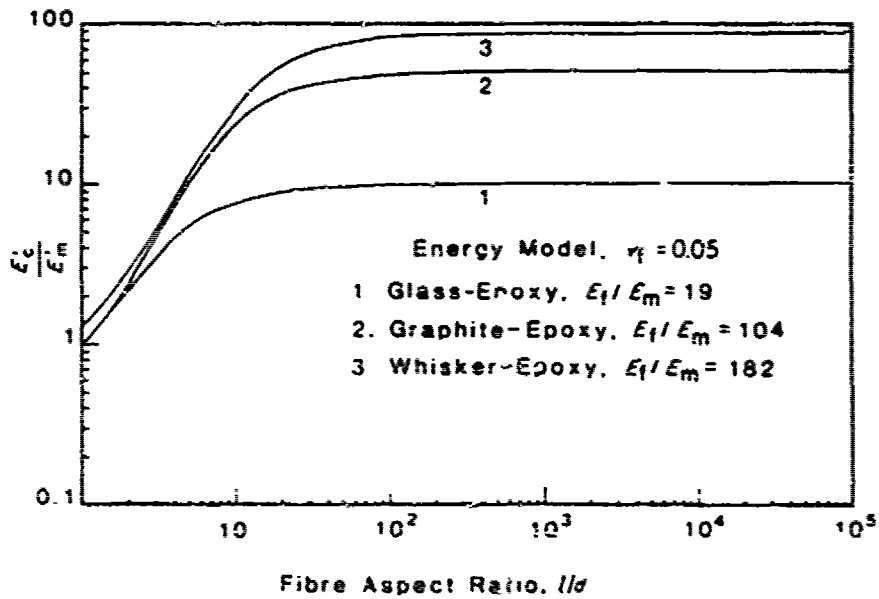
Figure 7.21. Comparison of predicted and measured Young's modulus and viscous damping ratio as a function of the outer ply fiber orientation.

Analytical methods have also been developed [7.69, 7.70, 7.71, 7.72] for predicting the modulus and damping in discontinuous or chopped aligned fiber composites. The correlation achieved between these methods and measured data is reasonable [7.71, 7.72]. This correlation can be improved by including fiber damping in the theory [7.71]. The characteristics of the discontinuous fiber composites are illustrated in Figure 7.22 which includes the variations, with fiber aspect ratio, of the loss modulus, E''_c , and the storage modulus, E'_c , of the composite, expressed in terms of the corresponding loss modulus, E''_m , and storage modulus, E'_m , of the matrix material. The composite is assumed to have a fiber volume, v_f , of fifty percent while the fiber is assumed to have no damping in the above figure. The loss and storage moduli are the real and imaginary part of the composite complex Young's modulus, respectively. The viscous damping ratio of the composite is given by $E''_c/2E'_c$. There appears to be an optimum value for the damping in the composite, obtained at the expense of a reduced stiffness. This behavior [7.71] is similar to that observed in a layered viscoelastic damping treatment [7.73]. In fact the material damping of a composite plate has also been increased significantly [7.22] by the use of randomly distributed discontinuous fiber composite material in the outer layers, providing an effect similar to that observed in extensional and constrained layer viscoelastic damping treatments.

Fiberglass Composites - The earliest damping tests concentrated on glass fiber composites. The measured damping data obtained from these and later tests are summarized in Table 7.6. The measured viscous damping ratio for axially fiber reinforced beams range from a low of 0.00051, measured in vacuum with free-free beams [7.58], to a high of 0.0016, measured in air with double cantilever beams [7.59], using the third mode to reduce the air damping effect (Figure 7.23). The difference between the measured aluminum beam damping in the third mode (Figure 7.23) and that indicated by the Zener curve in Figure 7.14 is approximately 0.0004. This result suggests that the actual material damping is closer to 0.0012 in the third mode, which is comparable to other test data measured at comparable fiber volume fractions. Similar double cantilever beams that were tested in vacuum, but at a higher dynamic strain level [7.58], yielded a viscous damping ratio of approximately 0.0008.



(a) LOSS MODULUS



(b) STORAGE MODULUS

Figure 7.22. Effect of fiber aspect ratio on the loss and storage moduli of discontinuous aligned composites.

TABLE 7.6. SUMMARY OF MEASURED FIBERGLASS COMPOSITE MATERIAL DAMPING (Sheet 1 of 4)

Material	Fiber Angle Degrees (0° = Axial)	Fiber Volume Fraction V_f	Dynamic Modulus MSI	Frequency Hz	Viscous Damping Ratio ζ	Type of Test*	Ref.	Test Conditions/Comments
3M 1009-2S (Estimated $V_f \approx 72\%$)	0	0.72	7.79	16 to 170	0.00051	F	7.58	Free-free beams; near vacuum; 76°F; damping constant with frequency.
	0/90	(Est.)	5.26	17 to 158	0.00126	F		
3M Scotch Ply 1002 (E-Glass)	0	0.45	5.16	159	0.0016	F	7.57	Double cantilever beams; in air, ambient temperature, third mode low strain data presented containing minimum contribution from air damping.
	22.5	0.45	2.77	503	0.0065	F		
	45	0.45	1.69	388	0.0092	F		
	90	0.45	1.57	86	0.0085	F		
3M Scotch Ply 1002	(0,±60)S (0,90,±45)S	0.45	4.01	735	0.0024	F	7.66	Aluminum beam viscous damping ratio in third mode is 0.0008 at 635 Hz, and low strain. Fixture and some air damping could be present in the data. Damping data from 3 dB bandwidth method (see Figure 7.23).
		0.45	4.02	915	0.0028	F		
Epon 815 Epoxy	--	--	0.42	317	0.0117	F	7.57	

*F Flexure
E Extensional
T Torsion

TABLE 7.6. SUMMARY OF MEASURED FIBERGLASS COMPOSITE MATERIAL DAMPING (Sheet 2 of 4)

Material	Fiber Angle Degrees (0° = Axial)	Fiber Volume Fraction V_f	Dynamic Modulus MSI	Frequency Hz	Viscous Damping Ratio ζ	Type of Test	Ref.	Test Conditions/Comments
E-Glass/ Polyester	0	0.40	3.75	290 to 420	0.0014	F	7.23	Free-free beams; in air; 70°F; damping values corrected for air and support damping; mate- rial damping constant with surface dynamic stress.
	0	0.54	4.95		0.0012	F		
	0	0.66	6.2		0.0011	F		
Polyester Rosin	0	0.38	0.46	15 to 30	0.0072	S	7.23	Fixed-fixed beam torsion test, in air; 70°F; damping constant with shear stress.
	0	0.60	0.76		0.0058	S		
	0	0.71	1.26		0.005	S		
E-Glass/ Polyester	--	--	0.5	290 to 420	0.0077	F	7.23	Same as above.
	--	--	0.2		0.0108	S		
	0	0.48	--		0.0014	F		
E-Glass/ Polyester	0	0.54	--	Between 70 to 700	0.0013	F	7.63	Free-free beams; in air; 25°C; data contains small contribution from air damping
	0	0.64	--		0.0009	F		
	0	0.65	7.24		0.00085	E		
E-Glass/ ERL 2256 Epoxy	0	0.65	7.3	300 to 900	0.0009	E	7.59	Free-free beam tested in extension; in air; 75°F, 130°F, 172°F and 220°F; Damping at 266°F approxi- mately three times greater. Damping increases with frequency.
	0	0.65	7.3		to 0.0016	E		
	0	0.65	7.3		to 0.0016 to 0.0031	E		

TABLE 7.6. SUMMARY OF MEASURED FIBERGLASS COMPOSITE MATERIAL DAMPING (Sheet 3 of 4)

Material	Fiber Angle Degrees ($0^\circ = \text{Axial}$)	Fiber Volume Fraction V_f	Dynamic Modulus MSI	Frequency Hz	Viscous Damping Ratio ζ	Type of Test	Ref.	Test Conditions/Comments
E-Glass/ ERL 2256 Epoxy	0	0.65	1.25	4000 to 30,000	0.014 to 0.015	S	7.59	Free-free beam tested in torsion; in air 75°F; other temperatures as above. Shear damping falls with temperature with minimum at 220°F but increases with frequency. Epoxy damping shows same general behavior as shear damping.
	--	--	0.54 to 0.6,	150 to 5000	0.013 to 0.029	E	7.59	
	--	--	0.21 to 0.22	1500 to 7000	0.022 to 0.038	S		
Scotchply 1002 (E-glass)	0	0.53	5 to 4.6	43 to 430	0.00065 to 0.0013	F	7.67	Double cantilever beam; near vacuum; 25°C. Damping increases with frequency but is constant with dynamic strain.
	90	0.53	1.52 to 1.5	32 to 450	0.0039 to 0.0068	F		
	0/90	0.53	3.25 to 3.15	34 to 440	0.0013 to 0.0023	F		
Scotchply 1002 Epoxy	0/90	--	--	30 to 440	0.0012 to 0.002	F	7.74	Epoxy damping increases with frequency.
	--	--	0.55 to 0.61	42 to 460	0.0058 to 0.0085	F	7.67	

LE 7.6. SUMMARY OF MEASURED FIBERGLASS COMPOSITE MATERIAL DAMPING (Sheet 4 of 4)

Material	Fiber Angle Degrees (0° = Axial)	Fiber Volume Fraction V_f	Dynamic Modulus MSI	Frequency Hz	Viscous Damping Ratio ζ	Type of Test	Ref.	Test Conditions/Comments
E-Glass/ LY556 - Hz 978	0°	0.60	6.52	4.88	0.001	F	7.75	Large free-free beam; in air; ambient temperature. Damping data includes air damping.
Glass/ DX-210	0° 90° 0°	0.5	5.48	--	0.0007	F	7.68	Basic material data used in analysis of composites. Analysis shows a good correlation with test data for other fiber orientations. Data applicable to low frequencies around 50 Hz.
		0.5	1.58	--	0.0040	S		
DX-210 Resin	-- --	--	0.465	--	0.0052	F	7.68	
		--	0.174	--	0.0053	S		
Chopped E-Glass Fibers and Polyester Resin, Fillers, Etc. (see Figure 7.24)	0°	0.5	See Figure 7.24(a)	10 to 1500	See Figure 7.24(b)	F	7.76	Double cantilever specimens, near vacuum; 20°C to 25°C. Damping constant with frequency.
			5.45	--	0.00128	F	7.22	Quoted values.
E-Glass/ DX-210	0°	0.5	5.45	--	0.00128	F	7.22	
DX-210 Resin	--	--	0.50	--	0.0056	F	7.22	

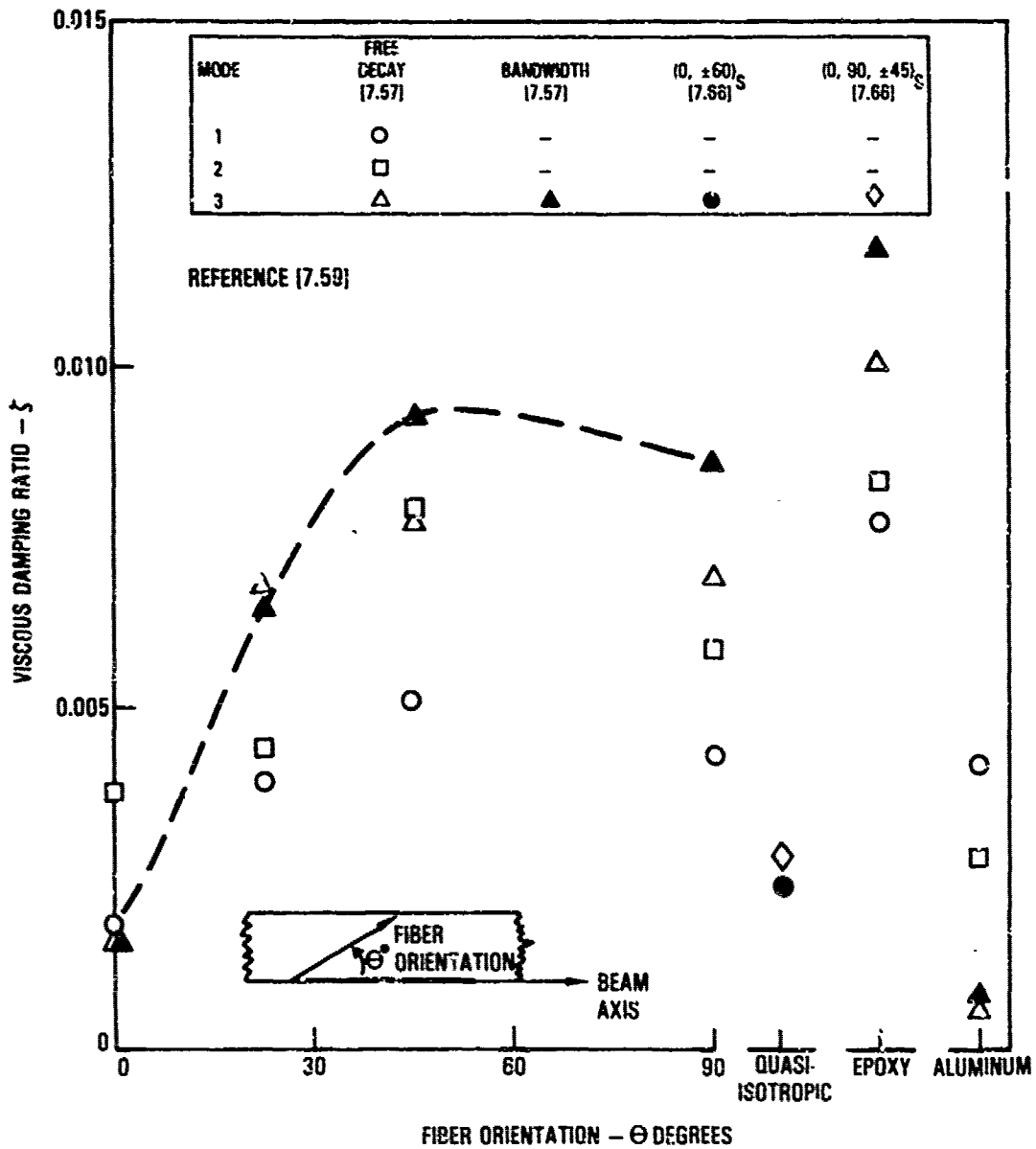


Figure 7.23. Variation of damping with uniaxial fiber orientation relative to beam axis for Scotchply 1002 measured by double cantilever beam tests in air.

DATA FROM REFERENCE (7.76)

MATERIAL	PERCENT CHOPPED E GLASS FIBER	PERCENT CONTINUOUS E GLASS FIBER	SYMBOL
PPG SMC 825	25	0	○
PPG SMC 885	85	0	□
PPG SMC 3	25	50 (17.5%)	◇
OCF SMC 825	25	0	●
OCF C/SMC 30	30	20 (6%)	△
PPG SMC 885	MATRIX	8828	■
PPG SMC 825	MATRIX	8828	●

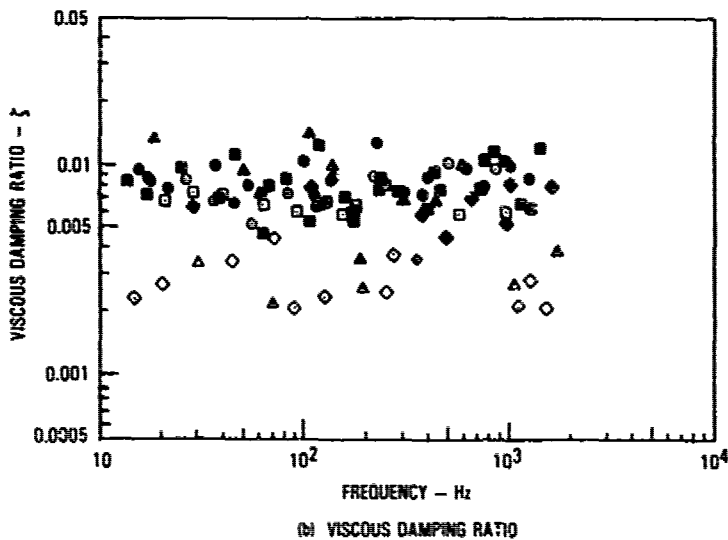
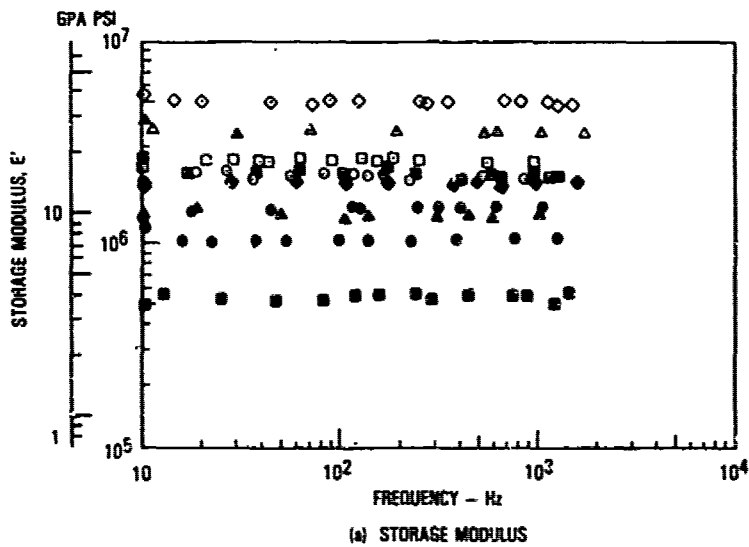


Figure 7.24. Variation of storage modulus and damping with frequency for chopped E-glass/polyester composites.

This result indicates that the damping could contribute as much as 0.0003 to the viscous damping ratio of the beams.

In general, the material damping is highly dependent on the fiber volume fraction, v_f , of the composite. The fiber volume fraction for the beams with the 0.00051 viscous damping ratio was estimated from the dynamic modulus to be around 0.72. This fiber volume is higher than normally used. A more common value is around 0.50. At this volume fraction, the viscous damping ratio is around 0.0007 [7.67, 7.68] at the lower frequencies (50 Hz). The viscous damping ratio increases with frequency, reaching a value of 0.0013 at 430 Hz [7.67]. However, the data in Reference [7.59] indicate viscous damping ratios of 0.0009 and 0.0016 at frequencies of 900 Hz and 5000 Hz, respectively. The viscous damping ratio remains constant with amplitude or surface stress level up to the damage level in the composite [7.74]. The damping is increased by the damage. A significant increase in the damping can be obtained by using other than axial fiber orientations at the expense of reduced composite stiffness. The damping is controlled by the damping in the resin. This result is also true for chopped fiber composites (Figure 7.24) [7.67]. The damping for these composite materials is constant with frequency. However, when this damping is measured in air, it increases with frequency [7.76].

Graphite-Epoxy and Graphite-Polyester Composites - The polyester resins used in fabricating some of the earliest test beams have given way to epoxy resins. The damping data for graphite fiber reinforced composites made with both resin systems are summarized in Table 7.7. In general, the damping of axially reinforced composites made with polyester resin [7.23, 7.63] tended to be higher than those made with epoxy resins (Figure 7.19). The viscous damping ratio for the graphite/polyester composites varies typically from 0.0009 to 0.0012, corresponding to fiber volumes of 62 to 50 percent, respectively, at ambient temperature. The viscous damping ratio for axially reinforced graphite fiber composites made with epoxy resins tends to be between 0.00024 [7.78] to 0.00068 [7.22, 7.63, 7.75, 7.77] for fiber volumes above 50 percent although viscous damping ratios as low as 0.00012 have been measured [7.61].

TABLE 7.7. SUMMARY OF MEASURED GRAPHITE-EPOXY AND POLYESTER COMPOSITE MATERIAL DAMPING (Sheet 1 of 7)

Material	Fiber Angle Degrees (0° = Axial)	Fiber Volume Fraction V _f	Dynamic Modulus MSI	Frequency Hz	Viscous Damping Ratio ζ	Type of Test*	Ref.	Test Conditions/Comments
HM/Polyester	0	0.47	22-24	230 to 420	0.0009- 0.0011	F	7.23	Free-free beams, in air; 70°F, damping values corrected for air and support damping. Material damping constant with surface dynamic stress for flexure.
	0	0.51	23.5		0.0012	F		
	0	0.58	24.2		0.00095	F		
Graf11 A/ Polyester BIP836	0	0.42	0.47	15 to 30	0.0058- 0.0065	S	7.25	Fixed-fixed beam torsion test; in air; 70°F; material damping increasing slightly with shear stress.
	0	0.48	0.53		0.006	S		
	0	0.53	16.8	Between 70 and 700	0.0010	F	7.63	Free-free beam; in air, 250C data contains small contribution from air damping.
Graf11 A/ Epoxy Epikote 828	0	0.62	19.7		0.0009	F		
	0	0.049	14.5	Between 70 and 700	0.00068	F	7.63	Effect of temperature (-200C to 500C) on damping very small in the 0.5 to 0.65 volume fraction range.
	0	0.58	18.9		0.00061	F		
	0	0.64	19.1		0.00061	F		

*F = Flexure
E = Extensional
T = Torsion

TABLE 7.7. SUMMARY OF MEASURED GRAPHITE-EPOXY AND POLYESTER COMPOSITE MATERIAL DAMPING (Sheet 2 of 7)

Material	Fiber Angle Degrees (0° = Axial)	Fiber Volume Fraction V_f	Dynamic Modulus MSI	Frequency Hz	Viscous Damping Ratio ζ	Type of Test	Ref.	Test Conditions/Comments
Grafil HT-S/ Polyester	0	0.40	13.9	72 to 700	0.0012- 0.0008	F	7.63	The damping in the graphite/polyester beams appears to fall slowly with frequency.
	0	0.53	22.8	Between 70 and 700	0.00123	F		
	0	0.61	26.8	700	0.00113	F		
Grafil HM-S/ Polyester	0	0.54	25.8	Between 70 and 700	0.0011	F	7.63	
	0	0.55	29.6		0.00117	F		
	0	0.61	33.6		0.00088			
Type A/ Epoxy ERLA 4617	0	0.50	12.9	140-600	0.00042	F	7.22	Free-free beams; near vacuum; ambient temperature. Damping of axially reinforced continuous fiber beams constant with frequency. Damping of laterally reinforced beams increases slightly with frequency.
	90	0.5	1.29	35-200	0.0045	F		
HT-S/Epoxy ERLA 4617	0	0.6	19	--	0.00053	F	7.22	
	0	0.6	21.2	--	0.00068	F		
HT-S/Epoxy DX-210	--	--	0.68	20-40	0.0083	F	7.22	
	--	--	--	20-40	0.0130	S		
DX-210 Epoxy	--	--	0.5	20-40	0.0056	F	7.22	

TABLE 7.7. SUMMARY OF MEASURED GRAPHITE-EPOXY AND POLYESTER COMPOSITE MATERIAL DAMPING (Sheet 3 of 7)

Material	Fiber Angle Degrees (0° = Axial)	Fiber Volume Fraction V_f	Dynamic Modulus MSI	Frequency Hz	Viscous Damping Ratio ζ	Type of Test	Ref.	Test Conditions/Comments	
HM-S/CY 209 - HT972	0	0.5	23.7	520	0.00049	F	7.75	Free-free and longitudinal beam tests, in air, ambient temperature. Air damping is present in free-free beam measurements. First mode data are only included in this table. Reference contains data for temperatures between -90°C to 95°C. The damping at zero fiber orientation is constant with temperature but follows the resin damping curve for the ±45° and 90° fiber orientations. (Figure 7.26). Additional data is presented in Figure 7.25. Reference also contains test data from cantilever beams, honeycomb panels and wind turbines.	
	±22.5	0.5	6.7	270	0.0027	F			
	±45	0.5	1.56	120	0.0050	F			
	±67.5	0.5	0.85	90	0.0073	F			
	90	0.5	0.8	90	0.0076	F			
	---	--	0.5	0.5	300	0.011			F
CY 209 - HT972 Epoxy				Approximate values			7.75		
HT-S/LY558	0	0.5	14	--	0.0002	F	7.61	Free-free beams; near vacuum; ambient temperature. Tested out a dynamic strain level of 5000 psi. These damping levels are lower than any reported damping as noted in the reference.	
	0	0.6	17.9	--	0.00015	F			
	0	0.7	19.7	--	0.00012	F			

TABLE 7.7. SUMMARY OF MEASURED GRAPHITE-EPOXY AND POLYESTER COMPOSITE MATERIAL DAMPING (Sheet 4 of 7)

Material	Fiber Angle Degrees (0° = Axial)	Fiber Volume Fraction V_f	Dynamic Modulus MSI	Frequency Hz	Viscous Damping Ratio ζ	Type of Test	Ref.	Test Conditions/Comments
HT-S/ F/MNA	0	0.5	13.8	--	0.00015	F	7.61	
LY588 Epoxy	0	0.7	20.5	--	0.00012	F	7.61	
	--	--	5.3	--	0.0053	F	7.61	
F/MNA Epoxy	--	--	0.193	--	0.0055	S	7.61	
	--	--	5.71	--	0.0025	F	7.61	
	--	--	0.21	--	0.0025	S	7.61	
HM-S/Epoxy DX-209	0	0.5	--	--	0.004	F	7.61	Free-free beam with length to width ratio of 90.
Modmor II/ Epoxy	0°	0.5	16	300 to 1620	0.00075-- 0.0012	F	7.64	Cantilever beam; in air ambient temperature.
Narmco 2387 Epoxy	--	--	0.6	--	0.0015	F	7.64	
AS1/3501-6	±45	--	--	25 to 175	0.0056-- 0.0065	F	7.29	Free-free beams in zero "g" tests; near vacuum; ambient temperature. Damping essentially constant with dynamic surface stress.

TABLE 7.7. SUMMARY OF MEASURED GRAPHITE-EPOXY AND POLYESTER COMPOSITE MATERIAL DAMPING (Sheet 5 of 7)

Material	Fiber Angle Degrees (0 = Axial)	Fiber Volume Fraction V_f	Dynamic Modulus MSI	Frequency Hz	Viscous Damping Ratio ζ	Type of Test	Ref.	Test Conditions/Comments
ASI/3501-6	0	--	--	50 to 300	0.0005	F	7.77	Free-free beams in zero "g" tests, near vacuum; ambient temperature.
	± 45	--	--	25 to 175	0.0055- 0.0065	F		
	90	--	--	50 to 150	0.0055- 0.0065	F		
Celion 3000/ 5208 Narmco	0	--	21.1	833	0.00033	F	7.78	Free-free beam; in air; ambient conditions. Air damping very small as shown by test data on aluminum free-free beam; $\zeta = 0.000158$ at 469 Hz.
	(0, $\pm 45, 90$) _B	--	6.9	510	0.0019	F		
	90	--	1.8	673	0.00625	F		
Celion 3000/ 5213 Narmco	0	--	19.7	881	0.00024	F	7.78	
	90	--	1.53	685	0.0036	F		
	0	--	20.2	882	0.00038	F	7.78	
Celion 6000/ 5208	90	--	1.68	699	0.0069	F		
	0	--	19.2	909	0.00026	F	7.78	
Celion 6000/ 5213	90	1.49	700	0.0038	F			

TABLE 7.7. SUMMARY OF MEASURED GRAPHITE-EPOXY AND POLYESTER COMPOSITE MATERIAL DAMPING (Sheet 6 of 7)

Material	Fiber Angle Degrees ($0^\circ = \text{Axial}$)	Fiber Volume Fraction V_f	Dynamic Modulus MSI	Frequency Hz	Viscous Damping Ratio ζ	Type of Test	Ref.	Test Conditions/Comments
GY-70/934 Fibrite	0	--	42.3	1090	0.00046	F	7.78	As above
	($0/\pm 45/90$) ^s	--	10.6	670	0.00156	F		
	90	--	1.01	437	0.0081	F		
Chopped Graphite/ Fibers, Aligned, Type A, and Random, HT-S, in ERLA 4617 Epoxy	See Table 7.9 and Figure 7.27	0.5	See Table 7.9 and Figure 7.27	40 - 700	See Table 7.9 and Figure 7.27	F	7.22	Free-free beam, in air and near vacuum; ambient temperature. Reference also contains damping data on plates made from these materials.

TABLE 7.7. SUMMARY OF MEASURED GRAPHITE-EPOXY AND POLYESTER COMPOSITE MATERIAL DAMPING (Sheet 7 of 7)

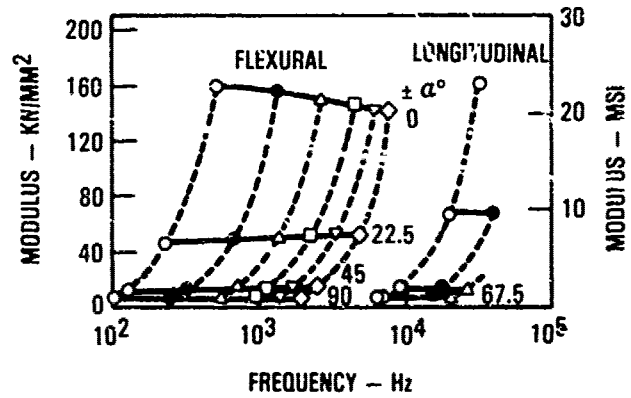
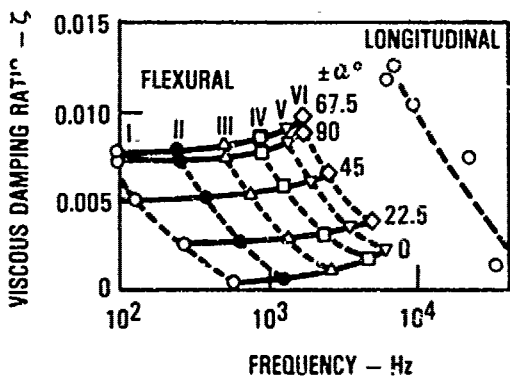
Material	Fiber Angle Degrees (0° = Axial)	Fiber Volume Fraction V_f	Dynamic Modulus MSI	Frequency Hz	Viscous Damping Ratio ζ	Type of Test	Ref.	Test Conditions/Comments
HM-S/DX-210 Aligned Chopped Fibers	0	0.48	21.3	--	0.00065	F	7.72	Free-free beam; ambient temperature 0.12 inch long, fibers
	0	0.63	27.1	--	0.0005	F		
	0	0.55	19.6	--	0.00096	F	7.72	Free-free beam; ambient temperature 0.02 inch long fibers. Damping appears to rise with fiber volume above 65% due to interaction between fibers.
	0	0.68	21.3	--	0.0015	F		
	0	0.73	19.6 to 23.9	--	0.0012-0.0018	F		Effect of resin damping on composite illustrated in Table 7.8.
T300/934 Fiberite Continuous and Chopped Fibers	0°	0.65	17	60	0.001	F	7.79	Cantilever beam; near vacuum; ambient temperature. The continuous fiber beam damping appears to be high. Damping data also contained in Figure 7.28.

The damping in these composites is constant with both frequency [7.22, 7.29] and surface dynamic stress level [7.29]. The damping increases substantially when other fiber orientations are included [7.22, 7.29, 7.75, 7.77, 7.78] at the expense of reduced stiffness as illustrated in Figure 7.25(b). Increased shear damping effect [7.61] is present in the higher beam flexural modes, which is responsible for the increase in the damping with frequency observed in Figure 7.25(a), starting with the second mode. As a consequence, data for the first mode only are included in Table 7.7 and in Figure 7.25(b).

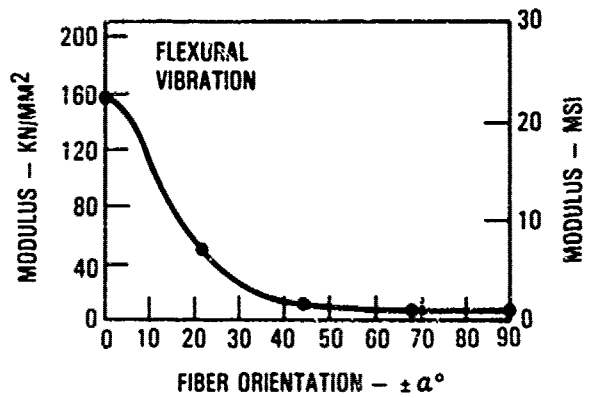
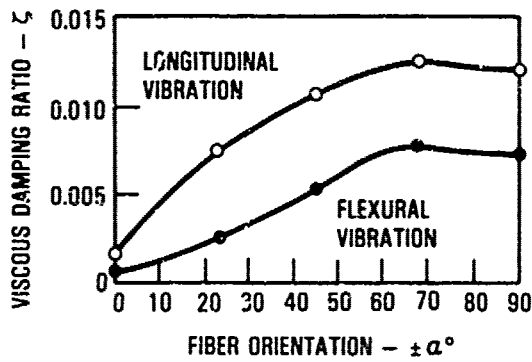
The variation of the damping with temperature of both the epoxy resin and the graphite/epoxy beams is illustrated in Figures 7.26(a) and (b), respectively. The resin, being a polymer, behaves in a similar manner with temperature as the damping materials, previously discussed in Section 2, with the peak damping occurring in this instance at 0°C (Figure 7.26(a)). The axially reinforced beam damping remains essentially constant over the temperature range shown in Figure 7.26(b). However, the damping in the beams with $\pm 45^\circ$ and 90° fiber orientations basically follows the shape of the resin damping curve. All fiber reinforced polymeric composite materials are expected to behave in a similar manner.

The damping in the resin determines the damping in the uniaxial composite [7.61, 7.65]. The effect of resin damping on the damping of the axially fiber reinforced composite can be observed in the data in Table 7.7 from Reference [7.78], although damping data were not available for the Normco 5208 and 5213 epoxies. The 5208 epoxy appears to have the greater damping. The effect of resin damping can be seen more clearly in Table 7.8 in damping studies [7.72] performed with chopped fibers although the resins were not identified. A significant increase in composite material damping can be obtained by the use of a highly damped resin.

Chopped fibers [7.22, 7.72, 7.79] provide another means of increasing the material damping in composites. The data indicating the increase in damping possible by the use of chopped fibers and combinations of continuous, chopped random fibers [7.22] are illustrated in Table 7.9 and Figures 7.27



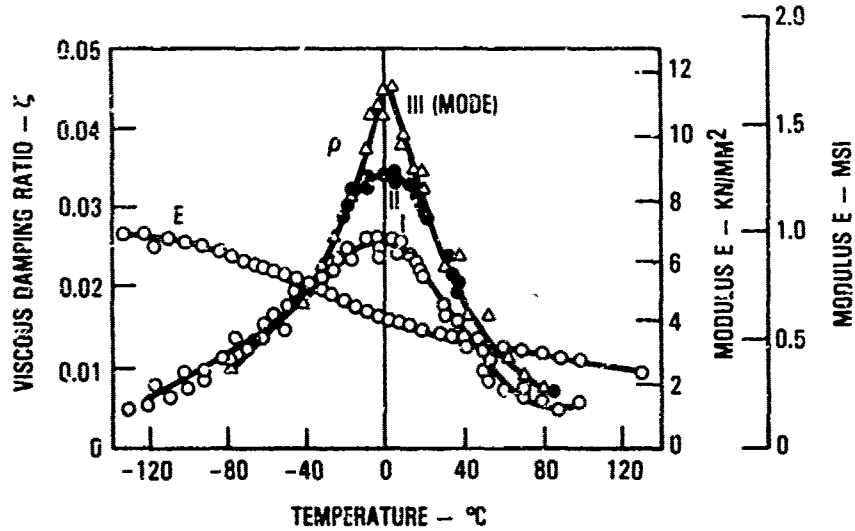
(a) VARIATION OF DAMPING AND YOUNG'S MODULUS WITH FREQUENCY FOR FIRST SIX MODES (7.75)



(b) VARIATION OF DAMPING AND YOUNG'S MODULUS WITH FIBER ORIENTATION IN THE FIRST MODE (7.75)

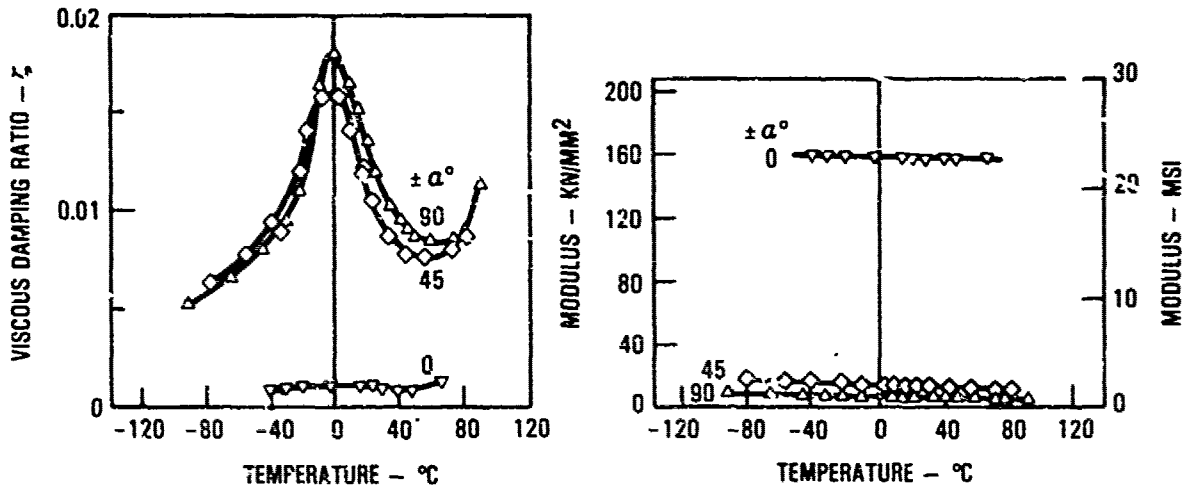
Figure 7.25. Measured Young's modulus and damping for graphite/epoxy composite at ambient temperature.

LONGITUDINAL VIBRATION - FIRST THREE MODES



(a) VARIATION OF MODULUS AND DAMPING OF CY209/NT972 EPOXY WITH TEMPERATURE [7.75]

LONGITUDINAL VIBRATION - FIRST MODE



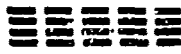
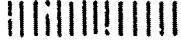
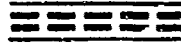
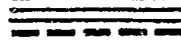
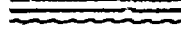
(b) VARIATION OF MODULUS AND DAMPING OF HM-S GRAPHITE/EPOXY COMPOSITE WITH TEMPERATURE AND FIBER ORIENTATION \pm $^{\circ}$ [7.75]

Figure 7.26. Comparison between the damping behavior of epoxy and that of graphite/epoxy composite, as a function of temperature.

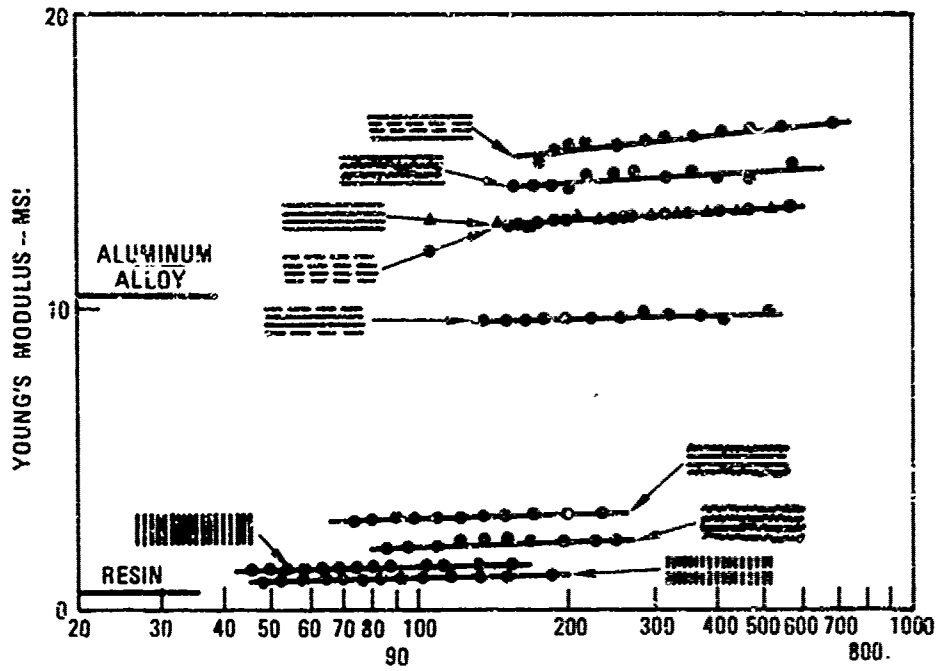
TABLE 7.8. EFFECT OF RESIN DAMPING ON THE DAMPING OF CHOPPED ALIGNED GRAPHITE FIBER COMPOSITE

Material Identified by Resin Number Only [7.72]	Resin		Chopped Fiber Composite ($V_f = 0.6$)	
	Modulus MSI	Viscous Damping Ratio, ζ	Modulus MSI	Viscous Damping Ratio, ζ
1	0.144	0.075	13.25	0.004
5	0.475	0.0035	17.62	0.00025
6	0.249	0.075	16.69	0.005

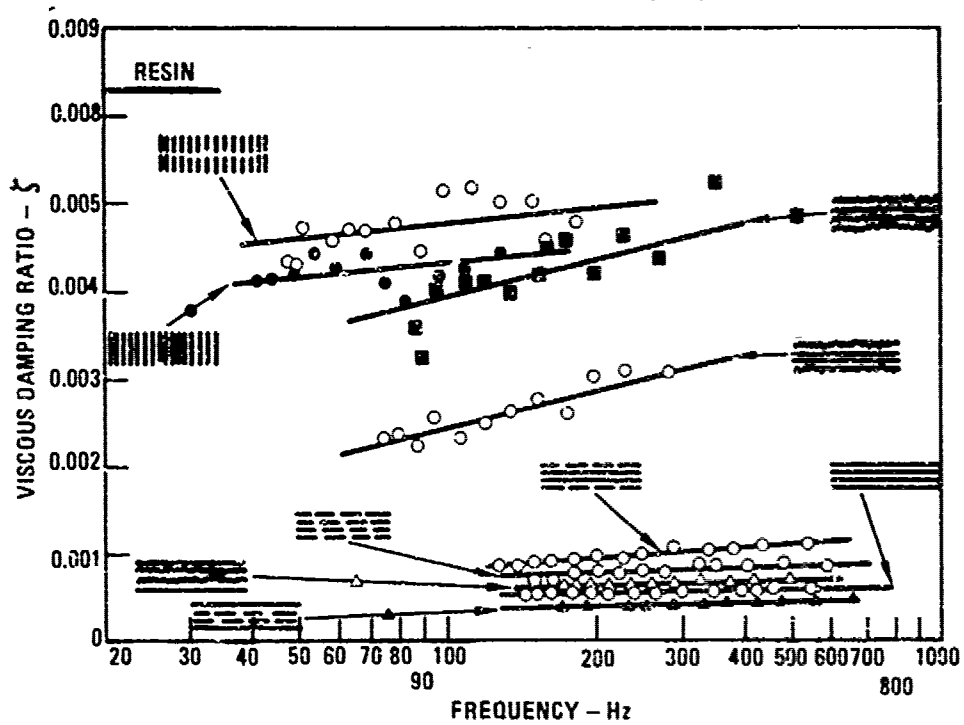
TABLE 7.9. DAMPING IN DISCONTINUOUS ALIGNED AND RANDOM FIBER GRAPHITE/EPOXY COMPOSITES

Beam Construction [7.22]	Young's Modulus MSI		Viscous Damping Ratio, ζ	
	1st Mode	2nd Mode	1st Mode	2nd Mode
	12.9	12.8	0.00043	0.00062
	12.8	12.9	0.00039	0.00044
	1.12	1.11	0.0038	0.0034
	1.28	1.3	0.0042	0.0047
	13.9	13.9	0.0003	0.00084
	14.9	15.4	0.00025	0.00043
	9.5	9.6	0.0006	0.00095
	2.97	3.1	0.0019	0.0023
	1.96	1.97	0.0023	0.0023

 Continuous Type A Fiber
 Chopped Aligned Type A Fiber
 Random HT-S Fiber



(a) FLEXURAL MODULUS [7-22]



(b) VISCOUS DAMPING RATIO [7-22]

Figure 7.27. Young's modulus and damping of discontinuous aligned and random fiber graphite/epoxy composites.

and 7.28. The increase in damping is obtained at the expense of reduced stiffness.

Boron/Epoxy Composites - The increased damping data on boron/epoxy composites [7.60, 7.62, 7.75] is summarized in Table 7.10. In general good agreement has been obtained by the various researchers on the damping in the boron/epoxy composites. The damping of the axially fiber reinforced composite is around 0.0006. The measured modulus in Reference [7.62] falls with frequency while the damping increases with frequency. This behavior is attributed to the previously discussed near effect in the higher modes. The variation of the damping and modulus with fiber orientation [7.75] is illustrated in Figure 7.29(a). The damping of the axially reinforced composite appears to change slightly with temperature whereas the damping for the $\pm 45^\circ$ and 90° fiber orientations takes on the form of the resin damping (Figure 7.29(b)).

Kevlar/Epoxy Composites - The damping data [7.10, 7.75, 7.79] on Kevlar/epoxy is summarized in Table 7.11. Initial damping measurements were made on free-free Kevlar cloth Style 181/epoxy honeycomb panels [7.11] with a $\pm 45^\circ$ fiber orientation in the face sheets. The damping data, included in Figure 7.30, indicated a higher damping for the panel with the thicker honeycomb core. Core shear was not a factor. As a consequence some Kevlar/epoxy uni-axial and cloth beams were tested in 1974 to see if the cloth affected the damping. The results [7.10] are summarized in Figure 7.30 and average values included in Table 7.11. There is reasonably good correlation between the cloth beams and one of the honeycomb panels. The reason for the higher damping in the other free-free honeycomb panels remains unknown.

In general, there is good agreement between the measured damping of the axial fiber reinforced Kevlar composites, from the limited sources, with a value around 0.006 being typical. The damping value of 0.0044 recorded in Reference [7.80] appears to be on the low side as compared to the other data.

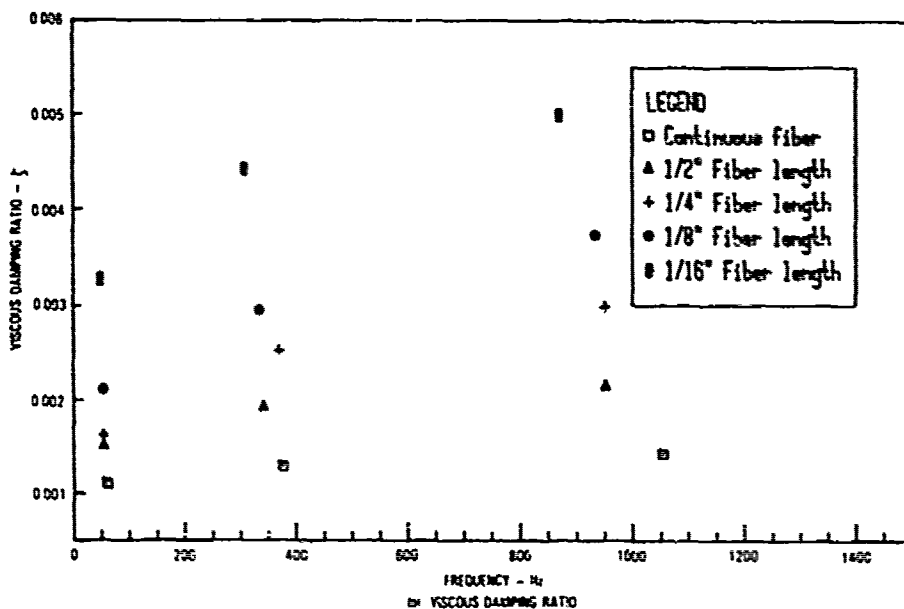
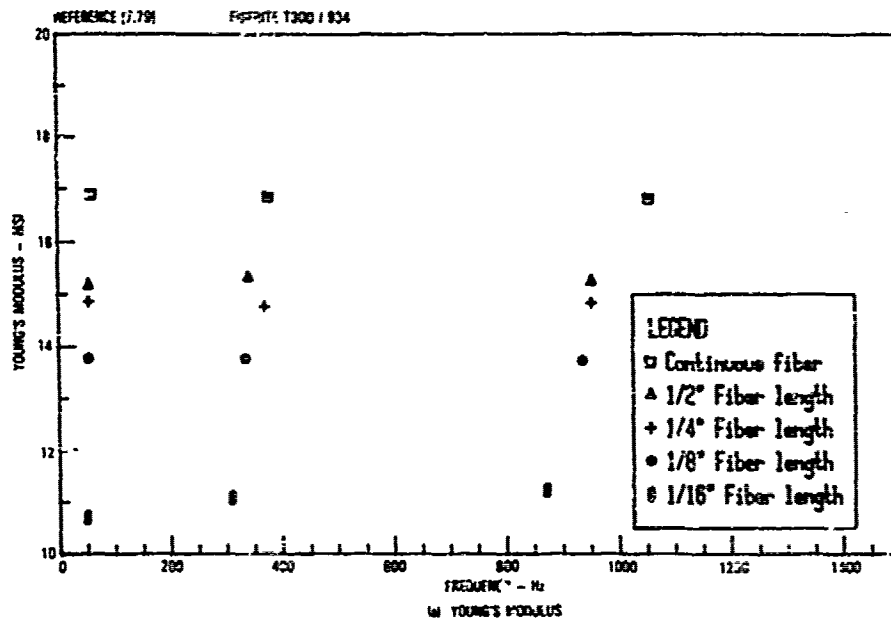
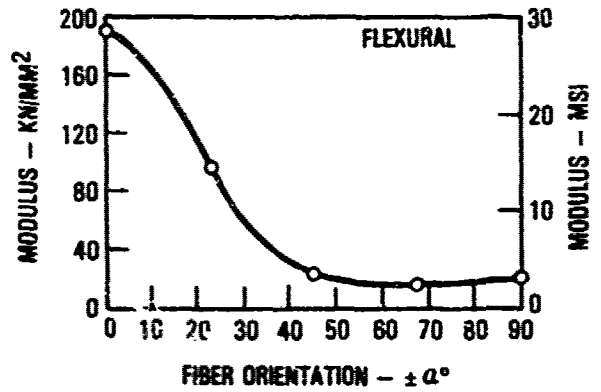
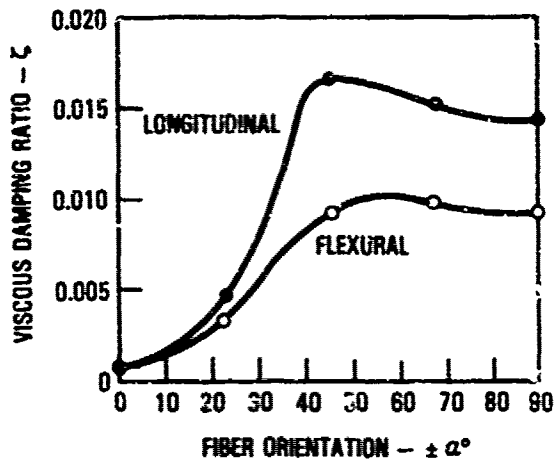


Figure 7.28. Graphite/epoxy composite Young's modulus and viscous damping ratio as a function of frequency for difference fiber lengths.

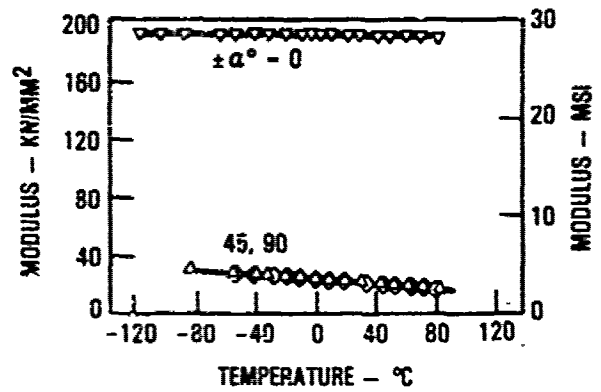
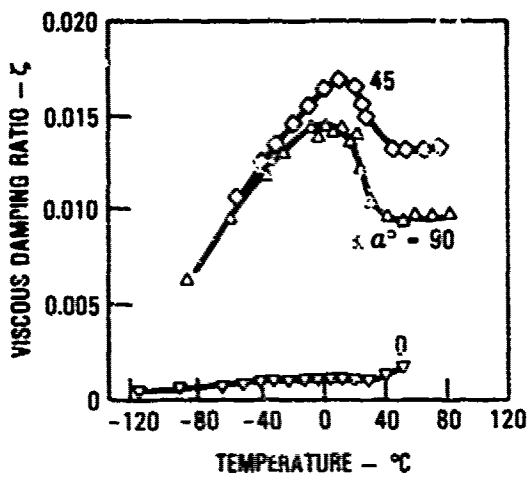
TABLE 7.10. SUMMARY OF MEASURED BORON/EPOXY COMPOSITE MATERIAL DAMPING

Material	Fiber Angle Degrees (0° = Axial)	Fiber Volume Fraction V _f	Dynamic Modulus MSI	Frequency Hz	Viscous Damping Ratio ζ	Type of Test	Ref.	Test Conditions/Comments
Boron/5505 NARMCO	0		26.5	34.2	0.00058	F	7.58	Free-free beams; near vacuum; 70° - 90°F. Double cantilever beam specimens also tested in vacuum but at higher dynamic strain levels. Damping was also higher. Modulus values taken from double cantilever data at the nearest frequency.
	0		23.5	140.0	0.00061	F	7.62	
	0		22.5	300.0	0.00067	F		
	±45		3.95	28.3	0.0094	F	7.58	
	±45		3.70	144.5	0.0107	F	7.62	
	±45		--	300.0	0.0110	F		
	90		3.87	25.0	0.0081	F	7.58	
	90		3.95	40.0	0.0083	F	7.62	
	90		2.88	123.3	0.0097	F		
Boron/Epoxy	0		2.81	300.0	0.0100	F		Free-free beams; in air; ambient temperature and first mode data reported here. Effect of temperature between -120°C and 80°C in Reference and Figure 7.29.
	±22.5	55	27.6	490	0.00064	F		
	±45	55	13.6	340	0.0032	F	7.75	
	±67.5	55	3.3	160	0.0092	F		
	90	55	2.5	140	0.0095	F		
Boron/Epoxy	0		2.9	150	0.0092	F	7.60	Free-free beams; main; ambient temperature tested in flexure and torsion.
	90					F		
	0					E		

*F = Flexure
 E = Extensional
 T = Torsion



(a) VARIATION OF DAMPING AND MODULUS WITH FIBER ORIENTATION FOR FUNDAMENTAL MODE (7.75)



(b) VARIATION OF DAMPING AND MODULUS WITH TEMPERATURE FOR FIRST LONGITUDINAL MODE (7.75)

Figure 7.29. Measured damping and Young's modulus for boron/epoxy composite.

TABLE 7.11. SUMMARY OF MEASURED KEVLAR/EPOXY MATERIAL DAMPING

Material	Fiber Angle Degrees (0° = Axial)	Fiber Volume Fraction V_f	Dynamic Modulus MSI	Frequency Hz	Viscous Damping Ratio ζ	Type of Test*	Ref.	Test Conditions/Comments
Kevlar/ Epoxy	0	0.59	8.77	116.8	0.0067	F	7.10	Free-free beam; in air; ambient temperature. Air damping is small compared to material damping. Test data average of three test specimens. More detailed test data in Figure 7.30.
	90	0.59	0.72	32.6	0.0092	F	7.10	
Kevlar Type 181 Cloth/ Epoxy	±45	0.45	0.74	39.2	0.0085	F	7.10	
	0/90	0.45	3.1	82.4	0.0073	F		
Kevlar/ Epoxy	0	0.55	--	4.23	0.0064	F	7.75	Free-free beam; in air; ambient temperature.
Kevlar/ Epoxy HY-E1734A2	0	0.65	9.75	42	0.0056	F	7.79	Cantilever beam; near vacuum; ambient temperature. First mode data reported here. Other data in Figure 7.31 together with chopped fiber data.
Kevlar/ Epoxy Chopped Fibers	0	0.65	See Figure 7.31	See Figure 7.31	See Figure 7.31	F	7.79	
Kevlar/ Epoxy	0	--	--	56	0.0044	F	7.80	Cantilever beam, in air; ambient temperature first mode

*F = Flexure
E = Extensional
T = Torsion

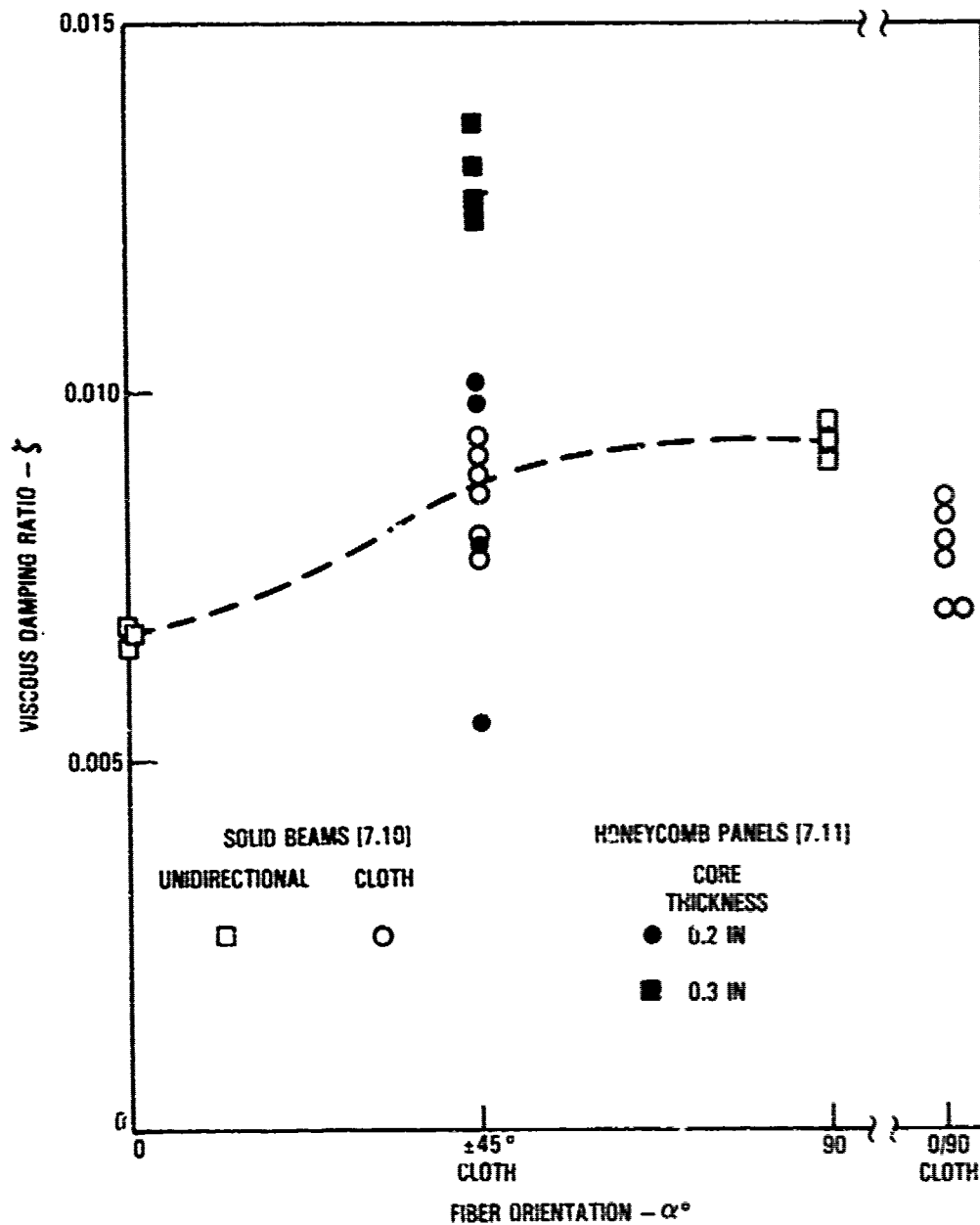


Figure 7.30. Measured damping in free-free Kevlar honeycomb panels and beams.

Metal Matrix Composites — The measured damping data on metal matrix composites is summarized in Table 7.12. Boron/aluminum, the first metal matrix composite, appears to have a viscous damping ratio around 0.00038 [7.75]. The most comprehensive damping data to date, on later types of metal matrix composites, is contained in References [7.81] and [7.82], the former addressing the variation of the damping with frequency (Figures 7.32 to 7.34) and the latter dealing with variation of damping with surface stresses at ambient, 200°F and 400°F temperatures. The highest damping was measured in the graphite/aluminum and graphite/magnesium composites with viscous damping ratios of 0.00066 and 0.00067, respectively. The damping appears to be constant with frequency. The damping in the FP/aluminum and FP/magnesium composites also appears to be constant with frequency, with viscous damping ratios of around 0.00045. Some measurement problems were encountered at higher frequencies [7.81] which may account for the subsequent rise in damping above 1000 Hz for these materials. The FP in these metal matrix composites is Al₂O₃ fiber. The damping in the silicon carbide reinforced aluminum composites continues to fall off with frequency similar to the Zener curve with values as low as 0.0002 around 6000 Hz and as high as 0.001 around 10 Hz. The graphite/AZ916-T [7.77] composites also exhibited a low damping with a viscous damping ratio of 0.0004. The graphite/AZ916-Mg [7.77] had a higher viscous damping ratio of 0.001 consistent with that expected from the Zener curve for magnesium, as illustrated in Figure 7.35. The damping data in Reference [7.83] for various metal matrix composites appears to be high. This conclusion is supported by the comparison with the damping measured in Reference [7.77] for P100/AZ916-Mg composite. There appears to be a factor of six difference. The damping of the aluminum beam also appears to be high.

7.2.4.5 Current Methods for Measuring Material Damping

The basic methods currently used for measuring the material damping in both metals and composites, in the low to intermediate audio frequency range, involve resonant testing of thin beam type test specimens, either in flexure or torsion. Longitudinal resonant vibration testing is generally used in the highest audio frequency range while nonresonant testing is used in the lowest frequency range, down to almost zero frequency. Many of the test methods are

TABLE 7.12. SUMMARY OF MEASURED METAL MATRIX COMPOSITE MATERIAL DAMPING (Sheet 1 of 3)

Material	Fiber Angle Degrees (0° = Axial)	Fiber Volume Fraction V _f	Dynamic Modulus MSI	Frequency Hz	Viscous Damping Ratio ζ	Type of Test*	Ref.	Test Conditions/Comments
Boron BB4C/6061 Aluminum	0	57	34.1	9.7	0.00038	F	7.75	Free-free beam; in air; ambient temperature.
P55/6061 Al	0	-	26.4	6 to 2200	0.00088	F	7.81	Cantilever beam; in air; ambient temperature. Air damping present in the data. The damping appears to be constant with frequency for graphite/aluminum and graphite/magnesium composites (see Figure 7.32).
P100/6061 Al	0	-	42.5	7 to 7000	0.00085	F		
P55/ZE41A Mg	0	-	23.1	6 to 9000	0.00070	F	7.81	
P100/ZE41A Mg	0	-	40.8	8 to 6000	0.00065	F		
FP-Al ₂ O ₃ /Li Al	0	-	32.0	10 to 1000	0.00045	F	7.81	Damping increases to 0.0002 from 1000 Hz to 9000 Hz (see Figure 7.33).
FP-Al ₂ O ₃ /Ze41A Mg	0	-	30.0	10 to 1000	0.00045	F		
FP-Al ₂ O ₃ /C.P. Mg	0	-	30.0	10 to 1000	0.00045	F		
Particulate SiC/6061 Al	0	0.45	22.0	10 to 6000	0.001 to 0.0002	F	7.81	Damping generally decreases with frequency (see Figure 7.34).
Whiskers SiC/6061 Al	0	0.20	14.1	10 to 6000	0.001 to 0.0002	F		

*F = Flexure
E = Extensional
T = Torsion

TABLE 7.12. SUMMARY OF MEASURED METAL MATRIX COMPOSITE MATERIAL DAMPING (Sheet 2 of 3)

Material	Fiber Angle Degrees (0° = Axial)	Fiber Volume Fraction V_f	Dynamic Modulus MSI	Frequency Hz	Viscous Damping Ratio ζ	Type of Test	Ref.	Test Conditions/Comments
Same Materials as described in Reference [7.81]						F	7.82	Cantilever beam: in air; ambient, 200°F and 400°F. Includes the effect of surface dynamic stress. Damping increases with surface stress for all materials, but at different rates. Contribution from air damping calculated.
	0	-	-	-	0.0004	F	7.77	Free-free beam; near vacuum under zero 'g' loading, ambient temperature. See Figure 7.35.
	0	-	-	-	0.0004	F		
P100/ AZ91C-T1	0	-	-	-	0.001	F		

TABLE 7.12. SUMMARY OF MEASURED METAL MATRIX COMPOSITE MATERIAL DAMPING (Sheet 3 of 3)

Material	Fiber Angle Degrees ($0^\circ = \text{Axial}$)	Fiber Volume Fraction V_f	Dynamic Modulus MSI	Frequency Hz	Viscous Damping Ratio ζ	Type of Test	Ref.	Test Conditions/Comments
$\text{SiC}_v/\text{6061-T6}$	0	0.17	14.7	32.1	0.0025	F	7.83	Cantilever beam; in air; ambient temperature. Air damping present in the data. Damping of aluminum beam appears to be high. Could also have additional damping due to clamping.
$\text{SiC}_p/\text{6061-T6}$	0	0.20	15.2	120.0	0.0046	F	7.83	
$\text{SiC}_p/\text{6061-T6}$	0	0.30	17.5	20 105	0.0037 0.0014	F	7.83	
P55/AZ91C/AZ31B	0	0.127	12.4	13	0.0034- 0.0071	F	7.83	
	90	0.127	4.6	11	0.0054- 0.0079	F	7.83	
P100/AZ91C/AZ31B	0	0.265	32.4	13.6	0.0061	F	7.83	
	90	0.265	4.8	8.7	0.0067- 0.013	F	7.83	
P100/6061/6061	0	0.34	37.1	35.5-47.6	0.0046- 0.0057	F	7.83	
	90	0.34	5.4	38	0.0093- 0.0153	F	7.83	
6061-T6	-	-	10	15.2-53.9	0.0029- 0.0025	F	7.83	

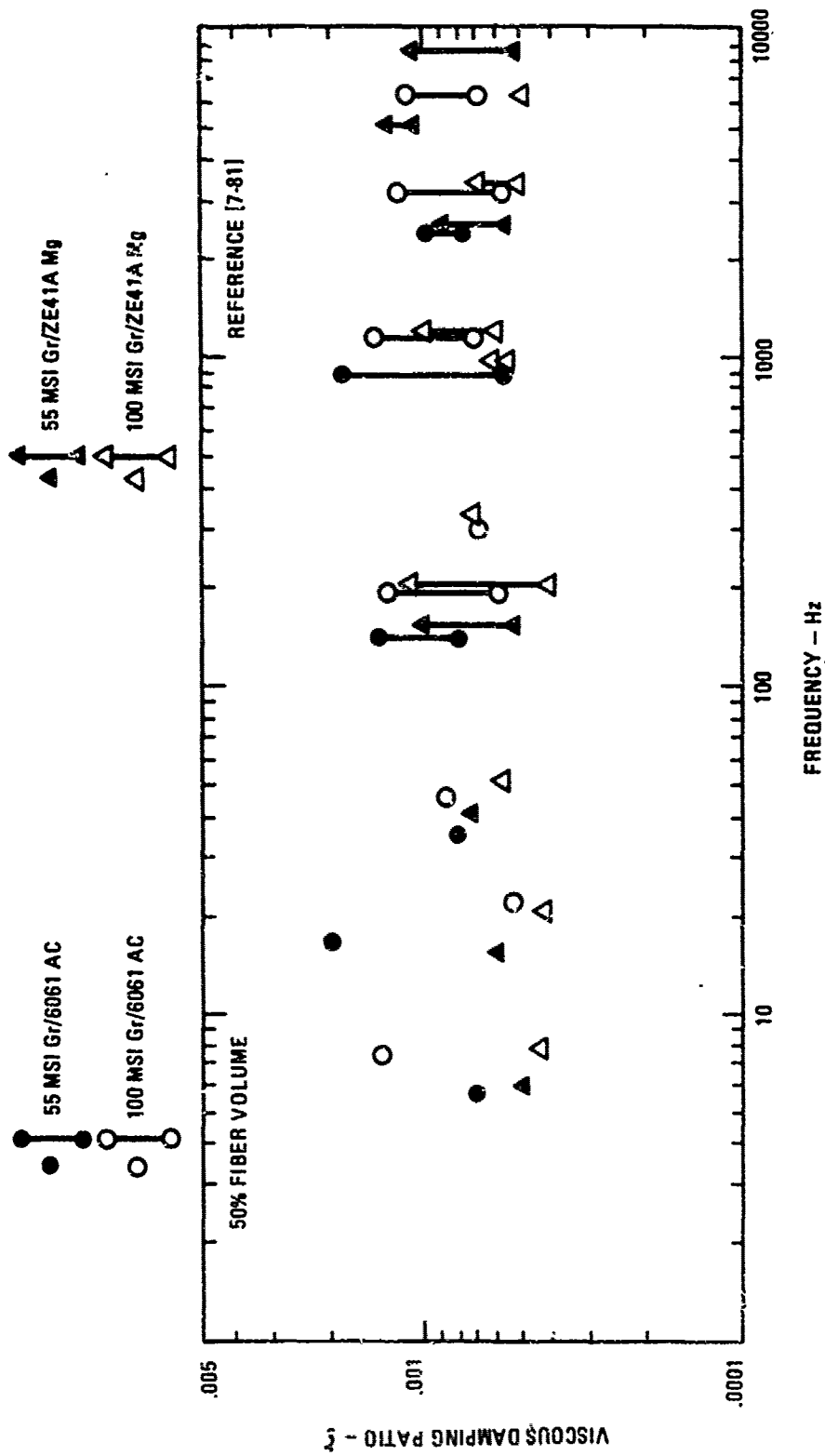


Figure 7.32. Variation of damping with frequency of graphite reinforced aluminum and magnesium matrix composites.

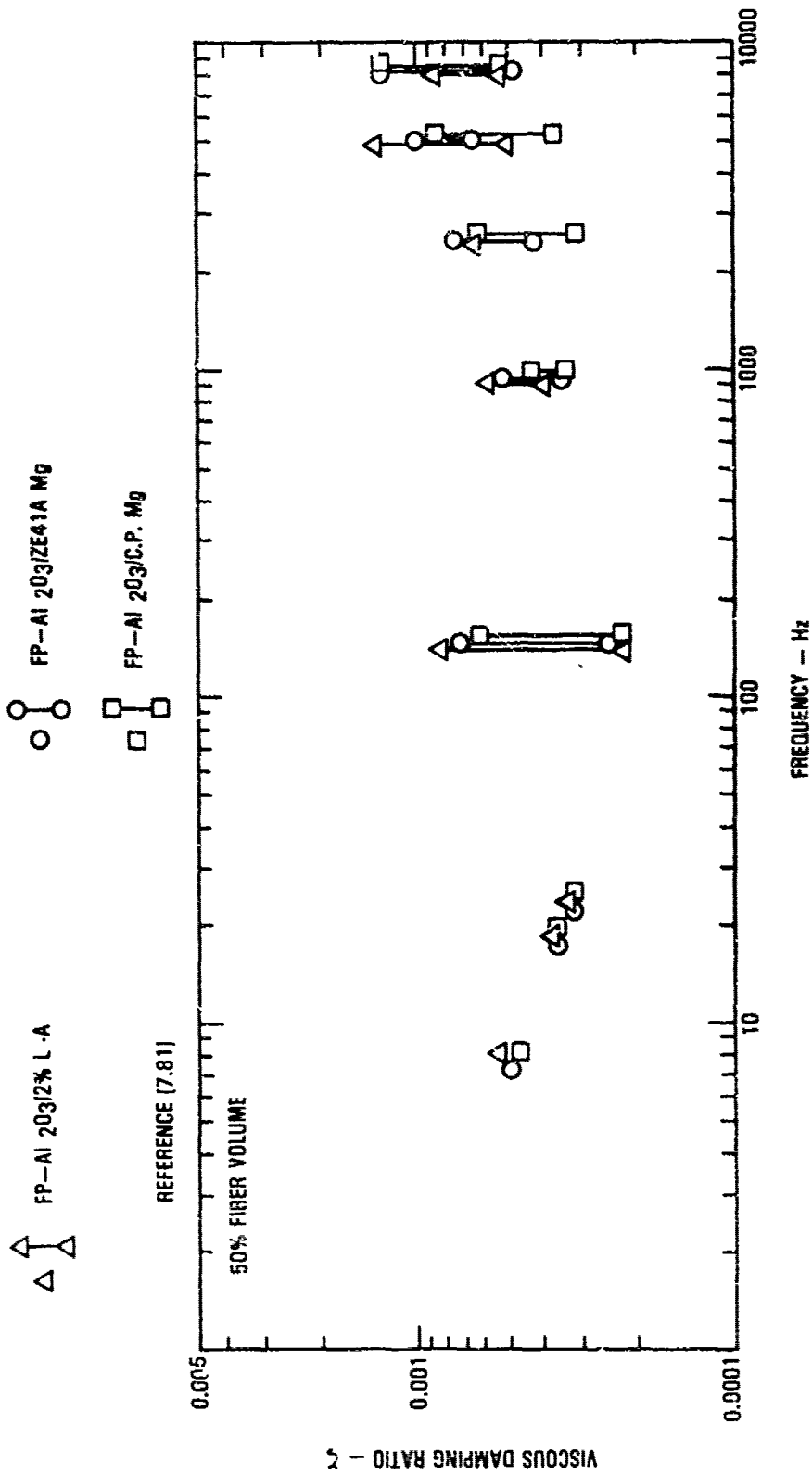


Figure 7.33. Variation of damping with frequency of aluminum oxide fiber reinforced lithium-aluminum and magnesium matrix composites.

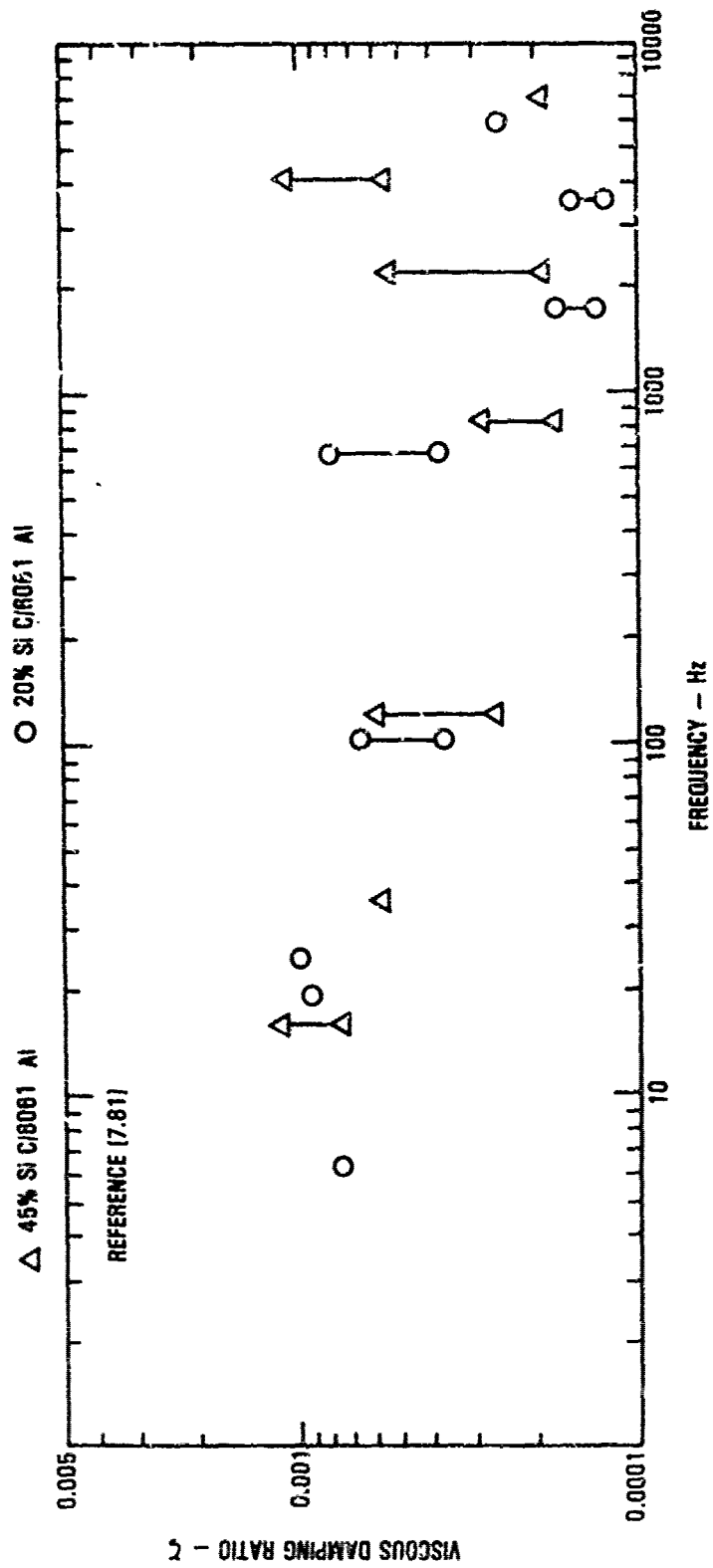


Figure 7.34. Variation of damping with frequency of silicon carbide reinforced aluminum matrix composites.

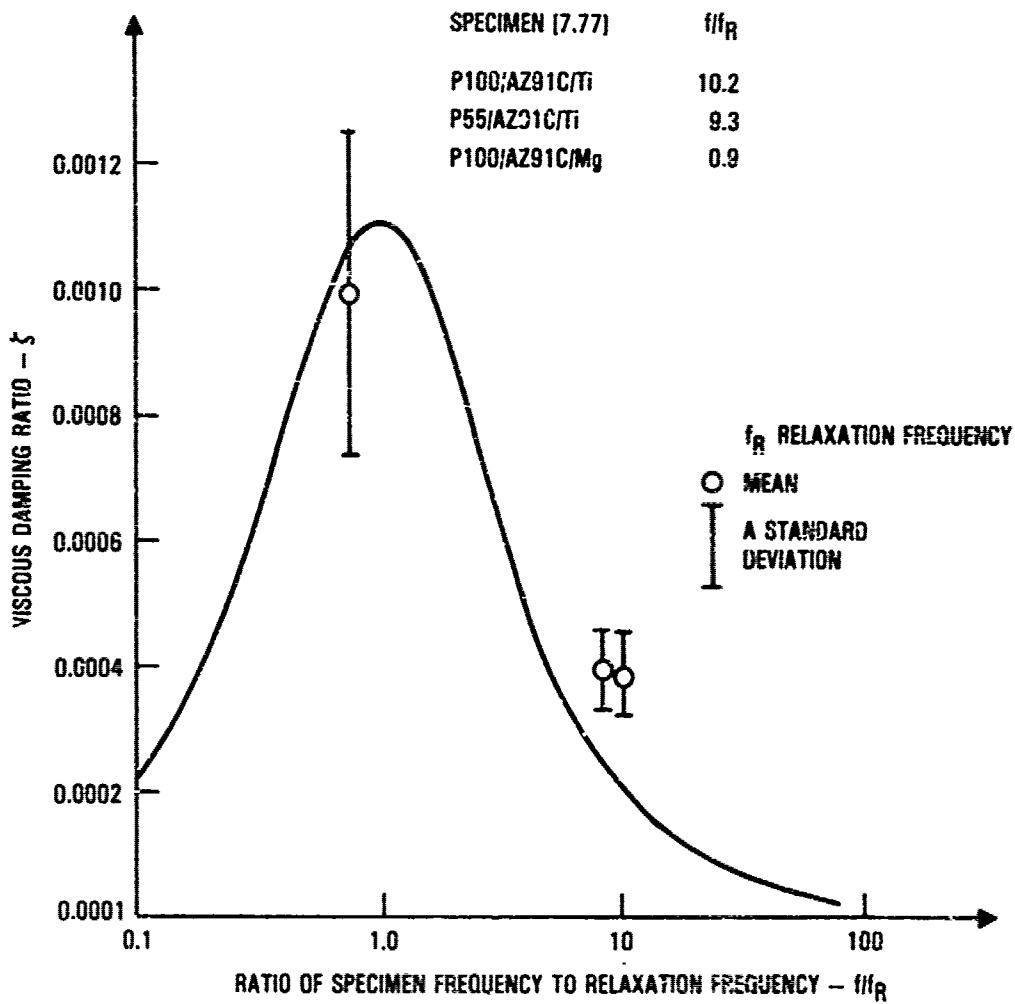


Figure 7.35. Damping of metal matrix specimens versus frequency superimposed on the Zener curve for AZ916 magnesium.

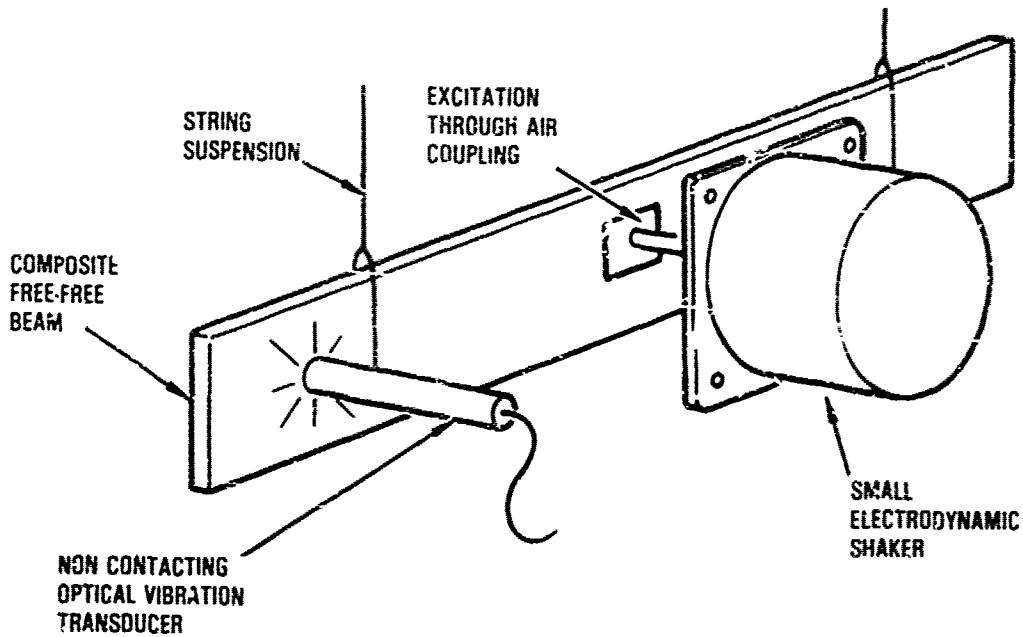
discussed in References [7.84], [7.85] and [7.86]. The basic resonant frequency equation for many of the test specimens and the methods for correcting these equations for added masses, magnetic drive effects and some test fixture effects are summarized in Reference [7.84].

The material damping in aluminum has been well established by experiment (Figure 7.14) and is, in general, in good agreement with the theoretically predicted damping (equation 7.9). Consequently, aluminum has [7.87] become the standard reference material for evaluating and, indeed, calibrating test methods used in measuring material damping.

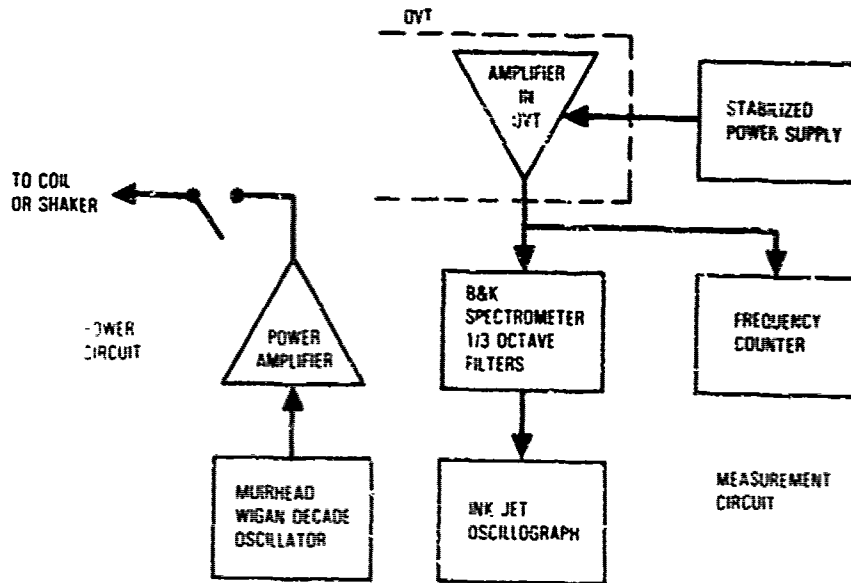
Nonresonant Testing - The main problem with nonresonant testing is that specified test fixtures [7.51] have to be developed to introduce the loads into the test specimen without any friction or damping losses, especially when testing very stiff metals. These problems are less severe when testing the much softer polymer type materials [7.84]. The above test fixtures often require the use of complex specimen shapes [7.51] that can be expensive to manufacture, at least in comparison to the more common beam type specimens. The advantages are a highly controlled force level, and the ability to measure the material damping as a function of stress amplitude, especially in the presence of a static load. Thus, the widest possible loading combinations can be used in the tests, albeit over a small frequency range.

Free-Free Resonant Flexural and Torsional Testing - The free-free beam represents one of the most commonly used test methods for measuring the material damping. The free-free beam test method requires only a minimal test fixture, but is usually restricted to the lower dynamic strain region by the availability of only a limited input force level. This test method has recently been extended into the higher dynamic flexural strain region by the development of a controlled impulse launch mechanism for the specimen.

In the simplest form of the free-free beam flexural test [7.24], the specimen is suspended at the nodal lines by two long vertical nylon strings as illustrated in Figure 7.36a. The specimen has a length to thickness ratio



(a) TEST SETUP



(b) CIRCUIT DIAGRAM

Figure 7.36. Typical method for measuring material damping in air with a free-free resonant beam.

typically around 250 to minimize the effect of transverse shear on the resonant frequencies and, in composite beams, on the damping of the lowest flexural modes. The excitation is provided through air coupling by a plate mounted parallel to the test specimen and attached to an electrodynamic shaker. The response of the specimen is measured by a noncontacting optical vibration transducer (OVT) [7.24]. The harmonic excitation is first tuned onto the resonant mode of interest and the power to the shaker is then open circuited. The resulting single mode free decay response of the beam is recorded either on a strip chart by means of an ink jet oscillograph (Figure 7.36(b)), or on magnetic tape for subsequent analysis on the computer. Since the excitation is normal to the support direction, and since noncontacting excitation and response transducer are used, all extraneous sources of damping, except for acoustic radiation (air damping), have been eliminated. The beam is tested in its manufactured state without any added mass. Consequently, the error in calculating the flexural modulus from the beam geometry, density and measured resonant frequency is also expected to be a minimum. However, this test method can only be used in air due to the nature of the excitation.

Magnetic transducers have also been used [7.58, 7.60, 7.62, 7.84] to excite free-free beam specimens in material damping tests. These transducers can be used down to near vacuum conditions (Figure 7.37) [7.62], but require small magnetic steel targets to be bonded onto the center of the beam, or to the end of the beam, on one side for flexural tests and on opposite sides and corners for torsional tests [7.60, 7.34]. Optical [7.62] or proximity probes [7.84] can be used to measure the beam vibration response. The probes also require thin steel or aluminum foil targets to be bonded onto the specimen. Except for some possible magnetic effect [7.84], the added masses do not effect the material damping of the beam, but must be accounted for, when extracting the flexural Young's modulus from the test data. It is, generally, recommended [7.84] that the added mass be less than 3 percent of the total beam weight. Lightweight coil and magnet drives [7.22, 7.23] have also been used in the measurement of the material damping in free-free beams [7.23] and in free-free composite honeycomb panels [7.11], as illustrated in Figure 7.38.

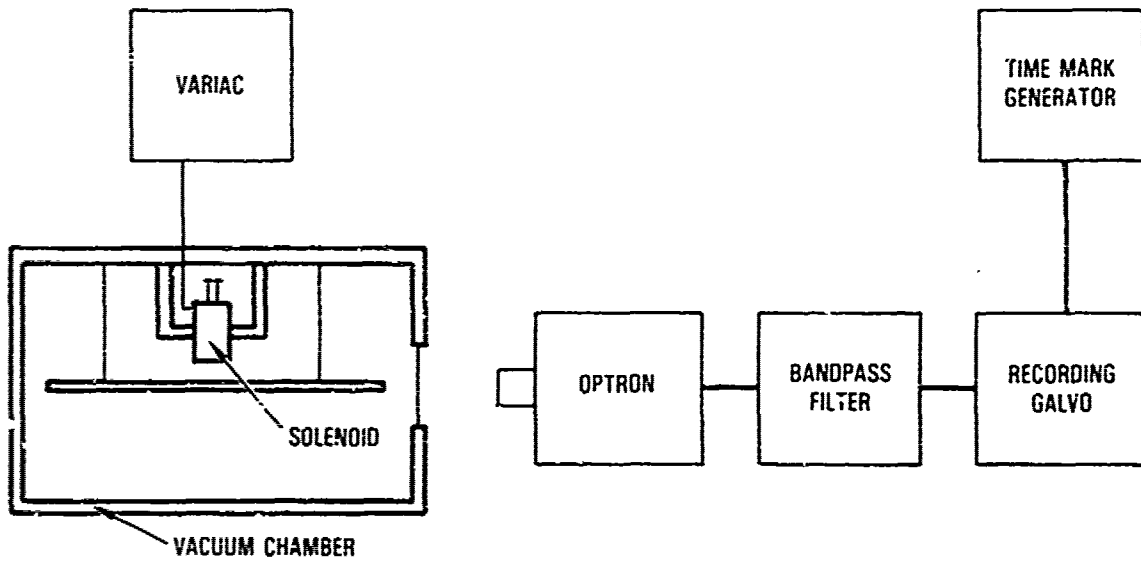


Figure 7.37. A method for measuring material damping under near vacuum conditions with a free-free resonant beam.

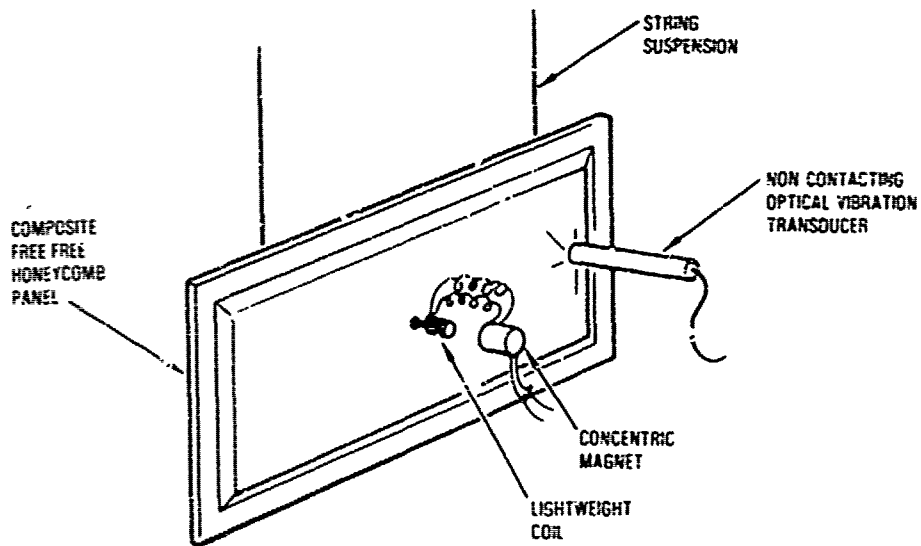


Figure 7.38. Schematic of coil and magnet drive used with large test specimens.

This form of magnetic drive provides a negligible contribution to the material damping in air and can also be used under near vacuum conditions.

The free-free test beams can also be mounted horizontally [7.58, 7.62, 7.84] supported at the nodal lines by two cotton or nylon string loops or by two thin steel wires [7.84], or even mounted on two polyurethane foam wedges [7.23]. Care must be taken to locate these supports exactly at the nodal lines since any relative motion between the supports and the specimen can generate friction damping [7.84, 7.23]. This type of support can also introduce rigid body modes into the beam response [7.84], with frequencies high enough to be mistaken for a flexural mode.

The final form of free-free flexural beam test involves the use of impulsive type excitation. The most interesting test method [7.88] involves the use of a spring-cocked launcher, as illustrated in Figure 7.39. The specimen is simultaneously excited and lofted into a vertical free-fall trajectory, that lasts about 1 second, by the above launcher. This launcher

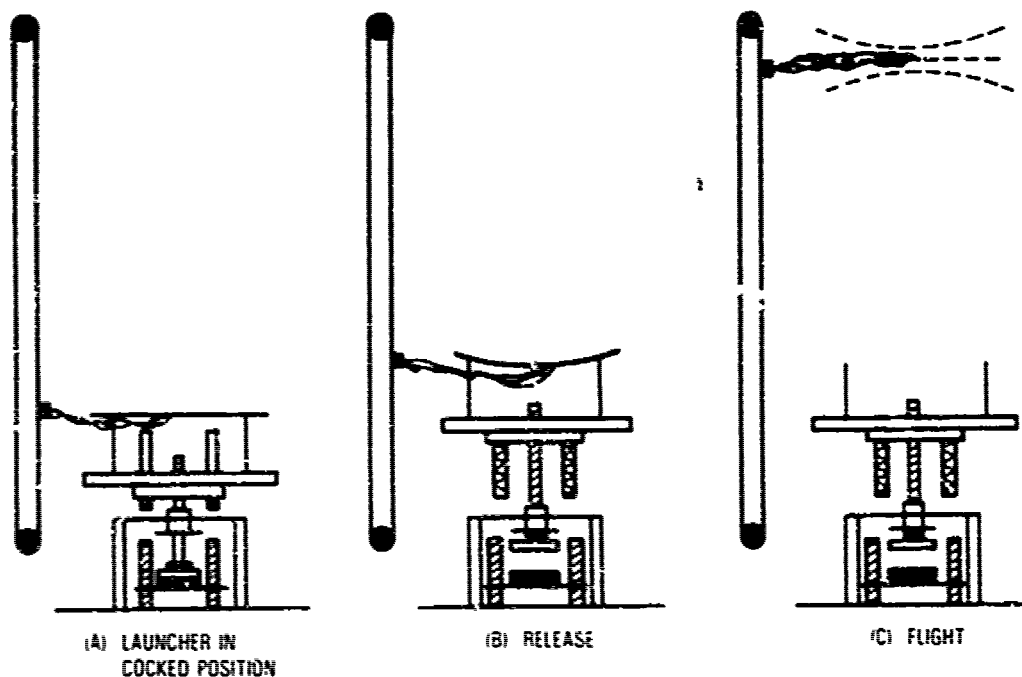


Figure 7.39. Test sequence of the tunable excitation launch mechanism, showing the launcher, specimen and signal wire carrier.

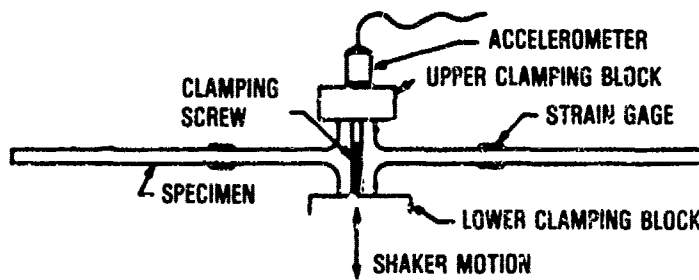
permits, within limits, the elastic dynamic stress amplitude to be varied while maintaining the same rigid body launch velocity. Dynamic stress levels as high as 20 KSI have been measured in some specimens [7.29]. The dynamic response is measured by two axial strain gages located in opposite sides at the center of the test beam. The thin lead wires are supported, in part, by a wire carrier which follows the vertical trajectory of the beam (Figure 7.39) under computer control. The contribution to the material damping from the lead wires is very small, as demonstrated by the good agreement obtained [7.88] with other test data and with the theoretically predicted relaxation damping to aluminum alloy. This test method overcomes the problem of support damping and acoustic radiation damping, the latter through enclosure in a vacuum chamber to simulate near vacuum test conditions.

The impulse head hammer tap method can also be used to measure the damping of larger free-free test specimens that are supported by nylon string. The resulting rigid body motion may take the specimen beyond the measuring limits of noncontacting transducer. The use of a lightweight accelerometer raises the question of lead wire damping. Unless a remote hammer tap mechanism is used, this method is also restricted to testing in air.

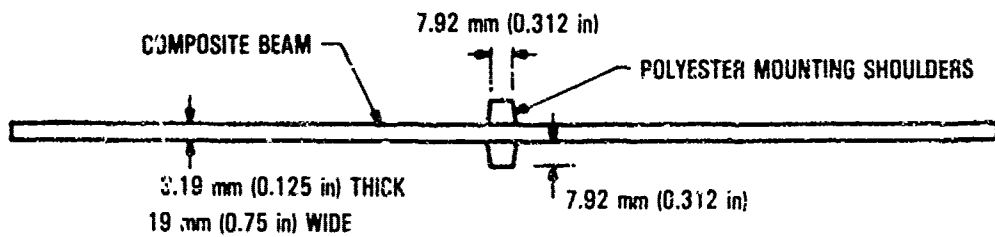
Flexural and Torsional Resonant Testing with Fixed Supports - The test specimens in resonant flexural tests can be a single cantilever beam [7.25, 7.26, 7.84] that is mounted in a rigid test fixture and excited by a magnetic transducer, a double cantilever beam [7.27, 7.57, 7.58, 7.62, 7.67] (Figure 7.40) that is bolted to an electrodynamic shaker or a single cantilever beam that is attached to a cantilevered mass [7.81], which is in turn, attached to an electrodynamic shaker (Figure 7.41). A typical test set-up [7.62], used with a double cantilever beam, is illustrated in Figure 7.42. A tip mass can be added [7.81] to permit testing at lower frequencies. The electrodynamic shaker provides sufficient force to produce significant dynamic stress levels in the cantilever test specimens. In the resonant torsional tests, either one end or both ends of either a square [7.23], or a rectangular [7.29, 7.84] test specimen can be clamped in a fixture. The test specimens can be excited at the free end by two magnetic transducers [7.84] located at



METAL TEST SPECIMEN (7.26)



TEST SPECIMEN INSTRUMENTATION (7.67)



COMPOSITE TEST SPECIMEN (7.67)

Figure 7.40. Typical double cantilever test specimens used in measuring material damping.

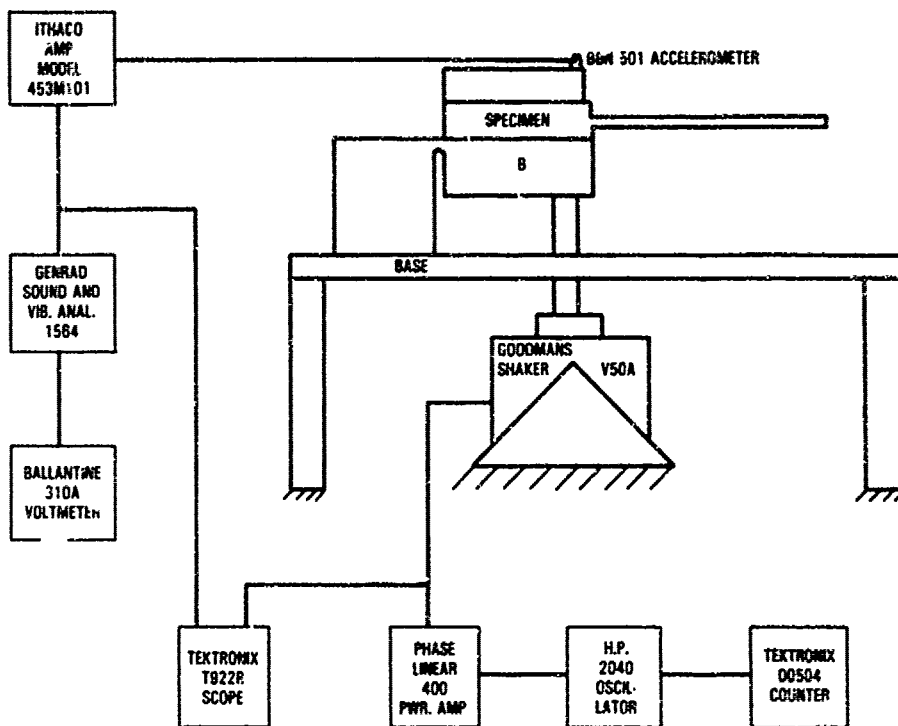


Figure 7.41. Experimental arrangement for resonant dwell tests.

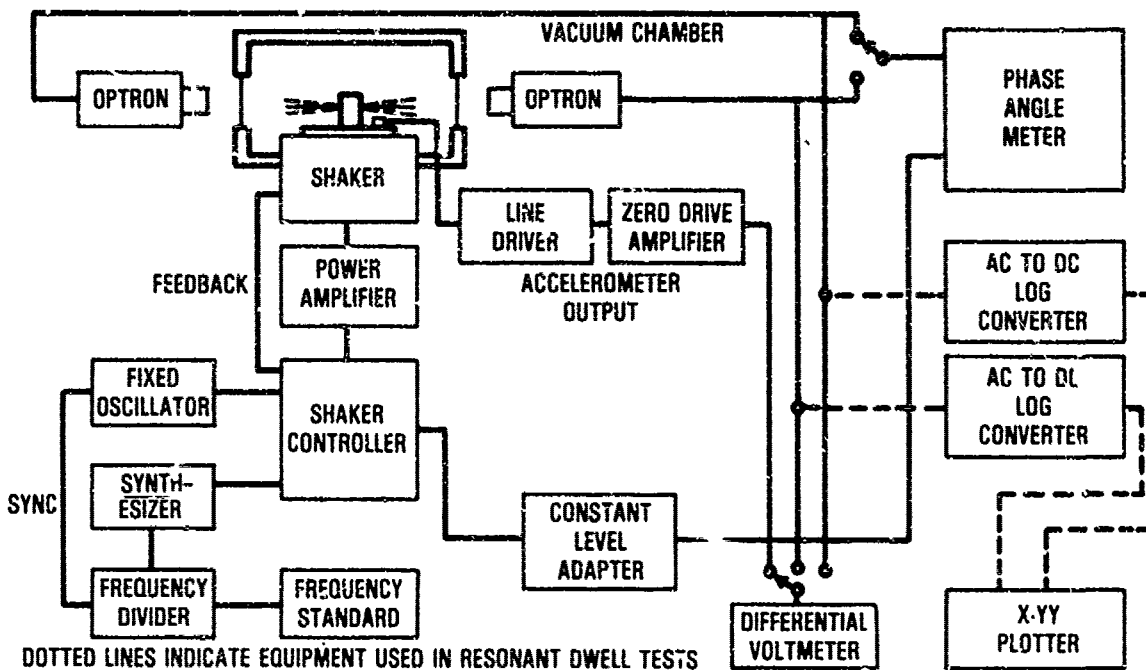


Figure 7.42. Forced vibration test setup used for frequency sweep tests.

two opposite corners, or at the center, with two coil and magnet drive [7.22, 7.23] positioned to provide a torque to the clamped-clamped specimen (Figure 7.43). A torsional pendulum [7.84] is used to test at lower frequencies.

The cantilever beam suffers from frictional losses at the root, requiring the use of special machined test specimens [7.27, 7.67, 7.81], for high stiffness metals and composites, such as illustrated in Figure 7.40 and 7.41. Similar test specimens are also used in measuring the damping and Young's modulus properties of viscoelastic damping materials as previously discussed in Section 2.3.1 of this volume. The clamping is not so critical for torsional test specimens because of the relatively low torsional stiffness of the test specimens. The cantilever beam is also subjected to significant damping from acoustic radiation as previously discussed. Consequently, the cantilever beam test method should be used under near vacuum conditions when measuring the material damping. The errors encountered in the above test methods and means of estimating these errors are discussed in more detail in Reference [7.84].

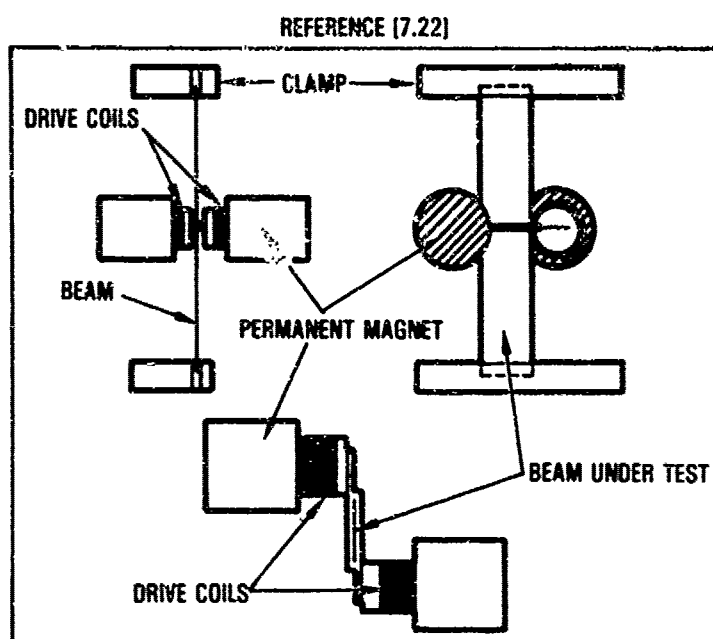


Figure 7.43. Driving arrangement for shear tests.

More recently, impulse test methods have been developed [7.79, 7.80] that utilize remotely controlled hammer tap mechanisms with cantilever beams under near vacuum conditions. Results, comparable to those from forced vibration tests, have been obtained [7.79].

Longitudinal Resonance Testing - The longitudinal resonance testing is generally used to measure the damping in the high frequency range, typically above 2000 Hz [7.59, 7.75]. The short [7.84] or long [7.59] rectangular specimen is excited at one end with a magnetic or piezoelectric transducer, or a small explosive charge [7.59]. The response is measured at the other end by lightweight accelerometer, proximity probe, or condenser microphone. The damping is obtained from the free decay of each longitudinal resonant mode on termination of the harmonic excitation [7.84]. The Young's modulus extracted by this method has to be corrected for [7.84] the added end masses and, in the higher modes, for the lateral inertia related to the Poisson's ratio effect.

Resonance Testing Under Combined Loads - Three resonance test methods have recently been developed to measure the damping of materials under combined loading. The first two methods [7.72] [7.89] involve the application of combined dynamic loads to the test specimen, while the third method [7.42] involves the application of only a static tension load with a dynamic bending load.

In the test method described in Reference [7.89], the combined dynamic bending and torsion loads are applied simultaneously to a hollow cylindrical test specimen by means of four magnetic drives mounted on an inertia bar that is clamped to the end of the test specimen (Figure 7.44). The magnetic drives excite the specimen in a coupled bending-torsion mode. The mode shape can be varied such that any combined loading condition, between all bending, no torsion and no bending, all torsion, can be obtained. Damping data for six highly damped metals, two alloys of manganese-copper and four grades of cast iron, were determined from energy input during steady state vibration. Prior combined loads test methods are also discussed in this reference.

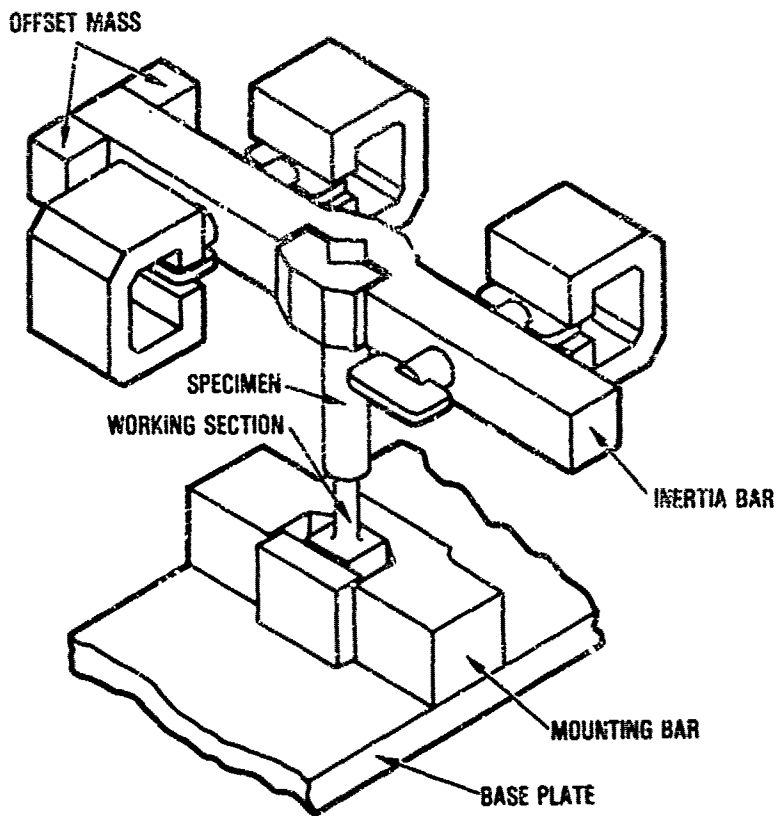


Figure 7.44. Combined loading apparatus [7.89].

A test apparatus, Figure 7.45, is being developed [7.72], for measuring the damping properties of rods also under combined dynamic torsion and bending loads. The rods in this test method can be pretwisted and/or pretensioned. Oscillatory torque and bending forces are applied through a central inertia bar by two concentric coil and magnet drives.

The final test method [7.41] is designed to measure the damping of turbine blades under a simulated centrifugal force. The test specimen consists of a pair of turbine blades that are welded at the tips (Figure 7.46) and installed in the loading frame by the fir tree roots. The axial load is applied by pressured load cells. The whole test fixture is enclosed in an environmental chamber. The specimen is excited, in both the lateral and tangential directions, by a remote striker. The damping is determined from the free decay by means of the computer aided data acquisition system illustrated in Figure 7.47.

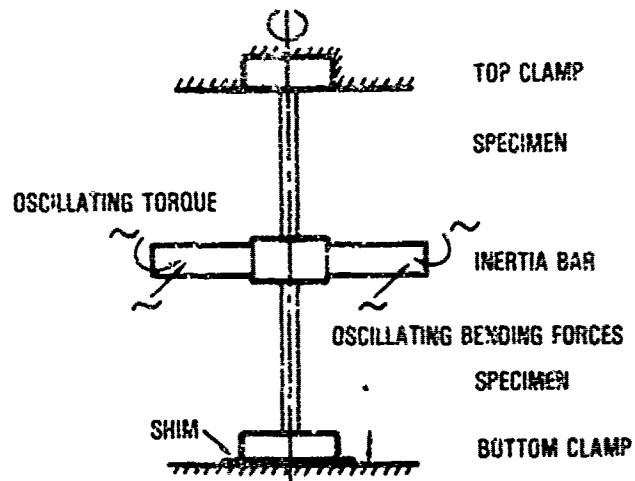


Figure 7.45. Combined loading apparatus [7.72].

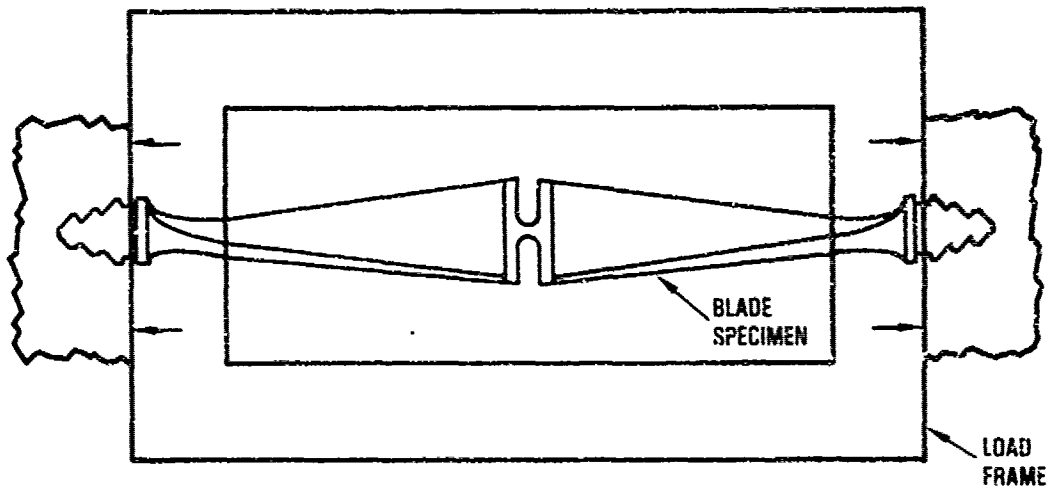


Figure 7.46. Principle of blade test rig [7.41].

7.3 DAMPING LEVELS IN AEROSPACE STRUCTURES

The damping levels, primarily in lightweight aerospace structures, are reviewed in this section. The most common type of structure consists of riveted multi-bay stringer-and-frame-stiffened aluminum panels [7.12, 7.15, 7.90, 7.91, 7.92, 7.93] and single bay stiffened aluminum honeycomb panels [7.12, 7.90, 7.91] used primarily in secondary aircraft structures. Damping data are also available for stiffened curved panels [7.90], corrugated and beaded panels [7.94, 7.95, 7.96], integrally machined panels in built-up structures [7.90, 7.91], chemically milled panels [7.90], bonded skin-stringer multi-bay aluminum panels [7.97, 7.98], bonded [7.99] and integrally stiffened [7.13, 7.100] composite multi-bay panels, stiffened composite honeycomb panels [7.10, 7.11, 7.101] fastener attached composite [7.102] and aluminum [7.92, 7.103] box structures, weldbond panels and composite rudders [7.104], and trailing edge wedges [7.90, 7.91]. The damping data for the above structures have been obtained mostly during sonic fatigue tests. Damping measurements have also been made on stiffened fuselage shell structure [7.106] and stiffened cylinders, with and without the acoustic trim [7.107], in connection with interior noise studies. Data on the effects of fluid loading on the damping of shells [7.108] and stiffened panel type structures [7.109] are available. Damping also plays an important part in the design of structures as diverse as engine components [7.110, 7.111] and circuit boards [7.112] in electronic boxes to name a few. Damping levels in spacecraft vary from spacecraft-to-spacecraft. Typical spacecraft damping levels have been previously discussed in Section 7.2.2.1 and will not be included in this section.

The damping data are usually presented in the form of a graph of viscous damping ratio as a function of frequency, for each structural configuration, plotted on a log-log graph such as illustrated in Figure 7.48 for skin-stringer panels. On account of the past emphasis on predominant single fundamental mode response in acoustic fatigue studies, most of the damping data recorded in literature for skin-stringer and other stiffened panel type structures is only for the fundamental mode. Some higher mode damping data may also be included in the above damping-frequency plots.

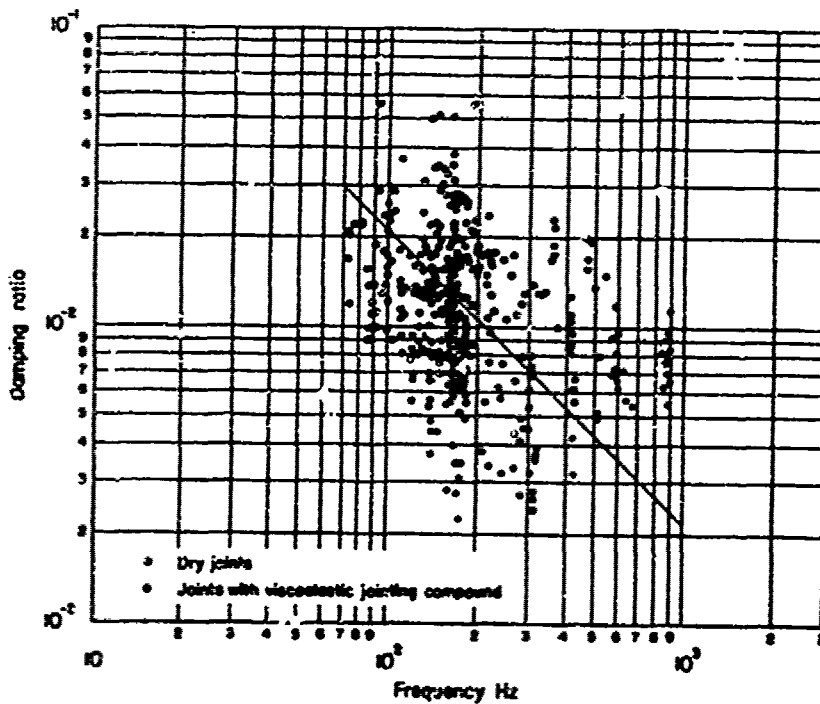


Figure 7.48. Measured viscous damping ratios for flat skin-stringer panels

Some damping measurements have been made at high dynamic strain levels [7.95, 7.113] where nonlinear panel response is encountered. When the 3 dB bandwidth method is used to extract the damping data from the power spectral density of the panel strain response, obtained during high level random excitation tests, higher than actual damping values are obtained [7.113]. These damping values do not correlate with the root mean square (rms) strain levels, measured during the same random excitation tests, when attempting to curve fit test data to simplified theory [7.114]. In previous studies [7.12], reasonable correlation was obtained between the measured rms strains and damping values obtained at low excitation levels, in spite of the simplicity of the theory used in the curve fit. The measured damping values are degraded by poor signal-to-noise ratios, providing a further temptation for using higher excitation levels. The analysis bandwidth used in the spectral analysis of the strain response must also be sufficiently narrow to avoid smoothing

errors, as discussed in more detail in Section 6. Acoustic edge conditions can also affect the damping measurements, as can the method of mounting the panels in the test facility. It is, therefore, not surprising that the measured damping data are characterized by a large scatter such as illustrated in Figure 7.48.

The one-over-the-frequency type variation, assumed in the least squares linear curve fit to the test data in Figure 7.48 and, indeed, to the test data for other panels [7.90], as illustrated in Figure 7.49, is based on the variations of the viscous damping ratio with resonant frequency that is predicted by the single degree-of-freedom system response theory [7.90]. The author of Reference [7.90] joked, when presenting the original damping data for these structures, that there is an equal justification for drawing a horizontal line through the damping data. This comment was received with appreciative laughter. Little did he know how close to the truth he came.

The damping data for stiffened aluminum and composite honeycomb panels is discussed first in the following section since some recent work [7.10, 7.47] has thrown a considerable amount of light on the nature of the damping in these structures. Honeycomb panels have the advantage over skin-stringer panel arrays in being tested one panel at-a-time, on account of their relatively large size. The modes are usually well separated and clearly defined. Consequently it is much easier to see modal trends with these panels than with stiffened multi-bay type panels.

7.3.1 Damping in Stiffened Aluminum and Composite Honeycomb Panels

Most of the available damping data for aluminum honeycomb panels [7.12], composite honeycomb panels [7.10, 7.11] and honeycomb rudder wedges [7.90, 7.91] are summarized in Figure 7.50. The damping data for the composite honeycomb panels and the rudder wedges also contain higher order modes, in addition to the fundamental mode. Lines can be drawn through these data in the traditional manner to indicate the trends with frequency. There are in fact several trend

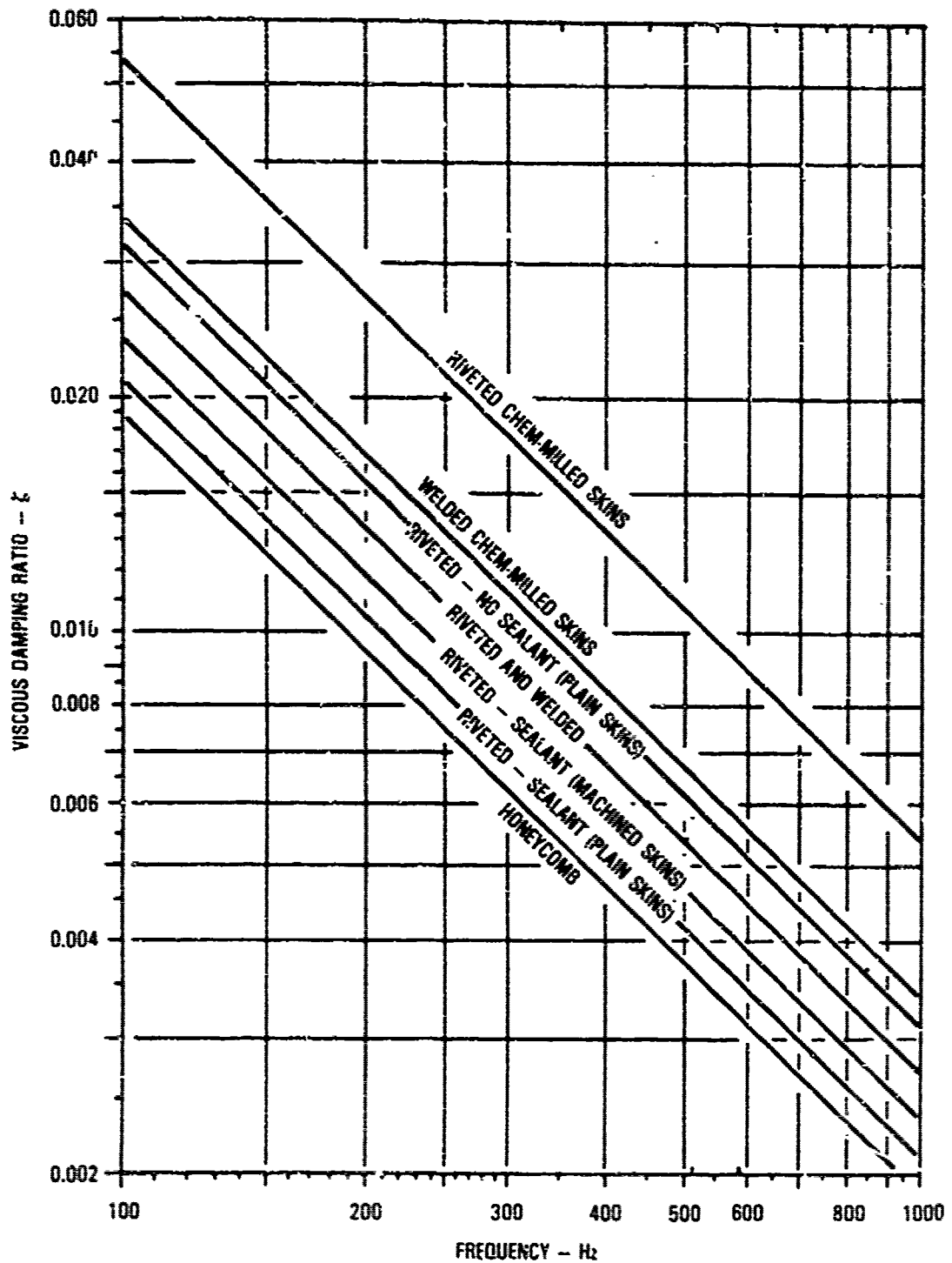


Figure 7.49. Damping ratio versus frequency for typical structure.

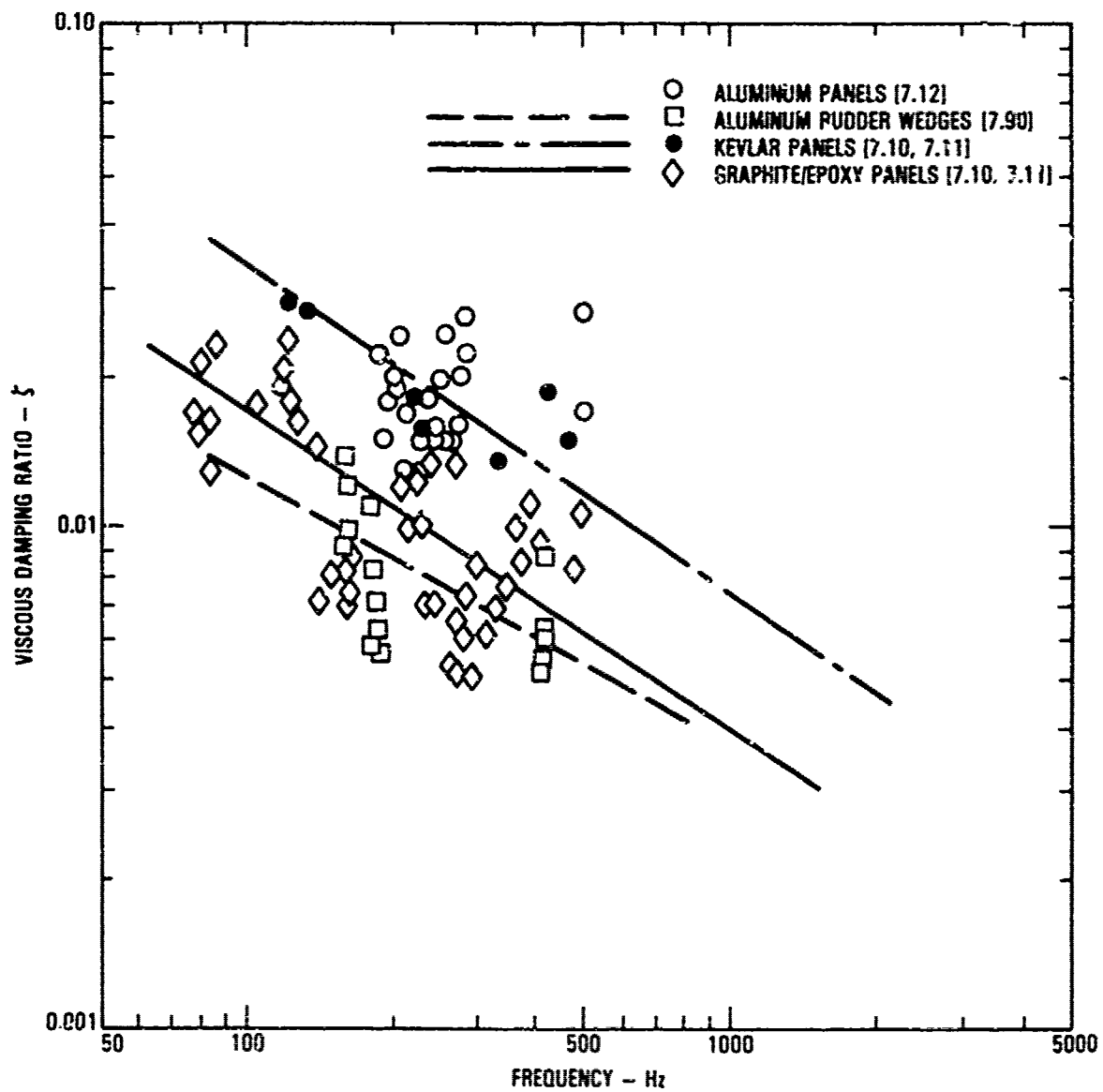


Figure 7.50. Measured stiffened aluminum and composite honeycomb panel damping.

lines, dependent on the type of honeycomb panel (Figure 7.50). The trend lines are different even for the three types of composite honeycomb panels tested [7.47], as illustrated in Figure 7.51. If only the fundamental mode damping is plotted against frequency for both the composite and aluminum honeycomb panels, a constant variation of the damping with frequency is obtained [7.47], as illustrated in Figure 7.52. The damping is the same for the graphite/epoxy and the aluminum honeycomb panels while that for the Kevlar honeycomb panels is higher, reflecting a significant contribution from the material damping [7.10]. The above result is consistent with the fact that the dominant contribution to the honeycomb panel damping is due to acoustic radiation [7.10, 7.11] as previously discussed in Section 7.2.1. The difference in the fundamental mode frequencies between the composite and aluminum honeycomb panels are due to the use of thicker honeycomb cores in the aluminum honeycomb panels. Although the damping is the same for the fundamental mode of the graphite/epoxy honeycomb panels, differences in the higher order mode damping (Figure 7.52) start to appear due to different stiffness characteristics of these honeycomb panels.

Although the damping of these panels can now be predicted [7.10] reasonably accurately (Figures 7.2 and 7.3), scatter is still present in the test data that cannot be explained by theory alone. It is reasonable to assume [7.47] that the mechanisms responsible for producing, for example, an above average damping in a panel fundamental mode, will also contribute to the above average damping in the higher order modes. On this basis there would be a great advantage in being able to predict the damping in the higher modes based on the damping and frequency in the fundamental mode, especially if the expression for the damping is relatively simple. Such a theory has been developed in Reference [7.47].

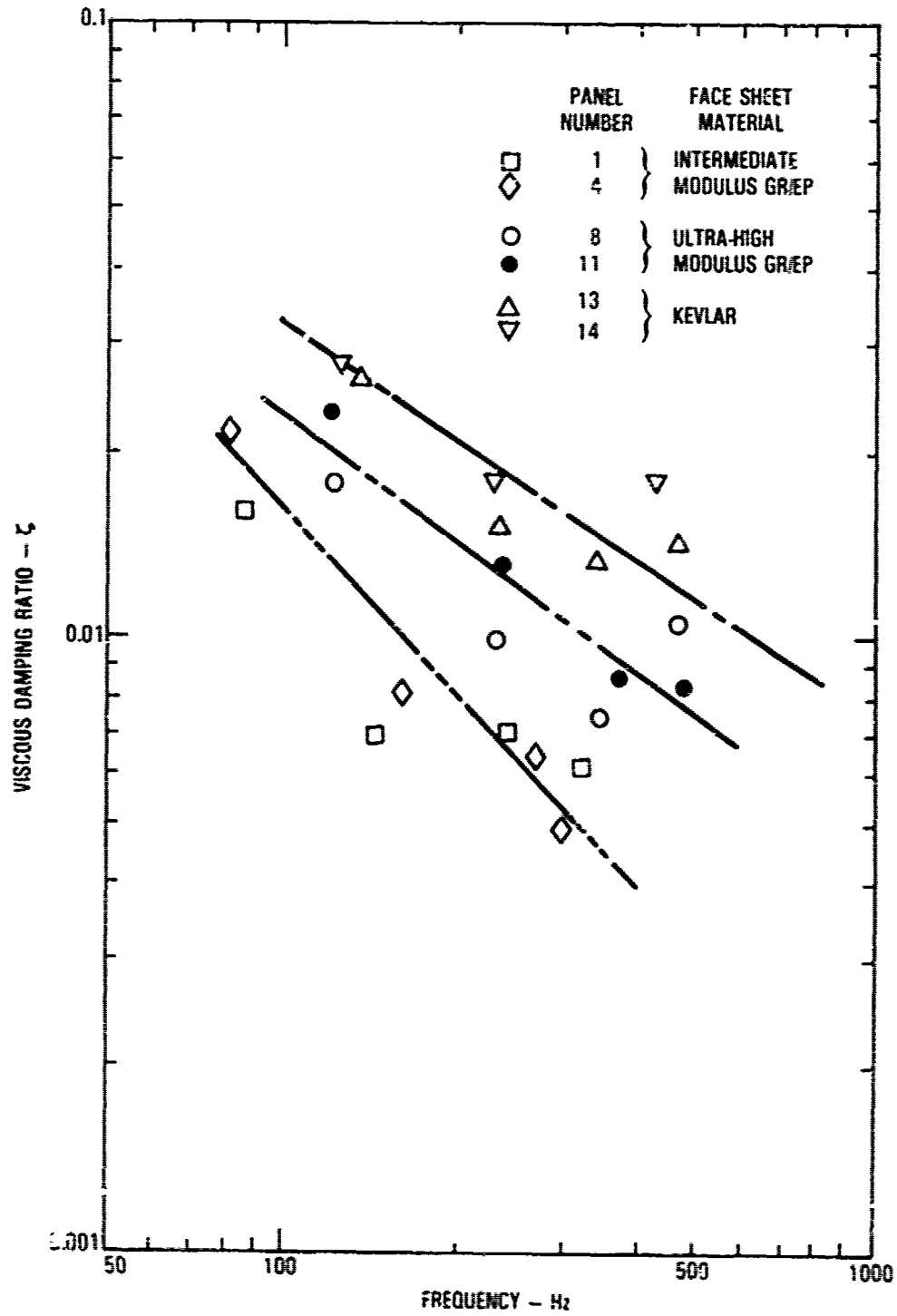


Figure 7.51. Measured fundamental and higher mode damping in selected composite honeycomb panels

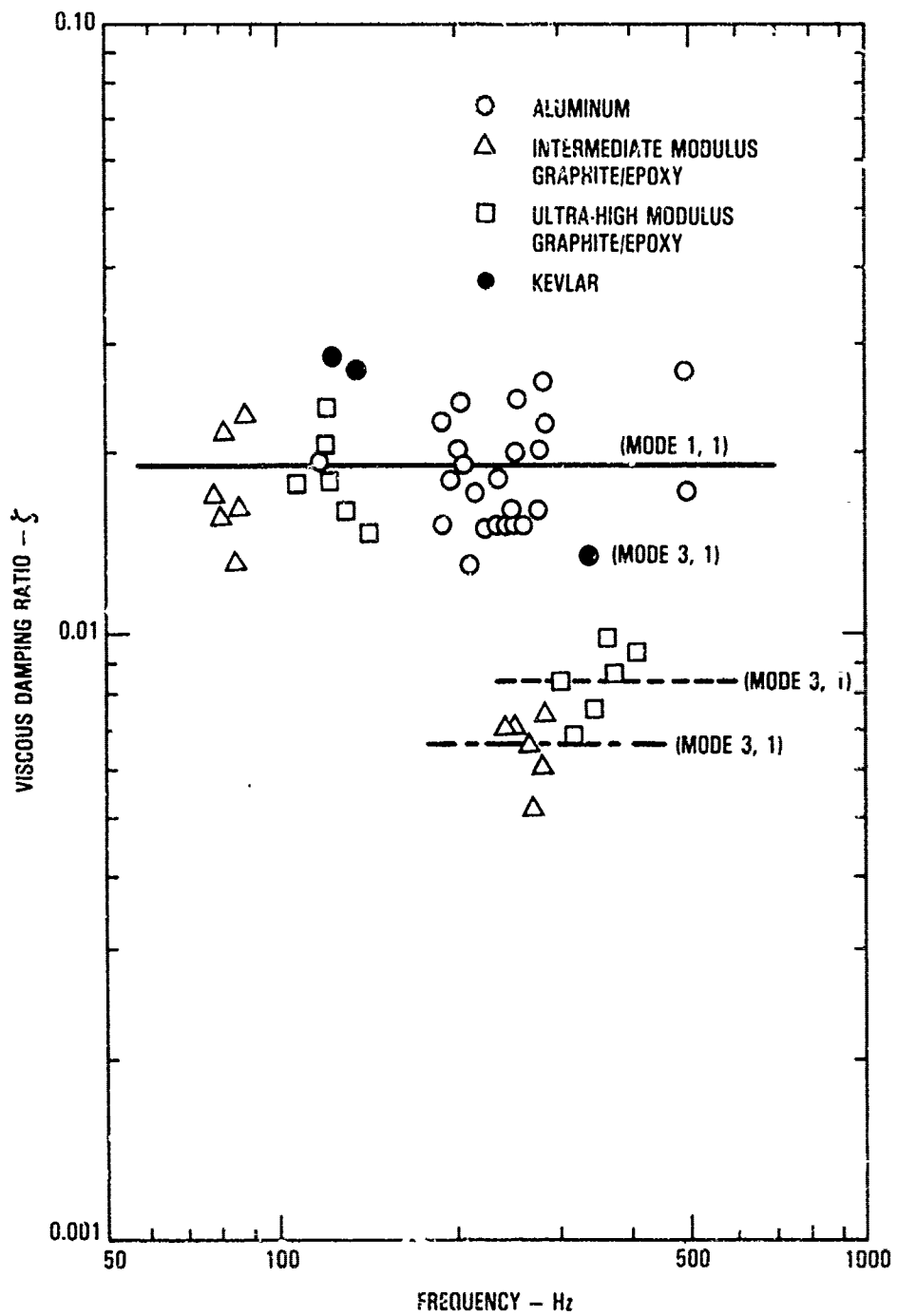


Figure 7.52. Actual measured variation of fundamental mode damping with frequency for stiffened honeycomb panels.

The viscous damping ratio for the m,n^{th} honeycomb panel mode is given, in the most general form, by [7.47]

$$\zeta_{mn} = (\zeta_{11} - \zeta_M - \zeta_F) \left(\frac{f_{mn}}{f_{11}} \cdot \frac{1}{m^2 n^2} \right) + \zeta_M + \zeta_F \quad (7.11)$$

where

- ζ_{mn} = m,n^{th} mode viscous damping ratio
- ζ_{11} = fundamental mode viscous damping ratio
- ζ_M = contribution from material damping
- ζ_F = contribution from friction damping of the rivet line
- f_{mn} = m,n^{th} mode resonant frequency
- f_{11} = fundamental mode resonant frequency

The friction and material damping used in the analysis of the honeycomb panels [7.47], are summarized in Table 7.13. The degree of correlation achieved in predicting the higher mode damping, based on the fundamental mode frequency and damping, is illustrated in Figure 7.53. Means of improving this correlation even further are discussed in Reference [7.47]. This method represents a significant improvement over the current damping-frequency plot approach. Advantage can also be taken of the existing fundamental mode data. This method has also been extended to skin-stinger panel arrays as discussed in the following section.

TABLE 7.13. VALUES OF FRICTION AND MATERIAL DAMPING ASSUMED IN HONEYCOMB PANEL ANALYSIS

Honeycomb Panels	ζ_M	ζ_F
Aluminum	0	0
Graphite/Epoxy	0	0
Kevlar	0.008	0

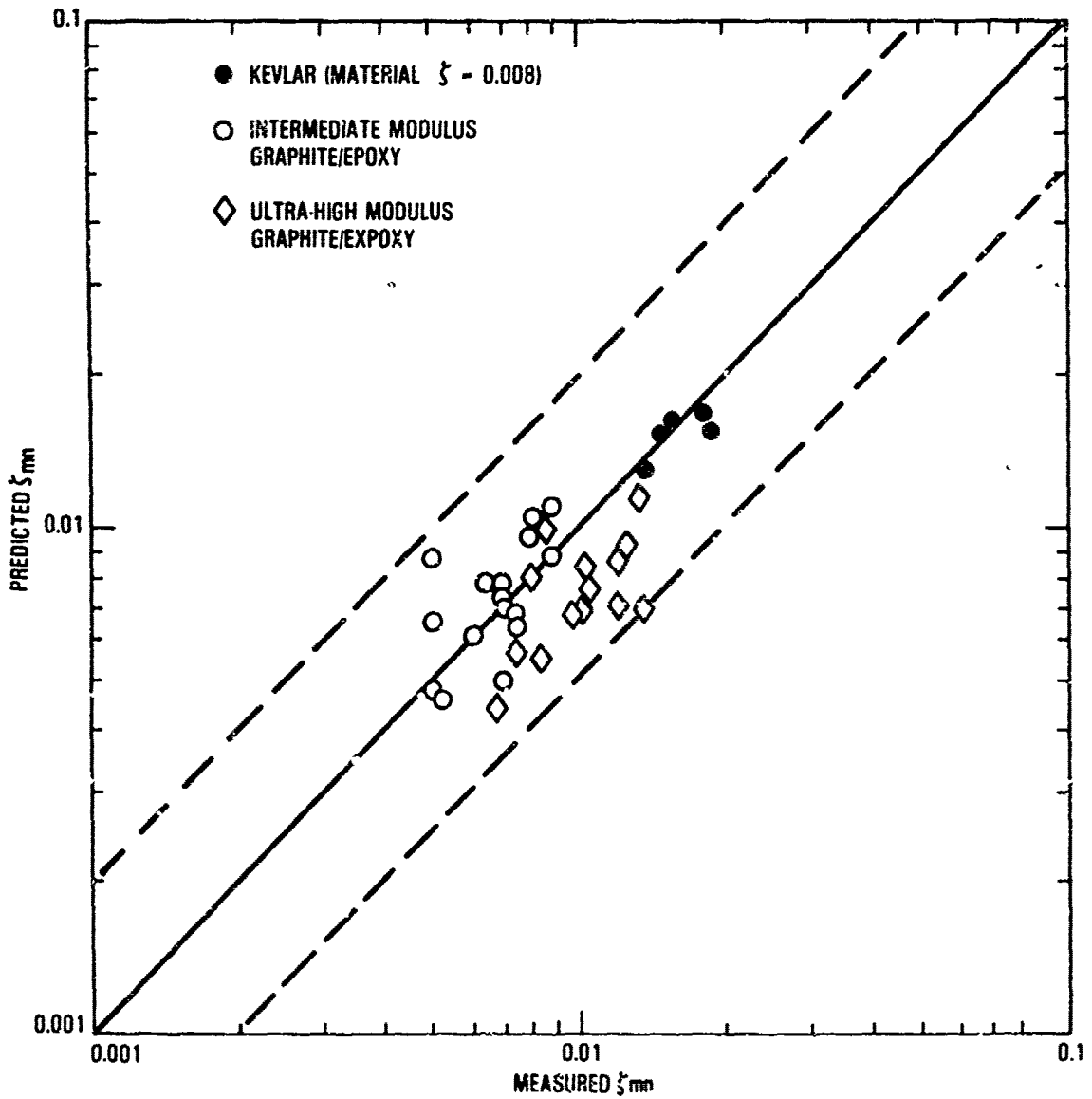


Figure 7.53. Correlation achieved in predicting the higher order panel damping on the basis of the fundamental mode damping.

7.3.2 Damping in Riveted and Bonded Multibay Metal Panels and Box Structures

The damping in, basically, the fundamental mode of riveted [7.12] and bonded [7.97] multibay aluminum panels, riveted multibay aluminum panels [7.92] and box structures [7.92, 7.103], and riveted multibay titanium and aluminum panels [7.93], are illustrated in Figures 7.54, 7.55 and 7.56, respectively, as a function of resonant frequency [7.47]. The constant damping trend line with frequency is the same in each figure, and based on the riveted panel data in Figure 7.54. This trend line represents a good fit to the test data in Figure 7.55 and is slightly on the low side for the data in Figure 7.56. Based on these results, it was concluded in Reference [7.47] that the damping in the fundamental mode can be considered to be essentially constant with frequency, confirming the result previously obtained with stiffened honeycomb panels. The constant fundamental mode damping trend line for flat skin-stringer panels appears to be equally applicable to curved skin-stringer panels as illustrated in Figure 7.57. The fundamental mode damping for built up structures with integrally machined skins (Figures 7.58 and 7.59) and with corrugated and hat stiffened skins (Figure 7.59) is also constant with frequency. The damping is lower for the integrally machined skins and higher for the corrugated and hat stiffened skins than the average damping for the skin-stringer panels. It can therefore be concluded that the concept of a constant fundamental mode damping with frequency, developed in Reference [7.47], is valid for a wide range of stiffened panel type structures.

A method for predicting the damping of the skin-stringer panels was also developed in Reference [7.47]. The damping of these panels is due primarily to friction damping at the fastener line and acoustic radiation damping. The acoustic radiation damping, as indicated in References [7.14] and [7.15], can be predicted by the simple theory, described in Reference [7.3], if double sided acoustic radiation is used. The acoustic radiation viscous damping ratio, ζ_a , for a simple supported panel that is mounted in a baffle, is given by

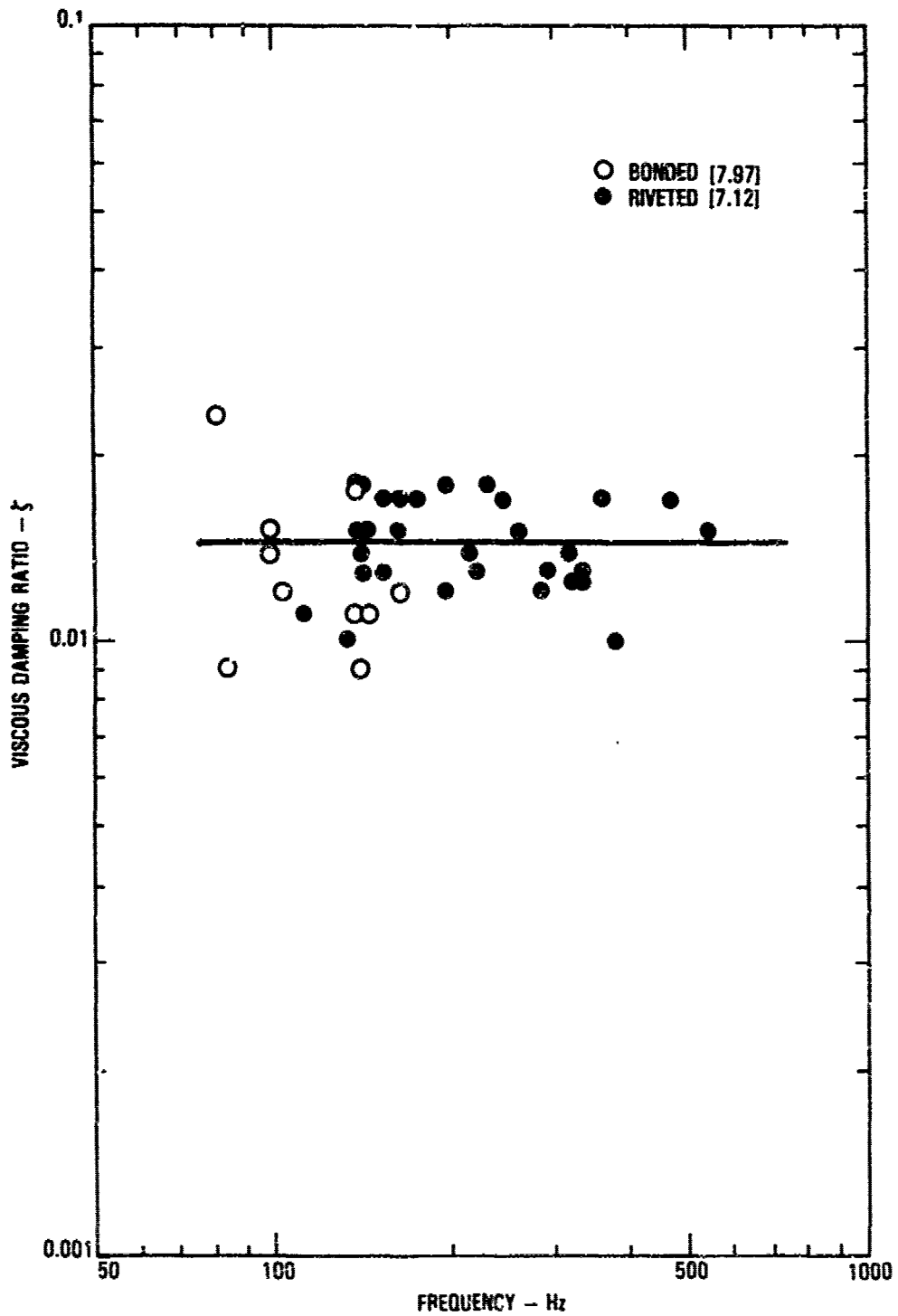


Figure 7.54. Variation of the measured damping in the fundamental mode of riveted and bonded multi-bay skin-stringer aluminum panels with frequency.

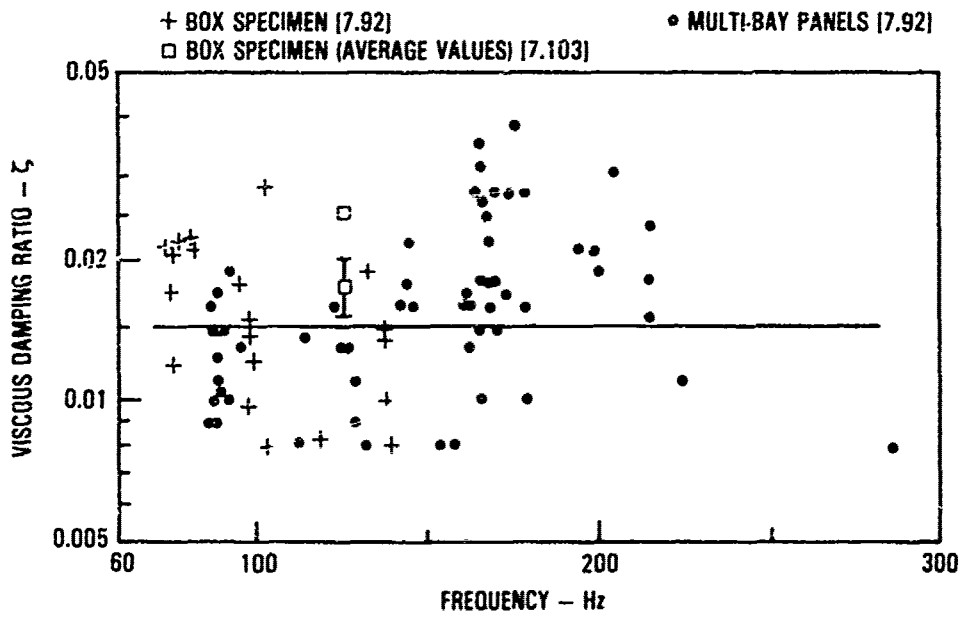


Figure 7.55. Measured damping in aluminum multi-bay panels and box specimens.

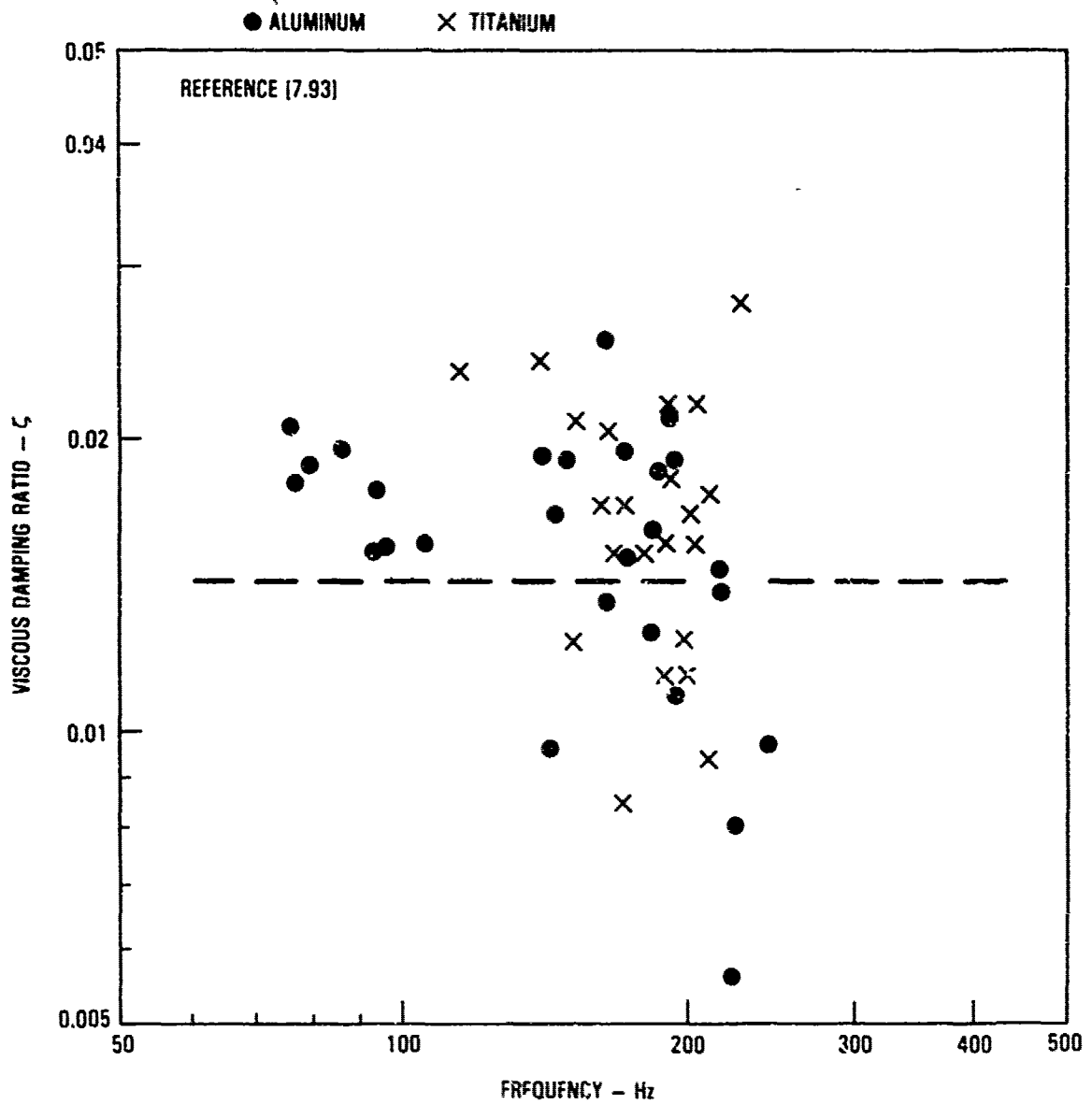


Figure 7.56. Measured damping in aluminum and titanium multi-bay panels.

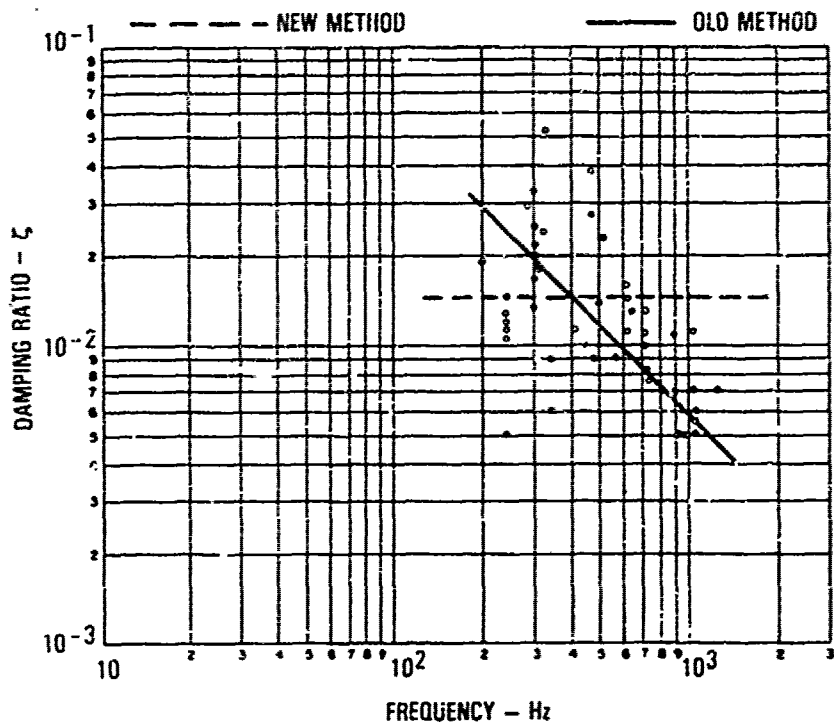


Figure 7.57. Curved skin and stringer panels.

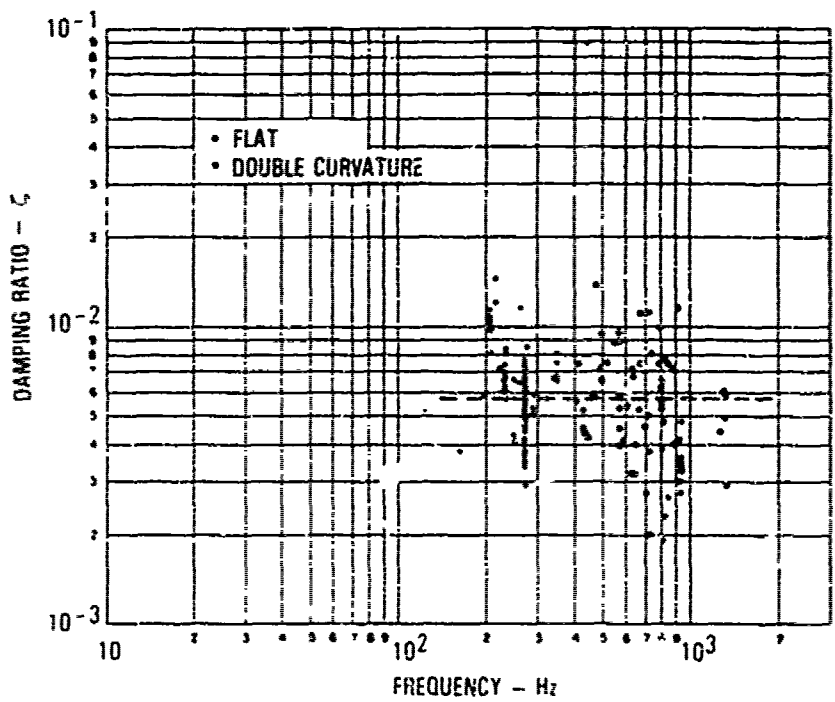


Figure 7.58. Built-up structures with integrally machined skins.

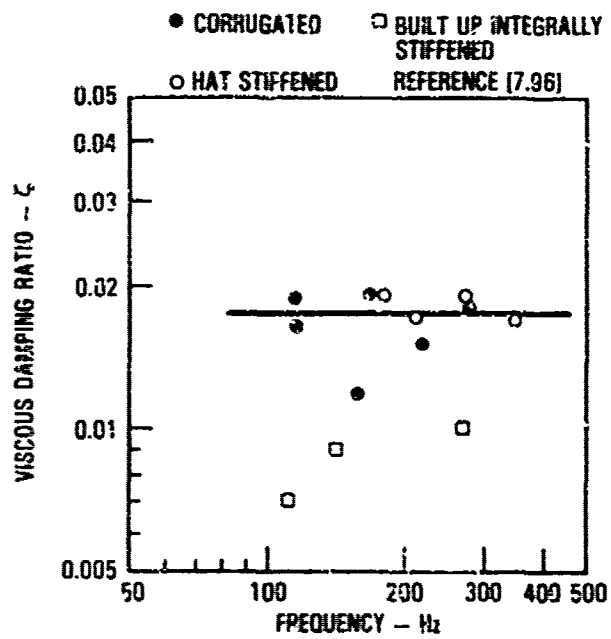


Figure 7.59. Damping in hat stiffened, corrugated and built-up integrally stiffened panels.

$$\zeta_a = \frac{64}{\pi^4} \frac{\rho}{c} \frac{f_n}{M} \frac{a}{m^2} \frac{b}{n^2} \quad (7.12)$$

where .

ρ = density of air

c = speed of sound in air

f_n = natural frequency of the m, n^{th} mode

M = panel surface density

a, b = panel length and width

m, n = mode number in the length and width direction, respectively

The above equation provides the basis for the expression for the viscous damping ratio in equation 7.11. It must be pointed out that the variation of the higher mode damping with frequency is not a simple one-to-the-frequency relationship. In the case of riveted panels, the relationship is further modified by presence of friction.

Experimental evidence indicates that friction damping is both constant with frequency and velocity [7.28] and independent of the load amplitude at the fastener line [7.19]. Consequently, it was concluded, in Reference [7.47], that the friction damping at the fastener line is dependent only on the number of fastener along the panel periphery. The viscous damping ratio of 0.0085, measured in a panel array under near vacuum conditions, was assumed as a reference value for the friction damping. As a consequence the following semi-empirical equation was developed [7.47] for the friction viscous damping ratio ζ_F :

$$\zeta_F = 0.0253 \frac{\left[s(a+b) - \frac{n}{s} - \frac{m}{s} \right]}{ab} \quad (7.13)$$

where s is the number of fasteners per inch, and all the other dimensions are in inches. The above value of 0.0085, used in deriving equation 7.13, can vary in practice from panel to panel depending, for example, on the quality of the fabrication. This value could be as low as 0.0034, as previously measured on an un baffled curved panel array [7.115].

The viscous damping ratio ζ_{mn} for the m,n^{th} mode of a single panel is given simply by

$$\zeta_{mn} = \zeta_a + \zeta_F + \zeta_M \quad (7.14)$$

where ζ_M is the material damping. The above equations can be applied to single panels vibrating in a panel array. Most of the multi-bay test panels consist of 9-bays with a large center bay. Thus the dominant response tends to occur in the center bay vibrating alone. For a panel array with equal panels equation 7.12 has to be modified to account for the number of panels vibrating in-phase and out-of-phase in the panel array [7.47]. If all of the panels are vibrating in phase, then equation 7.12 can still be used, since the damping in each panel will be the same.

The degree of correlation achieved [7.47] in predicting the damping of both riveted skin-stringer and bonded panels using equation 7.14 is illustrated in Figure 7.60. In this correlation, the material damping ζ_m was assumed to be zero for both panels and the friction damping ζ_F was assumed to be zero for the bonded panels. The correlation appears to be very promising. The variation in the damping of higher modes, as predicted by equation 7.14 with ζ_m equal to zero, is illustrated in Figure 7.61. The old trend line (Figure 7.48) is included in Figure 7.61 since it may have been influenced by the presence of higher modes in the data. The old trend line appears to fit the data although there are higher order modes, such as the (1,3) modes, that have a viscous damping ratio almost as high as that in the fundamental mode. This result is due to the influence of the acoustic radiation damping which tends to increase with frequency, even in the fundamental mode.

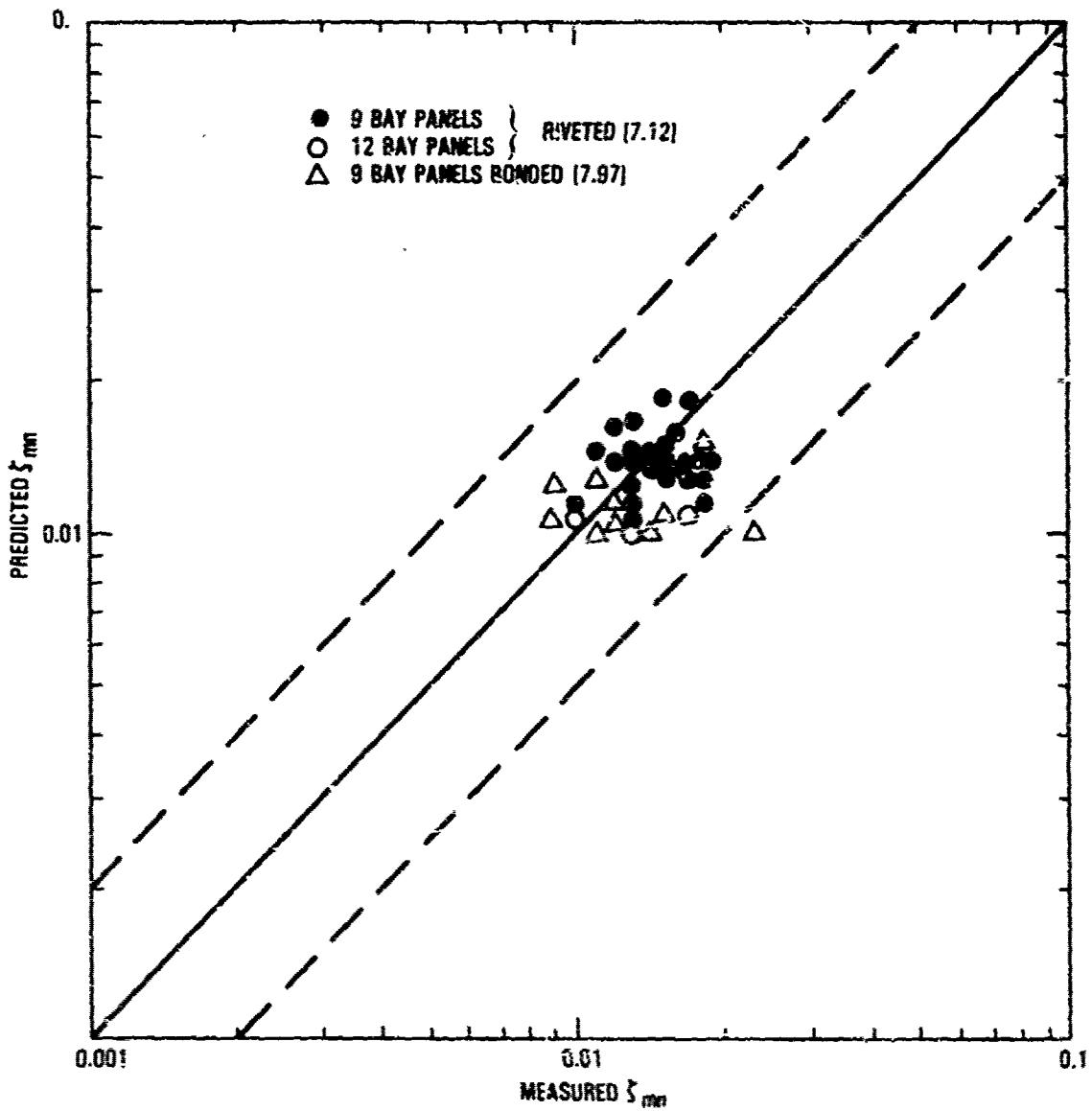


Figure 7.60. Comparison of measured and predicted damping in the fundamental mode of riveted and bonded multi-bay skin-stringer aluminum panels.

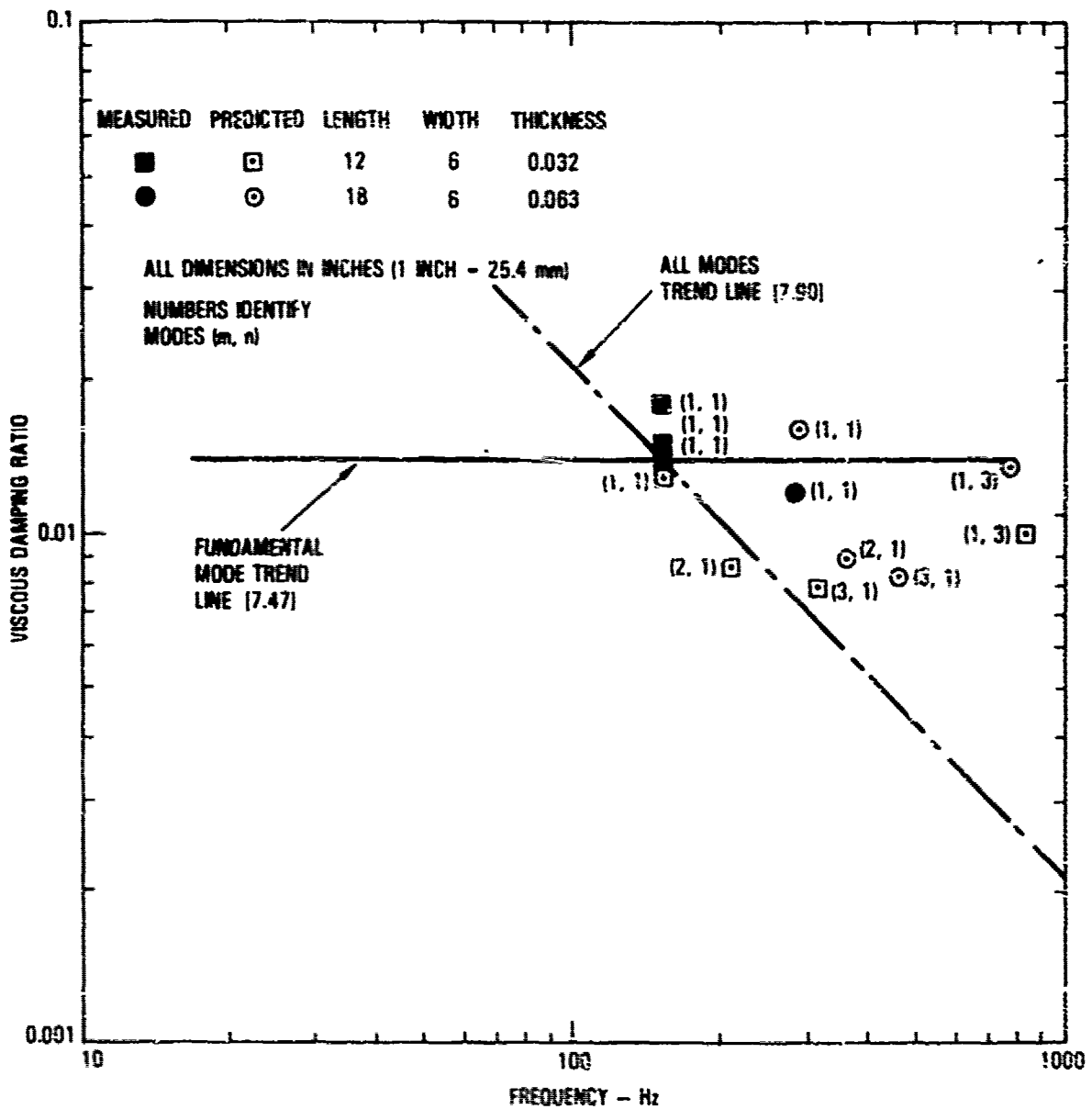


Figure 7.61. Comparison of measured and predicted damping of riveted multi-bay aluminum panels with predictions for higher mode damping.

Since a lot of experimental data are available for the damping in the fundamental mode of many structures, it is more convenient to use these data to predict the damping in the higher modes rather than to perform the acoustic radiation calculation. This approach is based on equation 7.11, by assuming that the form of this equation is applicable to most stiffened panel structures. The value of ζ_F must be first calculated from equation 7.13, with m and n equal to one for fastener attached panels, and also for the corrugated panels, although these latter panels may have a greater frictional damping. The friction damping is zero for integrally stiffened and bonded panels.

7.3.3 Damping in Bonded and Integrally Stiffened Multi-bay Composite Panels and Fastener Attached Box Structure

The prediction of the damping in bonded and integrally stiffened composite panels is simplified by the absence of friction damping. Except for some material damping in Kevlar composites, the damping is due entirely to acoustic radiation damping [7.13, 7.14]. The critical item in predicting the damping is therefore the number and the size of the panels in the panel array, since they affect the vibration response of the array. The mode shape is very critical, as can be illustrated by comparing the damping (Figure 7.4) from an integrally blade stiffened panel [7.13, 7.14] with a large center bay that is vibrating by itself in the fundamental mode (Figure 7.62), with the damping (Figure 7.63) of an integrally J-stiffened panel [7.15, 7.14] with nearly identical bays, all vibrating out of phase (Figure 7.64) in the fundamental mode. The viscous damping ratio predicted by equation 7.12 for the fundamental mode, should be closer to 0.01, if all the panels are assumed to have equal mode shapes, instead of the viscous damping ratio of approximately 0.005 (Figure 7.63) actually measured. The difference is due entirely to the mode shapes. The trend line for the damping of the composite panel in Figure 7.63 is due to the presence of higher modes.

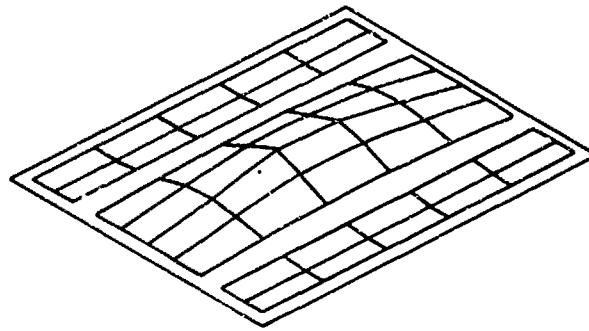


Figure 7.62. Fundamental mode shape of integrally blade stiffened graphite/epoxy minisandwich panel.

The damping measured on a composite aileron box structure [7.102] is also included in Figure 7.63. Thus the acoustic damping in composite structures can be very low, but predictable by acoustic radiation theory, at least for simple skin-stiffener type panels. Other damping data for bonded skin-stringer [7.99] and integrally hat stiffened [7.100] composite panels are contained in Tables 7.14 and 7.15, respectively.

7.3.4 Damping in Stiffened Panels under Inplane Axial, Tension, Compression and Shear Load

The effect of axial inplane tension and compression loading on the damping of a stiffened aluminum panel has been studied as part of an investigation into the crack growth of stiffened panels under combined loading [7.18]. The variation of the un baffled panel damping with axial inplane load is illustrated in Figure 7.5. The damping remains constant with tension loading but increases with compression loading on approaching buckling. The damping in the compression region is nonlinear, as indicated by a different decay rate with amplitude measured with the free decay method.

Fuselage panels are often designed to be near buckling at one g. Considerable interest was expressed in determining the effect of acoustic loading, from the close proximity jet engine exhausts, on these fuselage panels. A three-bay

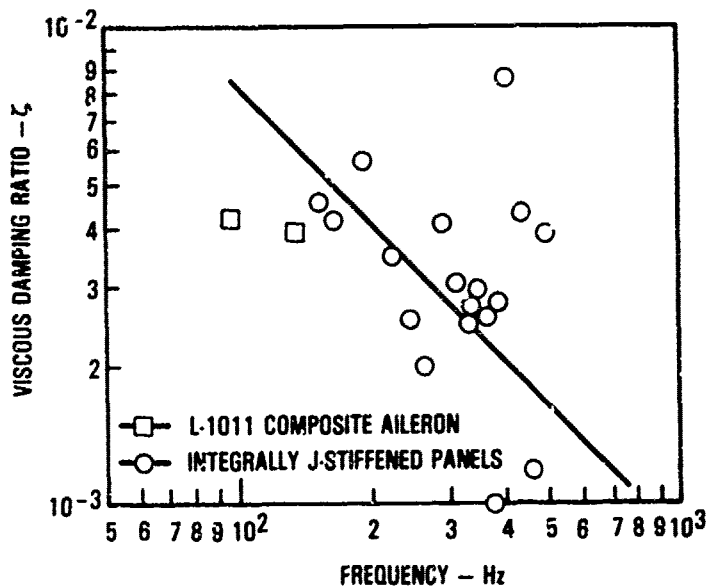


Figure 7.63. Measured damping in multibay integrally J-stiffened graphite/epoxy panels and graphite/epoxy box structure assembled with fasteners.

integrally J-stiffened monolithic and minisandwich graphite/epoxy panels were tested under combined acoustic and shear loading [7.20] to study this problem. The variation of the resonant frequencies and the corresponding viscous damping ratios with shear load through buckling was determined. The variation of the resonant frequency and viscous damping ratio with shear load are illustrated in Figures 7.65 and 7.66 respectively for the minisandwich panel. The damping in the critical 2,1 mode increases very rapidly on approaching buckling. The damping in the noncritical modes is also increased on approaching buckling, as illustrated in Figure 7.67 for the monolithic panel, even when a much higher order panel mode is the critical mode.

7.3.5 Damping in Stiffened Cylinders

The damping in stiffened shells has been measured in connection with interior noise studies [7.105, 7.106, 7.107] on aircraft. The damping data measured on a bare Metroliner fuselage, on a bare L-1011 rear fuselage and a small diameter stiffened shell, both with and without interior acoustic trim, are illustrated in Figure 7.68 as a function of frequency. The damping data

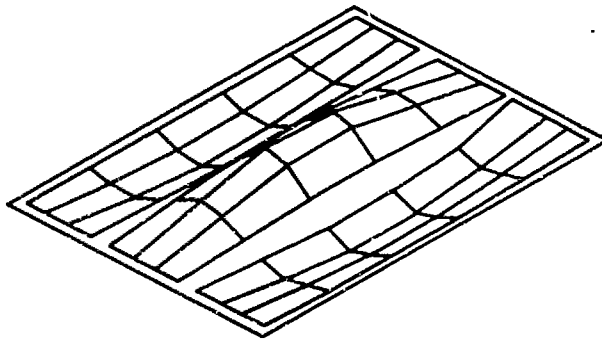


Figure 7.64. Fundamental mode of integrally J-stiffened graphite/epoxy panel.

TABLE 7.14. MEASURED DAMPING IN BONDED GRAPHITE/EPOXY PANELS

Panel	Frequency Hz	Viscous Damping Ratio - ζ
A-66-B1	167	—
	184	0.023
	219	--
	233	0.014
	277	0.017
	343	0.017
A-66-B3	170	0.013
	177	0.0125
	288	--
	348	0.015
	517	0.016
	563	0.016

Reference [7.99].

TABLE 7.15. MEASURED DAMPING IN INTEGRALLY HAT STIFFENED GRAPHITE/EPOXY FLAT AND CURVED PANELS

Panel A-1		Panel AA-1		Panel AA-2		Panel AA-5		Panel AA-6		Panel N-1		Panel N-2		Panel N-3	
Natural Frequency Hz	ζ														
194	0.025	147	0.025	77	0.018	84	Beats	79	0.026	170	0.014	128	0.004	107	0.042
250	0.012	164	Beats	120	Clfp	346	Beats	132	0.019	251	0.005	222	0.016	167	0.003
377	0.005	210	0.009	223	Beats			230	0.024	304	0.004	248	0.005	182	0.014
412	0.005	242	0.022	274	Beats					315	0.008	325	0.005	271	0.015
456	0.009	291	Beats	343	0.010					365	0.005	400	0.002	531	0.004
511	0.006			411	0.015					431	0.008				
										466	0.005				
										495	0.008				

ζ is the nondimensional viscous damping ratio.
Reference [7.100]

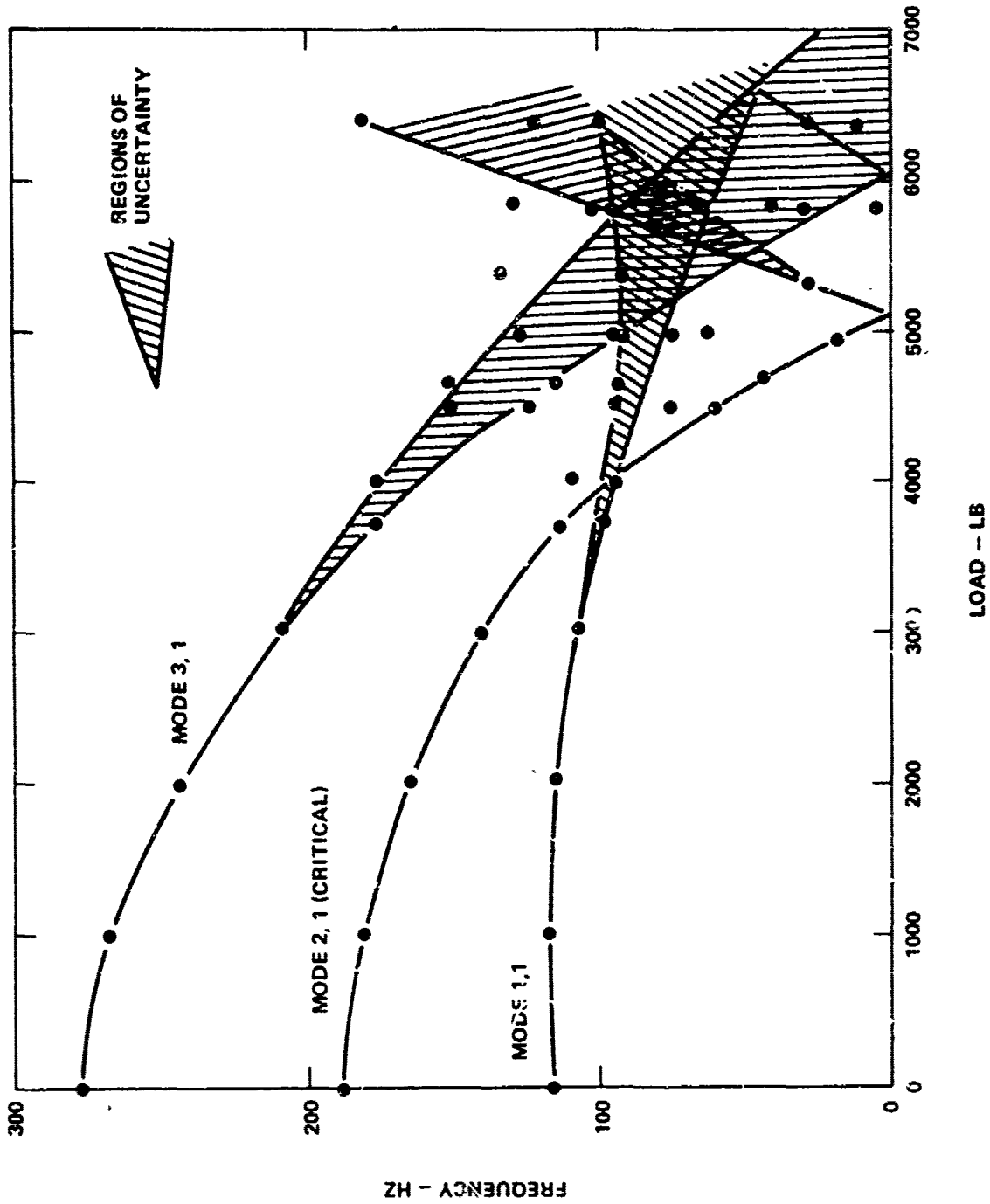


Figure 7.65. Variation of the J-stiffened minisandwich panel resonant frequencies with jack load.

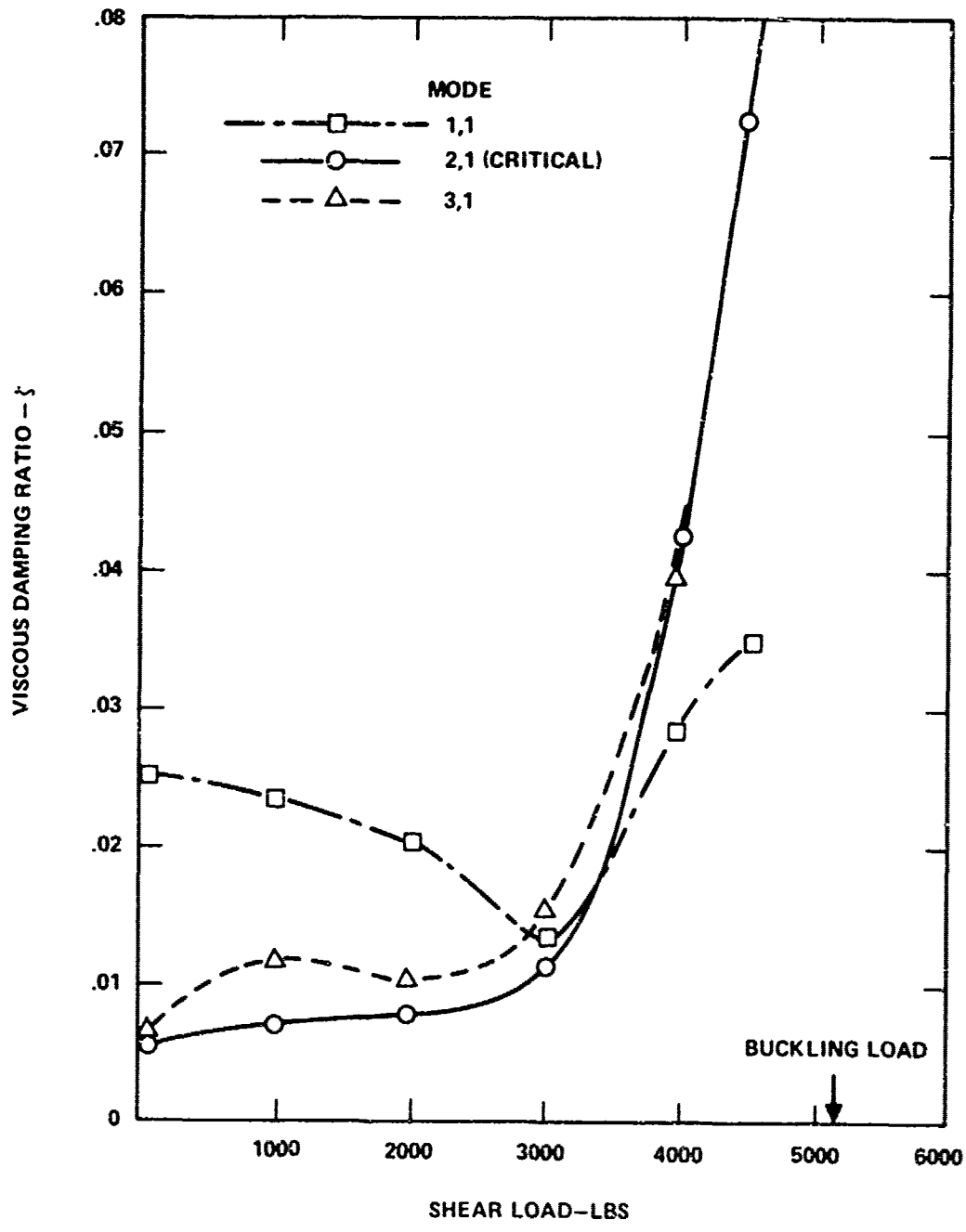


Figure 7.66. Variation of damping with jack load for J-stiffened minisandwich panel.

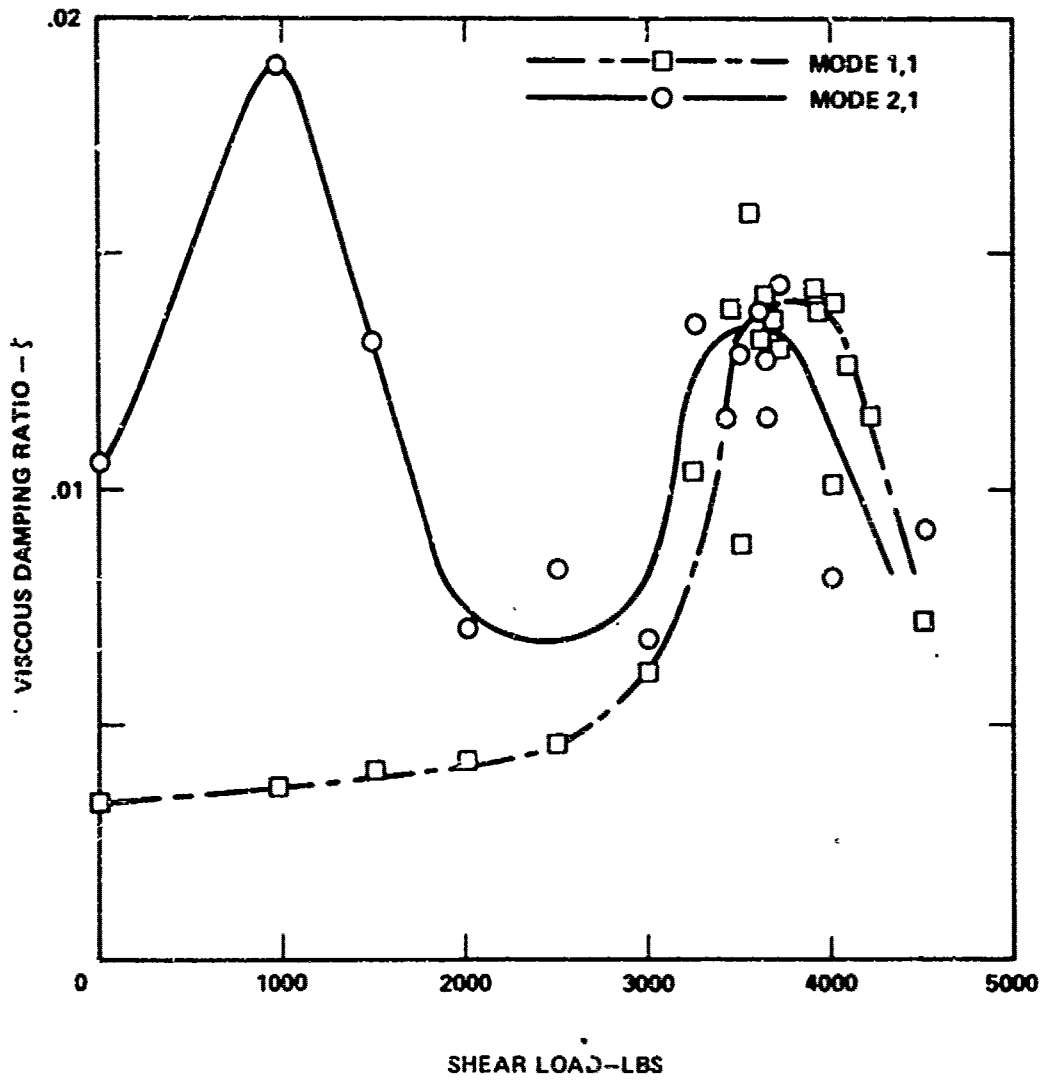


Figure 7.67. Variation of J-stiffened monolithic panel damping with jack load.

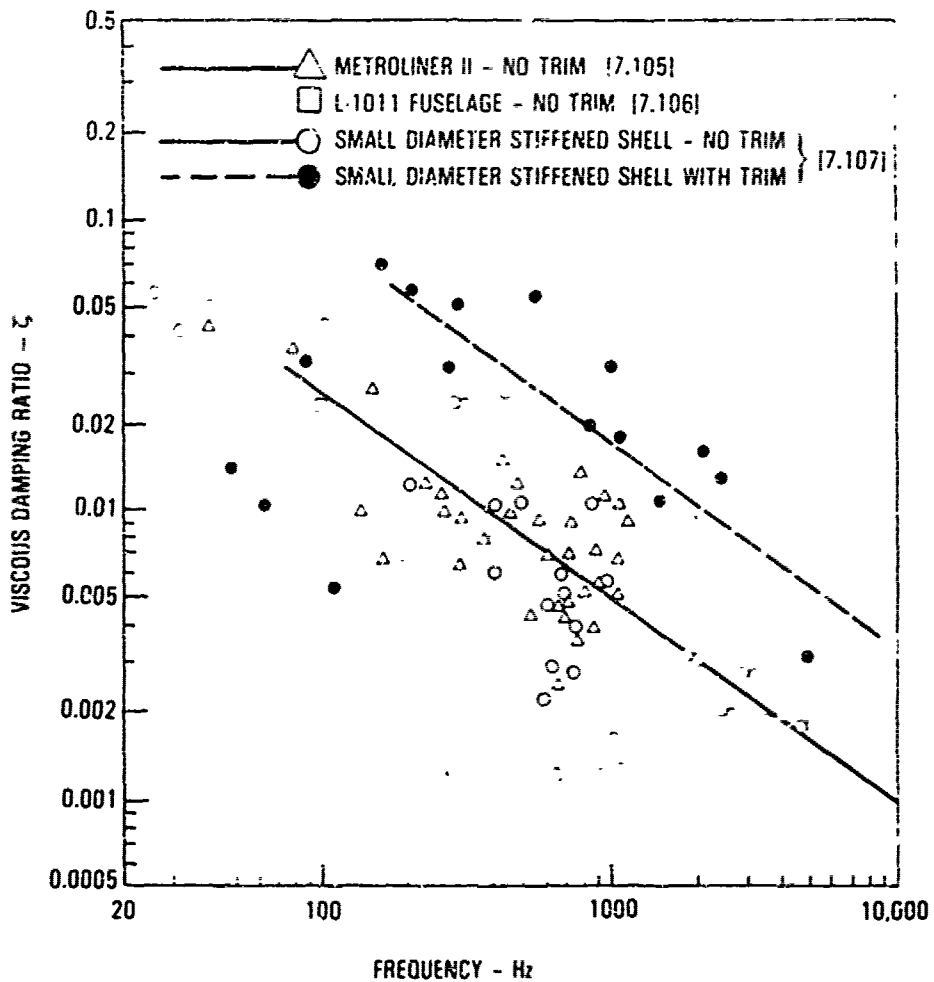


Figure 7.68. Damping measured on bare stiffened shells and a trimmed stiffened shell as a function of frequency.

for all of these bare shells appears to collapse onto a single line. This trend line decreases with frequency since many shell modes are involved. Another interesting result is that the acoustic trim, even when not in contact with the shell, increases the shell damping significantly.

7.3.6 Effect of Fluid Loading on Stiffened Panels

A study was conducted [7.109] to measure the damping of a hull panel, in a motor torpedo boat, both in air and in contact with water. The structure consists of T stringers and frames welded to the hull skin. The measured damping is illustrated in Figure 7.69. The interesting result is that there is virtually no difference in the damping of the panel when in air or in contact with the water. There is a shift in frequency due to the combination of mass loading and hydrodynamic pressure [7.109]. This result is important when investigating fuel slosh loading in outer wing tanks and in liquid fuel rockets.

7.3.7 Measured Damping in Jet Engine Components

Jet engines often use welded components, which have very low damping, and as a consequence often experience failures due to excessive vibration. Typical damping levels measured on a variety of components are summarized in Table 7.16. These data have been obtained from the examples and case histories in Section 6 of Volume II of this design guide. The low damping levels and the high frequencies are self evident.

7.3.8 Printed Circuit Board Damping

Another area of interest that can affect the reliability of the avionics is the vibration and, indeed, the damping in printed circuit boards (PCB's). Reference [7.112] is devoted to the design of circuit boards to minimize the possibility of failure in electronic components mounted on the PCB's from vibration. A range of measured circuit board damping levels are included in Table 7.17 together with an empirical equation for estimating the damping.

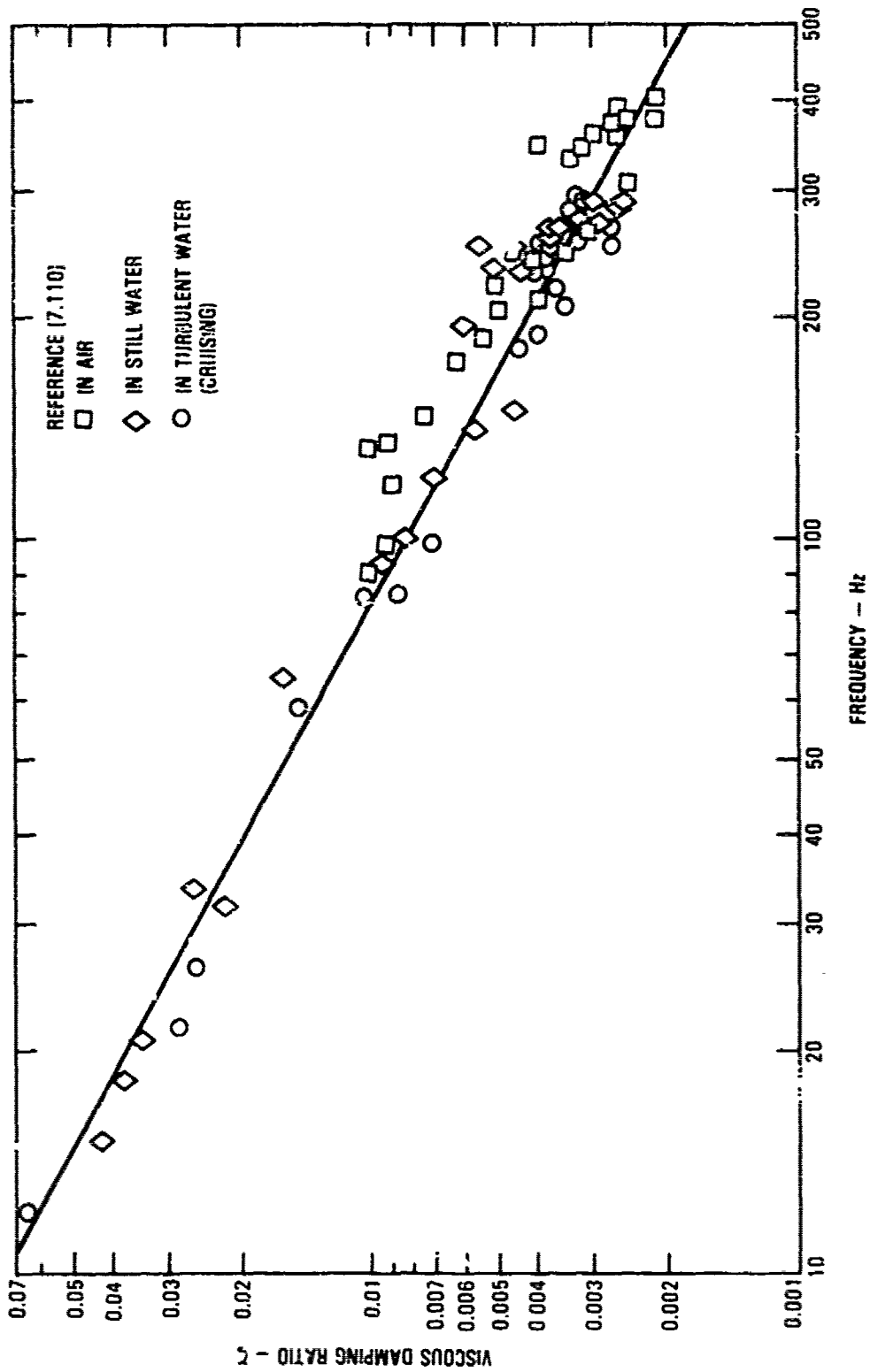


Figure 7.69. Damping measured on a welded stiffened steel structure in air and immersed in water

TABLE 7.16. MEASURED DAMPING VALUES FOR ENGINE COMPONENTS

Description of Structure	Frequency Hz	Viscous Damping Ratio - ζ
TF-41 Jet Engine Inlet Extension	3140	0.0011 to 0.0027*
RF-33-P3 Turbojet Engine Welded Inlet Guide Vanes (IGV) and Shrouds	1000 to 5000	0.0012 to 0.0023*
Engine Rear Mount Ring	374 403 903 1172 1396 3515 4325	0.0037 0.0033 0.0045 0.0030 0.0037 0.0040 0.0049
TF-30 Jet Engine Welded Titanium Guide Vanes	3000 to 4000	0.0009 to 0.0018*
Helicopter Turbine Engine Exhaust Stacks	50 to 500	0.0005 to 0.005
Jet Engine Turbine Blade	746 Bending 824 Torsion	0.001 to 0.002
Exducer - Turbing Blade Assembly	5300 8500	0.0022 to 0.0039* 0.0009 to 0.0014

*Damping varies with temperature

TABLE 7.17. TYPICAL RANGE OF MEASURED PRINTED CIRCUIT BOARD DAMPING VALUES

Frequency f_n Hz	ζ	Q	K	Reference
65	0.0142	35	4.3	7.116
165	0.023	22	1.71	7.116
215 (2g's input)	0.033	15	1.023	7.112
182 (5g's input)	0.045	11.2	-	
161 (10g's input)	0.061	8.2	-	

Empirical relationship [7.112]

$$Q \approx K (f_n)^{1/2}$$

$$\zeta = \frac{1}{2Q}$$

$K \approx 0.5 + 2$ Typical
Input 2g's and less

REFERENCES

- 7.1 Ungar, E.E., "The Status of Engineering Knowledge Concerning the Damping of Built-Up Structures", *Journal of Sound and Vibration* Vol. 26, No. 1, 1973.
- 7.2 Kerwin, E.M., "Acoustic Damping Mechanisms", WADC-TR-59-676, March 1961, p. 286.
- 7.3 Mead, D.J., "The Effect of Certain Damping Treatments on the Response of Idealized Aeroplane Structures Excited by Noise", AFML-TR-65-284, August 1965.
- 7.4 Beranek, L.L., "Noise and Vibration Control", McGraw Hill, 1971.
- 7.5 Maidanik, G. and Ungar, E.E., "Panel Loss Factor Due to Gas-Pumping at Structural Joints", NASA CR-854, November 1967.
- 7.6 Mead, D.J., "The Damping, Stiffness and Fatigue Properties of Joints and Configurations Representative of Aircraft Structures", NADC-TR-59-676, March 1961, p. 275.
- 7.7 Ungar, E.E., "Energy Dissipation of Structural Joints, Mechanisms and Magnitude", FDL-TDR-64-98, August 1964.
- 7.8 Pian, T.H.J., "Structural Damping", *Random Vibration*, Technology Press and John Wiley & Sons, 1958, p. 91.
- 7.9 Wada, B.K. and DesForges, D.T., "Spacecraft Damping Considerations in Structural Design", AGARD-CP-277, October 1979, p. 6-1.
- 7.10 Soovere, J., "Dynamic Response of Acoustically Excited Stiffened Composite Honeycomb Panels", Ph.D. Thesis, Institute of Sound and Vibration Research, Southampton University, England, March 1984.

- 7.11 Soovere, J., "Dynamic Properties of Graphite Fibre Honeycomb Panels", AIAA Dynamics Specialists Conference, Williamsburg, Virginia, March 1973, Paper No. 73-326.
- 7.12 Ballentine, J.R., Rudder, F.F., Mathis, J.T. and Plumblee, H.E., "Refinement of Sonic Fatigue Structural Design Criteria", AFFDL-TR-67-156, January 1968.
- 7.13 Soovere, J., "Effect of Acoustic/Thermal Environments on Advanced Composite Fuselage Panels", Journal of Aircraft, Volume 22, No. 4, April 1985.
- 7.14 Soovere, J., "Dynamic Response and Acoustic Fatigue of Stiffened Composite Structures", Proceeding of the Second International Conference on Recent Advances in Structural Dynamics, M. Petyt and H.F. Wolfe Editors, University of Southampton, 9-13 April, 1984, p. 775.
- 7.15 Clarkson, B.L. and Ford, R.D., "The Response of Typical Aircraft Structure to Jet Noise", Journal of the Royal Aeronautical Society, Vol. 66, January 1962, p. 31.
- 7.16 Wilby, J.F. and Gloyna, F.L., "Vibration Measurements of an Airplane Fuselage Structure; i. Turbulent Boundary Layer Excitation", Journal of Sound and Vibration, Vol. 25, No. 4, 1972.
- 7.17 Szechenyi, E., "The Response of, and Acoustic Radiation from Panels Excited by Turbulent Boundary Layer", AFFDL-TR-70-94, June 1970.
- 7.18 Soovere, J. and Chiu, S.T., "Effect of Combined Acoustics and Flight Loads on Crack Growth", AFFDL-TR-76-68, July 1976.
- 7.19 Mead, D.J., "Prediction of the Structural Damping of a Vibrating Stiffened Plate", AGARD-CP-277, October 1979, p. 2-1.

- 7.20 ... J., "Dynamic Response of Flat Integrally Stiffened Graphite/epoxy Panels Under Combined Acoustic and Shear Loads", Recent Advances in Composites in the United States and Japan, J.R. Vinson and M. Taya Editors, ASTM Special Technical Publication 864, July 1985.
- 7.21 Crandall, S.H., "The Role of Damping in Vibration Theory", Journal of Sound and Vibration, Volume 11, No. 1, 1970.
- 7.22 White, R.G., "Some Measurements of the Dynamic Properties of Mixed Carbon Fiber Reinforced, Plastic Beams and Plates", Aeronautical Journal, July 1975, p. 318.
- 7.23 Adams, R.D., Fox, M.A.O., Flood, R.J.L., Friend, R.J. and Hewitt, R.L., "The Dynamic Properties of Unidirectional Carbon and Glass Fiber Reinforced Plastics in Torsion and Flexure", J. Composite Materials, Vol. 3, October 1969, p. 594.
- 7.24 Wright, G.C., "The Dynamic Properties of Fiber Reinforced Beams", ISVR Technical Report 51, September 1971.
- 7.25 Baker, W.E., Woolam, W.E. and Young, D., "Air and Internal Damping of Thin Cantilever Beams", Int. J. Mech. Sci., Pergamon Press, Ltd., Vol. 9, 1967, p. 743.
- 7.26 Stephens, D.G. and Scarvullo, M.A., "Investigation of Air Damping of Circular and Rectangular Plates, a Cylinder and a Sphere", NASA TND-1865, April 1965.
- 7.27 Granick, N. and Stern, J.E., "Material Damping of Aluminum by Resonance-Dwell Technique", Shock and Vibration Bulletin, Vol. 34, No. 5, 1966.
- 7.28 Srinivasan, A.V., Cassenti, B.N. and Cutts, D.G., "Characteristics of Dry Friction Damping", Vibration Damping 1984 Workshop Proceedings, Dr. Lynn Rogers Editor, AFWAL-TR-84-3064, p. 1-3.

- 7.29 Crawley, E.F., Sarver, G.L. and Mohr, D.G., "Experimental Measurement of Passive Material and Structural Damping for Flexible Space Structures", Vibration Damping 1984 Workshop Proceedings, Dr. Lynn Rogers Editor, AFWAL-TR-84-3064, p. A-26.
- 7.30 Beards, C.F. and Williams, J.L., "Damping of Structural Vibration by Rotational Slip Joints", Journal of Sound and Vibration, Vol. 53, No. 3, 1977.
- 7.31 Beards, C.F. and Imam, I.M.A., "Damping of Plate Vibration by Interface Slip Between Layers", Int. J. Mach. Tool. Des. Res., Vol. 18, 1978.
- 7.32 Beards, C.F., "The Damping of Structural Vibration by Controlled Interfacial Slip in Joints", ASME Design Engineering Technical Conference, Hartford, Conn., September 1981, Paper No. 81-DET-86.
- 7.33 Trubert, M., "Assessment of Galileo Modal Test Results for Mathematical Model Verification", AIAA Dynamics Specialists Conference, Palm Springs, California, May 1984, Paper No. 84-1066
- 7.34 Wada, B.K., "Spacecraft Damping Considerations in Structural Design", AGARD-CP-277, October 1979, p. 6-1.
- 7.35 Chen, J.C., "Evaluation of Modal Test Methods", AIAA Dynamics Specialists Conference, Palm Springs, California, May 1984, Paper No. 84-1071.
- 7.36 Wada, B.K. and Chen, J.C., "A Comparison of Measured Spacecraft Modal Damping Values", Vibration Damping 1984 Workshop Proceedings, Dr. Lynn Rogers Editor, AFWAL-TR-84-3064, p. Y-2.
- 7.37 Jensen, D.L., "Structural Damping of the Space Shuttle Orbiter and Ascent Vehicles", Vibration Damping 1984 Workshop Proceedings, Dr. Lynn Rogers Editor, AFWAL-TR-84-3064, p. Z-2.

- 7.38 Stokes, J., "Comparative Evaluation of Operability of Large Space Structure Connectors".
- 7.39 Hertz, T.J. and Crawley, E.F., "Damping in Space Structure Joints", AIAA Dynamics Specialists Conference, Palm Springs, California, May 1984, Paper No. AIAA-84-1039-CP.
- 7.40 Kerley, J., "Concepts and Effects of Damping in Isolators", Vibration Damping 1984 Workshop Proceedings, Dr. Lynn Rogers, Editor AFWAL-TR-84-3064, p. L-1.
- 7.41 Jay, R.L. and Burns D.W., "Damping Applications in Turbine Engines", Vibration Damping 1984 Workshop Proceedings, Dr. Lynn Rogers Editor, AFWAL-TR-84-3064, p. H-1.
- 7.42 Rieger, N.F., "Damping Properties of Steam Turbine Blades", Vibration Damping 1984 Workshop Proceedings, Dr. Lynn Rogers Editor, AFWAL-TR-84-3064, p. K-1.
- 7.43 Soovere, J., "Theory for Predicting the Dynamic Edge Strain in Stiffened Honeycomb Panels", Tenth Biennial ASME Design Engineering Division Conference on Mechanical Vibration and Noise, Cincinnati, Ohio, 10-13 September 1985.
- 7.44 McGowan, P.R., et al, "Structural Design for Acoustic Fatigue", ASD-TDR-62-820, October 1963.
- 7.45 Rasor, J.E., "Sonic Fatigue Test of 0.045 lb/FT² Adhesive for Honeycomb Sandwich Panels", Lockheed Report ER-9028, March 1967.
- 7.46 Rasor, J.E., "Sonic Fatigue Tests on Low Density Core Honeycomb Panels", Lockheed Report ER 8601, July 1966.

- 7.47 Soovere, J., "Method for Predicting the Damping in Stiffened Structures", Paper to be Presented at the Vibration Damping Workshop II, Las Vegas, 5-9 March 1986.
- 7.48 Lazan, B.J., "Damping of Materials and Members in Structural Mechanics", Oxford: Pergamon Press, 1968.
- 7.49 Bert, C.W., "Material Damping: An Introductory Review of Mathematical Models, Measures and Experimental Techniques", Journal of Sound and Vibration, Vol. 29, No. 3, 1973.
- 7.50 Zener, C., "Elasticity and Aeroelasticity of Metals", University of Chicago Press, 1948.
- 7.51 Vandeurzen, U., "Identification of Damping in Materials and Structures - Optimization of the Dynamic Behavior of Mechanical Structures", A University of Leuven Report, Leuven, Belgium.
- 7.52 Birchak, J.R., "Damping Capacity of Structural Materials", Published After 1976 - Babcock and Wilcox, Lynchburg Research Center.
- 7.53 Keine, J.C., "The Stress and Frequency Dependence of Material Damping in Some Engineering Alloys", Ph.D. Thesis, M.I.T., Cambridge, Mass., June 1966.
- 7.54 Vandeurzen, U., "Physical Aspects, Dynamic Properties and Applications of High Damping Materials", A University of Leuven Report, Leuven, Belgium.
- 7.55 Lee, L.T., "A Graphic Compilation of Damping Properties of Both Metallic and Nonmetallic Materials", AFML-TR-66-169, May 1966.
- 7.56 Lundin, K., "Dynamic Mechanical Data of Nonreinforced Plastics", Royal Institute of Technology, Stockholm, TRITA-TAK-8203, December 1982.

- 7.57 Schultz, A.B. and Tsai, S.W., "Dynamic Moduli and Damping in Fiber-Reinforced Composites", J. Composite Materials, Vol. 2, No. 3, July 1968.
- 7.58 Mazza, L.T., Paxson, E.B. and Rodgers, R.L., "Measurement of Damping Coefficients and Dynamic Modulus of Fiber Composites", VSAAVLABS Technical Note 2, February 1970.
- 7.59 Lifshitz, J.M., "Specimen Preparation and Preliminary Results in the Study of Mechanical Properties of Fiber Reinforced Materials", AFML-TR-69-89 Part 1, July 1969.
- 7.60 Clary, R.R., "Vibration Characteristics of Uni-Directional Filamentary Composite Material Panels", Composite Materials: Testing and Design (second conference), ASTM STP 497, 1971, p. 415.
- 7.61 Adams, R.D. and Bacon, D.G.C., "The Dynamic Properties of Unidirectional Fibre Reinforced Composites in Flexure and Torsion", J. Composite Materials, Vol. 7, January 1973.
- 7.62 Paxson, E.B., "Real and Imaginary Parts of the Complex Viscoelastic Modulus of Boron Fiber Reinforced Plastics (BFRP)", Journal of the Acoustical Society of America, Vol. 57, No. 4, April 1975.
- 7.63 Wright, G.C., "The Dynamic Properties of Glass and Carbon Fibre Reinforced Plastic Beams", Journal of Sound and Vibration, Vol. 21, No. 2, 1972, p. 205.
- 7.64 Dudek, T.J., "Young's and Shear Moduli of Unidirectional Composites by a Resonant Beam Method", J. Composite Materials, Vol. 4, 1970, p. 323.
- 7.65 Hashin, Z., "Complex Moduli of Viscoelastic Composites - II. Fiber-Reinforced Materials", Int. J. Solids Struct., Vol. 6, 1970, p. 797.

- 7.66 Schultz, A.B. and Tsai, S.W., "Measurements of Complex Dynamic Moduli for Laminated Fiber-Reinforced Composites", J. Composite Materials, Vol. 3, July 1969.
- 7.67 Gibson, R.F. and Plunkett, R., "Dynamical Behavior of Fiber-Reinforced Composites: Measurement and Analysis", J. Composite Materials, Vol. 10, October 1967.
- 7.68 Ni, R.G. and Adams, R.D., "The Damping and Dynamic Moduli of Symmetric Laminated Composite Beams - Theoretical and Experimented Results", J. Composite Materials, Vol. 18, March 1984.
- 7.69 Cox, H.L., "The Elasticity and Strength of Paper and Other Fibrous Materials", British Journal of Applied Physics, 1952.
- 7.70 McLean, D. and Read, B.E., "Storage and Loss Moduli in Discontinuous Composites", Journal of Material Sciences, Vol. 10, 1975, p. 481.
- 7.71 Gibson, R.F., Chaturvedi, S.K. and Sun, C.T., "Complex Moduli of Aligned Discontinuous Fiber-Reinforced Polymer Composites", Journal of Material Sciences, Vol. 17, 1982, p. 3499.
- 7.72 White, R.G. and Palmer, T.A., "Control of the Material Properties and Structural Application of Carbon Fiber-Reinforced Plastics", 24th Structures, Structural Dynamics and Materials Conference, Lake Tahoe, Nevada, May 2-4, 1983, Paper No. 83-859.
- 7.73 Plunkett, R. and Lee, C.T., "Length Optimization for Constrained Viscoelastic Layer Damping", Journal of the Acoustic Society of America, Vol. 48, 1970, p. 150.
- 7.74 Gibson, R.F. and Plunkett, R., "A Forced Vibration Technique for Measuring Material Damping", Experimental Mechanics, Vol. 11, No. 8, August 1977, p. 297.

- 7.75 Georgi, H., "Dynamic Damping Investigations on Composites", Damping Effects in Aerospace Structures, AGARD-CP-277, October 1979.
- 7.76 Gibson, R.F., Yau, A. and Riegner, D.A., "Vibration Characteristics of Automotive Composite Materials", Short Fiber-Reinforced Composite Materials, ASTM STP 772, 1982, p. 153.
- 7.77 Crawley, E.F. and Sheen, R.L., "Experimental Measurement of Material Damping for Space Structures", Vibration Damping 1984 Workshop Proceedings, Dr. Lynn Rogers Editor, AFWAL-TR-84-3064, November 1984, p. F-2.
- 7.78 Haines, D.W., "Material Damping of Carbon/Epoxy Composites by Means of Free-Free Beam Resonance Tests", Vibration Damping 1984 Workshop Proceedings, Dr. Lynn Rogers Editor, AFWAL-TR-84-3064, November 1984, p. R-3.
- 7.79 Gibson, R.F., Suarez, S.A. and Deobald, L.R., "Improvement of Damping in Fiber-Reinforced Polymer Composites", Vibration Damping 1984 Workshop Proceedings, Dr. Lynn Rogers Editor, AFWAL-TR-84-3064, November 1984, p. S-1.
- 7.80 Sun, C.T., Lee, B.T. and Chaturvedi, S.K., "Composite Material Damping Using Impulse Techniques", Vibration Damping 1984 Workshop Proceedings, Dr. Lynn Rogers Editor, AFWAL-TR-84-3064, November 1984, p. P-2.
- 7.81 Timmerman, N.S., "Damping Characteristics of Metal Matrix Composites", AMMRC-TR-82-19, April 1982.
- 7.82 Timmerman, N.S. and Doherty, J., "Loss Factors Measured in Metal Matrix Composite Materials", AMMRC-TR-84-22, June 1984.
- 7.83 Misa, M.S. and La Greca, P.D., "Damping Behavior of Metal Matrix Composites", Vibration Damping 1984 Workshop Proceedings, Dr. Lynn Rogers Editor, AFWAL-TR-84-3064, November 1984, p. U-2.

- 7.84 Read, R.E. and Dean, C.D., "The Determination of Dynamic Properties of Polymers and Composites", John Wiley and Sons, 1978.
- 7.85 Bert, C.W. and Clary, R.R., "Evaluation of Experimental Methods for Determining Dynamic Stiffness and Damping of Composite Materials," Composite Materials: Testing and Design (third conference), ASTM STP 546, 1973, p. 250.
- 7.86 Plunkett, R., "Measurement of Damping", in Structural Damping, Structural Damping, Rusicka Editor, ASME, December 1959, p. 117.
- 7.87 Gibson, R.F. and Plunkett, R., "Dynamic Stiffness and Damping of Fiber-Reinforced Composite Materials", The Shock and Vibration Digest, Vol. 9, No. 2, February 1977.
- 7.88 Crawley, E.F. and Mohr, D.G., "Experimental Measurement of Material Damping in Free Fall with Tunable Excitation", AIAA/ASME/ASCE/AHS Structures, Structural Dynamics and Materials Conference, Lake Tahoe, Nevada, May 1983, Paper No. 83-0858-CP.
- 7.89 Hooker, R.J., "Damping in Metals Under Combined Loading", Journal of Sound and Vibration, Vol. 79, No. 2, 1981, p. 243.
- 7.90 Hay, J.A., "Experimentally Determined Damping Factors", Symposium on Acoustic Fatigue, AGARD-CP-113, May 1973.
- 7.91 Thomson, A.G.R. and Lambert, R.F., "Acoustic Fatigue Design Data", AGARD-AG-196 - Part III, December 1973.
- 7.92 Rudder, F.F., "Acoustic Fatigue Resistance of Internal Airframe Structure", AFFDL-TR-71-107, July 1971.

- 7.93 Schneider, C.W., "Acoustic Fatigue of Aircraft Structures at Elevated Temperatures," AFFDL-TR-73-155 - Part I, March 1974.
- 7.94 Van der Heyde, R.C.W., and Kolb, A.W., "Sonic Fatigue Resistance of Lightweight Aircraft Structures", Symposium on Acoustic Fatigue, AGARD - CP-113, May 1973.
- 7.95 Van der Heyde, R.C.W. and Wolf, N.D., "Comparison of Sonic Fatigue Characteristics of Four Structural Designs," AFFDL-TR-76, September 1976.
- 7.96 Baird, E.F., Beinstein, M. and Arcas, N., "Sonic Fatigue Failure Mechanisms in Potential Space Shuttle Orbiter Designs," AIAA/ASME/SAE 15th Structures, Structural Dynamics and Materials Conference, Las Vegas, Nevada, April 17-19, 1974.
- 7.97 Jacobson, M.J., "Sonic Fatigue Design Data for Bonded Aluminum Aircraft Structures", AFFDL-TR-77-45, June 1977.
- 7.98 Wolfe, H.F. and Holehouse, I, "Durability of Adhesively Bonded Structures Subjected to Acoustic Loads," AGARD Report No. 701, December 1981.
- 7.99 Jacobson, M.J., "Advanced Composite Joints; Design and Acoustic Fatigue Characteristics", AFFDL-TR-71-127.
- 7.100 Jacobson, M.J. "Fatigue of V/STOL Composite Fuselage Panels Under Acoustic-Thermal Environments", NADC-81045-60, March 1981.
- 7.101 Jacobson, M.J., "Acoustic Fatigue Design Information for Fiber Reinforced Structures", AFFDL-TR-68-107, October 1968.
- 7.102 Soovere, J. "Sonic Fatigue Testing of the NASAL-1011 Composite Aileron", The Shock and Vibration Bulletin, No. 50, Part 4, September 1980.

- 7.103 Clarkson, B.L., "Extraction of the Response of Box Type Structures to Acoustic Loading," Symposium on Acoustic Fatigue, AGARD-CP-113, May 1973.
- 7.104 Gordon, R.W., Wolfe, H.F. and Talmadge, R.D., "Modal Investigation of Lightweight Aircraft Structures Using Digital Techniques," AFFDL-TR-77-124, December 1977.
- 7.105 Prydz, R.A., Revelle, J.D., Hayward, J.L. and Balena, F.J., "Evaluation of Advanced Fuselage Design Concepts for Interior Noise Control on High Speed Propeller-Driven Aircraft," NASA Contractor Report 165960, September 1982.
- 7.106 Soovere, J., "High Modulus Graphite Fiber Constrained Layer Damping Treatment for Heavy Aerospace Structure", AFFDL-TM-78-78-FBA, July 1978.
- 7.107 Pope, L.D. and Wilby, E.G., "Analytical Prediction of the Interior Noise for Cylindrical Models of Aircraft Fuselages for Prescribed Exterior Noise Fields (Part II), NASA Contractor Report 165869, April 1982.
- 7.108 Silverman, S. and Abramson, H.N., "Damping in Liquid Motions and Lateral Sloshing", Dynamic Behaviour of Liquids in Moving Containers, H. N. Abramson, Editor, NASA SP-106, 1966, p 105.
- 7.109 White, R.G., "The Application of a Transient Test Technique to the Study of the Local Vibration Characteristics of Ship Structures," I.S.V.R. Technical Report No. 31, May 1970.
- 7.110 Sharp, J.D. and Breke, M.L., "An Example of Additive Damping as a Cost Savings Alternative to Redesign", Winter Annual Meeting ASME Turbine Division, Atlanta, Georgia, November 27, 1977.

- 7.111 Henderson, J.P., "Damping Applications in Aero-Propulsion Systems", ASME Booklet AMD Vol. 38, Damping Applications for Vibration Control, pp 145-148, 1980.
- 7.112 Steinberg, D.S., "Vibration Analysis for Electronic Equipment", John Wiley and Sons, 1973.
- 7.113 Hayes, J.A., "Sonic Fatigue Tolerance of Glen Filament Structure: Experimental Results", AFFDL-TR-66-78, December 1966.
- 7.114 Holehouse, Ian, "Sonic Fatigue Design Techniques for Advanced Composite Aircraft Structures," AFWAL-TR-80-3019, April 1980.
- 7.115 Clarkson, B.L. and Ford, R.D., "The Response of a Model Structure to Noise; Part II - Curved Panel." ASD-TDR-62-706, Part II, May 1963.
- 7.116 Medaglia, J.M., "Dynamic Integrity Methods Including Damping for Electronic Packages in Random Vibration," General Electric Space Division.

SECTION 8

EFFECT OF DAMPING ON INTERIOR NOISE IN AIRCRAFT

8.1 INTRODUCTION

The primary purpose in this section is to discuss the possibility of reducing interior noise in aircraft by increasing the damping of the fuselage structure through the application of viscoelastic damping. Increasing the fuselage damping by this means has been tried before many times. In most instances the expected interior noise reductions did not materialize. Some recent developments [8.1, 8.2] have thrown some light on the possible reason for this discrepancy.

A brief review of both the interior noise sources in aircraft and the important parameter in the basic noise transmission loss theory are included in Section 8.2 as an introduction to the subject of interior noise in aircraft. The effect of the acoustic trim on the damping of aircraft structures is discussed in Section 8.3 together with a discussion of test procedures used to verify the performance of the viscoelastic damping treatment in reducing interior noise. The topic is concluded by a brief summary of recent developments in aircraft interior noise prediction methodology in Section 8.4.

8.2 INTERIOR NOISE IN AIRCRAFT

8.2.1 Sources of Interior Noise

The main in-flight source of interior noise, in turbojet and turbofan powered transport aircraft is due to turbulent boundary layer excitation of the fuselage shell [8.1, 8.3, 8.4] although some contributions may be obtained in the rear fuselage from jet exhaust noise [8.5]. Jet noise is a dominant noise source during take-off, especially in high-powered military aircraft [8.6], and in other parts of the aircraft during landing, when reverse thrust is used. Both of these noise sources are broad band in nature and, therefore, capable of exciting structural resonances.

In propeller driven aircraft, the noise generated by the propellers is usually the dominant noise source, although engine exhaust noise may provide a significant contribution to the interior noise in the aft cabin of some light general aviation aircraft [8.7, 8.8]. The propeller noise tends to be tonal in nature, concentrated primarily at the blade passage frequency and, to a progressively lesser extent, at the higher harmonics. Large turboprop aircraft also tend to employ constant speed (revolutions per second) propellers [8.9] with fixed excitation frequencies.

Recent studies [8.9], have indicated that structure borne noise, in the form of engine vibration, can be transmitted to the fuselage through the wing structure. Synchronizing the engines, in multi-engined turboprop aircraft, can reduce this noise. The propeller wash striking the horizontal stabilizer can be a further source of interior noise [8.9]. Jet engine vibration, transmitted to the fuselage via the engine support structure, has produced significant interior noise problems [8.10] in the past.

Localized interior noise can be produced by equipment mounted in aircraft, localized areas of supersonic flow, and critical acoustic spinning modes in large fanjet intake ducts that are attached to the fuselage.

8.2.2 Basic Noise Transmission Loss Theory

The basic noise transmission loss theory was developed with plane wave acoustic excitation, impinging on an infinite panel (Figure 8.1) at angles of incidence between near-grazing and normal. The transmission loss, due to a reverberant acoustic field, can be obtained by simply averaging the plane wave effect over all angles of incidence, above the near-grazing incidence. The reverberant acoustic field is readily reproduced in current test facilities.

The current test facilities, typically, consist of a reverberant source room and a reverberant receiving room that are separated by a high transmission loss common wall containing an aperture for the test panel. The transmission loss, TL, of the finite test panel, mounted in the aperture, is given by [8.11]

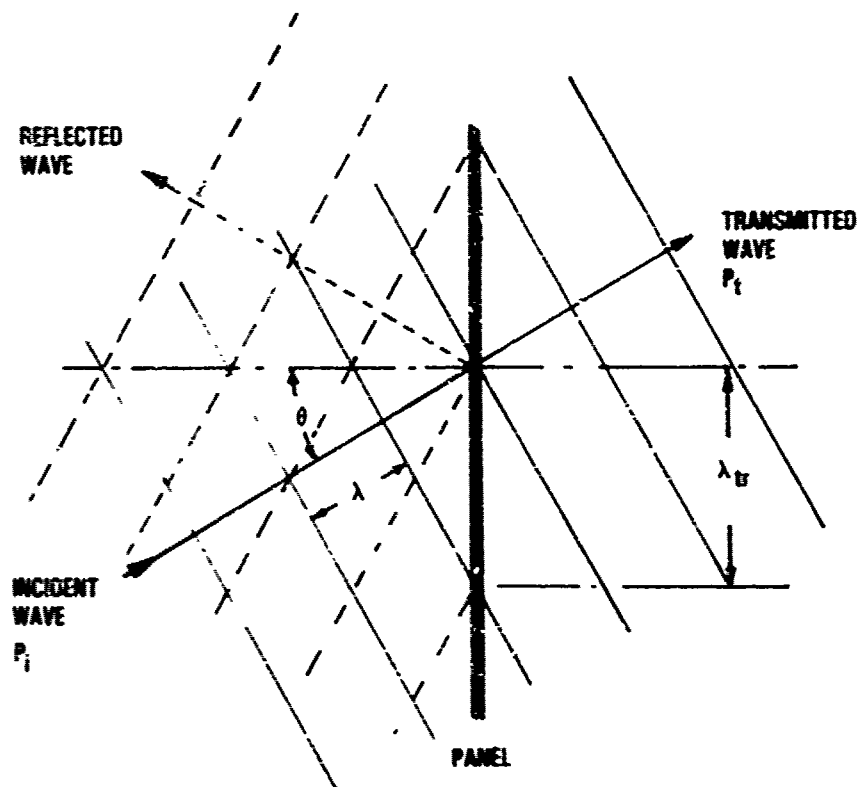


Figure 8.1. Plane acoustic wave incident on a panel

$$TL = NR + 10 \log_{10} \left(\frac{S}{A} \right) \quad (8.1)$$

where NR is the noise reduction of the panel, S is the area of the panel, and A is the absorption of the receiving room, usually determined from the reverberation time. The noise reduction is defined [8.11] as the difference between the space and time averaged random broadband noise measured in the source room and the space and time averaged transmitted sound measured in the receiving room. It is customary to present the transmission loss in one-third octave bands. The effects of the acoustic trim and viscoelastic damping can be determined by the difference in the measured noise reduction, between the treated and untreated panel.

The above noise transmission loss measurements involve the use of finite panels. The transmission loss curve for a finite panel (Figure 8.2), excited by an acoustic plane wave that is incident at an angle θ to the panel (Figure 8.1), is characterized by a low frequency stiffness controlled region, a resonant response region, a mass controlled region and a coincidence region, in ascending order of frequency. The transmission loss in the resonant response and the coincidence regions can be reduced by increasing the damping of the panel.

Resonances are introduced into a finite panel, by the initial flexural waves combining, at the same phase, with the flexural waves reflected by the panel boundaries, to set up standing flexural waves within the panel at each of the resonant frequencies. Coincidence is obtained when the trace wave λ_{tr} of the acoustic wave (Figure 8.1) matches the flexural wave length in the panel at the same frequency. The frequency at which coincidence is obtained, is known as the critical frequency (f_c).

8.2.2.1 Infinite Panel Transmission Loss Theory

There are no resonances in an infinite panel, although coincidence can still be obtained. The panel, in fact, behaves like a limp wall, obeying the mass law up to the coincidence region. This behavior simplifies the noise transmission loss analysis. The resulting infinite panel transmission loss equations have proven to be quite accurate in predicting the finite panel transmission loss, above the resonance region.

The transmission loss is determined from the transmission coefficient $\tau(\theta)$ [8.12, 8.13], which is defined as the ratio of transmitted acoustic power to incident acoustic power on the structure. The transmission coefficient for an infinite panel, that is excited by an acoustic plane wave at incidence θ to the panel, is given by the relationship

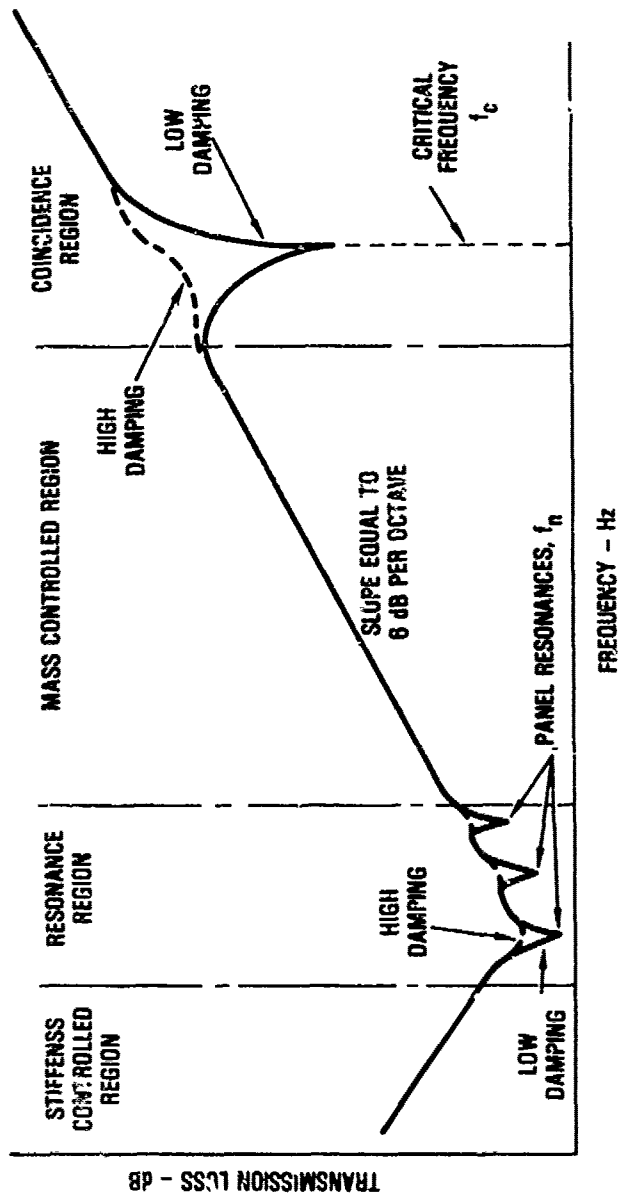


Figure 8.2. Schematic of acoustic transmission loss curve for a finite panel

$$\frac{1}{\tau(\theta)} = \left| \frac{p_i}{p_t} \right|^2 = \left[1 + \eta \left(\frac{\omega \mu}{2\rho c} \cos^4 \theta \right) \left(\frac{\omega^2 D}{c^4 \mu} \sin \theta \right) \right]^2 + \left[\left(\frac{\omega \mu}{2\rho c} \cos \theta \right) \left(1 - \frac{\omega^2 D}{c^4 \mu} \sin^4 \theta \right) \right]^2 \quad (8.2)$$

where p_i and p_t are the amplitudes of the incident and transmitted pressure waves, respectively; ω is the circular frequency; η , D and μ are the loss factor, the flexural stiffness and the surface density of the panel, respectively; ρ is the density of the air; and c is the speed of sound in air. The transmission loss, in dB, is expressed simply by

$$TL = 10 \log \frac{1}{\tau(\theta)} \quad (8.3)$$

The noise transmission loss in the mass controlled and coincidence regions are obtained by substituting equation 8.2 into equation 8.3. At coincidence, the noise transmission loss equation is reduced to

$$TL = 20 \log \left[1 + \eta \left(\frac{\omega \mu}{2\rho c} \cos \theta \right) \right] \quad (8.4)$$

The transmission loss at coincidence is controlled entirely by the loss factor η . The critical frequency, used in deriving equation 8.4 from equations 8.2 and 8.3, is given by [8.12, 8.13]

$$f_c = \frac{c^2}{2\pi \sin^2 \theta} \left| \frac{\mu}{D} \right|^{\frac{1}{2}} \quad (8.5)$$

Below the critical frequency, the transmission loss is approximated by the mass law; that is, by

$$TL \approx 10 \log \left[1 + \left(\frac{\omega \rho l}{2 \rho c} \cos \theta \right)^2 \right] \quad (8.6)$$

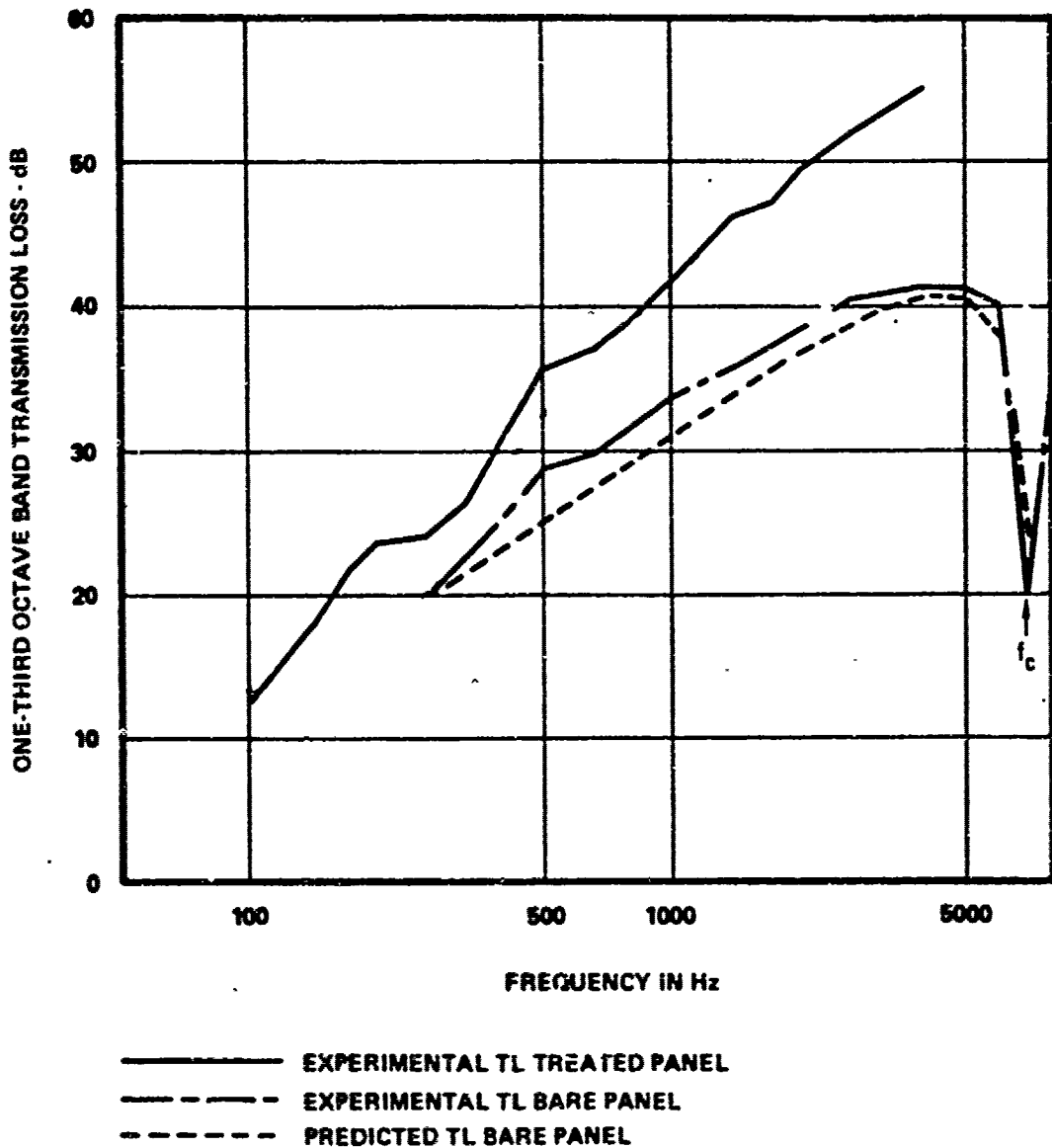
The transmission loss in this mass controlled region is not affected by the panel damping.

The normal incidence transmission loss is given by equation 8.6, when $\cos \theta = 1$. For the reverberant acoustic field, often used in noise transmission loss studies, the transmission coefficient $\tau(\theta)$ in equation 8.2 is replaced by an average transmission coefficient $\bar{\tau}$, defined by

$$\bar{\tau} = \frac{\int_0^{78^\circ} \tau(\theta) \cos \theta \sin \theta \, d\theta}{\int_0^{78^\circ} \cos \theta \sin \theta \, d\theta} \quad (8.7)$$

where the 78° limit provides the best fit to the test data. The noise transmission loss equation breaks down when θ approaches 90° . The transmission loss calculated with the average transmission coefficient is known as the field incidence transmission loss.

The above infinite panel noise transmission loss theory predicts the noise transmission loss of aluminum panels (Figure 8.3) and, in a slightly modified form [8.14], of composite panels (Figure 8.4) with good accuracy. The addition of acoustic trim increases the noise transmission loss even more (Figure 8.3). For an ideal double wall partition, i.e., with equal weight unconnected walls, the transmission loss increases at the rate of 12 dB/octave in the mass controlled region, above the double wall resonance [8.13].



SKIN	THICKNESS 0.070 INCHES AND WEIGHT DENSITY 172.00 LB/FT ³
AIRGAP	THICKNESS 1.00 INCHES
SEPTUM	SURFACE WEIGHT DENSITY 0.01 LB/FT ²
POROUS BLANKET	THICKNESS 2.00 INCHES AND WEIGHT DENSITY 1.20 LB/FT ³
	SPECIFIC FLOW RESISTANCE 68.00 CGS RAYLS/IN
SEPTUM	SURFACE WEIGHT DENSITY 0.01 LB/FT ²

Figure 8.3. Panel transmission loss both with and without acoustic treatment

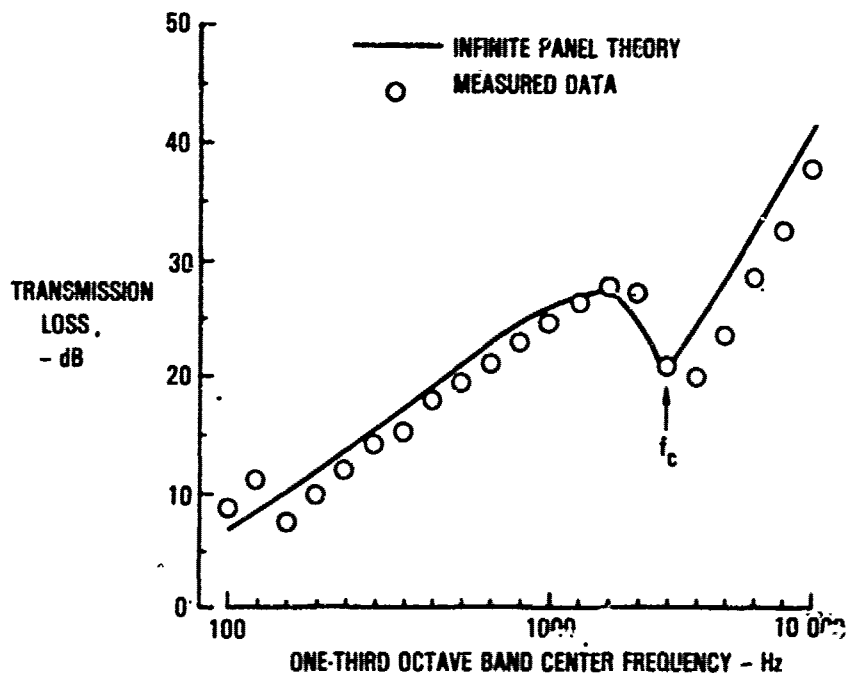


Figure 8.4. Transmission loss characteristics of graphite/epoxy mini-sandwich panel with a 1mm thick syntactic core

8.2.2.2 Radiation Efficiency of a Panel

The critical frequency is important also for another reason. At and above the critical frequency, the panel becomes a very efficient radiator of sound [8.13], with a radiation ratio, σ_{rad} , above unity at the critical frequency, and tending to unity, above the critical frequency. The radiation ratio is defined as the power radiated by a plate into a half space divided by the power radiated by an infinite rigid piston into the same half space, both vibrating with the same root mean square (rms) velocity. For a finite panel, the acoustic power W_A radiated by a set of resonant panel modes within a frequency band, can be expressed by

$$W_A = \sigma_{rad} \rho c S \langle v^2(\omega) \rangle \quad (8.8)$$

where S is the panel area and $\langle v^2(\omega) \rangle$ is the space-time average of the panel mean square velocity within the frequency band, centered at a circular frequency ω . Typical variation of the finite panel radiation ratio [8.15] with normalized frequency is illustrated in Figure 5. Noise is also radiated by these resonant modes below the critical frequency. This noise is produced by uncancelled acoustic radiation, emanating primarily from the panel boundaries [8.15, 8.16]. The radiation efficiency of this noise is, however, very low below the critical frequency. In the near field, within about half a wave length from the surface of the panel, these panel modes can still produce very intense sound pressure [8.13], in spite of the cancellation effect.

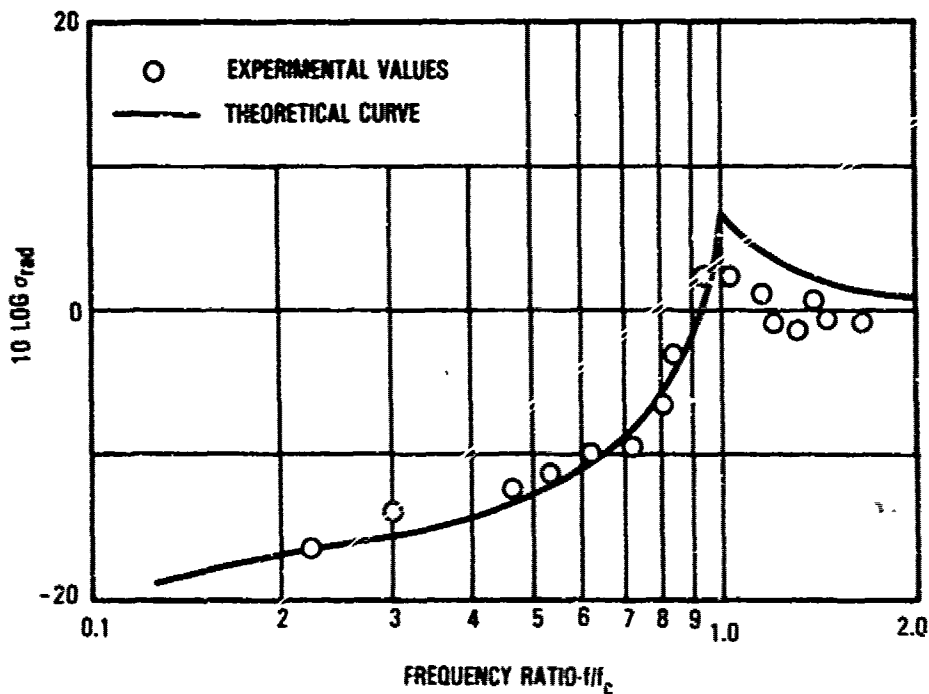


Figure 8.5. Typical radiation ratio for a baffled panel as a function of frequency normalized to the critical frequency

8.2.2.3 Transmission Loss Characteristics of a Stiffened Panel

The typical field incidence transmission loss of a large metal panel, that is stiffened by frames and stringers [8.16, 8.17] and subjected to a reverberant acoustic excitation, is illustrated in Figure 8.6. The noise transmission loss, at the lower frequencies, can be calculated by the single panel field incidence transmission loss equation applied to the whole panel in which the weight of stringers and frames are averaged over the area of the panel and added to the skin weight per unit area [8.13, 8.17]. The lowest vibration frequencies are usually controlled by the stiffness and mass of the frames which are assumed to be simply supported at the panel boundary. Above the fundamental panel resonant frequency, the field incidence transmission loss drops to that of the unstiffened panel.

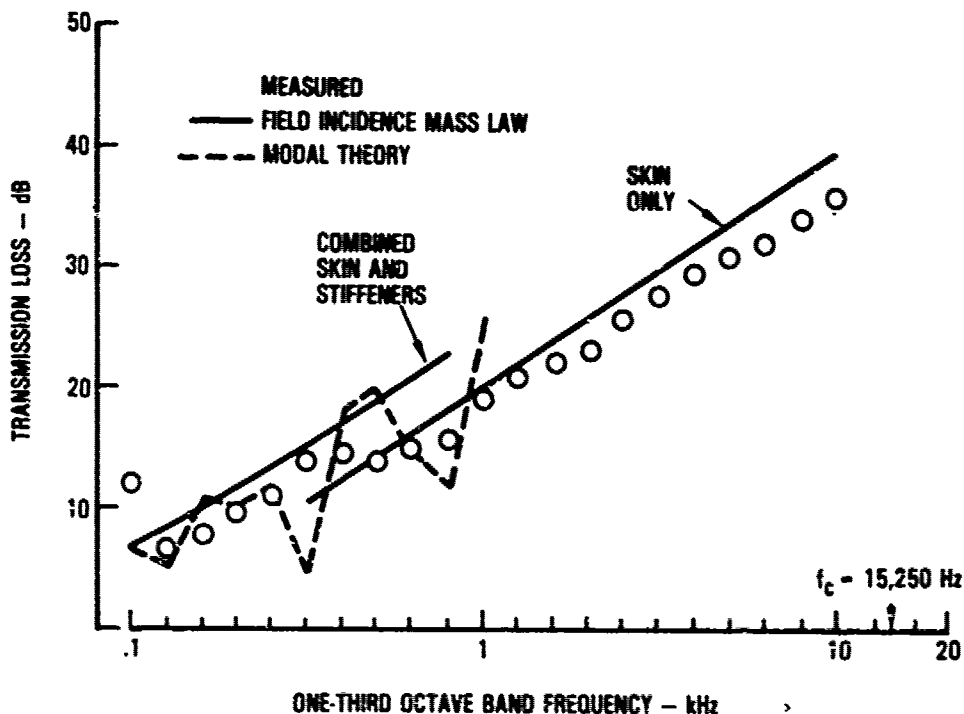


Figure 8.6. Field incidence transmission loss of a stiffened flat panel [8.17]

8.2.3 Behavior of Stiffened Aircraft Panels

The noise transmission phenomenon becomes more difficult to visualize when dealing with more complex structures. Analytical methods for predicting the noise transmission into trimmed aircraft fuselage structure are still in the process of evolution. Before discussing the noise transmission characteristics of more complex stiffened shell structures, it is necessary to understand how the acoustic plane wave excitation relates to the actual environment on aircraft, and how the stiffened panels on aircraft behave in response to these environments.

The acoustic plane wave can be used, with the appropriate noise spectrum, to model both the random jet noise and the harmonic propeller noise directly by the use of the appropriate angle of incidence for the plane wave relative to the surface of the fuselage. Grazing incidence acoustic plane wave excitation also reproduces some of the characteristics of the turbulent boundary layer excitation, although there are differences as to their effect on the structural vibration. The acoustic plane wave tends to be more efficient in exciting the lower frequency panel modes than turbulent boundary layer. The reverse is true for the higher frequency modes where the structural wave lengths provide a better match with the turbulent boundary layer wave lengths. The boundary layer characteristics are, themselves, dependent on the frequency, boundary layer thickness and aircraft speed. In spite of these differences, some conclusions, based on near-grazing incidence acoustic excitation, are also applicable to turbulent boundary layer excitation.

The fuselage structure, in general aviation and transport aircraft, usually consists of panels supported by open section frames and stringers. The lighter stringers usually run parallel to the fuselage axis. Experimental evidence involving both turbulent boundary layer [8.4] and jet noise excitation [8.18] of aircraft fuselage structure, indicates that very little correlation is obtained between the vibration of panels on either side of frames, that are fastened to the skin. The correlation, that was obtained with jet noise excitation, was restricted to a number of adjacent circumferential bays with equal stringer spacing [8.18].

In the panel array, between two adjacent frames, the stringer torsion and bending modes couple up with the panel bending modes to form group modes (Figure 8.7) that are bounded by the frequency of the coupled stringer torsion and bending modes. The number of modes within each group is equal to the number of equal adjacent bays. A similar group of modes is repeated at a higher frequency, bounded by the corresponding higher order stringer torsion and bending modes. This type of panel array vibration has been reproduced in the laboratory with grazing incidence jet noise [8.19]. Theory [8.20, 8.21, 8.22, 8.23] has also been developed for predicting the vibration response of these panels. Simplified method for predicting the frequencies of the group modes is given in Reference [8.24].

Acceleration measurements [8.4] taken in flight, on an untrimmed fuselage subjected to turbulent boundary layer excitation, indicated that very little coherence was obtained between the vibration of adjacent panels in the

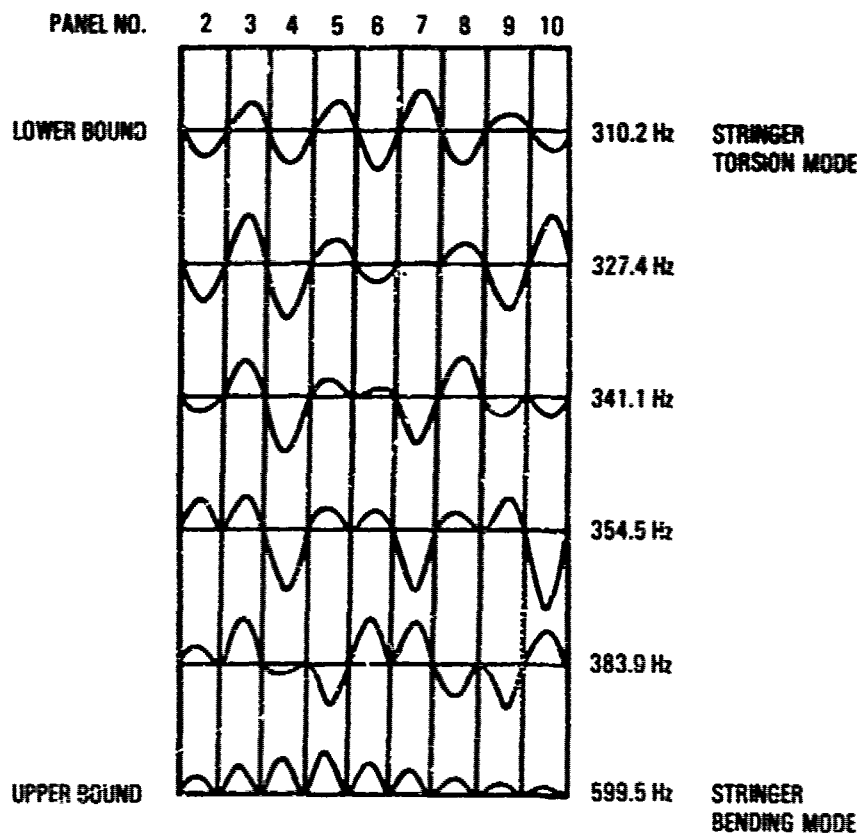


Figure 8.7. Mode shapes of a stiffened panel array

circumferential direction. Coherence is a measure of the amount of correlation obtained. Where the upstream and downstream panel boundaries (frames) provided weak "discontinuities" good coherence was obtained between two adjacent axial panels at coincidence. Turbulent boundary layer [8.25, 8.26] has a relatively long correlation length in the axial direction and a short correlation length in the later (circumferential) direction, which provides an explanation of the above observations.

The above result, of low circumferential coherence between adjacent panels across a stringer, has also been reproduced by analysis [8.27, 8.28], using realistic analytical models of turbulent boundary layer. The analysis in reference [8.29] indicated that an upper bound to the noise radiated by the group modes, that are excited by turbulent boundary layer, can be obtained by summing the radiation from the individual panels.

The vibration response of single panels, excited by turbulent boundary layer, has also been studied by many authors [8.29, 8.30, 8.31]. In general, good correlation has been obtained between the predicted and measured response. The greatest problem involved the reproduction of the correct edge conditions encountered in practical aircraft panels. For open section stringers, the actual panel edge conditions are closer to those of the stringer torsional mode at the lowest resonant frequency and approach the simply supported edge condition at the higher panel resonant frequencies. The simply supported edge condition is, generally, considered to represent the lower bound for the panel resonant frequencies. However, the resonant frequencies of the higher order panel modes can, in some panels, fall below the corresponding simply supported panel frequencies, because of the increasing contribution from the stiffener rotational inertia.

Theory [8.27] indicates that the acoustic power radiated from a panel is proportional to $(a/h)^4 / (\eta l_0^{a/b})$ where, a, b and h are the panel length, width, and thickness, respectively, and η is the panel loss factor. Thus,

a considerable reduction in the radiated power can be obtained by the use of large aspect ratio panels. The power radiated is less for panels supported by stiffeners of finite width [8.27] than by line attached stiffeners.

The above behavior of single panels and panel arrays was partly responsible for the division of the vibration response of stiffened shell structures into three vibration regions, in the earlier development of interior noise prediction methodology [8.32] for large transport aircraft. The three regions are, in descending order of frequency, the vibration response of the individual panels, the group modes and the overall shell modes.

8.2.4 Behavior of Shells

Expressions for the noise transmission loss of infinite shallow shells [8.33], infinitely long unstiffened isotropic and orthotropic cylindrical shells [8.34] and infinitely long stringer stiffened cylindrical shells have been developed by Koval. The above cylindrical shells are assumed to be excited by an acoustic plane wave, incident on the surface of the cylindrical shell at an angle θ , as illustrated in Figure 8.8. Full absorption of the noise radiated into the interior of these shells is also assumed.

The predicted transmission loss is illustrated in Figure 8.9 [8.35] for an unstiffened and stringer stiffened shell with the plane wave impinging at near grazing incidence ($\theta = 30^\circ$). The transmission loss is characterized by a low frequency stiffness controlled region, the resonance region just below the ring frequency, f_R , the mass controlled region and the critical frequency, f_c , in ascending order of frequency. The noise transmission loss is seen to be a minimum at the ring frequency. The ring frequency is the fundamental breathing mode of the shell where all parts of the shell are moving simultaneously in or out during the vibration. The ring frequency is given by

$$f_R = \frac{1}{2\pi R} \left\{ \frac{E}{\rho_s} \right\}^{1/2} \quad (8.9)$$

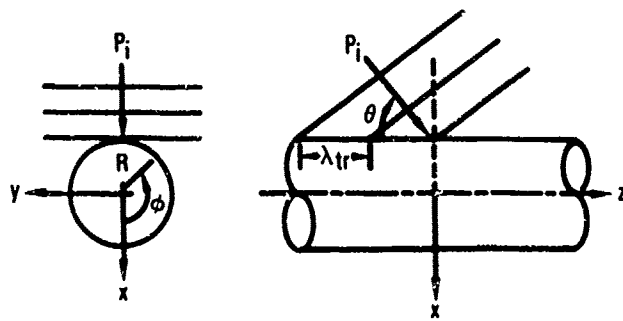


Figure 8.8. Acoustic plane wave excitation of infinite cylinder

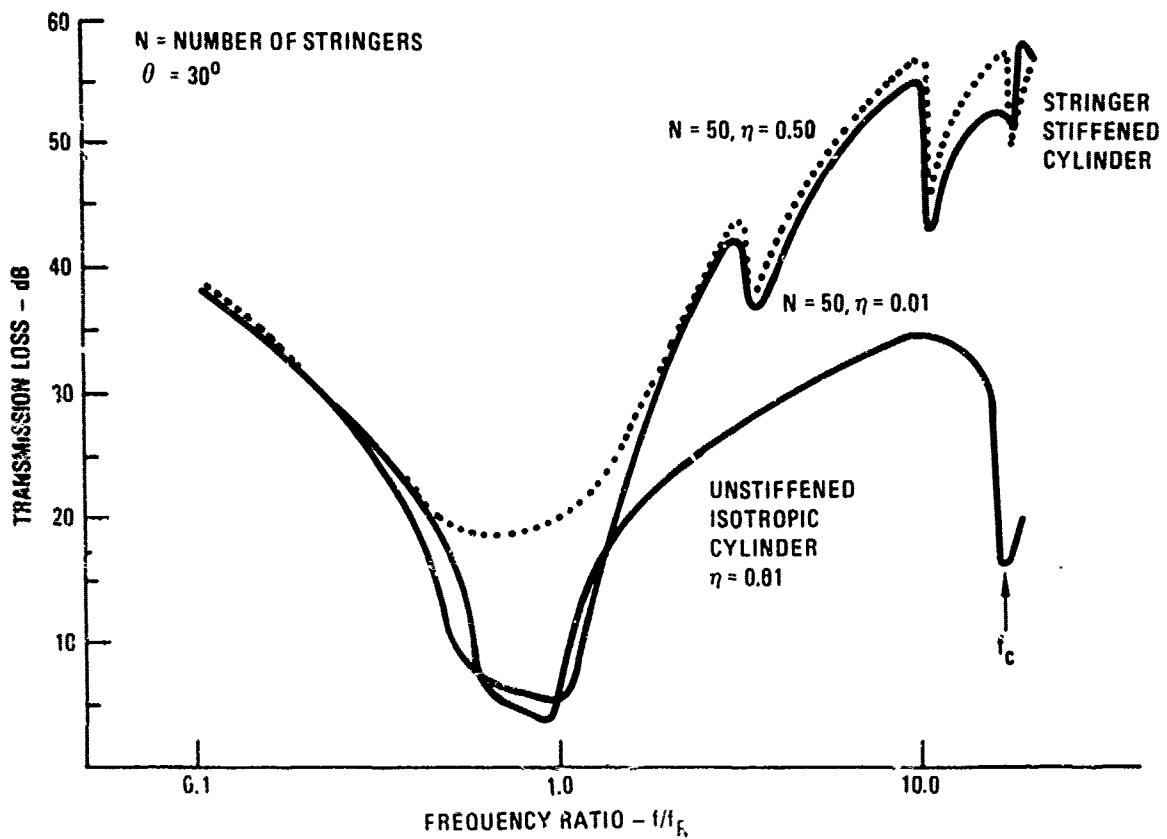


Figure 8.9. Transmission loss for stringer-stiffened infinite length shell

for an isotropic shell. Apart from the radius, R , it is a function of the shell material properties such as the Young's modulus E and the density ρ_s . Above the ring frequency, the curved panels also start to behave more like flat panels. The addition of stringers (Figure 8.9) tends to increase the transmission loss in the mass controlled region [8.35]. Dips in the transmission loss curves in this region are due to stringer torsional modes.

The transmission loss at the ring frequency and the critical frequency, is controlled by the damping in the shell. This result, at the ring frequency, is due to shell resonances which are responsible for the relatively wide band of low transmission loss in this region. These resonances below the ring frequency are actually circumferential modes which are excited when the trace wave length and frequency of the plane wave matches up with a circumferential mode that has the same axial characteristics and a non zero generalized force in the circumferential direction. The vibration response of the shell, both above and below the ring frequency, is modified by coupling of the shell vibration modes with the frame vibration mode [8.36]. The possible effect of this coupling is illustrated in Figure 8.10, where the unstiffened cylinder response is obtained only at the lowest frequencies. At slightly higher frequencies the unstiffened shell response is replaced by the frame dominated vibration response of the shell followed by the vibration of the shell between two adjacent frames.

For a finite length cylinder, the modal density is greatest around the ring frequency, increasing the resonant region beyond that indicated in Figure 8.9. Evidence is provided by vibration response tests [8.37] conducted on a stiffened cylindrical shell, cut from an old fighter aircraft fuselage. The free-free shell was excited over part of its circumference (Figure 8.11) by a broad band (80-3000 Hz) random noise, at grazing incidence. The typical strain response of a panel, located at the mid-section of the shell on the loudspeaker side, is illustrated in Figure 8.12. The greatest vibration response was obtained just above the ring frequency. Low frequency overall modes (Figure 8.13) of the stiffened shell were also excited. Flight test

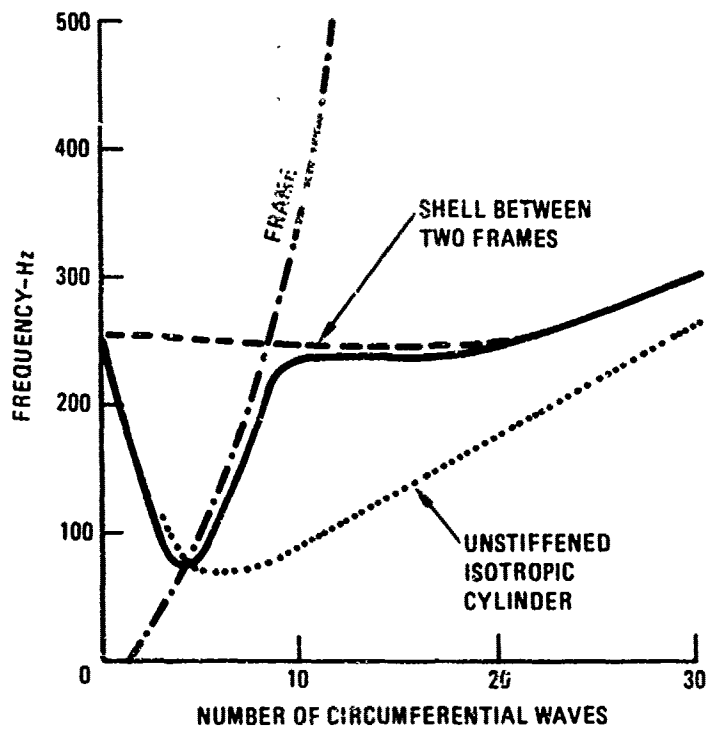


Figure 8.10. Natural frequencies of a finite, frame-stiffened cylinder



Figure 8.11. Stiffened cylinder mounted in acoustic test facility

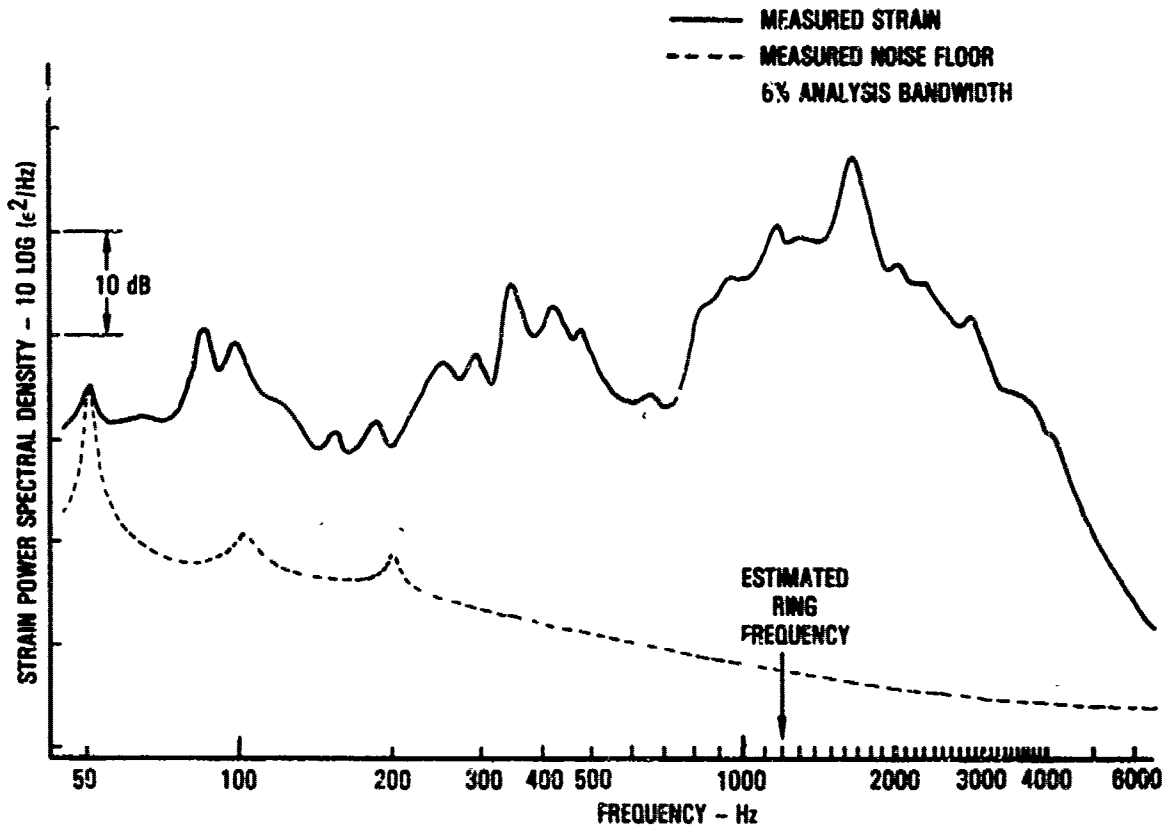


Figure 8.12. Typical strain response of a panel in a stiffened shell due to broad band random acoustic loading at grazing incidence

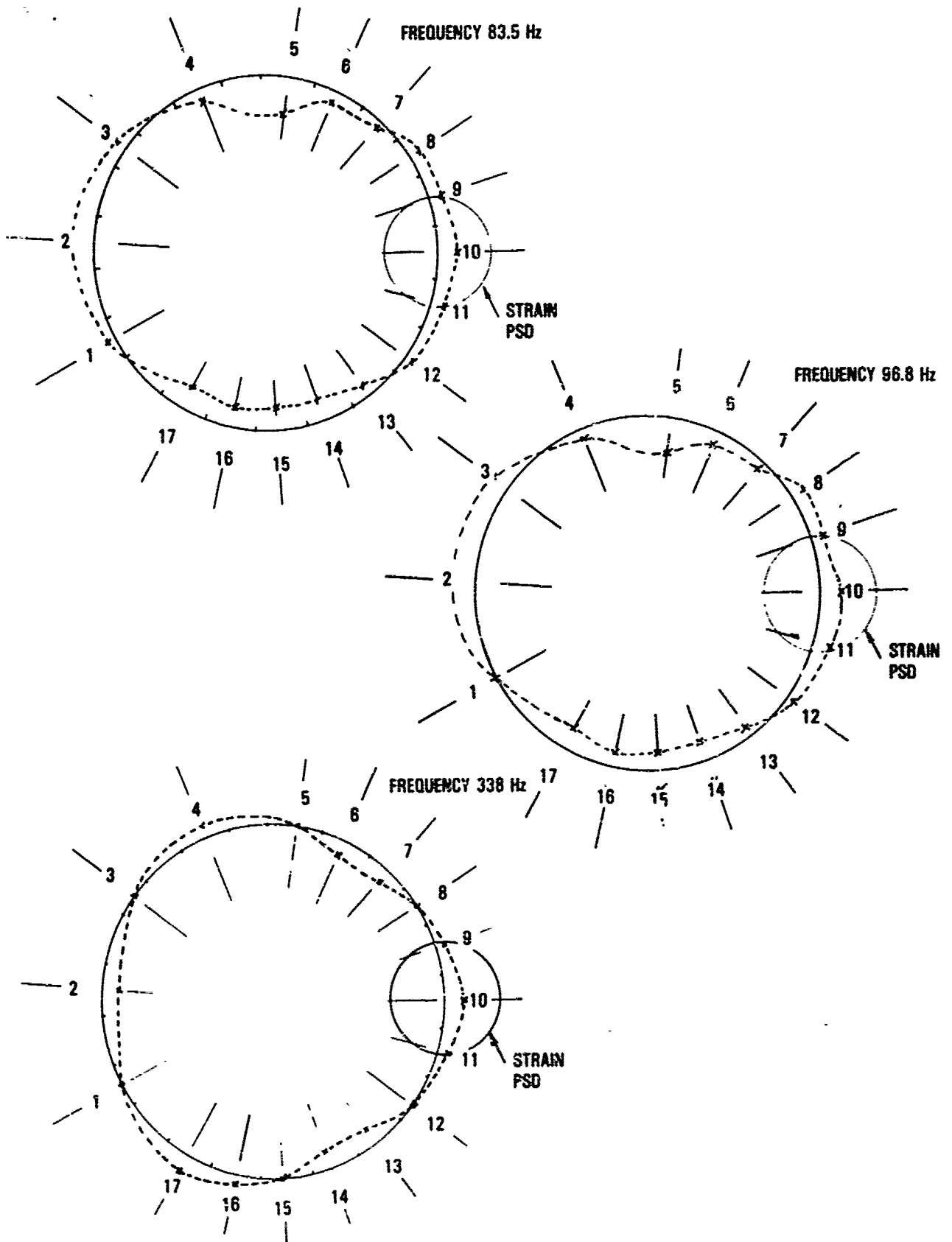


Figure 8.13. Typical measured stiffened shell overall mode shapes in the circumferential direction

results [8.31] on a bare fuselage, indicate (Figure 8.14) a similar type of panel response to turbulent boundary layer excitation above the ring frequency, and a similarly shaped noise radiation spectrum. The panel response in Figure 8.12 is proportional to displacement whereas the acceleration response is illustrated in Figure 8.

Pressure differential (Figure 8.14) and curvature increase the resonant frequencies of the panel and shell modes. This increase in frequency can be best demonstrated by considering two simply supported panels, each 20 inches (508 mm) long, 8 inches (203.2 mm) wide and 0.064 inch (1.63 mm) thick, one flat and the other curved with a radius of 72 inches (1829 mm). The

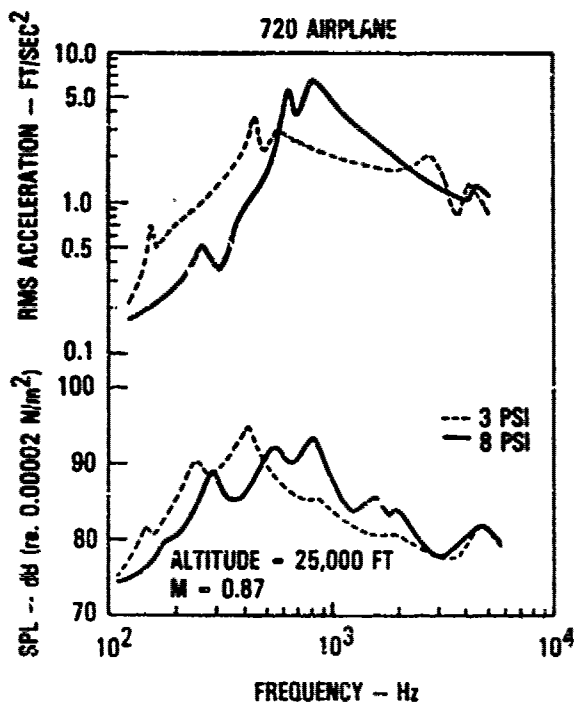


Figure 8.14. Typical in-flight fuselage acceleration response and radiated noise

fundamental frequency of the panels, with both a zero and an 8.5 psi (58.5 N/m²) pressure differential, are listed in Table 9.1.

TABLE 8.1 EFFECT OF CURVATURE AND PRESSURE

Pressure psi	Radius in.	Frequency Hz
0	-	108
8.5	-	409
0	72	124
8.5	72	414

By far the greatest effect is due to the pressure differential. A pressure differential of 8.5 psi (58.5 N/m²) is typical for a large transport aircraft fuselage.

The shell, at and above coincidence, is also a very efficient radiator of sound [8.16], similar to the panels. The radiation efficiency (Figure 8.15) is slightly less between the ring frequency and the critical frequency, but drops off rapidly below the ring frequency. The critical frequency is reduced by an increase in both the curvature and the pressure differential. The grazing incidence acoustic excitation and the turbulent boundary layer excitation have a significantly different effect on the critical frequency of both shells and panels. The convection velocity of the turbulent boundary layer fluctuating pressures is between 0.6 and 0.9 times the free stream velocity, depending on the frequency. At a flight speed of Mach 0.8 the critical frequency produced by turbulent boundary layer excitation could be more than fifty percent lower than that obtained with near grazing incidence acoustic excitation. The infinite panel critical frequency, with turbulent boundary layer excitation, is given by

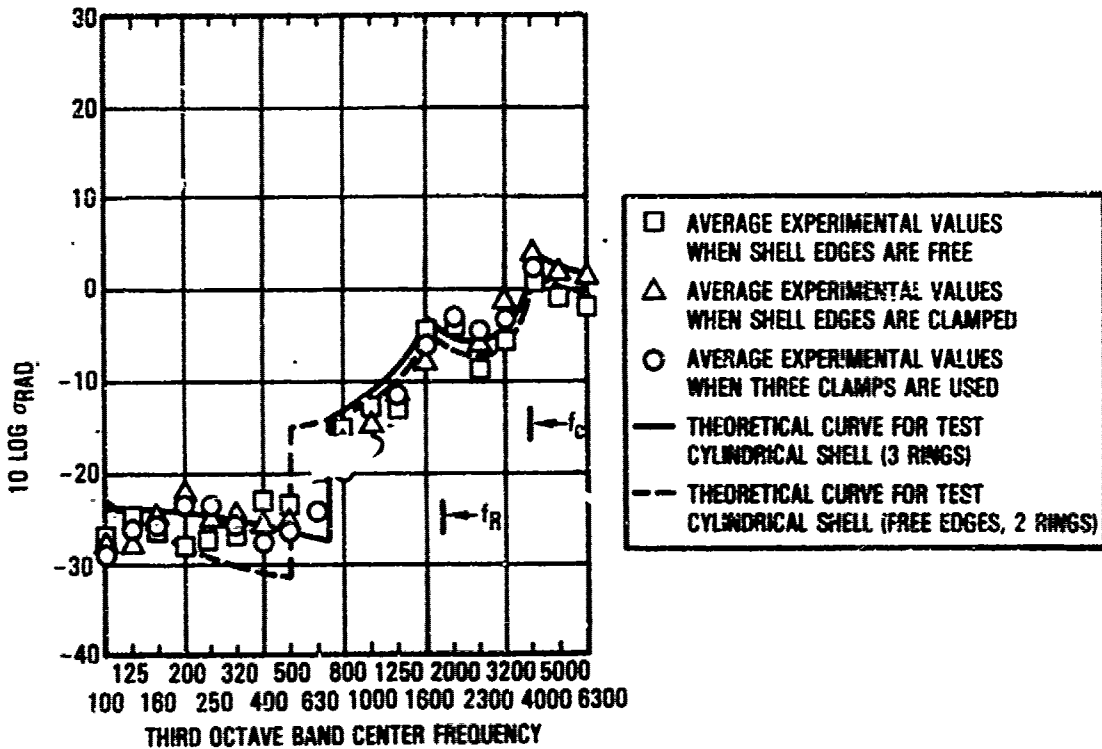


Figure 8.15. Radiation ratio of a cylindrical shell

$$f_c = \frac{U_c^2}{2\pi} \left\{ \frac{\mu}{D_x} \right\}^{1/2} \left\{ 1 - \frac{\Delta p R}{2\mu U_c^2} \right\}^{1/2} \quad (8.10)$$

where U_c is the convection velocity, D_x is the panel flexural difference in the axial direction and Δp is the pressure differential.

Flight test results [8.4] have also indicated that the critical frequency is affected by the presence of the stringers. It was assumed that the critical frequency can be related to the longitudinal component of the flexural wave length, λ_L , by the expression

$$\lambda_L \propto (f_c)^{-\beta}$$

where β is an empirically derived frequency index. The measured variation of this index with frequency is illustrated in Figure 8.16. For an infinite isotropic panel $\beta = 0.5$.

The evidence in this section suggests that there could be a wide frequency range, in the vibration response of a stiffened shell due to turbulent boundary layer excitation, where the noise transmission loss could be affected by the shell damping. This region could extend from just below the ring frequency to above the critical frequency. On account of the pressure differential effect and the relatively low convection velocity of the turbulent boundary layer relative to the speed of sound, the coincidence frequency is considerably lower than suggested by acoustic excitation in Figures 8.3 and 8.9. As a consequence, much more of the audio frequency range is included in the high radiation efficiency region. Turbulent boundary is also much more efficient than grazing incidence acoustic waves in exciting the panels in this higher frequency region.

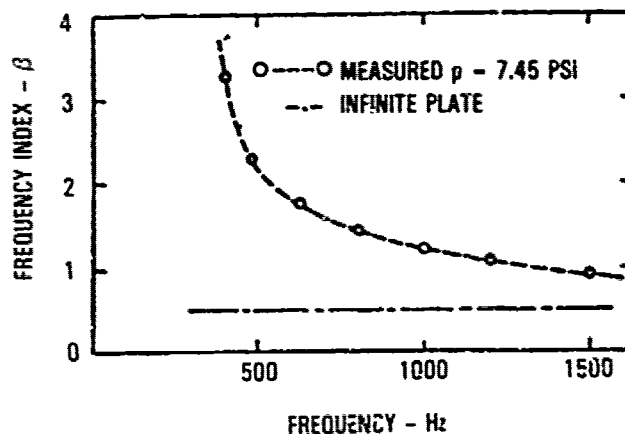


Figure 8.16. Variation of frequency index β with frequency

8.3 EFFECT OF ACOUSTIC TRIM AND DAMPING TREATMENT ON FUSELAGE DAMPING

8.3.1 Effect of Damping Treatment on Interior Noise

Many tests have been conducted that demonstrate the possibility of reducing interior noise by the application of viscoelastic damping treatments to the skin. The effectiveness of these treatments, when applied to the bare fuselage skin can be illustrated in a single figure (Figure 8.17), which represents measured in-flight data [8.3]. Similar results with minor differences were previously obtained in laboratory tests [8.31]. The rubber wedges, used at the upstream panel boundary, are thought to provide an increase in the panel damping as well as minimizing the reflection of the travelling waves at the upstream boundary. The rubber wedges were much heavier than the damping tape which could account for the greater effectiveness.

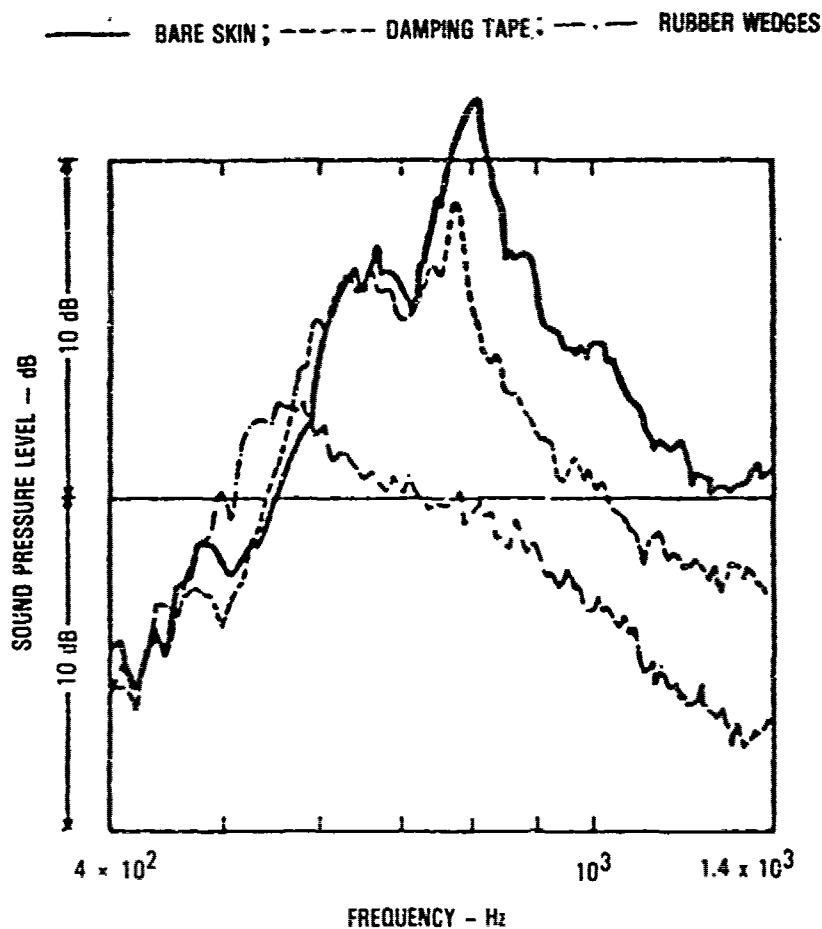


Figure 8.17. Power spectral density of interior noise (Mach 0.85)

Based on these results, it must be concluded that viscoelastic damping treatment is very effective in reducing interior noise. However, these and other similar results were obtained with a bare fuselage shell, devoid of any insulating blankets and interior trim. When the full acoustic trim was installed over the viscoelastically damped shell, the noise reduction, expected on the basis of bare shell measurements, usually failed to materialize.

8.3.2 Effect of Acoustic Trim on the Fuselage Damping

The standard aircraft interior trim, generally, consists of a fiberglass thermal insulating blanket, enclosed in thin plastic that represents a septum on either side of the blanket, all covered by an interior trim panel. Often, there is an air gap between the insulating blanket and the aircraft skin. This treatment increases the noise transmission loss significantly (Figure 8.3) above the double wall resonance frequency. It becomes highly effective, in this respect, above a frequency of approximately 1000 Hz.

Two recently completed, but totally independent studies [8.1, 8.2], have revealed the effect of the acoustic trim on the damping of the structure. One of these studies [8.2] involved noise transmission tests on a small diameter stiffened cylinder (Figure 8.18) both with and without the presence of the interior trim. This study was part of the latest interior noise prediction methodology development, that requires the use of a measured loss factor for each of the one-third-octave bands, as part of the input.

The measured loss factors, both with and without the presence of the interior trim, are summarized in Figure 8.19. These data include loss factors measured both for the individual modes and in the third-octave bands. The measured loss factors from an untrimmed metroliner fuselage [8.38] (Figure 8.20) and from an untrimmed wide body transport aircraft [8.39] are included for comparison. The loss factors for all three untrimmed cylindrical shells tend to lie along the same mean curve, indicating that the damping in shells may be dependent primarily on frequency and not on the structural parameters.

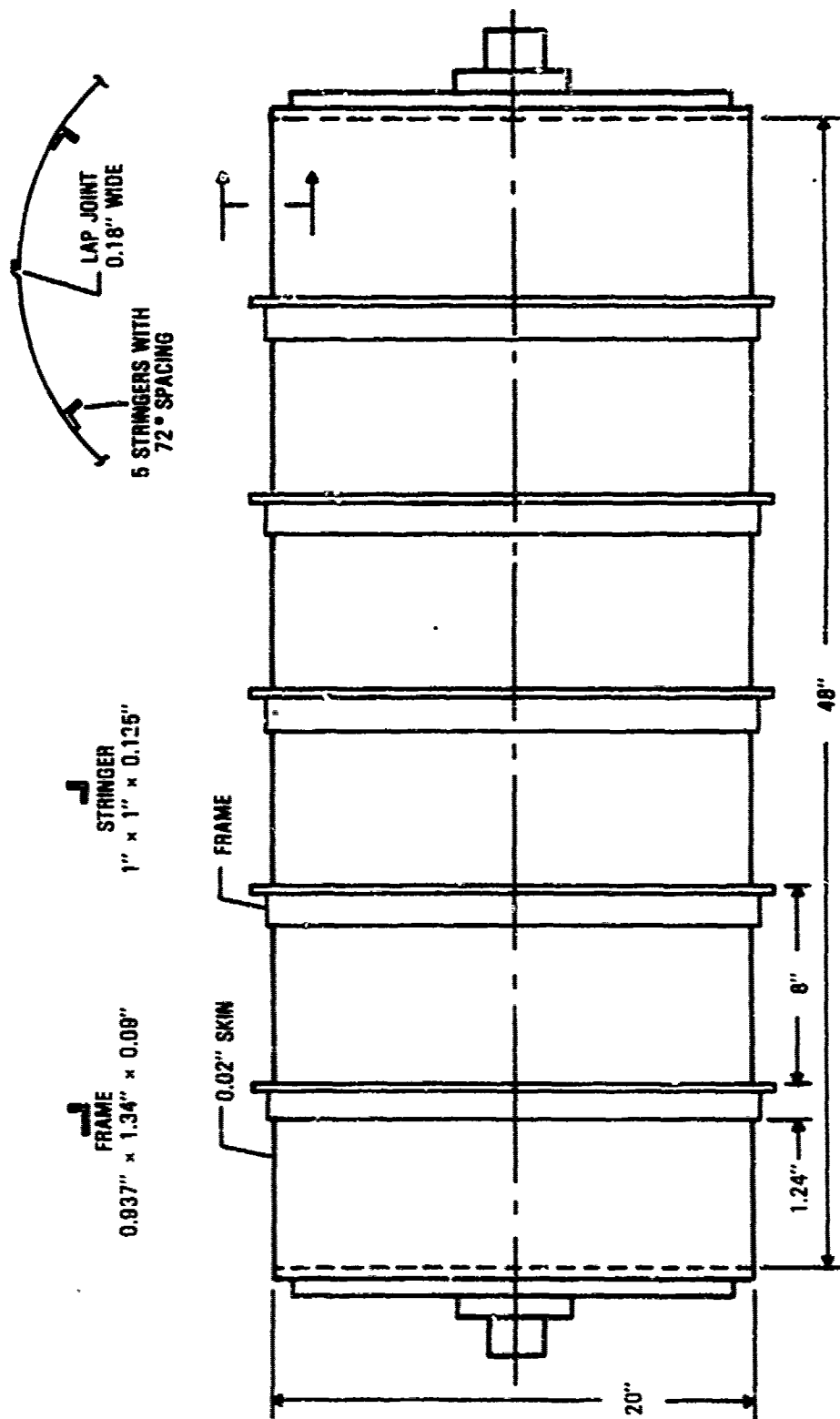


Figure 8.18. Small diameter stiffened cylinder

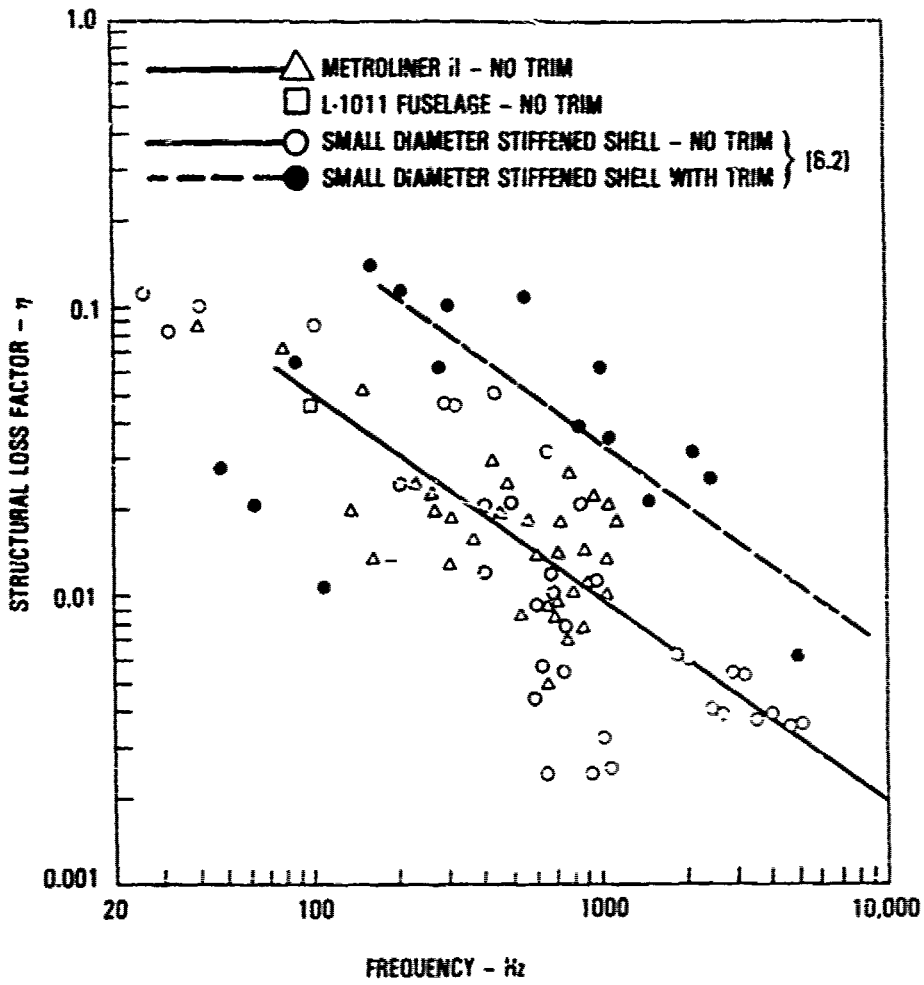
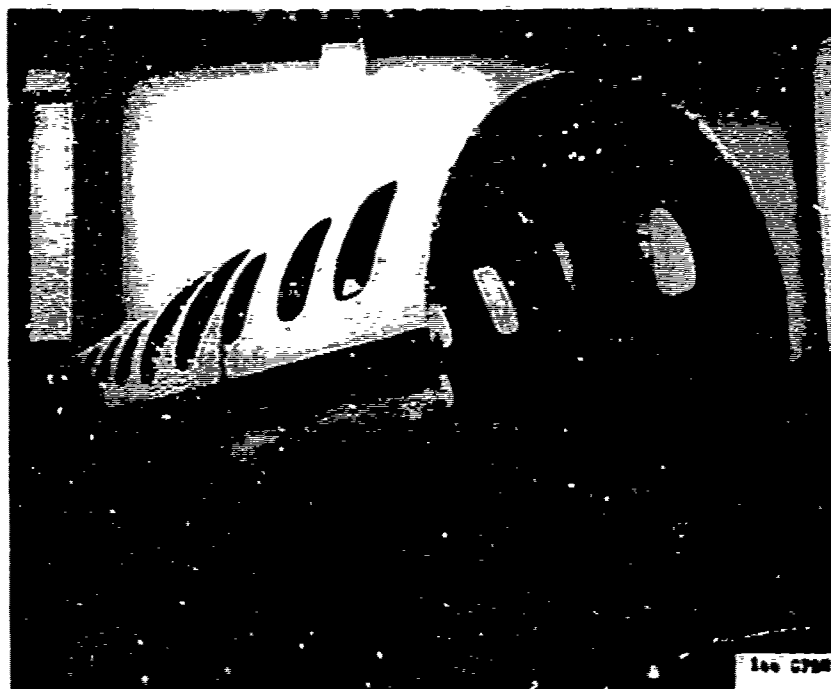


Figure 8.19. Summary of loss factors measured on bare shells and a trimmed shell



Exterior View



Interior View

Figure 8.20. Bare Metroliner Fuselage Shell

The loss factors, for the trimmed small diameter cylinder, appear to have the same trend with frequency as for the untrimmed shell, except that the level is approximately four times higher (Figure 8.19) above a frequency of 100 Hz.

The other program involved the development [8.1] of a unique I-beam viscoelastic damper for the upper level cabin on the 747 aircraft. Flight measurements made both with and without the trim (Figure 8.21) indicated that the presence of the trim increased the damping in the dominant panel modes, with the greatest effect occurring in the lowest frequency mode. This effect is similar to that observed [8.40] in acoustic progressive wave tunnels (Figure 8.22) when the test panel area approaches or exceeds the cross sectional area of the tunnel. Damping tape applied to the panels lowered the bare shell vibration levels in the lower frequencies that dominate the interior noise to the levels achieved with the trim (Figure 8.23). The damping tape did prove to be more effective at higher frequencies. Overall, the noise reduction produced by the damping tape proved to be quite small (Figure 8.24) in comparison to that achieved (Figure 8.25) by the use of the I-beam dampers which produced significantly higher damping than the damping tape.

The conclusion is that viscoelastic damping will reduce interior noise provided that it is correctly designed. The damping treatment must be designed to provide the maximum possible damping, certainly more than that provided by the acoustic trim, if the treatment is to succeed.

8.3.3 Flight Test Procedures for Developing Viscoelastic Damping Treatments

The reason why the effect of the acoustic trim on the shell damping was not discovered earlier rests with the test procedures used to design the damping treatments. The conventional approach [8.3] is based on a flight test program which includes the following steps:

1. Measure interior noise in a fully trimmed aircraft to identify the problem frequencies. (The use of sound intensity measurement [8.41, 8.42, 8.43] is proving to be very useful in identifying the problem noise sources.)

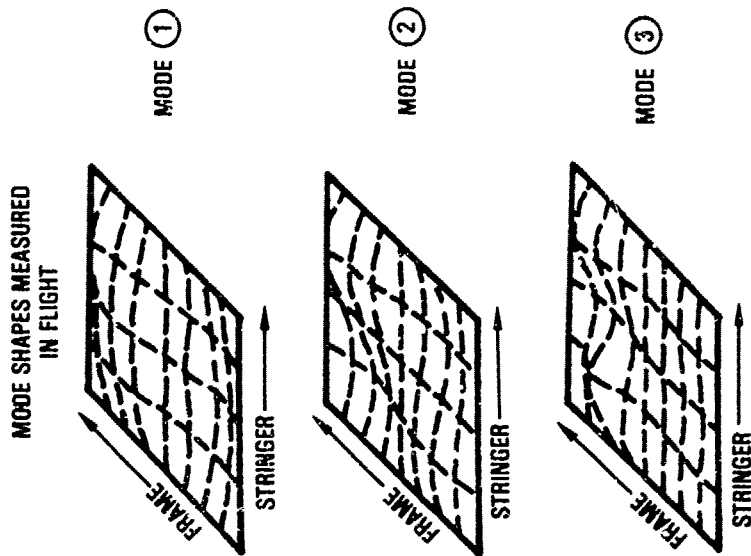
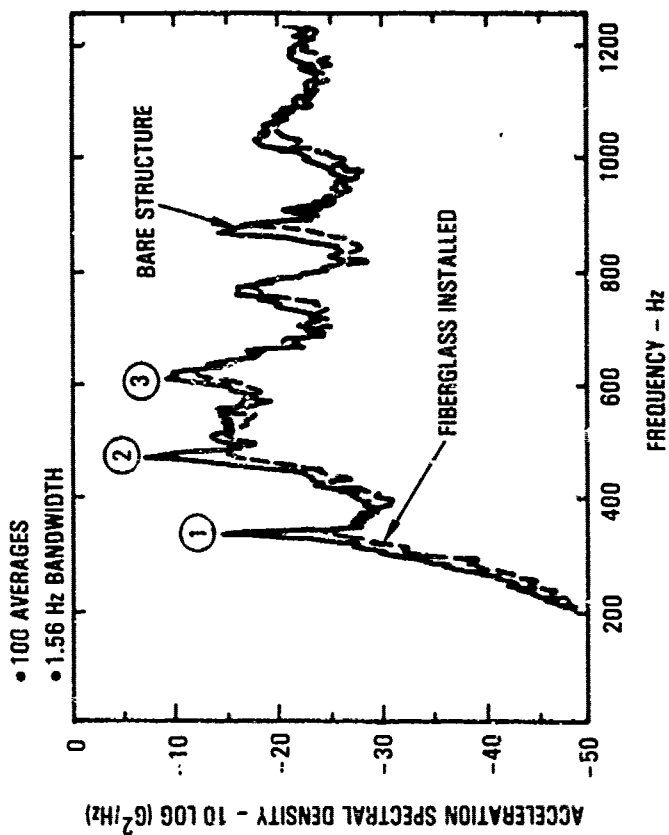


Figure 8.21. Vibration data measured during flight on the 747 upper deck panels both with and without acoustic trim

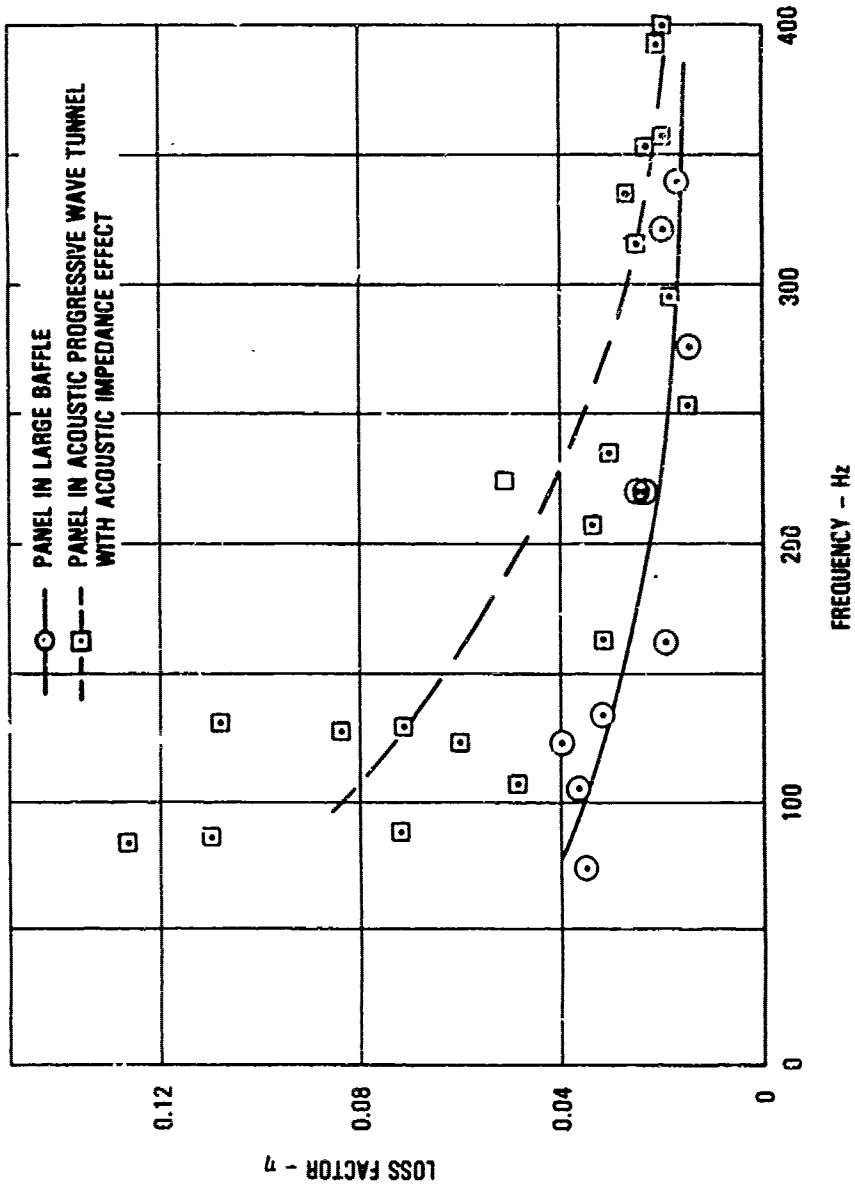


Figure 8.22. Honeycomb panel damping increased by acoustic impedance effect in acoustic progressive wave tunnel

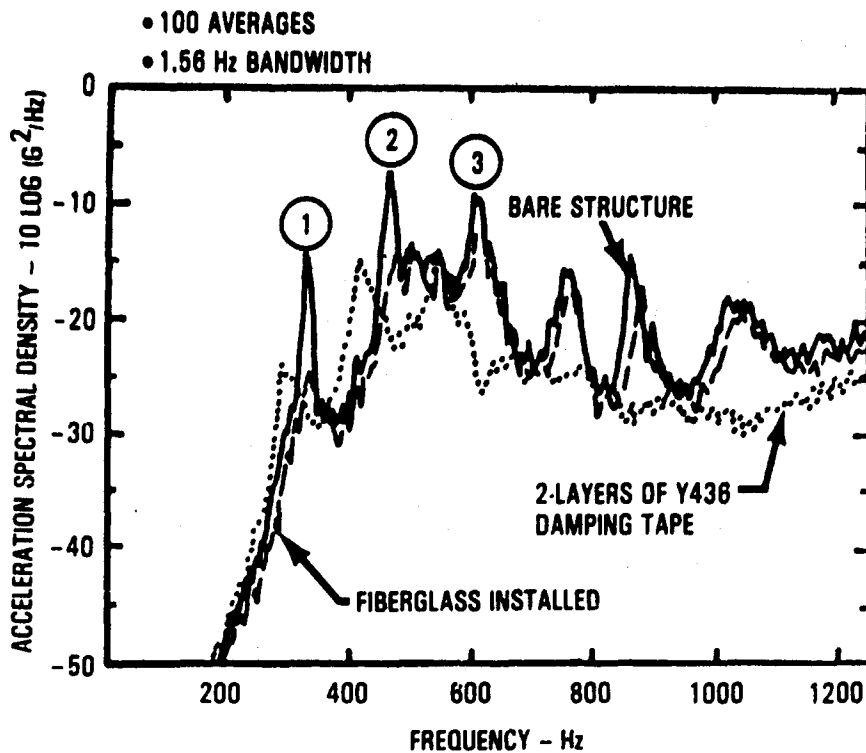


Figure 8.23. Effect of damping tape on bare panel vibration in comparison to that from acoustic trim

2. Remove all trim over a selected area of the fuselage to provide access to the structure for taking structural response measurements.
3. Use an acoustic enclosure to cover the exposed aircraft structure to restrict the noise within the enclosure to that radiated by the exposed structure.
4. Identify from the measured structural vibration response and radiated noise data the structural modes producing the radiated noise, their resonant frequencies, mode shapes and damping levels.
5. Design the damping treatment based on the above modal data, including the bare shell damping, and the skin temperature. (Most of the damping treatments fail at this stage because their design is based on the measured bare-shell damping.)
6. Install the damping treatment and repeat the flight test with the untrimmed aircraft. (This step provides a false sense of security because of the very encouraging measured noise and vibration level reductions.)
7. Measure the interior noise with the acoustic trim installed over the damping tape. (The usually poor level of noise reduction achieved is only discovered at this stage.)

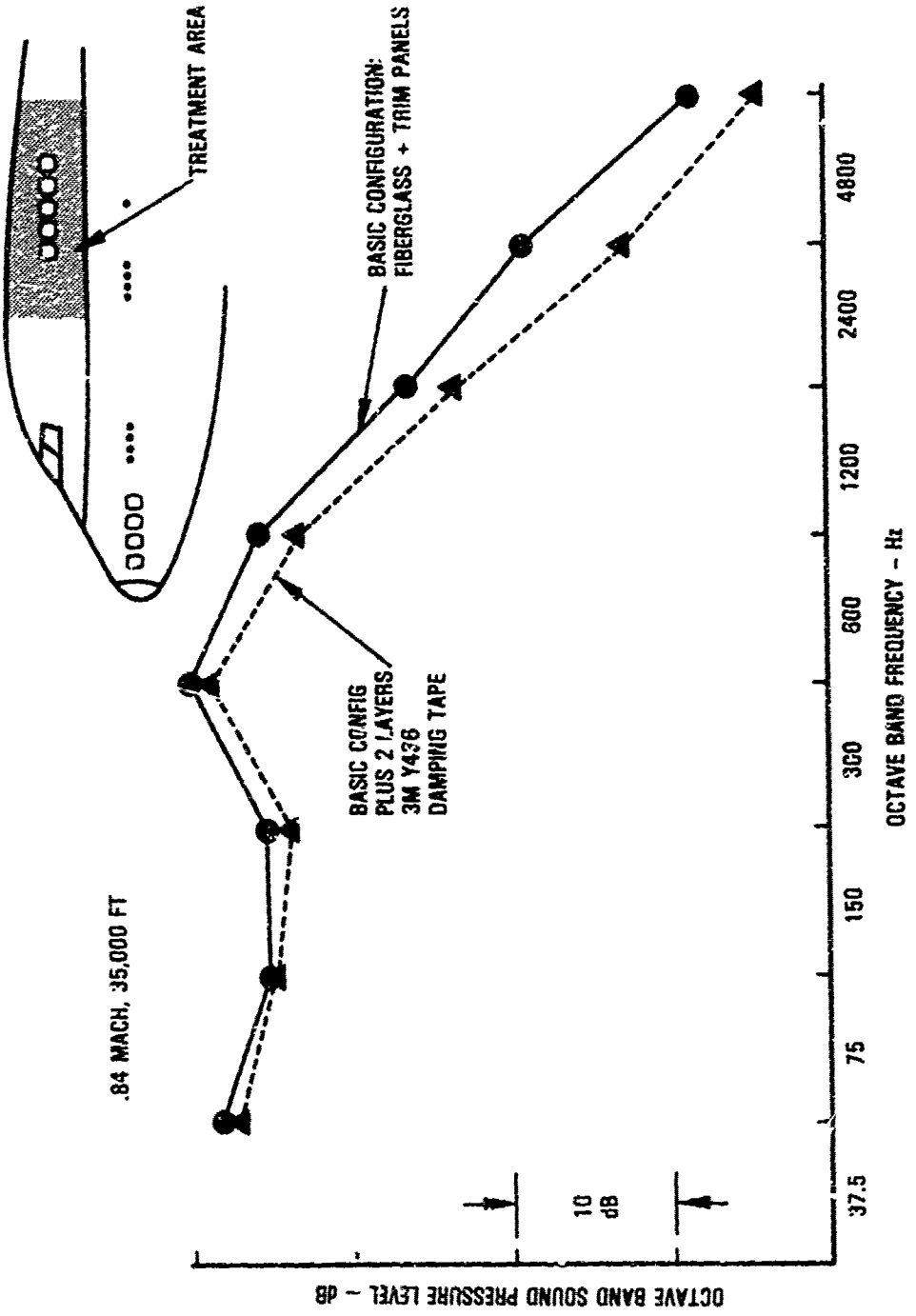


Figure 8.24. Effect of damping tape on 747 upper deck sound levels

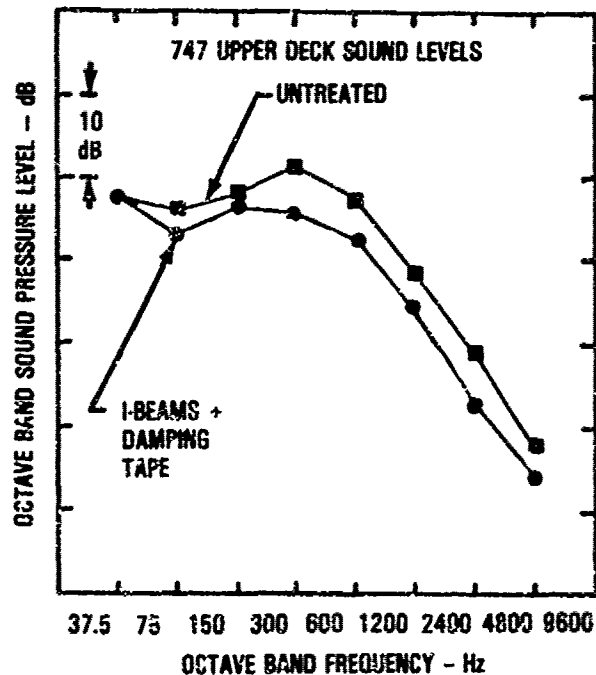


Figure 8.25. Noise reduction achieved with I-beam damping

The above approach can still be used to develop the damping treatment except that the acoustic trim is removed in step 2 only for installation of the instrumentation. Thereafter steps 3 to 7 are implemented with the acoustic trim installed.

Another method that has been used to design damping treatment, after first identifying the noise problem during flight, involves measuring the resonant frequencies, mode shapes and damping levels by means of impedance head hammer tap tests or by the use of electrodynamic shaker excitation. These tests are performed on the ground both with and without a pressure differential across the shell, since pressurization increases the shell frequencies. The easiest way to apply this method is from inside the aircraft, requiring the removal of the acoustic trim to provide access to the structure. Thus, the same mistake is repeated with this test method as with the previously described method. The damping treatment is first designed for the ground temperature and installed on the aircraft. The above tap or shaker

test is repeated to demonstrate that the desired vibration reduction has been achieved with the damping treatment. Thereafter, a similar damping treatment is designed for the flight temperature.

For the second design procedure to succeed, the acoustic trim must be left in place during the testing and the tap tests must be conducted on the outer surface of the aircraft. The instrumentation can be installed on the inside underneath the trim or attached to the outer surface of the skin. The shaker can still be installed inside the aircraft and attached to the structure through a small aperture in the trim. The shaker is generally used to excite the overall modes of the shell rather than the panel modes. The tap tests are more useful in measuring the panel modes.

8.4 SUMMARY OF CURRENT INTERIOR NOISE PREDICTION METHODOLOGY

The development of interior noise prediction methodology has focused, over the past few years, on propeller-generated noise both in general aviation and advanced transport aircraft. A summary of the most recent propeller noise related research are contained in References [8.44] and [8.45]. The prediction of the interior noise [8.46, 8.47, 8.48] within the cargo bay of the space shuttle orbiter vehicle due to the rocket noise at liftoff and fluctuating pressures during the ascent at maximum dynamic pressure represented a departure from the above trend in interior noise prediction.

The earlier development on interior noise prediction methodology [8.32] for large transport type aircraft concentrated on predicting the interior noise due to jet noise, turbulent boundary layer and reverberant noise excitations. The jet noise and turbulent boundary layer excitations are currently [8.49] being incorporated into the latest noise prediction methodology [8.2, 8.50] for use in the design of advanced composite fuselage structure for minimum interior noise.

This latest method involves a generalized power flow approach in which the conventional modal approach and the statistical energy analysis (SEA) are

integrated for improved computational efficiency. The power balance is applied at all frequencies, as opposed to the SEA approach, which is usually restricted to multimodal resonant response within the frequency bands. The net time-averaged acoustic power, flowing into the enclosed volume, is equated to the net time averaged power dissipated on the interior walls. Power flow into each individual acoustic mode is computed at the low frequencies, regardless of whether the mode is resonant or not. The sound radiated by resonant structural modes and nonresonant shell vibration is included. The power flow out of each acoustic mode to the wall of the cavity, is also computed mode by mode. By equating the power flows in and out of each mode, both the individual mode and overall levels can be obtained. This procedure includes expressions for the exterior excitation, the properties of the intervening structure and the acoustic trim, and the acoustic and structural "loss factors". At higher frequencies when the above mode by mode procedure becomes computationally inefficient, the same methodology is now applied to multimodal response within each of successive frequency bands.

REFERENCES

- 8.1 Miles, R.N., "Beam Dampers for Skin Vibration and Noise Reduction in the 747" Vibration Damping Workshop Sponsored by Air Force Wright Aeronautical Laboratories, Long Beach, California, February 27-29, 1984.
- 8.2 Pope, L.D. and Wilby, E.G., "Analytical Prediction of the Interior Noise for Cylindrical Models of Aircraft Fuselages for Prescribed Exterior Noise Fields (Part II)", NASA Contractor Report 165869, April, 1982.
- 8.3 Bhat, W.V. and Wilby, J.F., "Interior Noise Radiated by an Airplane Fuselage Subjected to Turbulent Boundary Layer Excitation and Evaluation of Noise Reduction Treatments", Journal of Sound and Vibration, Vol. 18, No. 4, 1971.
- 8.4 Wilby, J.F. and Gloyna, F.L., "Vibration Measurements of an Airplane Fuselage Structure; I. Turbulent Boundary Layer Excitation", Journal of Sound and Vibration, Vol. 23, No. 4, 1972.
- 8.5 Wilby, J.F. and Gloyna, F.L., "Vibration Measurements of an Airplane Fuselage Structure; II. Jet Noise Excitation", Journal of Sound and Vibration, Vol. 23, No. 4, 1972.
- 8.6 Tipton, A.G., "Viscoelastic Damping Applications in Aircraft", Conference on Aerospace Polymeric Viscoelastic Damping Technology for the 1980's, (Dr. Lynn Rogers, Editor), AFFDL-78-78-FBA, July 1980.
- 8.7 Catherines, J.J. and Mayes, W.H., "Interior Noise Levels of Two Propeller-Driven Light Aircraft", NADA TM X-72716, 1975.
- 8.8 Mixson, J.S. and Kearney, C., "Investigation of Interior Noise in a Twin-Engine Light Aircraft", Journal of Aircraft, Vol. 15, No. 4, April 1978.
- 8.9 Johnson, J.F. and Donham, R.E., "Attenuation of Propeller-Related Vibration and Noise", Journal of Aircraft, Vol. 19, No. 10, October 1982.
- 8.10 Van Dyke, J., Schendel, J., Gunderson, C. and Ballard, M., "Cabin Noise Reduction in the DC-9", AIAA Commercial Aircraft Design and Operation Meeting, Los Angeles, California, June 12-14, 1967.
- 8.11 "Standard Methods for Laboratory Measurement of Airborne Sound Transmission Loss of Building Partitions", ASTM Standard E90-75, in 1977 Annual Book of ASTM Standards, Part 18.
- 8.12 Richards, E.J. and Mead, D.J. (Editors), Noise and Acoustic Fatigue in Aeronautics, John Wiley & Sons, 1968.

REFERENCES (Continued)

- 8.13 Beranek, L.L. (Editor), Noise and Vibration Control, McGraw-Hill, 1971.
- 8.14 Roussos, L.A., Powell, C.A., Grosveld, F.N. and Koval, L.R., "Noise Transmission Characteristics of Advanced Composite Structural Materials", Paper presented at the AIAA 8th Aeroacoustics Conference, Atlanta, Georgia, April 11-13, 1983.
- 8.15 Maidanik, G., "Response of Ribbed Panels to Reverberent Acoustic Fields", Journal of Acoustical Society of America, Vol. 34, No. 6, June 1962.
- 8.16 Lyon, R.H., and Maidanik, G., "Statistical Methods in Vibration Analysis", AIAA Journal, Vol. 2, No. 6, 1964.
- 8.17 Mixson, J.S., Roussos, L.A., Barton, C.K. and Vaicaitis, R., "Laboratory Study of Efficient Add-On Treatments for Interior Noise Control in Light Aircraft," AIAA 7th Aeroacoustics Conference, Palo Alto, California, October 5-7, 1981.
- 8.18 Clarkson, B.L. and Ford, R.D., "The Response of a Typical Aircraft to Jet Noise", Journal of the Royal Aeronautical Society, January 1962.
- 8.19 Clarkson, B.L. and Ford, R.D., "The Response of Modal Structure to Noise - Part II: Curved Panel", ASD Tech. Rep., TDR-62-706, 1962.
- 8.20 Lin, Y.K., "Free Vibrations of Continuous Skin-Stringer Panels", J. Applied Mechanics, Vol. 27, 1960.
- 8.21 Lin, Y.K. and Donaldson, B.K., "A Brief Survey of Transfer Matrix Techniques with Special Reference to Analysis of Aircraft Panels", Journal of Sound and Vibration.
- 8.22 McDaniel, T.J., "Dynamics of Stiffened Cylindrical Shells with Spatially Varying Curvatures", AFML-TR-72-134, 1972.
- 8.23 Henderson, J.P., "Vibration Analysis of Curved Skin Stringer Structures Housing Tuned Elastomeric Dampers", AFML-TR-72-240, 1972.
- 8.24 "Natural Frequencies of Built-up Flat Periodic Skin-Stringer Structures - Part 1: Stringers Rigid in Bending", ESDU Data Item Number 72003, January 1972.
- 8.25 Willmarth, W.W. and Wooldridge, C.E., "Measurement of the Fluctuating at the Wall Beneath a Thick Turbulent Boundary Layer", J. Fluid Mechanics, Vol. 14, 1962.
- 8.26 Bull, M.K., "Wall Pressure Fluctuations in Boundary Layer Flow", University of Southampton AASU Report No. 243, March 1963.

REFERENCES (Continued)

- 8.27 Szechenyi, E., "The Response of, and the Acoustic Radiation from Panels Excited by Turbulent Boundary Layer", AFFDL-TR-70-94, June 1970.
- 8.28 Jacobs, L.D. and Lagerquist, D.R., "Response of Complex Structures to Turbulent Boundary Layers", AIAA 7th Aerospace Sciences Meeting, New York, USA, January 20-22, 1969.
- 8.29 Wilby, J.F., "The Response of Simple Panels to Turbulent Boundary Layer", AFFDL-TR-67-70, 1967.
- 3.30 Maestrello, L., "Measurement of Noise Radiated by Boundary Layer Excited Panels", Journal of Sound and Vibration, Vol. 2, No. 2, 1965.
- 8.31 Maestrello, L., "Use of Turbulent Model to Calculate the Vibration and Radiation Responses of a Panel with Practical Suggestions for Reducing Sound Level", Journal of Sound and Vibration, Vol. 5, No. 3, 1967.
- 8.32 Cockburn, J.A and Jolly, A.C, "Structural-Acoustic Response, Noise Transmission Losses and Interior Noise Levels of an Aircraft Fuselage, Excited by Random Pressure Fields", AFFDL-TR-68-2, 1968.
- 8.33 Koval, L.R., "Effect of Air Flow, Panel Curvature, and Internal Pressurization on Field-Incidence Transmission Loss", Journal of Acoustical Society of America, Vol. 59, No. 6, June 1976.
- 8.34 Koval, L.R., "On Sound Transmission into an Orthotropic Shell", Journal of Sound and Vibration (1979) 63 (7), pp 51-59.
- 8.35 Koval, L.R., "Effect of Longitudinal Stringers on Sound Transmission into a Thin Cylindrical Shell", Journal of Aircraft, Volume 15, Number 12, December 1978.
- 8.36 SenGupta, G., "Reduction of Cabin Noise During Cruise Conditions by Stringer and Frame Damping", AIAA Journal, Volume 17, Number 3, March, 1979.
- 8.37 Soovere, J., Unpublished Data from Tests Conducted at the Institute of Sound and Vibration Research, Southampton University, England in 1967.
- 8.38 Prydz, R.A., Revelle, J.D., Hayward, J.L. and Balena, F.J., "Evaluation of Advanced Fuselage Design Concepts for Interior Noise Control on High Speed Propeller-Driven Aircraft", NASA Contractor Report 165960, September 1982.
- 8.39 Soovere, J., "High Modulus Graphite Fiber Constrained Layer Damping Treatment for Heavy Aerospace Structures", AFFDL-TM-78-78-FBA, July 1978.

REFERENCES (Continued)

- 8.40 Soovere, J., "Dynamic Properties of Graphite Fiber Honeycomb Panels", AIAA Paper 73-326, March 1973.
- 8.41 Singh, R. "Acoustic Impedance Measurement Methods", The Shock and Vibration Digest, Vol. 14, No. 2, February 1982.
- 8.42 Gade, S., "Sound Intensity (Theory)", Brüel and Kjaer Technical Review No. 3, 1982.
- 8.43 Gade, S., "Sound Intensity (Instrumentation and Application)", Brüel and Kjaer Technical Review No. 4, 1982.
- 8.44 Mixson, J.S. and Powell, C.A., "A Review of Recent Research on Interior Noise of Propeller Aircraft", AIAA/NASA 9th Aeroacoustic Conference, Williamsburg, Virginia, October 15-17, 1984.
- 8.45 Dowell, E.H., "Master Plan for Prediction of Vehicle Interior Noise", AIAA 5th Aeroacoustic Conference, Seattle, Washington, March 12-14, 1979.
- 8.46 Wilby, J.F. and Pope, L.D., "The Development of a Method for Predicting the Noise Exposure of Payloads in the Space Shuttle Orbiter Vehicle", The Shock and Vibration Bulletin, No. 49, Part 1, September 1979.
- 8.47 Wilby, J.F. and Pope, L.D., "Prediction of the Acoustic Environment in the Space Shuttle Payload Bay", Journal of Spacecraft and Rockets, Vol. 17, No. 3, May-June 1980.
- 8.48 Pope, L.D. and Wilby, J.F., "Space Shuttle Payload Bay Acoustic Prediction Study. Volume II, Analytical Model", NASA Contractor Report 159956, March 1980.
- 8.49 "Transport Composite Fuselage Technology - Impact Dynamics and Acoustic Transmission", Current NASA Contract NAS1-176981, Lockheed-California Company, 1984.
- 8.50 Pope, L.D., Rennison, D.C., Willis, C.M. and Mayes, W.H., "Development and Validation of Preliminary Analytical Models for Aircraft Interior Noise Prediction", Journal of Sound and Vibration, Vol. 82, No. 4, 1982.